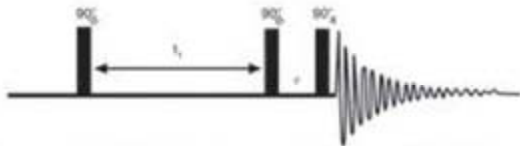
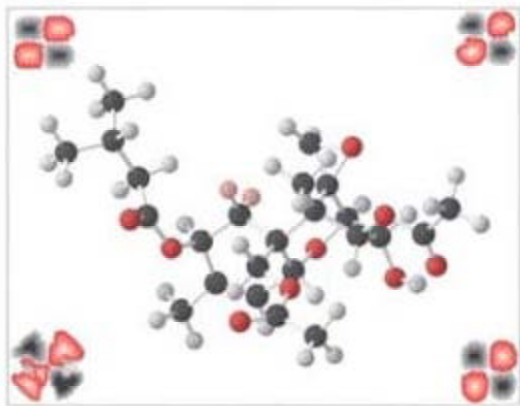


NUCLEAR MAGNETIC RESONANCE SPECTROSCOPY

*An Introduction to Principles,
Applications, and Experimental Methods*



JOSEPH B. LAMBERT • EUGENE P. MAZZOLA

Nuclear Magnetic Resonance Spectroscopy

*An Introduction to Principles,
Applications, and Experimental Methods*

Joseph B. Lambert
Northwestern University

Eugene P. Mazzola
University of Maryland—
Food and Drug Administration
Joint Institute for Food Safety & Applied Nutrition



Pearson Education Inc.
Upper Saddle River, New Jersey 07458

Contents

Preface xi

1 Introduction 1

- 1-1 Magnetic Properties of Nuclei 1
- 1-2 The Chemical Shift 5
- 1-3 Excitation and Relaxation 8
- 1-4 Pulsed Experiments 11
- 1-5 The Coupling Constant 13
- 1-6 Quantitation and Complex Splitting 19
- 1-7 Commonly Studied Nuclides 21
- 1-8 Dynamic Effects 23
- 1-9 Spectra of Solids 25
 - Problems 27
 - Bibliography 30

2 Introductory Experimental Methods 31

- 2-1 The Spectrometer 31
- 2-2 Sample Preparation 33
- 2-3 Optimizing the Signal 34
 - 2-3a Sample Tube Placement 34
 - 2-3b Probe Adjustment 34
 - 2-3c Field/Frequency Locking 35
 - 2-3d Spectrometer Shimming 36
- 2-4 Determination of NMR Spectra: Acquisition Parameters 39
 - 2-4a Number of Data Points 41
 - 2-4b Spectral Width 41
 - 2-4c Filter Bandwidth 42
 - 2-4d Acquisition Time 42
 - 2-4e Transmitter Offset 43
 - 2-4f Flip Angle 43
 - 2-4g Receiver Gain 45
 - 2-4h Number of Scans 45
 - 2-4i Steady-State Scans 46
 - 2-4j Oversampling and Digital Filtration 46
 - 2-4k Decoupling for X Nuclei 46
 - 2-4l Typical NMR Experiments 47
- 2-5 Determination of NMR Spectra: Processing Parameters 48
 - 2-5a Exponential Weighting 48
 - 2-5b Zero Filling 49
 - 2-5c FID Truncation and Spectral Artifacts 50
 - 2-5d Resolution 51
- 2-6 Determination of NMR Spectra: Spectral Presentation 52
 - 2-6a Signal Phasing and Baseline Correction 52
 - 2-6b Zero Referencing 55
 - 2-6c Determination of Certain NMR Parameters 56

- 2-7 Calibrations 58
 - 2-7a Pulse Width (Flip Angle) 58
 - 2-7b Decoupler Field Strength 60
- Problems 61
- Bibliography 61

3 The Chemical Shift 62

- 3-1 Factors that Influence Proton Shifts 62
- 3-2 Proton Chemical Shifts and Structure 69
 - 3-2a Saturated Aliphatics 69
 - 3-2b Unsaturated Aliphatics 71
 - 3-2c Aromatics 73
 - 3-2d Protons on Oxygen and Nitrogen 75
 - 3-2e Programs for Empirical Calculations 76
- 3-3 Medium and Isotope Effects 76
- 3-4 Factors that Influence Carbon Shifts 79
- 3-5 Carbon Chemical Shifts and Structure 81
 - 3-5a Saturated Aliphatics 82
 - 3-5b Unsaturated Compounds 86
 - 3-5c Carbonyl Groups 88
 - 3-5d Programs for Empirical Calculation 88
- 3-6 Tables of Chemical Shifts 88
 - Problems 91
 - Bibliography 97

4 The Coupling Constant 98

- 4-1 First- and Second-Order Spectra 98
- 4-2 Chemical and Magnetic Equivalence 99
- 4-3 Signs and Mechanisms: One-Bond Couplings 104
- 4-4 Geminal Couplings 106
- 4-5 Vicinal Couplings 109
- 4-6 Long-Range Couplings 112
- 4-7 Spectral Analysis 115
- 4-8 Tables of Coupling Constants 119
 - Problems 122
 - Bibliography 129

5 Further Topics in One-Dimensional NMR 131

- 5-1 Spin-Lattice and Spin-Spin Relaxation 131
- 5-2 Reactions on the NMR Time Scale 136
- 5-3 Multiple Resonance 143
- 5-4 The Nuclear Overhauser Effect 148
- 5-5 Spectral Editing 153
- 5-6 Sensitivity Enhancement 156
- 5-7 Carbon Connectivity 162
- 5-8 Phase Cycling, Composite Pulses, and Shaped Pulses 163
 - Problems 166
 - Bibliography 170

6 Two-Dimensional NMR 172

- 6-1 Proton–Proton Correlation Through Coupling 172
- 6-2 Proton–Heteronucleus Correlation 187
- 6-3 Proton–Proton Correlation Through Space or Chemical Exchange 195
- 6-4 Carbon–Carbon Correlation 199
- 6-5 Higher Dimensions 201
- 6-6 Pulsed Field Gradients 203
- 6-7 Summary of Two-Dimensional Methods 207
 - Problems 208
 - Bibliography 232

7 Advanced Experimental Methods 233

- Part A.** One-Dimensional Techniques 233
 - 7-1 T_1 Measurements 233
 - 7-2 ^{13}C Spectral Editing Experiments 234
 - 7-2a The APT Experiment 235
 - 7-2b The DEPT Experiment 236
 - 7-3 NOE Experiments 237
 - 7-3a The NOE Difference Experiment 238
 - 7-3b The Double Pulsed Field Gradient Spin Echo-NOE Experiment 240
- Part B.** Two-Dimensional Techniques 240
 - 7-4 Two-Dimensional NMR Data-Acquisition Parameters 241
 - 7-4a Number of Data Points 241
 - 7-4b Number of Time Increments 241
 - 7-4c Spectral Widths 241
 - 7-4d Acquisition Time 242
 - 7-4e Transmitter Offset 242
 - 7-4f Flip Angle 242
 - 7-4g Relaxation Delay and Repetition Times 242
 - 7-4h Receiver Gain 243
 - 7-4i Number of Scans per Time Increment 243
 - 7-4j Steady-State Scans 243
 - 7-5 Two-Dimensional NMR Data-Processing Parameters 243
 - 7-5a Weighting Functions 244
 - 7-5b Zero Filling 246
 - 7-5c Digital Resolution 246
 - 7-5d Linear Prediction 247
 - 7-6 Two-Dimensional NMR Data Display 250
 - 7-6a Phasing and Zero Referencing 250
 - 7-6b Symmetrization 250
 - 7-6c Use of Cross Sections in Analysis 250
- Part C.** Two-Dimensional Techniques: The Experiments 251
 - 7-7 Homonuclear Chemical-Shift Correlation Experiments Via Scalar Coupling 251
 - 7-7a The COSY Family of Experiments 252
 - 7-7b The TOCSY Experiment 256
 - 7-8 Direct Heteronuclear Chemical-Shift Correlation Via Scalar Coupling 257
 - 7-8a The HMQC Experiment 258
 - 7-8b The HSQC Experiment 259
 - 7-8c The HETCOR Experiment 261

7-9	Indirect Heteronuclear Chemical-Shift Correlation Via Scalar Coupling	262
7-9a	The HMBC Experiment	262
7-9b	The FLOCK Experiment	264
7-9c	The HSQC-TOCSY Experiment	266
7-10	Homonuclear Chemical-Shift Correlation Via Dipolar Coupling	267
7-10a	The NOESY Experiment	268
7-10b	The ROESY Experiment	269
7-11	Miscellaneous 1D and 2D Experiments	270
7-11a	The 1D TOCSY Experiment	270
7-11b	The Multiplicity-Edited HSQC Experiment	271
7-11c	The 2J , 3J -HMBC Experiment	273
	Bibliography	276

8 Structural Elucidation: An Example 277

8-1	^1H NMR Data	277
8-2	^{13}C NMR Data	279
8-3	The DEPT Experiment	280
8-4	The HSQC Experiment	281
8-5	The COSY Experiment	282
8-6	The HMBC Experiment	284
8-7	General Molecular Assembly Strategy	284
8-8	A Specific Molecular Assembly Procedure	286
8-9	The NOESY Experiment	290

Appendix 1	Derivation of the NMR Equation	295
Appendix 2	The Bloch Equations	297
Appendix 3	Quantum Mechanical Treatment of the Two-Spin System	302
Appendix 4	Analysis of Second-Order, Three- and Four-Spin Systems by Inspection	312
Appendix 5	Relaxation	317
Appendix 6	Product-Operator Formalism and Coherence-Level Diagrams	322
	Bibliography	333
Appendix 7	Stereochemical Considerations	334
A7-1	Homotopic Groups	335
A7-2	Enantiotopic Groups	337
A7-3	Diastereotopic Groups	339
	Bibliography	341

Index I-1

Preface

Nuclear magnetic resonance (NMR) has become the chemist's most general structural tool. It is one of the few techniques that may be applied to all three states of matter. Some spectra may be obtained from less than a microgram of material. In the early 1960s, spectra were taken crudely on strip-chart recorders. The field has since seen one major advance after another, culminating in the Nobel prizes awarded to Richard R. Ernst in 1991 and to Kurt Wüthrich in 2002. The very richness of the field, however, has made it intimidating to many users. How can they take full advantage of the power of the method when so much of the methodology seems to be highly technical, beyond the grasp of the casual user? This text was written to answer this question. The chapters provide an essentially nonmathematical introduction to the entire field, with emphasis on structural analysis.

The early chapters introduce classical NMR spectroscopy. A thorough understanding of proton and carbon chemical shifts (Chapter 3) is required in order to initiate any analysis of spectra. The role of other nuclei is key to the examination of molecules containing various heteroatoms. An analysis of coupling constants (Chapter 4) provides information about stereochemistry and connectivity relationships between nuclei. The older concepts of chemical shifts and coupling constants are emphasized, because they provide the basis for the application of modern pulse sequences.

Chapter 5 and 6 describe the basics of modern NMR spectroscopy. The phenomena of relaxation, of chemical dynamics, and of multiple resonance are considered thoroughly. One-dimensional multipulse sequences are explored to determine the number of protons attached to carbon atoms, to enhance spectral sensitivity, and to determine connectivities among carbon atoms. Concepts that have been considered advanced, but are now moving towards the routine, are examined, including phase cycling, composite pulses, pulsed field gradients, and shaped pulses. Two-dimensional methods represent the current apex of the field. We discuss a large number of these experiments. It is our intention to describe not only what the pulse sequences do, but also how they work, so that the user has a better grasp of the techniques.

Two chapters are dedicated to experimental methodologies. Although many people are provided with spectra by expert technicians, increasing numbers of chemists must record spectra themselves. They must consider and optimize numerous experimental variables. These chapters address not only the basic parameters, such as spectral width and acquisition time, but also the parameters of more advanced techniques, such as spectral editing and two-dimensional spectra.

To summarize modern NMR spectroscopy, Chapter 8 carries out the total structural proof of a single complex natural product. This chapter illustrates the tactics and strategies of structure elucidation, from one-dimensional assignments to two-dimensional spectral correlations, culminating in stereochemical analysis based on Overhauser effects.

The theory behind NMR not only is beautiful in itself, but also offers considerable insight into the methodology. Consequently, a series of appendices presents a full treatment of this theoretical underpinning, necessary to the physical or analytical chemist, but possibly still edifying to the synthetic organic or inorganic chemist.

This text thus offers

- classical analysis of chemical shifts and coupling constants for both protons and other nuclei,
- modern multipulse and multidimensional methods, both explained and illustrated,
- experimental procedures and practical advice relative to the execution of NMR experiments,

- a chapter-long worked-out problem that illustrates the application of nearly all current methods to determine the structure and stereochemistry of a complex natural product,
- appendices containing the theoretical basis of NMR, including the most modern approach that uses product operators and coherence-level diagrams, and
- extensive problems throughout the book.

Joseph B. Lambert
jlambert@northwestern.edu

Eugene P. Mazzola
em105@umail.umd.edu

ACKNOWLEDGMENTS

The authors are indebted to numerous people for assistance in preparing this manuscript. For expert word processing, artwork, recording of spectra for figures, or general assistance, we thank Curtis N. Barton, Gwendolyn N. Chmurny, Frederick S. Fry, Jr., D. Aaron Lucas, Peggy L. Mazzola, Marcia L. Meltzer, William F. Reynolds, Carol J. Slingo, Mitchell J. Smith, Que N. Van, and Yuyang Wang. In addition, we are grateful to the following individuals for reviewing all or part of the manuscript: Lyle D. Isaacs (University of Maryland, College Park), William F. Reynolds (University of Toronto), Que N. Van (National Cancer Institute, Frederick, Maryland), and R. Thomas Williamson (Wyeth Research).

Symbols

B_0	main magnetic field
B_1	magnetic field due to transmitter
B_2	magnetic field in double-resonance experiments
Hz	hertz (a unit of frequency)
I	dimensionless spin
I_z	spin quantum number in the z direction
J	indirect spin–spin coupling constant
M	magnetization
p	coherence order
T	tesla (unit of magnetic flux density, commonly, the magnetic-field strength)
T_1	spin–lattice (longitudinal) relaxation time
$T_{1\rho}$	spin–lattice relaxation time (spin locked) in the rotating frame
T_2	spin–spin (transverse) relaxation time
T_2^*	effective spin–spin relaxation time (includes magnetic-field inhomogeneity effects on xy magnetization)
T_c	coalescence temperature
t_a	acquisition time
t_p	transmitter pulse duration or pulse width (in μs)
t_1	two-dimensional (2D) incremented time
t_2	two-dimensional (2D) acquisition time
W	designation for relaxation pathways, with units of rate constants
α	flip angle
α^0	optimum (Ernst) flip angle
γ	gyromagnetic or magnetogyric ratio
γB_0	resonance or Larmor frequency (ω_0)
γB_2	decoupler field strength (ω_2)
δ	chemical shift
η	nuclear Overhauser enhancement
μ	magnetic moment
ν	linear frequency
σ	magnetic shielding
τ	time delay or lifetime
τ_c	effective correlation time
τ_m	mixing time
ω	angular frequency

Abbreviations

APT	attached proton test
ASIS	aromatic solvent-induced shift
BIRD	bilinear rotation decoupling
COLOC	correlation spectroscopy via long-range coupling
COSY	correlation spectroscopy
CP	cross polarization
CW	continuous wave
CYCLOPS	cyclically ordered phase sequence
DANTE	delays alternating with nutation for tailored excitation
DEPT	distortionless enhancement by polarization transfer
DPFGSE	double pulsed field gradient spin echo
DQF	double quantum filtered
DR	digital resolution
DT	relaxation delay time
EXSY	exchange spectroscopy
FID	free-induction decay
F_n	Fourier number
FT	Fourier transform or transformation
HETCOR	heteronuclear chemical-shift correlation
HMBC	heteronuclear multiple bond correlation
HMQC	heteronuclear multiple quantum correlation
HSQC	heteronuclear single quantum correlation
INADEQUATE	incredible natural abundance double-quantum transfer experiment
INEPT	insensitive nuclei enhanced by polarization transfer
LP	linear prediction
MAS	magic angle spinning
MQC	multiple quantum coherence
MRI	magnetic resonance imaging
n_i	number of time increments
NMR	nuclear magnetic resonance
NOE	nuclear Overhauser effect or enhancement
NOESY	NOE spectroscopy
np	number of data points
ns	number of scans
ns/i	number of scans per time increment
PFG	pulsed field gradient
ppm	parts per million
ROESY	rotating frame nuclear Overhauser effect spectroscopy
RT	repetition time ($DT + t_a$)
S/N	signal-to-noise ratio
sw	spectral width
TMS	tetramethylsilane
TOCSY	total correlation spectroscopy
WALTZ	wideband, alternating-phase, low-power technique for zero residual splitting
WATERGATE	water suppression by gradient tailored excitation

1

Introduction



Structure determination of almost any organic or biological molecule, as well as that of many inorganic molecules, begins with nuclear magnetic resonance (NMR) spectroscopy. During the more-than-half-century existence of NMR spectroscopy, the field has undergone several internal revolutions, repeatedly redefining itself as an increasingly complex and effective structural tool. Aside from X-ray crystallography, which can uncover the complete molecular structure of some pure crystalline materials, NMR spectroscopy is the chemist's most direct and general tool for identifying the structure of both pure compounds and mixtures as either solids or liquids. The process often involves performing several NMR experiments to deduce the molecular structure from the magnetic properties of the atomic nuclei and the surrounding electrons.

1-1 Magnetic Properties of Nuclei

The simplest atom, hydrogen, is found in almost all organic compounds and is composed of a single proton and a single electron. The hydrogen atom is denoted ^1H , in which the superscript signifies the sum of the atom's protons and neutrons (i.e., the atomic mass of the element). For the purpose of NMR, the key aspect of the hydrogen nucleus is its angular momentum properties, which resemble those of a classical spinning particle. Because the spinning hydrogen nucleus is positively charged, it generates a magnetic field and possesses a *magnetic moment* μ , just as a charge moving in a circle creates a magnetic field (Figure 1-1). The magnetic moment μ is a vector, because it has both magnitude and direction, as defined by its axis of spin in the figure. The NMR experiment exploits the magnetic properties of nuclei to provide information on molecular structure.

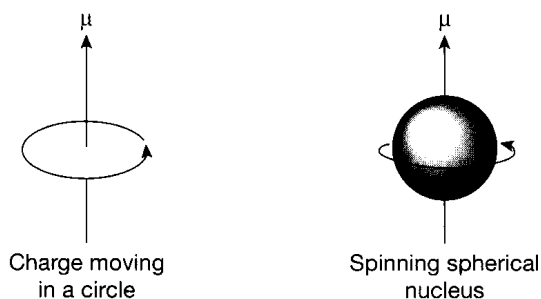
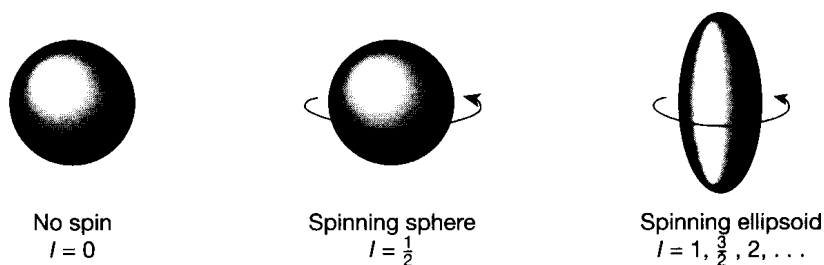


Figure 1-1 Analogy between a charge moving in a circle and a spinning nucleus.

Figure 1-2 Three classes of nuclei.



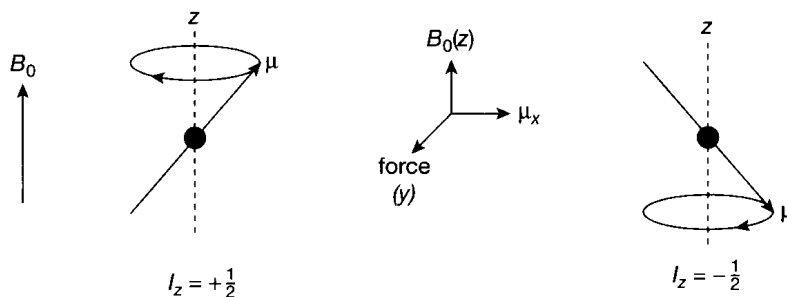
The spin properties of protons and neutrons in the nuclei of heavier elements combine to define the overall spin of the nucleus. When both the atomic number (the number of protons) and the atomic mass (the sum of the protons and neutrons) are even, the nucleus has no magnetic properties, as signified by a zero value of its *spin quantum number* I (Figure 1-2). Such nuclei are considered not to be spinning. Common nonmagnetic (nonspinning) nuclei are carbon (^{12}C) and oxygen (^{16}O), which therefore are invisible to the NMR experiment. When either the atomic number or the atomic mass is odd, or both are odd, the nucleus has magnetic properties and is said to be spinning. For spinning nuclei, the spin quantum number can take on only certain values. Those nuclei with a spherical shape have a spin of $\frac{1}{2}$, and those with a nonspherical, or quadrupolar, shape have a spin of 1 or more (in increments of $\frac{1}{2}$). Common nuclei with a spin of $\frac{1}{2}$ include ^1H , ^{13}C , ^{15}N , ^{19}F , ^{29}Si , and ^{31}P . Thus, many of the most common elements found in organic molecules (H, C, N, P) have at least one isotope with $I = \frac{1}{2}$ (although oxygen does not). The class of nuclei with $I = \frac{1}{2}$ is the most easily examined by the NMR experiment. Quadrupolar nuclei ($I > \frac{1}{2}$) include ^2H , ^{11}B , ^{14}N , ^{17}O , ^{33}S , and ^{35}Cl .

The magnitude of the magnetic moment produced by a spinning nucleus varies from atom to atom in accordance with the equation $\mu = \gamma\hbar I$. (See Appendix 1 for a derivation.) The quantity \hbar is Planck's constant divided by 2π , and γ is a characteristic of the nucleus called the *gyromagnetic* or *magnetogyric ratio*. The larger the gyromagnetic ratio, the larger is the magnetic moment of the nucleus. Nuclei that have the same number of protons, but different numbers of neutrons, are called *isotopes* ($^1\text{H}/^2\text{H}$, $^{14}\text{N}/^{15}\text{N}$). The term *nuclide* is generally applied to any atomic nucleus.

To study nuclear magnetic properties, the experimentalist subjects nuclei to a strong laboratory magnetic field B_0 whose units are tesla, or T (1 tesla = 10^4 gauss). In the absence of the laboratory field, all the nuclear magnets of the same isotope have the same energy. When the B_0 field is turned on along a direction designated as the z axis, the energies of the nuclei are affected. There is a slight tendency for magnetic moments to align in the general direction of B_0 ($+z$) over the opposite direction ($-z$). Nuclei with a spin of $\frac{1}{2}$ assume only these two arrangements. The splitting of spins into specific groups has been called the *Zeeman effect*.

The interaction is illustrated in Figure 1-3. At the left is a magnetic moment with a $+z$ component, and at the right is one with a $-z$ component. The nuclear magnets are not actually lined up parallel to the $+z$ or $-z$ direction. Rather, the force of B_0 causes the magnetic moment to move in a circular fashion about the $+z$ direction in the first case and about the

Figure 1-3 Interaction between a spinning nucleus and an external field.



$-z$ direction in the second, a motion called *precession*. In terms of vector analysis, the B_0 field in the z direction operates on the x component of μ to create a force in the y direction (Figure 1-3, inset in the middle). The force is the cross, or vector, product of the magnetic moment and the magnetic field; that is, $\mathbf{F} = \boldsymbol{\mu} \times \mathbf{B}$. The nuclear moment then begins to move toward the y direction. Because the force of B_0 on μ is always perpendicular to both B_0 and μ (according to the definition of a cross product), the motion of μ describes a circular orbit around the $+z$ or the $-z$ direction, in complete analogy to the forces present in a spinning top or gyroscope.

As only two directions of precession exist for a spin- $\frac{1}{2}$ nucleus (Figure 1-3), two assemblages or spin states are created, designated as $I_z = +\frac{1}{2}$ for precession with the field ($+z$) and $-\frac{1}{2}$ for precession against the field ($-z$). (Some texts refer to the quantum number I_z as m_I .) The assignment of signs (+ or -) is entirely arbitrary. The $I_z = +\frac{1}{2}$ state has a slightly lower energy. In the absence of B_0 , the precessional motions are absent, and all nuclei have the same energy.

The tendency toward $+z$ precession in the presence of B_0 is defined by Boltzmann's law,

$$\frac{n\left(+\frac{1}{2}\right)}{n\left(-\frac{1}{2}\right)} = \exp\left(\frac{\Delta E}{kT}\right) \quad (1-1)$$

in which n is the population of a spin state, k is Boltzmann's constant, T is the absolute temperature in kelvins, and ΔE is the energy difference between the spin states. Figure 1-4a depicts the energies of the two states and the difference ΔE between them.

The precessional motion of the magnetic moment around B_0 occurs with angular frequency ω_0 , called the *Larmor frequency*, whose units are radians per second (rad s^{-1}). As B_0 increases, so does the angular frequency; that is, $\omega_0 \propto B_0$, as is demonstrated in Appendix 1. The constant of proportionality between ω_0 and B_0 is the gyromagnetic ratio γ , so that $\omega_0 = \gamma B_0$. The natural precession frequency can be expressed as linear frequency in Planck's relationship $\Delta E = h\nu_0$ or angular frequency in Planck's relationship $\Delta E = \hbar\omega_0$ ($\omega_0 = 2\pi\nu_0$). In this way, the energy difference between the spin states is related to the Larmor frequency by the formula

$$\Delta E = \hbar\omega_0 = h\nu_0 = \gamma\hbar B_0. \quad (1-2)$$

Thus, as the B_0 field increases, the difference in energy between the two spin states increases, as illustrated in Figure 1-4b. Appendix 1 provides a complete derivation of these relationships.

The foregoing equations indicate that the natural precession frequency of a spinning nucleus ($\omega_0 = \gamma B_0$) depends only on the nuclear properties contained in the gyromagnetic

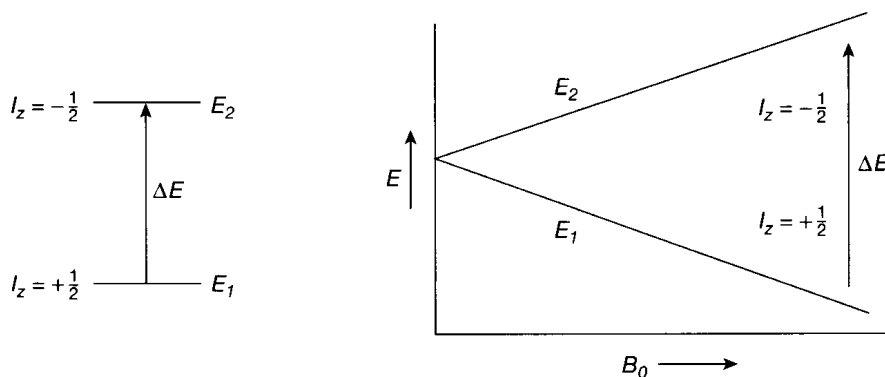
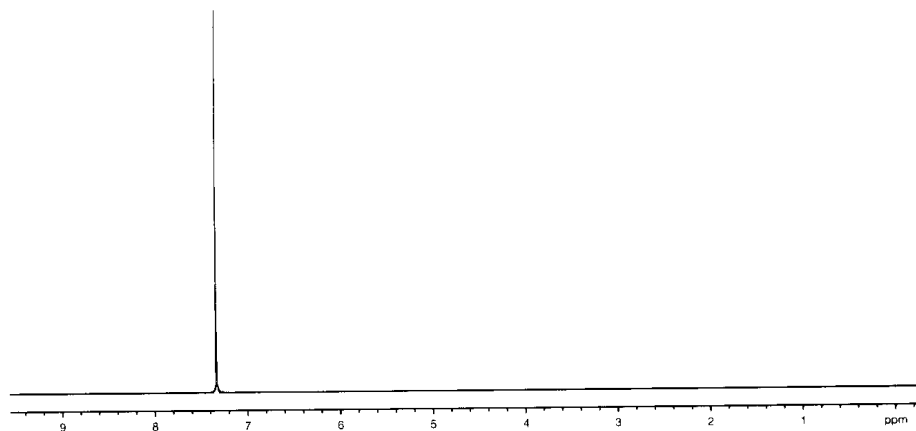


Figure 1-4 The energy difference between spin states as a function of the external magnetic field B_0 .

Figure 1-5 The 300 MHz ^1H spectrum of benzene.



ratio γ and on the laboratory-determined value of the magnetic field B_0 . For a proton in a magnetic field B_0 of 7.05 tesla (T), the frequency of precession is 300 megahertz (MHz), and the difference in energy between the spin states is only $0.0286 \text{ cal mol}^{-1}$ (0.120 J mol^{-1}). This value is extremely small in comparison with the energy differences between vibrational or electronic states. At a higher field, such as 14.1 T, the frequency increases proportionately, to 600 MHz in this case.

In the NMR experiment, the two states illustrated in Figure 1-4 are made to interconvert by applying a second magnetic field B_1 at radio frequencies. When the frequency of the B_1 field is the same as the Larmor frequency of the nucleus, energy can flow by absorption and emission between this newly applied field and the nuclei. Absorption of energy occurs as $+\frac{1}{2}$ nuclei become $-\frac{1}{2}$ nuclei, and emission occurs as $-\frac{1}{2}$ nuclei become $+\frac{1}{2}$ nuclei. Since the experiment begins with an excess of $+\frac{1}{2}$ nuclei, there is a net absorption of energy. The process is called *resonance*, and the absorption may be detected electronically and displayed as a plot of frequency vs. amount of energy absorbed. Because the resonance frequency ν_0 is highly dependent on the structural environment of the nucleus, NMR has become the structural tool of choice for chemists. Figure 1-5 illustrates the NMR spectrum for the protons in benzene. Absorption is represented by a peak directed upwards from the baseline.

Because gyromagnetic ratios vary among elements and even among isotopes of a single element, resonance frequencies also vary ($\omega_0 = \gamma B_0$). There is essentially no overlap in the resonance frequencies of different isotopes. At the field strength (7.05 T) at which protons resonate at 300 MHz, ^{13}C nuclei resonate at 75.45 MHz, ^{15}N nuclei at 30.42 MHz, and so on.

The magnitude of the gyromagnetic ratio γ also has an important influence on the intensity of the resonance. The difference in energy, $\Delta E = \gamma \hbar B_0$ (eq. 1-2), between the two spin states is directly proportional not only to B_0 , as illustrated in Figure 1-4b, but also to γ . From Boltzmann's law (eq. 1-1), when ΔE is larger, there is a greater population difference between the two states. A greater excess of $I_z = +\frac{1}{2}$ spins (the E_1 state) means that more nuclei are available to flip to the E_2 state and the resonance intensity is larger. The proton has one of the largest gyromagnetic ratios, so its spin states are relatively far apart, and the value of ΔE is especially large. The proton signal, consequently, is very strong. Many other important nuclei, such as ^{13}C and ^{15}N , have much smaller gyromagnetic ratios and hence have smaller differences between the energies of the two spin states (Figure 1-6). Thus, their signals are much less intense.

When spins have values greater than $\frac{1}{2}$, there are more than two available spin states. For $I = 1$ nuclei such as ^2H and ^{14}N , the magnetic moments may precess about three directions relative to B_0 : parallel ($I_z = +1$), perpendicular (0), and opposite (-1). In general, there are $(2I + 1)$ spin states—for example, six for $I = 5/2$ (^{17}O has this spin). The values of I_z extend from $+I$ to $-I$ in increments of 1 ($+I, +I - 1, +I - 2, \dots -I$). Hence, the energy-state picture is more complex for quadrupolar than for spherical nuclei.

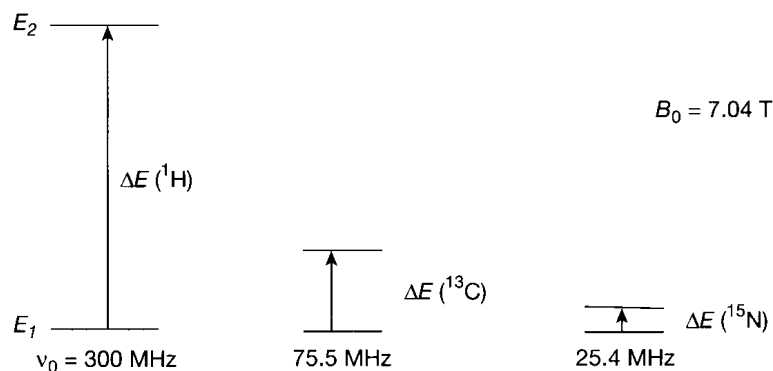


Figure 1-6 The energy difference between spin states for three nuclides with various relative magnitudes of the gyromagnetic ratio ($|\gamma|$): 26.75 for ^1H , 6.73 for ^{13}C , and 2.71 for ^{15}N .

In summary, the NMR experiment consists of immersing magnetic nuclei in a strong field B_0 to distinguish them according to their values of I_z ($+\frac{1}{2}$ and $-\frac{1}{2}$ for spin- $\frac{1}{2}$ nuclei), followed by the application of a B_1 field whose frequency corresponds to the Larmor frequency ($\omega_0 = \gamma B_0$). This application of energy results in a net absorption, as the excess $+\frac{1}{2}$ nuclei are converted to $-\frac{1}{2}$ nuclei. The resonance frequency varies from nuclide to nuclide according to the value of γ . The energy difference between the I_z spin states, $\Delta E = h\nu$, which determines the intensity of the absorption, depends on the value of B_0 (Figure 1-4) and on the gyromagnetic ratio of the nucleus ($\Delta E = \gamma\hbar B_0$) (Figure 1-6).

1-2 The Chemical Shift

NMR is a valuable structural tool because the observed resonance frequency ν_0 depends on the molecular environment as well as on γ and B_0 . The electron cloud that surrounds the nucleus also has charge, motion, and, hence, a magnetic moment. The magnetic field generated by the electrons alters the B_0 field in the microenvironment around the nucleus.

The actual field present at a given nucleus thus depends on the nature of the surrounding electrons. This electronic modulation of the B_0 field is termed *shielding*, which is represented quantitatively by the Greek letter σ . The actual field at the nucleus becomes B_{local} and may be expressed as $B_0(1 - \sigma)$, in which the electronic shielding σ normally is positive. The variation of the resonance frequency with shielding has been termed the *chemical shift*.

By substituting B_{local} for B_0 in eq. 1-2, the expression for the resonance frequency in terms of shielding becomes

$$\nu_0 = \frac{\gamma B_0(1 - \sigma)}{2\pi} \quad (1-3)$$

Decreased shielding thus results in a higher resonance frequency ν_0 at constant B_0 , since σ enters the equation after a negative sign. For example, the presence of an electron-withdrawing group in a molecule reduces the electron density around a proton, so that there is less shielding and, consequently, a higher resonance frequency than in the case of a molecule that lacks the electron-withdrawing group. Hence, protons in fluoromethane (CH_3F) resonate at a higher frequency than those in methane (CH_4), because the fluorine atom withdraws electrons from around the hydrogen nuclei.

Figure 1-7 shows the separate NMR spectra of the protons and the carbons of methyl acetate ($\text{CH}_3\text{CO}_2\text{CH}_3$). Although 98.9% of naturally occurring carbon is the nonmagnetic ^{12}C , the carbon NMR experiment is carried out on the 1.1% of ^{13}C , which has an I of $\frac{1}{2}$. Because of differential electronic shielding, the ^1H spectrum contains separate resonances

Figure 1-7 The 300 MHz ^1H spectrum (top) and the 75.45 MHz ^{13}C spectrum (bottom) of methyl acetate in CDCl_3 . (The resonance at δ 77 is from solvent.) The ^{13}C spectrum has been decoupled from the protons.

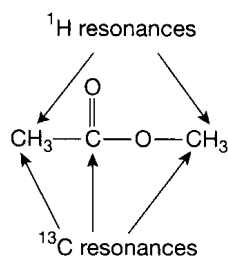
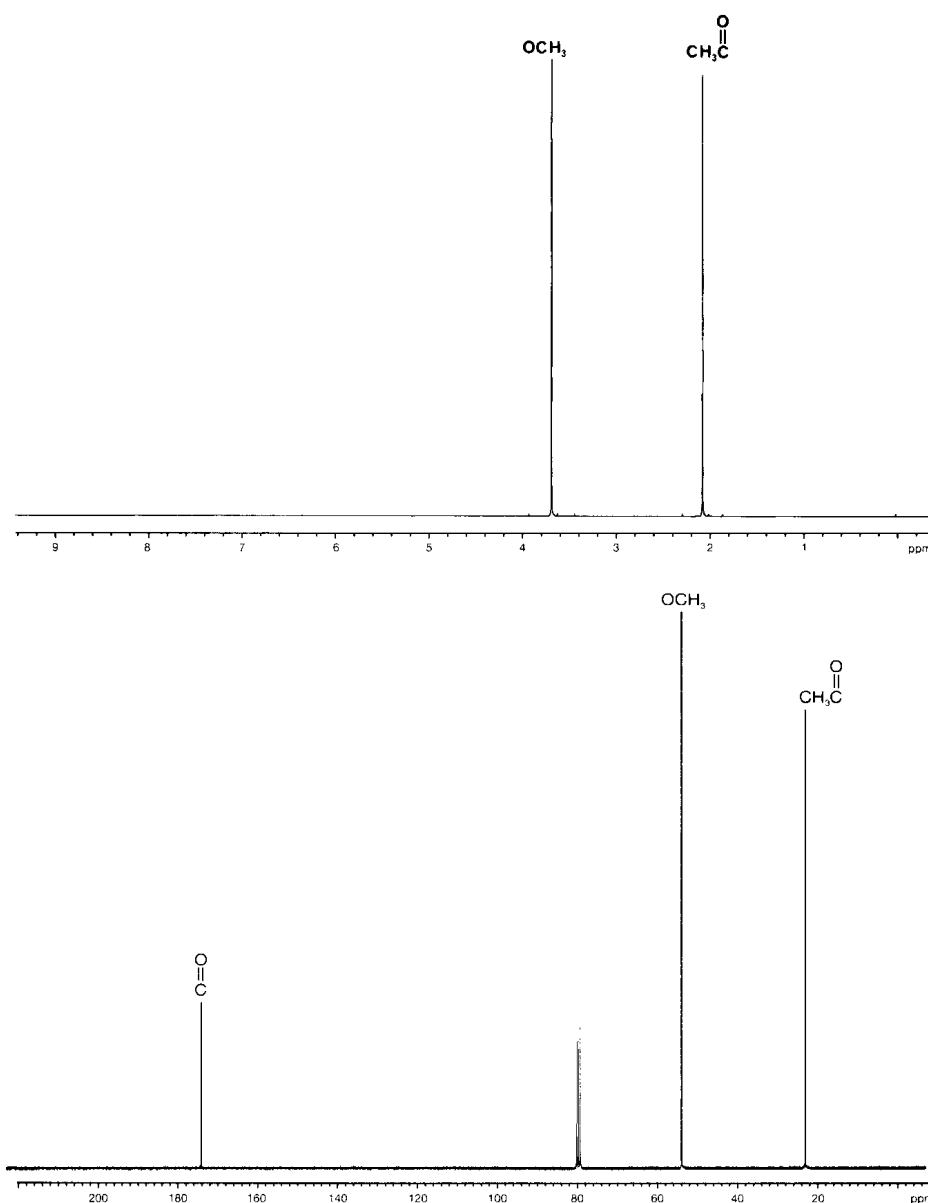


Figure 1-8 The different resonances expected for methyl acetate.

for the two types of protons ($\text{O}-\text{CH}_3$ and $\text{C}-\text{CH}_3$), and the ^{13}C spectrum contains separate resonances for the three types of carbons ($\text{O}-\text{CH}_3$, $\text{C}-\text{CH}_3$, and carbonyl) (Figure 1-8).

The proton resonances may be assigned on the basis of the electron-withdrawing abilities, or electronegativities, of the neighboring atoms. The ester oxygen is more electron withdrawing than the carbonyl group, so the $\text{O}-\text{CH}_3$ resonance occurs at a higher frequency than (and to the left of) the $\text{C}-\text{CH}_3$ resonance. By convention, frequency in the spectrum increases from right to left, for consistency with other forms of spectroscopy. Therefore, shielding increases from left to right.

The system of units depicted in Figure 1-7 and used throughout this book has been developed to overcome the fact that chemical information often is found in small differences between large numbers. An intuitive system might be absolute frequency—for example, in Hz. At the common field of 7.05 T, for instance, all protons resonate in the vicinity of 300 MHz. A scale involving numbers like 300.000764, however, is cumbersome. Moreover, frequencies would vary from one B_0 field to another (eq. 1-3). Thus, for every element or isotope, a reference material has been chosen and assigned a relative frequency of zero. For both protons and carbons, the substance is tetramethylsilane $[(\text{CH}_3)_4\text{Si}]$, usually called TMS, which is soluble in most organic solvents, is unreactive, and is volatile. In addition,

the low electronegativity of silicon means that the protons and carbons are surrounded by a relatively high density of electrons. Hence, they are highly shielded and resonate at very low frequency. Shielding by silicon in fact is so strong that the proton and carbon resonances of TMS are placed at the right extreme of the spectrum, providing a convenient spectral zero. In Figures 1-5 and 1-7, the position marked "0 ppm" is the hypothetical position of TMS.

The chemical shift may be expressed as the distance from a chemical reference standard by writing eq. 1-3 twice—once for an arbitrary nucleus i as

$$\nu_i = \frac{\gamma B_0(1 - \sigma_i)}{2\pi} \quad (1-4a)$$

and again for the reference (i.e., TMS) as

$$\nu_r = \frac{\gamma B_0(1 - \sigma_r)}{2\pi}. \quad (1-4b)$$

The distance between the resonances in the NMR frequency unit (Hz, or cycles per second) then is given by the formula

$$\Delta\nu = \nu_i - \nu_r = \frac{\gamma B_0(\sigma_r - \sigma_i)}{2\pi} = \frac{\gamma B_0 \Delta\sigma}{2\pi}. \quad (1-5)$$

This expression for the frequency differences, however, still depends on the magnetic field B_0 . In order to have a common unit at all B_0 fields, the chemical shift of nucleus i is defined by

$$\delta = \frac{\Delta\nu}{\nu_r} = \frac{\sigma_r - \sigma_i}{1 - \sigma_r} \sim \sigma_r - \sigma_i, \quad (1-6)$$

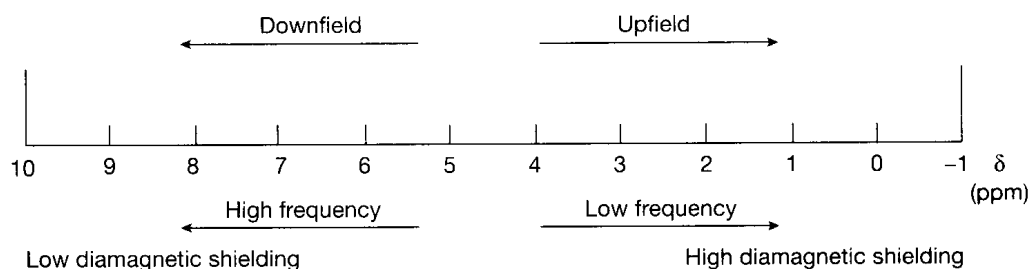
in which the frequency difference in Hz is divided by the reference frequency in MHz (eq. 1-5 divided by eq. 1-4b; the constants cancel out). The δ scale is thus in units of Hz/MHz, or parts per million (ppm). Because the reference shielding is chosen to be much less than 1.0 [$(1 - \sigma_r) \sim 1$], δ corresponds to the differences in shielding of the reference and the nucleus. An increase in σ_i thus results in a decrease in δ_i in accordance with eq. 1-6.

As seen in the ^1H spectrum of methyl acetate (Figure 1-7), the δ value for the C—CH₃ protons is 2.07 ppm and that for the O—CH₃ protons is 3.67 ppm. These values remain the same in spectra taken at a B_0 field of either 1.41 T (60 MHz) or 21.2 T (900 MHz), which represent the extremes of spectrometers currently in use. Chemical shifts in Hz, however, vary from field to field. Thus, a resonance that is 90 Hz from TMS at 60 MHz is 450 Hz from TMS at 300 MHz, but always has a δ value of 1.50 ppm ($\delta = 90/60 = 450/300 = 1.50$). Note that a resonance to the right of TMS has a *negative* value of δ . Also, since TMS is insoluble in water, other internal standards are used for this solvent, including 3-(trimethylsilyl)-1-propanesulfonic acid [(CH₃)₃Si(CH₂)₃SO₃Na] and 3-(trimethylsilyl)propionic acid [(CH₃)₃SiCH₂CH₂CO₂Na] (sodium salts).

In the first generation of spectrometers, the range of chemical shifts, such as those in the scale at the bottom of Figures 1-5 and 1-7, was generated by varying the B_0 field while holding the B_1 field, and hence the resonance frequency, constant. As eq. 1-3 indicates, an increase in shielding (σ) requires B_0 to be raised in order to keep ν_0 constant. Since nuclei with higher shielding resonate at the right side of the spectrum, the B_0 field in this experiment increases from left to right. Consequently, the right end came to be known as the high field, or upfield, end, and the left end as the low field, or downfield, end. This method was termed *continuous-wave field sweep*.

Modern spectrometers vary the B_1 frequency while the B_0 field is kept constant. An increase in shielding (σ) lowers the right side of eq. 1-3, so that ν_0 must decrease in order to maintain a constant B_0 . Thus, the right end of the spectrum, as noted before, corresponds to lower frequencies for more shielded nuclei. The general result is that frequency increases

Figure 1-9 Spectral conventions.



from right to left and field increases from left to right. Figure 1-9 summarizes the terminology. The right end of the spectrum still is often referred to as the high field or upfield end, in deference to the old field-sweep experiment, although it is more appropriate to call it the low-frequency or more shielded end.

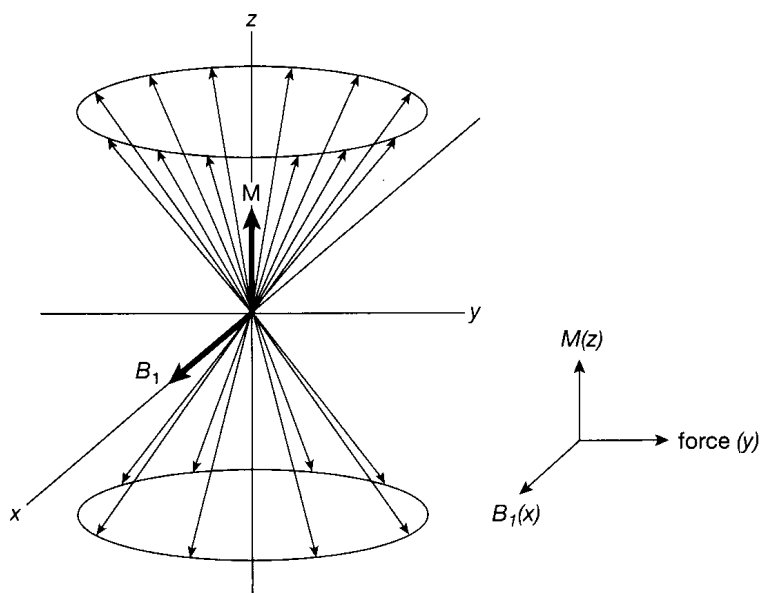
The chemical shift is considered further in Chapter 3.

1-3 Excitation and Relaxation

To understand the NMR experiment more fully, it is useful to consider Figure 1-3 again—this time in terms of a collection of nuclei (Figure 1-10). At equilibrium, the $I_z = +\frac{1}{2}$ nuclei precess around the $+z$ axis, and the $-\frac{1}{2}$ nuclei precess around the $-z$ axis. Only 20 spins are shown on the surface of the double cone in the figure, and the excess of $+\frac{1}{2}$ over $-\frac{1}{2}$ nuclei is exaggerated (12 to 8). The actual ratio of populations of the two states is given by the Boltzmann equation (1-1). Inserting the numbers for $B_0 = 7.04$ T yields the result that, for every million spins, there are only about 50 more with $+\frac{1}{2}$ than $-\frac{1}{2}$ spin. If the magnetic moments are added vectorially, there is a net vector in the $+z$ direction because of the excess of $+\frac{1}{2}$ over $-\frac{1}{2}$ spins. The sum of all the individual spins is called the *magnetization* (\mathbf{M}), and the boldface arrow pointing along the $+z$ direction in the figure represents the resultant \mathbf{M} . Because the spins are distributed randomly around the z axis, there is no net x or y magnetization; that is, $M_x = M_y = 0$, and hence, $\mathbf{M} = M_z$.

Figure 1-10 also shows the vector that represents the B_1 field placed along the x axis. When the B_1 frequency matches the Larmor frequency of the nuclei, some $+\frac{1}{2}$ spins turn over and become $-\frac{1}{2}$ spins, so that M_z decreases slightly. The vector B_1 exerts a force on \mathbf{M} whose result is perpendicular to both vectors (inset at lower right of the figure; the force arises from the cross product $\mathbf{F} = \mathbf{M} \times \mathbf{B}$). If B_1 is turned on just briefly, the magnetization

Figure 1-10 Spin- $\frac{1}{2}$ nuclei at equilibrium, prior to application of the B_1 field.



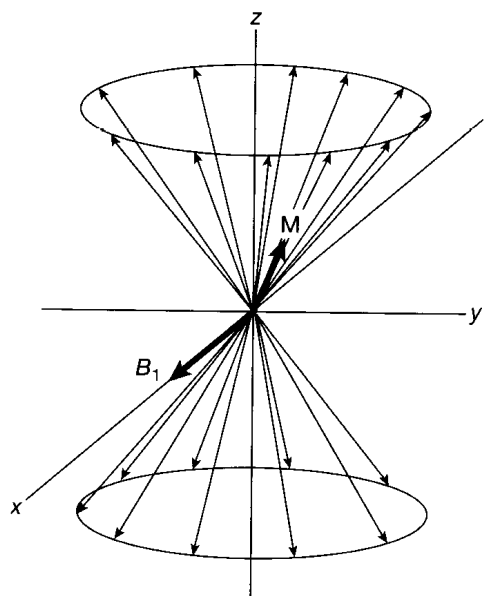


Figure 1-11 Spin- $\frac{1}{2}$ nuclei immediately after application of the B_1 field.

vector \mathbf{M} tips only slightly off the z axis, moving toward the y axis, which represents the mutually perpendicular direction. Figure 1-11 illustrates the result.

The 20 spins of Figure 1-10 originally had 12 nuclei of spin $+\frac{1}{2}$ and 8 of spin $-\frac{1}{2}$; these nuclei are shown in Figure 1-11 as 11 nuclei of spin $+\frac{1}{2}$ and 9 of spin $-\frac{1}{2}$ after application of the B_1 field. That is, only 1 nucleus has changed its spin. The decrease in M_z is apparent, as is the tipping of the magnetization vector off the axis. The positions on the circles, or *phases*, of the 20 nuclei no longer are random, because the tipping requires bunching of the spins toward the y axis. Thus, the phases of the spins now have some *coherence*, and there are x and y components of the magnetization. The xy component of the magnetization is the signal detected electronically as the resonance. The so-called absorption of energy as $+\frac{1}{2}$ nuclei become $-\frac{1}{2}$ nuclei is not measured directly.

The B_1 field in Figures 1-10 and 1-11 oscillates back and forth along the x axis. As Figure 1-12 illustrates from a view looking down the z axis, B_1 may be considered either (1) to oscillate linearly along the x axis at so many times per second (with frequency ν) or (2) to move circularly in the xy plane with angular frequency ω ($2\pi\nu$) in radians per second. The two representations are essentially equivalent. (See Appendix 2, and Figure A2-1 in particular, for an expansion of these concepts.) Resonance occurs when the frequency and phase of B_1 match that of the nuclei precessing at the Larmor frequency.

Figure 1-11 represents a snapshot in time, with the motion of both the B_1 vector and the precessing nuclei frozen. In real time, each nuclear vector is precessing around the z axis, so that the magnetization \mathbf{M} also is precessing around that axis. Another way to look at the freeze frame is to consider that the x and y axes are rotating at the frequency of the B_1 field. In terms of Figure 1-12, the axes are following the circular motion. Consequently, B_1 appears to be frozen in position and in magnitude along the x axis, instead of oscillating in the fashions shown in that figure. This *rotating coordinate system* is used throughout the book to simplify magnetization diagrams. In the rotating frame, the individual nuclei and the

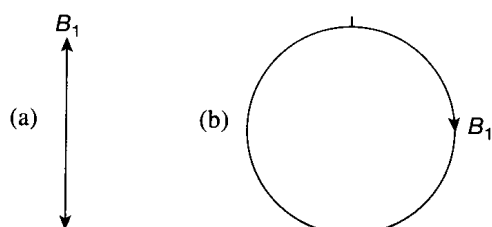


Figure 1-12 Analogy between linearly and circularly oscillating fields.

magnetization \mathbf{M} no longer precess around the z axis but are frozen for as long as they all have the same Larmor frequency matched by the frequency (B_1) of the rotating x and y axes.

Application of B_1 at the resonance frequency results in both energy absorption ($+\frac{1}{2}$ nuclei become $-\frac{1}{2}$) and emission ($-\frac{1}{2}$ nuclei become $+\frac{1}{2}$). Because initially there are more $+\frac{1}{2}$ than $-\frac{1}{2}$ nuclei, the net effect is absorption. As B_1 irradiation continues, however, the excess of $+\frac{1}{2}$ nuclei disappears, so that the rates of absorption and emission eventually become equal. Under these conditions, the sample is said to be approaching *saturation*. The situation is ameliorated, however, by natural mechanisms whereby nuclear spins move toward equilibrium from saturation. Any process that returns the z magnetization to its equilibrium condition with the excess of $+\frac{1}{2}$ spins is called *spin-lattice*, or *longitudinal, relaxation* and is usually a first-order process with time constant T_1 . For a return to equilibrium, relaxation also is necessary to destroy magnetization created in the xy plane. Any process that returns the x and y magnetizations to their equilibrium condition of zero is called *spin-spin*, or *transverse, relaxation* and is usually a first-order process with time constant T_2 .

Spin-lattice relaxation (T_1) derives from the existence of local oscillating magnetic fields in the sample that correspond to the resonance frequency. The primary source of these random fields is other magnetic nuclei that are in motion. As a molecule tumbles in solution in the B_0 field, each nuclear magnet generates a field caused by its motion. If this field is at the Larmor frequency, excess spin energy of neighboring spins can pass to this motional energy ($-\frac{1}{2}$ nuclei become $+\frac{1}{2}$ nuclei). The resonating spins are relaxed, and the absorption experiment can be repeated to increase intensities through signal averaging.

For effective spin-lattice relaxation, the tumbling magnetic nuclei must be spatially close to the resonating nucleus. For ^{13}C , attached protons provide effective spin-lattice relaxation. A carbonyl carbon or a carbon attached to four other carbons thus relaxes very slowly and is more easily saturated because the attached atoms are nonmagnetic (^{12}C and ^{16}O are nonmagnetic, so their motion provides no relaxation). Protons are relaxed by their nearest neighbor protons. Thus, CH_2 and CH_3 groups are relaxed by geminal protons, but CH protons must rely on vicinal ($\text{CH}-\text{CH}$) or more distant protons.

Spin-lattice relaxation also is responsible for generating the initial excess of $+\frac{1}{2}$ nuclei when the sample is first placed in the probe. In the absence of the B_0 field, all spins have the same energy. When the sample is immersed in the B_0 field, magnetization begins to build up as spins flip through interaction with surrounding magnetic nuclei in motion, eventually creating the equilibrium ratio of $+\frac{1}{2}$ and $-\frac{1}{2}$ states.

For x and y magnetization to decay towards zero (spin-spin, or T_2 , relaxation), the phases of the nuclear spins must become randomized. (cf. Figures 1-10 and 1-11.) The mechanism that gives the phenomenon its name involves the interaction of two nuclei with opposite spin. The process whereby one spin goes from $+\frac{1}{2}$ to $-\frac{1}{2}$ while the other goes from $-\frac{1}{2}$ to $+\frac{1}{2}$ involves no net change in z magnetization and hence no spin-lattice relaxation. The switch in spins results in dephasing, because the new spin state has a different phase from the old one. In terms of Figure 1-11, a spin vector disappears from the surface of the upper cone and reappears on the surface of the lower cone (and vice versa) at a new phase position. As this process continues, the phases become randomized around the z axis, and xy magnetization disappears. This process of two nuclei simultaneously exchanging spins is sometimes called the flip-flop mechanism.

A similar result arises when the B_0 field is not perfectly homogeneous. Again in terms of Figure 1-11, if the spin vectors are not located in exactly identical B_0 fields, they differ slightly in Larmor frequencies and hence precess around the z axis at different rates. As the spins move faster or more slowly relative to each other, eventually their relative phases become randomized. When nuclei resonate over a range of Larmor frequencies, the line width of the signal naturally increases. The spectral line width at half height and the spin-spin relaxation are related by the expression $w_{\frac{1}{2}} = 1/\pi T_2$. Both mechanisms (flip-flop and field inhomogeneity) can contribute to T_2 .

The subject of relaxation is discussed further in Section 5-1 and Appendix 5.

1-4 Pulsed Experiments

In the pulsed NMR experiment, the sample is irradiated close to the resonance frequency with an intense B_1 field for a very short time. For the duration of the pulse, the B_1 vector on the x axis (in the rotating coordinate system) exerts a force (see inset in Figure 1-10) on the M vector, which is on the z axis, pushing the magnetization toward the y axis. Figure 1-13 simplifies Figures 1-10 and 1-11 by eliminating the individual spins. Only the net magnetization vector M is shown in Figure 1-13. Thus, (a) is equivalent to Figure 1-10 and (b) is equivalent to Figure 1-11, but without showing the individual nuclear spins.

As long as the strong B_1 field is on, the magnetization continues to rotate, or precess, around B_1 . The strength of the B_1 field is such that, when it is on, precession occurs preferentially around its direction (y), rather than around the natural direction of B_0 (z). Consequently, the primary field present at the nuclei is B_1 , so the expression for the precession frequency becomes $\omega = \gamma B_1$. More precisely, this equation holds at the resonance frequency $\omega_0 = \gamma B_0$. Farther and farther from the resonance frequency, the effect of B_1 wanes, and precession around B_0 returns. A full mathematical treatment requires the inclusion of terms in both B_0 and B_1 , but, qualitatively, our interest focuses on the events at the resonance frequency.

The angle θ of rotation increases as long as B_1 is present (Figure 1-13). A short pulse might leave the magnetization at a 30° angle relative to the z axis (Figure 1-13b). A pulse three times as long (90°) aligns the magnetization along the y axis (Figure 1-13c). A pulse of double this duration (180°) brings the magnetization along the $-z$ direction (Figure 1-13d), meaning that there is an excess of $-\frac{1}{2}$ spins, or a population inversion. The exact angle θ caused by a pulse thus is determined by its duration t_p . The angle θ is therefore ωt_p , in which ω is the precession frequency in the B_1 field. Since $\omega = \gamma B_1$, it follows that $\theta = \gamma B_1 t_p$.

If the B_1 irradiation is halted when the magnetization reaches the y axis (a 90° pulse), and if the magnetization along the y direction is detected over time at the resonance frequency, then the magnetization would be seen to decay (Figure 1-14). Alignment of the magnetization along the y axis is a nonequilibrium situation. The x and y magnetization

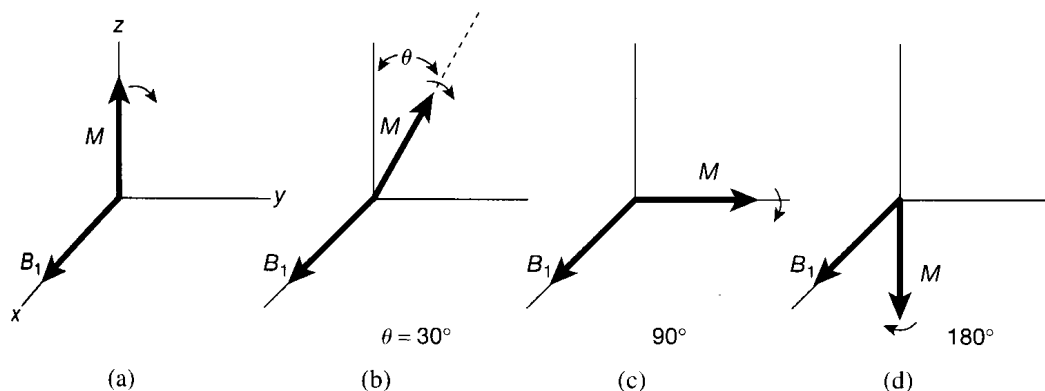


Figure 1-13 Net magnetization M as a function of time, following application of the B_1 field.

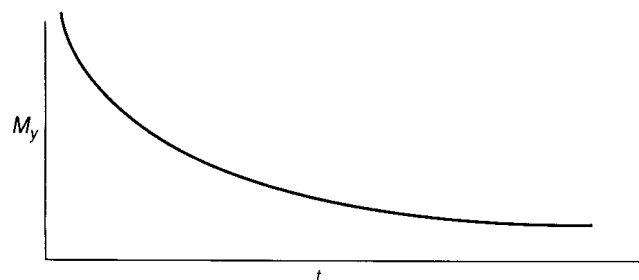


Figure 1-14 The induced magnetization along the y axis as a function of time (the free-induction decay).

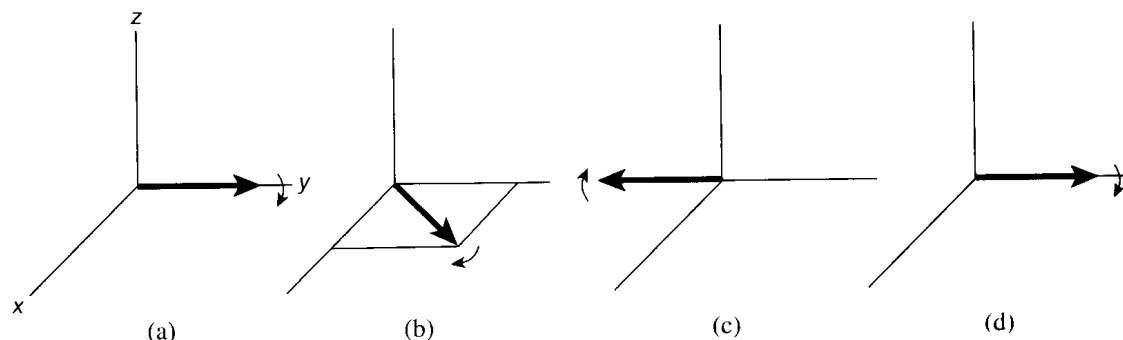


Figure 1-15 Time dependence of the magnetization M following a 90° pulse.

decays by spin–spin relaxation (T_2). At the same time, z magnetization reappears by spin–lattice relaxation (T_1). The reduction in y magnetization with time shown in the figure is called the *Free Induction Decay* (FID) and is a first order process with time constant T_2 .

The illustration in Figure 1-14 is artificial, because it involves only a single type of nucleus for which the resonance frequency γB_0 corresponds to the frequency of rotation of the x and y axes. Most samples have quite a few different types of protons or carbons, so that several resonance frequencies are involved, but the rotating frame can have only a single, or reference, frequency. What happens when there are nuclei with a variety of resonance frequencies? First, imagine again the case of a single resonance, like that of benzene in Figure 1-5. At the end of the 90° B_1 pulse (Figure 1-15), the spins are lined up along the y axis (Figure 1-15a), and precession about the z axis returns. In the rotating coordinate system, the x and y axes are rotating at γB_0 around the z axis. Nuclei with resonance frequency γB_0 appear not to precess about the z axis. If, however, the xy coordinate system is rotating at a frequency slightly different from the Larmor frequency, then the nuclear magnet moves off the y axis within the xy plane (Figure 1-15b). Only nuclei precessing at the reference frequency appear to be stationary in the rotating coordinate system. After additional time, the magnetization continues to rotate, reaching the $-y$ axis (Figure 1-15c) and eventually returning to the $+y$ axis (Figure 1-15d). The detected y magnetization during this cycle first decreases, then falls to zero as it passes the $y = 0$ point, next moves to a negative value in the $-y$ region (Figure 1-15c), and finally returns to positive values (Figure 1-15d). The magnitude of the magnetization thus varies periodically like a cosine function. When it is again along the $+y$ axis (Figure 1-15d), the magnetization is slightly smaller than at the beginning of the cycle, because of spin–spin relaxation (T_2). Moreover, it has moved out of the xy plane (not shown in the figure) as z magnetization returns through spin–lattice relaxation (T_1). The magnetization varies as a cosine function with time, continually passing through a sequence of events illustrated by Figure 1-15.

Figure 1-16a shows what the FID looks like for the protons of acetone. The horizontal distance between each maximum is the reciprocal of the difference between the Larmor frequency and the B_1 frequency. The intensities of the maxima decrease as y magnetization is lost through spin–spin relaxation. Because the line width of the spectrum is determined by T_2 , the FID contains all the necessary information to display a spectrum: frequency and line width, as well as overall intensity.

Now consider the case of two nuclei with different resonance frequencies, each different from the reference frequency. Their decay patterns are superimposed, reinforcing and interfering to create a complex FID, as in Figure 1-16b for the protons of methyl acetate. By the time there are four frequencies, as in the carbons of 3-hydroxybutyric acid shown in Figure 1-16c, it is nearly impossible to unravel the frequencies visually. The mathematical process called Fourier analysis matches the FID with a series of sinusoidal curves and obtains from them the frequencies, line widths, and intensities of each component. The FID is

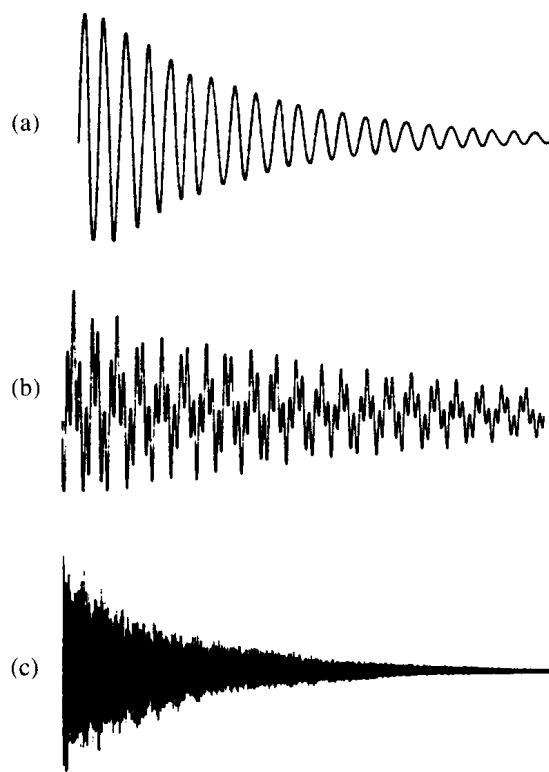


Figure 1-16 The free-induction decay for the ^1H spectra of (a) acetone and (b) methyl acetate. (c) The free-induction decay for the ^{13}C spectrum of 3-hydroxybutyric acid. All samples are without solvent.

a plot in time (see Figures 1-14 and 1-16), so the experiment is said to occur in the *time domain*. The experimentalist, however, wants a plot of frequencies, so the spectrum must be transformed to a *frequency domain*, as shown in Figures 1-5 and 1-7. The Fourier transformation (FT) is carried out rapidly by computer, and the experimentalist does not need to examine the FID.

1-5 The Coupling Constant

The form of a resonance can be altered when other magnetic nuclei are nearby. In 1-chloro-4-nitrobenzene (**1-1**), for example, there are two types of protons, labeled A and X, which are, respectively, ortho to nitro and ortho to chloro. For the time being, we will ignore any effects from the identical A and X protons across the ring. Each proton has a spin of $\frac{1}{2}$ and therefore can exist in two I_z spin states, $+\frac{1}{2}$ and $-\frac{1}{2}$, which differ in population only in parts per million. Almost exactly half the A protons have $+\frac{1}{2}$ X neighbors, and half have $-\frac{1}{2}$ X neighbors. The magnetic environments provided by these two types of X protons are not identical, so the A resonance is split into two peaks (Figures 1-17a and 1-18). By the same token, the X nucleus exists in two distinct magnetic environments, because the A proton has two spin states. The X resonance also is split into two peaks (Figures 1-17b and 1-18). Quadrupolar nuclei, such as the nuclei of the chlorine and nitrogen atoms in molecule **1-1**,

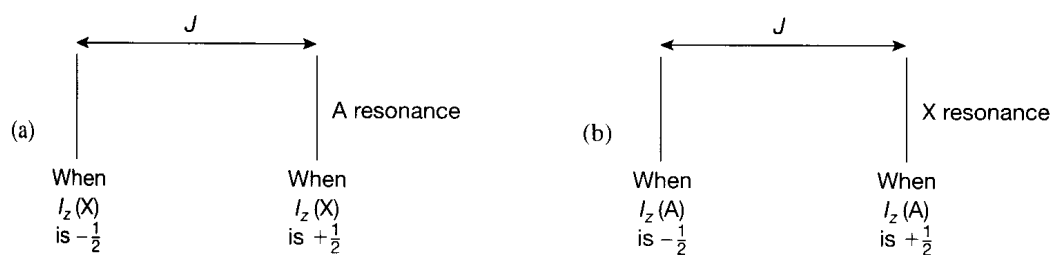
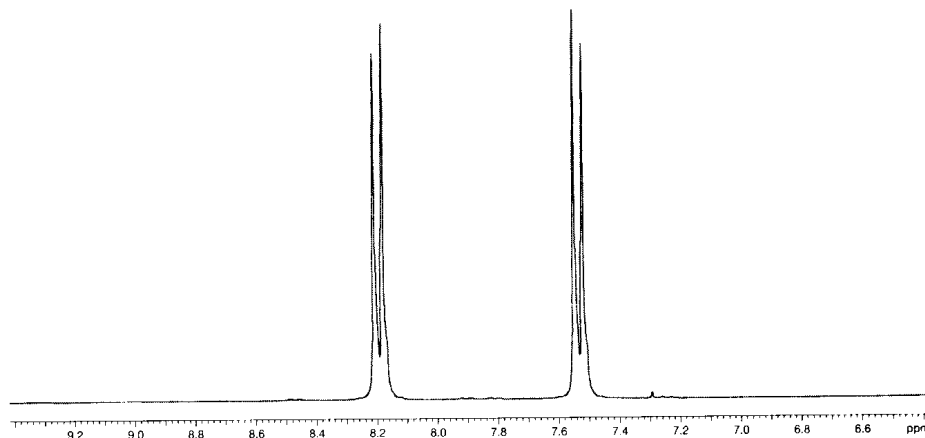
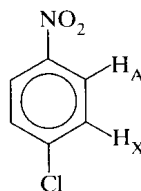


Figure 1-17 The four peaks of a first-order, two-spin system (AX).

Figure 1-18 The 300 MHz ^1H spectrum of 1-chloro-4-nitrobenzene in CDCl_3 .



often act as if they are nonmagnetic and may be ignored in this context. Thus, the proton resonance of chloroform (CHCl_3) is a singlet; the proton resonance is not split by chlorine. This phenomenon is considered in detail in Section 5-1.



1-1

The influence of neighboring spins on the multiplicity of peaks is called *spin-spin splitting* or *indirect coupling*. The distance between the two peaks for the resonance of one nucleus split by another is a measure of how strongly the nuclear spins influence each other and is called the *coupling constant J* , measured in hertz (Hz). In 1-chloro-4-nitrobenzene (**1-1**), the coupling between A and X is 10.0 Hz, a relatively large value of J for two protons. In general, when there are only two nuclei in the coupled system, the resulting spectrum is referred to as AX. Notice that the splitting in both the A and the X portions of the spectrum is the same (Figure 1-18), since J is a measure of the interaction between the nuclei and must be identical for both nuclei. Moreover, J is independent of B_0 , because the magnitude of the interaction depends only on nuclear properties and not on external quantities such as the field. Thus, in 1-chloro-4-nitrobenzene (**1-1**), J is 10.0 Hz when measured either at 7.05 T (300 MHz), as in Figure 1-18, or at 14.1 T (600 MHz).

For two nuclei to couple, there must be a mechanism whereby information about spin is transferred between them. The most common mechanism involves the interaction of electrons along the bonding path between the nuclei. (See Figure 1-19 for an abbreviated coupling pathway over two bonds.) Electrons, like protons, act like spinning particles and have a magnetic moment. The X proton (H_X) influences, or polarizes, the spins of its surrounding

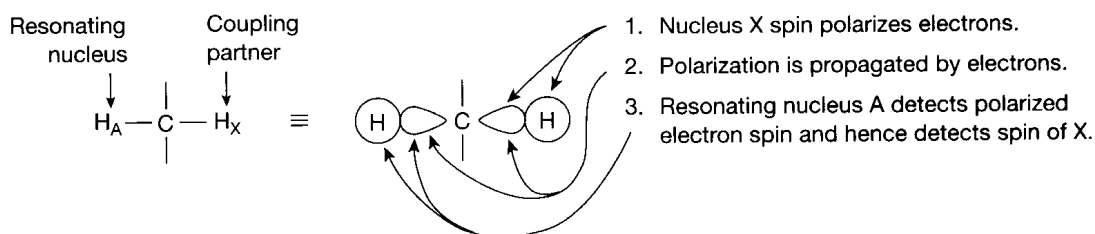


Figure 1-19 The mechanism for indirect spin-spin coupling.

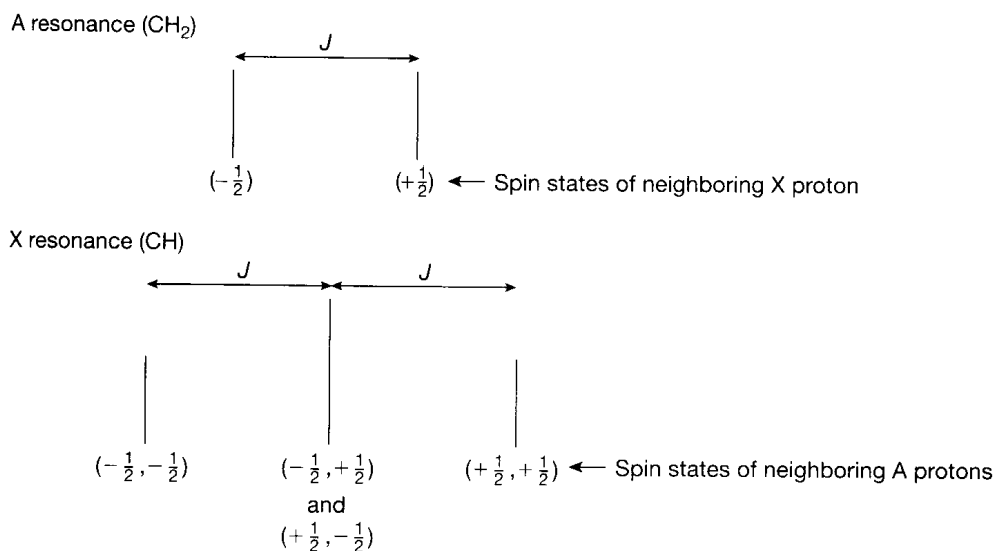
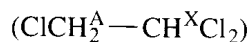


Figure 1-20 The five peaks of a first-order, three-spin system (A_2X).

electrons very slightly, making the electron spins favor one I_z state slightly. Thus, a proton of spin $+\frac{1}{2}$ polarizes the electron to $-\frac{1}{2}$. The electron in turn polarizes the other electron of the C—H bond, and so on, finally reaching the resonating A proton (H_A). (This mechanism is discussed further in Section 4-3.) Because J normally represents an interaction through bonds, it is a useful parameter in drawing conclusions about molecular bonding, such as bond strengths and steric arrangements.

Additional splitting occurs when a resonating nucleus is close to more than one nucleus. For example, 1,1,2-trichloroethane (**1-2**) has two types of protons, which we label H_A (CH_2) and H_X (CH). The A protons are subject to two different environments, from the $+\frac{1}{2}$ and $-\frac{1}{2}$ spin states of H_X , and therefore are split into a 1/1 doublet, analogous to the situations shown in Figures 1-17 and 1-18. The X proton, however, is subject to *three* different magnetic environments, because the spins of H_A must be considered collectively: both may be $+\frac{1}{2}$ ($++$), both may be $-\frac{1}{2}$ ($--$), and one may be $+\frac{1}{2}$ while the other is $-\frac{1}{2}$ (the two equivalent possibilities are $+-$ and $-+$). The three different A environments—($++$), ($+-$)/($-+$), and ($--$)—therefore result in three X peaks in the ratio 1 : 2 : 1 (Figure 1-20). Thus, the spectrum of **1-2** contains a doublet and a triplet and is referred to as A_2X (or AX_2 if the labels are switched) (Figure 1-21). The value of J is found in three different spacings in the spectrum, between any two adjacent peaks of a multiplet (Figures 1-20 and 1-21).



1-2

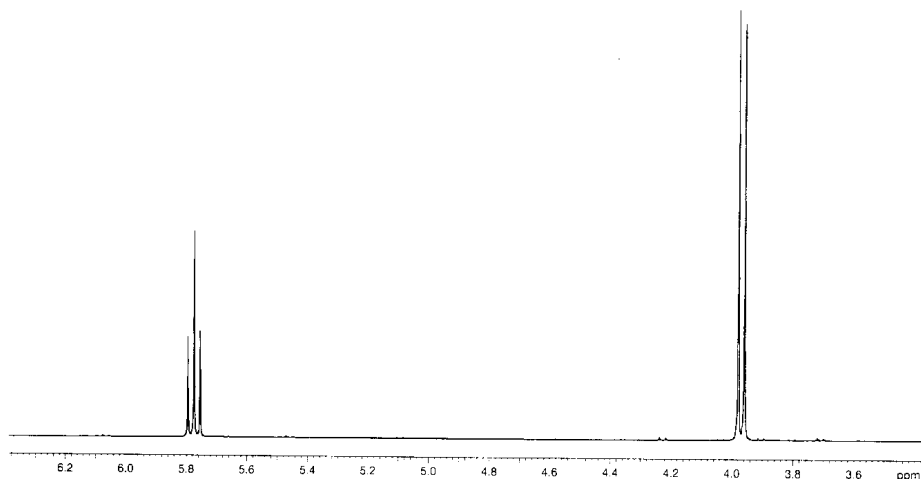
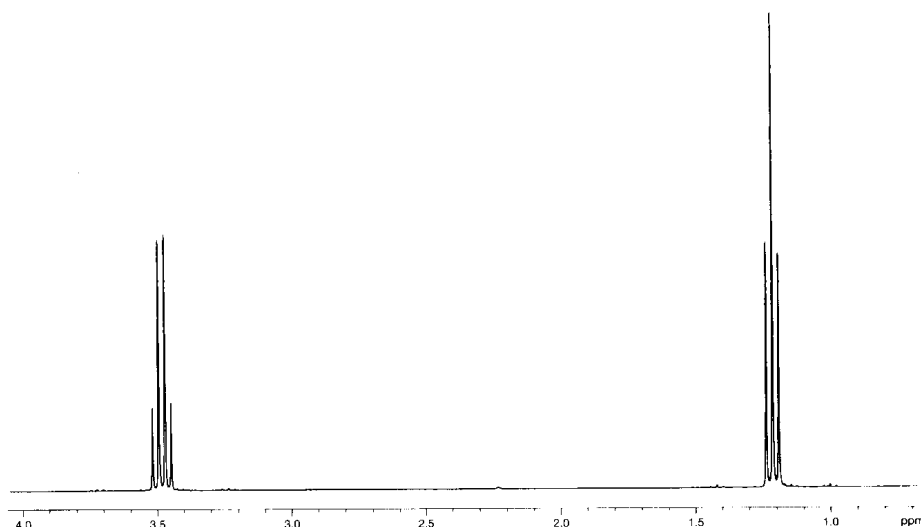


Figure 1-21 The 300 MHz 1H Spectrum of 1,1,2-trichloroethane in $CDCl_3$.

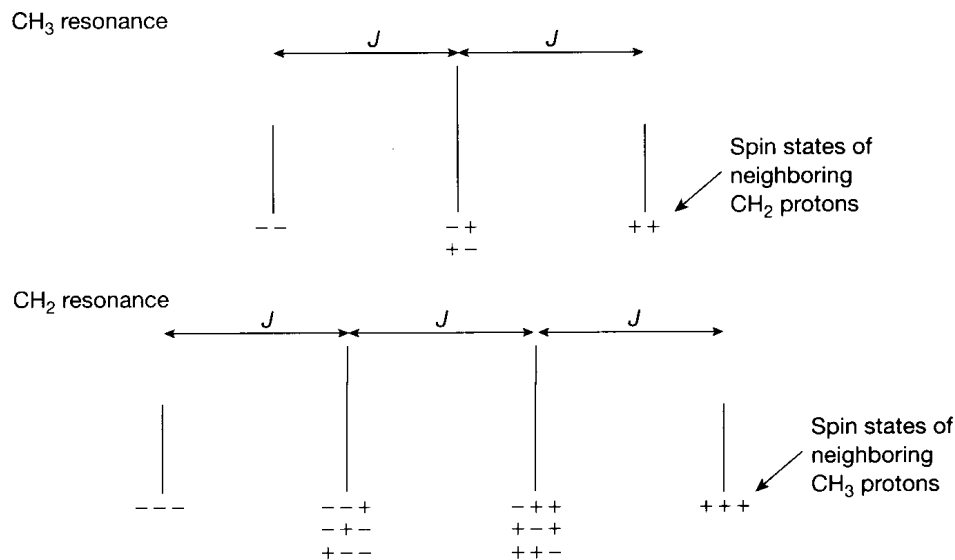
Figure 1-22 The 300 MHz ^1H spectrum of diethyl ether in CDCl_3 .



As the number of neighboring spins increases, so does the complexity of the spectrum. The ethyl groups in diethyl ether form an A_2X_3 spectrum (Figure 1-22). The methyl protons are split into a 1 : 2 : 1 triplet by the neighboring methylene protons, as in the X resonance of Figure 1-20. Because the methylene protons are split by three methyl protons, there are four peaks in the methylene resonance. The neighboring methyl protons can have all positive spins (+++), two spins positive and one negative (in three ways: ++-, +-+, and -++), one spin positive and two negative (also in three ways: +--, -+-, --+), or all negative spins (---). The result is a 1 : 3 : 3 : 1 quartet (Figure 1-23). The triplet–quartet pattern seen in Figure 1-22 is a reliable indicator for the presence of an ethyl group.

The splitting patterns of larger spin systems may be deduced in a similar fashion. If a nucleus is coupled to n equivalent nuclei with $I = \frac{1}{2}$, there are $n + 1$ peaks, unless second-order effects, discussed in Chapter 4, are present. The intensity ratios, to a first-order approximation, correspond to the coefficients in the binomial expansion and may be obtained from Pascal's triangle (Figure 1-24), since arrangements of I_z states are statistically independent events. Pascal's triangle is constructed by summing two horizontally adjacent integers and placing the result one row lower and between the two integers. Zeros are imagined outside the triangle. The first row (1) gives the resonance multiplicity when there is no

Figure 1-23 The seven peaks of the first-order A_2X_3 spectrum.



				1							
			1	1							
		1	2	1							
	1	3	3	1							
	1	4	6	4	1						
	1	5	10	10	5	1					
	1	6	15	20	15	6	1				
	1	7	21	35	35	21	7	1			
	1	8	28	56	70	56	28	8	1		
	1	9	36	84	126	126	84	36	9	1	
	1	10	45	120	210	252	210	120	45	10	1

Figure 1-24 Pascal's triangle.

neighboring spin, the second row (1 1) when there is one neighboring spin, and so on. We have already seen that two neighboring spins give a 1 : 2 : 1 triplet and three give a 1 : 3 : 3 : 1 quartet. Four neighboring spins are present for the CH proton in the arrangement $-\text{CH}_2-\text{CHX}-\text{CH}_2-$ (X is nonmagnetic), and the CH resonance is a 1 : 4 : 6 : 4 : 1 quintet (AX_4). The CH resonance from an isopropyl group, $-\text{CH}(\text{CH}_3)_2$, is a 1 : 6 : 15 : 20 : 15 : 6 : 1 septet (AX_6). Several common spin systems are given in Table 1-1.

Except in cases of second-order spectra (discussed in Chapter 4), coupling between protons that have the same chemical shift does not lead to splitting in the spectrum. It is for this reason that the spectrum of benzene in Figure 1-1 is a singlet, even though the protons are coupled to each other. For the same reason, protons within a methyl group normally do not cause splitting of the methyl resonance. Examples of unsplit spectra (singlets) include those of acetone, cyclopropane, and dichloromethane. The absence of splitting between coupled nuclei with identical resonance frequencies is quantum mechanical in nature and is explained in Appendix 3.

All the coupling examples given so far have been between vicinal protons, over three bonds ($\text{H}-\text{C}-\text{C}-\text{H}$). Coupling over four or more bonds usually is small or unobservable. It is possible for geminal protons ($-\text{CH}_2-$) to split each other, provided that each proton of the methylene group has a different chemical shift. Geminal splittings are observed when the carbon is part of a ring with unsymmetrical substitution on the upper and lower faces, when there is a single chiral center in the molecule, or when an alkene lacks an axis of symmetry ($\text{XYC}=\text{CH}_2$), as is discussed in Section 4-2.

Coupling can occur between ^1H and ^{13}C , as well as between two protons. Because ^{13}C is in such low natural abundance (about 1.1%), these couplings are not important in analyzing

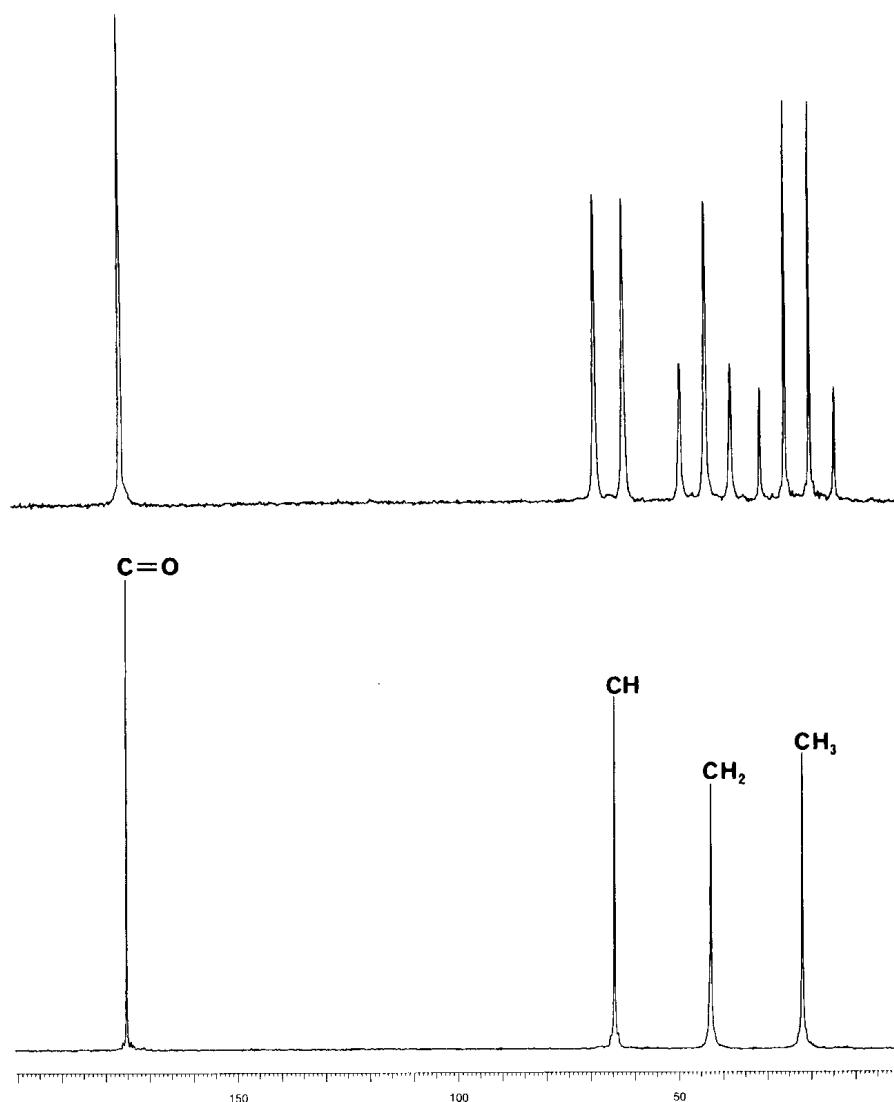
Table 1-1 Common First-Order Spin-Spin Splitting Patterns

Spin System	Molecular Substructure	A Multiplicity	X Multiplicity
AX	$-\text{CH}^{\text{A}}-\text{CH}^{\text{X}}-$	doublet (1 : 1)	doublet (1 : 1)
AX_2	$-\text{CH}^{\text{A}}-\text{CH}_2^{\text{X}}-$	triplet (1 : 2 : 1)	doublet (1 : 1)
AX_3	$-\text{CH}^{\text{A}}-\text{CH}_3^{\text{X}}$	quartet (1 : 3 : 3 : 1)	doublet (1 : 1)
AX_4	$-\text{CH}_2^{\text{X}}-\text{CH}^{\text{A}}-\text{CH}_2^{\text{X}}-$	quintet (1 : 4 : 6 : 4 : 1)	doublet (1 : 1)
AX_6	$\text{CH}_3^{\text{X}}-\text{CH}^{\text{A}}-\text{CH}_3^{\text{X}}$	septet (1 : 6 : 15 : 20 : 15 : 6 : 1)	doublet (1 : 1)
A_2X_2	$-\text{CH}_2^{\text{A}}-\text{CH}_2^{\text{X}}-$	triplet (1 : 2 : 1)	triplet (1 : 2 : 1)
A_2X_3	$-\text{CH}_2^{\text{A}}-\text{CH}_3^{\text{X}}$	quartet (1 : 3 : 3 : 1)	triplet (1 : 2 : 1)
A_2X_4	$-\text{CH}_2^{\text{X}}-\text{CH}_2^{\text{A}}-\text{CH}_2^{\text{X}}-$	quintet (1 : 4 : 6 : 4 : 1)	triplet (1 : 2 : 1)

^1H spectra. In 99 cases out of 100, protons are attached to nonmagnetic ^{12}C atoms. Small satellite peaks from the 1.1% of ^{13}C sometimes can be seen in ^1H spectra. In the ^{13}C spectrum, the carbon nuclei are coupled to nearby protons. The largest couplings occur with protons that are directly attached to the carbon. Thus, the ^{13}C resonance of a methyl carbon is split into a quartet, that of a methylene carbon into a triplet, and that of a methine carbon (CH) into a doublet; a quaternary carbon is not split by one bond coupling. Figure 1-25 (top) shows the ^{13}C spectrum of 3-hydroxybutyric acid ($\text{CH}_3\text{CH}(\text{OH})\text{CH}_2\text{CO}_2\text{H}$), which contains a carbon resonance with each type of multiplicity. From right to left are seen a quartet (CH_3), a triplet (CH_2), a doublet (CH), and a singlet (CO_2H). Hence, the splitting pattern in the ^{13}C spectrum is an excellent indicator of each of these types of groupings within a molecule.

Instrumental procedures, called *decoupling*, are available by which spin-spin splittings may be removed. These methods, discussed in Section 5-3, involve irradiating one nucleus with an additional field (B_2) while observing another nucleus resonating in the B_1 field. Because a second field is being applied to the sample, the experiment is called *double resonance*. This procedure was used to obtain the ^{13}C spectrum of methyl acetate in Figure 1-7 (bottom) and the spectrum of 3-hydroxybutyric acid at the bottom of Figure 1-25. It is commonly employed to obtain a very simple ^{13}C spectrum, so that each carbon gives a singlet. Measurement of both decoupled and coupled ^{13}C spectra then

Figure 1-25 Top: The 22.6 MHz ^{13}C spectrum of 3-hydroxybutyric acid, $\text{CH}_3\text{CH}(\text{OH})\text{CH}_2\text{CO}_2\text{H}$, without solvent. Bottom: The ^{13}C spectrum of the same compound with proton decoupling.



produces in the first case a simple picture of the number and types of carbons and in the second case the number of protons to which they are attached (Figure 1-25). (Coupling is treated in more detail in Chapter 4.)

1-6 Quantitation and Complex Splitting

The signal detected when nuclei resonate is directly proportional to the number of spins present. Thus, the protons of a methyl group (CH_3) produce three times the signal of a methine proton (CH). This difference in intensity can be measured through electronic integration and exploited to elucidate molecular structure. Figure 1-26 illustrates electronic integration for the ^1H spectrum of ethyl *trans*-crotonate ($\text{CH}_3\text{CH}=\text{CHCO}_2\text{CH}_2\text{CH}_3$). The vertical displacement of the continuous line above or through each resonance provides a measure of the area under the peaks. The vertical displacements show that the doublet at δ 5.84, the quartet at δ 4.19, and the triplet at δ 1.28 are respectively in the ratio 1:2:3. The integration provides only relative intensity data, so that the experimentalist must select a resonance with a known or suspected number of protons and normalize the other integrals to it. Usually, integrals are provided digitally by the spectrometer.

Each of the peaks in the ^1H spectrum of ethyl crotonate illustrated in Figure 1-26 may be assigned by examining the integral and splitting pattern. The triplet at the lowest frequency (the highest field, δ 1.28) has a relative integral of 3 and must come from the methyl part of the ethyl group. Its J value corresponds to that of the quartet in the middle of the spectrum at δ 4.19, whose integral is 2. This latter multiplet then must come from the methylene group. The mutually coupled methyl triplet and methylene quartet form the resonances for the ethyl group attached to oxygen ($-\text{OCH}_2\text{CH}_3$). The methylene resonance is at a higher frequency than the methyl resonance because CH_2 is closer than CH_3 to the electron-withdrawing oxygen.

The remaining resonances in the spectrum come from protons coupled to more than one type of proton. Coupling patterns are then more complex, as seen in the three spectral expansions in Figure 1-26. The highest-frequency (lowest-field) resonance (δ 6.98) has an intensity of unity and comes from one of the two alkenic ($-\text{CH}=\text{}$) protons. This resonance is split into a doublet ($J = 16$ Hz) by the other alkenic proton, and then each member of the doublet is further split into a quartet ($J = 7$ Hz) by coupling to the methyl group on carbon

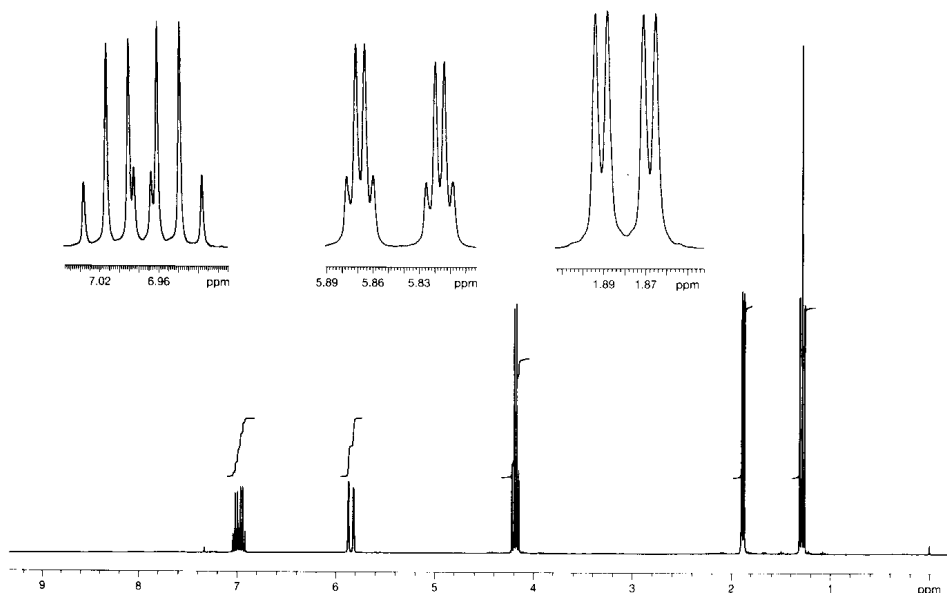
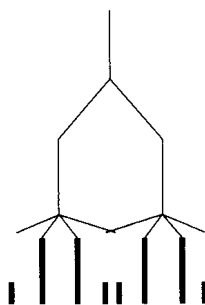


Figure 1-26 The 300 MHz ^1H spectrum of ethyl *trans*-crotonate in CDCl_3 . The upper multiplets are expansions of three resonances.

Figure 1-27 Overlapping peaks (δ 6.98 resonance) that arise when nuclei are unequally coupled to more than one other set of spins.



Resonance at δ 6.98 if there were no coupling

Splitting by the other CH \equiv (δ 5.84) into a 1:1 doublet ($J = 16$ Hz)

Splitting by each member of the doublet into a 1:3:3:1 quartet ($J = 7$ Hz) by coupling to CH $_3$ (δ 1.88) (note the crossover of the two middle peaks)

with a crossover of the inner two peaks. Stick diagrams (often called a tree) are useful in analyzing complex multiplets, as in Figure 1-27 for the resonance at δ 6.98.

The resonance of unit integral at δ 5.84 is from the other alkenic proton and is split into a doublet ($J = 16$ Hz) by the proton at δ 6.98. There is a small coupling (1 Hz) over four bonds to the methyl group, giving rise to a quartet (Figure 1-28). (The significance of these differences in the magnitude of couplings is discussed in Chapter 4.) The resonance at δ 6.98 can be recognized as originating from the proton closer to the methyl. (J is larger because it is over three, rather than four, bonds.)

The resonance at δ 1.88 has an integral of 3 and hence comes from the remaining methyl group, attached to the double bond. Because it is split by both of the alkenic protons, but with unequal couplings (7 and 1 Hz), four peaks result (Figure 1-29). This grouping is called a doublet of doublets; the term *quartet* normally is reserved for 1:3:3:1 multiplets. The two unequal couplings in the resonance at δ 1.88 correspond precisely to the quartet splittings found, respectively, in the two alkenic resonances. The final assignments are as follows:

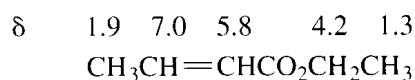
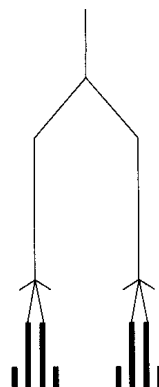


Figure 1-28 Overlapping peaks for the δ 5.84 resonance (not to scale).



Resonance at δ 5.84 if there were no coupling

Splitting by the other CH \equiv (δ 6.98) into a 1:1 doublet ($J = 16$ Hz) (note same splitting as for δ 6.98 resonance)

Splitting by each member of the doublet ($J = 1$ Hz) into a 1:3:3:1 quartet by coupling to CH $_3$ (δ 1.88)

Figure 1-29 Overlapping peaks for the δ 1.88 resonance (not to scale).



Resonance at δ 1.88 if there were no coupling

Splitting by CH \equiv with $J = 7$ Hz (δ 6.98)

Splitting by CH \equiv with $J = 1$ Hz (δ 5.84)

Integration also may be used as a measure of the relative amounts of the components of a mixture. In this case, after normalizing for the number of protons in a grouping, the proportions of the components may be calculated from the relative integrals of protons in different molecules. An internal standard with a known concentration may be included. Comparisons of other resonances with those of the standard thus can provide a measure of the absolute concentration.

1-7 Commonly Studied Nuclides

Which nuclei (in this context, "nuclides") are useful in chemical problems? The answer depends on one's area of specialty. Certainly, for the organic chemist, the most common elements are carbon, hydrogen, oxygen, and nitrogen (Table 1-2). The biochemist would add phosphorus to the list. The organometallic or inorganic chemist would focus on whichever

Table 1-2 NMR Properties of Common Nuclei

Nuclide	Spin	Natural Abundance (N_a) (%)	Natural Sensitivity		NMR Frequency (at 7.05 T)	Reference Substance
			(N_s) (for equal numbers of nuclei) (vs. ^1H)	Receptivity (vs. ^{13}C)		
Proton	$\frac{1}{2}$	99.985	1.00	5680	300.00	(CH_3) ₄ Si
Deuterium	1	0.015	0.00965	0.0082	46.05	(CD_3) ₄ Si
Lithium-7	$\frac{3}{2}$	92.58	0.293	1540	38.86	LiCl
Boron-10	3	19.58	0.0199	22.1	32.23	$\text{Et}_2\text{O} \cdot \text{BF}_3$
Boron-11	$\frac{3}{2}$	80.42	0.165	754	96.21	$\text{Et}_2\text{O} \cdot \text{BF}_3$
Carbon-13	$\frac{1}{2}$	1.108	0.0159	1.00	75.45	(CH_3) ₄ Si
Nitrogen-14	1	99.63	0.00101	5.69	21.69	$\text{NH}_3(\text{l})$
Nitrogen-15	$\frac{1}{2}$	0.37	0.00104	0.0219	30.42	$\text{NH}_3(\text{l})$
Oxygen-17	$\frac{5}{2}$	0.037	0.0291	0.0611	40.68	H_2O
Fluorine-19	$\frac{1}{2}$	100	0.833	4730	282.27	CCl_3F
Sodium-23	$\frac{3}{2}$	100	0.0925	525	79.36	NaCl (aq)
Aluminum-27	$\frac{5}{2}$	100	0.0206	117	78.17	$\text{Al}(\text{H}_2\text{O})_6^{3+}$
Silicon-29	$\frac{1}{2}$	4.70	0.00784	2.09	59.61	(CH_3) ₄ Si
Phosphorus-31	$\frac{1}{2}$	100	0.0663	377	121.44	85% H_3PO_4
Sulfur-33	$\frac{3}{2}$	0.76	0.00226	0.0973	23.04	CS_2
Chlorine-35	$\frac{3}{2}$	75.53	0.0047	20.2	29.40	NaCl (aq)
Chlorine-37	$\frac{3}{2}$	24.47	0.00274	3.8	24.47	NaCl (aq)
Potassium-39	$\frac{3}{2}$	93.1	0.000509	2.69	14.00	K^+
Calcium-43	$\frac{7}{2}$	0.145	0.00640	0.0527	20.19	CaCl_2 (aq)
Iron-57	$\frac{1}{2}$	2.19	0.0000337	0.0042	9.71	$\text{Fe}(\text{CO})_5$
Cobalt-59	$\frac{7}{2}$	100	0.277	1570	71.19	$\text{K}_3\text{Co}(\text{CN})_6$
Copper-63	$\frac{3}{2}$	69.09	0.0931	365	79.58	$\text{Cu}(\text{CH}_3\text{CN})_4^+ \text{BF}_4^-$
Selenium-77	$\frac{1}{2}$	7.58	0.00693	2.98	57.22	$\text{Se}(\text{CH}_3)_2$
Rhodium-103	$\frac{1}{2}$	100	0.0000312	0.177	9.56	Rh metal
Tin-119	$\frac{1}{2}$	8.58	0.0517	25.2	37.29	(CH_3) ₄ Sn
Tellurium-125	$\frac{1}{2}$	7.0	0.0315	12.5	78.51	$\text{Te}(\text{CH}_3)_2$
Platinum-195	$\frac{1}{2}$	33.8	0.00994	19.1	64.38	Na_2PtCl_6
Mercury-199	$\frac{1}{2}$	16.84	0.00567	5.42	53.73	(CH_3) ₂ Hg
Lead-207	$\frac{1}{2}$	22.6	0.00920	11.8	62.57	$\text{Pb}(\text{CH}_3)_4$

For a more complete list, see J. B. Lambert and F. G. Riddell, *The Multinuclear Approach to NMR Spectroscopy* (Dordrecht: D. Reidel, 1983).

elements are of potential use, possibly boron, silicon, tin, mercury, platinum, or some of the low-intensity nuclei, such as iron and potassium. The success of the experiment depends on several factors.

Spin. The overall spin of the nucleus is determined by the spin properties of the protons and neutrons, as discussed in Section 1-1. (See the second column in Table 1-2.) By and large, spin- $\frac{1}{2}$ nuclei exhibit more favorable NMR properties than quadrupolar nuclei ($I > \frac{1}{2}$). Nuclei with odd mass numbers have half-integral spins ($\frac{1}{2}, \frac{3}{2}$, etc.), whereas those with even mass and odd charge have integral spins (1, 2, etc.). Quadrupolar nuclei have a unique mechanism for relaxation that can result in extremely short relaxation times, as is discussed in Section 5-1. The relationship between lifetime (Δt) and energy (ΔE) is given by the Heisenberg uncertainty principle, which states that their product is constant: $\Delta E \Delta t \sim \hbar$. When the lifetime of the spin state, as measured by the relaxation time, is very short, the larger uncertainty in energies implies a larger band of frequencies, or a broadened signal, in the NMR spectrum. The relaxation time, and hence the broadening of the spectral lines, depends on the distribution of charge within the nucleus, as determined by the quadrupole moment. For example, quadrupolar broadening makes ^{14}N ($I = 1$) a generally less useful nucleus than ^{15}N ($I = \frac{1}{2}$), even though ^{14}N is much more abundant.

Natural Abundance. Nature provides us with nuclides in varying amounts. (See the third column in Table 1-2.) Whereas ^{19}F and ^{31}P are 100% abundant and ^1H nearly so, ^{13}C is present only to the extent of 1.1%. The most useful nitrogen (^{15}N) and oxygen (^{17}O) nuclides occur to the extent of much less than 1%. The NMR experiment, of course, is easier with nuclides with higher natural abundance. Because so little ^{13}C is present, there is a very small probability of having two ^{13}C atoms at adjacent positions in the same molecule ($0.011 \times 0.011 = 0.00012$, or about 1 in 10,000). Thus, J couplings are not easily observed between two ^{13}C nuclei in ^{13}C spectra, although procedures to measure them have been developed.

Natural Sensitivity. Nuclides have differing sensitivities to the NMR experiment, as determined by the gyromagnetic ratio and the energy difference $\Delta E (= \gamma \hbar B_0)$ between the spin states (Figure 1-6) (see the fourth column in Table 1-2). The larger the energy difference, the more nuclei are present in the lower spin state (see eq. 1-1), and hence the more are available to absorb energy. With its large γ , the proton is one of the most sensitive nuclei, whereas ^{13}C and ^{15}N , unfortunately, are rather weak (Figure 1-6). Tritium (^3H) is useful to the biochemist as a radioactive label. It has $I = \frac{1}{2}$ and is highly sensitive. Since it has zero natural abundance, it must be introduced synthetically. As a hydrogen label, deuterium also is useful, but it has very low natural sensitivity. Nuclei that are of interest to the inorganic chemist vary from poorly sensitive iron and potassium to highly sensitive cobalt. Thus, it is important to be familiar with the natural sensitivity of a nucleus before designing an NMR experiment.

Receptivity. The intensity of the signal for a spin- $\frac{1}{2}$ nucleus is determined by both the natural abundance (in the absence of synthetic labeling) and the natural sensitivity of the isotope. The mathematical product of these two factors is a good measure of how amenable a specific nucleus is to the NMR experiment. Because chemists are quite familiar with the ^{13}C experiment, the product of natural abundance and natural sensitivity for a nucleus is divided by the product for ^{13}C to give the factor known as the receptivity. (See the fifth column in Table 1-2.) Thus, the receptivity of ^{13}C is, by definition, 1.00. The ^{15}N experiment then is seen to be about 50 times less sensitive than that for ^{13}C , since the receptivity of ^{15}N is 0.0219.

In addition to these factors, Table 1-2 also contains the NMR resonance frequency at 7.05 T. (See the sixth column.) The last column contains the reference substance for each nuclide, for which $\delta = 0$.

1-8 Dynamic Effects

According to the principles outlined in the previous sections, the ^1H spectrum of methanol (CH_3OH) should contain a doublet of integral 3 for the CH_3 (coupled to OH) and a quartet of integral 1 for the OH (coupled to CH_3). Under conditions of high purity or low temperature, such a spectrum is observed (Figure 1-30, bottom). The presence of a small amount of acidic or basic impurity, however, can catalyze the intermolecular exchange of the hydroxyl proton. When this proton becomes detached from the molecule by any mechanism, information about its spin states is no longer available to the rest of the molecule. For coupling to be observed, the rate of exchange must be considerably slower than the magnitude of the coupling, in Hz. Thus, a proton could exchange a few times per second and still maintain coupling. If the rate of exchange is faster than J , no coupling is observed between the hydroxyl proton and the methyl protons. Hence, at high temperatures (Figure 1-30, top), the ^1H spectrum of methanol contains only two singlets. If the temperature is lowered or the amount of acidic or basic catalyst is decreased, the exchange rate slows down. The coupling constant continues to be washed out until the exchange rate reaches a critical value at which the proton resides sufficiently long on oxygen to permit the methyl group to detect the spin states. As can be seen from the figure, the transition from *fast exchange* (upper) to *slow exchange* (lower) can be accomplished for methanol over an 80°C temperature range. Under most spectral conditions, there are minor amounts of acid or base impurities, so hydroxyl protons do not usually exhibit couplings to other nuclei. The integral is still unity for the OH group, because the amount of catalyst is small. Sometimes the exchange rate is intermediate, between fast and slow exchange, and broadened peaks are observed. The situation as regards amino protons (NH or NH_2) is similar.

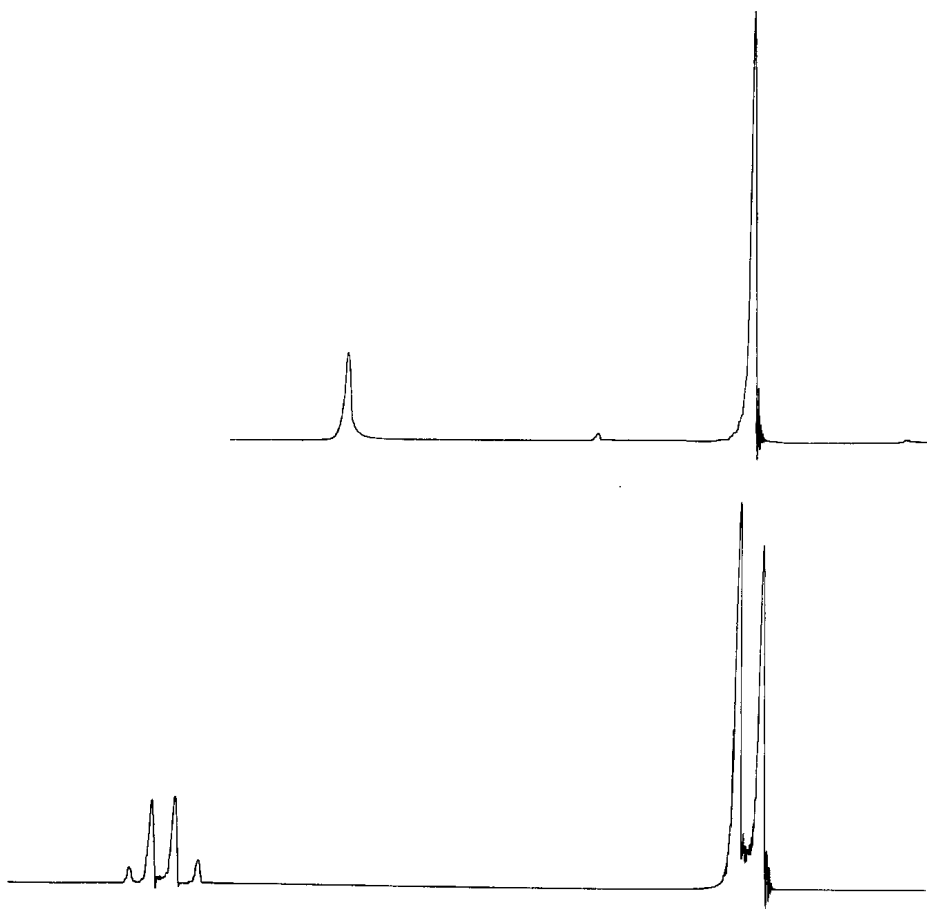
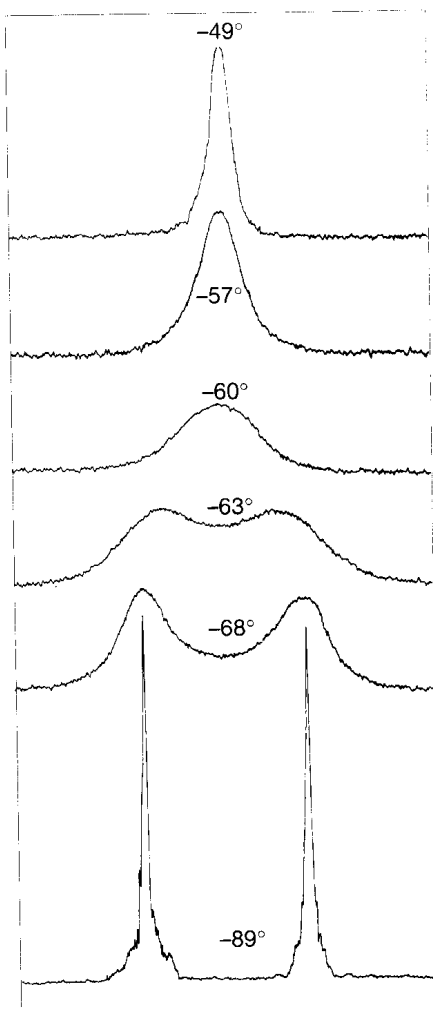


Figure 1-30 The 60 MHz ^1H spectrum of CH_3OH at $+50^\circ\text{C}$ (top) and at -30°C (bottom).

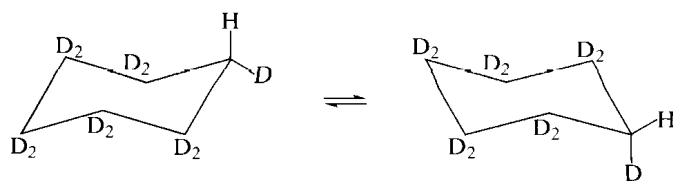
A process that averages coupling constants also can average chemical shifts. A mixture of acetic acid and benzoic acid can contain only one ^1H resonance for the CO_2H groups from both molecules. The carboxyl protons exchange between molecules so rapidly that the spectrum exhibits only the average of the two. Moreover, if the solvent is water, exchangeable protons such as OH in carboxylic acids or alcohols do not give separate resonances. Thus, the ^1H spectrum of acetic acid ($\text{CH}_3\text{CO}_2\text{H}$) in water contains two, not three, peaks: the water and carboxyl protons appear as a single resonance whose chemical shift falls at the weighted average of those of the pure materials. If the rate of exchange between $-\text{CO}_2\text{H}$ and water could be slowed sufficiently, separate resonances would be observed.

Intramolecular (unimolecular) reactions also can influence the appearance of the NMR spectrum if the rate is comparable to that of chemical shifts. The molecule cyclohexane, for example, contains distinct axial and equatorial protons, yet the spectrum exhibits only one sharp singlet at room temperature. There is no splitting, because all protons have the same average chemical shift. Flipping of the ring interconverts the axial and equatorial positions. When the rate of this process is greater (in s^{-1}) than the chemical-shift difference between the axial and equatorial protons (in Hz, which, of course, is s^{-1}), the NMR experiment does not distinguish the two types of protons, and only one peak is observed. (This situation is called *fast exchange*.) At lower temperatures, however, the process of ring flipping is much slower. At -100°C , the NMR experiment can distinguish the two types of protons, so two resonances are observed (*slow exchange*). At intermediate temperatures, broadened peaks are observed that reflect the transition from fast to slow exchange. Figure 1-31 illustrates the spectral changes as a function of temperature for cyclohexane in which all protons but one

Figure 1-31 The 60 MHz ^1H spectrum of cyclohexane- d_{11} as a function of temperature. (Reproduced with permission from F. A. Bovey, F. P. Hood, III, E. W. Anderson, and R. L. Kornegay, *J. Chem. Phys.* **41**, 2042 [1964].)



have been replaced by deuterium to remove vicinal proton–proton couplings and simplify the spectrum (1-3).



1-3

These processes that bring about averaging of spectral features occur reversibly, whether by acid-catalyzed intermolecular exchange or by unimolecular reorganization. NMR is one of the few methods for examining the effects of reaction rates when a system is at equilibrium. Most other kinetic methods require that one substance be transformed irreversibly into another. The dynamic effects of the averaging of chemical shifts or coupling constants provide a nearly unique window into processes that occur on the order of a few times per second. (The subject is examined further in Section 5-2.)

1-9 Spectra of Solids

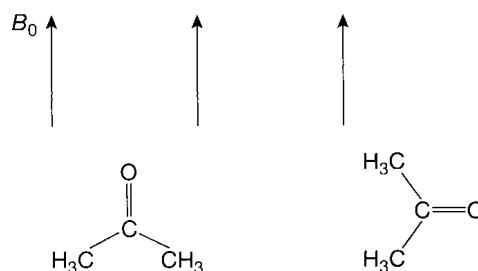
All of the examples and spectra illustrated thus far have been for liquid samples. Certainly, though, it would be useful to be able to take NMR spectra of solids, so why have we avoided discussing solid samples? Under conditions normally used for liquids, the spectra of solids are broad and unresolved, providing only modest amounts of information. There are two primary reasons for the poor resolution of solid samples. In addition to the indirect spin–spin (J) interaction that occurs between nuclei through bonds, nuclear magnets also can couple through the direct interaction of their nuclear dipoles. This *dipole–dipole coupling* occurs through space, rather than through bonds. The resulting coupling is designated with the letter D , and is much larger than J coupling.

In solution, dipoles are continuously reorienting themselves through molecular tumbling. Just as two bar magnets have no net interaction when averaged over all mutual orientations, two nuclear magnets have no net dipolar interaction because of the randomizing effect of tumbling. Thus, the D coupling normally averages to zero in solution. The indirect J coupling does not average to zero, because tumbling cannot average out an interaction that takes place through bonds. In contrast, nuclear dipoles in the solid phase are held rigidly in position, so that the D coupling does not average to zero. The dominant interaction between nuclei in solids is in fact the D coupling, which is on the order of several hundred to a few thousand hertz. One nucleus might have a dipolar coupling with several nearby nuclear spins. Since such interactions are much larger than J couplings and even than most chemical shifts, very broad signals are produced.

As with the J coupling, the D coupling may be eliminated by the application of a strong B_2 field. Power levels required for the removal of D must be much higher than those for J decoupling, since D is two to three orders of magnitude larger than J . High-powered decoupling is used routinely to reduce the line width of the spectra of solids. In practice, dipolar decoupling is most easily brought about between different spin- $\frac{1}{2}$ nuclei, as when ^{13}C is observed with decoupling of ^1H . The analogous all-proton experiment is more difficult, since both observed and irradiated nuclei have the same frequency range. Thus, the acquisition of solid-state ^{13}C spectra is much simpler than that of ^1H spectra. Quadrupolar nuclei such as ^{27}Al also are more difficult to observe.

The second factor that contributes to line broadening for solids is *chemical shielding anisotropy* (the term “chemical shift anisotropy” should be avoided in this context, since, strictly speaking, chemical shift is a scalar quantity and cannot be anisotropic). In solution, the observed chemical shift is the average of the shielding of a nucleus over all orientations in space, as the result of molecular tumbling. In a solid, shielding of a specific nucleus in a

Figure 1-32 Anisotropy of shielding in the solid state.



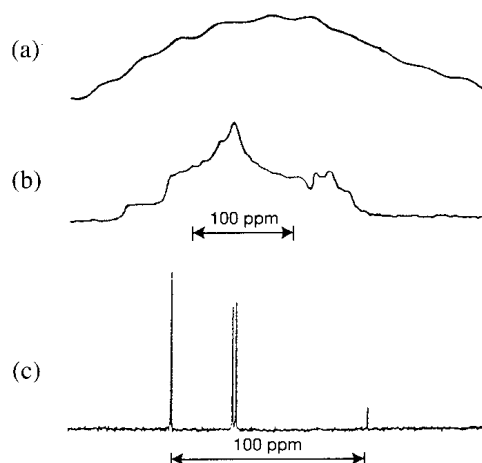
molecule depends on the orientation of the molecule with respect to the B_0 field. Consider the carbonyl carbon of acetone. When the B_0 field is parallel to the $C=O$ bond, the nucleus experiences a different shielding from when the B_0 field is perpendicular to the $C=O$ bond (Figure 1-32). The ability of electrons to circulate and give rise to shielding varies according to the arrangement of bonds in space. Differences between the abilities of electrons to circulate in the two arrangements shown in the figure, as well as in all other arrangements, generate a range of shieldings and hence a range of resonance frequencies.

Double irradiation does not average chemical shielding anisotropy, since the effect is entirely geometrical. The problem is largely removed by spinning the sample to mimic the process of tumbling. The effects of spinning are optimized when the axis of spin is set at an angle of $54^\circ 44'$ to the direction of the B_0 field. This is the angle between the edge of a cube and the adjacent solid diagonal. Spinning of a cube along this diagonal averages each Cartesian direction, just as tumbling in solution does. When the sample is spun at that angle to the field, the various arrangements of Figure 1-32 average, and the chemical shieldings are reduced to the isotropic chemical shift. The technique therefore has been called *Magic-Angle Spinning* (MAS). Because shielding anisotropies are generally a few hundred to several thousand hertz, the rate of spinning must exceed this range in order to average all orientations. Typical minimum spinning rates are 2–5 kHz, but rates up to 50 kHz are possible.

The combination of strong irradiation to eliminate dipolar couplings and magic-angle spinning to eliminate chemical shielding anisotropy results in ^{13}C spectra of solids that are almost as high in resolution as those of liquids. Spectra of protons or of quadrupolar nuclei in a solid can be obtained, but require more complex experiments. Figure 1-33 shows the ^{13}C spectrum of polycrystalline β -quinolmethanol clathrate. The broad, almost featureless spectrum at the top (Figure 1-33a) is typical of solids. Strong double irradiation (Figure 1-33b) eliminates dipolar couplings and brings out some features. Magic-angle spinning in addition to decoupling (Figure 1-33c) produces a high-resolution spectrum.

Relaxation times are extremely long for solids because the motion of nuclei necessary for spin–lattice relaxation is slow or absent. Carbon-13 spectra could take an extremely long

Figure 1-33 The ^{13}C spectrum of polycrystalline β -quinolmethanol clathrate (a) without dipolar decoupling, (b) with decoupling, and (c) with both decoupling and magic-angle spinning. (Reproduced with permission from T. Terao, *JEOL News*, **19**, 12 [1983].)



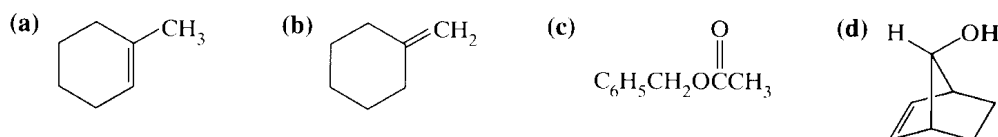
time to record because the nuclei must be allowed to relax for several minutes between pulses. The problem is solved by taking advantage of the more favorable properties of the protons that are coupled to the carbons. The same double-irradiation process that eliminates J and D couplings is used to transfer some of the proton's higher magnetization and faster relaxation to the carbon atoms. The process is called *Cross Polarization (CP)* and is standard for most solid spectra of ^{13}C . After the protons are moved onto the y axis by a 90° pulse, a continuous y field is applied to keep the magnetization precessing about that axis, a process called *spin locking*. The frequency of this field ($\gamma_{\text{H}}B_{\text{H}}$) is controlled by the operator. When the ^{13}C channel is turned on, its frequency ($\gamma_{\text{C}}B_{\text{C}}$) can be set equal to the ^1H frequency (the *Hartmann-Hahn condition*, $\gamma_{\text{H}}B_{\text{H}} = \gamma_{\text{C}}B_{\text{C}}$). Both protons and carbons then are precessing at the same frequency and hence have the same net magnetization, which, for carbon, is increased over that used in the normal pulse experiment. Carbon resonances thus have enhanced intensity and faster (protonlike) relaxation. When carbon achieves maximum intensity, B_{C} is turned off (ending the *contact time*) and carbon magnetization is acquired, while B_{H} is retained for dipolar decoupling.

The higher resolution and sensitivity of the cross-polarization-and-magic-angle-spinning experiment (CP/MAS) opened vast new areas to NMR. Inorganic and organic materials that do not dissolve may now be subjected to NMR analysis. Synthetic polymers and coal were two of the first materials to be examined. Biological and geological materials, such as wood, humic acids, and biomembranes, became general subjects for NMR study. Problems unique to the solid state—for example, structural and conformational differences between solids and liquids—also may be examined.

Problems

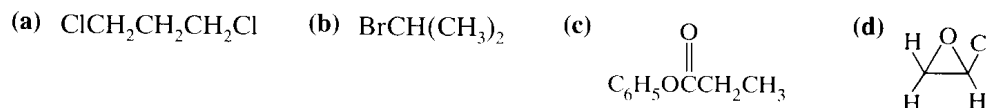
In the following problems, assume fast rotation around all single bonds:

1.1 Determine the number of chemically different hydrogen atoms and their relative proportions in the following molecules:

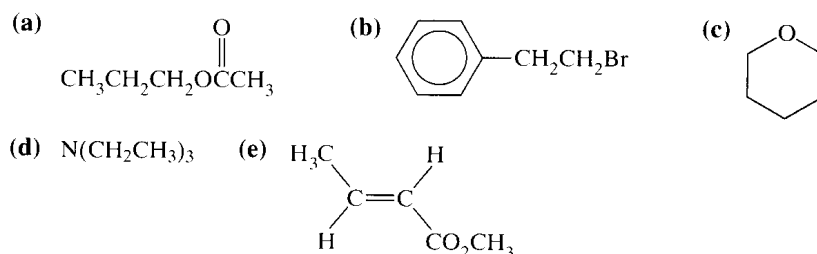


Do the same for carbon atoms.

1.2 What is the expected multiplicity for each proton resonance in the following molecules?



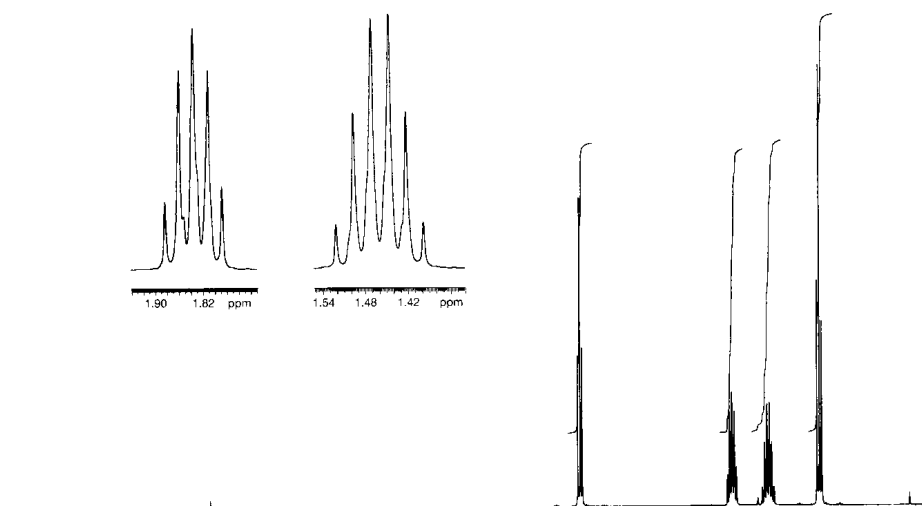
1.3 Predict the multiplicities for the ^1H and the ^{13}C resonances in the absence of decoupling for each of the following compounds:



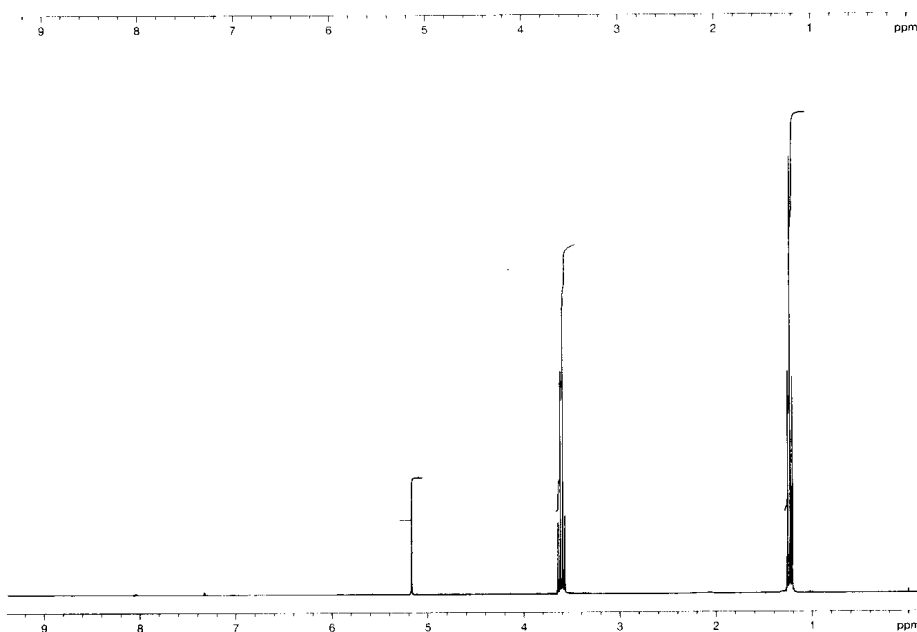
For the ^{13}C spectra, give only the multiplicities caused by coupling to attached protons. For the ^1H spectra, give only the multiplicities caused by coupling to vicinal protons (HCCH).

- 1.4 For each of the following 300 MHz ^1H spectra, carry out the following operations: (i) From the elemental formula, calculate the unsaturation number U [$U = C + 1 - \frac{1}{2}(X - N)$, in which U is number of unsaturations (1 for a double bond, 2 for a triple bond, and 1 for each ring), C is the number of tetravalent elements (C, Si, etc.), X is the number of monovalent elements (H and the halogens), and N is the number of trivalent elements (N, P, etc.)]. (ii) Calculate the relative integrals for each group of protons. Then convert the integrals to absolute numbers by selecting one group to be of a known integral. (iii) Assign a structure to each compound; be sure that your structure agrees with the spectrum in all aspects: number of different proton groups, integrals, and splitting patterns.

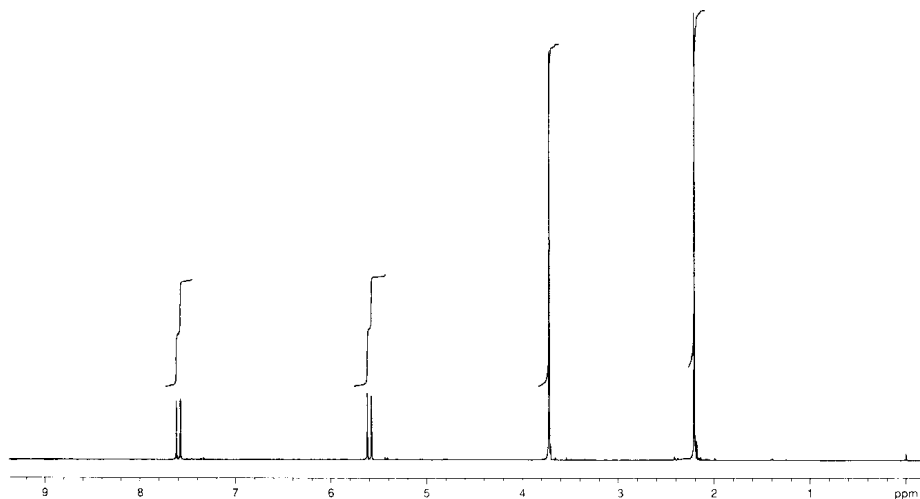
(a) $\text{C}_4\text{H}_9\text{Br}$



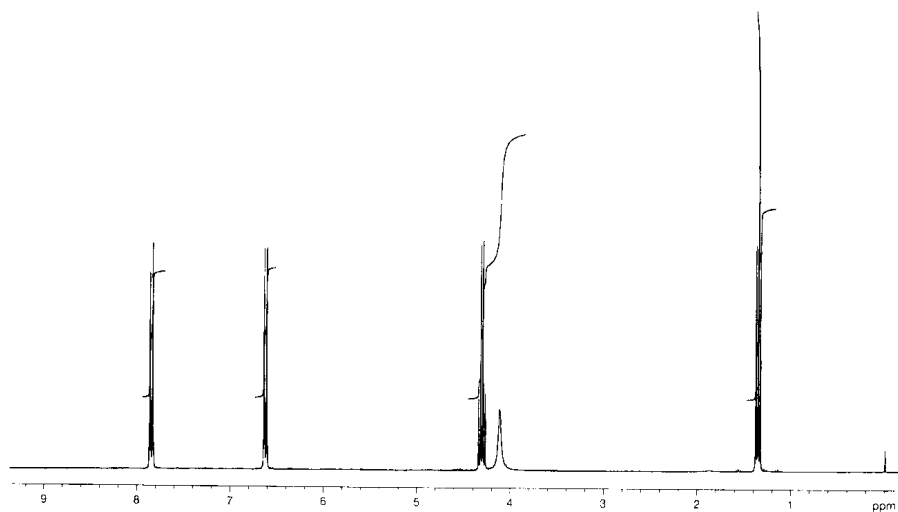
(b) $\text{C}_7\text{H}_{16}\text{O}_3$ (The resonance at δ 1.2 is a 1:2:1 triplet and that at δ 3.6 is a 1:3:3:1 quartet.)



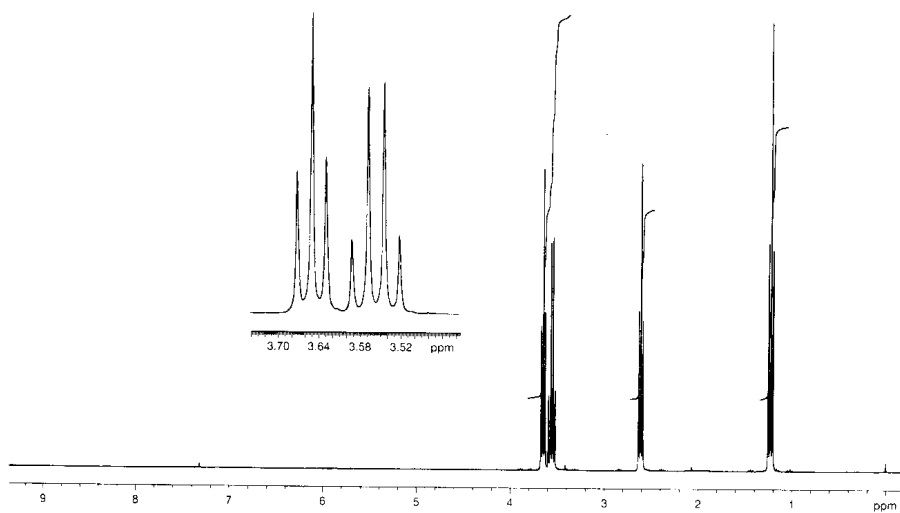
(c) $C_5H_8O_2$ (Ignore stereochemistry at this stage.)



(d) $C_9H_{11}O_2N$ (*Hint*: The highest-frequency resonances (δ 6.6–7.8) come from a *para*-disubstituted phenyl ring. They are doublets. The resonance at δ 4.3 is a quartet, and that at δ 1.4 is a triplet.)



(e) C_5H_9ON (The resonances at δ 1.2 and 2.6 are triplets.)



Bibliography

- 1.1. L. M. Jackman and S. Sternhell, *Applications of Nuclear Magnetic Resonance Spectroscopy in Organic Chemistry*, 2d ed. Oxford, UK: Pergamon Press, 1969.
- 1.2. R. K. Harris, *Nuclear Magnetic Resonance Spectroscopy*. London: Pitman Publishing, Ltd., 1983.
- 1.3. C. A. Fyfe, *Solid State NMR for Chemists*. Guelph, ON: C. F. C. Press, 1983.
- 1.4. A. E. Derome, *Modern NMR Techniques*. Oxford, UK: Pergamon Press, 1987.
- 1.5. N. Chandrakumar and S. Subramanian, *Modern Techniques in High-Resolution FT-NMR*. New York: Springer-Verlag, 1987.
- 1.6. F. A. Bovey, L. W. Jelinski, and P. A. Mirau, *Nuclear Magnetic Resonance Spectroscopy*, 2d ed. San Diego: Academic Press, 1988.
- 1.7. T. C. Farrar, *Pulse Nuclear Magnetic Resonance Spectroscopy*, 2d ed. Chicago: Farragut Press, 1989.
- 1.8. L. D. Field and S. Sternhell (eds.), *Analytical NMR*. Chichester, UK: John Wiley & Sons, Ltd., 1989.
- 1.9. H. Duddle and W. Dietrich, *Structure Elucidation by Modern NMR*. Darmstadt, Germany: Steinkopf Verlag, 1989.
- 1.10. E. Breitmaier, *Structure Elucidation by NMR in Organic Chemistry*. Chichester, UK: John Wiley & Sons Ltd., 1993.
- 1.11. J. K. M. Sanders and B.K. Hunter, *Modern NMR Spectroscopy*, 2d ed. Oxford, UK: Oxford University Press, 1993.
- 1.12. H. Günther, *NMR Spectroscopy*, 2d ed., Chichester, UK: John Wiley & Sons, Ltd., 1995.
- 1.13. E. D. Becker, *High Resolution NMR*, 3d ed. New York: Academic Press, 2000.

2

Introductory Experimental Methods

Now that the principles of NMR spectroscopy have been introduced, we will see how NMR spectra of the two most common nuclei—hydrogen and carbon-13—are obtained. The principles described for carbon-13 are applicable to many other spin- $1/2$ nuclei, such as nitrogen-15, fluorine-19, silicon-29, and phosphorus-31. Topics to be discussed include the components of a typical NMR spectrometer, preparation of a sample, signal optimization techniques, spectral acquisition, selection of processing parameters, spectral presentation, and calibration of the spectrometer.

2-1 The Spectrometer

Although a wide variety of NMR instrumentation is available, common components are (i) a magnet to supply the B_0 field, (ii) devices to generate the B_1 pulse and receive the resulting NMR signal, (iii) a probe for positioning the sample in the magnet, (iv) hardware for stabilizing the B_0 field and optimizing the signal, and (v) computers for controlling much of the operation and for processing the NMR signals.

The first NMR spectrometers relied on electromagnets and operated in the *continuous-wave* (CW) mode, much the way many of today's ultraviolet-visible spectrophotometers do. Although a generation of chemists used these spectrometers, the magnets had low sensitivity and poor stability. Less popular permanent magnets were simpler to maintain, but still had low sensitivity. Most research-grade instruments today use a superconducting magnet and operate in the *pulse Fourier transform* (commonly referred to as FT-NMR; Section 1-4) mode. These magnets have field strengths of 3.5–18.8 tesla (T) (150–800 MHz for protons) and provide high sensitivity and stability. Perhaps most important, the very high fields produced by superconducting magnets result in better separation of resonances, because chemical shifts, and hence the differences in them, (both expressed in Hz) increase with field strength. The superconducting magnet has a double Dewar-jacket arrangement, resembling a solid cylinder with a central axial hole. The outer Dewar is filled with liquid nitrogen, the inner Dewar with liquid helium. The solenoid coils are immersed in liquid helium and kept at approximately 4.2°K. The central bore tube on current solenoids is manufactured with a diameter of 53 mm or 89 mm, the latter being considerably more expensive. The bore tube is maintained at room temperature, and the direction of the B_0 field (z) is aligned with the axis of the cylinder. While most samples are examined as liquids in cylindrical NMR tubes,

the study of solid-state samples has become increasingly important for those materials that either cannot be dissolved in suitable NMR solvents or are more appropriately examined in the solid state. For liquid samples, the axis of the tube is placed parallel to the z axis of the superconducting cylinder; magic-angle spinning is used for solid samples (Section 1-9).

Separate from the magnet is a console that contains, among other components, two or more transmitter channels (up to five or more for protein NMR applications), each with a frequency synthesizer and power amplifier. The B_1 field of the transmitter in the pulse experiment is 1–40 mT. In spectrometers designed to record the resonances of several nuclides (multinuclear spectrometers), the B_1 field must be tunable over a range of frequencies. The console also has a broadband receiver and preamplifiers to magnify the inherently weak (relative to other spectroscopic methods, such as infrared and ultraviolet) NMR signals from the probe. Other standard features include a variable-temperature controller, a shim coil power supply, and an analog-to-digital converter. Optional, but very important, extras include (i) a pulsed field generator and waveform generators on one or more channels to produce shaped pulses and (ii) decoupler pulse sequences needed to irradiate specific regions of the spectrum.

Modern spectrometers typically have a dedicated acquisition controller/processor, plus a main computer. The latter is usually UNIX based with as much RAM and as much permanent data storage as possible. Ideally, one or more workstations are linked to the host computer to permit data processing and spectral plotting away from the spectrometer. In addition, a recorder to display the signals and a printer to list spectral parameters, chemical shifts, coupling constants, and integral values (all described later) are usually located next to the main computer and monitor.

The sample is placed in the most homogeneous region of the magnetic field by means of an adjustable probe that contains (i) a holder for the sample, (ii) mechanical means for adjusting the position of the holder in the field, (iii) transmitter coils for supplying the B_1 and B_2 (double-resonance) fields, (iv) coils for receiving the NMR signals, (v) coils for the field/frequency lock circuitry, and (vi) devices for improving the homogeneity of the magnetic field. The arrangement of receiver coils depends on the primary purpose of the probe. A probe used mainly for observing protons has an inner coil for ^1H detection and an outer X-nucleus coil. The inner coil is located closer to the sample to maximize the probe's sensitivity. For nuclei (including ^{13}C), other than protons, the X-nucleus coil is positioned on the inside, the ^1H -coil on the outside. Probes are available for sample tubes ranging in diameter from 30 mm down to 1.7 mm. The most common size of sample tube is 5 mm, which requires a volume of 500–650 μl of solvent. Sample tubes larger than 10 mm are generally used only for biological samples.

If a particular sample is in short supply and solubility is not a problem, microtubes (120–150 μl) and submicrotubes (25–30 μl) can be used. With their receiver coils placed very close to the small, but concentrated, samples, these microprobes are excellent at scavenging their signals. Conversely, the use of wider diameter tubes, such as 10 or 15 mm, is appropriate for (i) a relatively large amount of sample that can be readily put in solution, (ii) a relatively small quantity of sample that cannot be adequately dissolved, and (iii) the experimental examination of low-sensitivity nuclei for which microprobes have not been developed. For commonly studied nuclei, microtubes should be considered when one is *sample* limited, while large-diameter tubes should be employed when one is *solubility* limited.

There are two additional approaches to increasing the NMR signal of either small or relatively dilute (due to a high molecular weight) samples. One technique is very old and consists of increasing the magnetic field strength because sensitivity increases with the $3/2$ power of B_0 . A second, very recent, development is the construction of probes for which the receiver coils or preamplifier is kept at very low temperatures to minimize noise and, thereby, increase the signal-to-noise ratio.

2-2 Sample Preparation

The first important step in preparing a sample is the selection of good-quality NMR tubes. Tube quality is especially important for higher field spectrometers (400 MHz and up), for which only tubes of very high quality should be used. Previously used tubes should be carefully cleaned and dried prior to reuse. A suitable procedure is as follows: (i) washing with a glassware detergent solution, (ii) thoroughly rinsing (10 times or so, to remove all detergent) with water, (iii) rinsing with acetone and then diethyl ether (although methanol followed by CDCl_3 is also used), and (iv) air drying an inverted tube or drying the tube on a vacuum pump. Alternatively, NMR sample-tube cleaners that spray a jet of solvent up into the tube are available commercially. The cleaners are easily connected to a laboratory aspirator and permit large quantities of NMR tubes to be cleaned in a very short time. Tubes that cannot be cleaned completely should be discarded. Most problems with cleaning tubes are related to the evaporation of solvent from samples whose NMR spectra were determined several weeks or months previously. An obvious solution, which requires some discipline, is to make it a policy to transfer samples made up in volatile NMR solvents to inexpensive vials soon after their spectra have been recorded and then clean the NMR tubes immediately after the transfer. Chromic acid–sulfuric acid (“cleaning solution”) should never be used for NMR tubes, since paramagnetic chromium ions that remain on the glass will broaden the signals (especially from protons) of the next samples to be placed in the tubes. In addition, oven drying of NMR tubes should be avoided, since the practice may warp the tubes.

The sample must have good solubility in a solvent, which must have no resonances in the regions of interest. NMR solvents generally are deuterated to provide a ^2H lock signal (Section 2-3c). The most commonly used organic NMR solvent is CDCl_3 . For polar compounds that are sparingly soluble in CDCl_3 , CD_3OD and acetone- d_6 are good choices. $\text{DMSO}-d_6$ is an excellent solvent for polar compounds and compounds containing hydroxyl groups. $\text{DMSO}-d_6$ solutions, however, rapidly absorb water, and good vacuum pumps are required to recover samples from them. D_2O is a good solvent for highly polar and ionic compounds. If the solution to be observed is dilute, however, a water-suppression technique may have to be used because of the intense HOD solvent signal that arises from D_2O exchange with H_2O in the atmosphere. Lastly, if the spectrum is to be recorded above or below room temperature, the solvent chosen must not boil or freeze during the experiment.

Because magnetic field homogeneity is crucial to the NMR experiment (Section 2-3d), the depth to which sample tubes are filled is important. Tubes must be neither under- nor overfilled. The probe or spectrometer manual should indicate the optimum sample solution depth in the NMR tube. Underfilling the sample tube adversely affects the field homogeneity in the region of the sample, while overfilling results in a poorer signal-to-noise ratio, since some of the sample will remain outside of the receiver coils. If the NMR tube is accidentally overfilled, there are several options. If the sample in the tube represents just part of the total solution (i.e., more remains in a vial or test tube), the excess can simply be withdrawn. If, however, (i) the entire sample is in the material in the tube (ii) there is a relatively small quantity of sample, and (iii) there is not enough time to evaporate off the excess solvent, then the first option may not be attractive. In this case, consideration should be given to how the sample tube is placed in the magnet. This subject is addressed in Section 2-3a.

Solid particles remaining in the sample solution after preparation (e.g., dust, dirt, or undissolved sample) should be filtered off before the solution is transferred to the NMR tube. If the sample needs to be filtered, there are two common procedures for doing so. The first is to filter the solution through a small plug of glass wool, or a small piece of tissue, such as a Kimwipe™, that has been inserted into the tip of a transfer pipette. If glass wool is used, it is important first to rinse the glass wool filter with a small amount of the deuterated solvent, to remove any fine glass particles. A better approach is to pour the sample into a

syringe and pass it through a Millipore™, or equivalent, filter assembly. Contaminants such as phthalates, however, can be a problem with this method. Suspected particles in the NMR tube can be detected by inverting the sample tube, turning it right side up, and then holding it at about a 45° angle. Any suspended particles can be easily observed in the swirling solvent at the bottom of the sample tube as the solvent runs back down the NMR tube.

If ultrahigh-resolution NMR spectra are required, particularly for small molecules, degassing the sample to remove dissolved oxygen may be helpful. To avoid the glassblowing difficulties associated with sealing NMR tubes, screw-top tubes are commercially available. Degassing must be done when absolute relaxation times (Section 7-1) are being determined.

In practice, ¹H NMR spectra can be obtained from less than 1 μg of material, although the result depends on the molecular weight of the compound in question, the magnet field strength, the design of the probe, and the preparation of the sample, among other factors. ¹³C NMR spectra typically require samples in the milligram range. Micro- and submicro-probes have recently pushed this limit down to the nanogram and microgram ranges for proton and carbon spectra, respectively.

2-3 Optimizing the Signal

2-3a Sample Tube Placement

The positioning of the NMR sample tube in the probe, which in turn is in the magnet, is another factor to be considered. Correct NMR tube placement in the *spinner turbine* (why sample tubes are spun during spectral acquisition is discussed in Section 2-3d) is usually accomplished in one of two ways. Most instrument and probe manufacturers provide depth charts, which show a drawing of the spinner turbine containing an NMR tube. A much better means of ensuring proper tube placement is through the use of a *depth gauge*, which can be purchased from spectrometer manufacturers or made by a machine shop. In either case, the NMR tube is inserted into the spinner turbine, and the turbine either is placed against the depth chart or is inserted into the depth gauge. The sample tube is then pushed down until the bottom matches the drawing on the depth chart or touches the bottom of the depth gauge.

Proper placement of the NMR tube in the spinner turbine is important. If the tube is not inserted far enough, some of the sample will be outside of the receiver coils. (The effect is similar to overfilling the sample tube.) If the tube is inserted too deeply, the consequences can be far worse. Temperature sensors, glass inserts, etc., are located in nearly all probes at depths slightly below where the bottom of a sample tube should be. An NMR tube that has been inserted too far could easily damage the very expensive probe and, again, place some of the sample outside of the receiver coils. In the previous section, the question was raised concerning accidental overflow of an NMR tube when removal of the excess sample is not a viable option. An answer may present itself in the nature of the depth chart or gauge. Some of these guides indicate the location of the center of the receiver coils. If this information is given, the overfilled sample tube may be able to be positioned so that the receiver coils are centered with respect to the height of the solution. Then, some of the sample will be above the RF coils, and an equal amount will be below. It is important, however, to remember that this maneuver will work only if further insertion of the NMR tube will not take it below the maximum depth of the tube.

2-3b Probe Adjustment

The NMR experiment is plagued by the twin problems of sensitivity and resolution. In order to achieve maximum sensitivity, modern probes are designed to give optimum performance over a narrow frequency range. Therefore, they must be carefully adjusted to match the specific frequency of the sample and dielectric constant of the solution. Probes usually have a *tuning* capacitor and a *matching* capacitor for each coil. The first part of the adjustment process (tuning) sets the coil to the radiofrequency of the nucleus being studied. (See, e.g.,

Table 1-2). This operation is analogous to rotating a radio knob to the desired station. Proper tuning is necessary for optimum probe sensitivity. The second part of the adjustment process (matching) sets the total effective resistance (i) to an alternating current (impedance) of the coil, (ii) to the solvent with the sample, and (iii) to the NMR tube equal to that of the transmitter and receiver. Matching is required for passage of the maximum possible radiofrequency energy from the transmitter to the sample and then on to the receiver. Adjustment of the two capacitors is interactive, and at least two cycles of probe tuning are typically required. The tuning procedure is carried out by adjusting the capacitors to give either (i) a minimum level on a probe-tuning meter or an oscilloscope display or (ii) a V-shaped signal that is horizontally (indicating a tuning error) or vertically (indicating a matching error) displaced from its correct position. Probe-tuning circuits are delicate, and tuning should be done very carefully.

As was discussed earlier in the chapter, probes typically include two coils: ^1H and X nucleus (e.g., ^{13}C or ^{15}N). The inner (or observation) coil is more sensitive and requires more careful adjustment. Normal ^1H NMR spectra usually have such good signal-to-noise ratios that probe tuning is not critical for relatively concentrated samples. Tuning, however, is very important for both one- and two-dimensional X-nucleus-detected experiments and for many two-dimensional ^1H -detected techniques. A surprising number of these experiments have failed simply because the X coil was not tuned to the correct nucleus! In addition, if X-nucleus detection is to be conducted with proton broadband decoupling, as is usually the case (Section 1-5), then it is important that the ^1H decoupling coil also be tuned optimally.

2-3c Field/Frequency Locking

All magnets are subject to field drift, the effects of which can be compensated by electronically locking the field to the resonance of a substance contained in the sample. In pulsed experiments, the nucleus to whose signal the magnetic field is to be locked cannot be of the same type that is being either observed or decoupled. Thus, ^1H cannot be used for locking. Deuterium, however, is an excellent candidate for the role of lock nucleus. Almost all common organic solvents have protons that can be replaced by deuterons. A large variety of deuterated solvents are frequently used for this purpose and are available commercially. The type of lock just described is called an *internal* lock. By contrast, in some instruments, the field is locked to a sample contained in a separate tube permanently located elsewhere in the probe. This type of *external* lock is mostly found in spectrometers designed for a highly specific use, such as taking only ^1H spectra in the CW mode or studying solid-state samples.

In the former case, an internal lock is established at the deuterium frequency of the solvent by adjusting the frequency of the lock transmitter until it matches that frequency. The operator typically observes a decreasing number of interference-pattern sine waves as the lock transmitter frequency approaches that of the deuterium nuclei in the solvent. A null appears when the two frequencies are identical; the operator then turns the lock control to "On." On most modern spectrometers, autolocking procedures are also available that search for the deuterium resonance and automatically lock the spectrometer when the signal is found.

The deuterium lock system can be regarded as another NMR experiment being conducted simultaneously, and largely invisibly, with the desired one. Just as there is an observation transmitter and receiver for the nucleus of interest, so there is a lock transmitter and receiver for the deuterium nucleus. The stability of the lock signal depends on (i) the magnetic field homogeneity, (ii) the power of the lock transmitter, and (iii) to a much lesser degree, the phase of the lock signal. Certain lock signal behavior is indicative of specific problems. If the lock signal bounces up and down *erratically*, there may be suspended particles in the sample that have to be filtered off. If the lock signal bounces in a *rhythmic* fashion, the lock power is set too high, and the lock signal is becoming saturated. A simple test for saturation is to lower the lock power and observe the lock level. If saturation is taking place, the lock level falls initially, but then climbs back to a higher level than before.

It is important to avoid lock instability due to either saturation or suspended particles, because instability interferes with magnet field regulation by the lock channel and, in severe cases, can result in loss of the lock signal altogether. When a stable lock level is achieved somewhere around midrange, the *lock phase* (see next subsection) should be maximized. Only an approximately maximum lock phase, however, is desired at this point, because the lock phase is dependent on the homogeneity of the magnetic field.

2-3d Spectrometer Shimming

As stated previously, the NMR experiment suffers inherently from both sensitivity and resolution problems. Peak separations of less than 0.5 Hz may need to be resolved, so the B_0 field homogeneity must be uniform to a very high degree. (For a separation of 0.3 Hz at 300 MHz or 0.5 Hz at 500 MHz, the field homogeneity must be better than 1 part in 10^9). The stringency of this homogeneity requirement can, perhaps, be appreciated by considering it in optical terms. James Shoolery, of Varian NMR Systems, has suggested that such resolution corresponds to training a telescope on the moon and being able to distinguish two cats separated by one cat length. Corrections to field homogeneity are made for small gradients in B_0 by the use of *shim coils*, in a process called *shimming*. The name derives from the early days of NMR, when small pieces of nonmagnetic metal (shims) were used to improve the homogeneity of electromagnets by changing the distance between the halves of the magnet. For today's magnets, the field along the z direction usually is slightly greater at one point than another. Such a gradient may be compensated for by applying a small current through a shim coil built into the probe. Shim coils are available for correcting gradients in all three Cartesian coordinates (primary gradients, x , y , and z), as well as higher order (z^2 , x^3 , z^4 , etc.) and combination (xz , yz , x^2-y^2 , and so on) gradients.

The amount of shimming required depends on (i) how well the sample was prepared (Section 2-2), (ii) the quality of the initial shim set, and (iii) whether very high resolution is required for the sample in question. Therefore, after placing a sample in the magnet, tuning the probe, and engaging the field/frequency lock, the operator adjusts the various homogeneity controls to achieve a highly homogeneous magnetic field in the region of the sample. One approach is to optimize, as nearly as possible, the primary and secondary spinning controls (z and z^2 for superconducting magnets, y and y^2 for permanent magnets or electromagnets) and take a quick proton spectrum to assess the homogeneity of the magnet. If the proton spectrum is reasonably good in terms of exhibiting a symmetrical line shape and overall appearance, the operator can proceed to shim the magnet as described next. If, however, the ^1H NMR spectrum indicates that the homogeneity is quite poor, the operator might recall a stored shim set (for the *same* probe, either from (i) an earlier ^1H spectrum taken with, ideally, the same solvent or from (ii) the NMR laboratory shim library if such a library has been created). In either case, this set can provide a starting shim set.

Shimming may be carried out either by maximizing the lock level or by adjusting with a strong signal in the sample. The former procedure is simpler to carry out, but the latter is better if very high resolution is critical. Shimming in the latter case is done by maximizing the area of the free-induction decay (FID) signal and not by actually observing a resonance in the spectrum. In either case, it is important to remember that shimming is an interactive process. As the field homogeneity is improved and the lock level thereby increased, the phase of the lock signal (analogous to that of NMR signals, Section 2-6a) must also be readjusted for a maximum lock signal level at the start of each cycle of the shimming procedure.

Normally, the sample is spun for one-dimensional experiments along the axis of the NMR sample tube at a rate of 20–25 Hz by an airflow, in order to improve the magnetic-field homogeneity. Spinning improves the resolution of the spectrum because the field near a nucleus at a particular location in the tube is averaged over a circular path. In a superconducting magnet, the axis of the NMR tube is in the z direction, while in electromagnets it lies along the y axis. Spinning does not average gradients along the axis of the NMR tube, so shimming is required primarily for the z gradients of a superconducting magnet or the y

gradients of an electromagnet. If there are significant spinning sidebands (signals on either side of an intense signal at a distance from the central signal that is equal to the spinning frequency), however, then adjustment of the nonspinning gradient (x_y or x_z) is recommended.

Shimming is an art, and sometimes there seem to be almost as many shimming routines as there are NMR spectroscopists. Before magnet shimming is undertaken, the lock level should be set to midrange. Just as saturation of the lock signal due to excess lock power (Section 2-3c) must be avoided, lock levels that are too high because of the lock gain setting also are undesirable. It is difficult to see whether the lock level is being improved by the shimming process when that level is very close to the maximum value. An exhaustive shimming procedure is given by Braun et al. (1998). The following abbreviated method for superconducting magnets suffices in most cases. (1) With the sample spinning, adjust Z1 and Z2 (*coarse* and then *fine*) interactively for a maximum. (2) With the spinner turned off, interactively maximize Z1 and the lower order, nonspinning controls (X, Y, XZ, and YZ). (3) Turn the spinner back on, and when the spinning speed has returned to its original value, interactively adjust the higher order Z controls (Z3, Z4, and Z5 if present). (4) With the spinner again turned off, interactively maximize the higher order, nonspinning controls (X2-Y2, X3, Y3, etc.). If good proton spectra can be recorded in eight or fewer scans, it is helpful to take such spectra somewhere between the steps just listed to see how—or if—the spectra are improving with shimming. If major changes in lock level or FID area are noted for the steps beyond the Z1, Z2 optimization, the first step and possibly others, depending on the appearance of the test spectra, should be repeated. For two-dimensional spectra, which are performed *without* sample spinning, the z controls should, likewise, be adjusted with the sample not spinning.

In practice, with a well-prepared sample and a good starting shim set, it is frequently not necessary to go beyond the first step. If additional shimming is required, then the computerized shimming routines included in the spectrometer software can be of great help. These automatic procedures iteratively optimize sets of interacting gradient shim coils. They are particularly useful in dealing with lock signals that are relatively insensitive to small changes, since the operator often has little idea as to whether a specific shim control is being moved in the correct direction during shimming.

The results of shimming are best judged by observing spectral (most often proton) line shapes. Examples of NMR signals in which one or more shims are misadjusted are shown in Figure 2-1. If one of the odd-order gradients is misset, the resulting line is *symmetrically*

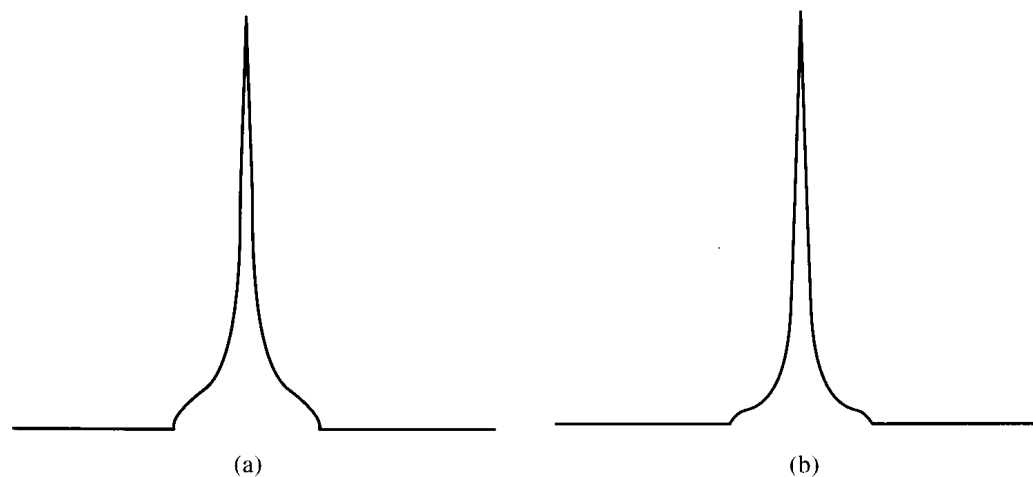


Figure 2-1 Effects of misadjusted shim settings. (a) Z3 misset. (b) Z5 misadjusted. (c) Z2 misset. (d) Z4 misadjusted. (e) First-order spinning sidebands: X, Y, XZ, and YZ misset. (f) Second-order spinning sidebands: XY and X2-Y2 misadjusted on top of first-order sidebands. (g) High-order nonspin shims: X3, Y3, Z3X, and Z3Y misset. (h) Z1, Z2, and Z4 misadjusted. These spectral effects have been exaggerated for the purpose of illustration. (Courtesy of Varian Inc. Technical Publications.)

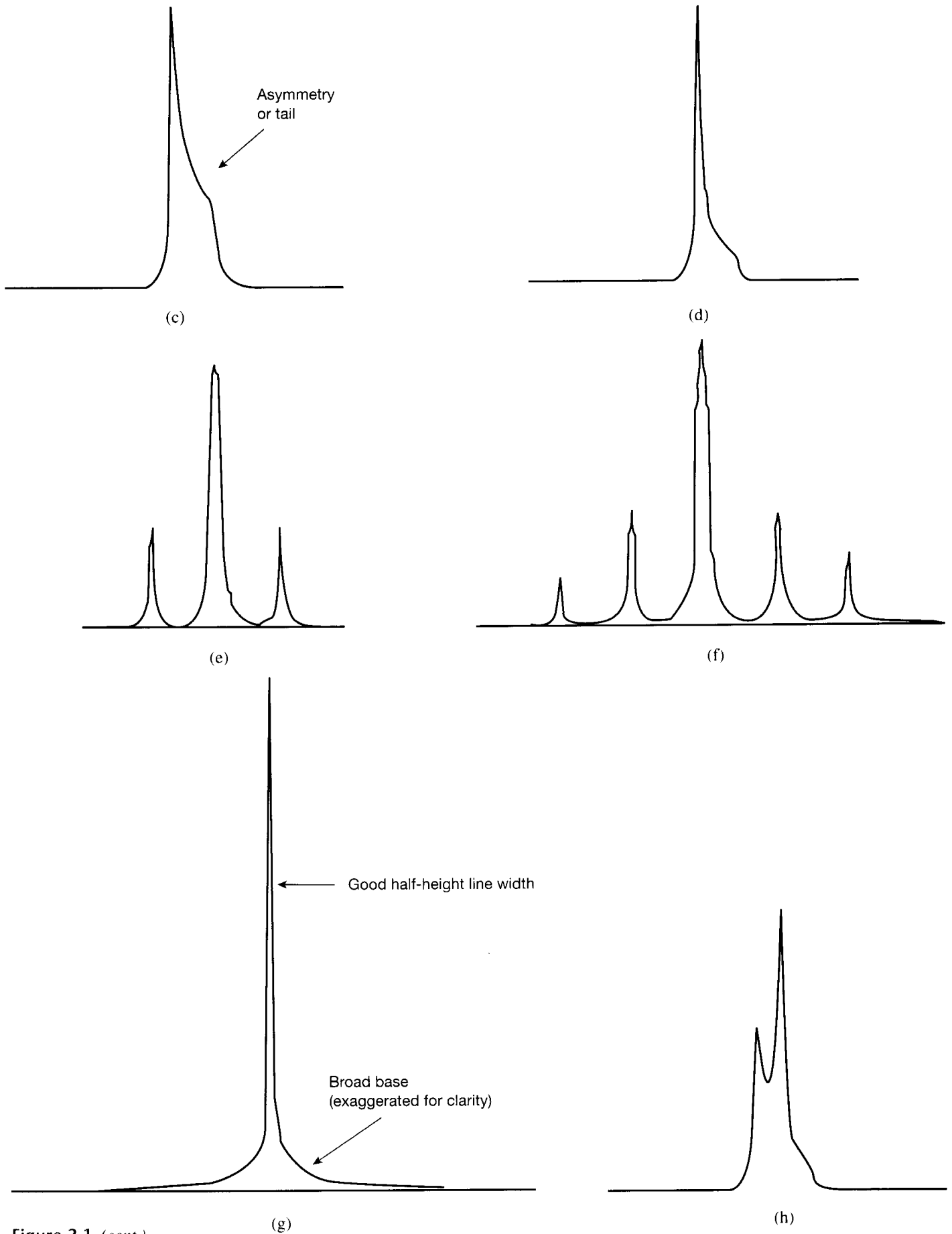


Figure 2-1 (cont.)

broadened, considerably so for Z1. If Z3 or Z5 is misadjusted, as in (a) and (b), respectively, the amount of broadening not only is less, but occurs closer to the baseline for increasingly higher order gradients. Thus, the Z5 line broadening in (b) can be seen to appear lower on the signal than the Z3 broadening in (a).

If Z2 or Z4 is misset, as in (c) and (d), respectively, the resulting signal is *asymmetrically* broadened. The same inverse relationship between the height of the line-broadening effect and the order of the gradient is observed for these even-order gradients. Likewise, Z2 broadening in (c) appears higher on the signal than that of Z4 in (d). In addition, the *direction* of the asymmetry (to a higher or lower frequency) is related to both the sign of the misadjustment in the gradient and the manufacturer of the magnet. In the examples shown in Figures 2-1c and d, asymmetric broadening occurs on the low-frequency (up-field) side of the signal when Z2 or Z4 is misset in a positive sense (i.e., is too large). If Z2 or Z4 is misadjusted in a negative sense (i.e., is too small), then the asymmetry appears on the high-frequency (downfield) side of the resonance line. For magnets having the opposite polarity, the Z2 and Z4 asymmetries just described are reversed.

When the sample is poorly adjusted without spinning, *x* and *y* gradients produce unusually large spinning sidebands. These sidebands occur on either side of a signal (commonly, a sharp single line) and are separated from it by multiples of the spinning speed (e.g., 20 Hz or 20 and 40 Hz). If a first-order shim (X, Y, XZ, or YZ) is misset (Figure 2-1e), then disproportionately large first-order (inner) spinning sidebands are observed. Conversely, if XY or X²-Y² are misadjusted, then atypically large second-order (outer) sidebands appear. First- and second-order spinning sidebands are seen (Figure 2-1f) when members of both of the preceding shim groups are misset. Lastly, misadjustment of a higher order, nonspinning shim (X³, Y³, Z³X, or Z³Y) results in broad signal bases (Figure 2-1g). In most cases, of course, several shims are misset, giving rise to complex line shapes and complicating the foregoing visual analysis. Such an example is (Figure 2-1h), in which Z1 can be misadjusted in either direction, Z2 is too small, and Z4 is too large. Note that for well-maintained NMR spectrometers, usually nothing more than Z1 and Z2 adjustment is required for each sample.

An alternative, rapid, and highly effective approach to shimming is available for spectrometers with pulsed field gradient accessories and probes with gradient coils (Section 6-6). The procedure is known as *gradient shimming*. The pulse gradient accessory can be used to generate a field map of inhomogeneity along a particular axis and then determine the optimum settings for the shim coils relevant to that axis. In most cases, probes contain only a z gradient coil; therefore, only the Z1-Z5 controls can be optimized in this manner. These controls, however, are the most critical, and this method is highly recommended if the appropriate gradient accessories are available.

2-4 Determination of NMR Spectra: Acquisition Parameters

In the FT-NMR experiment, a number of acquisition parameters must be considered before NMR data are collected. The first of these parameters is *spectral resolution*, which is controlled directly by the amount of time taken to acquire the signal. To distinguish two signals separated by $\Delta\nu$ (in Hz), data must continue to be acquired for at least $1/\Delta\nu$ seconds. For example, a desired resolution of 0.5 Hz in a ¹³C spectrum requires an acquisition time of $1/0.5$ Hz, or 2.0 s. Sampling for a longer time would improve the spectral resolution; for example, acquisition for 4.0 s would yield a resolution of 0.25 Hz. Thus, longer acquisition times are necessary to produce narrower lines until the natural line width is reached.

A second parameter concerns the range of frequencies (the *spectral width*) to be detected. The spectral width is determined by how often the detector samples the value of the FID—that is, the *sampling rate*. The FID is made up of a collection of sinusoidal signals

Figure 2-2 (a) Sampling a sine wave exactly two times per cycle. (b) Sampling a sine wave less than twice per cycle. (c) The lower frequency sine wave that contains the same points as in (b) and is sampled more than twice per cycle. The frequency of (b) is not detected, but appears as an aliased peak at the frequency of (c). (Reprinted with permission from J. W. Cooper and R. D. Johnson, *FT NMR Techniques for Organic Chemists*, IBM Instruments, Inc., 1986.)

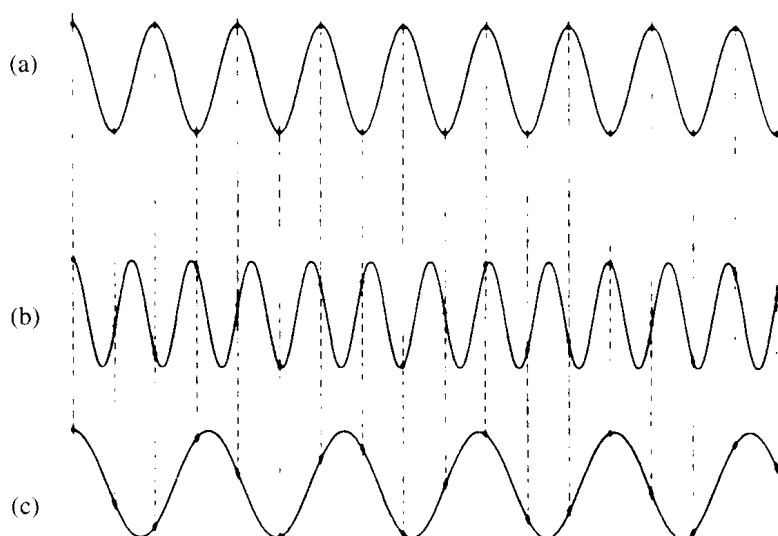


(Figure 1-16). A single specific signal must be sampled at least twice within one sinusoidal cycle (the Nyquist condition) to identify its frequency. For a collection of signals up to a frequency of N Hz, the FID thus must be sampled at a rate of $2N$ Hz. For example, for a ^{13}C spectral width of 20,000 Hz (200 ppm at 100 MHz), the signal must be sampled 40,000 times per second. Figure 2-2 illustrates this situation. The top signal (a) is sampled exactly twice per cycle. (Each dot represents a sampling.) The higher frequency signal in (b) is sampled at the same rate, but not often enough to identify its frequency. In fact, the lower frequency signal in (c) gives exactly the same collection of points as in (b). A real signal from the points shown in (b) is indistinguishable from an *aliased*, or *fold-over*, signal (discussed in Section 2-4b) with the frequency illustrated in (c). For the aforementioned example of ^{13}C , if the spectral width is reduced to 10,000 Hz (100 ppm at 100 MHz) and sampled only 20,000 times per second, a signal with a frequency of 150 ppm (15,000 Hz) appears as a distorted peak in the 0–100-ppm region. In this case, the highest frequency that can be accurately identified is half of the sampling rate, or 10,000 Hz. Since the test frequency is greater than the maximum allowed frequency, the degree of aliasing of this signal is then calculated: $15,000 \text{ Hz}_{\text{actual}} - 10,000 \text{ Hz}_{\text{limit}} = 5,000 \text{ Hz} = 50 \text{ ppm at } 100 \text{ MHz}$.

If a signal is sampled 20,000 times per second, the detector spends $50 \mu\text{s}$ on each point. The reciprocal of the sampling rate is called the *dwelt time*, which signifies the amount of time between samplings. Reducing the dwelt time means that more data points are collected in the same period, so that a larger computer memory is required. If the acquisition time is 4.0 s (for a resolution of 0.25 Hz) and the sampling rate is 20,000 times per second (for a spectral width of 10,000 Hz) the computer must store 80,000 data points. Making do with fewer points because of computer limitations would require either lowering the resolution of the spectrum or decreasing its spectral width.

In the early days of FT-NMR, the dedicated spectrometer computers were quite slow by today's standards and had very limited memory. Consequently, NMR spectroscopists had to consider a trade-off between spectral width and resolution. Today, we are fortunate to have dedicated computers that are very fast and have abundant memory. For the most part, NMR spectroscopists now can let science, rather than computer limitations, dictate how they set the parameters of their experiments.

Like the shim libraries of many NMR laboratories discussed in Section 2-3d, spectrometers usually have standard sets of proton and ^{13}C acquisition parameters that will suffice in most routine instances. It is important, however, to have an understanding of these spectral parameters and their interaction.

2-4a Number of Data Points

The computer algorithms that carry out the discrete Fourier transform calculation work most efficiently if the number of data points (np) is an integral power of 2. Generally, for basic ^1H and ^{13}C spectra, at least 16,384 (referred to as “16K”) data points, and 32,768 (“32K”) points should be collected for full ^1H and ^{13}C spectral windows, respectively. With today’s higher field instruments and large-memory computers, data sets of 64K for ^1H and 64–128K for ^{13}C and other nuclei are now commonly used.

2-4b Spectral Width

The spectral width (sw) is the range of frequencies over which NMR signals are to be detected and, of course, represents the range of frequencies over which these signals are expected. For ^1H NMR, this range is usually less than 10 ppm, but, on rare occasions, can be as large as 20 ppm (Chapter 3). For ^{13}C NMR, the normal range of frequencies can exceed 220 ppm (also Chapter 3), and ^{13}C spectral widths are typically set at 220 ppm. Which spectral width is used for ^1H NMR depends on whether the sample is a known or an unknown compound. If it is the former, with no unusually deshielded protons (resulting in signals at a very high frequency, or downfield), a 10-ppm spectral width almost always suffices. If the identity of the sample is unknown to the operator, an initial 15-ppm spectral width might be appropriate, just in case there are any unexpected high-frequency signals. If none are present, succeeding ^1H NMR spectra can be with the use of a standard 10-ppm spectral width.

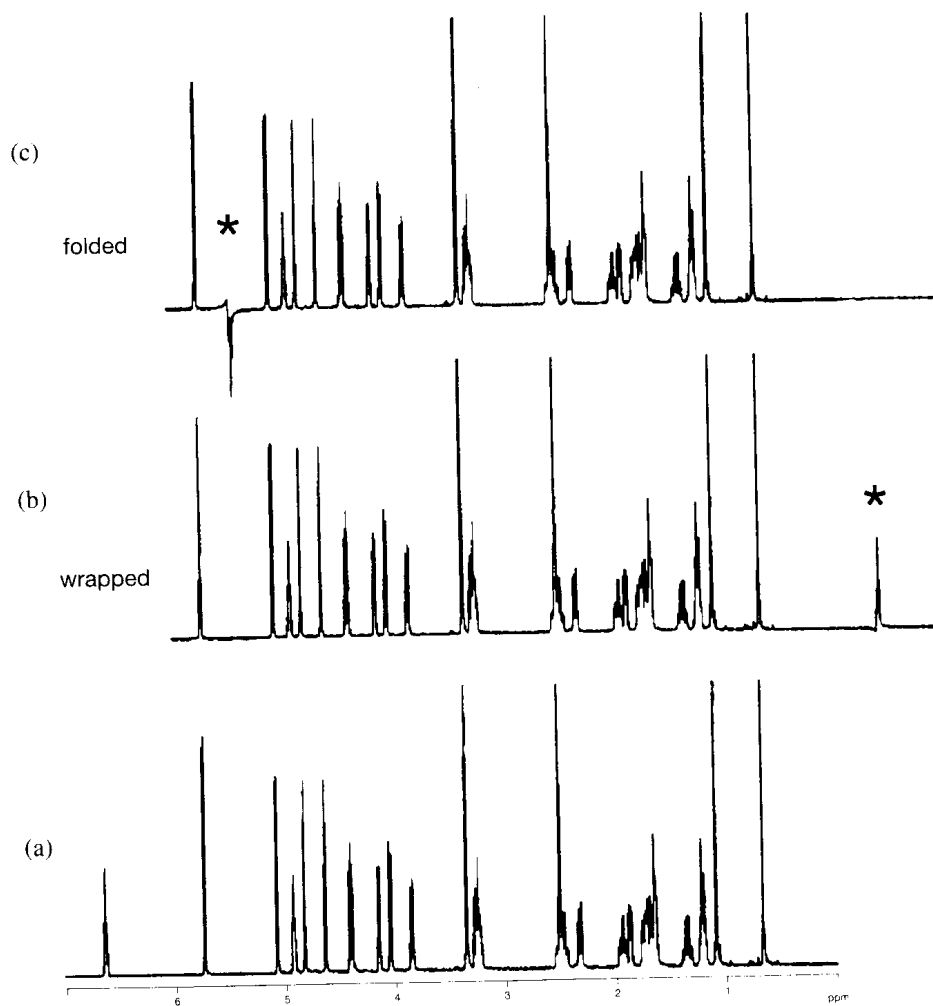
At the beginning of this section, the concept of aliasing, or fold-over, was discussed in terms of the sampling rate. A signal whose frequency lies outside of the spectral window was described as appearing as a distorted peak at a frequency inside the spectral window. Just how such aliasing of signals occurs depends on the manner in which the detection of the signals is done. Quadrature phase detection (Section 5-8) is now standard practice on all modern spectrometers and is accomplished in one of two ways: using two phase-sensitive detectors whose reference phases differ by 90° and using only one detector, but incrementing the phase of the receiver by 90° after each measurement. It is important for the operator to know which type of quadrature detection method is being used, because these two methods produce very different results with respect to aliased signals.

NMR signals that are aliased appear in the spectral window in one of the following two ways. If a single phase detector is used, signals fold into the spectral window on the *same* side on which they are situated. Thus, higher frequency resonances fold in at the high-frequency end and vice versa (Figure 2-3c). If two phase detectors are employed, signals wrap into the spectral window on the side *opposite* that where they are located. For example, resonances that lie outside of the spectral window to higher frequencies wrap into the window at the low-frequency end (Figure 2-3b), while those that are at lower frequencies wrap in at the high-frequency end (not illustrated).

When the operator suspects the presence of an aliased signal, the testing procedure for such aliasing also depends on the type of quadrature detection being used. For either type of quadrature phase detection system, the sw parameter can be significantly increased. The position of the putative aliased resonance then changes in relation to the rest of the signals.

In addition, for single-phase detection systems, the transmitter offset (Section 2-4e) can be changed by several hundred Hz. The position of a supposed folded signal then moves in a direction opposite that of the rest of the resonance lines. The transmitter offset-changing test procedure assumes that folding has occurred an *odd* number of times. Multiple folding is virtually unheard of for ^1H and ^{13}C NMR. It is something, however, for which the operator should be watchful in the investigation of less common nuclei, because in that case signals tend to be few in number and chemical shift ranges often are very large. When folding takes place an *even* number of times, it is more difficult to detect because the change in the transmitter offset test may not work. (All of the resonances may move in the *same* direction.) Increasing the sw also may not be a definitive test for either type of quadrature

Figure 2-3 Aliasing of signals. (a) Normal spectrum, with all of the signals at their correct chemical shifts. (b) The highest-frequency signal has wrapped around into the spectrum at the lowest-frequency end. (c) The same signal has folded back into the spectrum at the high-frequency end. The appearance of aliased signals (denoted by an asterisk) is distorted in both cases. (Reprinted from T. D. W. Claridge, *High-Resolution NMR Techniques in Organic Chemistry*, 1999, p. 63; with permission from Elsevier Science.)



detection system if the multiply (even number) aliasing signal is the only one in the spectrum. Here, the sw has to be reduced, perhaps several times, and the position of the resonance noted until the signal is made to fold, or wrap, an odd number of times.

2-4c Filter Bandwidth

In addition to signals that lie accidentally outside of the spectral window, noise also folds, or wraps, back into the spectrum. Such noise can be greatly reduced by placing filters near the edges of the desired spectral window. Care must be taken, however, in positioning the filters, since they do not cut off sharply and can reduce the intensities of signals near the ends of the spectrum. The positioning of filters is controlled by a parameter known as the *filter bandwidth*, which typically has values from 1.1 to 1.25 sw . In general, the filter bandwidth is automatically set by the spectrometer software once the spectral width has been selected.

2-4d Acquisition Time

The acquisition time (t_a) is related to the two previous parameters by the formula

$$np = 2(sw)t_a \quad (2-1)$$

For ^1H spectra determined with $np = 32\text{K}$ and $sw = 4,000$ Hz (10 ppm at 400 MHz), t_a is approximately 4.1 s. For ^{13}C spectra recorded with $np = 32\text{K}$ and $sw = 22,000$ Hz (220 ppm at 100 MHz), t_a is about 0.75 s. The acquisition time normally is set by the spectrometer after the number of data points and spectral width have been selected.

2-4e Transmitter Offset

The transmitter offset describes the location of the observation frequency and is closely related to the spectral width. With quadrature phase detection of sample signals (Section 5-8), the frequency of the transmitter is positioned in the middle of the spectral width. In so doing, the operator has the best chance of irradiating, with equal intensity, those nuclei whose resonances are both close to and far from the transmitter frequency. Irradiation is not a problem for protons, with their small chemical shift range, but it can be for nuclei with large chemical shift ranges (Chapter 3).

Standard sets of acquisition parameters include typical transmitter offset values. If wider spectral widths are required, simple trial and error with concentrated samples or standards permits the operator to widen the spectral window in a selective manner. For example, the operator may suspect the presence of highly deshielded ^1H signals and wish to open the ^1H spectral width from the usual 10 ppm (4,000 Hz at 400 MHz) to 15 ppm (6,000 Hz). In order to add all of the additional 5 ppm (2,000 Hz) worth of sw capacity to the *downfield* (high-frequency) end of the spectral range (i.e., from 10–15 ppm), the transmitter offset value is increased by approximately 2.5 ppm (1,000 Hz at 400 MHz). This procedure also keeps the transmitter offset positioned in the middle of the widened spectral window.

2-4f Flip Angle

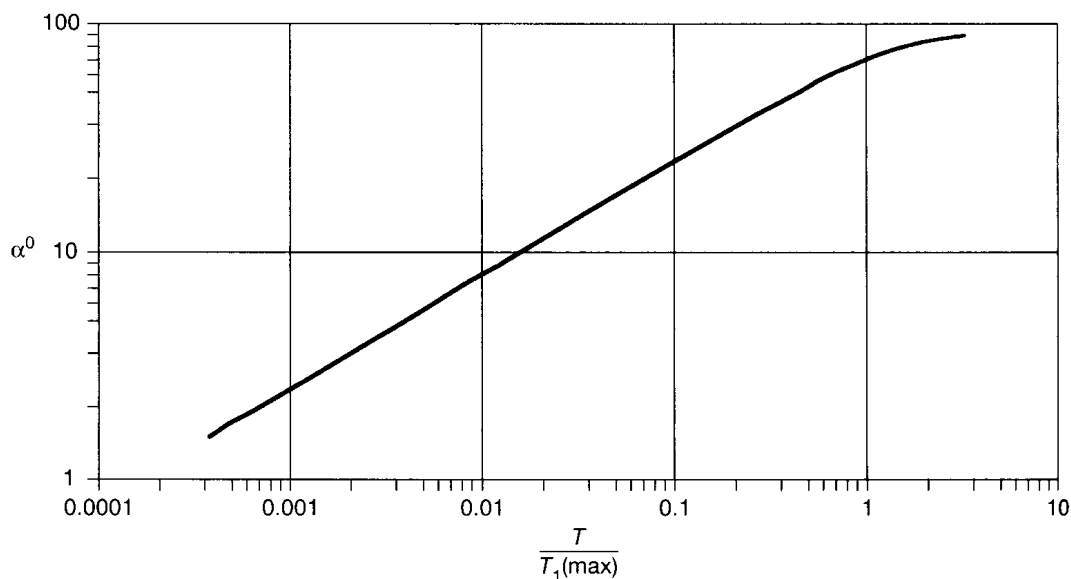
The flip-angle (α) parameter has generated considerable debate. The root of the problem can be seen in Figure 1-13. If we have a *given* amount of time in which to record spectral data, the signal can be acquired in basically two ways: (i) we can use a series of 90° pulses (as in Figure 1-13c) and wait a certain length of time (the acquisition time, plus a relaxation delay time) between pulses for the equilibrium magnetization (M_{z0}) to be reestablished, or (ii) we can employ a series of shorter pulses (as in Figure 1-13b, where θ might be 30°) without any waiting time between them. With the latter approach, M_{z0} has to be entirely reestablished during t_a .

The flip-angle problem can be resolved by the following analysis. Let us subject a generalized nuclear vector to a series of pulses of various duration, as shown in Figure 1-13, and find out how much of the original magnetization is deposited on the y axis for detection by the receiver. We already have seen that a 90° pulse aligns *all* of the starting magnetization along the y axis (Figure 1-13c). By contrast, a 30° pulse positions the magnetization at a 30° angle to the z axis (similar to that shown in Figure 1-13b). Trigonometry demonstrates that the quantity of magnetization deposited on the y axis bears a sinusoidal relationship to the angle θ . Therefore, a 30° pulse places *half* of the original magnetization ($\sin 30^\circ$) on the y axis, but also leaves approximately 87% ($\cos 30^\circ$) remaining aligned along the z axis. Consequently, recovery of the z magnetization is considerably faster if 30° , rather than 90° , pulses are used. The 30° pulses can be administered more rapidly than their 90° counterparts. Of course, less magnetization is detected per pulse with the former method.

Richard Ernst, who won the 1991 Nobel Prize in Chemistry, conclusively demonstrated that the second method of using less-than- 90° pulses with no delay times is superior (Ernst and Anderson, 1966). He calculated the ratio $T/T_1(\max)$ and related it to the optimum angle of rotation, α^0 (the Ernst angle). In this expression, T is the total time between pulses, which includes (i) the acquisition time and (ii) any relaxation delay time, and $T_1(\max)$ is the longest longitudinal relaxation time of interest. Figure 2-4 contains a plot of various $T/T_1(\max)$ ratios against α^0 . To use the figure, one divides the estimated, or known, $T_1(\max)$ into t_a and then reads the optimum flip angle that corresponds to this ratio. If a series of 90° pulses is being used, $T = 1.27T_1(\max)$.

While the Ernst angle relationship has worked very well for many years, problems can arise if $T/T_1(\max)$ moves, for a variety of reasons, off scale (to the left) or if the resulting α^0

Figure 2-4 Plot used to identify optimum flip angle (Ernst angle).



necessitates a pulse width that is too short for the spectrometer. Relaxation delays are used if $T_1(\max)$ is unusually long or if the t_a 's run the risk of becoming too short at higher magnetic-field strengths (14.1 T; 600 MHz, proton), which are becoming increasingly prevalent. When B_0 increases, so does sw , expressed in Hz, and from eq. 2-1, t_a is seen to decrease as sw increases. In such instances, the introduction of a relaxation delay effectively moves the $T/T_1(\max)$ ratio back on scale.

Even if the t_a does not appear to be too short for the relaxation times involved, we saw at the beginning of this section that spectral resolution and t_a are inversely related. Desirable ^1H and ^{13}C spectral resolution values are about 0.25 and 1 Hz, respectively, and such numbers, in turn, require t_a 's of approximately 4 and 1 s, respectively. One remedy for the problem of short t_a 's is to use a larger number of data points. If $n_p = 65,536$ (64K), t_a also is doubled (assuming that sw remains constant). This approach, however, increases both the memory and speed requirements of the spectrometer computer.

The consequences of this relationship are considerably different for ^1H and ^{13}C NMR. In Section 2-4d, we saw that proton t_a 's are around 4 s for standard 10-ppm spectral widths at 400 MHz, while those for ^{13}C are about 0.75 s for common 220-ppm spectral windows at 100 MHz. The numerators of the $T/T_1(\max)$ ratio for ^1H and ^{13}C , therefore, are considerably different if T is essentially equal to t_a (t_p is in μs , and its contribution to T can be ignored). The denominators of this ratio are less different for ^1H and ^{13}C than one would imagine when quaternary carbons are ignored. The T_1 values of protons and many protonated carbons are similar in magnitude ($<2-3$ s) if very small molecules are discounted (Section 5-1). Nonprotonated carbons are another matter and have significantly longer T_1 values. The T_1 's of these carbons, however, are usually considered only indirectly when NMR spectroscopists determine $T/T_1(\max)$ ratios.

Because ^1H and ^{13}C T_1 's are not generally known, the selection of α often is done in the following manner. For ^1H NMR experiments with $T = t_a \sim 4$ s and $T_1(\max) = 2-3$ s, the α^0 's are $76-83^\circ$. Since these T_1 values are approximations, many operators just take $\alpha = 90^\circ$. In this approach, the equilibrium magnetization of more slowly relaxing protons is not quite complete, and the intensities of their signals are somewhat diminished, but this seldom causes problems.

For ^{13}C NMR experiments, the situation is less well defined. With $T = t_a \sim 0.75$ s and with a protonated-carbon T_1 range of 2-3 s, the α^0 's are $40-45^\circ$. If there are nonprotonated carbons in the molecule, however, then, assuming that we wish to observe them, a smaller α should be used so that the carbons will appear in the spectrum, albeit with reduced

intensities. Many operators compromise and set $\alpha = 45^\circ$ for situations in which the longest T_1 's of the nonprotonated carbons are expected to be about 10 s. When longer T_1 's are anticipated, the procedure is to set $\alpha = 30^\circ$.

2-4g Receiver Gain

The degree to which the receiver is turned on to detect the faint, transient signals that the previously excited excess nuclei produce as they lose phase coherence and reestablish equilibrium z magnetization is determined empirically. A proper receiver gain setting is important because (i) too high a setting causes baseline distortions of the signals after Fourier transformation and (ii) too low a setting causes a precious part of the sample signal to be lost. Modern spectrometers have *autogain setting* routines in which a pulse, at the selected flip angle, is first delivered with full receiver gain. If the pulse causes a receiver overload, the gain is decreased by 10% and the spectrometer is pulsed again. The process is repeated until a suitable gain is found that does not cause receiver overload.

2-4h Number of Scans

The number of scans (ns, or transients) that is collected depends not only on the desired quality of the spectrum, but also, to some degree, on the amount of spectrometer time available to the operator and its cost. Moreover, consideration must be given to the manner in which spectral signal-to-noise (S/N) ratio is improved in multiple-scan, or signal-averaging, NMR experiments. In this procedure, a digitized FID is stored in the computer memory. Additional FIDs are then recorded a certain number of times and added to the same memory locations. Any signals present are reinforced, while noise tends to cancel out. The theory of random processes states that if n scans are carried out and added digitally, the amplitude of the signal is proportional to n and the noise is proportional to $n^{1/2}$. The S/N ratio, therefore, increases by $n/n^{1/2}$, or $n^{1/2}$. For example, for ^1H NMR, if ns is initially set to a very large number, such as 1,024, four scans might be taken for a preliminary spectrum. If this ns is then found to be too small, an additional 60 scans can be added and another FT performed. The S/N ratio in the two experiments would be increased by $(64/4)^{1/2} = 4$. Multiple scanning is a routine part of FT-NMR, and nuclei such as ^{13}C and ^{15}N cannot be observed at their natural abundance without it.

For ^1H NMR spectra, the number of scans should be a multiple of 4, since this is the length of the CYCLOPS phase cycle used to minimize imperfections associated with quadrature signal detection (Section 5-8). Anywhere from 4 to 128 scans are usually sufficient to obtain a good spectrum with a relatively flat baseline. This number, however, depends heavily on the concentration of the sample. Nevertheless, accumulation times of over 1 hour are relatively rare.

In this regard, a useful feature of many spectrometers is the *block-size* parameter. For ^1H NMR, and in general, block sizes are set to 4 or a multiple of 4, again depending on the concentration of the sample. The number of scans is set to an accumulation time that might correspond to the total time that the operator has reserved. (Modern spectrometers also have programs that calculate the total experimental time from the number of scans, t_a , and any delay times.) At the end of each block, the summed FIDs (see earlier) are written into the computer memory, where they can be Fourier transformed. When the spectrum displays a sufficient S/N ratio, the acquisition is halted. Remember, from the square-root relationship just discussed, in order to double the S/N ratio, we must quadruple ns.

For ^{13}C and other low-sensitivity nuclei, the number of scans required to obtain a good spectrum is much larger than for ^1H . A procedure similar to that of ^1H NMR can be employed, by which the number of scans is again set to the equivalent of the maximum spectrometer time (now several hours) that the operator has reserved. Because of the larger number of scans, the block size is now set typically to 32 or 64. For small-sized samples whose spectra cannot be determined in two hours, it is better to think in terms of an overnight experiment. (Again, doubling a 2-hour S/N ratio requires 8 hours, and even this accumulation time might not be enough.)

2-4i Steady-State Scans

Steady-state, or dummy, scans are used to allow a sample to come to equilibrium before data collection begins. As in a regular experiment, a number of scans are taken, but data are not collected during what would be the normal acquisition time. Steady-state scans are usually performed before the start of an experiment, but, for certain experiments on older instruments, may be acquired before the start of each incremented time value. This technique is not necessary in typical one-dimensional NMR experiments, but is employed in one-dimensional methods that involve spectral subtraction (e.g., DEPT; Section 7-2b) and virtually all two-dimensional experiments.

Steady-state scan numbers given in the experimental sections of this chapter and Chapter 7 are performed at the beginning of the experiment described, unless stated otherwise.

2-4j Oversampling and Digital Filtration

We saw in Section 2-4g that the receiver gain must be set neither too high nor too low. A potential problem arises, especially in the ^1H NMR spectroscopy of mixtures, when one wishes to observe the small signals of minor components in the presence of much larger signals from major components. In such a situation, the receiver gain is, of course, set to a low value to avoid overload; the trouble is that the signals of the minor components then tend to be weak.

This difficulty, which has recently been addressed by *oversampling* the FID, involves digitizing spectral data at a rate that is much faster than that required to satisfy the Nyquist condition (Section 2-4, introduction). Since we usually think of appropriate signal digitization in terms of adequate spectral widths rather than sufficient sampling rates, oversampling can be thought of as the acquisition of NMR data with much larger spectral width than would ordinarily be necessary. The decrease in *digitization noise* (not the same as the *thermal noise* encountered in Section 2-4h) follows a pattern similar to that of S/N enhancement observed in Section 2-4h: oversampling by a factor of N reduces digitization noise by a factor of $N^{1/2}$. Common oversampling factors for ^1H NMR are 16 and 32.

One potential problem that appears to arise from this solution is related to data processing. As we saw in eq. 2-1, if the spectral width is increased to several hundred kHz, the number of data points required to describe the FID is augmented commensurately. This, in turn, necessitates much greater computer data storage capacity and results in slower data processing. Modern spectrometers avoid these limitations by a combination of oversampling and *digital signal filtration* techniques. The FID is reduced to the usual number of data points (16K or 32K) prior to storage by averaging the oversampled data. Data points are taken at intervals that satisfy the Nyquist condition for the desired spectral width. The final FID thus has the same number of data points as would have been taken if an ordinary 16K or 32K FID had been acquired in the usual manner.

A second potential problem concerns aliased noise due to the increased spectral width. Digital filters, when combined with analog ones (Section 2-4c), do an excellent job of keeping unwanted noise (and signals, too!) from aliasing into the selected spectral window. This very efficient filtration can become a liability, however, if spectral widths are not carefully chosen, because the presence of signals that have been accidentally left outside of the spectral window is not revealed by the appearance of aliased resonances.

2-4k Decoupling for X Nuclei

As we saw in Section 1-5, spectra of X nuclei (e.g., ^{13}C or ^{15}N) are usually recorded and presented under conditions of ^1H decoupling for several reasons, the main one being sensitivity. X-nucleus spectra are, generally speaking, inherently weak, due to the low natural abundance of most X nuclei (Section 1-7) and the presence of both direct and longer range X-H couplings (Section 1-5). The effect of these two factors is to divide intrinsically small singlet signals into even smaller multiplets, and the problem is especially serious for ^{13}C .

^1H decoupling not only removes this difficulty for X-nucleus spectra, but also enhances the resulting singlet signals considerably by means of the nuclear Overhauser effect (NOE, Section 5-4). ^1H decoupling also is carried out for ^{13}C spectra to eliminate spectral congestion. For instance, if we consider the methylene region of a fatty acid, it is often difficult to ascertain the exact number of CH_2 carbons even in ^1H -decoupled ^{13}C spectra. The task would be impossible in the presence of severely overlapping multiplets.

In some respects, the ^1H -decoupling operation can be viewed as a simultaneous ^1H NMR experiment. Just as there is a transmitter offset that positions the X-nucleus observation frequency, so is there a corresponding decoupler offset for the ^1H -decoupling frequency. Many spectrometers have both transmitter and decoupler power levels. Three parameters, however, are specific to decoupling and have no counterparts among the spectral observation parameters that have been discussed.

Among the various types of decoupling, the one considered here is nonselective, or broadband, in nature. What is meant by these terms is that the entire ^1H NMR spectrum is irradiated in a continuous fashion, so that the X nuclei do not experience spin-coupling effects from their ^1H neighbors. An example of such ^1H decoupling is shown in Figure 1-25. For NMR spectrometers whose magnetic field strengths are 7.05 T or below (or whose ^1H frequencies are 300 MHz or less), the removal of proton effects can be accomplished by standard *broadband decoupling*.

For field strengths of 9.4 T or above, corresponding to ^1H frequencies of 400 MHz or more, broadband decoupling cannot be employed, because too much heat is generated in the decoupling process. Several proton-decoupling techniques, however, have been developed that are appropriate for higher field instruments. The most popular of these is the WALTZ decoupling scheme of Freeman, discussed in Section 5-8. At this point, let us just state that a *decoupler field strength* has to be determined for WALTZ decoupling. The procedures by which this WALTZ parameter and various transmitter pulse times (used for generating flip angles of varying magnitude) are determined are discussed in Section 2-7b.

2-4I Typical NMR Experiments

Now that the various spectral parameters have been introduced, let us consider an ordinary ^1H FT-NMR experiment. The pulse sequence used in this experiment is shown in Figure 2-5, in which the duration of the observation t_p pulse is greatly exaggerated. The sequence begins with an optional relaxation delay time (DT, in s), in which equilibrium z magnetization can be restored. This period is followed by the observation pulse [t_p , called the *pulse width* (Section 2-7a), in μs], during which the transmitter is turned on for a certain length of time and the z magnetization is rotated through the desired flip angle α (Section 2-4f). Finally, the receiver detects the signal during the acquisition time (t_a , in s, Section 2-4d). This sequence is repeated as necessary to provide a spectrum with a desired S/N ratio (Section 2-4h) upon Fourier transformation.

In a typical ^{13}C FT-NMR experiment performed with proton decoupling, we must consider both nuclei in the pulse sequence shown in Figure 2-6. The ^{13}C part of the sequence (bottom) is the same as that pictured in Figure 2-5. The ^1H part (top) indicates the status of the decoupler during the experiment. There are four types of ^{13}C NMR experiments in which the decoupler can be turned on or off during both t_p and t_a and similarly during DT: (i) standard decoupling, wherein the decoupler is ON continuously, producing

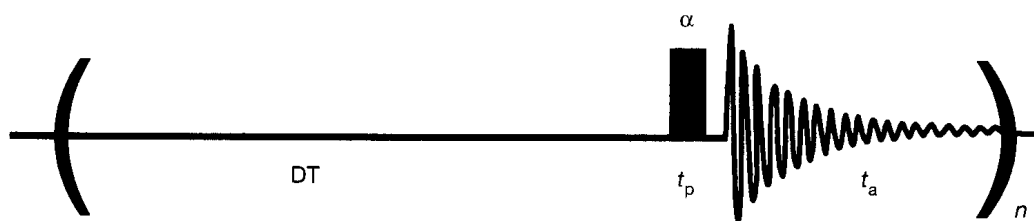
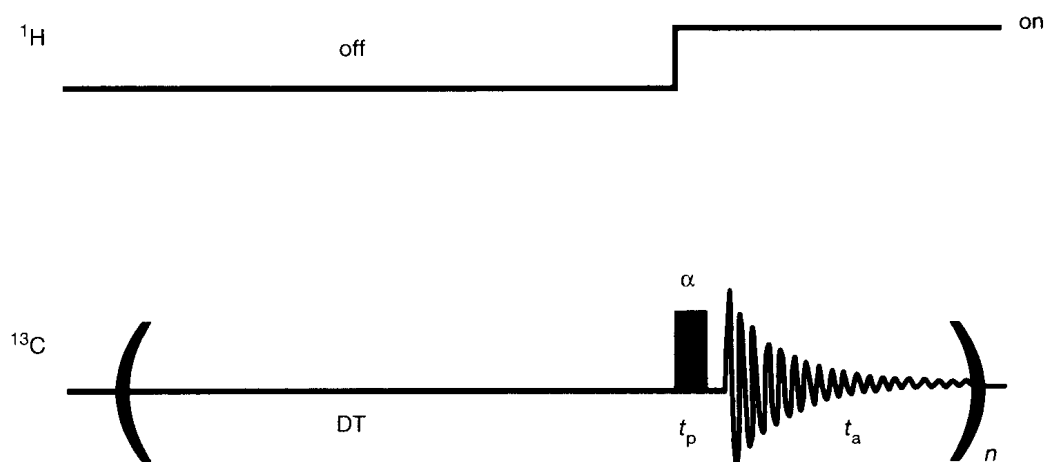


Figure 2-5 A typical ^1H NMR pulse sequence.

Figure 2-6 A typical pulse sequence for the observation of ^{13}C (bottom) while irradiating ^1H (top).



^1H -decoupled ^{13}C spectra (Figure 1-25, lower) with NOE enhancement of individual signal intensities (Section 5-4), (ii) an experiment in which the decoupler is OFF continuously, yielding fully ^1H -coupled ^{13}C spectra without NOE enhancements (Figure 1-25, upper), (iii) *gated* decoupling, wherein the decoupler is ON during DT and OFF during t_p and t_a , giving ^1H -coupled ^{13}C spectra with NOE enhancements, and (iv) *inverse-gated* decoupling, in which the decoupler is OFF during DT and ON during t_p and t_a , producing ^1H -decoupled ^{13}C spectra without NOE enhancements. Experiments (iii) and (iv) are employed either to take advantage of, or to suppress, respectively, the nuclear Overhauser effect. The former yields ^{13}C spectra with signals of greater intensity than those of experiment (ii), while the latter is useful for counting the number of carbons that give rise to each signal in a ^{13}C spectrum.

2-5 Determination of NMR Spectra: Processing Parameters

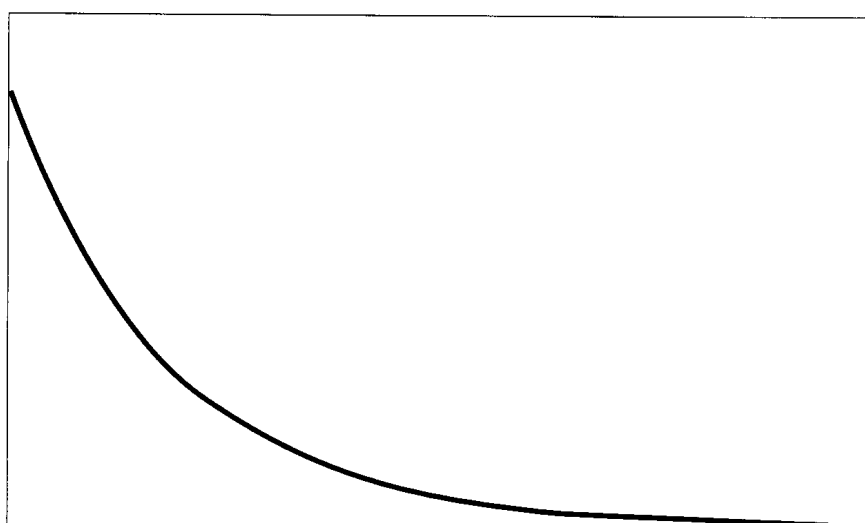
After data acquisition has been completed, it is a good habit to save the NMR data in the operator's disk space. In this way, the original data are safe (especially after long accumulations such as overnight or overweekend runs) from a power failure, accidental deletion, or simply forgetting to save the data after a workup (it happens).

2-5a Exponential Weighting

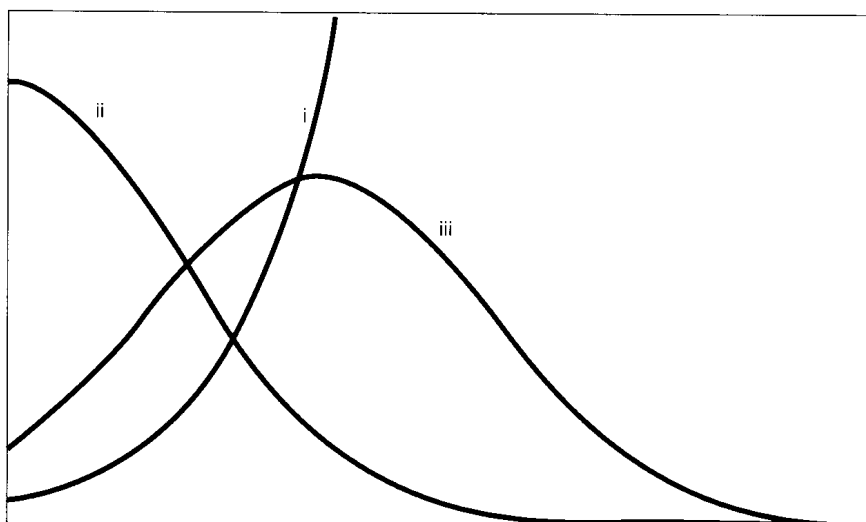
The FID, which is displayed on the monitor after data acquisition is complete (Section 1-4 and Figure 1-16), has two distinct regions. The front part, on the left, contains most of the intensity of the signals to be observed in the spectrum after Fourier transformation. In contrast, the tail of the FID, on the right, contains mostly noise mixed with those parts of the signals that give rise to narrow lines and is, therefore, the resolution part of the FID. There are two basic weighting functions that can be applied to the FID before Fourier transformation.

If sensitivity is a primary concern, as is usually the case in ^{13}C NMR, an *exponential weighting function* (Figure 2-7a) can be applied to the later portions of the FID. This process improves the S/N ratio at the expense of resolution. The use of such weighting necessarily results in some line broadening and a concomitant loss of resolution, because it attenuates the resolution portion of the FID. For this reason, sensitivity-enhancing weighting functions are usually listed as *line-broadening functions* in spectrometer manuals. ^{13}C NMR spectra are typically presented with a 0.5–3-Hz line broadening.

When resolution is a primary concern, as is almost always the case in ^1H NMR, exponential weighting normally is not done. After viewing the spectrum, however, the operator may choose to use a *resolution enhancement function*. Such a function improves the



(a)



(b)

Figure 2-7 Weighting functions. (a) Sensitivity enhancement. (b) Resolution enhancement.

resolution at the expense of the S/N ratio by attenuating the beginning part of the FID and emphasizing the latter part. An example of a resolution function is shown in Figure 2-7b. The function is the resultant (iii) of a negative line-broadening function (i)—the opposite of Figure 2-7a—and a Gaussian function (ii). The effects of line broadening and resolution enhancement on ^1H spectra are seen in Figures 2-8 and 2-9, respectively. Ordinarily, such line broadening is not introduced into ^1H NMR spectra, but it can be helpful in quantitative work (Section 2-6c).

2-5b Zero Filling

After the application of weighting functions (primarily in ^{13}C NMR), the next step in data processing is to *zero fill* the data to at least a factor of two (called one level of zero filling). The reason for this step is that the complex Fourier transform of np data points consists of a real part (from the cosine part of the FT) and an imaginary part (from the sine part of the FT), each containing $np/2$ points in the frequency domain. Therefore, the actual spectrum displayed is described by only *half* of the original number of points. The technique of zero

Figure 2-8 The effect of multiplying a free-induction decay by a line-broadening factor of 3, 2, 1, and 0 Hz. (Reprinted with permission from J. W. Cooper and R. D. Johnson, *FT NMR Techniques for Organic Chemists*, IBM Instruments, Inc., 1986.)

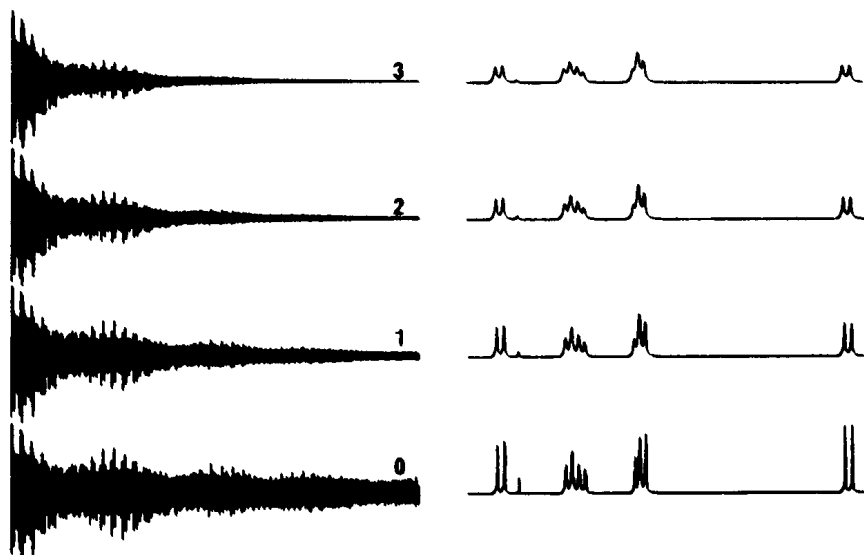
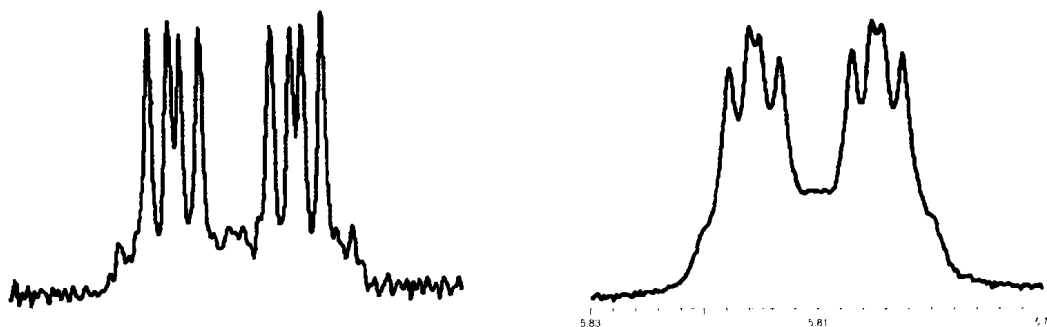


Figure 2-9 The effect of multiplying a free-induction decay by a resolution enhancement (left) and the normal spectrum (right).



filling effectively allows all of the experimental data points to be used to generate the real spectrum. It accomplishes this goal by retrieving information that would otherwise be lost in discarding the imaginary spectrum and thus halves the *digital resolution*. In this method, n_p is doubled by adding an equal number of zeros after the collected data points. If, as is usually the case, $n_p = 32,768$, then, for one level of zero filling, the Fourier transform number $F_n = 2n_p = 65,536$. In this manner, the number of points that describe the spectrum is 32,768, rather than just 16,384. The only experimental requirement for the performance of zero filling is that the FID must have decayed to zero by the end of the acquisition time.

Zero filling beyond a factor of two also can be done, but does not produce further improvement in line width. It is useful, however, in quantitative work (Section 2-6c), because it provides more data points to define line shapes and the positions of signals.

2-5c FID Truncation and Spectral Artifacts

Acquisition times (Section 2-4d, eq. 2-1) depend inversely on the field strength of the magnet, as (i) the number of points used to determine a spectrum are largely the same, irrespective of the nucleus, and (ii) the spectral widths for ^1H and ^{13}C NMR are directly proportional to the magnetic-field strength. Distorted NMR signals can arise if the FID does not decay to zero by the end of the acquisition time. In this case, the FID is said to be *truncated*, and symmetrical oscillations appear at the base of strong signals, as illustrated in Figure 2-10a. When such truncation oscillations, or wiggles, are observed, the situation can be remedied by applying an exponential weighting function (Figure 2-10b) to the FID in order to drive the tail of the FID to zero by the end of t_a (Figure 2-10c). This process is called *apodization* (which means “removing the feet”).

Truncation artifacts are rarely a problem in ^1H NMR, because acquisition times usually are long enough (2–4 s) to permit essentially complete decay of the FID. The

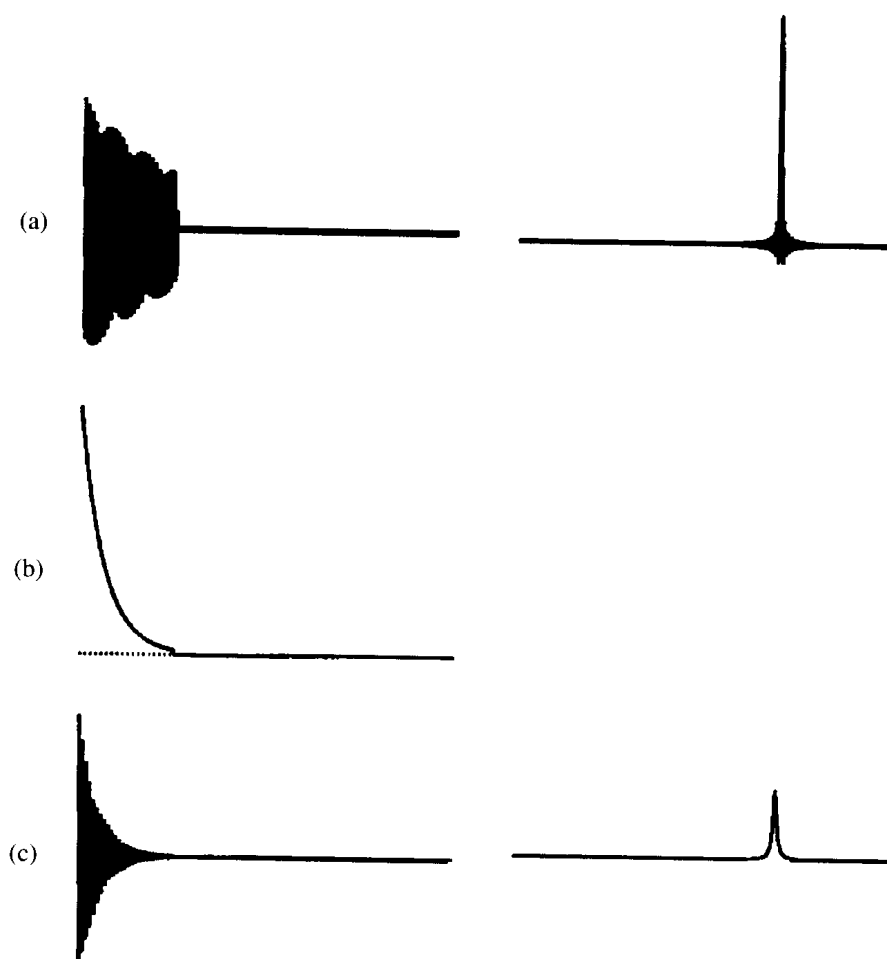


Figure 2-10 The effects of truncating a signal. (a) A truncated FID showing truncation wiggles at its base. (b) Apodization using an exponential decay function yields the data in (c). While the truncation wiggles have been reduced, the resulting signal has been broadened. (Reprinted from J. C. Hoch and A. S. Stern, *NMR Data Processing*, 1996, by permission of Wiley-Liss, Inc., a subsidiary of John Wiley & Sons, Inc.)

situation is quite different for ^{13}C NMR, with much larger spectral widths and t_a 's typically in the range from 0.5 to 1 s. FID's often are truncated—especially those of carbons, with relatively long T_2 's in small molecules. The types of truncation effects shown in Figure 2-10, however, are usually not observed even here, because apodization is performed by the sensitivity-enhancing weighting functions (e.g., Figure 2-7a), which are almost always applied to ^{13}C FID's. As described in Chapter 7, apodization is very important in two-dimensional NMR experiments.

2-5d Resolution

Several terms pertaining to resolution are used widely in NMR spectroscopy. It is appropriate to define them further at this point to avoid confusion. *Spectral resolution* (SR) concerns the acquisition time employed to acquire the spectral data. We saw in Section 2-4 (introduction) that this number is the reciprocal of t_a and is expressed in Hz. If $np = 32,768$ and $sw = 4,000$ Hz, then $t_a = 4.1$ s, and SR is given by

$$\text{SR} = \frac{1}{t_a} = \frac{1}{4.1 \text{ s}} = 0.24 \text{ Hz.} \quad (2-2)$$

Digital resolution (DR) is related to both sw (in Hz) and the number of points actually used to describe the final Fourier-transformed spectrum. DR is an important concept because the distinction between two signals whose separation is $\Delta\nu$ (the signals can be two single lines or a coupling constant) necessitates a DR of about $\frac{1}{2}(\Delta\nu)$ [e.g., for $\Delta\nu \sim 1$ Hz,

a DR of $\frac{1}{2}$ (~ 1 Hz), or approximately 0.5 Hz, is required]. For the previous SR example, DR is calculated from the formula

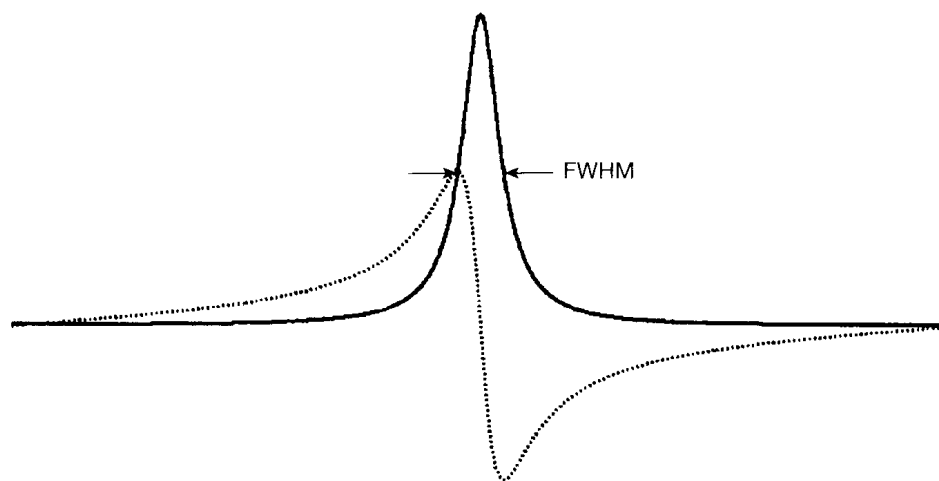
$$\text{DR} = \frac{\text{sw}}{(\text{np}/2)} = 4,000 \text{ Hz}/(32,768/2 \text{ points}) = 0.24 \text{ Hz/point.} \quad (2-3)$$

With the very large data sets currently used in one-dimensional experiments (32 or 64 K), digital resolution is seldom a problem. Equation 2-3 also demonstrates that SR and DR are the same. Both are derived from eq. 2-1 in Section 2-4d. DR, however, provides the entry to zero filling and the recovery of lost data points (Section 2-5b). Again, for the previous SR example, with one level of zero filling to 65,536 total points, we have

$$\text{DR} = \frac{\text{sw}}{(\text{np}/2)} = 4,000 \text{ Hz}/(65,536/2 \text{ points}) = 0.12 \text{ Hz/point.} \quad (2-4)$$

Resolution, of course, also refers to *magnetic-field homogeneity*. It is a measure of how well the magnet has been shimmed (Section 2-3d) and is unrelated to the preceding terms. This kind of resolution is quoted in terms of the narrowness of a line at half-height and is shown as the full width at half maximum (FWHM) in Figure 2-11. Spectroscopists describe shimming results with expressions such as half-Hz (acceptable) or quarter-Hz (good) resolution. These numbers assume that a suitable t_a (for SR) and np (for DR) have been selected and, perhaps, even zero filling has been performed to allow the operator actually to observe the level of resolution sought.

Figure 2-11 Comparison of shapes of absorption (solid line) and dispersion (dotted line) signals. Spectra are usually phase corrected to give pure absorption-mode peaks. The arrows indicate the full width at half maximum. (Reprinted from J. C. Hoch and A. S. Stern, *NMR Data Processing*, 1996 by permission of Wiley-Liss, Inc., a subsidiary of John Wiley & Sons, Inc.)



2-6 Determination of NMR Spectra: Spectral Presentation

2-6a Signal Phasing and Baseline Correction

When the accumulated FID's have been zero filled, perhaps exponentially weighted, and Fourier transformed, the next step is to phase correct the resulting resonances to give a spectrum consisting of pure absorption-mode signals. (See shortly and Appendix 2.) In an NMR experiment, there usually are many vectors, such as those pictured in Figure 1-13. These vectors correspond to nuclei with varying chemical shifts and, accordingly, varying Larmor frequencies. The vectors are initially placed partially (Figure 1-13b) or completely (Figure 1-13c) along the y axis by the observation pulse. They begin to evolve (rotate away from the y axis in the xy plane), however, during both the finite pulse and the delay period between the pulse and when the receiver is gated on.

Signal phasing is usually necessary for a number of reasons. For simplicity, let us suppose that the magnetization vectors we just referred to are rotating (Figure 1-13c) in the xy plane. When the receiver is turned on, their initial phases generally do not exactly match that of the receiver. Since these phase differences are approximately the same for all of the vectors (independently of their resonance frequencies), the correction applied is referred to as a *zero-order* phase correction. A further complication arises, however, as the vectors become dispersed in the xy plane. Those vectors with the greatest frequencies move the farthest, and if they do not lap the slowest-moving vectors, require the largest phase corrections. Since these corrections are dependent on the resonance frequencies of the vectors, they are known as *first-order* phase corrections.

The two basic types of signals that can be detected in an NMR experiment are an *absorption* signal (due to the detection of a signal perpendicular to B_1) and a *dispersion* signal (due to a signal parallel to B_1), as shown in Figures 2-11 and A2-2). For analysis purposes, NMR spectra are displayed with completely absorptive signals. Phase errors are manifested by the dispersive character that they introduce into these signals prior to phase correction. Zero- and first-order phase errors are illustrated in Figure 2-12. Resonances with zero-order phase errors exhibit the *same* degree of dispersive character across the spectrum (Figure 2-12a) and are adjusted to give absorption signals with the *zero-frequency* phase control (also called the *zero-order*, or *right-phase*, control). Those resonances with first-order phase errors display *varying* degrees of dispersive character across the spectrum (Figure 2-12b) and are phase corrected by applying a *first-order*, or *left-phase*, correction that varies linearly with frequency.

Typically, both types of phase correction have to be performed, and the usual phasing procedure is to first correct the phase of the lowest-frequency signals with the zero-order

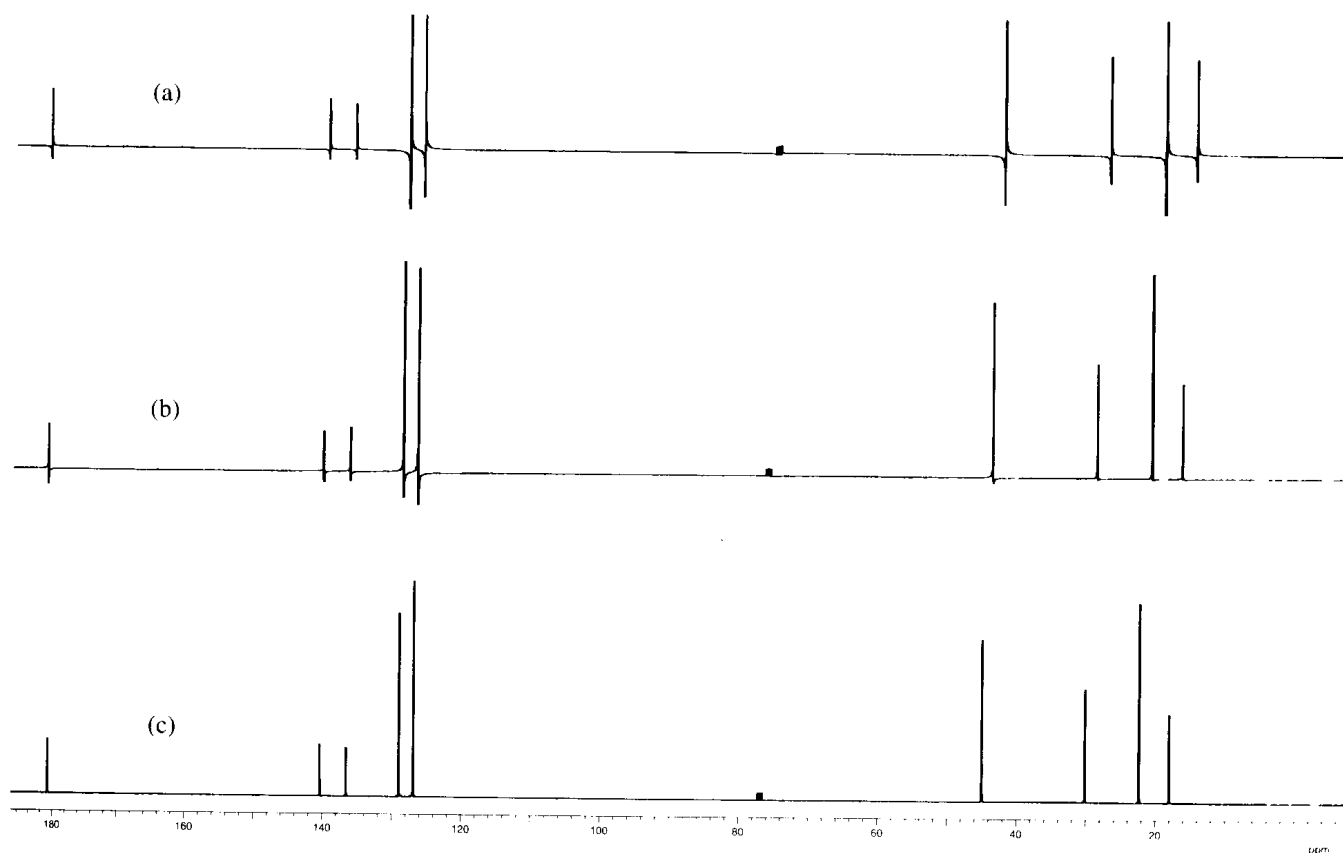


Figure 2-12 ^1H spectra showing zero- and first-order phase errors. (a) The spectrum with frequency-independent (zero-order) phase errors. (b) The spectrum with frequency-dependent (first-order) phase errors. (c) The correctly phased spectrum.

control and then move across the spectrum to increasingly higher frequencies, phasing groups of resonances with the first-order control. The process is interactive, so that by the time that the highest-frequency signals have been phase corrected, the lowest-frequency resonances may require further correction. Two to three passes through the spectrum usually suffice to correct the phase of all of the signals. The correctly phased spectrum is displayed in Figure 2-12c. Most modern spectrometers have automatic-phasing routines, which generally do a relatively good job of phasing spectra instantaneously.

A situation that appears to be a phasing problem, but is actually a case of FID truncation (Section 2-5c), is illustrated in Figure 2-13a. Note that most of the signals can be phased properly, but slight distortions (some with opposite phase) are observed for the resonances at approximately δ 17, 30, 44, 136, and 140. Attempted phasing will convince the operator that these distortions are not phasing errors. Comisarow has demonstrated that they are, in fact, due to the truncation of certain FID's owing to acquisition times that are too short. These effects are most often found in the ^{13}C spectra of small molecules for the signals of those carbons with relatively long T_2 's. FID truncation effects are most easily eliminated by either (i) applying an even greater line-broadening weighting function (Section 2-5a) or (ii) introducing a relaxation delay time (Section 2-4f), as was done in Figure 2-13b.

If the spectrum displayed on the monitor is not level, a *baseline correction* can be applied. This procedure is accomplished with a simple spectrometer command, and the correction, like autophasing, is done immediately.

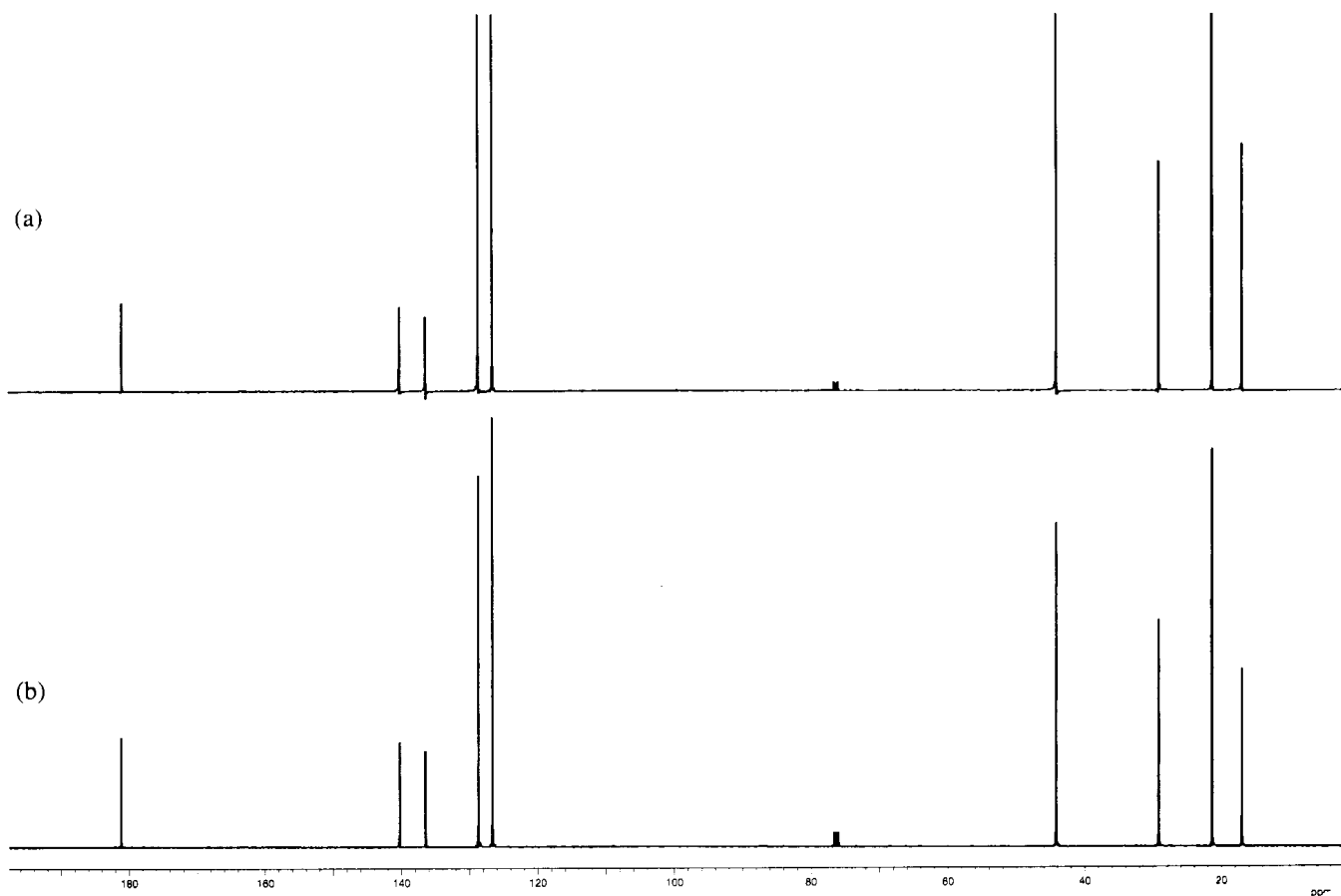


Figure 2-13 Apparent phase errors due to signal-truncation effects. (a) The distorted spectrum caused by an acquisition time that is too short ($DT = 0$ s). (b) The distortion-free spectrum after the introduction of a relaxation delay time ($DT = 1$ s).

2-6b Zero Referencing

The last matter to be dealt with before the spectrum is plotted is selecting an appropriate *zero reference* for the signals in the spectrum. This subject was mentioned briefly in Section 1-2, where we saw that reference materials have been agreed upon, for the most part, for each nuclide (Table 1-2) and assigned a relative frequency of zero. We also learned that the compound tetramethylsilane (TMS) serves as an internal zero reference for protons, carbon, and silicon.

TMS is an almost ideal reference material, in that it appears at such low frequency (high field) that very few proton and carbon signals appear to its right. Nevertheless, its great volatility makes it very difficult to add a small amount of TMS (even right out of the freezer) to a sample tube. Years ago, with relatively insensitive spectrometers, this was not a major concern. However, with today's highly sensitive instruments, several drops of TMS would easily result in its signal being the most intense resonance in a ^1H spectrum recorded in a customary, deuterated NMR solvent.

An attractive alternative to the use of TMS as a primary reference is its use as a secondary reference. In this method, a ^1H spectrum is referenced to the signal of the residual proton(s) in a deuterated solvent (e.g., the small amount of CHCl_3 at δ 7.26 in CDCl_3), while a ^{13}C spectrum is referenced to the carbon(s) of the solvent (e.g., the middle line of the three-line resonance of CDCl_3 at δ 77.00). The chemical shifts of the carbons and residual protons of the more common solvents are presented in Table 2-1. The two water soluble,

Table 2-1 Chemical-Shift Data of Common Deuterated NMR Solvents^a

Solvent	^1H Chemical Shift(s) ^b	^{13}C Chemical Shift(s)
Acetic acid- d_4	2.04 (5)	20.0 (7)
	11.65 (1)	178.99 (1)
Acetone- d_6	2.05 (5)	29.92 (7)
		206.68 (1)
Acetonitrile- d_3	1.94 (5)	1.39 (7)
		118.69 (1)
Benzene- d_6	7.16 (1)	128.39 (3)
Chloroform- d	7.26 (1)	77.00 (3)
Deuterium oxide	4.8 ^c	(NA)
Dichloromethane- d_2	5.32 (3)	54.00 (5)
<i>N,N</i> -Dimethylformamide- d_7	2.75 (5)	29.76 (7)
	2.92 (5)	34.89 (7)
	8.03 (1)	163.15 (3)
Dimethyl sulfoxide- d_6	2.50 (5)	39.51 (7)
1,4-Dioxane- d_8	3.53 (m)	66.66 (5)
Methanol- d_4	3.31 (5)	49.15 (7)
	4.87 (1)	
Pyridine- d_5	7.22 (1)	123.87 (3)
	7.58 (1)	135.91 (3)
	8.74 (1)	150.35 (3)
Tetrahydrofuran- d_8	1.73 (1)	25.37 (5)
	3.58 (1)	67.57 (5)

^a Multiplicities in parentheses.

^b Signals of residual solvent protons.

^c Chemical shift highly dependent on pH and temperature.

(Courtesy of Cambridge Isotope Laboratories, Andover, MA)

internal proton and carbon standards mentioned in Section 1-2 [the sodium salts of 3-(trimethylsilyl)propionic acid and 3-(trimethylsilyl)-1-propanesulfonic acid] also present some problems. Again, with today's very sensitive spectrometers, only small amounts of the powdery compounds need be added to NMR sample tubes. Handling these materials is thus somewhat inconvenient. Even worse is the fact that the chemical shifts of the trimethylsilyl groups of both compounds are appreciably dependent on pH and temperature. As we saw previously with TMS, an alternative, secondary reference material exists for both protons and carbons: 1,4-dioxane. This diether is water soluble, and one drop in a 5-mm tube is sufficient to produce a signal that is easily visible, but not too intense. The eight protons of 1,4-dioxane appear as a singlet at δ 3.68, and its four carbons also appear as a singlet, at δ 67.06. These chemical-shift values are somewhat dependent on temperature, but less so than those of the aforementioned solid standards.

2-6c Determination of Certain NMR Parameters

Chemical Shifts and Coupling Constants. After NMR spectra have been zero referenced, determining ^{13}C chemical shifts is straightforward, since the spectra are almost always collected under proton-decoupling conditions and therefore appear as single lines. Modern spectrometers have *peak-picking* programs in which a threshold value is first set and then the line positions of all signals that exceed this threshold are recorded.

^1H chemical shifts are another matter, since the signals of most protons are multiplets. Strictly speaking, spectral analysis is required to determine the chemical shifts and coupling constants of those protons whose signals display second-order behavior (Chapter 4 and Appendix 4). For those protons whose spectra are first order or even pseudo first order, chemical shifts and couplings can be determined from the spectra by inspection, but some care should be exercised in this endeavor.

^1H spectra should first be spread out so that only one multiplet or one region containing several multiplets is displayed on the monitor. Vertical cursors or arrows should be set so that they are either (i) between the middle signals of a multiplet containing an even number of lines or (ii) on top of the middle resonance of a multiplet containing an odd number of signals. Cursor or arrow positions can then be recorded in the laboratory notebook.

Peak-picking programs often are misused in the determination of coupling constants. The reason is that coupling constants have to be just that—*constant*. The spin coupling that is determined for the methyl triplet ($\sim\delta$ 1.2) of diethyl ether in Figure 1-22 has to be the same as that for the methylene quartet ($\sim\delta$ 3.5), both being approximately 7 Hz. If we request a line listing for the seven lines of the diethyl ether spectrum and do the subtraction, however, we will quickly discover that the line separations, and thus the apparent coupling constants, almost always are *not* exactly the same. The reason for the inconsistency is that the peak-picking routine reads either the highest data point that describes each spectral line or an interpolated maximum as the position of that line. This procedure is adequate for the determination of ^{13}C chemical shifts because the horizontal scale is in thousands of Hz and moving the shift-determining data point(s) a small amount to either side does not make a significant difference. ^1H coupling constants, however, are generally less than 20 Hz, so moving the corresponding data points is now sufficient to produce unequal spacings. The spreading out and averaging procedure described previously for the determination of ^1H chemical shifts avoids this problem, but can be tedious.

An attractive alternative in which spectrometer line-listing routines are used is as follows. After the spectral data have been Fourier transformed and saved, the proton FID is zero filled three to four times. If $n_p = 32\text{K}$, then F_n should be set to 256 or 512K. The resulting spectral lines should then have sufficient definition for peak picking. This expectation can easily be tested by examining a known multiplet, such as a triplet or quartet. The two- or three-line spacings are, of course, identical, and their equivalence must be reflected in the line listings displayed on the monitor. No matter what technique is used, J values between spin-coupled nuclei should always be reported as identical.

^1H Integration. As we saw in Section 1-6, ^1H NMR spectra are almost always recorded in such a manner that the detected signals are directly proportional to the number of protons giving rise to those signals. For most ^1H -decoupled ^{13}C spectra, however, a spread of T_1 's and the nuclear Overhauser effect (Section 5-4) combine to produce signals whose intensities are *not* proportional to the number of carbons present.

The process of measuring the intensities of NMR signals is called *integration* and is normally performed only for ^1H spectra. The integral of the total spectrum is a line that starts at the left side of the spectrum and increases in a stepwise fashion at each ^1H signal. The areas of the sections into which this continuous line is cut correspond to the number of protons giving rise to the signals below them and are known as *integrals*. An example of a typical integrated ^1H spectrum can be seen in Figure 8-1 for the fungal metabolite T-2 toxin.

Proton spectra, for which integration is to be performed, are commonly determined in one of two ways, depending upon whether the sample in question is predominantly a single compound or a mixture of two or more compounds. In the former case, integration is more easily carried out, because the areas of the signals must be integral ratios of one another. These spectra can be acquired in the manner described earlier (e.g., with acquisition times of approximately 4 s), because proton relaxation is essentially complete at the end of t_a . For mixtures, however, integration must be performed with much greater care, because the integral values are seldom simple multiples of one another. For good quantitative results, it is critical that proton relaxation be essentially complete between scans. Since proton T_1 's tend to be short (on the order of milliseconds to a few seconds), this condition can best be achieved by using small flip angles and relaxation delay times of several seconds.

The initial approach to integration is to determine where the spectrum can be cut between groups of signals and to identify the largest continuous run of signals where the integral of that group cannot be cut to the baseline. This region likely contains the largest number of proton signals. It is now spread out on the screen and its integral amplitude essentially maximized (i.e., set to a round number like, say, 2,000, that can easily be doubled, tripled, etc). The idea is next to cut the rest of the signals into regions (which are generally less spread out than they are for the determination of ^1H chemical shifts and coupling constants; see the previous section) that can be integrated accurately.

If the operator wishes, the integral amplitudes of these smaller regions also can be maximized so that they are multiples of the first amplitude. In this approach, integrals that would be less accurate because they are small, compared with the largest integral, can be increased in size and better compared. By keeping track of the multiplication factors, all of the integrals can be recorded and then scaled back to the same integral amplitude. This technique is especially helpful if mixtures of compounds are being analyzed, since the integrals are only infrequently integer ratios of one another.

Like shimming, there are many ways to perform integration. The following parameters of Gard, Pagel, and Yang represent a general approach to obtaining precise ^1H NMR quantitative measurements:

Acquisition parameters:

1. Set $\alpha \sim 30^\circ$ with $DT = 1$ s.
2. Increase the filter bandwidth by 500–1,000 Hz if there are signals near the edges of the spectral window.
3. Take enough scans to ensure a good S/N ratio and thus smoother integrals.
4. Adjust the receiver's dead time (the time between the end of the pulse and the beginning of acquisition of the signal) to minimize pulse breakthrough, which is manifested by a baseline roll. Certain spectrometers carry out this operation in the following way. First, a spectrum is recorded and phased as usual. Then, a software command calculates the dead time such that the first-order (left) phase control equals zero in a repeated spectrum.

Processing parameters:

1. Set line broadening = 0.2–0.3 Hz.
2. Use three levels of zero filling (8 np) (e.g., if np is 32K, then Fn is 256K).

Spectral display:

1. Careful phasing is very important.
2. Make integral regions five to seven line widths, if possible, to get the full integral. Even more critical, however, is that all integral regions be the *same width* and extend the same distance on either side of each signal.
3. Use baseline corrections on each integral cut if spectral tilt is noticeable. Extensive zero filling (see step 2) is useful, because it provides more data points to define line shapes better (Section 2-5b). Slight line broadening produces smoother spectral and integral lines with less baseline noise.
4. Consistently include, or exclude, ^{13}C satellite signals.

2-7 Calibrations

In Section 2-4, we encountered a number of spectral acquisition parameters. The selection of these parameters is relatively direct and straightforward, with the exception of the flip angle α and the decoupler modulation frequency (for WALTZ decoupling). Neither α nor the decoupler modulation frequency is entered directly, and both parameters require that the spectrometer be calibrated.

2-7a Pulse Width (Flip Angle)

In Section 1-4, it was demonstrated that magnetization vectors can be rotated along the x axis through various angles θ . As we have seen, a 90° pulse places all of the original z magnetization along the y axis and leads to the detection of a full signal (Figure 1-13c). In contrast, a 180° pulse places the entire magnetization vector along the $-z$ axis and therefore results in no signal at all (Figure 1-13d). A 270° pulse aligns the z magnetization along the $-y$ axis, producing a full negative signal, and a 360° pulse returns the magnetization vector to its original position along the z axis. As θ increases from 0 to 360° , the detected magnetization exhibits the behavior shown in Figure 2-14. The maximum signal, therefore, is obtained when $\theta = 90^\circ$.

The length of time that the transmitter has to be turned on (i.e., the *pulse width* t_p) in order to achieve a certain vector rotation is determined empirically in the following manner. In principle, any particular sample can be used to ascertain the ^1H 90° pulse width. In practice, however, the sample should have at least one well-defined signal (ideally, an intense singlet) that can be observed with one pulse. More important is the requirement that the T_1 of the test signal not be excessively long, because the z magnetization must be reestablished between pulses. (This important criterion is considered further later in the section.) A sample of 10% acetone in CDCl_3 is a possible ^1H 90° pulse width standard. It is better if this sample is *not* a sealed and degassed reference standard, because the T_1 value of the methyl protons in these latter standards is approximately 30 s!

With the test sample in the magnet, the probe is tuned to ^1H and the magnet homogeneity maximized. Next, a test spectrum is determined in which the t_p used is unimportant. This spectrum then serves as a starting point for another spectrum, which has a reduced spectral width. The original sw is now reduced to about 500 Hz, and the transmitter offset is adjusted so that it is in the middle of the reduced sw. Many spectrometers have programs that do both operations with one command. Since sw has been considerably reduced, the number of data points should also be decreased, to approximately 4,000, so as to maintain an acquisition time of around 4 s.

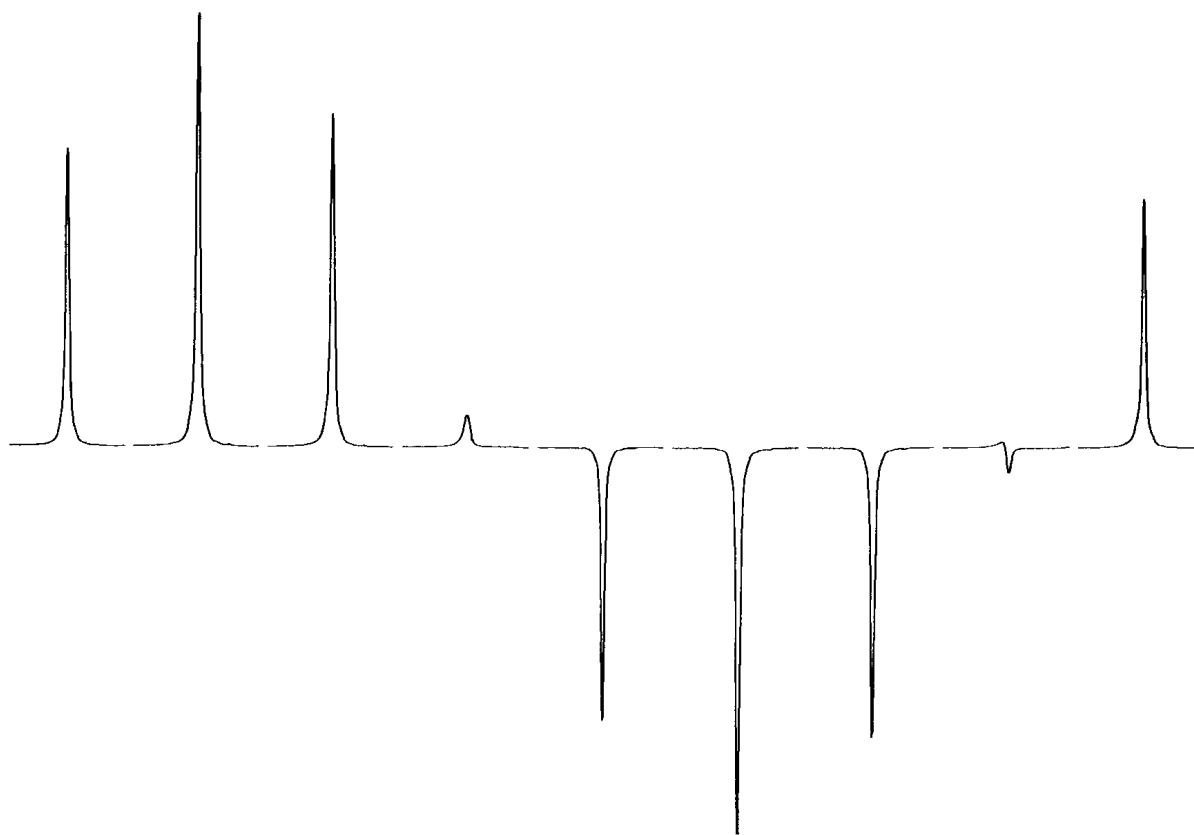


Figure 2-14 A typical 90° pulse width calibration plot.

A reduced one-scan spectrum is then taken and displayed in the *absolute-intensity* mode, with t_p set to about one-half of the value given for the $90^\circ t_p$ in the instrument specifications (e.g., set $t_p = 5 \mu\text{s}$ for a $90^\circ t_p = 10 \mu\text{s}$). The resulting one-line spectrum should be processed with a 1-Hz line broadening, phased properly, and presented such that the baseline appears at about midscreen and the height of the signal occupies about one-half of the vertical size of the screen.

A series of experiments is then queued in which t_p is increased from this first value to a final one that is about five times the specified $90^\circ t_p$. For the example given in Figure 2-14, the suggested $90^\circ t_p$ is approximately $6 \mu\text{s}$. The queued t_p 's are then 3, 6, 9, 12, 15, 18, 21, 24, and $27 \mu\text{s}$. In addition, a relaxation delay time estimated to be greater than $3T_1$ of the test proton(s) ($\sim 30\text{--}45\text{s}$) was inserted before each pulse in the series. Modern spectrometers have programs for displaying the accumulated signals, which appear like those shown above in the figure.

A plot like Figure 2-14 gives us only an approximate idea of the $90^\circ t_p$, but that is all right because we are really interested in the $360^\circ t_p$. Determining a $360^\circ t_p$, rather than a $90^\circ t_p$, is a better procedure for several reasons. First, it is much easier to see where a series of signals crosses over from negative to positive, in the case of a series of t_p 's arrayed around 360° (e.g., 350° to 10°), than to decide on a maximum for a corresponding series arrayed around 90° (e.g., 80° to 100°). Second, if the T_1 of the test proton(s) is not known, the relaxation delay time might be insufficient to permit complete reestablishment of z magnetization between pulses. If complete relaxation does not occur, the resulting signal amplitudes are decreased from their true intensities and displaced toward smaller pulse widths as incomplete z magnetization recovery increases and reaches a steady state. The problem of

incomplete relaxation is much more severe for a series of t_p 's arrayed around 90° , where nearly complete z magnetization has to be reestablished after each pulse, than for a corresponding series arrayed around 360° , where the z magnetization is little disturbed from its equilibrium value with each pulse.

A second series of experiments is now carried out in which the t_p 's are arrayed around 360° and the relaxation delay time is set to approximately 30 s. Additional series of t_p 's can be used as one closes in on the $360^\circ t_p$. Values of t_p do not change appreciably between common organic solvents and therefore do not have to be determined for each sample. Since ionic samples require retuning of a probe with respect to nonionic ones, the t_p 's of the former have to be redetermined relative to those of the latter. Observe, however, that the 90° pulse width thus determined is likely to be slightly longer than $360^\circ/4$, since the rise time (the time required for the transmitter to reach full strength after it is turned on) of a 90° pulse is slightly less than that of a 360° pulse. Nevertheless, the potential errors cited, due to both incomplete relaxation and the difficulty of determining signal maxima encountered in ascertaining 90° pulse widths (and avoided with 360° pulses), generally make the second procedure the method of choice.

^{13}C $90^\circ t_p$'s are determined in much the same manner. Since carbon signals are considerably weaker than proton resonances, however, only ^{13}C -enriched or highly concentrated samples, which give good one-scan spectra, are suitable as ^{13}C $90^\circ t_p$ reference materials. One such candidate is the ^{13}C sensitivity reference standard, 60% $\text{C}_6\text{D}_6/40\%$ dioxane, in which the dioxane resonance is observed. Since reference standards are, as a rule, degassed, special care must be taken to ensure that suitable relaxation delay times ($\sim 45\text{--}60$ s) are used between initial spectral acquisitions. Shorter DT's can be employed for t_p 's arrayed around 360° . With the test sample in the magnet, the probe is tuned to both ^{13}C (the transmitter) and ^1H (the decoupler), and the magnet homogeneity is maximized. ^{13}C spectra are recorded with full ^1H decoupling and are displayed in the same manner (with, perhaps, a line broadening of 3–4 Hz) as described for ^1H $90^\circ t_p$ calibration. Values of t_p for both nuclei should be recalibrated at least once a month.

As a general rule, the transmitter and decoupler power levels are set so that both the ^1H and ^{13}C $90^\circ t_p$'s are in the range of 5–10 μs . Pulse widths less than 5 μs are inaccurate, because pulse rise and fall times are in the microsecond range. Probes having t_p 's appreciably greater than 10 μs may be unable to execute those pulse sequences which require several transmitters to be rapidly switched on and off.

2-7b Decoupler Field Strength

We saw in Section 2-4k that (i) ^{13}C NMR spectra are usually recorded with WALTZ proton decoupling for spectrometers whose field strengths are 9.4 T or above (or whose ^1H frequencies are 400 MHz and above) and (ii) one of the components of WALTZ decoupling, the *decoupler field strength* γB_2 , has to be determined for each individual spectrometer. The quantity γB_2 is a function of both the decoupler power level and characteristics of the probe. In addition, γB_2 can even depend on the sample itself if highly ionic solutions are being examined, which, as we have seen, require a different probe tuning relative to common organic solvents.

The standard method for calibrating γB_2 is a technique known as *off-resonance decoupling* (Section 5-3 and Figure 5-8). In Figure 1-25, we saw that methyl carbons appear as quartets, methylene carbons as triplets, and methine carbons as doublets in fully proton-coupled ^{13}C NMR spectra. In off-resonance proton-coupled ^{13}C spectra, the same patterns are observed (doublets, triplets, etc.), but the proton–carbon coupling constants are reduced to a residual value J_{res} . The ^{13}C sensitivity reference standard, 60% $\text{C}_6\text{D}_6/40\%$ dioxane (to which we were introduced in the previous section) is a good test sample for this calibration.

In the off-resonance decoupling method, the residual carbon–hydrogen coupling constant J_{res} of the methylene group of dioxane is measured. Two sequential, off (proton)-resonance experiments are performed, one with the decoupler situated at a higher frequency than the chemical shift of the methylene protons and a second with the decoupler located at

a lower frequency. This technique results in two carbon spectra, which are both triplets and in which the values of the reduced carbon–hydrogen couplings are a function of γB_2 and the two distances that the decoupler is positioned off resonance ($\Delta\nu$).

With the test sample in the magnet, the probe is tuned to both ^{13}C (observation) and ^1H (decoupling) and the magnet homogeneity maximized. A test spectrum is then determined, and, as in the $90^\circ t_p$ calibrations already described, sw is reduced to about 500 Hz and the transmitter offset is adjusted so that it is in the middle of the reduced sw. Since sw has been reduced considerably, np is also decreased, to approximately 4,000 (for a $t_a \sim 4$ s). The resulting spectrum should be processed with a 3–4-Hz line broadening, phased properly, and presented so that the height of the middle signal of the triplet occupies the full vertical size of the screen and the three lines of the spectrum occupy about three-fourths of the horizontal size of the screen.

The first partially decoupled spectrum is acquired with the decoupler frequency situated approximately +1,000 Hz off resonance. The residual coupling is best determined by measuring the distance between the outer lines of the residual triplet and dividing the result by two (the coupling constant appears twice in a triplet; Section 1-5). This high-frequency, residual coupling is then recorded in the lab notebook. The second spectrum is acquired with the decoupler frequency located about –1,000 Hz off resonance and the low-frequency residual coupling similarly measured and noted. Most modern spectrometers have programs that calculate γB_2 from these two residual couplings, as well as the value of the full carbon–hydrogen coupling constant of dioxane (J), which is 142 Hz. γB_2 also can be calculated from the formula

$$\Delta\nu = \frac{\gamma B_2 J_R}{2\pi(J^2 - J_{\text{res}}^2)^{1/2}} \quad (2-5)$$

in which J_{res} is the residual C–H coupling constant of dioxane described previously, J is the natural, one-bond C–H coupling of dioxane (~ 142 Hz), and $\Delta\nu$ is the difference between the resonance frequency of the equivalent dioxane carbons and the decoupler frequency.

The *decoupler modulation frequency* employed in WALTZ decoupling is $4(\gamma B_2)$.

Problems

- 2-1 (a) What is the spectral resolution of an experiment whose acquisition time is 0.66 s?
 (b) What is the minimum sampling rate required to avoid aliasing for a spectral width of 25 kHz?
- 2-2 (a) How many data points are required to describe a spectrum for an experiment whose desired digital resolution is 1.22 Hz/point and whose spectral width is 20 kHz?
 (b) What acquisition time is required for an experiment in which 32,768 data points are used and whose spectral width is 20 kHz?
- 2-3 What is the difference in the amounts of signal acquired for the following two experiments: (a) four 90° pulses with a 3-s delay time between pulses and (b) twelve 30° pulses with no delay time between pulses? Assume in both cases that $t_p = 1$ s and that relaxation is complete by the time the next pulse is delivered.
- 2-4 (a) By how much would a signal increase if the number of scans went from 4 to 16?
 (b) How much would the signal of a 15-hour experiment increase if the operator decided to continue acquisition for another hour? What conclusion can be drawn from the two observations?

Bibliography

- 2.1. S. Braun, H.-O. Kalinowski, and S. Berger, *150 and More Basic NMR Experiments*, 2d ed. New York: Wiley-VCH, 1998.
- 2.2. R. R. Ernst and W. A. Anderson, *Rev. Sci. Instr.*, **37**, 93 (1966).
- 2.3. M. L. Martin, G. J. Martin, and J.-J. Delpuech, *Practical NMR Spectroscopy*. Philadelphia: Heyden, 1980.
- 2.4. E. Fukushima and S. B. W. Roeder, *Experimental Pulse NMR*. Reading, MA: Addison-Wesley, 1981.

3

The Chemical Shift

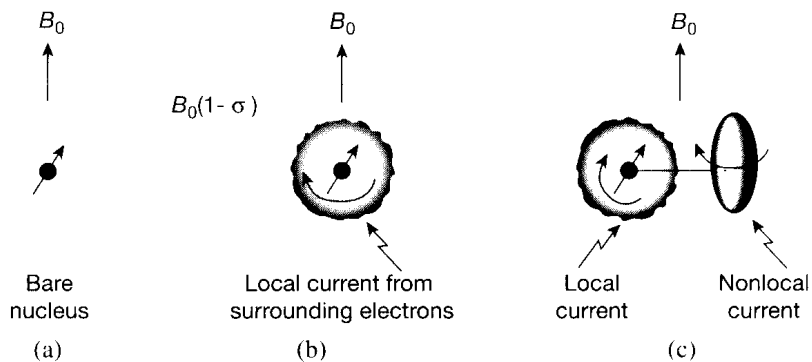
3-1 Factors that Influence Proton Shifts

The magnetic field in the vicinity of a nucleus is altered by the surrounding electrons, from B_0 to a value $B_0(1 - \sigma)$, in which the quantity σ is called the *shielding* (Figure 3-1a and b). Because the magnetic field induced by the electrons opposes the static B_0 field, the effect is said to be *diamagnetic* (or σ^d) and is directly proportional to the electron density.

For the proton, the electronic effects of physical organic chemistry (induction and resonance) conveniently describe the role of structure vis-à-vis electron density. In this way, both the atom to which the proton is attached and those atoms somewhat farther removed can modulate the electron density at the proton and hence alter the shielding effect. An attached or nearby electron-withdrawing atom or group can decrease the shielding and move the resonance of the attached proton towards the left of the chart (to a higher frequency, or downfield; see Figure 1-9). By contrast, an electron-donating atom or group increases the shielding and moves the resonance towards the right of the chart (to a lower frequency, or upfield). Although the effects of shielding on chemical shift are more properly described in terms of frequency, we include field terminology parenthetically, since it still enjoys wide usage.

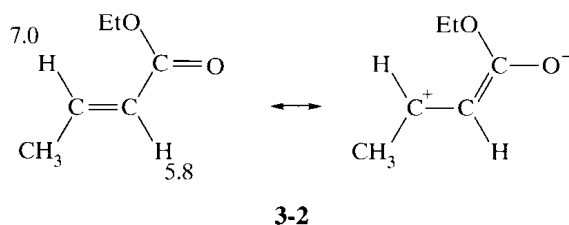
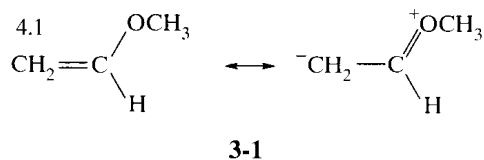
The progressive replacement of hydrogen with chlorine on a methane molecule moves the chemical shift to higher frequency (downfield) because of chlorine's ability to remove electron density from the remaining protons: δ 0.23 for CH_4 , 3.05 for CH_3Cl , 5.30 for

Figure 3-1 Shielding by local (b) and nonlocal (c) currents.



CH_2Cl_2 , and 7.27 for CHCl_3 . The trend for a series of methyl resonances often can be explained in the same fashion by the inductive or polar effect. The chemical shifts for the series CH_3X for which X may be F, HO, H_2N , H, Me_3Si , and Li, respectively, are δ 4.26, 3.38, 2.47, 0.23, 0.0 (TMS, the standard), and -0.4 (this value is considerably dependent on the solvent; the minus sign indicates a lower frequency than TMS), following the electronegativity of the atom attached to CH_3 .

Electron density is influenced by resonance (mesomerism), as well as by inductive effects, as seen in unsaturated molecules such as alkenes and aromatics. The donation of electrons through resonance by a methoxy group increases the electron density at the β position of a vinyl ether (**3-1**) and at the para position of anisole ($\text{C}_6\text{H}_5\text{OCH}_3$). Thus, the

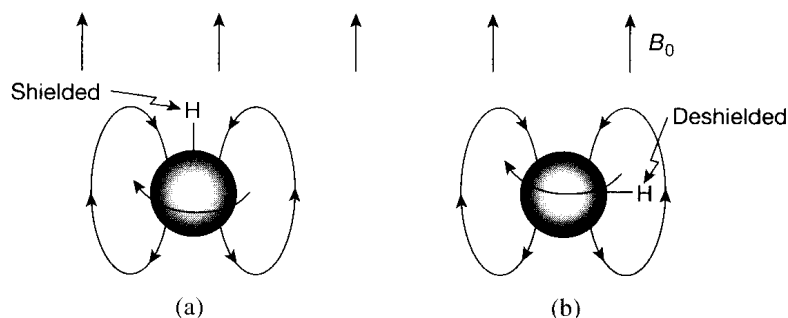


chemical shift of the β protons in **3-1** is at about δ 4.1, in comparison with δ 5.28 in ethene. The resonance frequency decreases, as is expected with the increased shielding from electron donation. The electron-withdrawing inductive effect of CH_3O is overpowered by the resonance effect. Groups such as nitro, cyano, and acyl withdraw electrons by both resonance and induction, so they can bring about significant shifts to a higher frequency (downfield). Ethyl *trans*-crotonate (**3-2**; see also Section 1-6) illustrates this effect. The electron-withdrawing group shifts the β proton strongly to a high frequency (δ 7.0). Although the α proton is not subjected to this strong resonance effect, it is close enough to the electron-withdrawing carboethoxy group to be shifted slightly to a higher frequency (δ 5.8) by the inductive effect.

Hybridization of the carbon to which a proton is attached also influences electron density. As the proportion of s character increases from sp^3 to sp^2 to sp orbitals, bonding electrons move closer to carbon and away from the protons, which then become deshielded. For this reason, methane and ethane resonate at δ 0.23 and 0.86, respectively, but ethene resonates at δ 5.28. Ethyne (acetylene) is an exception in this regard, as we shall see. Hybridization contributes to shifts in strained molecules, such as cyclobutane (δ 1.98) and cubane (δ 4.00), for which hybridization is intermediate between sp^3 and sp^2 .

Induction, resonance, and hybridization modulate electron density at the proton itself, as the result of local electron currents around the nucleus (Figure 3-1b). In the absence of changes in electron density, purely magnetic effects of substituents also can have a major influence on proton shielding, but only when the groups have a nonspherical shape. The drawing in Figure 3-1c represents the combined effects of local fields and nonlocal fields. The group giving rise to the nonlocal field could be, for example, methyl, phenyl, or carbonyl, and the resonating nucleus need not be attached directly to the group. To see why a spherical or isotropic ("same in all directions") group contributes no nonlocal effect, consider a proton attached to such a group—for instance, chlorine. The local effect arises from the

Figure 3-2 Shielding by a spherical (isotropic) group.



electrons that surround the resonating proton. The electrons in the substituent, which are not around the proton, also precess in the applied field (Figure 3-1c). They induce a magnetic field that opposes B_0 and that can have a nonzero value at the position of the proton. The nonlocal induced field may be represented by magnetic lines of force. If the bond from the spherical substituent to the resonating proton is parallel to the direction of B_0 , as in Figure 3-2a, the lines of force from the induced field oppose B_0 at the proton, thereby shielding it. If the bond from the substituent to the proton is perpendicular to B_0 , as in Figure 3-2b, the induced lines of force reinforce those of B_0 , deshielding the proton. Because the group is isotropic, the two arrangements are equally probable. As the molecule tumbles in solution, the effects of the induced field cancel out. Other orientations cancel each other in a similar fashion. Thus, an isotropic substituent has no effect over and above what it provides to local currents from induction or resonance.

Most substituents, however, are not spherical. The flat shape of an aromatic ring, for example, resembles an oblate ellipsoid, and the elongated shape of single or triple bonds resembles a prolate ellipsoid. For a proton situated at the edge of an oblate ellipsoid, such as a benzene ring, there again are two extremes (Figure 3-3). When the flat portion is perpendicular to the static field (Figure 3-3a), a proton at the edge is deshielded, since the induced lines of force reinforce the B_0 field. For the same geometry, a proton situated over the middle of the ellipsoid is shielded, as the induced lines of force oppose B_0 . For this geometry, the induced field is large because aromatic electrons circulate easily above and below the ring. When the ring is parallel to B_0 (Figure 3-3b), however, induced currents would have to move from one ring face to the other. As a result, little current or field is induced from this geometry. The cancellation seen for the sphere as the molecule tumbles in solution does not occur for aromatic rings. A group that has appreciably different currents induced by B_0 from different orientations in space is said to have *diamagnetic anisotropy*. Because an oblate ellipsoid has the larger effect for the geometry shown in Figure 3-3a, a proton at the edge of an aromatic ring is deshielded and one at or over the center is shielded. It is for this reason that benzene resonates at such a high frequency (low field, δ 7.27), compared with the frequency of alkenes (e.g., ethene, at δ 5.28).

Figure 3-3 Shielding by an oblate ellipsoid, the model for aromatic rings.

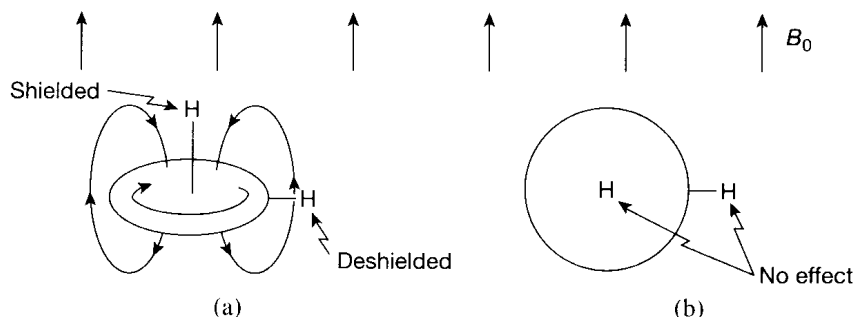


Figure 3-4 illustrates how the diamagnetic effect of benzene is shielding (+) above and below the ring, but deshielding (-) around the edge. This effect was modeled quantitatively by McConnell as the influence of a magnetic dipole on the point in space at which a proton resides. He derived the formula

$$a_A(r, \theta) = \frac{(\chi_L - \chi_T)(3 \cos^2 \theta - 1)}{3r^3} \quad (3-1)$$

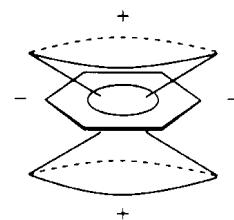
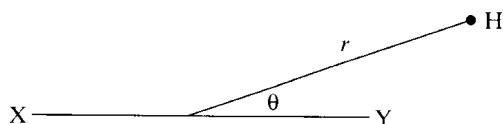
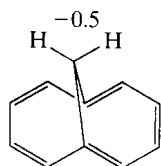


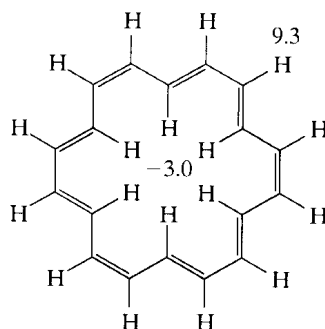
Figure 3-4 Shielding geometry for a benzene ring.

for the shielding σ_A by an anisotropic group (represented by the dipole X-Y) of a hydrogen atom at an arbitrary point in space with polar coordinates (r, θ) . In this equation, r is the distance from the midpoint of the group to the point, θ is the angle subtended by the line representing the longitude of the group on the line from the midpoint of the group to the point, and χ_L and χ_T are the diamagnetic susceptibilities of the group along its longitude and its transverse (e.g., Figure 3-3a and b, respectively). The effect changes sign at a null point at which the angle from the ring is $54^\circ 44'$, the so-called magic angle at which the expression $(3 \cos^2 \theta - 1)$ goes to zero.

Although the protons of benzene reside in the deshielded portion of the cone, molecules have been constructed to explore the full range of the effect. The methylene protons of methano[10]annulene (**3-3**) are constrained to positions above the aromatic 10π electron



3-3

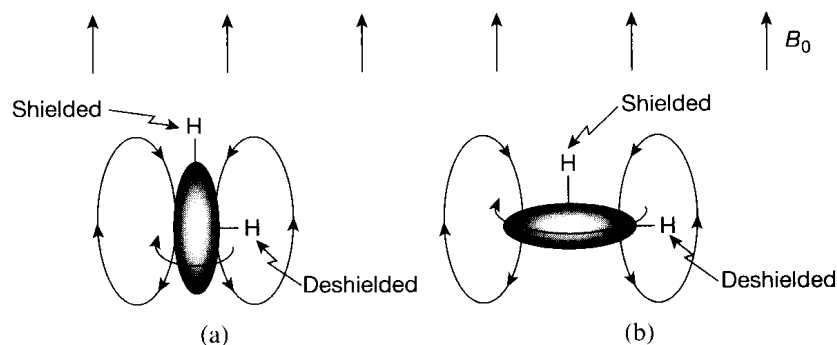


3-4

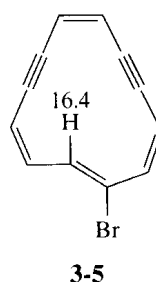
system and consequently are shielded to a position ($\delta -0.5$) at an even lower frequency (higher field) than TMS. [18]Annulene (**3-4**) has one set of protons around the edge of the aromatic ring that resonates at a deshielded position of $\delta 9.3$ and a second set located toward the center of the ring that resonates at a shielded position of $\delta -3.0$.

The presence of $(4n + 2)\pi$ electrons is a requirement for the existence of a diamagnetic circulation of electrons. Pople showed that an external magnetic field can induce a paramagnetic circulation in a $4n\pi$ electron system. Under such circumstances, the conclusions drawn from the configuration in Figure 3-3a are reversed (i.e., outer protons are shielded and inner protons deshielded). The spectrum of [16]annulene is consistent with this interpretation (inner protons at $\delta 10.3$, outer at 5.2), but the most dramatic example is

Figure 3-5 Shielding by a prolate ellipsoid, the model for a chemical bond.



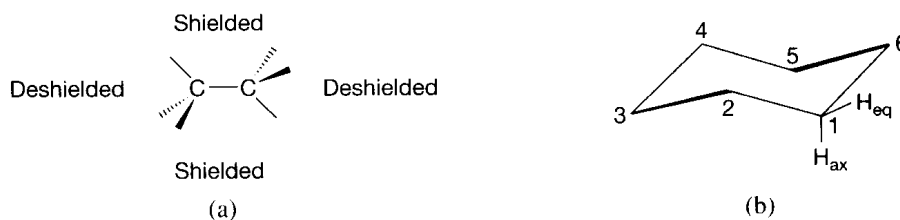
the [12]annulene (**3-5**). The bromine atom was included to prevent a conformational inter-conversion of the inner and outer protons. The indicated inner proton of **3-5** resonates at δ 16.4, compared with δ -3.0 for the inner protons of [18]annulene (**3-4**).



The two arrangements of a prolate ellipsoid, used as a model for a chemical bond, may be considered in a similar fashion (Figure 3-5). In this case, it is not always clear which arrangement has a stronger induced current. The π electrons of acetylene (ethyne) provide one clear-cut example. When the axis of the molecule is parallel to the B_0 field (as in Figure 3-5a), the π electrons are particularly susceptible to circulation around the cylinder. The alternative arrangement in Figure 3-5b is ineffective for acetylene and therefore does not provide a canceling effect. The acetylenic proton is attached to the end of the array of electrons and hence is shielded. For this reason, the acetylene resonance (δ 2.88) falls between those of ethane (δ 0.86) and ethene (δ 5.28). The effects of hybridization thus are superseded by those of diamagnetic anisotropy. In terms of the McConnell equation (eq. 3-1), the longitudinal susceptibility is much greater than the transverse susceptibility (i.e., $\chi_L > \chi_T$). Thus, σ_A is positive at the end of the bond ($\theta = 0^\circ$), resulting in a shift to a lower frequency (higher field).

The circulation of charge around a carbon-carbon single bond is less strong than that of a triple bond, and the larger effect is seen when the axis of the bond is perpendicular to B_0 (as in Figure 3-5b—i.e., $\chi_T > \chi_L$). Thus, a proton at the side of a single bond is more shielded than one along its end (Figure 3-6a). The axial and equatorial protons of a rigid cyclohexane ring exemplify these arrangements (Figure 3-6b). The two protons illustrated are equivalently positioned with respect to the 1,2 and 6,1 bonds, which thus produce no differential effect. The 1-axial proton, however, is in the shielding region of the farther removed 2,3 and 5,6 bonds (darkened), whereas the 1-equatorial proton is in their deshielding

Figure 3-6 (a) Shielding region around a carbon-carbon single bond. (b) Geometry of a cyclohexane ring.



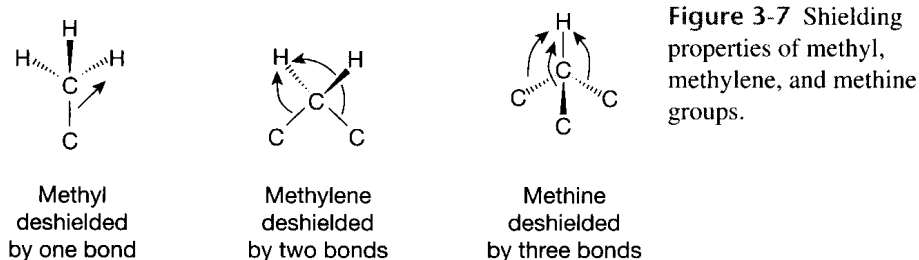


Figure 3-7 Shielding properties of methyl, methylene, and methine groups.

region. In general, axial protons are more shielded and resonate at a lower frequency (higher field) than do equatorial protons, typically by about 0.5 ppm.

The high-frequency position for methine compared with methylene protons and for methylene compared with methyl protons [CH_3X to $\text{CH}_3\text{CH}_2\text{X}$ to $(\text{CH}_3)_2\text{CHX}$] for a single X group may be attributed to the anisotropy of the additional C—C bonds (Figure 3-7), although changes in hybridization also may contribute.

The highly shielded position of cyclopropane resonances (δ 0.22, vs. 1.43 in cyclohexane) may be attributed either to an aromatic-like ring current or to the anisotropy of the C—C bond that is opposite to a CH_2 group in the three-membered ring. The effect is much larger than the indicated 1.2 ppm ($1.4 - 0.2$), because the sp^2 cyclopropane carbon orbital to hydrogen (compared with the sp^3 orbital in cyclohexane) deshields the proton. A cyclopropane ring also can shield adjacent hydrogens. In spiro[2.5]octane (**3-6**), the indicated equatorial proton resonates 1.2 ppm lower frequency (higher field) than does the axial proton. Since



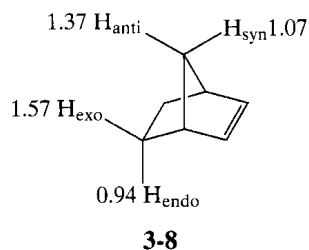
H_{ax} is normally at 0.5 ppm to lower frequency, the differential effect is 1.7 ppm. In **3-6**, H_{eq} is perched over the shielding region of the cyclopropane ring, so it undergoes a very strong shift to a lower frequency (upfield).

Most common single bonds (C—O, C—N) have shielding properties that parallel those of the C—C bond. There appears to be a sign reversal, however, for the C—S bond. In all these heteroatomic cases, the geometry is more complex than that for the C—C bond. In some instances, a lone electron pair can have a special effect. In *N*-methylpiperidine (**3-7**), the axial lone pair shields the vicinal H_{ax} by an $n - \sigma^*$ interaction without any effect on H_{eq} . As a result, $\Delta\delta_{\text{ax}}$ increases to about 1.0 ppm or more.

The anisotropy of double bonds is more difficult to assess, because they have three non-equivalent axes. Thus, the McConnell equation, with only two axes, does not apply. Protons situated over double bonds are, in general, more shielded than those in the plane (Figure 3-8), both for alkenes (Figure 3-8a) and for carbonyl groups (Figure 3-8b). The position of the methylene protons in norbornene (**3-8**) may be explained in this fashion,



Figure 3-8 Shielding properties of (a) the $\text{C}=\text{C}$ double bond and (b) the $\text{C}=\text{O}$ double bond.



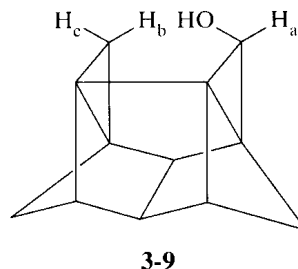
since the syn and endo protons, respectively, are shielded with respect to the anti and exo protons. The highly deshielded position of aldehydes (δ 9.7) is attributed to a combination of a strong inductive effect and the diamagnetic anisotropy of the carbonyl group.

The nonspherical array of lone pairs of electrons may exhibit diamagnetic anisotropy, although, alternatively, the effect may be considered a perturbation of local currents. A proton that is hydrogen bonded to a lone pair invariably is deshielded. Thus, the hydroxyl proton in ethanol as a dilute solute in a non-hydrogen-bonding solvent such as CCl_4 resonates at δ 0.7, but, in pure ethanol with extensive hydrogen bonding, it resonates at δ 5.3. Carboxylic protons (CO_2H) resonate at an extremely high frequency (low field), because every proton is hydrogen bonded within a dimer. Lone-pair anisotropy also has been invoked to explain trends in ethyl groups ($\text{CH}_3\text{CH}_2\text{X}$). The resonance positions of the CH_2 group attached to X are well explained by induction [for X = F (δ 4.36), Cl (3.47), Br (3.37), I (3.16)], but the trend for the more distant methyl group is opposite (in the same order, δ 1.24, 1.33, 1.65, and 1.86). As the size of X increases, the lone pair moves closer to the methyl group and deshields it more strongly.

Functional group effects on proton chemical shifts may be explained largely by the two general effects just described. (1) Electron withdrawal or donation by resonance or induction (including hybridization) alters the electron density and hence the local field around the resonating proton. Higher electron density shields the proton and moves its resonance position to a lower frequency (downfield). (2) Diamagnetic anisotropy of nonspherical substituents is largely responsible for the proton resonance positions of aromatics, acetylenes, aldehydes, cyclopropanes, cyclohexanes, alkenes, and, possibly, hydrogen-bonded species.

Two other, less general diamagnetic effects also influence chemical shifts. As discussed, a substituent may deshield a neighboring proton (i.e., decrease σ^d) by inductive electron withdrawal. If the substituent is distant by a sufficient number of bonds, the effect becomes negligible. When a substituent atom is held rigidly at a distance from the resonating nucleus that is less than the sum of the van der Waals radii, the atom repels electrons from the vicinity of the resonating atom. The net effect, therefore, is a decrease in σ^d . The nucleus is deshielded, and its resonance is shifted downfield. The phenomenon arises from the mutual repulsion of induced dipoles (by van der Waals or dispersion forces). The magnitude of the effect (σ_w) falls off very rapidly with increasing internuclear distance and depends critically on the size and polarizability of the nuclei. A proton is not deshielded by another proton until they are within about 2.5 Å of each other. A bromine atom can deshield a proton from a much greater distance, and a fluorine atom is intermediate.

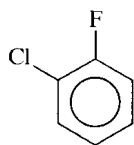
The 0.2-ppm downfield shift of the *tert*-butyl protons in *ortho*-di-*tert*-butylbenzene with respect to the *tert*-butyl resonances in the meta and para isomers has been attributed to a van der Waals effect. Possibly the most dramatic example is in the partial cage compound **3-9**, in



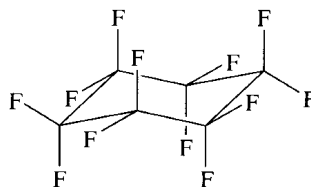
which the chemical shifts of H_b and H_c are δ 3.55 and 0.88, respectively. By comparison, the methylene protons of cyclohexane resonate at about δ 1.4. The oxygen atom therefore deshields H_b by over 2 ppm. Interestingly, the electron density displaced from H_b is in part shifted to H_c , which is shielded by about 0.5 ppm.

A polar bond in a molecule generates an electric field that can have an appreciable value at the position of a nearby resonating nucleus. This electric field distorts the electronic structure around the nucleus and causes a deshielding by diminishing σ^d . Unlike the inductive effect, the electric-field effect can be derived from a polar group that is many bonds removed from the resonating nucleus. For a significant value of σ_E , the polar bond must be reasonably close to the nucleus, but need not be in van der Waals contact.

Many examples of electric-field shielding have come from ^{19}F spectra, since the larger shifts of the fluorine nuclei magnify the effect. The ^{19}F resonance of 1-chloro-2-fluorobenzene (**3-10**) is more than 20 ppm to a higher frequency than a simple inductive effect could explain. The interpretation that this large additional shift is due to the electric field of the C—Cl bond has been substantiated by calculations. The 18-ppm chemical shift between the axial and equatorial fluorines in perfluorocyclohexane (**3-11**) compares with a 0.5-ppm difference for the corresponding protons in cyclohexane. The effect of diamagnetic anisotropy (σ_A) is not sufficient to explain the large ^{19}F separation. The electric field at axial and equatorial fluorine atoms in **3-11** is different from the electric field at the other polar bonds in the molecule. For both of these atoms, there may be a van der Waals contribution as well, since the nuclei are relatively close. An analysis of ^{19}F chemical shifts is not complete unless both effects are taken into consideration. The importance of these effects has not been fully explored in many systems or for many nuclei, so much work remains to be done.



3-10



3-11

3-2 Proton Chemical Shifts and Structure

The assignment of structure on the basis of NMR spectra requires knowledge of the relationship between chemical shifts and functional groups. Normally, both proton and carbon spectra are recorded and analyzed. This section considers the relationship between proton resonances and structure. Figure 3-9 summarizes the resonance ranges for common proton functionalities.

3-2a Saturated Aliphatics

Alkanes. Cyclopropane has the lowest-frequency position (δ 0.22) of any simple hydrocarbon, because of a ring current or the anisotropy of the carbon-carbon bonds. Unsubstituted methane has essentially the same chemical shift (δ 0.23). The progressive addition of saturated carbon-carbon bonds to methane results in a shift to a higher frequency (downfield), as in the series consisting of ethane (CH_3CH_3 , δ 0.86), propane ($\text{CH}_3\text{CH}_2\text{CH}_3$, δ 1.33), and isobutane [$(\text{CH}_3)_3\text{CH}$, δ 1.56]. The resonance position of cyclobutane is at an unusually high frequency (δ 1.98). Cyclic structures other than cyclopropane and cyclobutane have resonance positions similar to those of open-chain systems—for example, δ 1.43 for cyclohexane. In complex natural products such as steroids or alkaloids, a large number of structurally similar alkane protons lead to overlapping resonances in the region δ 0.8–2.0, the analysis of which requires the highest possible field.

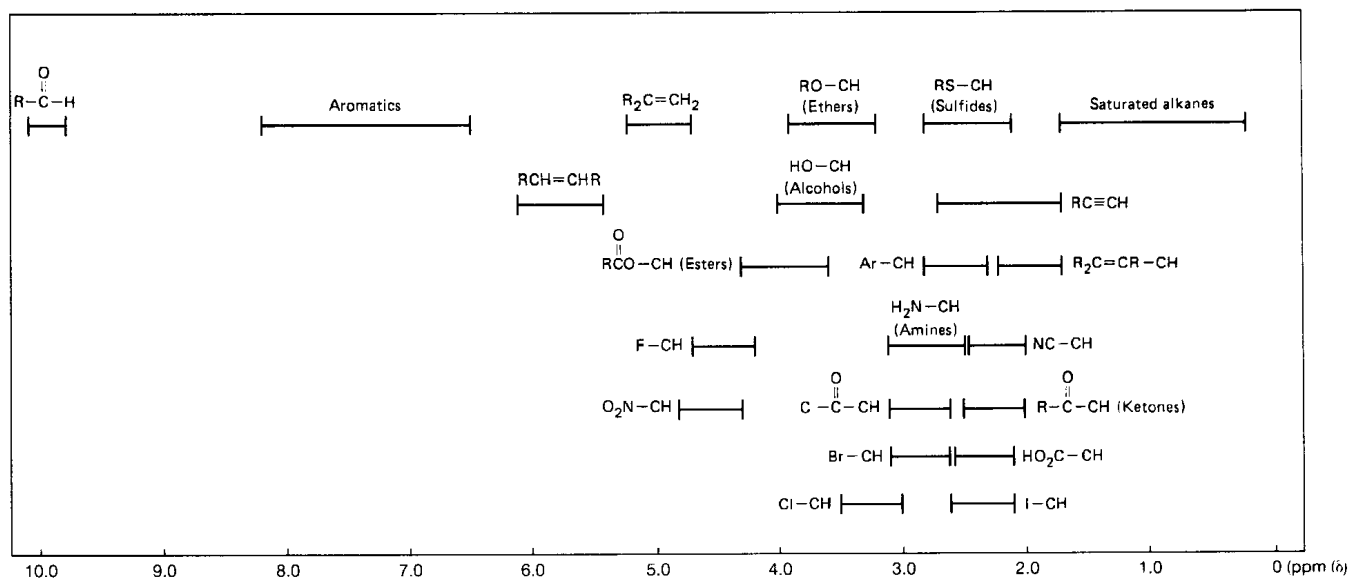
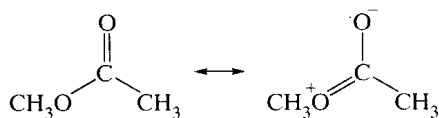
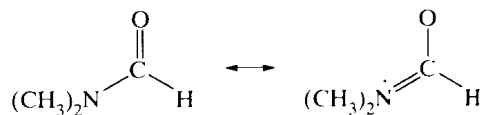


Figure 3-9 Proton chemical-shift ranges for common structural units. The symbol CH represents methyl, methylene, or methine, and R represents a saturated alkyl group. The range for $-\text{CO}_2\text{H}$ and other strongly hydrogen-bonded protons is off scale to the left. The indicated ranges are for common examples; actual ranges can be larger.

Functionalized Alkanes. The presence of a functional group alters the resonance position of neighboring protons according to the inductive effect of the group and its diamagnetic anisotropy. Ethane (δ 0.86) is a useful point of reference for methyl groups. The replacement of one methyl group in ethane with hydroxyl yields methanol (CH_3OH), whose resonance position is δ 3.38. The electron-withdrawing effect of the oxygen atom is the primary cause of the large shift to a higher frequency (lower field). Just as in unfunctionalized alkanes, methylene groups ($\text{CH}_3\text{CH}_2\text{OH}$, δ 3.56) and methine groups [$(\text{CH}_3)_2\text{CHOH}$, δ 3.85] are found at progressively higher frequencies. In general, methylene and methine protons resonate about 0.3 and 0.6 ppm, respectively, to a higher frequency than do analogous methyl groups. There is considerable variation from one example to another, depending on the remainder of the structure, so that resonances for a given functionality can range over 1 ppm. Ether resonances are similar to those for alcohols (CH_3OCH_3 , δ 3.24). Ester alkoxy groups, however, usually resonate at an even higher frequency ($\text{CH}_3\text{O}(\text{CO})\text{CH}_3$, δ 3.67), because the attached oxygen is more electron withdrawing as the result of ester resonance (3-12).



3-12



3-13

Since nitrogen is not so electron withdrawing as oxygen, amines resonate at a somewhat lower frequency (higher field) than ethers— δ 2.42 for methylamine (CH_3NH_2 in aqueous solution). Introducing a positive charge through quaternization induces increased electron withdrawal and causes a shift to a high frequency, as with $(\text{CH}_3)_4\text{N}^+$ (δ 3.33), compared with $(\text{CH}_3)_3\text{N}$ (δ 2.22). An intermediate charge, as is produced in amides through resonance, results in an intermediate shift, as with *N,N*-dimethylformamide (3-13, δ 2.88).

Table 3-1 Substituent Parameters for Shoolery's Rule
(R = H or Alkyl)

Substituent	Δ_i	Substituent	Δ_i
CH ₃	0.47	C ₆ H ₅	1.83
CR=CR ₂	1.32	Br	2.33
C≡CR	1.44	OR	2.36
NR ₂	1.57	Cl	2.53
SR	1.64	OH	2.56
CN	1.70	O(CO)R	3.01
CO—R	1.70	NO ₂	3.36
I	1.82	F	4.00

The lower electronegativity of sulfur means that sulfides are at a lower frequency (higher field), δ 2.12 for dimethyl sulfide (CH₃SCH₃). Halogens move resonances to higher frequency according to the electronegativity of the atom: δ 2.15 for CH₃I, 2.69 for CH₃Br, 3.06 for CH₃Cl, and 4.27 for CH₃F. In all these cases, the shifts probably are affected by the anisotropy of the C—X bond, but this factor is hard to assess and is somewhat diminished by free rotation in open-chain systems. Other electron-withdrawing substituents also cause shifts to higher frequencies, as, for example, does cyano in acetonitrile (CH₃CN, δ 2.00) and nitro in nitromethane (CH₃NO₂, δ 4.33). Electron-donating atoms, such as silicon in TMS (δ 0.00), cause shifts to lower frequencies.

Methyl groups attached to unsaturated carbons are usually found in the region δ 1.7–2.5, as are the allyl protons in isobutylene [(CH₃)₂C=CH₂, δ 1.70], the propargylic protons in methylacetylene (CH₃C≡CH, δ 1.80), and the benzylic protons in toluene (C₆H₅CH₃, δ 2.31). Methyl groups on carbon–oxygen double bonds are found in the region δ 2.0–2.7. [Cf. acetone (CH₃(CO)CH₃, δ 2.07), acetic acid (CH₃CO₂H, δ 2.10), acetaldehyde (CH₃CHO, δ 2.20), and acetyl chloride (CH₃COCl, δ 2.67).] These functionalities exhibit an appreciable range determined by further substitution.

Empirical correlations between structure and proton chemical shift have been developed for common structural units. The earliest, called Shoolery's rule, provides the chemical shift of protons in a Y—CH₂—X group by adding substituent parameters Δ_i to the chemical shift of methane (see Table 3-1):

$$\delta = 0.23 + \Delta_X + \Delta_Y. \quad (3-2)$$

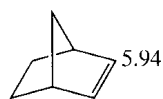
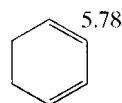
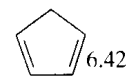
The calculation is reasonably successful for CH₂XY, but additivity fails due to interactions between groups for many CHXYZ examples. For instance, the calculated shift for CH₂Cl₂ is $0.23 + (2 \times 2.53) = 5.29$ (observed at δ 5.30), but for CHCl₃ it is $0.23 + (3 \times 2.53) = 7.82$ (observed at δ 7.27). Corrections may be made for tertiary systems.

3-2b Unsaturated Aliphatics

Alkynes. The anisotropy of the triple bond results in a relatively low frequency (upfield) position for protons on sp-hybridized carbons. For acetylene (ethyne) itself, the chemical shift is δ 2.88, and the range is about δ 1.8–2.9.

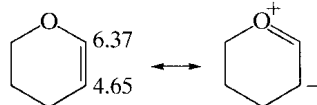
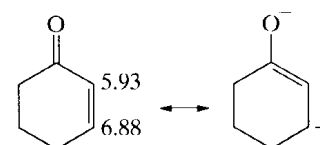
Alkenes. The increased electronegativity of the sp² carbon and the modest anisotropy of the carbon–carbon double bond result in a high-frequency (low-field) position for protons on alkene carbons. The range is quite large (δ 4.5–7.7), as the exact resonance position depends on the nature of the substituents on the double bond. The value for ethene is δ 5.28. 1,1-Disubstituted hydrocarbon alkenes (vinylidenes), including exomethylene groups on rings (=CH₂), resonate at a somewhat lower frequency; cf. isobutylene [(CH₃)₂C=CH₂,

δ 4.73]. The CH₂ part of a vinyl group, —CH=CH₂, is also usually at a lower frequency than δ 5. 1,2-Disubstituted alkenes, as found, for example, in endocyclic ring double bonds (—CH=CH—) and trisubstituted double bonds, generally resonate at a higher frequency than δ 5; cf. *trans*-2-butene (CH₃CH=CHCH₃, δ 5.46). Angle strain on the double bond moves the resonance position to a higher frequency, as with norbornene (**3-14**, δ 5.94). Conjugation also usually moves the resonance position to a higher frequency; cf. 1,3-cyclohexadiene (**3-15**, δ 5.78). The double bonds in 1,3-cyclopentadiene (**3-16**) are both strained

**3-14****3-15****3-16**

and conjugated, so the chemical shift is at an even higher frequency, δ 6.42. The phenyl ring of styrene (C₆H₅CH=CH₂) withdraws electrons from the double bond by induction, so the position of the nearer CH (α) proton is moved to a high frequency, δ 6.66. The more distant CH₂ (β) protons resonate at δ 5.15 and 5.63. The anisotropy of the aromatic ring is largely responsible for the difference between the β protons. (The closer *cis* proton is shifted to a higher frequency.) The nonaromatic portion of styrene, —CH=CH₂, is a *vinyl* group, and the term should be restricted to that structure. The term *alkenic*, not *vinyllic*, should be used generically for protons on double bonds.

Carbonyl groups are strongly electron withdrawing by both induction and resonance. Thus, the β protons on double bonds conjugated with a carbonyl group have very high frequency (downfield) resonances—for example, δ 6.83 in the α, β-unsaturated ester *trans*-CH₃CH₂O₂CCH=CHCO₂CH₂CH₃. Compounds **3-17** and **3-18** illustrate the effects

**3-17****3-18**

of conjugation on alkene chemical shifts. Whereas the alkenic protons of cyclohexene resonate at a normal δ 5.59, the oxygen atom in the unsaturated ether **3-17** donates electrons to the β position by resonance and moves the β proton to a lower frequency (δ 4.65). The oxygen withdraws electrons inductively from the α position, whose proton resonance moves to a higher frequency (δ 6.37). In contrast, the carbonyl group in the unsaturated ketone **3-18** withdraws electrons from the β position by resonance and moves the β proton to a higher frequency (δ 6.88). In this case, the inductive effect of the carbonyl group causes a small shift to higher frequency for the α proton (δ 5.93).

These effects were quantified in the empirical approach of Tobey and of Pascual, Meier, and Simon, who used the formula

$$\delta = 5.28 + Z_{\text{gem}} + Z_{\text{cis}} + Z_{\text{trans}} \quad (3-3)$$

to calculate the chemical shift of a proton on a double bond. Substituent constants Z_i (Table 3-2) for groups geminal, *cis*, or *trans* to the proton under consideration are added to the chemical shift of ethene. For example, the resonances of a crotonaldehyde (CH₃—CH_β=CH_α—CHO) at δ 6.87 and 6.03 may be assigned and the stereochemistry of the molecule determined. For the *cis* stereochemistry, the calculated shift for H_β is 6.93 (5.28 + 0.44 + 1.21) and for H_α is 6.02 (5.28 + 1.03 - 0.29); for the *trans* stereochemistry, the calculated shift for H_β is 6.69 (5.28 + 0.44 + 0.97) and for H_α is 6.05

Table 3-2 Substituent Parameters for the Tobey–Simon Rule

Substituent	Z_{gem}	Z_{cis}	Z_{trans}
H	0.0	0.0	0.0
Alkyl	0.44	-0.26	-0.29
CH ₂ O, CH ₂ I	0.67	-0.02	-0.07
CH ₂ S	0.53	-0.15	-0.15
CH ₂ Cl, CH ₂ Br	0.72	0.12	0.07
CH ₂ N	0.66	-0.05	-0.23
C=C	0.50	0.35	0.10
C≡N	0.23	0.78	0.58
C=C (isolated)	0.98	-0.04	-0.21
C=C (conjugated)	1.26	0.08	-0.01
C=O (isolated)	1.10	1.13	0.81
C=O (conjugated)	1.06	1.01	0.95
CO ₂ H (isolated)	1.00	1.35	0.74
CO ₂ R (isolated)	0.84	1.15	0.56
CHO	1.03	0.97	1.21
OR (R aliphatic)	1.18	-1.06	-1.28
OCOR	2.09	-0.40	-0.67
Aromatic	1.35	0.37	-0.10
Cl	1.00	0.19	0.03
Br	1.04	0.40	0.55
NR ₂ (R aliphatic)	0.69	-1.19	-1.31
SR	1.00	-0.24	-0.04

(5.28 + 1.03 - 0.26). The *cis* stereochemistry is supported and the resonances are assigned. Although the parameters Z_i incorporate inductive and resonance effects, steric effects can cause deviations from observed positions.

Aldehydes. The aldehydic proton is shifted to a very high frequency (low field) by induction and diamagnetic anisotropy of the carbonyl group. For acetaldehyde (CH₃CHO), the value is δ 9.80, and the range is relatively small, generally δ 10 \pm 0.3.

3-2c Aromatics

Diamagnetic anisotropy of the benzene ring augments the already deshielding influence of the sp² carbon atoms to yield a very high frequency (low field) position for benzene, δ 7.27. Inductive and resonance effects of substituents are similar to those in alkenes. For toluene (C₆H₅CH₃), the electronic effect of the methyl group is small, and all five aromatic protons resonate at about δ 7.2. A narrow range thus is typical for saturated hydrocarbon substituents (arenes). Conjugating substituents, however, result in a large spread in the aromatic resonances and in spectral multiplicity from spin–spin splitting. For nitrobenzene (Figure 3-10), the inductive effect of the nitro group (3-19) moves all resonances to a higher frequency with

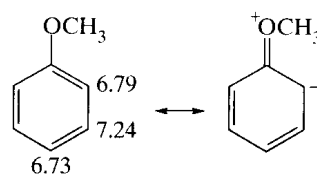
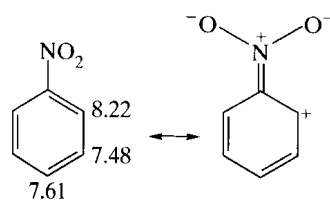
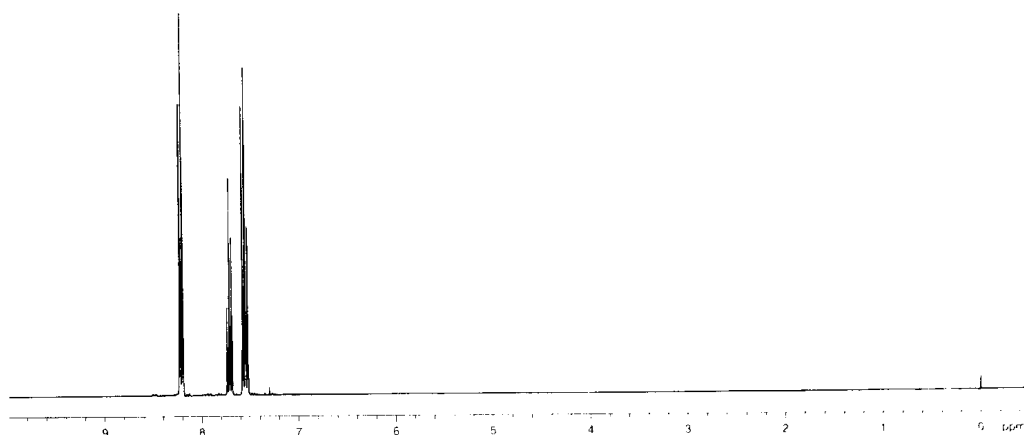
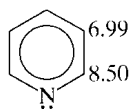


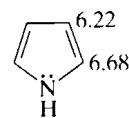
Figure 3-10 The 300 MHz ^1H spectrum of nitrobenzene in CDCl_3 .



respect to benzene, but the ortho and para protons are shifted further by electron withdrawal by resonance. By contrast, the methoxy group in anisole (**3-20**) donates electrons by resonance, so the ortho and para positions are at a lower frequency than that for benzene. The α protons in heterocycles generally are shifted to a high frequency, as in pyridine (**3-21**) and pyrrole (**3-22**), largely because of the inductive effect of the heteroatom.



3-21

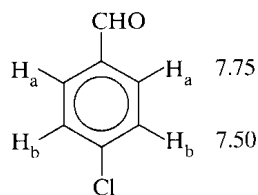


3-22

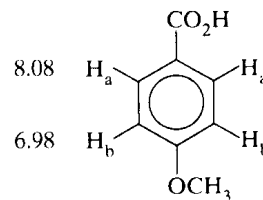
Aromatic proton resonances also may be treated empirically, provided that no two substituents are ortho to each other (producing steric effects). The shift of a particular proton is obtained by adding substituent parameters to the shift of benzene, as shown in the relationship

$$\delta = 7.27 + \sum S_i \quad (3-4)$$

and in Table 3-3 (which was compiled from many sources by Jackman and Sternhell). For example, the spectrum of 4-chlorobenzaldehyde (**3-23**) contains two doublets, centered at δ 7.75 and 7.50. The calculated position for H_a is 7.79 ($7.27 + 0.58 - 0.06$) and for H_b is 7.50 ($7.27 + 0.02 + 0.21$). Similarly, the observed resonances for 4-methoxybenzoic acid (**3-24**) are at δ 8.08 and 6.98, and the calculated positions are 7.98 for H_a and 6.98 for H_b .



3-23



3-24

Spectral assignments therefore often can be made with confidence. For multiply substituted aromatic rings, the identity of the substituents, but not their relative positions, may be known. Calculation of chemical shifts for all possible substitution possibilities and comparison with the observed positions can produce a structural assignment.

Table 3-3 Substituent Parameters for Aromatic Proton Shifts

Substituent	S_{ortho}	S_{meta}	S_{para}
CH ₃	-0.17	-0.09	-0.18
CH ₂ CH ₃	-0.15	-0.06	-0.18
NO ₂	0.95	0.17	0.33
Cl	0.02	-0.06	-0.04
Br	0.22	-0.13	-0.03
I	0.40	-0.26	-0.03
CHO	0.58	0.21	0.27
OH	-0.50	-0.14	-0.40
NH ₂	-0.75	-0.24	-0.63
CN	0.27	0.11	0.30
CO ₂ H	0.80	0.14	0.20
CO ₂ CH ₃	0.74	0.07	0.20
COCH ₃	0.64	0.09	0.30
OCH ₃	-0.43	-0.09	-0.37
OCOCH ₃	-0.21	-0.02	-0.13
N(CH ₃) ₂	-0.60	-0.10	-0.62
SCH ₃	0.37	0.20	0.10

3-2d Protons on Oxygen and Nitrogen

The NMR properties of protons attached to highly electronegative atoms such as oxygen or nitrogen are strongly influenced by the acidity, basicity, and hydrogen-bonding properties of the medium. For hydroxyl protons, minute amounts of acidic or basic impurities can bring about rapid exchange, as illustrated in Figure 1-30. Such protons then are averaged with other exchangeable protons, either in the same molecule or in other molecules, such as the solvent. Only a single resonance is observed for all the exchangeable protons at a weighted-average position. In addition, no coupling is observed with other protons in the molecule. The resonance may vary from being quite sharp to having a characteristically slightly broadened shape, depending on the exchange rate. A convenient experimental procedure to identify hydroxyl resonances in organic solvents such as CDCl₃ is to add a couple of drops of D₂O to the NMR tube. Shaking the tube briefly results in exchange of the OH protons with deuterium, which is in molar excess. The aqueous layer separates out, usually to the top in halogenated solvents, and is located above the receiver coil. Consequently, hydroxyl resonances in the original spectrum may be identified by their absence in the two-phase case. In highly purified basic solvents, such as dimethyl sulfoxide, exchange is slow and coupling between OH and adjacent protons can be observed.

At infinite dilution in CCl₄ (no hydrogen bonding), the OH resonance of alcohols may be found at about δ 0.5. Under more normal conditions of 5% to 20% solutions, hydrogen bonding results in resonances in the δ 2–4 range. More acidic phenols (ArOH) have resonances at a higher frequency (lower field), δ 4–8. If the phenolic hydroxyl can hydrogen bond fully with an ortho group, the position moves to δ 10 or higher. Most carboxylic acids (RCO₂H) exist as hydrogen-bonded dimers or oligomers, even in dilute solution. Because essentially every OH proton is hydrogen bonded, the acid protons resonate at the very high frequency range of δ 10–14 (δ 11.37 for acetic acid, CH₃CO₂H). Other highly hydrogen-bonded protons also may be found in this range, such as sulfonic acids (RSO₃H) or the OH proton of enolic acetylacetone. Because of the variable position and appearance of hydroxy resonances, including that of water, one must be very careful of spectral assignments for the group.

Protons on nitrogen have similar properties, but the slightly lower electronegativity of nitrogen results in lower frequency (higher field) shifts than those of analogous OH protons: δ 0.5–3.5 for aliphatic amines, δ 3–5 for aromatic amines (anilines), δ 4–8 for amides, pyrroles, and indoles, and δ 6–8.5 for ammonium salts. The most common nuclide of nitrogen is ^{14}N , which is quadrupolar and possesses unity spin. (See Sections 1-7 and 5-1.) The three resulting spin states could conceivably split the resonance of attached protons into a 1 : 1 : 1 triplet, but such a pattern is seen only in highly symmetrical cases, such as NH_4^+ or NMe_4^+ . Otherwise, the rapid relaxation of quadrupolar nuclei averages the spin states. The resonance of a proton on nitrogen thus can vary from a triplet to a sharp singlet, depending on the relaxation rate, but the most common result is a broadened resonance representing incomplete averaging. In some cases, the broadening can render NH resonances almost invisible. In addition, amino protons can exchange rapidly with solvent or other exchangeable protons to achieve an averaged position.

3-2e Programs for Empirical Calculations

Tables 3-1 through 3-3 contain data on which empirical calculations of chemical shifts can be made. The tables represent a fraction of the data available on the fundamental alkane, alkene, and aromatic structures. Moreover, corrections must be applied in order to avoid non-additivity caused primarily by steric effects. Thus, three groups on a single carbon atom, two large groups cis to each other on a double bond, or any two ortho groups can cause deviations from the parameters listed in the tables. If sufficient model compounds are available, the corrections shown can be applied. Further empirical calculations are possible for any structural entity, so that the eclipsing strain in cyclobutanes, the variety of steric interactions in cyclopentanones, or the variations in angle strain in norbornanes may be taken into account.

Commercial software for carrying out these calculations, based on hundreds of thousands of chemical shifts in a database, is widely available. The procedure is begun by drawing the structure of the compound under study. The program then searches the database for molecules with protons whose structural environment resembles that of the compound under study. From the available data, the program calculates and displays the expected proton spectrum. Such information is extremely valuable, because the amount of empirical data available from the program vastly exceeds either the amount resident in the minds of most experimentalists or even in all published compilations.

The approach, however, is subject to four limitations. (1) The specific skeleton or functional group may not exist in the database. (2) The database may not include sufficient information to assess steric effects that can lead to nonadditivity within an available series. (3) Solvent effects, to be described in Section 3-3, are not fully taken into consideration. (4) Coupling constants are calculated from simple relationships, such as the Karplus equation (Section 4-5). Because the calculations are not quantitatively reliable, couplings generally are represented more poorly than chemical shifts by these commercial programs. Usually, the program provides a list of the compounds used to calculate chemical shifts, so that the experimentalist can judge their relevancy. Sometimes, the compound under study in fact proves to be in the database, so that the real spectrum is reproduced. If not, the experimentalist always should review the structures of the compounds used for the calculations and decide whether they are sufficiently similar to trust the calculations.

3-3 Medium and Isotope Effects

The observed shielding of a particular nucleus consists of intramolecular components σ_{intra} (discussed in regard to protons in Section 3-2) and intermolecular components σ_{inter} . The total shielding is given by

$$\sigma = \sigma_{\text{intra}} + \sigma_{\text{inter}} \quad (3-5)$$

Buckingham, Schaefer, and Schneider pointed out five sources of intermolecular shielding, given in the equation

$$\sigma_{\text{inter}} = \sigma_{\text{B}} + \sigma_{\text{W}} + \sigma_{\text{E}} + \sigma_{\text{A}} + \sigma_{\text{S}}. \quad (3-6)$$

We shall consider each contribution in turn and then give several illustrations of the effects of the medium.

The solvent has a bulk diamagnetic susceptibility that is dependent on the shape of the sample container. Thus, the solvent in a spherical container shields the solute to an extent that is slightly different from the shielding afforded by the solvent in a cylindrical container. The shielding is

$$\sigma_{\text{B}} = \left(\frac{4}{3}\pi - \alpha \right) \chi_{\text{V}}, \quad (3-7)$$

in which α is a geometric parameter and χ_{V} is the volume susceptibility of the solvent. For a sphere, $\alpha = 4\pi/3$, so there is no effect, but for a cylinder, $\alpha = 2\pi/3$, and σ_{B} is $2\pi\chi_{\text{V}}/3$. Normally, the solute and the standard (TMS) are present in the same solution. Under these circumstances, they experience parallel bulk effects, and no correction for σ_{B} on the relative shift is necessary. Since internal standards are common, the effect of bulk susceptibility is largely discounted. A correction would be necessary only if chemical shifts had to be compared in examining data obtained without an internal standard from containers of different shapes (e.g., the normal cylinder and a spherical microtube) or from solvents with different volume susceptibilities.

Close approach of the solute and the solvent can distort the shape of the electron cloud around a proton and deshield it, even when both components are nonpolar. Such a phenomenon (σ_{W}) is analogous to the van der Waals effect on the chemical shift. The magnitude is rarely more than 0.1 ppm. If chemical shifts are measured from the resonance of an internal standard, the contribution from σ_{W} should affect the solute and the standard similarly. Chemical shifts so measured should be largely independent of σ_{W} .

A polar solute, or even a nonpolar molecule with polar groups, induces an electric field in the surrounding dielectric medium. This reaction field, proportional to $(\epsilon - 1)/(\epsilon + 1)$ (ϵ is the dielectric constant), can influence the shielding of protons elsewhere in the molecule. Generally, the effect (σ_{E}) is largest for protons close to the polar group. The sign can be either positive or negative because of an angular dependence, but more often it is negative (indicating deshielding). This effect is not compensated for by the use of an internal standard. Even within the solute molecule, the effect can be quite variable for different protons. For polar molecules in solvents of high dielectric constant, σ_{E} can range up to 1 ppm. The effect may be minimized by the use of solvents with small dielectric constants.

An anisotropic solvent will not orient itself completely randomly with respect to the solute. Thus, even a nonpolar molecule such as methane will be exposed preferentially to the shielding face of benzene or to the deshielding side of acetonitrile. In general, aromatic (dishlike) solvents induce shifts (σ_{A}) to a lower frequency (upfield) and rodlike solvents (acetylene, nitriles, and CS_2) induce shifts to a higher frequency. In the absence of any special solute-solvent interaction (charge transfer, dipole-dipole, or hydrogen bond), the internal standard and the solute exhibit similar anisotropic shifts, so that σ_{A} is compensated for in the δ value. As often as not, however, there is a special interaction between the solvent and a polar group in the solute molecule. As a result, the anisotropic solvent has a different effect on different protons, and solute resonances can undergo real shifts up to 0.5 ppm with respect to the internal standard. In some cases, only certain protons near a functional group are affected. The solvent effect can then be used to bring about differential shifts within the spectrum of a molecule. This technique is useful in spectral analysis to alter, for example, a case of accidental overlap. Because dishlike and rodlike solvents cause shifts in opposite directions, the investigator has some control over the movement of the resonances. The chemical shift alterations caused by aromatics have been termed *Aromatic Solvent-Induced*

Shifts, with the acronym ASIS. The chemical shift in the aromatic solvent is compared with the resonance position in CDCl_3 via the formula

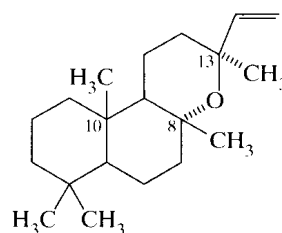
$$\Delta_{\text{C}_6\text{H}_6}^{\text{CDCl}_3} = \delta_{\text{CDCl}_3} - \delta_{\text{C}_6\text{H}_6} \quad (3-8)$$

Because the shift is usually to a lower frequency (upfield), Δ is normally positive. Although anisotropic shifts are frequently strongest close to a polar group, they may be differentiated from electric-field effects by the dependence of the latter on the dielectric constant of the solvent.

Specific interactions between solvent and solute, such as hydrogen bonding, can cause quite large effects (σ_S). It is not known whether the ASIS is caused by a time-averaged cluster of solvent molecules about a polar functional group or by a 1:1 solute-solvent charge transfer complex. In the latter case, the ASIS is more legitimately classified under σ_S than under σ_A .

In an early study of solvent shifts, Buckingham, Schaefer, and Schneider examined the solute methane. For this molecule, σ_E and σ_S are zero and σ_B may be calculated. Thus, only σ_W and σ_A should affect the solute chemical shift. The authors plotted the difference between the chemical shift of methane in a given solvent and that in the gas phase vs. the heat of vaporization of the solvent at the boiling point. The latter quantity was taken as a measure of the van der Waals interaction. More than a dozen solvents, including neopentane, cyclopentane, hexane, cyclohexane, the 2-butenes, ethyl ether, acetone, SiCl_4 , and SnCl_4 , fell on a straight line with a small negative slope. The shifts to a higher frequency (downfield) from gaseous methane ranged from 0.13 (neopentane) to 0.32 ppm (SnCl_4), largely as a function of atomic polarizability. The linear relationship with ΔH_v indicates that these shifts are due solely to σ_W . Well above this line are the dish-shaped aromatic molecules: benzene, toluene, and chlorobenzene, but also nitromethane and nitroethane. Below the line are the rodlike molecules acetonitrile, methylacetylene, dimethylacetylene, butadiyne, and carbon disulfide. Deviations from the Δv -vs.- ΔH_v line are due to true anisotropic shifts (σ_A), since the nonpolar, isotropic methane molecule has no direct (σ_S) interactions with the solvent. The largest positive displacement from the line was nitrobenzene (0.72 ppm), and the largest negative displacement was $\text{NC}-\text{C}\equiv\text{C}-\text{CN}$ (0.53 ppm).

Molecule **3-25** provides an interesting example of the electric-field effect.



3-25

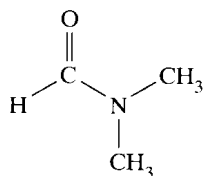
Table 3-4 shows the resonance positions of the methyl groups on C-8, C-10, and C-13 in cyclohexane ($\epsilon = 2.02$) and in methylene chloride ($\epsilon = 9.1$). These solvents were chosen for a low σ_A effect; σ_W and σ_B are discounted by the use of an internal standard. The methyl groups close to the ether linkage (C-8, C-13) are shifted about 4 Hz (0.067 ppm) to a higher

Table 3-4 Methyl Chemical Shifts, in Hz from TMS, at 60 MHz as a Function of Solvent (Laszlo)

Solvent	ϵ	ν_{10}	ν_8	ν_{13}
Cyclohexene	2.02	51.3	60.4	67.1
CH_2Cl_2	9.1	51.1	64.2	71.7

frequency by an electric-field effect. There is little or no shift of the C-10 methyl resonance, since the reaction field diminishes rapidly with distance.

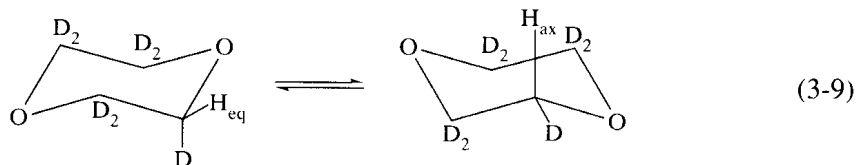
A large ASIS appears on the relative chemical shifts of the nonequivalent methyl groups in *N,N*-dimethylformamide (3-26). The distance between the two methyl peaks increases



3-26

by up to 1.7 ppm upon replacement of CHCl_3 by benzene. Interestingly, the lower frequency peak is responsible for almost all of the shift. This observation was explained in terms of a short-lived 1:1 solvent-solute complex in which one of the DMF methyl groups is situated over the benzene ring and the other is directed away from the ring. The model of a 1:1 complex between cyclohexanone and benzene has been used to justify the shift of the 2,6-axial protons (located above the benzene ring) to a lower frequency and the negligible shift of the 2,6-equatorial protons (near the region of no effect at $\theta = 55^\circ 44'$). These shifts have also been explained in terms of a time-averaged solvent cluster, which produces the same effect without recourse to a short-lived 1:1 complex.

Isotopic changes within a molecule can alter the chemical shifts of neighboring nuclei. The methyl group in toluene is 0.015 ± 0.002 ppm higher frequency than the corresponding protons in toluene- α - d_1 . The protons in cyclohexane are 0.057 ppm higher frequency than the lone proton in cyclohexane- d_{11} . The effect is larger on other nuclei, such as ^{19}F , but falls off very rapidly with distance. The isotope shift has been explained in terms of zero-point vibrational energy differences. An alternative explanation that the shift is a purely inductive phenomenon is probably not valid, because the effect is not strictly additive. Differential isotope effects have been exploited in a study of the ring reversal of 1,4-dioxane:



In undeuterated dioxane, H_{eq} and H_{ax} coincidentally have the same chemical shift (at the field studied), so they cannot be differentiated at low temperatures. (See Sections 1-8 and 5-2.) In 1,4-dioxane- d_7 (an impurity in commercial 1,4-dioxane- d_8), both H_{ax} and H_{eq} exhibit isotope shifts to a lower frequency, but H_{ax} is shifted somewhat farther. As a result, the axial and equatorial protons give separate resonances at low temperatures, in contrast to the undeuterated material. Because of a chlorine isotope effect, chloroform is a poor substance for an internal lock or a resolution standard at fields above about 9.4 T. At high resolution, the chloroform proton resonance shows up as several closely spaced peaks, due to $\text{CH}(^{35}\text{Cl})(^{37}\text{Cl})_2$, $\text{CH}(^{35}\text{Cl})_2(^{37}\text{Cl})$, $\text{CH}(^{35}\text{Cl})_3$, and $\text{CH}(^{37}\text{Cl})_3$.

3-4 Factors that Influence Carbon Shifts

Carbon is the defining element in organic compounds, but its major nuclide (^{12}C) has a spin of zero. The advent of pulsed Fourier transform methods in the late 1960s made the examination of the low-abundance nuclide ^{13}C (1.11%) a practical spectroscopic technique. The low probability $[(0.0111)^2 = 0.0001, \text{ or } 0.01\%]$ of having two adjacent ^{13}C nuclei in a single molecule removes complications from carbon-carbon couplings. When

carbon–hydrogen couplings are removed by decoupling techniques, the spectrum is essentially free of spin–spin coupling, and one singlet arises for each distinct type of carbon. Spectral analysis therefore is simpler for ^{13}C than for ^1H spectra. Integration is less reliable, because carbons have a much larger range of relaxation times than do protons and because the decoupling field perturbs intensities, as is discussed in Chapter 5. The analysis of ^{13}C chemical shifts, however, is straightforward and often more useful than that of proton shifts.

Diamagnetic shielding (σ^d) responsible for proton chemical shifts is caused by circulation of the electron cloud about the nucleus, as depicted in Figure 3-1b. Hindrance to free electron circulation creates an additional contribution called *paramagnetic shielding* (σ^p). Although *s* electrons circulate freely, *2p* electrons can have an angular momentum that hinders free circulation. Protons are surrounded solely by *s* electrons and consequently exhibit only diamagnetic shielding. Carbon nuclei (and almost all other nuclides as well) also are surrounded by *p* electrons and exhibit both forms of shielding. The term *paramagnetic* is appropriate because the effect is opposite in sign to diamagnetic contributions. In this context, the word should not be confused with its common usage to describe molecules with unpaired electrons.

The paramagnetic contribution can be quite large. Whereas the chemical-shift range for protons is only a few parts per million, paramagnetic shifts can extend over a range of hundreds or even thousands of ppm for other nuclei. Qualitatively, angular momentum can arise from excited electronic states and from π bonding. The effects are larger when electron density about the nucleus increases. These three considerations were gathered into the following simple relationship by Ramsay, Karplus, and Pople:

$$\sigma^p \propto -\frac{1}{\Delta E} \langle r^{-3} \rangle \Sigma Q_{ij}. \quad (3-10)$$

The quantity ΔE is the average energy of excitation required to reach certain excited states. The radial term $\langle r^{-3} \rangle$ includes the average distance r of the *2p* electrons from the nucleus and serves as a measure of electron density. Finally, ΣQ_{ij} is a measure of π bonding to carbon. The negative sign in the equation indicates that shielding is in the opposite direction from σ^d .

Structural changes can affect all three components of the equation. The quantity ΔE in eq. 3-10 represents the weighted-average energy difference between the ground and excited states. Because of symmetry considerations, the $\pi \rightarrow \pi^*$ transition is excluded. Low-lying excited states (with small ΔE) make the largest contribution, since ΔE appears in the denominator. Saturated molecules, such as alkanes, typically have no low-lying excited states (and hence possess a large ΔE), so that σ^p is small and alkane carbon resonances are found at a very low frequency (high field). (Paramagnetic shielding causes shifts to a high frequency, whereas diamagnetic shielding causes shifts to a low frequency.) Similarly, the nitrogen atoms in aliphatic amines and the oxygen atoms in aliphatic ethers have no low-lying excited states, so their ^{15}N and ^{17}O resonances also are found at a low frequency. Carbonyl carbons, $\text{C}=\text{O}$, have a low-lying excited state involving the movement of electrons from the oxygen lone pair to the antibonding π orbital that generates a paramagnetic current. This $n \rightarrow \pi^*$ transition causes the large shift to a high frequency that characterizes carbonyl groups—up to 220 ppm from the zero of TMS. Even larger shifts to a high frequency, viz., δ 335, have been observed for carbocations, R_3C^+ .

The radial term in eq. 3-10 is responsible for effects related to electron density that parallel inductive effects on proton chemical shifts. Paramagnetic shielding is larger when the *p* electrons are closer to the nucleus. Thus, substituents that donate or withdraw electrons influence the paramagnetic shift. Electron donation increases repulsion between electrons, which can be relieved by an increase in r . The paramagnetic shielding then decreases, causing a shift to a lower frequency (upfield). Similarly, electron withdrawal permits electrons to move closer to the nucleus, increasing the paramagnetic shielding and causing a shift to higher frequency. Hence, placing a series of electron-withdrawing atoms on carbon results in progressively higher frequency shifts, as in the series CH_3Cl (δ 25), CH_2Cl_2 (δ 54), CHCl_3 , (δ 78), and CCl_4 (δ 97). The situation is qualitatively similar to that for protons, but

the numbers are much larger because the shift is from the paramagnetic term. Again, however, substituent effects generally follow the electronegativity of groups attached to carbon.

Electronegativity is a measure of the ability of a nucleus to attract electrons. A highly electronegative element, such as oxygen, attracts p electrons more than does carbon and reduces the value of r . Thus, ^{17}O shifts are correspondingly larger than ^{13}C shifts. A plot of the ^{17}O shifts of aliphatic ethers versus the ^{13}C shifts of the analogous alkanes is linear with a slope of about three. The linearity shows that oxygen and carbon chemical shifts are sensitive to the same structural factors, and the slope indicates that oxygen is more sensitive to these factors, because its 2p electrons are closer to the nucleus.

The third factor in eq. 3-10, $\sum Q_{ij}$, is related to charge densities and bond orders and can be considered to be a measure of multiple bonding. The greater the degree of multiple bonding, the greater is the shift to a high frequency (low field). This term provides a rationale for the series ethane (δ 6), ethene (δ 123), and the central sp-hybridized carbon of allene (δ 214). Arene shifts are similar to those of alkenes (benzene, δ 129). The effects of diamagnetic anisotropy on carbon chemical shifts are similar in magnitude to the effects on protons, but are small in relation to the range of carbon shifts. The chemical shifts of alkynes do not follow this pattern, but are at an intermediate position (δ 72 for acetylene), because their linear structure has zero angular momentum about the $\text{C}\equiv\text{C}$ axis.

Interpretation of the chemical shifts of most elements other than hydrogen is accomplished by analyzing the three factors in eq. 3-10: accessibility of certain excited states, distance of the p electrons, and multiple bonding. For carbon, the shifts of alkanes, alkenes, arenes, alkynes, and carbonyl groups and the effects of electron-donating or electron-withdrawing groups may be interpreted in this fashion. There are exceptions, the most prominent being the effect of heavy atoms. The series CH_3Br (δ 10), CH_2Br_2 (δ 22), CHBr_3 (δ 12), and CBr_4 (δ -29) defies any explanation based on electronegativity, unlike the analogous series given before for chlorine. The same series with iodine is monotonic to a lower frequency (δ -290 for CI_4)—that is, opposite to the chlorine series. This so-called heavy-atom effect has been attributed to a new source of angular momentum from *spin-orbit coupling*. These anomalous shifts to a low frequency (high field) can be expected when nuclei other than hydrogen have a heavy atom substituent.

3-5 Carbon Chemical Shifts and Structure

Figure 3-11 illustrates general ranges for ^{13}C chemical shifts.

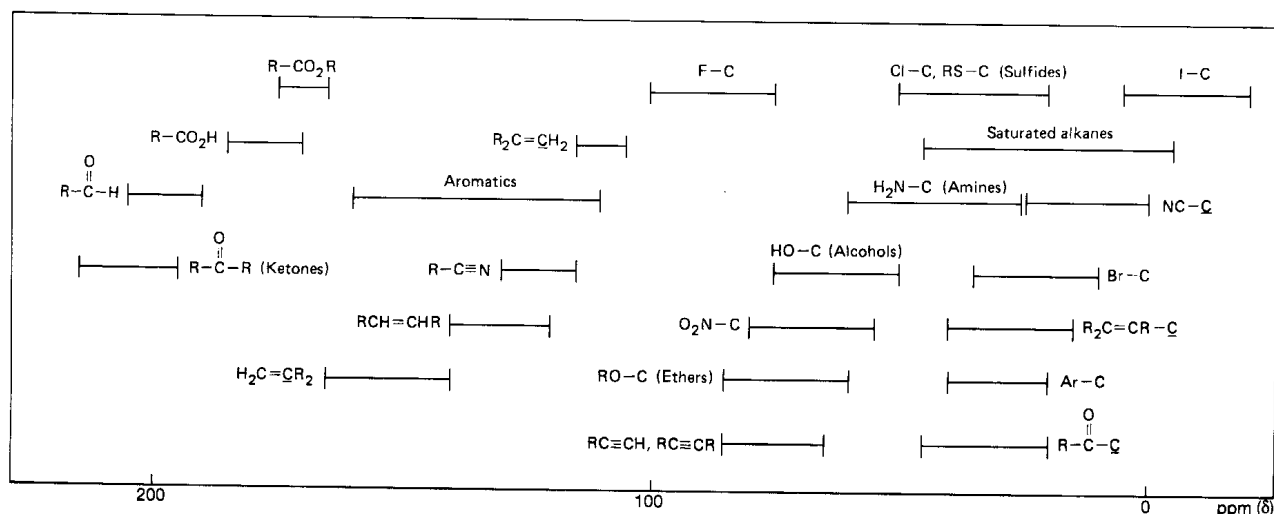
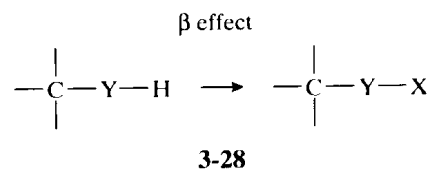
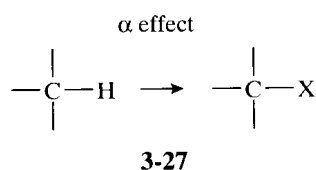


Figure 3-11 Carbon chemical-shift ranges for common structural units. The symbol C represents methyl, methylene, methine, or quaternary carbon; R represents a saturated alkyl group. The indicated ranges are for common examples; actual ranges can be larger.

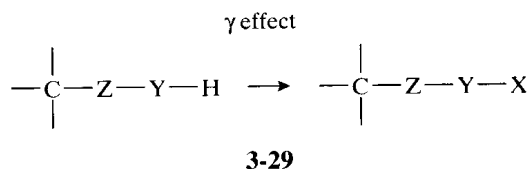
3-5a Saturated Aliphatics

Acyclic Alkanes. The absence of low-lying excited states and of π bonding minimizes paramagnetic shielding and places alkane chemical shifts at a very low frequency (high field). Methane itself resonates at $\delta -2.5$. The series ethane (CH_3CH_3), propane ($\text{CH}_3\text{CH}_2\text{CH}_3$), and isobutane ($(\text{CH}_3)_3\text{CH}$) follows a steady trend to a higher frequency, namely, δ 5.7, 16.1, 25.2, similar to the trend for the methyl, methylene, methine series of proton shifts. Replacement of H by CH_3 adds about 9 ppm to the chemical shift of the attached carbon. (The effect is similar for replacement by saturated CH_2 , CH, or C.) Because the added methyl group is attached directly to the resonating carbon, the shift has been termed the α effect (3-27). The effect is not restricted to the replacement of H by carbon.



Any group X that replaces hydrogen on a resonating carbon atom causes a relatively constant shift that depends primarily on the electronegativity of X.

The replacement of hydrogen by CH_3 (or by CH_2 , CH, or C) at a β position (3-28) also causes a constant shift of about +9 ppm. Thus, the central carbon in pentane ($\text{CH}_3\text{CH}_2\text{CH}_2\text{CH}_2\text{CH}_3$) is shifted by the α effects of the two methylene groups and by the β effects of the two methyl groups to δ 34.7. The replacement of a γ hydrogen (3-29) by CH_3 (or by CH_2 , CH, or C) causes a shift of about -2.5 ppm (to a low frequency, or upfield). Unlike the α



and β effects, this γ effect has an important stereochemical component. Because of the α , β , and γ effects, the alkane chemical shift range is relatively large. Methyl resonances in alkanes are typically found at δ 5–15, depending on the number of β substituents; methylene resonances are at δ 15–30, methine resonances at δ 25–45.

Carbon-13 chemical shifts lend themselves conveniently to empirical analysis, because these shifts are easily measured and tend to have well-defined substituent effects. For saturated, acyclic hydrocarbons, Grant developed the formula

$$\delta = -2.5 + \sum A_i n_i \quad (3-11)$$

as an empirical measure of chemical shifts. For any resonating carbon, a substituent parameter A_i for each carbon atom in the molecule, up to a distance of five bonds, is added to the chemical shift of methane ($\delta -2.5$). There are different substituent parameters for carbons (any of CH_3 , CH_2 , CH, and C) that are α (9.1), β (9.4), γ (-2.5), δ (0.3), or ϵ (0.1) to the resonating carbon. We already have alluded to the first three figures. If there is more than one α carbon, the substituent parameter is multiplied by the appropriate number n_i , and similar factors are applied for multiple substitution at other positions. Figure 3-12 illustrates the calculation for each carbon in pentane. The methyl chemical shift is calculated by adding contributions from single α , β , γ , and δ carbons to the shift (-2.5) of methane. The shift of the 2 carbon is calculated by adding contributions of two α carbons, one β carbon, and one γ carbon. Usually, the observed shifts are calculated to within 0.3 ppm, providing a reliable means for spectral assignment.

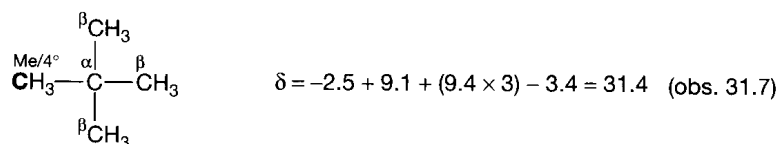
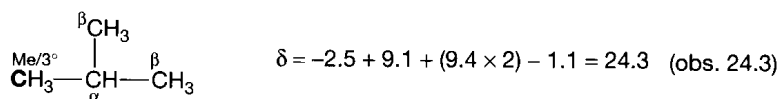
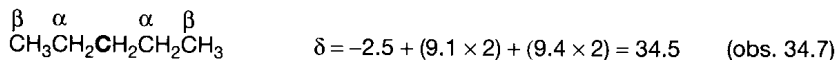
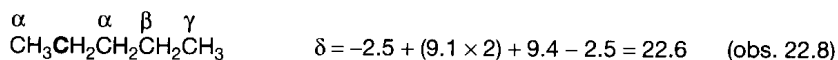
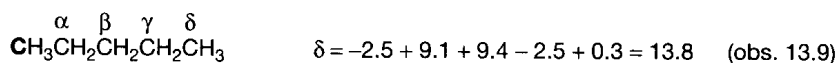


Figure 3-12 Calculation of the ^{13}C chemical shifts of pentane.

Figure 3-13 Calculation of the ^{13}C chemical shifts of the indicated carbon in 2-methylpropane (isobutane) and in 2,2-dimethylpropane (neopentane).

There are complications, however. Corrections must be applied if there is branching, because eq. 3-11 applies rigorously only to straight chains. The resonance position of a methyl group is corrected for the presence of an adjacent tertiary (CH) carbon by adding -1.1 and for an adjacent quaternary carbon by adding -3.4 . Methylene carbons have corrections of -2.5 and -7.2 , respectively, for adjacent tertiary and quaternary carbons. Methine carbons have respective corrections of -3.7 , -9.5 , and -1.5 for adjacent secondary, tertiary, and quaternary carbons. Finally, quaternary carbons have corrections of -1.5 and -8.4 for adjacent primary and secondary carbons. (Corrections for adjacent tertiary and quaternary carbons undoubtedly are significant, but are not known accurately.) For example, the methyl group in isobutane (see the first calculation in Figure 3-13) is adjacent to a tertiary carbon. The methyl chemical shift is calculated by adding the contributions of one α carbon, two β carbons, and the correction of -1.1 , since the methyl group is adjacent to a tertiary (3°) center. In the second calculation in Figure 3-13 (for neopentane), the methyl group is adjacent to a quaternary (4°) center.

It is noteworthy that the γ effect of a carbon substituent is negative (-2.5). A γ carbon can be either gauche or anti (Figure 3-14) to the resonating carbon, and the proportion of conformers can vary from molecule to molecule. The value -2.5 is a weighted average for open-chain conformers and does not serve accurately for all situations. For a pure γ -anti effect, the shift is about $+1$, and for a pure γ -gauche effect, it is about -6 . The average value of -2.5 measured by Grant clearly indicates a mix of the two conformations. Hydrocarbons with unusually large deviations from the average mix may give poor results with eq. 3-11. The α and β effects are determined by fixed geometries and have no stereochemistry component.

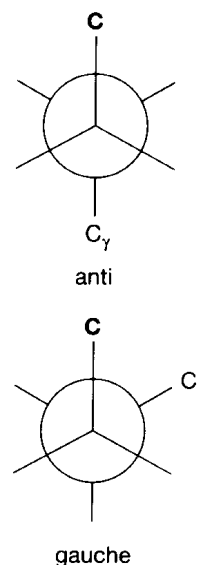


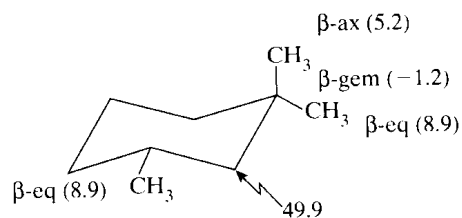
Figure 3-14 The anti and gauche geometries in a butane fragment.

Cyclic Alkanes. With a resonance position of $\delta -2.6$, cyclopropane has the lowest-frequency resonance of hydrocarbons. Cyclobutane resonates at $\delta 23.3$, and the remaining cycloalkanes generally resonate within 2 ppm of cyclohexane, at $\delta 27.7$. The fixed stereochemistry represented by cyclohexane requires an entirely new set of empirical parameters that depend on the axial or equatorial nature of the substituent, as well as on the distance from the resonating carbon. Table 3-5 lists Grant's parameters for methyl substitution that are added to the value for cyclohexane ($\delta 27.7$). The substituent parameter for a γ -axial methyl is large and negative (-5.4), reflecting the pure gauche stereochemistry between the perturbing and resonating carbons. A γ -equatorial group represents a γ -anti effect and has little perturbation in this case. Corrections again are needed for branching. For two α

Table 3-5 Substituent Parameters for Methyl Substitution on Cyclohexane

Stereochemistry	α	β	γ	δ
Equatorial	5.6	8.9	0.0	-0.3
Axial	1.1	5.2	-5.4	-0.1

methyls that are geminal (both on the resonating carbon), the correction is -3.4 ; for two β methyls that are geminal, it is -1.2 . Thus, the calculated resonance position for C2 of 1,1,3-trimethylcyclohexane (**3-30**) is $27.7 + 5.2 + (8.9 \times 2) - 1.2 = 49.5$ (observed value, 49.9).

**3-30**

A pair of vicinal, diequatorial methyls that are respectively α and β to the resonating carbon require a correction of -2.3 , and similar axial-equatorial vicinal methyls require a correction of -3.1 .

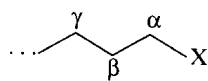
Functionalized Alkanes. The replacement of a hydrogen on carbon with a heteroatom or an unsaturated group usually results in shifts to a higher frequency (downfield) because of inductive effects on the radial term. Strongly electron-withdrawing groups thus have large positive α effects. In the halogen series CH_3X , the methyl chemical shifts are δ 75.4 for fluorine, 25.1 for chlorine, 10.2 for bromine, and -20.6 for iodine. Multiple substitution results in larger effects— δ 77.7 for CHCl_3 . Recall that the α effect of heavy atoms such as iodine or bromine is influenced by a spin-orbit mechanism and hence does not follow the simple order of electronegativity. The general range for the α halogen effect in hydrocarbons extends from the values given for the simple CH_3X systems to about a 25-ppm higher frequency (downfield) for CH_2X and CHX systems, since the α and β effects of the unspecified hydrocarbon pieces contribute to the shift to the higher frequency.

Methanol (CH_3OH) resonates at δ 49.2, and the range for hydroxy-substituted carbons is δ 49–75. Dimethyl ether [$(\text{CH}_3)_2\text{O}$] resonates at δ 59.5, and the range for alkoxy-substituted carbons is δ 59–80. The ether range is translated a few ppm to a higher frequency (downfield) from alcohols, because each ether must have one additional β effect with respect to the analogous alcohol.

The lower electronegativity of nitrogen moves the amine range to a somewhat lower frequency (upfield). Methylamine in aqueous solution resonates at δ 28.3, with the range for amines extending some 30 ppm to a higher frequency. The amine range is larger than the alcohol range because nitrogen can carry up to three substituents, with the possibility of more α and β effects. Dimethyl sulfide resonates at δ 19.5, acetonitrile at δ 0.3, and nitromethane at δ 57.3, with the respective ranges for thioalkoxy, cyano, and nitro substitution extending some 25 ppm to a higher frequency. The low-frequency position for cyano substitution is related to the cylindrical shape of the group.

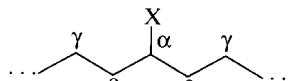
An attached double bond has only a small effect on a methyl group. The position for the methyls of *trans*-2-butene (*trans*- $\text{CH}_3\text{CH}=\text{CHCH}_3$) is δ 17.3, and that for the methyl of toluene ($\text{C}_6\text{H}_5\text{CH}_3$) is δ 21.3. The range for carbons on double bonds is about δ 15–40. Methyls on carbonyl groups are at a slightly higher frequency (lower field): δ 30.2 for acetone and δ 31.2 for acetaldehyde, with a range of about δ 30–45.

Introducing heteroatoms or unsaturation into alkane chains requires completely new sets of empirical parameters that depend on the substituent, on its distance from the resonating carbon (α , β , γ), and on whether the substituent is terminal (3-31) or internal (3-32) (Table 3-6). These numbers represent the effect on a resonating carbon of replacing a



Terminal

3-31



Internal

3-32

hydrogen atom at the respective position with a group X. With the exception of cyano, acetyleno, and the heavy atom iodine, the α effects are determined largely by the electronegativity of the substituent. It is interesting that the β effects are all positive and generally of similar magnitude (6 to 11) and that the γ effects are all negative and generally of similar magnitude (-2 to -5). Although the details are not entirely understood, it is clear that simple polar considerations do not dominate the β and γ effects.

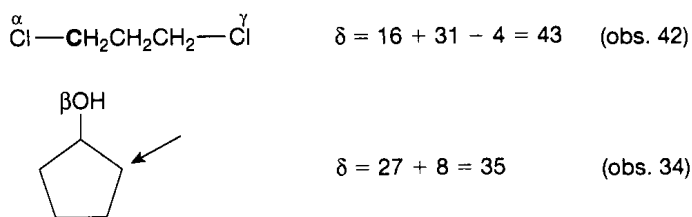
To utilize the substituent parameters given in Table 3-5, one adds the appropriate values to the chemical shift of the carbon in the analogous hydrocarbon, rounding off to the nearest ppm. As seen in Figure 3-15, the chemical shift of the 1 carbon of 1,3-dichloropropane may be calculated from the value (16) for the methyl carbon of propane and from the figures in Table 3-5. The chemical shift of the β carbon of cyclopentanol similarly may be calculated from the value (27) for cyclopentane.

Table 3-6 Carbon Substituent Parameters for Functional Groups*

X	Terminal X (3-30)			Internal X (3-31)		
	α	β	γ	α	β	γ
F	68	9	-4	63	6	-4
Cl	31	11	-4	32	10	-4
Br	20	11	-3	25	10	-3
I	-6	11	-1	4	12	-1
OH	48	10	-5	41	8	-5
OR	58	8	-4	51	5	-4
OAc	51	6	-3	45	5	-3
NH ₂	29	11	-5	24	10	-5
NR ₂	42	6	-3			-3
CN	4	3	-3	1	3	-3
NO ₂	63	4		57	4	
CH=CH ₂	20	6	-0.5			-0.5
C ₆ H ₅	23	9	-2	17	7	-2
C≡CH	4.5	5.5	-3.5			-3.5
(C=O)R	30	1	-2	24	1	-2
(C=O)OH	21	3	-2	16	2	-2
(C=O)OR	20	3	-2	17	2	-2
(C=O)NH ₂	22		-0.5	2.5		-0.5

* From F. W. Wehrli, A. P. Marchand, and S. Wehrli, *Interpretation of Carbon-13 NMR Spectra*, 2d ed., John Wiley & Sons, Ltd., Chichester, UK, 1988.

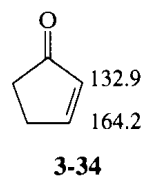
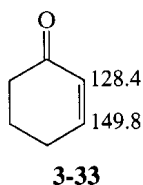
Figure 3-15 Calculation of the ^{13}C chemical shifts of the indicated carbon in 1,3-dichloropropane and in cyclopentanol.



3-5b Unsaturated Compounds

The effects of diamagnetic anisotropy on carbon and on a proton have similar magnitudes, but the much larger paramagnetic shielding renders the phenomenon relatively small for carbon. Thus, benzene (δ 128.7) and cyclohexene (δ 127.2) have almost identical carbon resonance positions, in contrast to the situation with their protons. The full range of alkene and aromatic resonances is about δ 100–170.

Alkenes. Alkenic carbons that bear no substituents ($=\text{CH}_2$) resonate at a low frequency (high field) (cf. isobutylene $[(\text{CH}_3)_2\text{C}=\text{CH}_2]$ at δ 107.7) and have a range of about δ 104–115 for hydrocarbons. Alkenic carbons that have one substituent ($=\text{CHR}$), like those in *trans*-2-butene (δ 123.3), resonate in the range δ 120–140. Finally, disubstituted alkenic carbons ($=\text{CRR}'$), like that in isobutylene (δ 146.4), resonate at the highest frequency (δ 140–165). Polar substituents on double bonds, particularly those in conjugation with the bond, can alter the resonance position appreciably. α , β -Unsaturated ketones, such as **3-33** and **3-34**, have lower frequency α resonances and higher frequency β

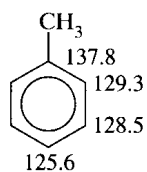


resonances. (The effect is reduced in acyclic molecules.) Electron donation, as in enol ethers, reverses the effect: $\text{CH}_2=\text{CHOCH}_3$ ($\delta(\alpha)$ 153.2, $\delta(\beta)$ 84.2). Electron donation or withdrawal alters the radial term through resonance (mesomerism).

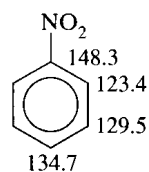
Alkene chemical shifts may be estimated from substituent parameters added to the shift for ethene (δ 123.3). For α , β , and γ carbons on the same end of the double bond as the resonating carbon, respective increments of 10.6, 7.2, and -1.5 are added. For α' , β' , and γ' carbons on the opposite end of the double bond from the resonating carbon, respective increments of -7.9 , -1.8 , and -1.5 are added. An increment of -1.1 is added if any pair of substituents are *cis* to each other. Thus, the shift of the unsubstituted carbon in 1-butene ($\text{CH}_3\text{CH}_2\text{CH}=\text{CH}_2$) is calculated to be $123.3 - 7.9 - 1.8 = 113.6$ (observed value, 113.3), and the shift of the substituted carbon ($\text{CH}_3\text{CH}_2\text{CH}=\text{CH}_2$) is $123.3 + 10.6 + 7.2 = 141.1$ (observed value, 140.2).

Alkynes and Nitriles. An alkyne carbon that carries a hydrogen substituent ($\equiv\text{CH}$) generally resonates in the narrow range δ 67–70. An alkyne carbon that carries a carbon substituent ($\equiv\text{CR}$) resonates at a slightly higher frequency (downfield, δ 74–85), because of α and β effects from the R group. Effects of conjugating, polar substituents expand the total range to δ 20–90. Nitriles resonate in the range δ 117–130. (Acetonitrile is at δ 117.2.) The $n \rightarrow \pi^*$ transition pushes the range to a high frequency.

Aromatics. Alkyl substitution, as in toluene (**3-35**), has its major (α) effect on the ipso carbon. Because this carbon has no attached proton, its relaxation time is much longer than

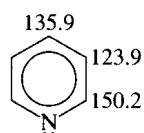


3-35

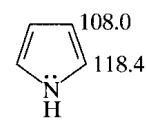


3-36

those of the other carbons, and its intensity is usually lower. Conjugating substituents like nitro (**3-36**) have strong perturbations on the aromatic resonance positions, as the result of a combination of traditional α , β , and γ effects and changes in electron density through delocalization (**3-19**, **3-20**). A similar interplay of effects is seen in the resonance positions of pyridine (**3-37**) and pyrrole (**3-38**). Aromatic resonances may be calculated empirically by adding increments to the benzene chemical shift (δ 128.7) for each substituent that is ipso, ortho, meta, or para to the resonating carbon (Table 3-7).



3-37



3-38

Table 3-7 Carbon Substituent Parameters for Aromatic Systems*

X	Ips0	Ortho	Meta	Para
CH ₃	8.9	0.7	-0.1	-2.9
CH ₂ OH	13.3	-0.8	-0.6	-0.4
CH=CH ₂	9.5	-2.0	0.2	-0.5
CN	-19.0	1.4	-1.5	1.4
CO ₂ CH ₃	1.3	-0.5	-0.5	3.5
CHO	9.0	1.2	1.2	6.0
CO-CH ₃	7.9	-0.3	-0.3	2.9
F	35.1	-14.1	1.6	-4.4
Cl	6.4	0.2	1.0	-2.0
Br	-5.4	3.3	2.2	-1.0
I	-32.0	10.2	2.9	1.0
NH ₂	19.2	-12.4	1.3	-9.5
OH	26.9	-12.6	1.8	-7.9
OCH ₃	30.2	-15.5	0.0	-8.9
SCH ₃	10.2	-1.8	0.4	-3.6
NO ₂	19.6	-5.3	0.8	6.0

* From J. B. Stothers, *Carbon-13 NMR Spectroscopy* (New York: Academic Press, 1973).

3-5c Carbonyl Groups

Carbonyl groups have no direct representation in proton NMR spectra, so carbon NMR provides unique information for their analysis. The entire carbonyl chemical shift range, δ 160–220, is well removed from that of almost all other functional groups. Like aromatic ipso carbons and nitriles, carbonyl carbons other than those in aldehydes carry no attached protons and hence relax more slowly and tend to have low intensities.

Aldehydes resonate toward the middle of the carbonyl range, about δ 190–205, with acetaldehyde (CH_3CHO) at δ 199.6. Unsaturated aldehydes, in which the carbonyl group is conjugated with a double bond or phenyl ring, are shifted to a lower frequency (up-field): benzaldehyde ($\text{C}_6\text{H}_5\text{CHO}$) at δ 192.4 and $\text{CH}_2=\text{CHCHO}$ at δ 192.2. The α , β , and γ effects of substituents on ketones add to the carbonyl chemical shift and hence are found at the high-frequency end of the carbonyl range. Their overall range is δ 195–220: acetone at δ 205.1, cyclohexanone at δ 208.8. Again, unsaturation shifts the resonances to a lower frequency.

Carboxylic derivatives fall into the range δ 155–185. The resonances for the series carboxylate (CO_2^-), carboxyl (CO_2H), and ester (CO_2R) often are well defined—for example, for sodium acetate (δ 181.5), acetic acid (δ 177.3), and methyl acetate (δ 170.7). The range for esters is about δ 165–175 and that for acids is δ 170–185. Acid chlorides are at a slightly lower frequency (higher field): δ 160–170, with δ 168.6 for acetyl chloride ($\text{CH}_3(\text{CO})\text{Cl}$). Anhydrides have a similar range: δ 165–175, with δ 167.7 for acetic anhydride ($\text{CH}_3(\text{CO})\text{O}(\text{CO})\text{CH}_3$). Lactones overlap the ester range, with the six-membered lactone at δ 176.5. Amides also have a similar range: δ 160–175, with δ 172.7 for acetamide ($\text{CH}_3(\text{CO})\text{NH}_2$). Oximes have a larger range, extending from δ 145–165. The central carbon of allenes ($\text{R}_2\text{C}=\text{C}=\text{CR}_2$) falls into the ketonic range, δ 200–215, although the outer carbons have a much lower frequency range, δ 75–95.

3-5d Programs for Empirical Calculation

The facility and accuracy of empirical calculations for carbon have been exploited through commercial computer programs for general predictions of ^{13}C chemical shifts. As with ^1H calculations (Section 3-2e), the results are only as good as the data set used in their creation. The programs assume that the effects of multiple substitution are additive, unless specific corrections have been incorporated. Unconsidered or nonadditive phenomena, such as conformational and other steric effects, can cause unexpected deviations between observed and calculated chemical shifts.

3-6 Tables of Chemical Shifts

Structural analysis of an unknown organic material normally begins with an examination of the ^1H and ^{13}C spectra. Resonance positions are analyzed, if possible, with the benefit of knowledge of the molecular formula and structural information based on synthetic precursors. Representative chemical shifts are given in Tables 3-8 through 3-12, drawn from references at the end of this chapter.

Table 3-8 Methyl and Methylene Groups

	$\delta(^1\text{H})$		$\delta(^{13}\text{C})$			$\delta(^1\text{H})$		$\delta(^{13}\text{C})$	
	CH_2	CH_3	CH_2	CH_3		CH_2	CH_3	CH_2	CH_3
CH_3Li		-0.4		-13.2	$(\text{CH}_3)_2\text{NCHO}$		2.88		36.0
CH_3CH_3		0.86		5.7			2.97		30.9
$(\text{CH}_3)_3\text{CH}$		0.89		25.2	CH_3Cl		3.06		25.1
$(\text{CH}_3)_4\text{C}$		0.94		31.7	$(\text{CH}_3)_2\text{O}$		3.24		59.5
$(\text{CH}_3)_3\text{COH}$		1.22		29.4	$(\text{CH}_3)_4\text{N}^+$		3.33		55.6
$\text{CH}_3\text{CH}=\text{CH}_2$		1.72		18.7	CH_3OH		3.38		49.2
$\text{CH}_3\text{C}\equiv\text{CH}$		1.80		-1.9	$\text{CH}_3\text{CO}_2\text{CH}_3$		3.67		51.0
$(\text{CH}_3)_3\text{P}=\text{O}$		1.93		18.6	$\text{CH}_3\text{OC}_6\text{H}_5$		3.73		54.8
CH_3CN		2.00		0.3	CH_3F		4.27		75.4
$\text{CH}_3\text{CO}_2\text{CH}_3$		2.01		18.7	CH_3NO_2		4.33		57.3
$\text{CH}_3(\text{CO})\text{CH}_3$		2.07		30.2	$(\text{CH}_3\text{CH}_2)_2\text{S}$	2.49	1.25	26.5	15.8
$\text{CH}_3\text{CO}_2\text{H}$		2.10		18.6	$\text{CH}_3\text{CH}_2\text{NH}_2$	2.74	1.10	36.9	19.0
$(\text{CH}_3)_2\text{S}$		2.12		19.5	$\text{CH}_3\text{CH}_2\text{C}_6\text{H}_5$	2.92	1.18	29.3	16.8
CH_3I		2.15		-20.6	$\text{CH}_3\text{CH}_2\text{I}$	3.16	1.86	0.2	23.1
CH_3CHO		2.20		31.2	$\text{CH}_3\text{CH}_2\text{Br}$	3.37	1.65	28.3	20.3
$(\text{CH}_3)_3\text{N}$		2.22		47.3	$\text{CH}_3\text{CH}_2\text{Cl}$	3.47	1.33	39.9	18.7
$\text{CH}_3\text{C}_6\text{H}_5$		2.31		21.3	$(\text{CH}_3\text{CH}_2)_2\text{O}$	3.48	1.20	67.4	17.1
CH_3NH_2		2.42		30.4	$\text{CH}_3\text{CH}_2\text{OH}$	3.56	1.24	57.3	15.9
$\text{CH}_3(\text{SO})\text{CH}_3$		2.50		40.1	$\text{CH}_3\text{CH}_2\text{F}$	4.36	1.24	79.3	14.6
$\text{CH}_3(\text{CO})\text{Cl}$		2.67		32.7	$\text{CH}_3\text{CH}_2\text{NO}_2$	4.37	1.58	70.4	10.6
CH_3Br		2.69		10.2	$\text{BrCH}_2\text{CH}_2\text{Br}$	3.63		32.4	
$(\text{CH}_3)_4\text{P}^+$		2.74		11.3	$\text{HOCH}_2\text{CH}_2\text{OH}$	3.72		63.4	
$\text{CH}_3(\text{SO}_2)\text{CH}_3$		2.84		42.6	$\text{ClCH}_2\text{CH}_2\text{Cl}$	3.73		51.7	

Table 3-9 Saturated Ring Systems

	^1H	^{13}C		^1H	^{13}C
Cyclopropane	0.22	-2.6	Oxane (tetrahydropyran)	(α) 3.52	68.0
Cyclobutane	1.98	23.3		(β) 1.51	26.6
Cyclopentane	1.51	26.5		(γ)	23.6
Cyclohexane	1.43	27.7	Pyrrolidine	(α) 2.75	47.4
Cycloheptane	1.53	29.4		(β) 1.59	25.8
Cyclopentanone	(α) 2.06	37.0	Piperidine	(α) 2.74	47.5
	(β) 2.02	22.3		(β) 1.50	27.2
Cyclohexanone	(α) 2.22	40.7		(γ) 1.50	25.5
	(β) 1.8	26.8	Thiirane		2.27
	(γ) 1.8	24.1	Tetrahydrothiophene	(α) 2.82	31.7
Oxirane	2.54	40.5		(β) 1.93	31.2
Tetrahydrofuran	(α) 3.75	69.1	Sulfolane	(α) 3.00	51.1
	(β) 1.85	26.2		(β) 2.23	22.7
			1,4-Dioxane		3.70
					66.5

Table 3-10 Alkenes

	¹ H	¹³ C		¹ H	¹³ C
CH ₂ =CHCN	(α) { 5.5–6.4 } (β)	107.7 137.8	(CH ₃) ₂ C=CHCO ₂ CH ₃	(α) — (β) 5.62	114.8 155.9
CH ₂ =CHC ₆ H ₅	(α) 6.66 (β) 5.15, 5.63	112.3 135.8	Cyclopentene		5.60 130.6
CH ₂ =CHBr	(α) 6.4 (β) 5.7–6.1	115.6 122.1	Cyclohexene		5.59 127.2
CH ₂ =CHCO ₂ H	(α) 6.5 (β) 5.9–6.5	128.0 131.9	1,3-Cyclopentadiene		6.42 132.2, 132.8
CH ₂ =CH(CO)CH ₃	(α) { 5.8–6.4 } (β)	138.5 129.3	1,3-Cyclohexadiene		5.78 124.6, 126.1
CH ₂ =CHO(CO)CH ₃	(α) 7.28 (β) 4.56, 4.88	141.7 96.4	2-Cyclopentenone	(α) 6.10 (β) 7.71	132.9 164.2
CH ₂ =CHOCH ₂ CH ₃	(α) 6.45 (β) 3.6–4.3	152.9 84.6	2-Cyclohexenone	(α) 5.93 (β) 6.88	128.4 149.8
CH ₃ ⁴ CH=C ³ CH ₃ = ² CH= ¹ CH ₂	(1) 5.02 (2) 6.40 (4) 5.70		<i>exo</i> -Methylenecyclohexane (=CH ₂)	4.55	106.5
			(C=)	—	149.7
			Allene (=CH ₂)	4.67	74.0
			(=C=)	—	213.0

Table 3-11 Aromatics

	¹ H			¹³ C			
	<i>o</i>	<i>m</i>	<i>p</i>	<i>i</i>	<i>o</i>	<i>m</i>	<i>p</i>
C ₆ H ₅ CH ₃	7.16	7.16	7.16	137.8	129.3	128.5	125.6
C ₆ H ₅ CH=CH ₂	7.24	7.24	7.24	138.2	126.7	128.9	128.2
C ₆ H ₅ SCH ₃	7.23	7.23	7.23	138.7	126.7	128.9	124.9
C ₆ H ₅ F	6.97	7.25	7.05	163.8	114.6	130.3	124.3
C ₆ H ₅ Cl	7.29	7.21	7.23	135.1	128.9	129.7	126.7
C ₆ H ₅ Br	7.49	7.14	7.24	123.3	132.0	130.9	127.7
C ₆ H ₅ OH	6.77	7.13	6.87	155.6	116.1	130.5	120.8
C ₆ H ₅ OCH ₃	6.84	7.18	6.90	158.9	113.2	128.7	119.8
C ₆ H ₅ O(CO)CH ₃	7.06	7.25	7.25	151.7	122.3	130.0	126.4
C ₆ H ₅ (CO)CH ₃	7.91	7.45	7.45	136.6	128.4	128.4	131.6
C ₆ H ₅ CO ₂ H	8.07	7.41	7.47	130.6	130.0	128.5	133.6
C ₆ H ₅ (CO)Cl	8.10	7.43	7.57	134.5	131.3	129.9	136.1
C ₆ H ₅ CN	7.54	7.38	7.57	109.7	130.1	127.2	130.1
C ₆ H ₅ NH ₂	6.52	7.03	6.63	147.9	116.3	130.0	119.2
C ₆ H ₅ NO ₂	8.22	7.48	7.61	148.3	123.4	129.5	134.7

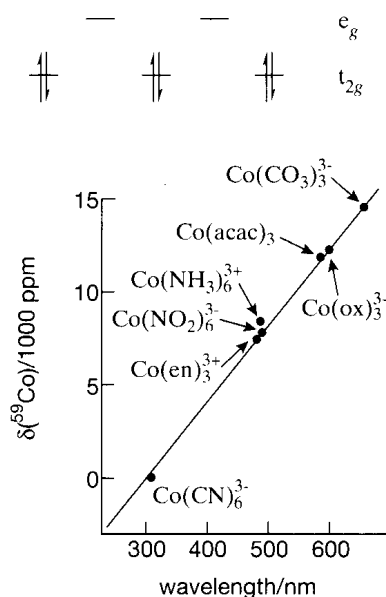
	¹ H			¹³ C		
	α	β	Other	α	β	Other
Naphthalene	7.81	7.46	—	128.3	126.1	—
Anthracene	7.91	7.39	8.31	130.3	125.7	132.8
Furan	7.40	6.30	—	142.8	109.8	—
Thiophene	7.19	7.04	—	125.6	127.4	—
Pyrrole	6.68	6.05	—	118.4	108.0	—
Pyridine	8.50	7.06	7.46	150.2	123.9	135.9

Table 3-12 Carbonyl Compounds

	$^1\text{H}(\text{CH}_3)$	$^1\text{H}(\text{other})$	$^{13}\text{C}(\text{C}=\text{O})$
$\text{H}(\text{CO})\text{OCH}_3$	3.79	8.05 (HCO)	160.9
$\text{CH}_3(\text{CO})\text{Cl}$	2.67	—	168.6
$\text{CH}_3(\text{CO})\text{OCH}_2\text{CH}_3$	2.02 (CH_3CO)	4.11 (CH_2), 1.24(CH_3C)	169.5
$\text{CH}_3(\text{CO})\text{N}(\text{CH}_3)_2$	2.10 (CH_3CO)	6.94, 7.04 (CH_3N)	169.6
$\text{CH}_3\text{CO}_2\text{H}$	2.10	1.37 (HO)	177.3
$\text{CH}_3\text{CO}_2^-\text{Na}^+$	—	—	181.5
$\text{CH}_3(\text{CO})\text{C}_6\text{H}_5$	2.62	—	196.0
$\text{CH}_3(\text{CO})\text{CH}=\text{CH}_2$	2.32	5.8–6.4 ($\text{CH}=\text{CH}_2$)	197.2
$\text{H}(\text{CO})\text{CH}_3$	2.20	9.80 (HCO)	199.6
$\text{CH}_3(\text{CO})\text{CH}_3$	2.07	—	205.1
2-Cyclohexenone	—	5.93, 6.88 ($\text{CH}_\alpha=\text{CH}_\beta$)	197.1
2-Cyclopentanone	—	6.10, 7.71 ($\text{CH}_\alpha=\text{CH}_\beta$)	208.1
Cyclohexanone	—	1.7–2.5	208.8
Cyclopentanone	—	1.9–2.3	218.1

Problems

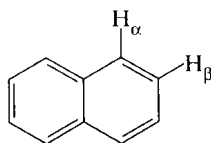
- From Shoolery's rule, calculate the expected resonance position for the CH_2 resonance in (a) $\text{CH}_3\text{CH}_2\text{I}$, (b) $\text{NC}-\text{CH}_2\text{CH}=\text{CH}_2$, (c) $\text{CH}_3\text{OCH}_2\text{C}_6\text{H}_5$, and (d) $\text{CH}_3\text{C}\equiv\text{CCH}_2\text{Br}$.
- The proton resonance positions of the *cis*- and *trans*-1, 2-dibromoethenes are δ 6.65 and 7.03. Which comes from the *cis* isomer and which from the *trans* isomer?
- A trisubstituted benzene possessing one bromine and two methoxy substituents exhibits three aromatic resonances, at δ 6.40, 6.46, and 7.41. What is the substitution pattern?
- Octahedral cobalt complexes, CoL_6 , have three filled t_{2g} and two empty e_g molecular orbitals. The ^{59}Co chemical shifts of several such complexes are linear with the wavelength of the first absorption (longest wavelength) in the UV/visible spectrum. Explain the linearity in terms of Ramsey's equation for shielding.



3.5 Calculate the expected ^{13}C resonance positions for all the carbon atoms in the following molecules:

- (a) $\text{CH}_3\text{CH}_2\text{CH}(\text{CH}_3)\text{CH}(\text{CH}_3)_2$ (c) $\text{CH}_3\text{CH}_2\text{CH}(\text{NO}_2)\text{CH}_3$
 (b) $\text{ICH}_2\text{CH}_2\text{CH}_2\text{Br}$ (d) $(\text{CH}_3)_3\text{CCN}$

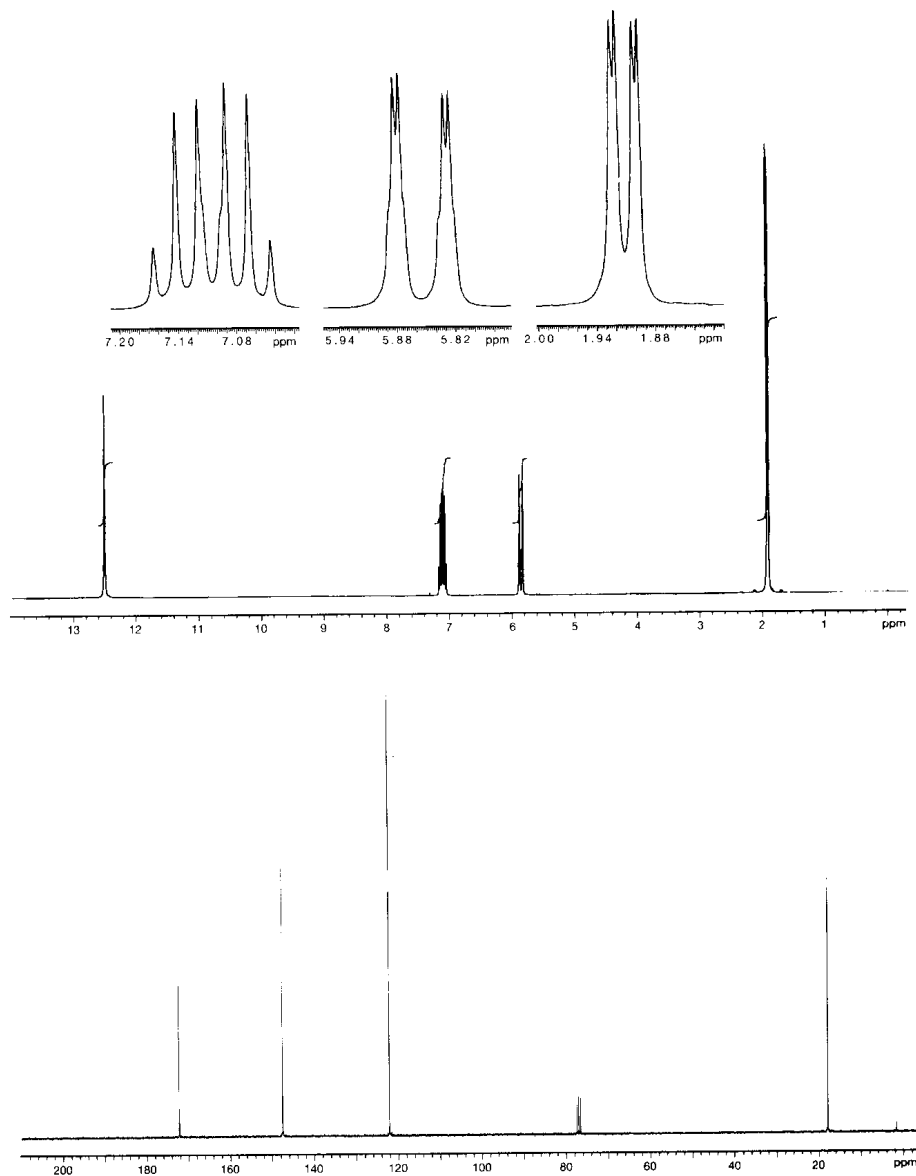
3.6 Of the α and β protons of naphthalene, which should resonate at a higher frequency? Why? Compare both resonance positions with that of benzene.

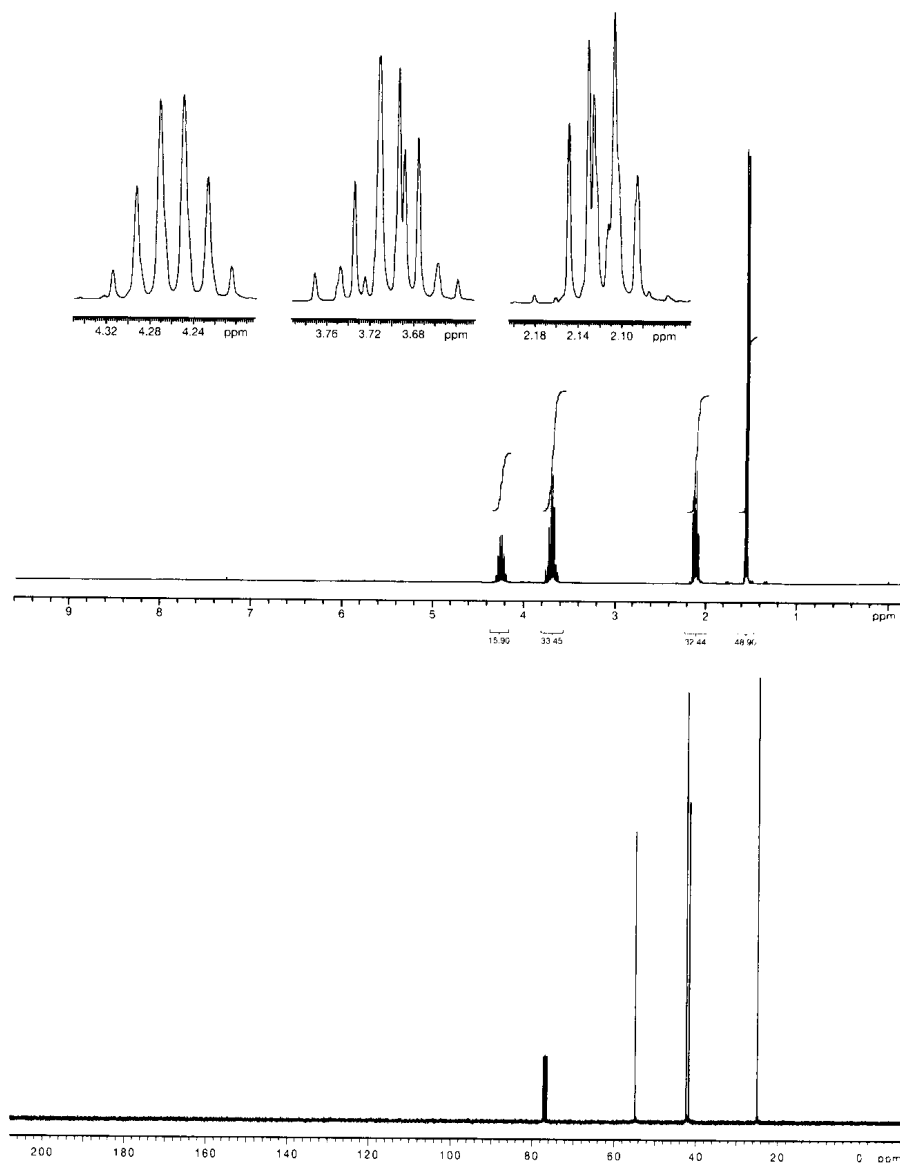


3.7 The $-\text{OH}$ proton resonance is found at δ 5.80 for phenol in dilute CDCl_3 and at δ 10.67 for 2-nitrophenol in dilute CDCl_3 . Explain.

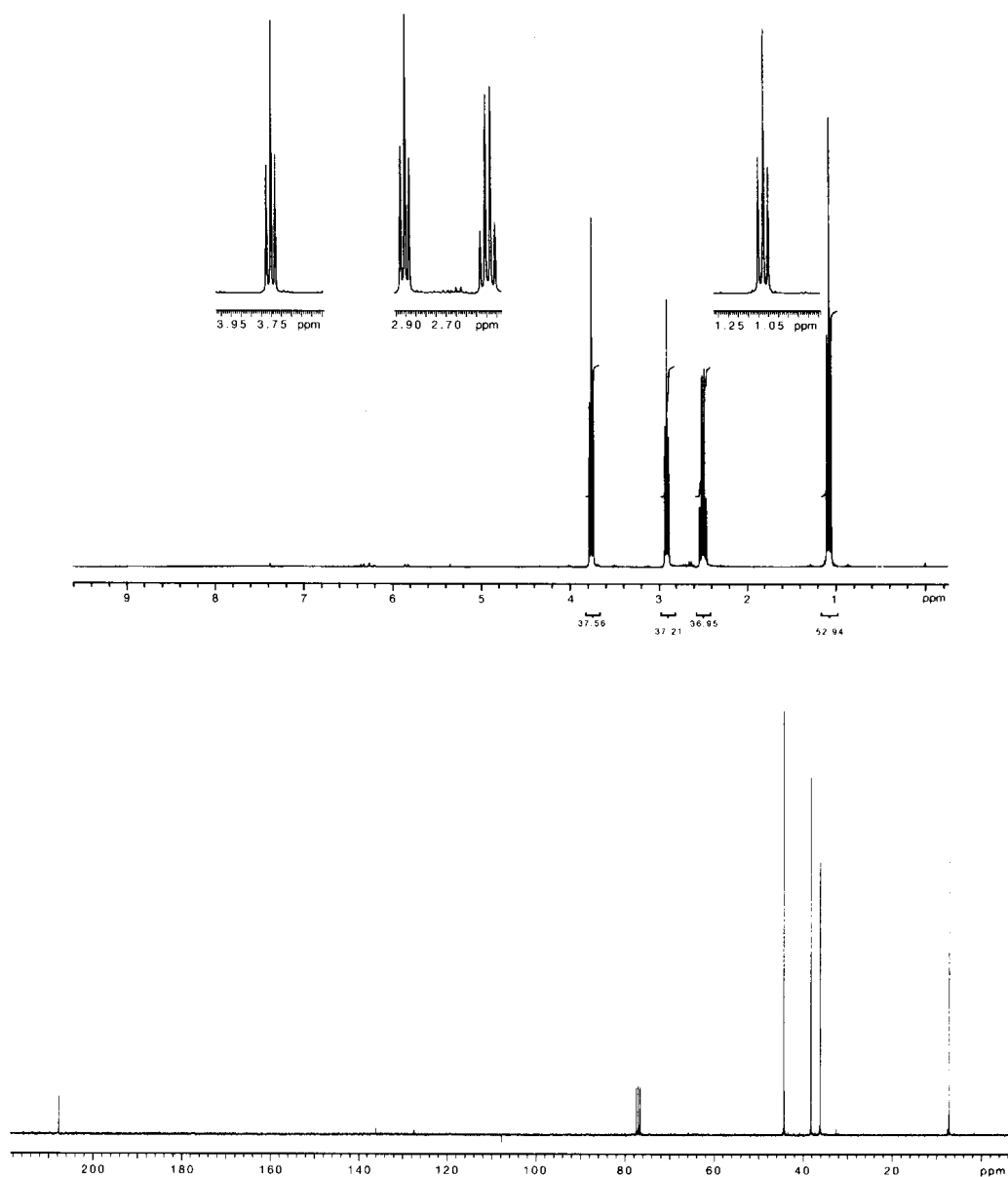
3.8 Derive the structures of the compounds that have the ^1H (300 MHz) and ^{13}C (75 MHz) spectra shown in parts (a)–(g). The 1 : 1 : 1 triplet at δ 78 in the ^{13}C spectra is from the solvent CDCl_3 (used in all cases except (f)).

(a) $\text{C}_4\text{H}_6\text{O}_2$

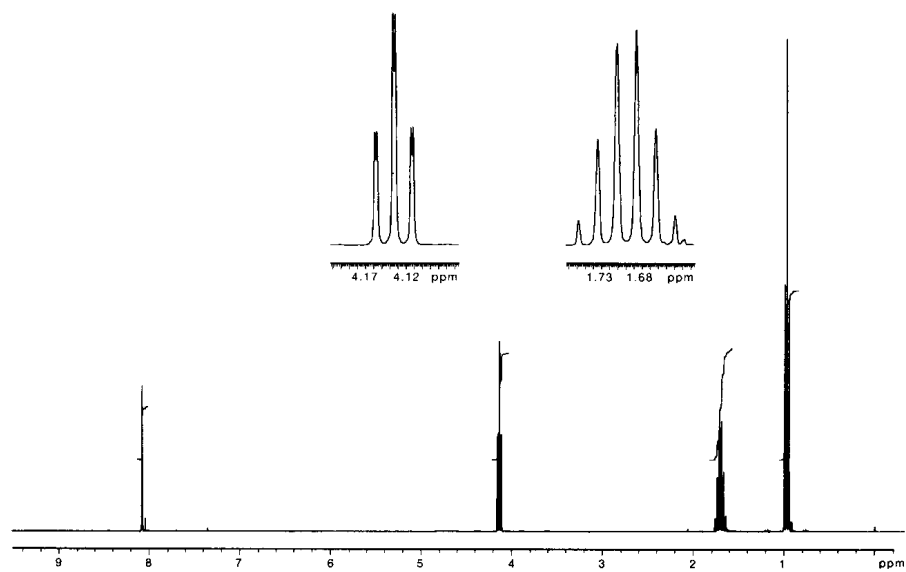


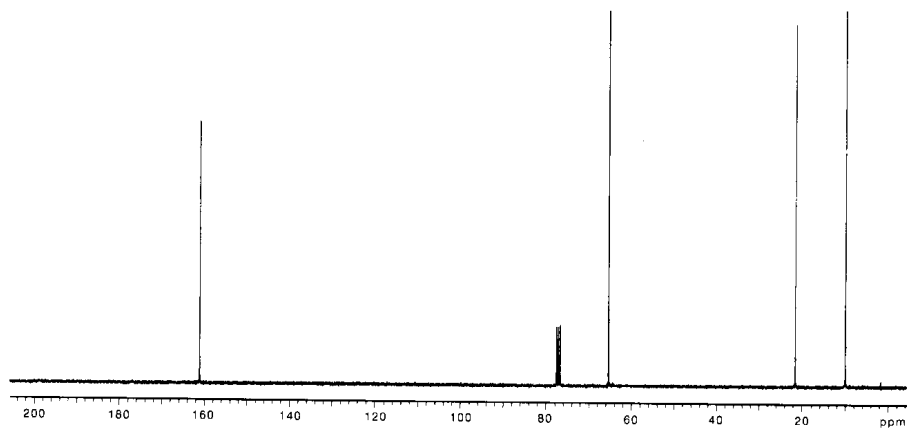
(b) $C_4H_8Cl_2$ 

(c) C_5H_9OCl

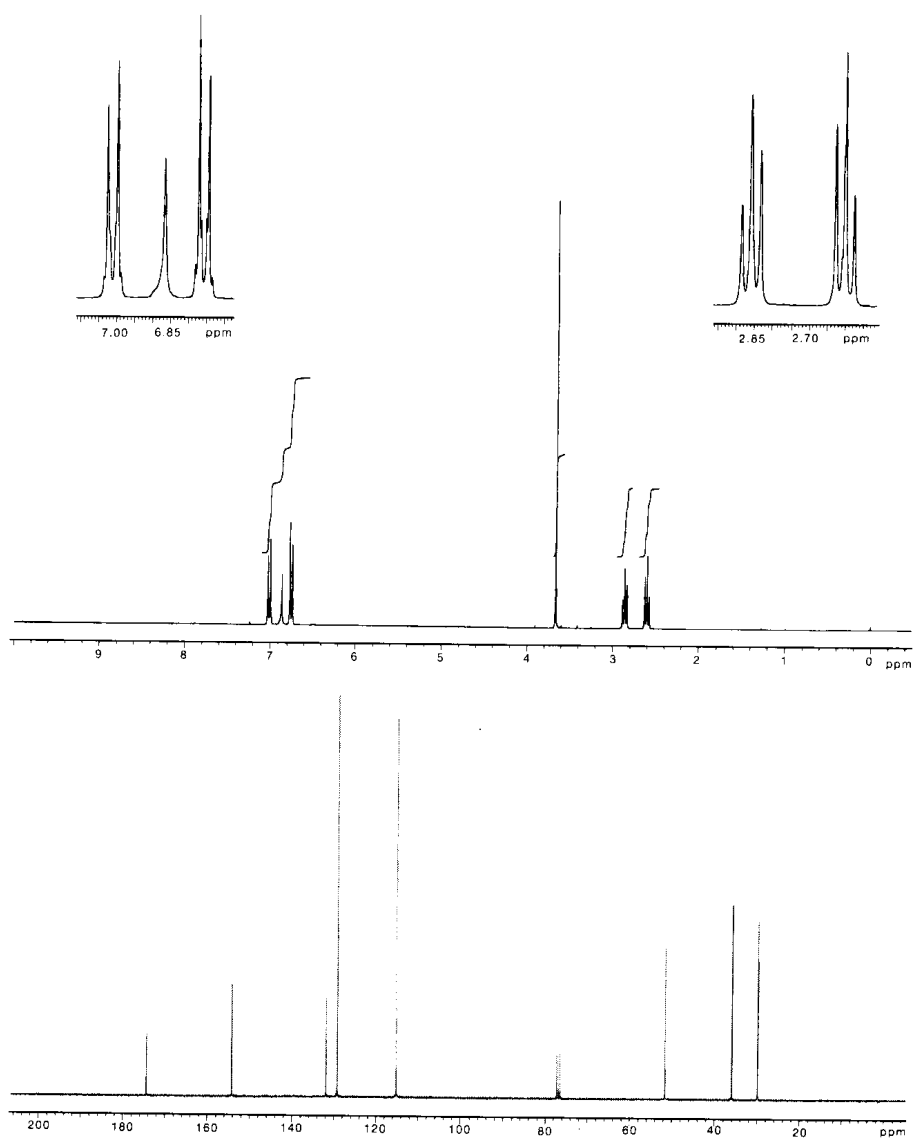


(d) $C_4H_8O_2$

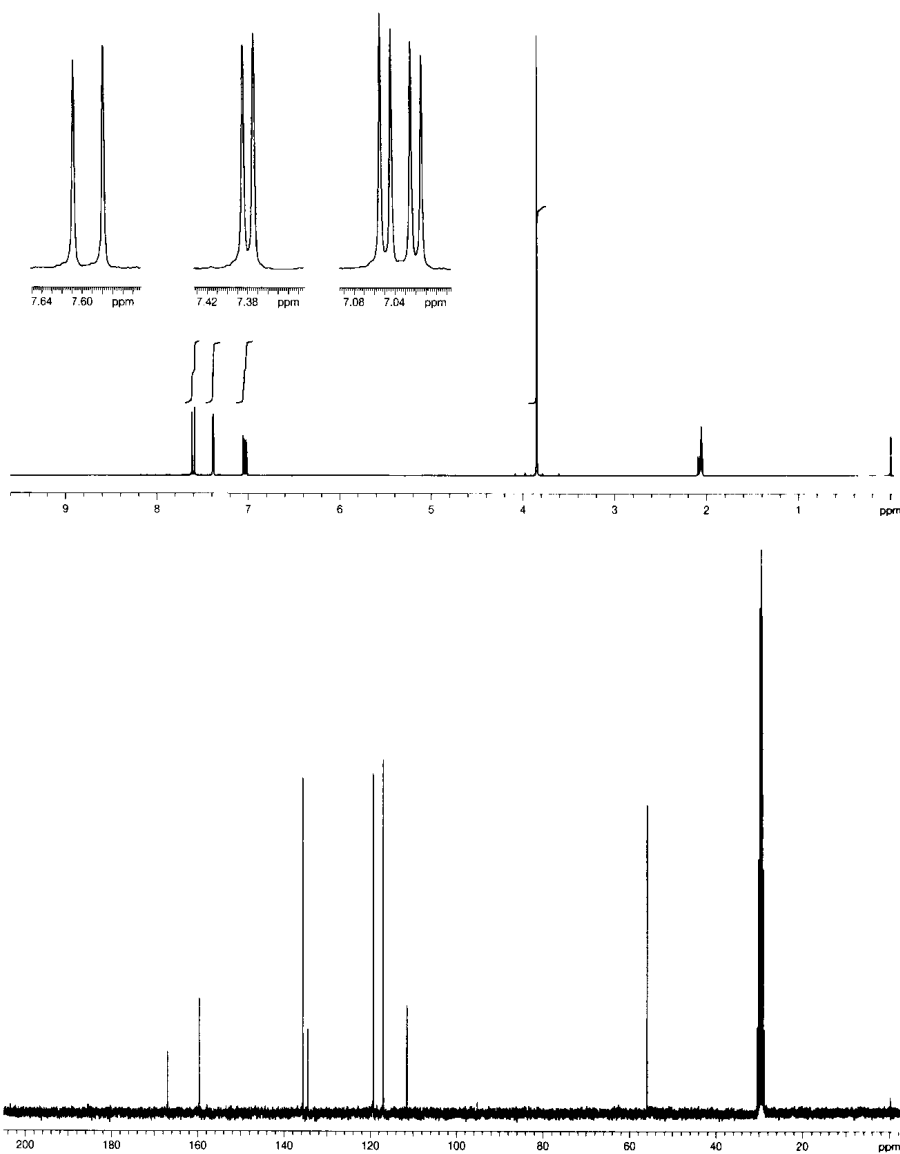




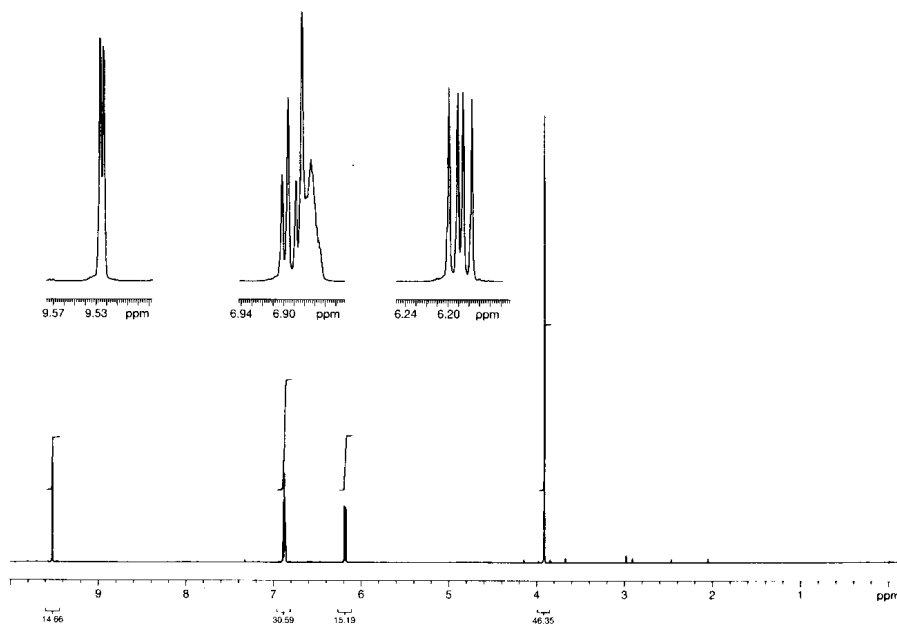
(e) $\text{C}_{10}\text{H}_{12}\text{O}_3$ (The peak at δ 6.87 disappears after adding D_2O and shaking.)

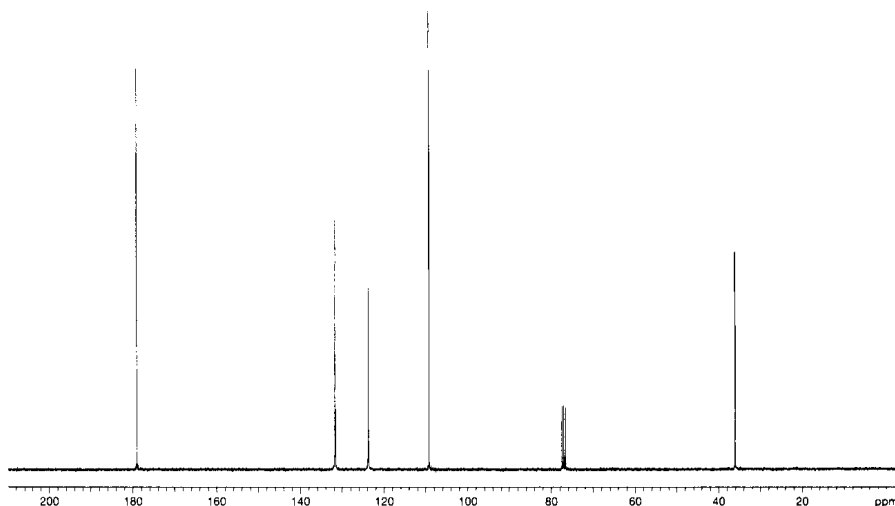


- (f) $C_8H_7BrO_3$ (A 1H resonance of unit integral at δ 12 is not shown; the 1H signals at δ 2.05 and the ^{13}C signals at δ 30 are from the solvent acetone- d_6 .)



- (g) C_6H_7NO





Bibliography

See also references 1.1, 1.2, 1.3, 1.5, 1.9, and 1.13.

Diamagnetic Anisotropy

- 3.1. R. C. Haddon, *Fortsch. Chem. Forsch.*, **16**, 105 (1971); C. W. Haigh and R. B. Mallion, *Progr. NMR Spectrosc.*, **13**, 303 (1979).

Empirical Correlations

- 3.2. C. Pascual, J. Meier, and W. Simon, *Helv. Chim. Acta*, **49**, 164 (1966); S. W. Tobey, *J. Org. Chem.*, **34**, 1281 (1969); E. C. Friedrich and K. G. Runkle, *J. Chem. Educ.*, **61**, 830 (1984); D. W. Brown, *J. Chem. Educ.*, **62**, 209–212 (1985).

Solvent Effects

- 3.3. P. Laszlo, *Progr. NMR Spectrosc.*, **3**, 231 (1967); J. Ronayne and D. H. Williams, *Ann. Rev. NMR Spectrosc.*, **2**, 83 (1969); J. Homer, *Appl. Spectrosc. Rev.*, **9**, 1 (1975).
- 3.4. J. B. Stothers, *Carbon-13 NMR Spectroscopy*. New York: Academic Press, 1973.
- 3.5. G. C. Levy, R. L. Lichter, and G. L. Nelson, *Carbon-13 Nuclear Magnetic Resonance Spectroscopy*, 2d ed. New York: Wiley-Interscience, 1980.

- 3.6. W. Bremser, B. Franke, and H. Wagner, *Chemical Shift Ranges in ¹³C NMR*, Weinheim, Germany: Verlag Chemie, 1982.
- 3.7. E. Breitmaier and W. Völter, *Carbon-13 NMR Spectroscopy*, 3d ed. Weinheim, Germany: VCH, 1987.
- 3.8. F. W. Wehrli, A. P. Marchand, and S. Wehrli, *Interpretation of Carbon-13 NMR Spectra*, 2d ed. Chichester, UK: John Wiley & Sons, Ltd., 1988.

Other Nuclei

- 3.9. R. K. Harris and B. E. Mann, *NMR and the Periodic Table*. London: Academic Press, 1978; C. Brevard and P. Granger, *Handbook of High Resolution Multinuclear NMR*. New York: Wiley-Interscience, 1981; J. B. Lambert and F. G. Riddell, eds., *The Multinuclear Approach to NMR Spectroscopy*. Dordrecht, the Netherlands: D. Reidel, 1983; P. Laszlo, ed., *NMR of Newly Accessible Nuclei*. New York: Academic Press, 1983; J. Mason, ed., *Multinuclear NMR*. New York: Plenum Press, 1987; B. E. Mann, *Ann. Rev. NMR Spectrosc.*, **23**, 141–207 (1991).

The Coupling Constant

4-1 First- and Second-Order Spectra

Most spectra illustrated up to this point are said to be *first order*. For a spectrum to be first order, the frequency difference ($\Delta\nu$) between the chemical shifts of any given pair of nuclei must be much larger than the value of the coupling constant J between them, approximately $\Delta\nu/J > 10$. In addition, an important symmetry condition discussed in the next section must hold. First-order spectra exhibit a number of useful and simple characteristics:

- Multiplicities that result from coupling reflect the $n + 1$ rule for $I = \frac{1}{2}$ nuclei exactly ($2nI + 1$, in general). Thus, two neighboring protons split the resonating nucleus into three peaks.
- The intensities of spin–spin multiplets correspond to the coefficients of the binomial expansion given by Pascal’s triangle for spin- $\frac{1}{2}$ nuclei. (See Figure 1-24.)
- Nuclei with the same chemical shift do not split each other, even when the coupling constant between them is nonzero.
- Spacings between adjacent components of a spin–spin multiplet are equal to the coupling constant J .
- Spin–spin multiplets are centered on their resonance frequency.

When the chemical-shift difference is less than about 10 times J ($\Delta\nu/J \lesssim 10$), *second-order* effects appear in the spectrum, including deviations in intensities from the binomial pattern and other exceptions from the preceding characteristics. By the Pople notation, nuclei that have a first-order relationship are represented by letters that are far apart in the alphabet (AX), and those that have a second-order relationship are represented by adjacent letters (AB). Figure 4-1 illustrates the progression for two spins from AB almost to AX. When $\Delta\nu/J$ is 0.4, the spectrum is practically a singlet. Intensity distortions increase peak heights toward the center of the multiplet. A second-order multiplet typically leans toward the resonances of its coupling partner. The peak intensities within a multiplet are not equal even when $\Delta\nu/J = 15$. With the wide availability of proton frequencies of 300 MHz and higher, first-order spectra have become common, but by no means exclusive.

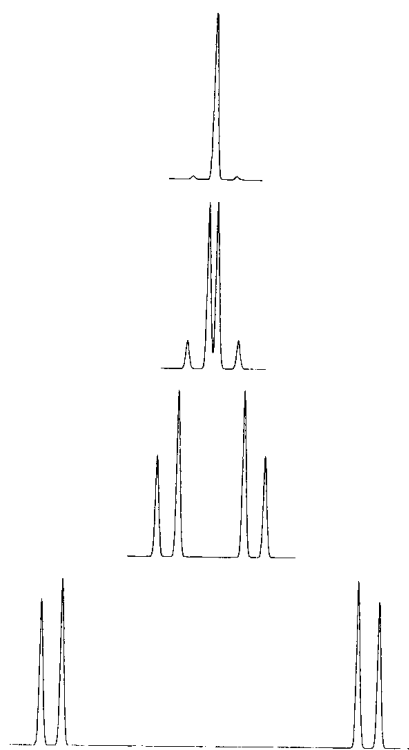
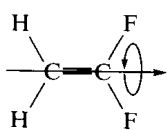


Figure 4-1 The two-spin spectrum with $\Delta\nu/J$ values of 0.4 (top), 1.0, 4.0, and 15.0.

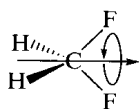
4-2 Chemical and Magnetic Equivalence

In addition to meeting the requirements concerning chemical-shift differences compared with coupling constants ($\Delta\nu/J$), first-order spectra must pass a symmetry test. Any pair of chemically equivalent nuclei must have the same coupling constant to any other nucleus. Nuclear pairs that fail this test are said to be *magnetically nonequivalent*. To apply the test, it is useful to understand the role of symmetry in the NMR spectrum.

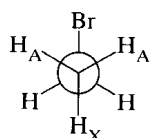
Nuclei are *chemically equivalent* if they can be interchanged by a symmetry operation of the molecule. Thus, the two protons in 1,1-difluoroethene (**4-1**) or in difluoromethane (**4-2**)



4-1



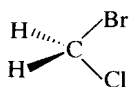
4-2



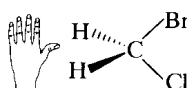
4-3

may be interchanged by a 180° rotation. Nuclei that are interchangeable by rotational symmetry are said to be *homotopic*. Rotation about carbon-carbon single bonds is so rapid that the chemist rarely considers the fact that the three methyl protons in $\text{CH}_3\text{CH}_2\text{Br}$ are not in fact equivalent. (Compare nuclei A and X in **4-3**.) Rapid C-C rotation, however, results in an average environment in which they are equivalent. (Dynamic effects are considered more thoroughly in Section 5-2.)

Nuclei related by other symmetry operations, such as passing a plane between them, are called *enantiotopic*, provided that there is no rotational axis of symmetry. For example, the protons in bromochloromethane (**4-4a**) are chemically equivalent and enantiotopic, because



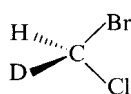
4-4a



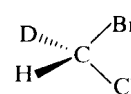
4-4b

they are related by the plane of symmetry containing C, Br, and Cl. If the molecule is placed in a chiral environment, this statement no longer holds true. Such an environment may be created by using a solvent composed of an optically active material or by placing the molecule in the active site of an enzyme. This kind of environment may be represented as shown in **4-4b**, in which bromochloromethane has a small hand placed to one side. The protons are no longer equivalent, because the hand is a chiral object. Because the plane of symmetry is lost in a chiral environment, the nuclei are not enantiotopic, but have become chemically nonequivalent. Enantiotopic nuclei may be expected to be chemically nonequivalent and give distinct resonances in an optically active solvent. In a biological context, enantiotopic protons may be rendered nonequivalent by an enzyme and may exhibit distinct chemical properties, such as acidity.

The term *enantiotopic* was invented because the replacement of one proton of the pair by another atom or group, such as deuterium, produces the enantiomer (nonsuperimposable mirror image, **4-4c**) of the molecule that results when the other proton is replaced by the

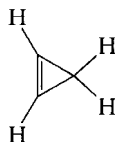


4-4c

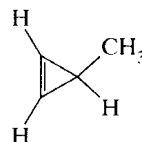


4-4d

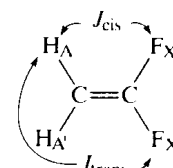
same group (**4-4d**). A pair of homotopic nuclei treated in this fashion produce identical molecules (superimposable mirror images). Enantiotopic or homotopic protons need not be on the same carbon atom. Thus, the alkenic protons in cyclopropene (**4-5**) are homotopic, but those in 3-methylcyclopropene (**4-6**) are enantiotopic. Chemically equivalent nuclei (either homotopic or enantiotopic) are represented by the same letter in the spectral shorthand of Pople. Cyclopropene (**4-5**) is A_2X_2 , as is difluoromethane (**4-2**), since the two fluorine atoms have spins of $\frac{1}{2}$. The ring protons of 3-methylcyclopropene (**4-6**) constitute an AX_2 group.



4-5



4-6



4-7

To be *magnetically equivalent*, nuclei that already are chemically equivalent must have the same coupling constant to any other nucleus in the molecule. This is a more stringent test than chemical equivalence, because it is necessary to go beyond considering just the symmetry of the overall molecule. The first two molecules discussed in this chapter provide contrasting results. In difluoromethane (**4-2**), each of the two hydrogen atoms has the same coupling to a specific fluorine atom, because they have the same spatial relationship to the fluorine. Consequently, the protons are magnetically equivalent. By the same token, the two fluorine atoms also are magnetically equivalent, by reference to coupling to either proton, and the spin system is labeled A_2X_2 .

In 1,1-difluoroethene (**4-1**), however, the two protons do not have the same spatial relationship to a given fluorine. Therefore, they have different couplings, one a J_{cis} and the other a J_{trans} (**4-7**), and are said to be magnetically nonequivalent. These spins are represented by the notation $AA'XX'$, so that the two couplings may be denoted by J_{AX} and $J_{AX'}$. (In contrast, an A_2X_2 system such as difluoromethane (**4-2**) or cyclopropene (**4-5**) has only one coupling, J_{AX} .) In an $AA'XX'$ system, J_{AX} and $J_{A'X'}$ are the same, as are $J_{AX'}$ and $J_{A'X}$. Any spin system that contains nuclei that are chemically equivalent, but magnetically nonequivalent, is, by definition, second order. Moreover, raising the intensity of the magnetic

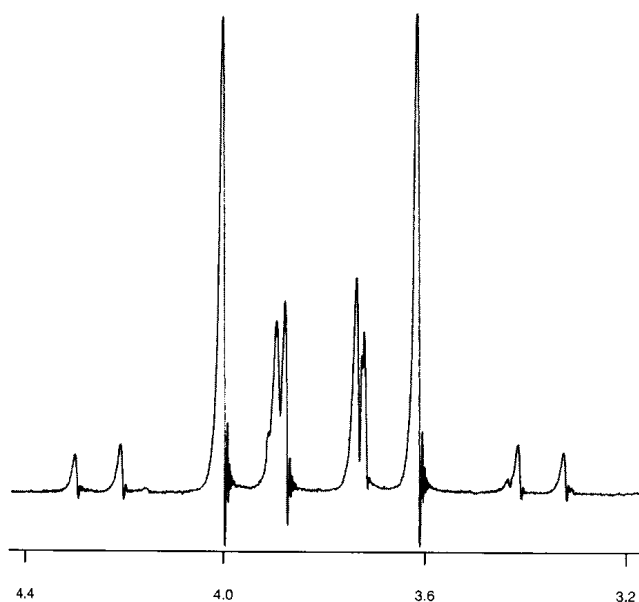
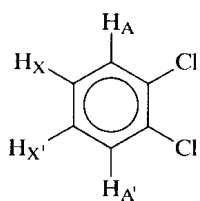


Figure 4-2 The 90 MHz ^1H spectrum of 1,1-difluoroethene in CDCl_3 .

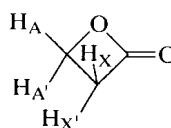
field cannot alter basic structural relationships between nuclei, so that the spectrum remains second order at the highest accessible fields.

The $\text{AA}'\text{XX}'$ notation may be interpreted as follows. The chemical shifts of the A and X nuclei are very far from each other (at opposite ends of the alphabet). The A and A' nuclei are chemically equivalent, but magnetically nonequivalent, as are the X and X' nuclei. Figure 4-2 illustrates the proton AA' part of the spectrum of 1,1-difluoroethene, in which 10 peaks are visible. This appearance is quite different from the simple 1 : 2 : 1 triplet expected in the first-order case. The multiplicity of peaks in Figure 4-2 in fact permits the measurement of $J_{\text{AA}'}$, the coupling between the equivalent protons.

Magnetic nonequivalence is not uncommon. The spin systems for both para- and ortho-disubstituted benzene rings are $\text{AA}'\text{XX}'$ (or $\text{AA}'\text{BB}'$ if the chemical shifts are close). Figure 4-3 illustrates the proton spectrum of 1,2-dichlorobenzene (**4-8**), which is $\text{AA}'\text{XX}'$ and relatively complex. Constraints of a ring frequently convey magnetic nonequivalence, as, for example, in butyrolactone (**4-9**). Even open-chain systems such as



4-8



4-9

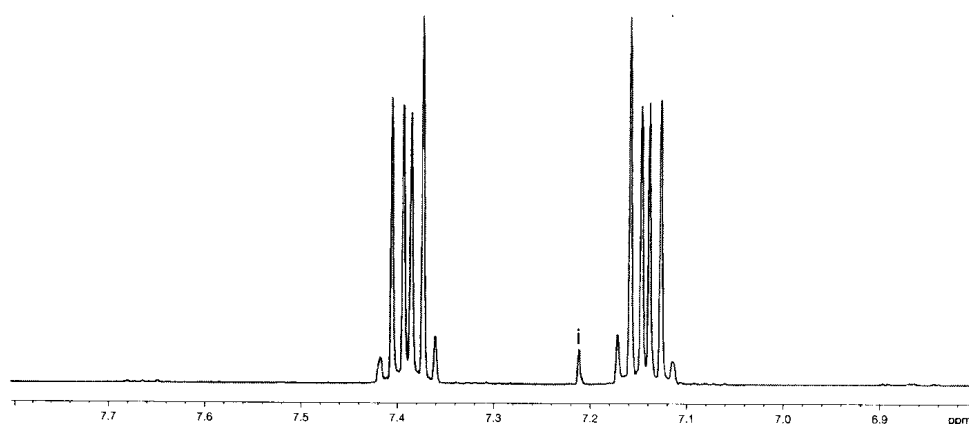
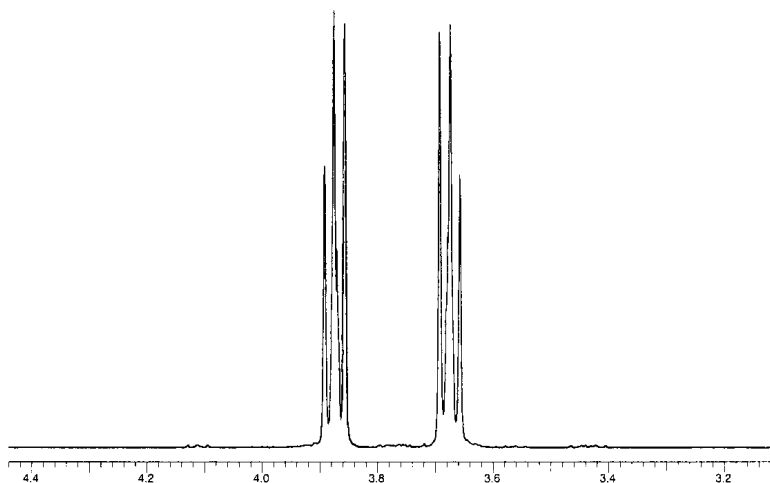


Figure 4-3 The 300 MHz ^1H spectrum of 1,2-dichlorobenzene in DCDI_3 . An impurity is signified by the letter *i*.

Figure 4-4 The 300 MHz ^1H spectrum of 2-chloroethanol (methylene resonances only) in CDCl_3 .

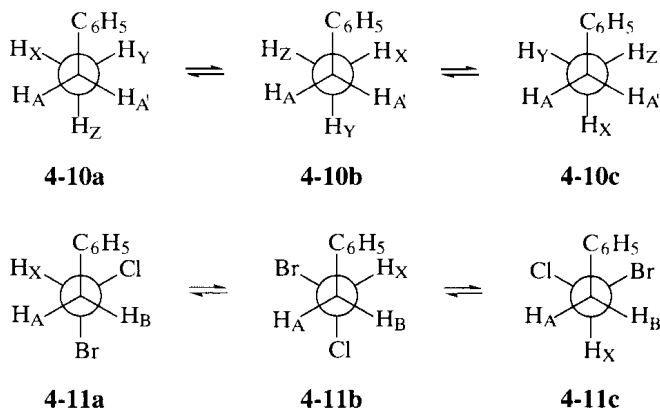


2-chloroethanol ($\text{ClCH}_2\text{CH}_2\text{OH}$; Figure 4-4) contain magnetically nonequivalent spin systems, although they are understandable only by examination of the contributing rotamers. (See problems at the end of the chapter.) Butyrolactone, chloroethanol, and both *o*- and *p*-dichlorobenzene thus all give $\text{AA}'\text{XX}'$ (or $\text{AA}'\text{BB}'$) spectra (if the hydroxyl proton is ignored in the alcohol).

In Figure 4-4, the second-order character of the spectrum is manifested in two ways. First, peaks do not have the binomial intensity relationship. Thus, the inner peaks of each resonance are larger than the outer peaks. (A first-order spectrum would have been two 1:2:1 triplets.) More careful examination, however, shows that the $n + 1$ rule fails. Instead of three peaks in each resonance, there are four. (The fourth peak requires spectral expansion, but is easily seen on the right side of the central peak of the high-frequency (low-field) resonance and less obviously on the left side of the central peak of the low-frequency resonance.)

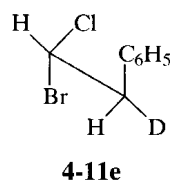
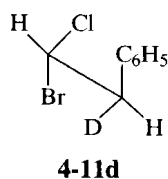
Magnetically equivalent nuclei must be chemically equivalent and hence must have the same chemical shift; that is, they must be *isochronous*. Nonequivalence resulting from unequal couplings to a single partner nucleus sometimes is referred to as *magnetic nonequivalence by the coupling-constant criterion*. The term is intended to provide a distinction from chemically nonequivalent nuclei, which have different chemical shifts and illustrate *magnetic nonequivalence by the chemical-shift criterion*.

When protons are on different carbons, it usually is straightforward to determine whether they are chemically equivalent on the basis of symmetry. Geminal protons (those on the same carbon, as in CH_2) can be more subtle. Consider the protons of ethylbenzene ($\text{C}_6\text{H}_5\text{CH}_2\text{CH}_3$) and of its β -bromo- β -chloro derivative ($\text{C}_6\text{H}_5\text{CH}_2\text{CHClBr}$). Rotation about the saturated C–C bond creates three rotamers for each molecule, which may be represented by the Newman projections shown in 4-10 and 4-11. For 4-10, the three rotamers



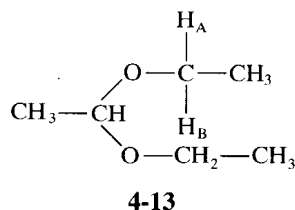
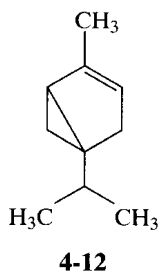
are identical. In the rotamer **4-10a**, H_A and $H_{A'}$ are chemically equivalent and enantiotopic by reason of the plane of symmetry. When methyl rotation is slow, H_A and $H_{A'}$ are magnetically nonequivalent, because each would couple unequally with both H_X and H_Y . The plane of symmetry actually requires that H_Y should be labeled $H_{X'}$, but we retain the different lettering to illustrate the effect of methyl rotation. Thus, the frozen structure **4-10a** would exhibit an $AA'XX'Z$ spectrum. Rapid methyl rotation averages the X, Y, and Z environments, so that the three methyl protons become chemically equivalent, on average, and the A and A' protons have equal couplings to all three methyl protons, on average, and hence become magnetically equivalent. On average, there is only one coupling constant, and the spectrum is A_2X_3 if the aromatic protons are ignored.

Molecule **4-11** contains a chiral or stereogenic center in place of the methyl group, so that the three rotamers are now distinct (**4-11a-c**). Moreover, no symmetry operation in any of them relates H_A to H_B . Consequently, even with rapid C-C rotation, H_A and H_B have different chemical shifts and exhibit a mutual coupling constant. The spin system is ABX (AMX if the chemical-shift differences are large). The AB protons in **4-11** exemplify chemically nonequivalent nuclei that are termed *diastereotopic*. Diastereoisomers are stereoisomers other than enantiomers. Replacing H_A by deuterium gives **4-11d**, a diastereoisomer of **4-11e**, which is formed when H_B is replaced by deuterium. The deuterated derivative has



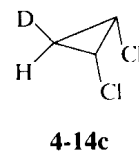
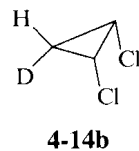
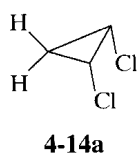
two stereogenic centers. In general, the protons of a saturated methylene group become diastereotopic when there is a stereogenic center elsewhere in the molecule, because there is no symmetry operation that relates the two protons. The protons in **4-4b** become diastereotopic because the hand provides the stereogenic center. Accidental degeneracy can occur when the chemical-shift difference is small or unobservable, so that diastereotopic protons can appear to be equivalent in the spectrum.

Methyl groups in an isopropyl group can be diastereotopic when stereogenic centers are present in the molecule, as in α -thujene (**4-12**). The proton resonance then appears as a pair



of doublets (coupled to the methine proton), and the carbon resonance appears as two singlets (with the proton decoupled). A stereogenic center is not necessary for methylene protons to be diastereotopic. The diethyl acetal of acetaldehyde (**4-13**) contains diastereotopic protons because the axis of symmetry of the molecule is not an axis of symmetry for the CH_2 protons. This situation may be understood by examining the rotamers or by replacing H_A with deuterium. The latter operation simultaneously creates two stereogenic centers, $-OCHD(CH_3)$ and $-OCH(CH_3)O-$, and the resulting molecule is a diastereoisomer of

the molecule in which H_B is replaced with deuterium. The methylene protons in *cis*-1,2-dichlorocyclopropane (**4-14a**) are diastereotopic because **4-14b** and **4-14c** are



diastereoisomers. The axial and equatorial protons on a single carbon in ring-frozen cyclohexane are diastereotopic because cyclohexane-axial-*d* and cyclohexane-equatorial-*d* are diastereoisomers. When ring flipping is fast on the NMR time scale, the geminal protons become equivalent, on average. Thus, the diastereotopic nature of protons can depend on the rate of molecular interconversions.

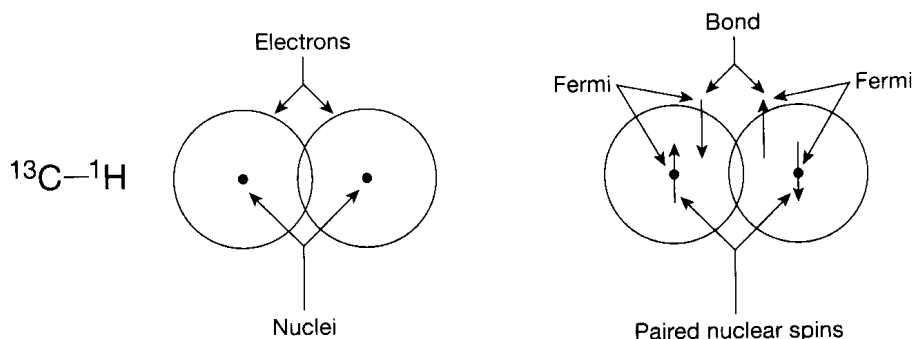
4-3 Signs and Mechanisms: One-Bond Couplings

Spin–spin coupling arises because information about nuclear spin is transferred from nucleus to nucleus via the electrons. Exactly how does this process occur? Several mechanisms have been considered, but the most important is the *Fermi contact mechanism*. According to this model, an electron in a bond X–Y, in which the nuclei of both X and Y are magnetic, spends a finite amount of time at the same point in space as, say, nucleus X. The electron and nucleus are then said to be in contact. If nucleus X has a spin of $I_x = +\frac{1}{2}$, then, by the Pauli exclusion principle, the spin of the electron must be opposite ($-\frac{1}{2}$), so that the two spins can occupy the same space at the same time. In this way, the nuclear spin polarizes the electron spin (gives one spin state a higher population). The electron in turn shares an orbital in the X–Y bond with another electron, which must have a spin of $+\frac{1}{2}$ when the spin of the first electron is $-\frac{1}{2}$. This second ($+\frac{1}{2}$) electron occupies the same point in space as nucleus Y only when Y has a spin of $-\frac{1}{2}$. Thus, whenever X has a spin of $+\frac{1}{2}$, a spin of $-\frac{1}{2}$ is slightly favored for Y, as shown in Figure 4-5 for a ^{13}C – ^1H coupling. (An upward-pointing arrow arbitrarily represents a $+\frac{1}{2}$ spin, a downward-pointing arrow a $-\frac{1}{2}$ spin.) Since the bonding electrons are used to pass the spin information, the contact term is not averaged to zero by molecular tumbling.

When one spin slightly polarizes another spin oppositely, as in the preceding model for coupling across X–Y, the coupling constant J between the spins is said by convention to have a positive sign. A negative coupling occurs when spins polarize each other in the same (parallel) direction. Qualitative models analogous to that shown in Figure 4-5 indicate that coupling over two bonds, as in H–C–H, is negative, while coupling over three bonds, as in H–C–C–H, is positive. There are numerous exceptions to this qualitative approach, but it is useful in understanding that J has sign as well as magnitude.

The magnetic dipoles of two magnetically active nuclei also may interact directly through space. This interaction, however, is averaged to zero for nuclei in solution by

Figure 4-5 Diagram of the Fermi contact mechanism for the indirect coupling of two spins.



molecular tumbling, whereby all possible relative orientations are populated. Direct coupling (D , to distinguish it from the indirect J coupling) may be manifested in the spectrum when molecular motion is inhibited in some way: by an external electric field, in liquid crystal solvents, in the solid, or even in liquids under certain circumstances, such as high viscosity. The D coupling can be a nuisance and lead to line broadening, or it can be exploited to obtain information about internuclear distances or absolute signs of coupling. When the sample is subjected to an external electric field, the absolute signs of D can be obtained. The relative signs of D and J can be derived from spectra of a partially oriented molecule, as in a liquid crystal solvent. In this manner, the absolute sign of J can be inferred from the electric-field experiment. In electric-field experiments, Buckingham and McLauchlan showed that the ortho coupling in 4-nitrotoluene has an absolute positive sign. In this way, the signs of all J coupling constants have been related back to a few whose absolute signs actually were measured.

High-resolution NMR spectra normally are not dependent on the absolute sign of coupling constants. Simultaneous reversal of the sign of every coupling constant in a spin system results in an identical spectrum. Many spectra, however, depend on the *relative signs* of component couplings. For example, the general ABX spectrum is determined in part by three couplings: J_{AB} , J_{AX} , and J_{BX} . (See Section 4-7.) Different spectra can be obtained when J_{AX} and J_{BX} have the same sign (both positive or both negative) from when they have opposite signs (one positive and the other negative), even when the magnitudes are the same.

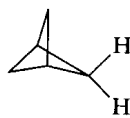
The usual convention for referring to a coupling constant is to denote the number of bonds between the coupled nuclei by a superscript to the left of the letter J and any other descriptive material by a subscript to the right or parenthetically. A two-bond (*geminal*) coupling between protons is then ${}^2J_{\text{HCH}}$ or ${}^2J(\text{HCH})$, and a three-bond (*vicinal*) coupling between a proton and a carbon is ${}^3J_{\text{HCCC}}$ or ${}^3J(\text{HCCC})$. Beyond three bonds, couplings between protons are said to be *long range*.

The one-bond coupling between carbon-13 and protons is readily measured from the ${}^{13}\text{C}$ spectrum when the decoupler is turned off. Although usually unobserved because of decoupling, this coupling provides useful information and illustrates several important principles. Because a p orbital has a node at the nucleus, only electrons in s orbitals can contribute to the Fermi contact mechanism. For protons, all electrons reside in the 1s orbital, but, for other nuclei, only that proportion of the orbital that has s character can contribute to coupling. When a proton is attached to an sp^3 carbon atom (25% s character), ${}^1J({}^{13}\text{C}-{}^1\text{H})$ is about half as large as that for a proton attached to an sp carbon atom (50%). The alkenic CH (sp^2) coupling is intermediate. The values of 1J for methane (sp^3), ethene (sp^2), benzene (sp^2), and ethyne (sp) are 125, 157, 159, and 249 Hz, respectively. These numbers define the following linear relationship between the percentage of s character of the carbon orbital and the one-bond coupling:

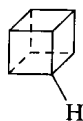
$$\%s(\text{C}-\text{H}) = 0.2J({}^{13}\text{C}-{}^1\text{H}). \quad (4-1)$$

The zero intercept of this equation indicates that there is no coupling when the s character is zero, in agreement with the Fermi contact model.

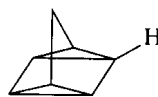
The one-bond CH coupling ranges from about 100 to 320 Hz, and much of the variation may be interpreted in terms of the J -s relationship. The coupling constant in cyclopropane (162 Hz) demonstrates that the carbon orbital to hydrogen is approximately sp^2 hybridized. Intermediate values in hydrocarbons may be interpreted in terms of fractional hybridization. The $J = 144$ Hz for the indicated CH bond in tricyclopentane (**4-15**) corresponds to 29% s character ($\text{sp}^{2.4}$), 160 Hz in cubane (**4-16**) to 32% s character (sp^2), and 179 Hz in quadricyclane (**4-17**)



4-15



4-16



4-17

to 36% s character ($sp^{1.8}$). Although the J - s relationship works well for hydrocarbons, there is some question as to its applicability to polar molecules. Variations in the effective nuclear charge, in addition to hybridization effects, alter the coupling constants.

Just as the resonance frequency of a nucleus is proportional to its gyromagnetic ratio γ , the coupling constant between two nuclei is proportional to the product of both gyromagnetic ratios; that is, $J(X-Y) \propto \gamma_X \gamma_Y$. Nuclei with very small gyromagnetic ratios, such as ^{15}N , tend to have correspondingly small couplings. Furthermore, in this case, $\gamma(^{15}\text{N})$ has a negative sign, whereas both $\gamma(^{13}\text{C})$ and $\gamma(^1\text{H})$ are positive. As a result, one-bond couplings between nitrogen-15 and hydrogen have a negative sign. The sign does not represent an exception to the Fermi model described (Figure 4-5), but only reflects the negative sign of the gyromagnetic ratio.

One-bond couplings have been measured between protons and many other types of nuclei. The coupling between nitrogen and hydrogen ranges from 51 Hz in diphenylketimine ($(\text{C}_6\text{H}_5)_2\text{C}=\text{NH}$) to 130 Hz in protonated acetonitrile ($\text{CH}_3\text{C}\equiv\text{NH}^+$). Typical values for sp^2 nitrogen, as in acetamide ($\text{CH}_3(\text{C}=\text{O})\text{NH}_2$) or protonated pyridine, are around 90 Hz, and typical values for sp^3 nitrogen, as in the ammonium ion, are 70–75 Hz. With the three points of hybridization provided by protonated acetonitrile, protonated pyridine, and ammonium, the relationship between coupling and hybridization can be established to be $s(\text{N}) = 0.43^1 J(^{15}\text{N}-\text{H}) - 6$, and the hybridization, for example, of nitrogen in ammonia ($^1 J = 61$ Hz) can be calculated to be sp^4 ($s = 20\%$). Because of the negative gyromagnetic ratio of nitrogen, all these couplings actually are negative, but the signs have been omitted.

One-bond coupling constants between ^{31}P and ^1H range from 186 Hz (PH_2-PH_2) to 707 Hz (H_3PO_3). Couplings of ^{11}B to ^1H range from 29 Hz (the bridging hydrogen in $\text{H}_2\text{BHBH}_2 \cdot \text{N}(\text{CH}_3)_3$) to 211 Hz in HBF_2 . Some extremely large couplings have been observed lower in the periodic table—for example, $^1 J(^{119}\text{Sn}-^1\text{H}) = 1,931$ Hz in SnH_4 , $^1 J(^{195}\text{Pt}-^1\text{H}) = 1,307$ Hz in $[\text{P}(\text{C}_2\text{H}_5)_3]_2\text{PtHCl}$, and $^1 J(^{207}\text{Pb}-^1\text{H}) = 2,379$ Hz in $(\text{CH}_3)_3\text{PbH}$.

When neither nucleus is a proton, the coupling constant depends on the product of the s characters of the orbitals from both nuclei that form the bond. Thus, $^1 J(^{13}\text{C}-^{13}\text{C})$ depends on the hybridization of both carbons. With two unknown hybridizations and only one measured coupling, s character can be measured only when the symmetry of the molecule is such that the two carbons are identical. Measurements with molecules such as ethane, ethene, and ethyne led to the relationship $s^2(\text{C}) = 17.4^1 J(^{13}\text{C}-^{13}\text{C}) + 60$. The range of $^{13}\text{C}-^{13}\text{C}$ couplings is from 34 Hz in $\text{C}_6\text{H}_5\text{CH}_2\text{CH}_3$ to 176 Hz in $\text{C}_6\text{H}_5\text{C}=\text{CH}$. The one-bond coupling between two carbon atoms is readily measured by the technique known as INADEQUATE (Section 5-7) and is extremely useful in mapping carbon connectivities in complex molecules. Coupling between nuclei with lone pairs, as in $^1 J(^{31}\text{P}-^{31}\text{P})$ or $^1 J(^{13}\text{C}-^{15}\text{N})$, appears to have complexities resulting from effects other than hybridization. Again, extremely large couplings have been observed between two nuclei when at least one is from lower in the periodic table (e.g., $^1 J(^{205}\text{Tl}-^{19}\text{F}) = 12,000$ Hz in TlF and $^1 J(^{195}\text{Pt}-^{31}\text{P}) = 5700$ Hz in $\{[(\text{C}_2\text{H}_5)_2\text{O}]_3\text{P}\}_2\text{PtCl}_2$).

4-4 Geminal Couplings

The geminal coupling between two protons ($\text{H}-\text{C}-\text{H}$) may be measured directly from the spectrum when the coupled nuclei are chemically nonequivalent, thus constituting, for example, the AB or AM part of an ABX, AMX, or ABX_3 , etc., spectrum. If the relationship is first order (AM), the coupling may be measured by inspection, but in second-order cases (AB), the spectrum must be simulated computationally (Section 4-7). When geminal nuclei are chemically equivalent, but magnetically nonequivalent, as in the AA' part of an $\text{AA}'\text{XX}'$ spectrum, the coupling constant often is accessible by computational methods.

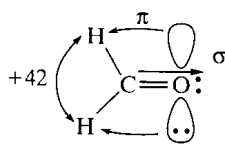
Splittings are not observed between coupled nuclei when they are magnetically equivalent, but the coupling constant may be measured by replacing one of the nuclei with deuterium. For example, in dichloromethane-*d* (CHDCl₂) the geminal H–C–D coupling is seen as the spacing between the components of the 1 : 1 : 1 triplet. (Deuterium has unity spin.) Since coupling constants are proportional to the product of the gyromagnetic ratios of the coupled nuclei, $J(\text{HCH})$ may be calculated from $J(\text{HCD})$ as follows:

$$J(\text{HH}) = \frac{\gamma_{\text{H}}}{\gamma_{\text{D}}} J(\text{HD}) = 6.51J(\text{HD}). \quad (4-2)$$

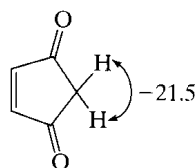
Geminal couplings depend strongly on the angle formed by the three atoms, H–C–H. The value decreases absolutely, but actually becomes less negative or more positive, when this angle increases, as in the cyclic hydrocarbon series (cyclohexane [–12.6 Hz], cyclopentane [–10.5 Hz], cyclobutane [–9 Hz], cyclopropane [–4.3 Hz]) or by comparison of acyclic alkanes (methane, –12.4 Hz) with acyclic alkenes (ethene, +2.3 Hz). Note that the sign of the coupling constant is important. Although most geminal couplings are negative, many of those for sp^2 carbons are positive.

The typical range for alkanes is –5 to –20 Hz and for alkenes is +3 to –3 Hz (or 0–3 Hz if the sign is ignored). Electron withdrawal by induction tends to make the coupling constant more positive, as pointed out by Pople and Bothner-By. For alkanes, the negative coupling thus decreases, from –12.4 Hz for methane to –10.8 Hz for CH₃OH, –9.2 Hz for CH₃I, and –5.5 Hz for CH₂Br₂. Electron donation makes the coupling less positive (or more negative), as in –14.1 Hz in TMS (Me₄Si). Analogous substitution on sp^2 carbon changes the coupling profoundly, as in the effect of electron withdrawal in the structure H₂C=X—for example, +2.3 Hz when X is CH₂ (ethene), +17 Hz when X is N(*tert*-butyl) (an imine), and +40 Hz when X is O (formaldehyde).

The effects of withdrawal or donation of electrons through the σ bonds (induction) can be augmented or decreased by π effects such as hyperconjugation. Pople and Bothner-By found that lone pairs of electrons can donate electrons and make J more positive, whereas the π orbitals of double or triple bonds can withdraw electrons and make J less positive. The aforementioned large increase in the geminal coupling of imines or formaldehyde compared with that of ethene results from reinforcement of the effects of σ withdrawal and π donation, as illustrated in structure 4-18. The effect of π withdrawal occurs for carbonyl, nitrile, and aromatic groups, as the values for acetone (–14.9 Hz), acetonitrile (–16.9 Hz),

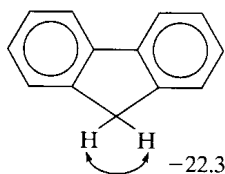


4-18

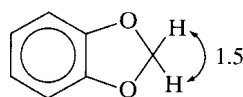


4-19

and dicyanomethane (–20.4 Hz) show. The π effect is somewhat reduced by free rotation in open-chain systems, but particularly large effects are created by constraints of rings, as seen in 4-19 and 4-20, as well as in the α protons of cyclopentanones and cyclohexanones. Structure 4-21 illustrates how π donation by lone pairs makes J more positive, an effect that



4-20

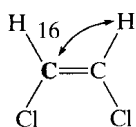


4-21

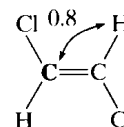
also explains the difference in the geminal couplings in three-membered rings [e.g., cyclopropane $(\text{CH}_2)_3$ (-4.3 Hz) and oxirane $(\text{CH}_2)_2\text{O}$ ($+5.5$ Hz)].

Geminal coupling between protons and other nuclei also has been studied. The $\text{H}-\text{C}-^{13}\text{C}$ coupling responds to substituents in much the same way as does the $\text{H}-\text{C}-\text{H}$ coupling. Most such couplings are relatively small in alkanes, as shown by $\text{H}-\text{CH}_2-\text{CH}_3$ (-4.8 Hz) and $\text{H}-\text{CCl}_2-\text{CHCl}_2$ ($+1.2$ Hz). Couplings from hydrogen to sp^2 carbon ($\text{H}-\text{CH}_2-\text{C}=\text{O}$) are typically -4 to -7 Hz, as in acetone (-5.9 Hz, $\text{H}-\text{CH}_2-\text{C}(=\text{O})\text{CH}_3$). When the intermediate carbon is sp^2 ($\text{H}-(\text{C}=\text{X})-\text{C}$), the coupling becomes larger and positive, as in aldehydes (26.7 Hz for acetaldehyde, $\text{H}-(\text{C}=\text{O})-\text{CH}_3$), but typically $5-10$ Hz in alkenes ($\text{H}-(\text{C}=\text{CR}_2)-\text{C}$).

Unlike the proton-proton case, the proton-carbon geminal-coupling pathway can include a double bond ($\text{H}-\text{C}=\text{C}$), a consequence of which is that factors not considered by Pople and Bothner-By become important. For sp^2 carbons, these couplings often are small (-2.4 Hz for ethene, $\text{H}-\text{CH}=\text{CH}_2$). With proper substitution, however, stereochemical differences may be observed, as in *cis*-dichloroethene (**4-22**, 16.0 Hz) and *trans*-dichloroethene (**4-23**, 0.8 Hz).



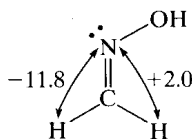
4-22



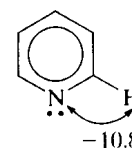
4-23

Such differences between alkene stereoisomers are common and may be exploited to prove stereochemistries. The geminal couplings in aromatics ($\text{H}-\text{C}=\text{C}$) are $4-8$ Hz. For sp carbons, the coupling becomes quite large: 49.3 Hz in ethyne ($\text{H}-\text{C}\equiv\text{CH}$) and 61.0 Hz in ($\text{H}-\text{C}\equiv\text{COPh}$).

The two-bond coupling between hydrogen and nitrogen-15 depends strongly on the presence and orientation of the nitrogen lone pair. The $\text{H}-\text{C}-^{15}\text{N}$ coupling in imines is large and negative when the proton is *cis* to the lone pair, but small and positive for a proton *trans* to the lone pair, as in **4-24**. Thus, $^2J(\text{HCN})$ is a useful structural diagnostic for *syn-anti*



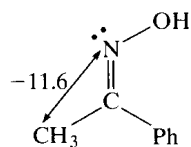
4-24



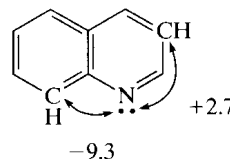
4-25

isomerism in imines, oximes, and related compounds. In saturated amines, however, values typically are small and negative (-1.0 Hz for methylamine, CH_3NH_2). The *cis* relationship between the nitrogen lone pair and hydrogen is also found in heterocycles such as pyridine (**4-25**), in which the coupling constant is -10.8 Hz.

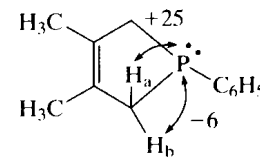
Two-bond couplings between ^{15}N and ^{13}C follow a similar pattern and also can be used for structural and stereochemical assignments. The carbon on the same side as the lone pair in imines again has a large negative coupling (-11.6 Hz in **4-26**). The isomer shown in **4-26**, in which the methyl is *syn* to hydroxyl (*anti* to the lone pair), has a $^2J(\text{CCN})$ of only 1.0 Hz.



4-26



4-27



4-28

The two indicated carbons in quinoline (**4-27**) have couplings of -9.3 and $+2.7$ Hz, respectively, as one is syn and the other anti to the nitrogen lone pair.

Couplings between ^{31}P and hydrogen also have been exploited stereochemically. The maximum positive value of $^2J(\text{HCP})$ is observed when the H-C bond and the phosphorus lone pair are eclipsed (syn), and the maximum negative value is seen when they are orthogonal or anti. The situation is similar to that for couplings between hydrogen and ^{15}N , but signs are reversed as a result of the opposite signs of the gyromagnetic ratios of ^{15}N and ^{31}P . The heterocycle **4-28** exhibits a coupling of $+25$ Hz between ^{31}P and H_a (syn) and of -6 Hz between ^{31}P and H_b (anti). The coupling also is structurally dependent, as it is larger for P(III) than for P(V), 27 Hz for $(\text{CH}_3)_3\text{P}$, and 13.4 Hz for $(\text{CH}_3)_3\text{P}=\text{O}$.

Geminal H-C-F couplings usually are close to $+50$ Hz for an sp^3 carbon (47.5 Hz for $\text{CH}_3\text{CH}_2\text{F}$) and $+80$ Hz for an sp^2 carbon (84.7 Hz for $\text{CH}_2=\text{CHF}$). Geminal F-C-F couplings are quite large ($+150$ – 250 Hz) for saturated carbon (240 Hz for 1,1-difluorocyclohexane), but less than 100 Hz for unsaturated carbon (35.6 Hz for $\text{CH}_2=\text{CF}_2$).

4-5 Vicinal Couplings

Coupling between protons over three bonds provided the most important early stereochemical application of NMR spectroscopy. In 1961, Karplus derived a mathematical relationship between $^3J(\text{HCCH})$ and the H-C-C-H dihedral angle ϕ . The simple formula

$$^3J = \begin{cases} A \cos^2 \phi + C & (\phi = 0^\circ\text{--}90^\circ) \\ A' \cos^2 \phi + C' & (\phi = 90^\circ\text{--}180^\circ) \end{cases} \quad (4-3)$$

illustrated in Figure 4-6, offers chemists a general and easily applied qualitative tool. The cosine-squared relationship results from strong coupling when orbitals are parallel and can overlap at the synperiplanar ($\phi = 0^\circ\text{--}30^\circ$) and antiperiplanar ($\phi = 150^\circ\text{--}180^\circ$) geometries and weak coupling when orbitals are staggered or orthogonal ($\phi = 60^\circ\text{--}120^\circ$).

The additive constants C and C' are usually neglected, as they are thought to be less than 0.3 Hz. When the constants A and A' can be evaluated, quantitation is possible. The inequality of A and A' ($A < A'$) means that J is different at the syn and anti maxima. Unfortunately, these multiplicative constants vary from system to system in the range 8–14 (larger for alkenes). Because of this variation, quantitative applications cannot be transferred easily from one structure to another.

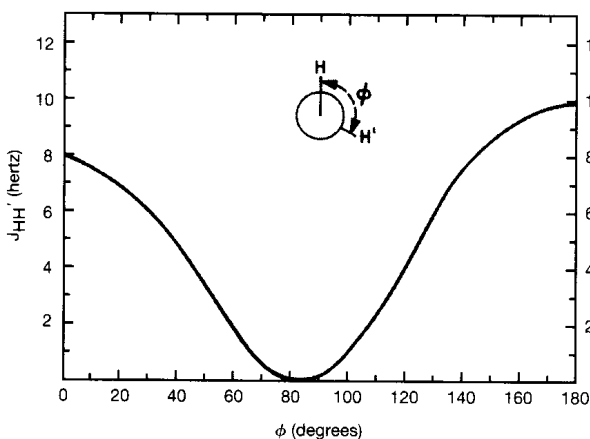


Figure 4-6 The vicinal H-C-C-H coupling constant as a function of the dihedral angle ϕ .

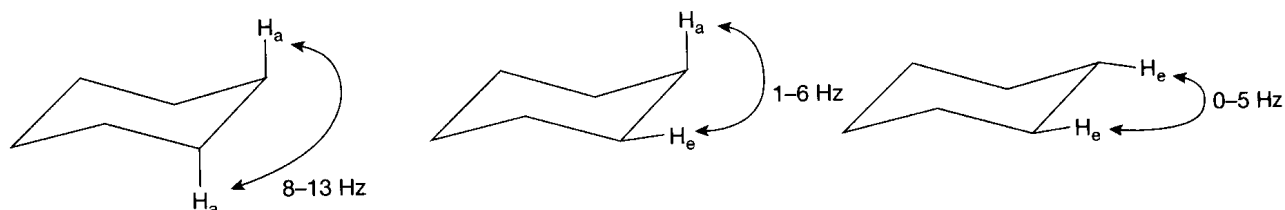
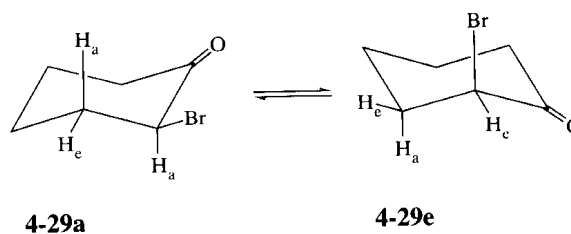


Figure 4-7 Coupling magnitudes between vicinal protons in chair six-membered rings.

The Karplus equation provides useful qualitative interpretations in a number of very fundamental systems. In chair cyclohexanes (Figure 4-7), J_{aa} is large (8–13 Hz) because ϕ_{aa} is close to 180° , whereas J_{ee} (0–5 Hz) and J_{ae} (1–6 Hz) are small because ϕ_{ee} and ϕ_{ae} are close to 60° . An axial proton that has an axial proton neighbor can easily be identified by its large J_{aa} . When cyclohexane rings are flipping between two chair forms, J_{aa} is averaged with J_{ee} to give a J_{trans} in the range 4–9 Hz, and J_{ae} is averaged with J_{ea} to give a J_{cis} in the range 1–6 Hz. In complex spin systems, axial proton resonances sometimes can be recognized by their larger line width or total spread than those of equatorial protons, because J_{aa} increases the width or spread more than does J_{ae} . By way of example, the 2 proton in 2-bromocyclohexanone (4-29) may be either axial (4-29a) or equatorial (4-29e). (The designations



a and e refer to the location of the proton geminal to bromine.) Because these two conformations are interconverting rapidly at room temperature, actual couplings of the 2 protons with the two vicinal protons at the 3 position are therefore averages, as given by the pair of equations

$$J_{cis} = aJ_{ea} + eJ_{ae} \quad (4-4a)$$

and

$$J_{trans} = aJ_{aa} + eJ_{ee}, \quad (4-4b)$$

in which a is the fraction of 4-29a and e is the fraction of 4-29e. Similar considerations apply to acyclic conformations.

In three-membered rings (4-30), J_{cis} ($\phi = 0^\circ$) is always larger than J_{trans} ($\phi = 120^\circ$), as a glance at the Karplus plot in Figure 4-6 will indicate. For the parent cyclopropane,



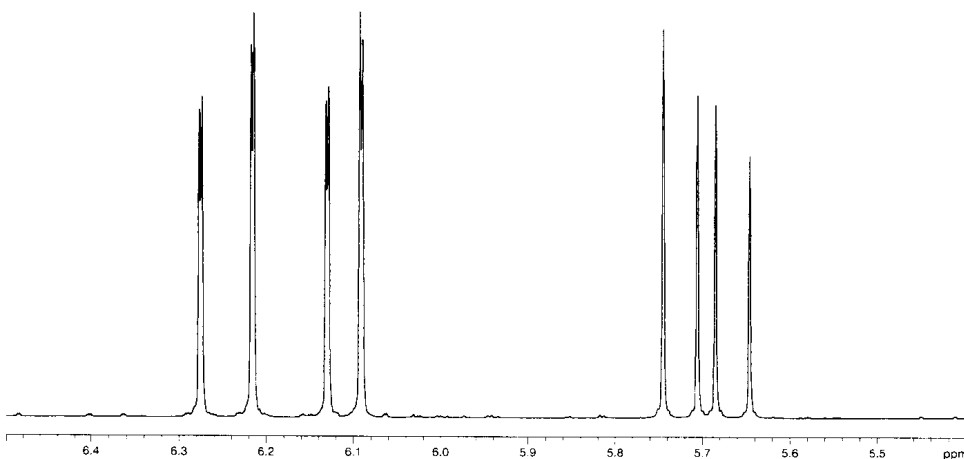


Figure 4-8 The 300 MHz ^1H spectrum of acrylonitrile ($\text{CH}_2=\text{CHCN}$) in CDCl_3 .

$J_{\text{cis}} = 8.97$ Hz and $J_{\text{trans}} = 5.58$ Hz. In four-membered rings, the cis coupling usually is larger than the trans coupling, but the two quantities can be close enough to be ambiguous. In five-membered rings, either J_{cis} or J_{trans} can be the larger, because the dihedral angles are toward the center of the Karplus curve.

In alkenes, $J_{\text{trans}} (\phi = 180^\circ)$ is always larger than $J_{\text{cis}} (\phi = 0^\circ)$ —for example, 18.2 and 11.3 Hz, respectively, in acrylonitrile (**4-31**). The spectrum of this compound is illustrated in Figure 4-8. The vinyl resonance is composed of three groupings, which constitute an AMX, ABX, or ABC spectrum, depending on the field strength. The three couplings (J_{AM} , J_{AX} , and J_{MX}) may be assigned by inspection with the knowledge that $^3J_{\text{trans}} > ^3J_{\text{cis}} > ^2J_{\text{gem}}$. The reader should carry out the measurements for **4-31** from Figure 4-8. The 12 peaks are located at δ 5.647, 5.684, 5.708, 5.744, 6.090, 6.093, 6.128, 6.132, 6.211, 6.215, 6.273, and 6.278. Finally, ortho protons in aromatic rings have a dihedral angle of 0° , so $^3J_{\text{ortho}}$ is generally quite large (6–9 Hz) and can be distinguished from the smaller J_{meta} and J_{para} .

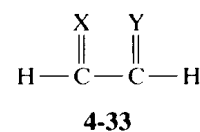
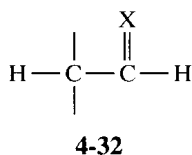
Despite the potentially general application of the Karplus equation to dihedral angle problems, there are quantitative limitations. The vicinal H–C–C–H coupling constant depends on the C–C bond length or bond order, the H–C–C valence angle, the electronegativity of substituents, and the orientation of substituents, in addition to the H–C–C–H dihedral angles. All of these other factors contribute to the multiplicative A and A' factors. A properly controlled calibration series of molecules must be rigid (monoconformational) and have unvarying bond lengths and valence angles. Several approaches have been developed to take the only remaining factor, the substituent electronegativity, into account. One approach is to derive the mathematical dependence of 3J on electronegativity. Another is empirical allowance by the use of chemical shifts that depend on electronegativity in a similar fashion as 3J . A third approach is to eliminate the problem through the use of the ratio (the R value) of two 3J coupling constants that respond to the same or related dihedral angles and that have the same multiplicative dependence on substituent electronegativity that divides out in R . These more sophisticated versions of the Karplus method have been used quite successfully to obtain reliable quantitative results.

The existence of factors other than the dihedral angle results in ranges of vicinal coupling constants at constant ϕ , even in structurally analogous systems. Saturated hydrocarbon chains (H–C–C–H) exhibit vicinal couplings in the range 3–9 Hz, depending on substituent electronegativity and rotamer mixes ($J = 3.06$ Hz for $\text{Cl}_2\text{CHCHCl}_2$ and 8.90 for $\text{CH}_3\text{CH}_2\text{Li}$). Higher substituent electronegativity always lowers the vicinal coupling constant. In small rings, the variation is almost entirely the result of substituent electronegativity, with cis ranges of 7–13 Hz and trans ranges of 4–10 Hz in cyclopropanes. Coupling constants in oxiranes (epoxides) are smaller, because of the effect of the electronegative oxygen atom. Couplings across a double bond (e.g., H–C=C–H) depend strongly on the

valence angles, as well as on the electronegativity of the other two substituents. In cycloalkenes, the value varies from 1.3 Hz in cyclopropene to 8.8 Hz in cyclohexene. In acyclic alkenes, J_{trans} has a range of 10–24 Hz, J_{cis} of 2–19 Hz. Because the ranges overlap between 10 and 19 Hz, the distinction between cis and trans isomers is fully reliable only when both isomers are in hand. When bonds are intermediate between single and double bonds, 3J is proportional to the overall bond order, as in ${}^3J_{12} = 8.6$ Hz and ${}^3J_{23} = 6.0$ Hz in naphthalene.

The ortho coupling in benzene derivatives varies over the relatively small range of 6.7–8.5 Hz, depending on the resonance and inductive effects of the substituents. The presence of heteroatoms in the ring expands the range at the lower end down to 2 Hz, because of the effects of electronegativity (pyridines) and of smaller rings (furans and pyrroles).

When one carbon is sp^3 and one is sp^2 (4-32) the range is 5–8 Hz for freely rotating acyclic hydrocarbons ($X = CR_2$) and 1–5 Hz for aldehydes ($X = O$). The value varies in hydrocarbon rings from 20.8 Hz in cyclobutene to 13.1 Hz in cyclohexene and 15.7 Hz in cycloheptene. For the central bond in dienes (4-33), the range is 10–12 Hz for transoid



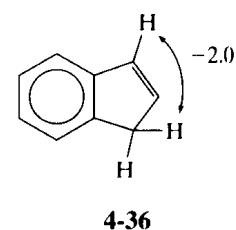
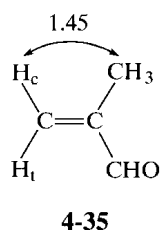
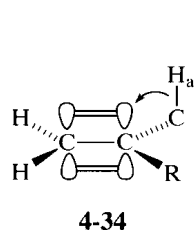
systems ($X, Y = CR_2$). When constrained to rings, the pathway is cisoid and the coupling is 1.9 Hz in cyclopentadiene and 5.1 Hz in 1,3-cyclohexadiene. In α, β -unsaturated aldehydes (4-33, $X = O, Y = CR_2$), the coupling is about 8 Hz if transoid and 3 Hz if cisoid.

The $H-C-X-H$ ($X = O, N, S, Si, \text{etc.}$), $H-C-C-C$, $H-C-C-F$, $H-C-N-F$, $H-C-X-P$ ($X = C, O, S$), and $C-C-C-C$ couplings also follow Karplus-like relationships. The ${}^3J(H-C-O-P)$ couplings are useful in determining backbone conformations of nucleotides. The ${}^3J(C-C-C-C)$ couplings have a range of values (3–15 Hz) that is larger than that in the two-bond case. (The range for ${}^2J(C-C-C)$ is 1–10 Hz.) The $F-C-C-F$ and $H-C-C-P$ couplings do not appear to follow the Karplus pattern.

4-6 Long-Range Couplings

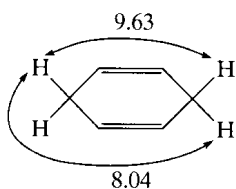
Coupling between protons over more than three bonds is said to be long range. Sometimes, coupling between ${}^{13}C$ and protons over more than one bond also is called long range, but the term is inappropriate for ${}^2J(CCH)$ and ${}^3J(CCCH)$. Long-range coupling constants between protons normally are less than 1 Hz and frequently are so small as to be unobservable. In at least two structural circumstances, however, such couplings commonly become significant.

Interactions of $C-H$ bonds with π electrons of double and triple bonds and aromatic rings along the coupling pathway often increase the magnitude of the coupling constant. One such case is the four-bond allylic coupling $HC-C=CH$, with a range of about +1 to -3 Hz and typical values close to -1 Hz. Larger values are observed when the saturated $C-H_a$ bond is parallel to the π orbitals (4-34).

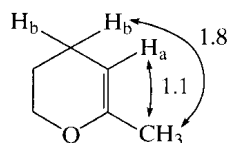


This σ - π overlap enables coupling to be transmitted more effectively. When the C-H_a bond is orthogonal to the π orbitals, there is no σ - π contribution and couplings are small (<1 Hz). In acyclic systems, the dihedral angle is averaged over both favorable and unfavorable arrangements, so an average 4J is found, as in 2-methylacryloin (**4-35**, ${}^4J = 1.45$ Hz). Ring constraints can freeze bonds into the favorable arrangement, as in indene (**4-36**, ${}^4J = -2.0$ Hz).

The five-bond doubly allylic coupling (also called homoallylic) HC-C=C-CH depends on the orientation of two C-H bonds with respect to the π orbitals. For acyclic systems such as the 2-butenes, 5J typically is 2 Hz, with a range of 0-3 Hz. When both protons are well aligned, the coupling can be quite large, as in the planar 1,4-cyclohexadiene (**4-37**), for which the cis coupling is 9.63 Hz and the trans coupling is 8.04 Hz. These couplings



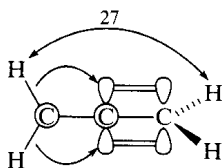
4-37



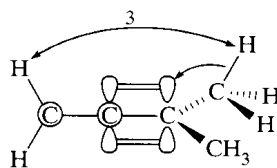
4-38

were measured by suitable deuterium labeling. It is not unusual for the doubly allylic coupling to be larger than the allylic, as in **4-38** (${}^4J(\text{CH}_3\text{-H}_a) = 1.1$ Hz, ${}^5J = 1.8$ Hz).

Coupling constants are particularly large in alkyne and allenic systems. In allene itself ($\text{CH}_2=\text{C}=\text{CH}_2$, **4-39**), 4J is 27 Hz. In 1,1-dimethylallene (**4-40**), 5J decreases to 3 Hz.



4-39

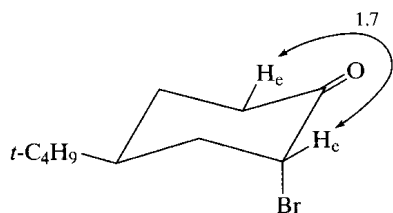


4-40

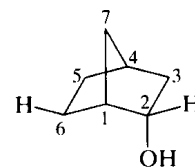
The allene stereochemistry is locked into a favorable stereochemistry for σ - π overlap, as is illustrated by the pair of arrows into the π orbitals of **4-39**. In both propyne (methylacetylene, ${}^4J = 2.9$ Hz) and 2-butyne (dimethylacetylene, ${}^5J = 2.7$ Hz), the long-range coupling is enhanced because the triple bond imposes no steric limitations on σ - π overlap. Appreciable long-range couplings have been observed over up to seven bonds in polyalkynes.

Conjugated double bonds provide a more complicated situation. In 1,3-butadiene, there are two four-bond (-0.86 and -0.83 Hz) and three five-bond ($+0.60$, $+1.30$, and $+0.69$ Hz) couplings. In aromatic rings, the meta coupling is a 4J (range 1-3 Hz) and the para coupling is a 5J (range 0-1 Hz). In benzene itself, ${}^3J_{\text{ortho}}$ is 7.54 Hz, ${}^4J_{\text{meta}}$ is 1.37 Hz, and ${}^5J_{\text{para}}$ is 0.69 Hz. None of these couplings in butadiene and benzene involves σ - π overlap. Protons on saturated carbon atoms attached to an aromatic ring ($\text{CH}_3\text{-C}_6\text{H}_5$) couple with all three types of protons on the ring. These benzylic couplings depend on the σ - π interaction between the substituent C-H bonds and the aromatic π electrons, much as the allylic coupling (${}^4J_{\text{ortho}} = 0.6\text{-}0.9$ Hz, ${}^5J_{\text{meta}} = 0.3\text{-}0.4$ Hz, ${}^6J_{\text{para}} = 0.5\text{-}0.6$ Hz) does. A doubly benzylic coupling can take place between protons on different saturated carbons that are directly attached to the benzene ring, as in the xylenes ($\text{CH}_3\text{-C}_6\text{H}_4\text{-CH}_3$, ${}^5J_{\text{ortho}} = 0.3\text{-}0.5$ Hz).

In the second major category of long-range coupling, enhanced values often are observed between protons that are related by a planar W or zigzag pathway. This geometry is seen, for example, in the 1,3-diequatorial arrangement between protons in six-membered rings (**4-41**, ${}^4J = 1.7$ Hz). The norbornane framework (**4-42**) contains several W arrangements,



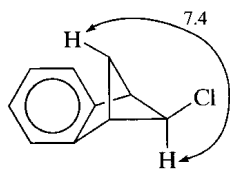
4-41



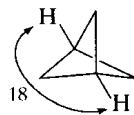
4-42

including that illustrated between the 2 and 6 exo protons, but also between the bridgehead protons (1 and 4) and between 3-endo and 7-anti protons.

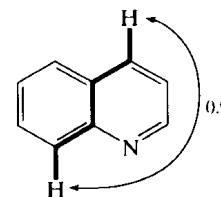
In the planar, zigzag arrangement, there is favorable overlap between parallel C–H and C–C bonds, analogous to the optimal vicinal coupling at $\phi = 180^\circ$. The large magnitude also has been explained in terms of a direct passing of spin information by interaction of the rear lobes of the C–H orbitals in the HC–C–CH pathway. When the first and third carbons are particularly close because of ring strain or when there are multiple zigzag pathways, the coupling can be quite large, as in **4-43** (${}^4J = 7.4$ Hz) and **4-44** (${}^4J = 18$ Hz). The zigzag pathways are entirely within the σ framework, but are important for many π systems,



4-43



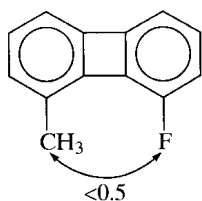
4-44



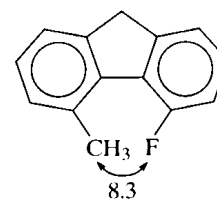
4-45

including aromatic meta couplings (hence the enhanced ${}^4J = 1.37$ Hz in benzene). Five-bond zigzag pathways similarly can give rise to enhanced long-range couplings, such as the ${}^5J = 1.3$ Hz in 1,3-butadiene ($\text{H}-\text{C}=\text{C}-\text{C}=\text{C}-\text{H}$) and the ${}^5J = 0.9$ Hz coupling between the indicated protons in quinoline (**4-45**). Zigzag pathways up to six bonds have been found to exhibit couplings.

Although coupling information is always passed via electron-mediated pathways, in some cases part of the through bond pathway may be skipped, as in allylic (**4-34**) and benzylic couplings with $\sigma-\pi$ overlap. Two nuclei that are within van der Waals contact in space over any number of bonds can interchange spin information if at least one of the nuclei possesses lone-pair electrons. These so-called through space couplings are found most commonly, but not exclusively, in H–F and F–F pairs. The six-bond CH_3-F coupling is negligible in **4-46** (H–F distance 2.84 Å), but is 8.3 Hz in **4-47** (1.44 Å). (The sum of the H



4-46



4-47

and F van der Waals radii is 2.55 Å.) In the latter case, coupling information is probably passed from the proton, through the lone-pair electrons, to the fluorine nucleus. Such a mechanism very likely is important in the geminal F–C–F coupling, which is unusually large. Values of ${}^2J(\text{FCF})$ are larger for sp^3CF_2 than for sp^2CF_2 , as the smaller tetrahedral angle brings the fluorine atoms closer together.

4-7 Spectral Analysis

We have not said much about how coupling constants are extracted from spectra. Measurement is straightforward when the spectrum is first order, as chemical shifts correspond to the midpoint of a resonance multiplet. The midpoint falls between the components of a doublet from coupling to one other spin, is coincident with the middle peak of a triplet from coupling to two other spins, and so on. The coupling constant corresponds to the distance between adjacent peaks in the resonance multiplet. These simple characteristics may fail in second-order spectra. Because most nuclei other than the proton have very large chemical-shift ranges and because the natural abundance of these nuclei often is low and hence the nuclei do not exhibit coupling with each other, second-order analysis is primarily a consideration for proton spectra alone. For protons, spectra measured above 500 MHz are usually first order, from the $\Delta\nu/J$ criterion. Magnetic nonequivalence (Section 4-2), however, is independent of the field and produces second-order spectra such as $\text{AA}'\text{XX}'$, even with the most expensive superconducting magnet.

The AX spectrum consists of two doublets, with all four components having equal intensities. (The spectra in Figure 1-18 and at the bottom of Figure 4-1 are very close to first order.) The doublet spacing is J_{AX} , and the midpoints of the doublets are ν_{A} and ν_{X} . The second-order, two-spin (AB) system also contains four lines, but the inner peaks are always more intense than the outer peaks. (See Figures 4-1 and 4-9.) The coupling constant (J_{AB}) still is obtained directly from the spacings between the doublets, but no specific peak position or simple average corresponds to the chemical shifts. The A chemical shift (ν_{A}) occurs at the weighted-average position of the two A peaks (and similarly for ν_{B}). The difference in chemical shift, $\Delta\nu_{\text{AB}} = (\nu_{\text{B}} - \nu_{\text{A}})$, is calculated easily from the formula

$$\Delta\nu_{\text{AB}} = (4C^2 - J^2)^{1/2}, \quad (4-5)$$

in which $2C$ is the spacing between alternate peaks. (See Figure 4-9.) The values of ν_{A} and ν_{B} are then readily found by adding and subtracting $\frac{1}{2}\Delta\nu_{\text{AB}}$ to the midpoint of the quartet. The ratio of intensities of the larger inner peaks to the smaller outer peaks is given by the expression $(1 + J/2C)/(1 - J/2C)$. (All of these relationships are developed in Appendix 3, which describes the quantum mechanical formulation of the two-spin system.)

Three-spin systems can be readily analyzed by inspection only in the first-order cases AX_2 and AMX . The second-order AB_2 spectrum can contain up to nine peaks—four from spin flips of the A proton alone, four from spin flips of the B protons alone, and one from simultaneous spin flips of both the A and the B protons. The ninth peak is called a *combination line* and is ordinarily forbidden and of low intensity. Although these patterns may be analyzed by inspection, recourse normally is made to computer programs. The other

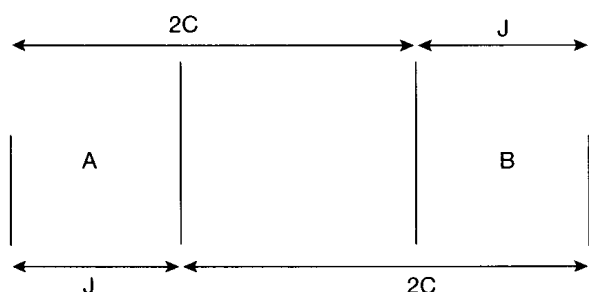


Figure 4-9 Notation for spacings in a second-order, two-spin system (AB).

second-order three-spin systems (AXX' , ABB' , ABX , and ABC) and almost all second-order systems of four spins ($AA'XX'$, $AA'BB'$, $ABXY$, etc.) or larger are seldom able to be analyzed by inspection, and computer methods frequently are employed. (Appendix 4 describes methods for analyzing some three- and four-spin systems.)

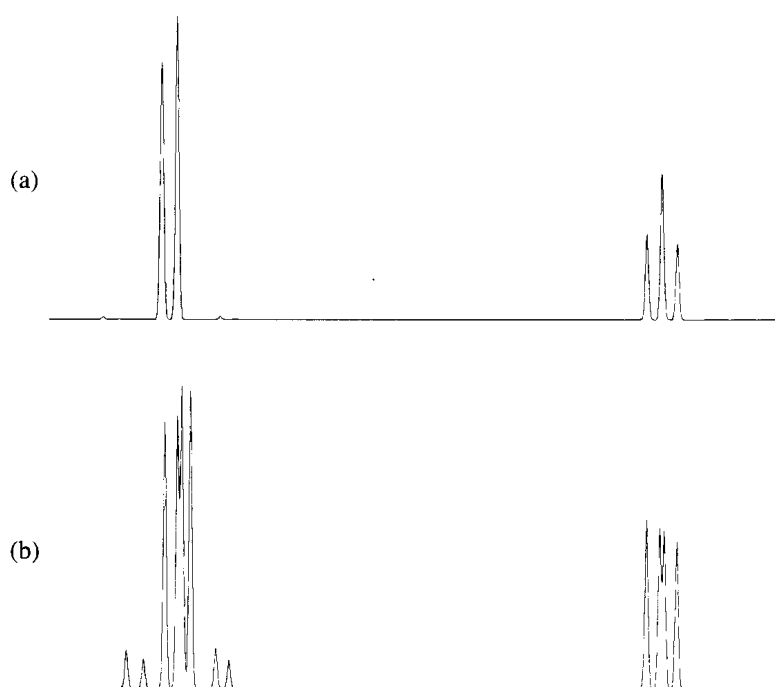
Most spectrometers today contain software that can calculate spectra for up to seven spins. The first step is a trial-and-error procedure of approximating the chemical shifts and coupling constants in order to match the observed spectrum through computer simulation. Chemical shifts are varied until the widths and locations of the observed and calculated multiplets approximately agree. Then the coupling constants or their sums and differences are varied systematically until a reasonable match is obtained. This method is relatively successful for three and four spins, but is difficult to employ with larger systems.

Refinements of direct calculations or of the preceding trial-and-error procedure utilize iterative computer programs. The program of Castellano and Bothner-By (LAOCN3) iterates on peak positions, but requires assignments of peaks to specific spin flips. The program of Stephenson and Binsch (DAVINS) operates directly on unassigned peak positions.

Second-order spectra are characterized by peak spacings that do not correspond to coupling constants, by nonbinomial intensities, by chemical shifts that are not at the midpoints of resonance multiplets, and by multiplicities that do not follow the $n + 1$ rules. (See Figures 4-1, 4-2, and 4-3.) Even when the spectrum has the appearance of being first order, it may not be. Lines can coincide in such a way that the spectrum assumes a simpler appearance than seems consistent with the actual spectral parameters (a situation called *deceptive simplicity*). For example, in the ABX spectrum, the X nucleus is coupled to two nuclei (A and B) that are themselves closely coupled. When $\Delta\nu_{AB}/J$ is extremely small, the A and B spin states are fully mixed, and X responds as if the nuclei were equivalent. The ABX spectrum then has the appearance of an A_2X spectrum, as if $J_{AX} = J_{BX}$. Figure 4-10 illustrates this situation. When $\Delta\nu_{AB} = 3.0$ Hz (Figure 4-10a), the calculated example looks like a first-order A_2X spectrum with one coupling constant. When $\Delta\nu_{AB} = 8.0$ Hz (Figure 4-10b), a typical ABX spectrum is obtained. Deceptive simplicity sometimes, but not always, can be removed by the use of a higher field. When the spectrum is deceptively simple, only sums or averages of coupling constants may be measured.

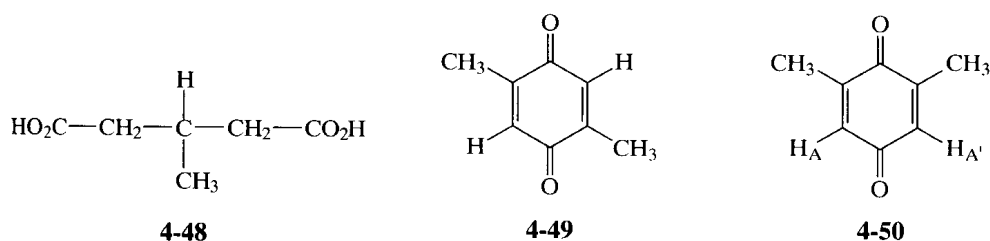
The $AA'XX'$ spectrum often is observed as a deceptively simple pair of triplets, resembling A_2X_2 . In this case, it is the A and A' nuclei that are closely coupled ($\Delta\nu_{AA'} = 0$ Hz

Figure 4-10 (a) A deceptively simple ABX spectrum: $\nu_A = 0.0$ Hz, $\nu_B = 3.0$ Hz, $\nu_X = 130.0$ Hz, $J_{AB} = 15.0$ Hz, $J_{AX} = 5.0$ Hz, and $J_{BX} = 3.0$ Hz. (b) The same parameters, except that $\nu_B = 8.0$ Hz. The larger value of $\Delta\nu_{AB}$ removes the deceptive simplicity and produces a typical ABX spectrum.



and $J_{AA'}$ is large). Such deceptive simplicity is not eliminated by raising the field, because A and A' are chemically equivalent. The chemist should beware of the pair of triplets that falsely suggests magnetic equivalence (A_2X_2) and equal couplings ($J_{AX} = J_{AX'}$) when the molecular structure suggests $AA'XX'$ instead. Sometimes the couplings between A and X may be observed by lowering the field to turn the $AA'XX'$ spectrum into $AA'BB'$, with a larger number of peaks that may permit a complete analysis.

A particularly subtle example of second-order complexity occurs in the ABX spectrum when A and B are very closely coupled, J_{AX} is large, and J_{BX} is zero. With no coupling to B, the X spectrum should be a simple doublet from coupling to A. Since A and B are closely coupled, however, the spin states of A and B are mixed, and the X spectrum is perturbed by the B spins. (The phenomenon has been termed *virtual coupling*, which is something of a misnomer, since, as stated, B is not coupled to X.) As an example in a slightly larger, but analogous, spin system, the CH and CH_2 protons of β -methylglutaric acid (4-48) are closely coupled. Although the CH_3 group is coupled only to the CH proton, its resonance is much



more complicated than that of a simple doublet (Figure 4-11). The CH and CH_2 protons are closely coupled, so their spin states are mixed. The CH_3 group thus interacts with a mixture of CH and CH_2 spin states, even though $J = 0$ between CH_3 and CH_2 . This problem is eliminated by a higher field, at which the CH and CH_2 resonances are well separated. Methyl, unmixed with the CH_2 spin states, then couples cleanly with CH.

The dimethylbenzoquinones provide a further example. The proton spectrum of the 2,5-dimethyl isomer (4-49) contains a first-order methyl doublet and an alkene quartet. The spectrum of the 2,6 isomer (4-50) is much more complicated. These spectra may be found

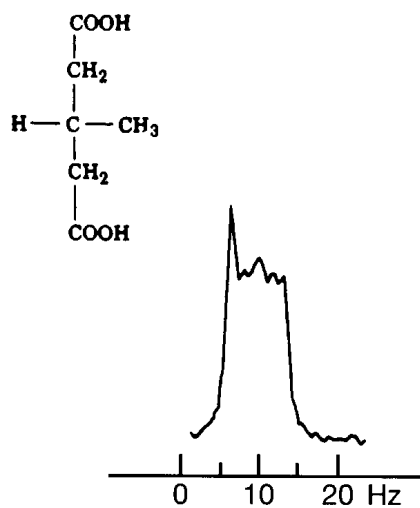


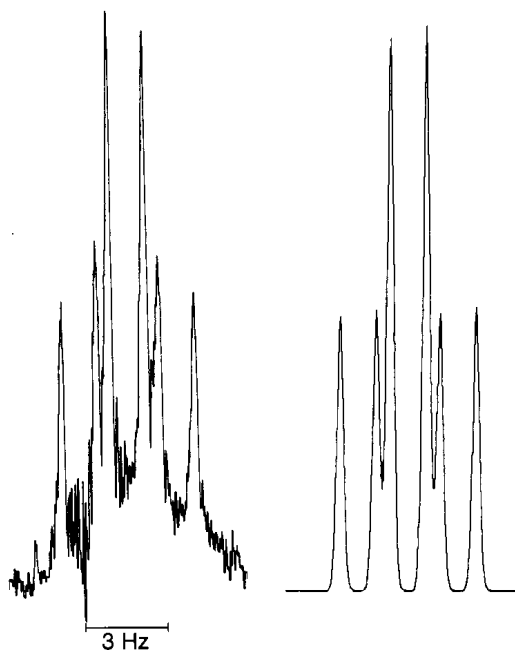
Figure 4-11 The 60 MHz methyl ^1H resonance of β -methylglutaric acid. (Reproduced with permission from F. A. L. Anet, *Can. J. Chem.*, **39**, 2267 [1961]).

on p. 166 of E.D. Becker, *High Resolution NMR*, 2d ed. (Orlando, FL: Academic Press, 1980). The alkenic protons in both molecules are equivalent (AA'). In **4-49** they are coupled only to the methyl protons ($J_{AA'} = 0$ Hz), but in **4-50** they are closely coupled to each other because of the zigzag pathway. The multiplicity of the methyl resonance is perturbed not only by the adjacent alkenic proton, but also by the one on the opposite side of the ring. In other words, **4-49** is $(AX_3)_2$, but **4-50** is $AA'X_3X'_3$. This effect is not altered at a higher field, because A and A' are chemically equivalent.

Some institutions still have available only iron-core 60 MHz spectrometers, which produce largely second-order proton spectra. These spectra may be clarified somewhat by the use of *paramagnetic shift reagents*, molecules that contain unpaired electron spins and that form Lewis acid–base complexes with dissolved substrates. The unpaired spin exerts a strong paramagnetic shielding effect (hence, to a higher frequency, or downfield) on nuclei close to it. The effect drops off rapidly with distance, so that those nuclei in the substrate with the fewest bonds to the site of acid–base binding are affected more. Consequently, the shift to a higher frequency varies through the substrate and leads to greater separation of peaks. Two common shift reagents—tris(dipivalomethanato)europium(III)·2(pyridine) (called $\text{Eu}(\text{dpm})_3$ without pyridine) and 1,1,1,2,2,3,3-heptafluoro-7,7-dimethyloctanedionateeuropium(III) (or $\text{Eu}(\text{fod})_3$)—contain lanthanides. Shift reagents are available with numerous rare earths, as well as with other elements. Almost all organic functional groups that are Lewis bases have been found to respond to these reagents. When the shift reagent is chiral, it can complex with the enantiomers and generate separate resonances from which enantiomeric ratios may be obtained.

Spectral analysis can sometimes be facilitated by taking advantage of dilute spins present in the molecule. Earlier in this chapter, cyclopropene (**4-5**) was mentioned as an example of an A_2X_2 spectrum, and in Section 4-5 the vicinal coupling between the protons on the double bond (J_{AA}) was quoted as being 1.3 Hz. How was such a coupling constant between two chemically equivalent protons measured? Its small value prohibits the use of deuterium, as J_{HD} would be only 0.2 Hz. For 1.1% of the molecules, the double-bond spin system is $\text{H}-^{12}\text{C}-^{13}\text{C}-\text{H}$. The proton on ^{12}C in such molecules resonates at almost the same position as in the molecules with no ^{13}C . The large one-bond $^{13}\text{C}-^1\text{H}$ coupling produces multiplets, called *satellites*, on either side of the center band and separated from it by about $\frac{1}{2}J(\text{CH})$. Small isotope effects can shift the center of the satellites. The separation of each satellite from the center band serves as an effective chemical-shift difference, so the H–H coupling between $\text{H}-^{12}\text{C}$ and $\text{H}-^{13}\text{C}$ is present in the satellite. Figure 4-12 shows the satellite

Figure 4-12 The 90 MHz ^1H spectrum of cyclopropene, showing the observed (left) and calculated (right) high-frequency ^{13}C satellite of the alkenic protons. (Reproduced with permission from J. B. Lambert, A. P. Jovanovich, and W. L. Oliver, Jr., *J. Phys. Chem.* **74**, 2221 (1970). Copyright 1970 American Chemical Society).



spectrum of the alkenic protons of cyclopropene. The satellite is a doublet of triplets, since the alkenic proton on ^{13}C is coupled to the other alkenic proton and to the two methylene protons. Other dilute spins produce satellite spectra that are commonly observed in proton spectra, including ^{15}N , ^{29}Si , ^{77}Se , ^{111}Cd , ^{113}Cd , ^{117}Sn , ^{119}Sn , ^{125}Te , ^{195}Pt , and ^{199}Hg .

The most general and effective method for analyzing complex proton spectra involves the use of two dimensions, as is described in Chapter 6. Even this method, however, has limitations imposed on it by the presence of second-order relationships.

4-8 Tables of Coupling Constants

Tables 4-1 through 4-5 summarize values of coupling constants by class of structure, extracted from the references found at the end of the chapter. Further examples may be obtained by examining these references.

Table 4-1 One-Bond Couplings (Hz)

$^{13}\text{C}-^1\text{H}$	CH_3CH_3	125	$^{13}\text{C}-^{19}\text{F}$	CH_2F_2	235	
	$(\text{CH}_3)_4\text{Si}$	118		CF_3I	345	
	CH_3Li	98		C_6F_6	362	
	$(\text{CH}_3)_3\text{N}$	132		$^{13}\text{C}-^{31}\text{P}$	CH_3PH_2	9.3
	CH_3CN	136			$(\text{CH}_3)_3\text{P}$	-13.6
	$(\text{CH}_3)_2\text{S}$	138			$(\text{CH}_3)_4\text{P}^+ \text{I}^-$	56
	CH_3OH	142	$^{13}\text{C}-^{15}\text{N}$	CH_3NH_2	-4.5	
	CH_3F	149		$\text{C}_6\text{H}_5\text{NH}_2$	-11.4	
	CH_3Cl	150		$\text{CH}_3(\text{CO})\text{NH}_2$	-14.8	
	CH_2Cl_2	177		$\text{CH}_3\text{C}\equiv\text{N}$	-17.5	
	CHCl_3	208		Pyridine	+0.62	
	Cyclohexane	125		$\text{CH}_3\text{HC}=\text{N}-\text{OH} (E, Z)$	-4.0, -2.3	
	Cyclobutane	136		$^{15}\text{N}-^1\text{H}$	CH_3NH_2	-64.5
	Cyclopropane	162	$\text{CH}_3(\text{CO})\text{NH}_2$		-89	
	Tetrahydrofuran (α, β)	145, 133	Pyridinium		-90.5	
	Norbornane (C1)	142	$\text{HC}\equiv\text{N}^+\text{H}$		-134	
	Bicyclo[1.1.1]pentane (C1)	164	$(\text{C}_6\text{H}_5)_2\text{C}=\text{NH}$		-51.2	
	Cyclohexene (C1)	157	$^{15}\text{N}-^{15}\text{N}$	Azoxybenzene	12.5	
	Cyclopropene (C1)	226		Phenylhydrazine	6.7	
	Benzene	159	$^{15}\text{N}-^{31}\text{P}$	$\text{C}_6\text{H}_5\text{NHP}(\text{CH}_3)_2$	53.0	
	1,3-Cyclopentadiene (C2)	170		$\text{C}_6\text{H}_5\text{NH}(\text{PO})(\text{CH}_3)_2$	-0.5	
	$\text{CH}_2=\text{CHBr} (\text{gem})$	197		$[(\text{CH}_3)_2\text{N}]_3\text{P}=\text{O}$	-26.9	
	Acetaldehyde (CHO)	172	$^{13}\text{C}-^{13}\text{C}$	CH_3CH_3	35	
	Pyridine (α, β, γ)	177, 157, 160		$\text{CH}_3(\text{CO})\text{CH}_3$	40	
	Allene	168		$\text{CH}_3\text{CO}_2\text{H}$	57	
	Propyne ($\equiv\text{CH}$)	248		$\text{CH}_2=\text{CH}_2$	68	
$(\text{CH}_3)_2\text{C}^+\text{H} (^+\text{CH})$	164	$\text{CH}\equiv\text{CH}$		171		
$\text{HC}\equiv\text{N}$	269	$^{31}\text{P}-^1\text{H}$		$\text{C}_6\text{H}_5(\text{C}_6\text{H}_5\text{CH}_2)(\text{PO})\text{H}$	474	
Formaldehyde	222		$^{31}\text{P}-^{31}\text{P}$	$(\text{CH}_3)_2\text{P}-\text{P}(\text{CH}_3)_2$	-179.7	
Formamide	191			$(\text{CH}_3)_2(\text{PS})(\text{PS})(\text{CH}_3)_2$	18.7	

Table 4-2 Geminal Proton-Proton (H—C—H) Couplings (Hz)

CH ₄	-12.4	Oxirane	+5.5
(CH ₃) ₄ Si	-14.1	CH ₂ =CH ₂	+2.3
C ₆ H ₅ CH ₃	-14.4	CH ₂ =O	+40.2
CH ₃ (CO)CH ₃	-14.9	CH ₂ =NOH	9.9
CH ₃ CN	-16.9	CH ₂ =CHF	-3.2
CH ₂ (CN) ₂	-20.4	CH ₂ =CHNO ₂	-2.0
CH ₃ OH	-10.8	CH ₂ =CHOCH ₃	-2.0
CH ₃ Cl	-10.8	CH ₂ =CHBr	-1.8
CH ₃ Br	-10.2	CH ₂ =CHCl	-1.4
CH ₃ F	-9.6	CH ₂ =CHCH ₃	2.1
CH ₃ I	-9.2	CH ₂ =CHCO ₂ H	1.7
CH ₂ Cl ₂	-7.5	CH ₂ =CHC ₆ H ₅	1.1
Cyclohexane	-12.6	CH ₂ =CHCN	0.9
Cyclopropane	-4.3	CH ₂ =CHLi	7.1
Aziridine	+1.5	CH ₂ =C=C(CH ₃) ₂	-9.0

Table 4-3 Vicinal Proton-Proton (H—C—C—H) Couplings (Hz)

CH ₃ CH ₃	8.0	CH ₂ =CH ₂ (cis, trans)	11.5, 19.0
CH ₃ CH ₂ C ₆ H ₅	7.62	CH ₂ =CHLi (cis, trans)	19.3, 23.9
CH ₃ CH ₂ CN	7.60	CH ₂ =CHCN (cis, trans)	11.75, 17.92
CH ₃ CH ₂ Cl	7.23	CH ₂ =CHC ₆ H ₅ (cis, trans)	11.48, 18.59
(CH ₃ CH ₂) ₃ N	7.13	CH ₂ =CHCO ₂ H (cis, trans)	10.2, 17.2
CH ₃ CH ₂ OAc	7.12	CH ₂ =CHCH ₃ (cis, trans)	10.02, 16.81
(CH ₃ CH ₂) ₂ O	6.97	CH ₂ =CHCl (cis, trans)	7.4, 14.8
CH ₃ CH ₂ Li	8.90	CH ₂ =CHOCH ₃ (cis, trans)	7.0, 14.1
(CH ₃) ₂ CHCl	6.4	ClHC=CHCl (cis, trans)	5.2, 12.2
ClCH ₂ CH ₂ Cl (neat)	5.9	Cyclopropene (1-2)	1.3
Cl ₂ CHCHCl ₂ (neat)	3.06	Cyclobutene (1-2)	2.85
Cyclopropane (cis, trans)	8.97, 5.58	Cyclopentene (1-2)	5.3
Oxirane (cis, trans)	4.45, 3.10	Cyclohexene (1-2)	8.8
Aziridine (cis, trans)	6.0, 3.1	Benzene	7.54
Cyclobutane (cis, trans)	10.4, 4.9	C ₆ H ₅ Li (2-3)	6.73
Cyclopentane (cis, trans)	7.9, 6.3	C ₆ H ₅ CH ₃ (2-3)	7.64
Tetrahydrofuran (α-β: cis, trans)	7.94, 6.14	C ₆ H ₅ CO ₂ CH ₃ (2-3)	7.86
Cyclopentene (3-4: cis, trans)	9.36, 5.72	C ₆ H ₅ Cl (2-3)	8.05
Cyclohexane (av.: cis, trans)	3.73, 8.07	C ₆ H ₅ OCH ₃ (2-3)	8.30
Cyclohexane (ax-ax)	12.5	C ₆ H ₅ NO ₂ (2-3)	8.36
Cyclohexane (eq-eq and ax-eq)	3.7	C ₆ H ₅ N(CH ₃) ₂ (2-3)	8.40
Piperidine (av. α-β: cis, trans)	3.77, 7.88	Naphthalene (1-2, 2-3)	8.28, 6.85
Oxane (av. α-β: cis, trans)	3.87, 7.41	Furan (2-3, 3-4)	1.75, 3.3
Cyclohexanone (av. α-β: cis, trans)	5.01, 8.61	Pyrrole (2-3, 3-4)	2.6, 3.4
Cyclohexene (3-4: (cis, trans)	2.95, 8.94	Pyridine (2-3, 3-4)	4.88, 7.67

Table 4-4 Carbon Couplings Other Than $^1J(^{13}\text{C}-^1\text{H})$ (Hz)

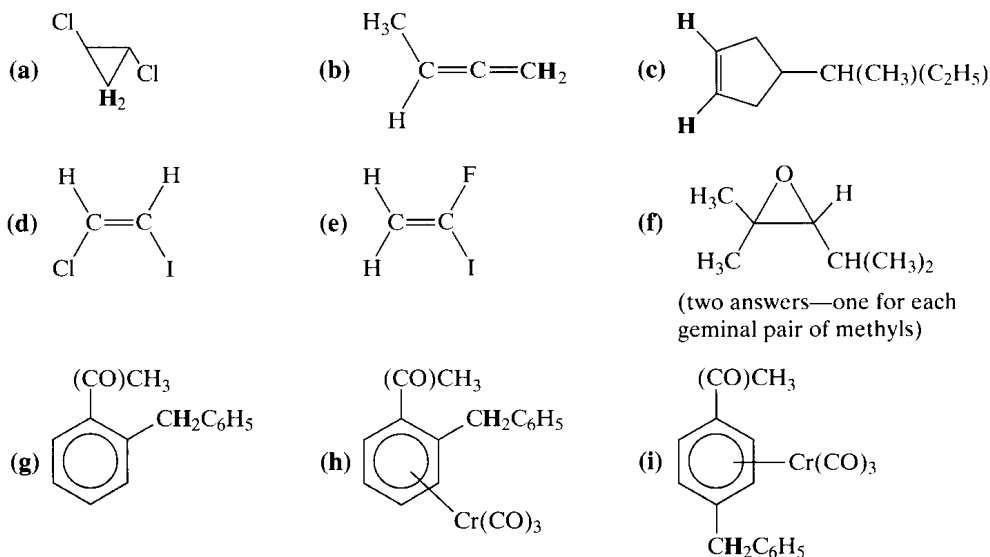
CH_3CH_3	-4.8	CH_3CH_3	34.6
$\text{CH}_3\text{CH}_2\text{Cl}$	2.6	$\text{CH}_3\text{CH}_2\text{OH}$	37.7
$\text{Cl}_2\text{CH}-\text{CHCl}_2$	+1.2	CH_3CHO	39.4
Cyclopropane [$^2J(\text{CH})$]	-2.6	$\text{CH}_3\text{C}\equiv\text{N}$	56.5
$(\text{CH}_3)_2\text{CHCH}_2\text{CH}(\text{CH}_3)_2$	5.	$\text{CH}_3\text{CO}_2\text{C}_2\text{H}_5$	58.8
$(\text{CH}_3)_2\text{C}=\text{O}$	5.9	$\text{CH}_2=\text{CH}_2$	67.2
$\text{CH}_3(\text{CO})\text{H}$	26.7	$\text{CH}_2=\text{CHCN}$	74.1
$\text{CH}_3\text{CH}=\text{C}(\text{CH}_3)_2$	4.8	$\text{C}_6\text{H}_5\text{CN}$ (ipso)	80.3
$\text{CH}_2=\text{CH}_2$	-2.4	$\text{C}_6\text{H}_5\text{NO}_2$ (1,2)	55.4
$\text{CHCl}=\text{CHCl}$ (cis, trans)	16.0, 0.8	$\text{HC}\equiv\text{CH}$	170.6
$\text{CH}_2=\text{CHBr}$ (cis, trans)	-8.5, -7.5	$(\text{CH}_3\text{CH}_2)_3\text{P}$	+14.1
Benzene [$^2J(\text{CH})$, $^3J(\text{CH})$]	+1.0, +7.4	$(\text{CH}_3\text{CH}_2)_4\text{P}^+ \text{Br}^-$	-4.3
$\text{CH}_3\text{C}\equiv\text{CH}$ (CH_3 , $\equiv\text{CH}$)	-10.6, -50.8	$(\text{CH}_3\text{O})_3\text{P}$	+10.1
CF_3CF_3	46.0	$(\text{CH}_3\text{O})_3\text{P}=\text{O}$	-5.8
$\text{CH}_3(\text{CO})\text{F}$	59.7	$(\text{CH}_3)_3\text{P}=\text{S}$	+56.1
$\text{Cl}_2\text{C}=\text{CF}_2$	44.2	$\text{CH}_3(\text{CH}_3\text{O})_2\text{P}=\text{O}$	+142.2

Table 4-5 Nitrogen-15 Couplings Beyond One Bond (Hz)

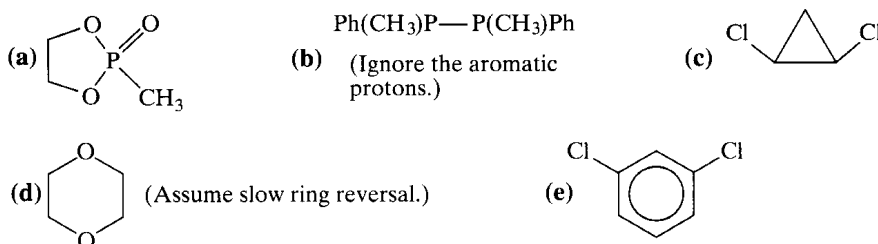
CH_3NH_2	-1.0	$\text{CH}_3\text{CH}_2\text{CH}_2\text{NH}_2$	1.2
Pyrrole (HNCH)	-4.52	CH_3CONH_2	9.5
Pyridine (NCH)	-10.76	$\text{CH}_3\text{C}\equiv\text{N}$	3.0
Pyridinium (HNCH)	-3.01	Pyridine (NCC)	+2.53
$(\text{CH}_3)_2\text{NCHO}$ (CH_3 , CHO)	+1.1, -15.6	Pyridinium (HNCC)	+2.01
$\text{H}-\text{C}\equiv\text{N}$	8.7	Aniline (NCC)	-2.68
$\text{H}_2\text{N}(\text{CO})\text{CH}_3$	1.3	Pyrrole (HNCC)	-3.92
Pyrrole (HNCCH)	-5.39	$\text{CH}_3\text{CH}_2\text{CH}_2\text{NH}_2$	1.4
Pyridine (NCCH)	-1.53	Pyridine (NCCC)	-3.85
Pyridinium (HNCCH)	-3.98	Pyridinium (HNCCC)	-5.30
$\text{CH}_3-\text{C}\equiv\text{N}$	-1.7	Aniline (NCCC)	-1.29

Problems

- 4.1 Characterize the indicated protons as (1) homotopic, enantiotopic, or diastereotopic and (2) magnetically equivalent or nonequivalent (by the coupling-constant criterion). In parts (h) and (i), the $\text{Cr}(\text{CO})_3$ ligand remains on one side of the benzene ring.

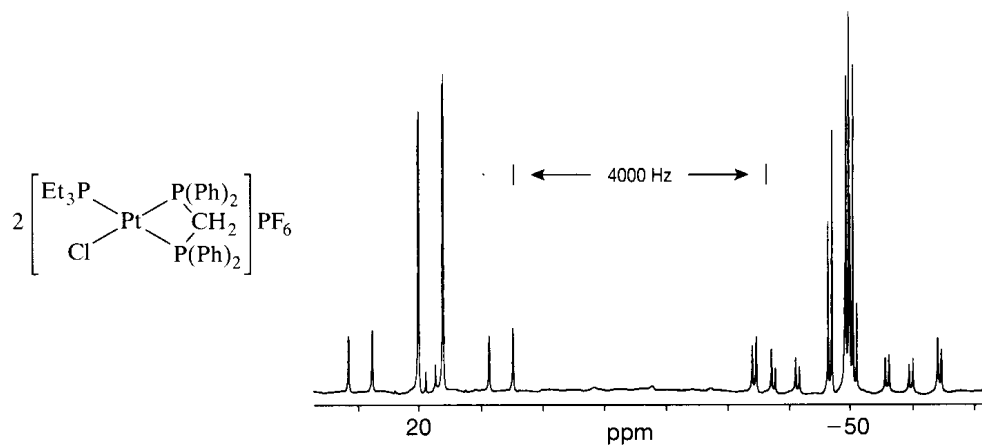


- 4.2 What is the spin notation for each of the following molecules (AX, AMX, AA'XX', etc.)?



Consider only major isotopes.

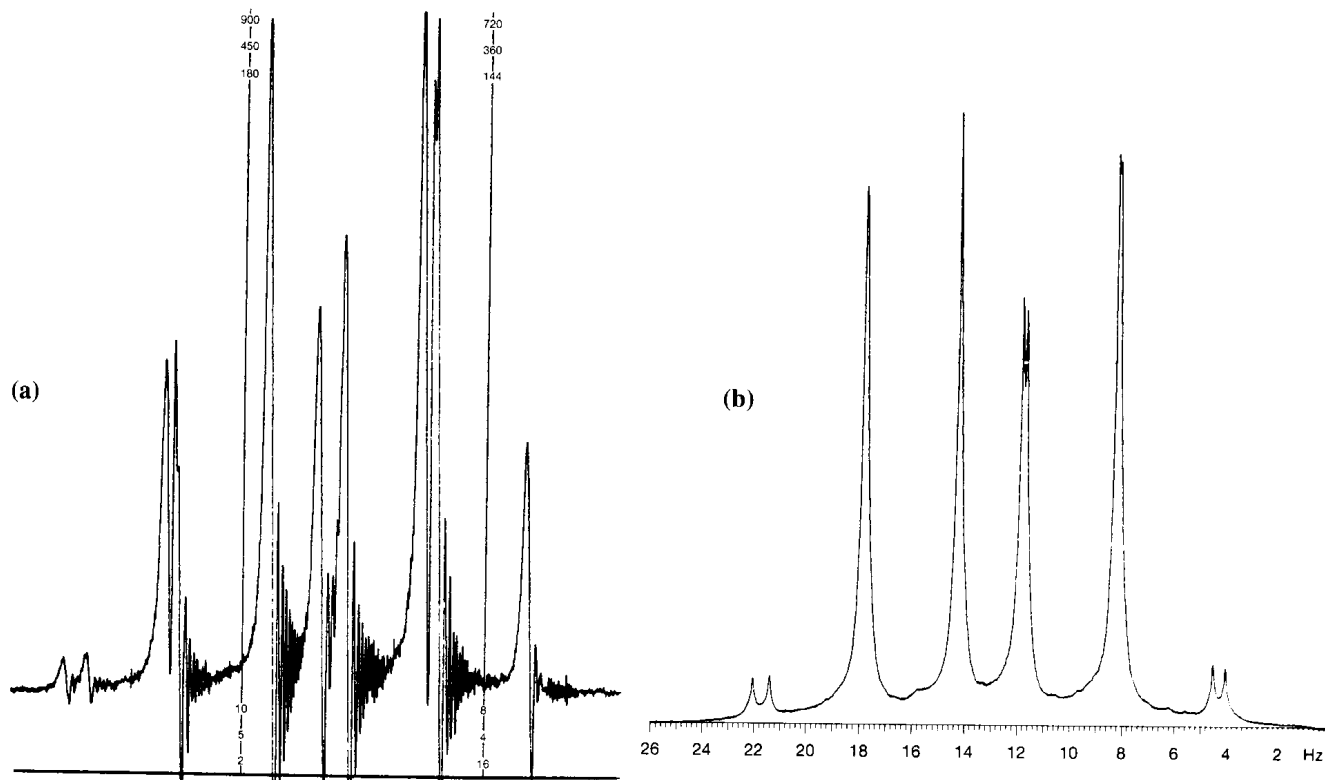
- 4.3 Write out the rotamers of 2-chloroethanol ($\text{ClCH}_2\text{CH}_2\text{OH}$). What is the spin notation at slow rotation for each rotamer and at fast rotation for the average?
- 4.4 Consider the following ^1H -decoupled ^{31}P spectrum* of the platinum complex with the structure illustrated (the resonances of the anion are omitted):



Explain all the peaks and give the spin notation. What should the ^{195}Pt spectrum look like?

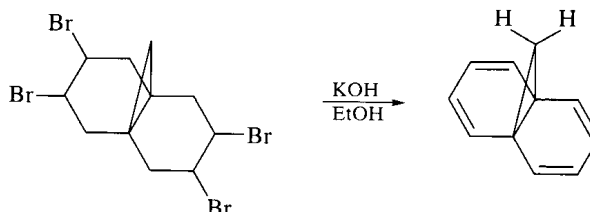
*From D. E. Berry, *J. Chem. Educ.*, **71**, 899–902 (1994). Copyright 1994 American Chemical Society. Reprinted by permission of the American Chemical Society.

- 4.5 The following is the ^1H spectrum of 1,2-dichlorobenzene at (a) 90 and (b) 750 MHz:



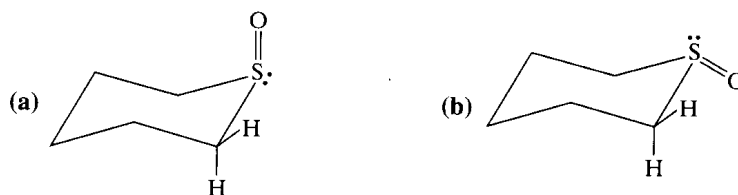
Examine each spectrum separately. Is it first or second order? Explain. What effect does the higher field have on the structure of the spectrum?

- 4.6 Eliminating 4 moles of HBr from the following molecule should give the indicated cyclopropane:



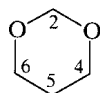
The $^1J(^{13}\text{C}-^1\text{H})$ for the bridge CH_2 group in the isolated product was measured to be 142 Hz. Explain in terms of product structures.

- 4.7 Examine the two isomers of thiane 1-oxide, (a) and (b):



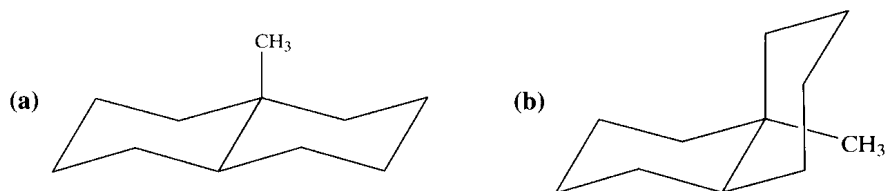
The observed geminal coupling constant between the α protons is -13.7 Hz in one isomer and -11.7 Hz in the other. Which coupling belongs to which isomer and why?

- 4.8 The ^1H spectrum of 1,3-dioxane at slow ring reversal contains three multiplets with geminal couplings -6.1 , -11.2 , and -12.9 Hz:



Without reference to any chemical shift data, assign the resonances.

4.9 Does the angular methyl group in *trans*-decalins (a) or in *cis*-decalins (b) have the larger line width? Explain.

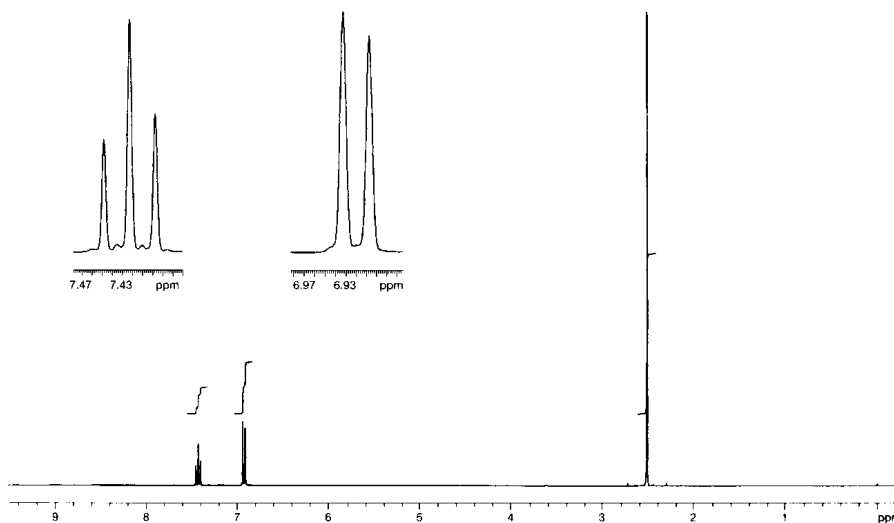


4.10 In cycloheptatriene (a), J_{23} is 5.3 Hz, whereas in the bistrifluoromethyl derivative (b), J_{23} is 6.9 Hz. Explain.

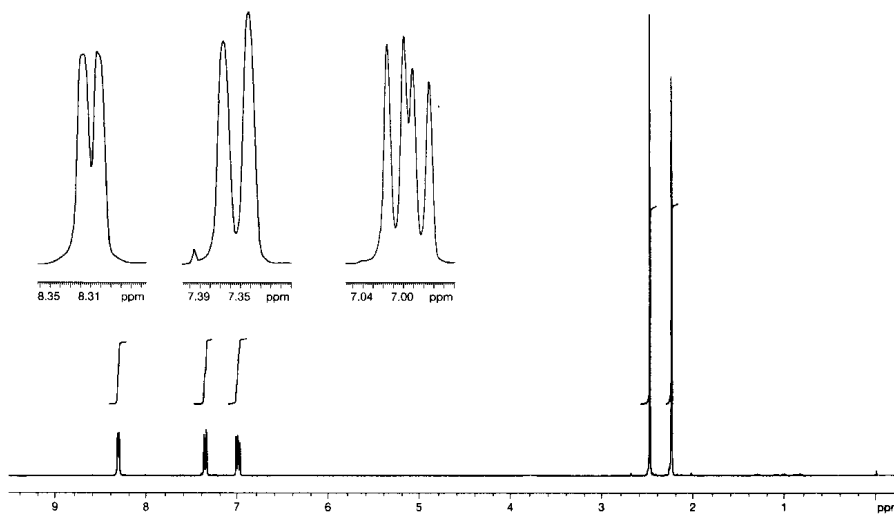


4.11 The following four 300 MHz ¹H spectra are of lutidines (dimethylpyridines):

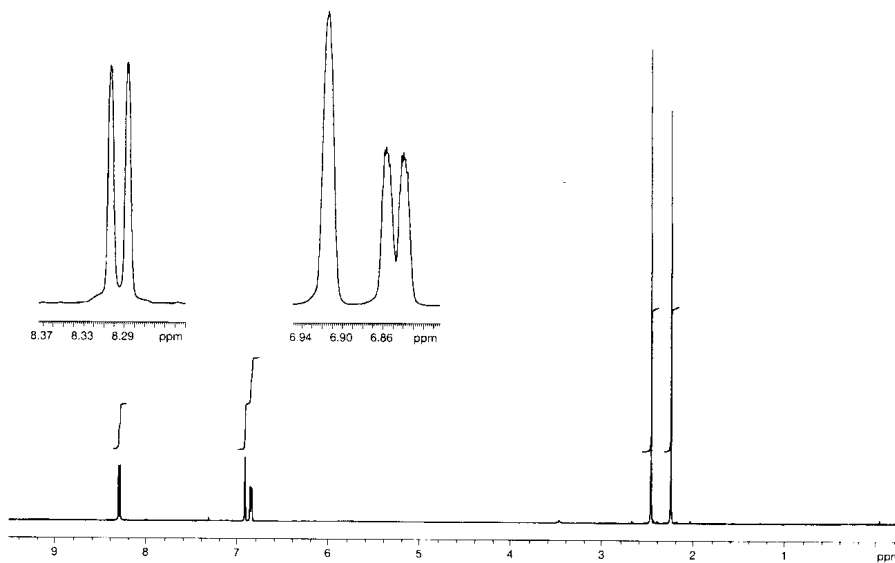
(a)



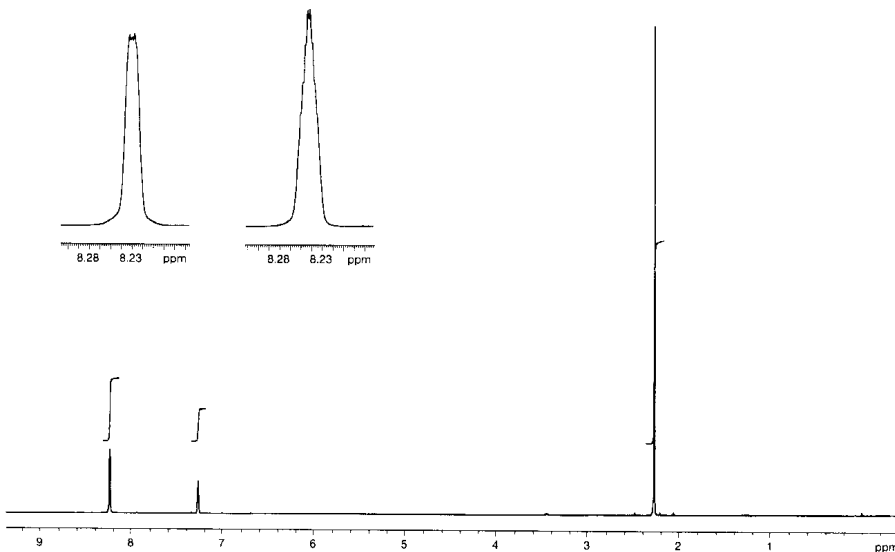
(b)



(c)



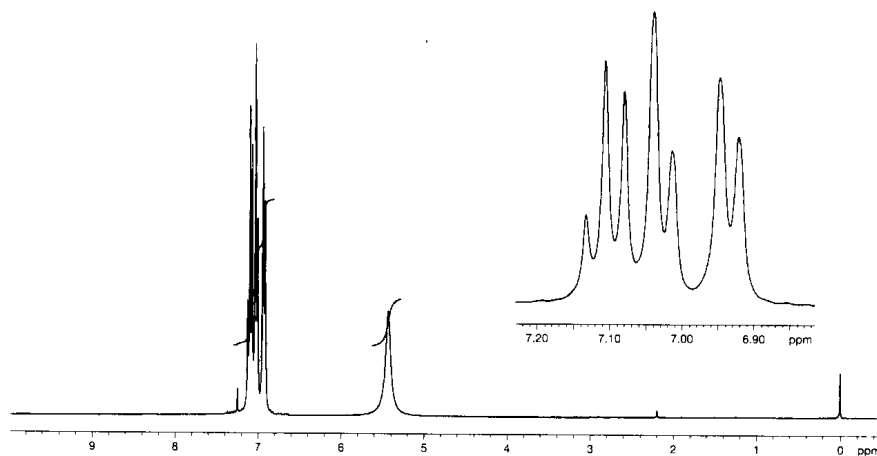
(d)



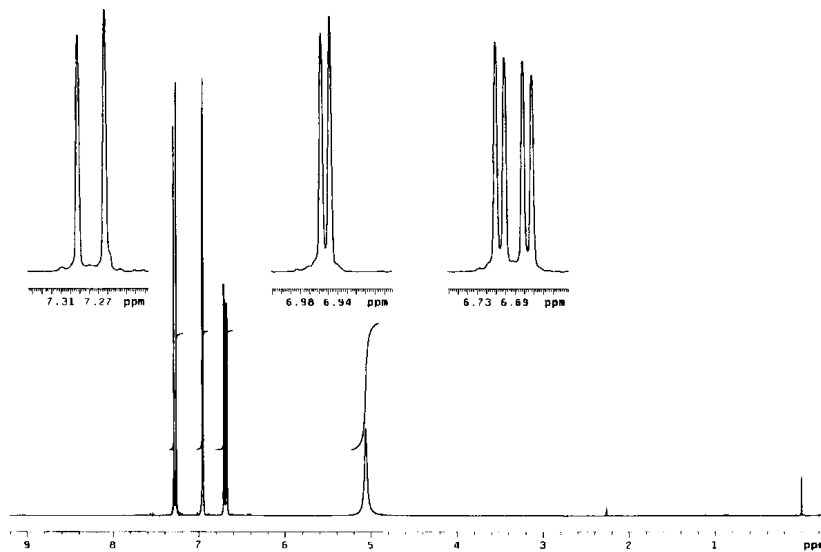
From the chemical shifts and coupling patterns, deduce the placement of methyl groups on each molecule. Assume that the spacings are first order.

4.12 Proceed as in Problem 4-11 with the following four 300 MHz ^1H spectra of dichlorophenols:

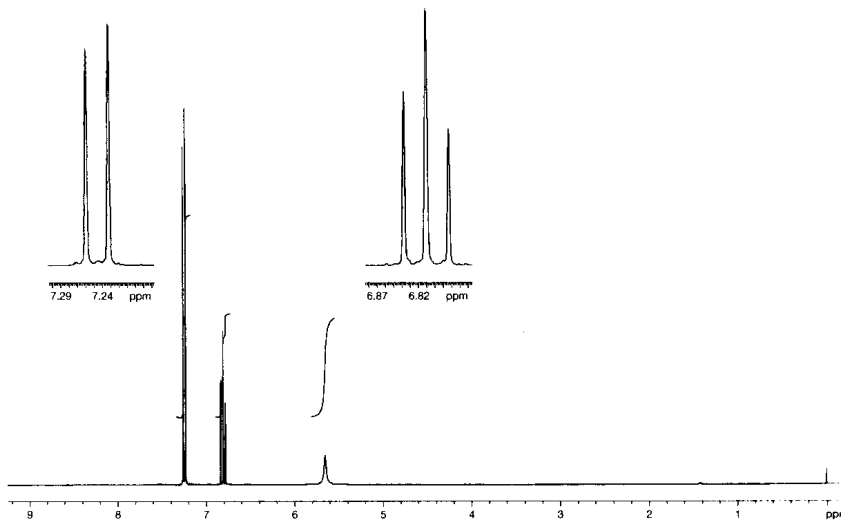
(a)



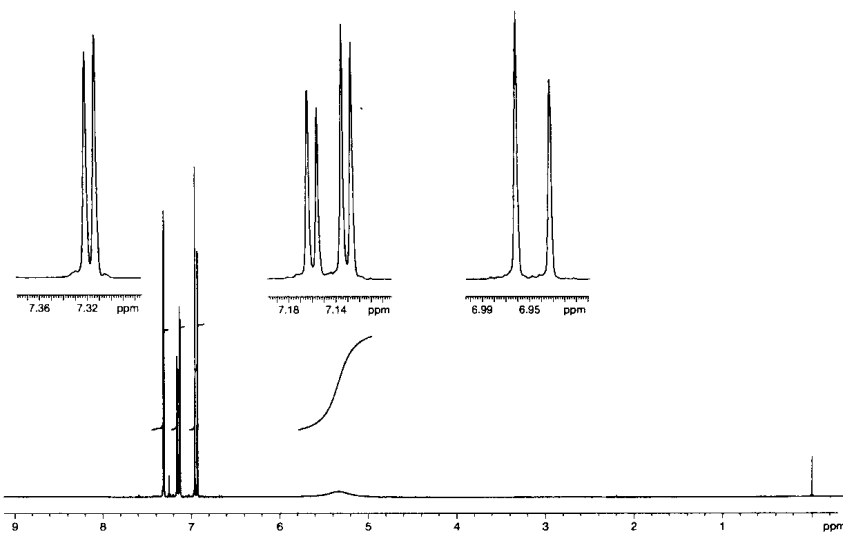
(b)



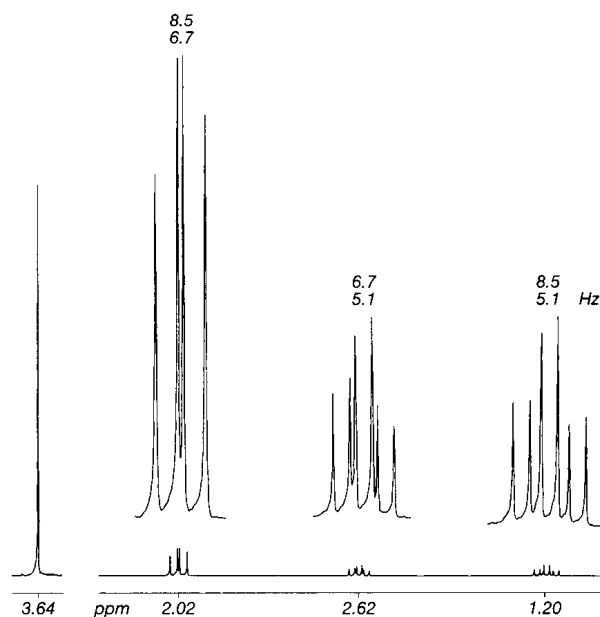
(c)



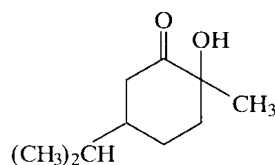
(d)



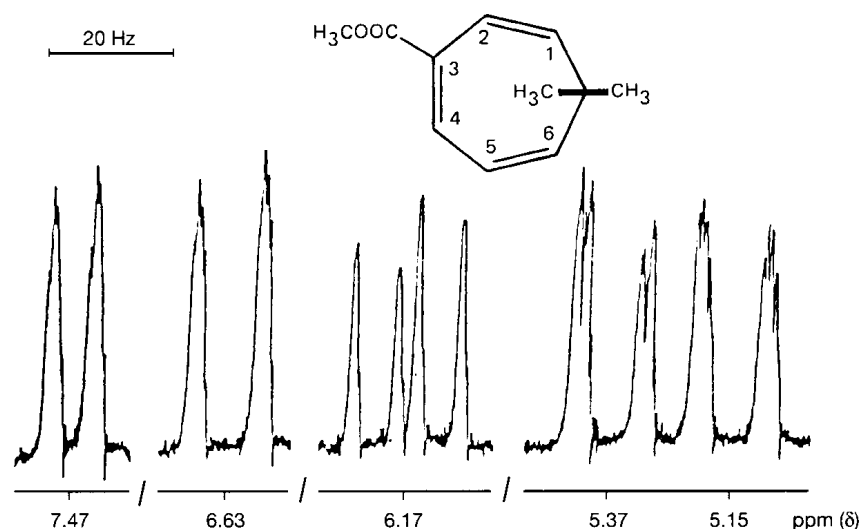
- 4.13 Is the following 400 MHz ^1H spectrum* (conditions: CDCl_3 , 25°C , 400 MHz) of the cis or the trans isomer of dimethyl 1,2-cyclopropanedicarboxylate? Explain.



- 4.14 The ^1H spectrum of 2-hydroxy-5-isopropyl-2-methylcyclohexanone has a $^3J_{56} = 3\text{ Hz}$ in benzene- d_6 , but 11 Hz in CD_3OD . Explain.



- 4.15 Analyze the following ^1H spectrum† of a thujic ester:

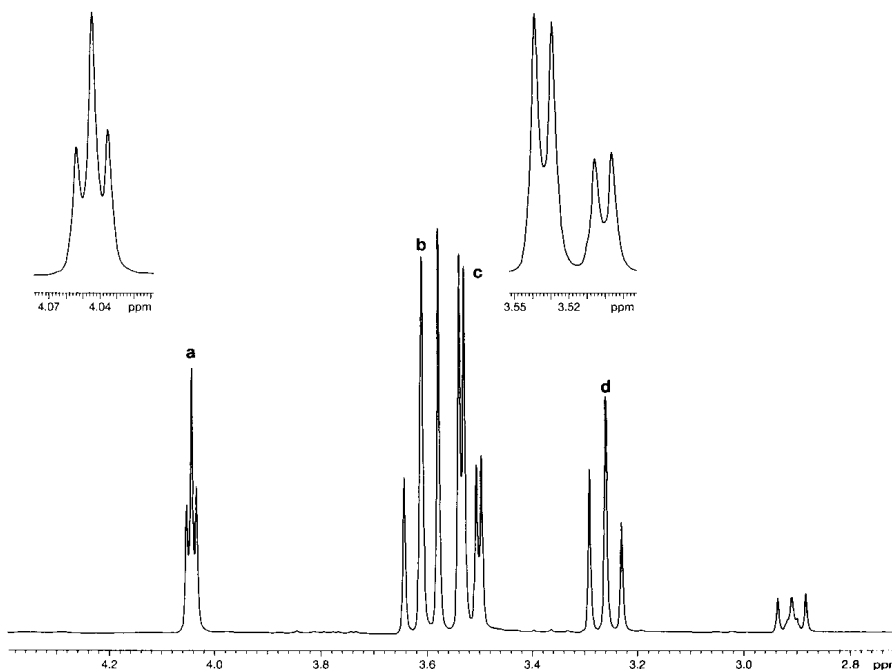


The CH_3 resonances are not shown. Assign the resonances to specific protons and give very approximate coupling constants. Explain your chemical-shift assignments.

*From E. Breitmaier, *Structure Elucidation by NMR in Organic Chemistry* (Chichester: Wiley, 1993), p. 71. Copyright 1993 John Wiley & Sons, Ltd. Reprinted by permission of John Wiley & Sons, Ltd.

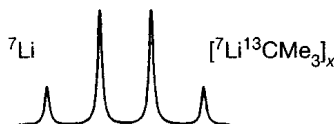
†From H. Günther et al., *Org. Magn. Reson.*, 6, 388 (1974). Copyright 1974 John Wiley & Sons, Ltd. Reprinted by permission of John Wiley & Sons, Ltd.

- 4.16 Deduce the structure (with relative stereochemistry) of the compound $C_6H_{12}O_6$ having the following 300 MHz 1H NMR spectrum in D_2O (the peaks at δ 2.9 are from the reference, 3-(trimethylsilyl)propionic acid):



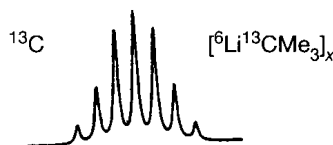
Hydroxyl resonances are not shown. The triplet (a) at δ 4.04 has integral 1 and $J = 2.8$ Hz. The second-order triplet (b) at δ 3.61 has integral 2 and $J = 9.6$ Hz. The second-order doublet of doublets (c) at δ 3.52 has integral 2 and $J = 2.8, 9.6$ Hz. The triplet (d) at δ 3.26 has integral 1 and $J = 9.6$ Hz. The ^{13}C NMR spectrum shows four resonances, all between δ 71 and 75.

- 4.17 The covalent and oligomeric nature of organolithium compounds has been demonstrated by examining the spectra of compounds fully labeled with ^{13}C or 6Li .
- (a) The $^7Li\{^1H\}$ spectrum of $[Li^{13}CMe_3]_x$ is a 1:3:3:1 quartet with $^1J(^7Li-^{13}C) = 14.3$ Hz:



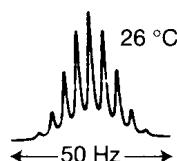
What can you conclude about the number of nearest neighbor *tert*-butyl groups to lithium in solution? Explain.

- (b) The $^{13}C\{^1H\}$ spectrum of $[^6Li^{13}CMe_3]_x$ at $-88^\circ C$ in cyclopentene is a 1:3:6:7:6:3:1 septet (recall that 6Li has a spin of 1), with $^1J(^6Li-^{13}C) = 5.4$ Hz:



How many nearest neighbor lithiums are indicated? Explain.

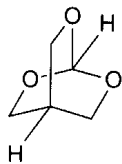
- (c) Suggest a structure for *tert*-BuLi under these conditions. Explain.
- (d) Above $-5^\circ C$, the septet is replaced by a nonet (nine lines) with $^1J = 4.1$ Hz:



Explain in terms of your structure.

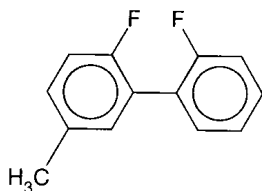
4.18 Explain the following couplings in terms of structure and mechanism:

(a)



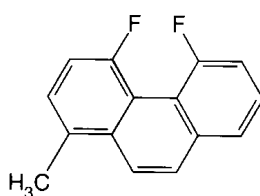
$${}^5J = 1.7 \text{ Hz}$$

(b)



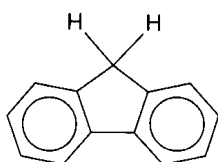
$${}^5J = 16.5 \text{ Hz}$$

(c)



$${}^5J = 170 \text{ Hz}$$

(d)



$${}^2J = -22.3 \text{ Hz}$$

Bibliography

Coupling (General)

- 4.1. I. Ando and G. A. Webb, *Theory of NMR Parameters*. London: Academic Press, 1983; *Nuclear Magnetic Resonance*, a specialist periodical report, Chemical Society, London, reviewed in each issue.

Magnetic Equivalence

- 4.2. K. Mislow and M. Raban, *Top. Stereochem.*, **1**, 1 (1966); W. H. Pirkle and D. J. Hoover, *Top. Stereochem.*, **13**, 263 (1982).

One-Bond Couplings

- 4.3. W. McFarlane, *Quart. Rev.*, **23**, 187 (1969); C. J. Jameson and H. S. Gutowsky, *J. Chem. Phys.*, **51**, 2790 (1969); J. H. Goldstein, V. S. Watts, and L. S. Rattet, *Progr. NMR Spectrosc.*, **8**, 103 (1971).

Geminal, Vicinal, and Long-Range ${}^1\text{H}$ - ${}^1\text{H}$ Couplings

- 4.4. S. Sternhell, *Rev. Pure Appl. Chem.*, **14**, 15 (1964); A. A. Bothner-By, *Advan. Magn. Reson.*, **1**, 195 (1965); M. Barfield and B. Charkrabarti, *Chem. Rev.*, **69**, 757 (1969); S.

Sternhell, *Quart. Rev.*, **23**, 236 (1969); V. F. Bystrov, *Russ. Chem. Rev.*, **41**, 281 (1972); J. Hilton and L. H. Sutcliffe, *Progr. NMR Spectrosc.*, **10**, 27 (1975); M. Barfield, R. J. Spear, and S. Sternhell, *Chem. Rev.*, **76**, 593 (1976).

Carbon-13 Couplings

- 4.5. J. B. Stothers, *Carbon-13 NMR Spectroscopy*. New York: Academic Press, 1973; J. L. Marshall, D. E. Müller, S. A. Conn, R. Seiwel, and A. M. Ihrig, *Acc. Chem. Res.*, **7**, 333 (1974); D. F. Ewing, *Ann. Rep. NMR Spectrosc.*, **6A**, 389 (1975); R. E. Wasylshen, *Ann. Rep. NMR Spectrosc.*, **7**, 118 (1977); P. E. Hansen, *Org. Magn. Reson.*, **11**, 215 (1978); V. Wray, *Progr. NMR Spectrosc.*, **13**, 177 (1979); G. C. Levy, R. L. Lichter, and G. L. Nelson, *Carbon-13 Nuclear Magnetic Resonance Spectroscopy*, 2d ed. New York: Wiley-Interscience, 1980; V. Wray and P. E. Hansen, *Ann. Rep. NMR Spectrosc.*, **11A**, 99 (1981); P. E. Hansen, *Ann. Rep. NMR Spectrosc.*, **11A**, 65 (1981); P. E. Hansen, *Progr. NMR Spectrosc.*, **14**, 175 (1981); W. H. Pirkle and D. J.

Hoover, *Top. Stereochem.*, **13**, 263 (1982); J. L. Marshall, *Carbon–Carbon and Carbon–Proton NMR Couplings*. Deerfield Beach, FL: Verlag Chemie, 1983; L. B. Krivdin and G. A. Kalabia, *Progr. NMR Spectrosc.*, **21**, 293 (1989); L. B. Krivdin and E. W. Della, *Progr. NMR Spectrosc.*, **23**, 301 (1991).

Fluorine-19 Couplings

4.6. J. M. Emsley, L. Phillips, and V. Wray, *Progr. NMR Spectrosc.*, **10**, 82 (1977).

Phosphorus-31 Couplings

4.7. E. G. Finer and R. K. Harris, *Progr. NMR Spectrosc.*, **6**, 61 (1970).

Spectral Analysis

4.8. J. D. Roberts, *An Introduction to the Analysis of Spin–Spin Splitting in High-Resolution Nuclear Magnetic Resonance Spectra*. New York: W. A. Benjamin, 1961; K. B. Wiberg and B. J. Nist, *The Interpretation of NMR Spectra*. New York: W. A. Benjamin, 1962; R. J. Abraham, *The Analysis of High Resolution NMR Spectra*. Amsterdam: Elsevier Science, Inc., 1971; R. A. Hoffman, S. Forsén, and B. Gestblom, *NMR Basic Princ. Progr.*, **5**, 1 (1971); C. W. Haigh, *Ann. Rep. NMR Spectrosc.*, **4**, 311 (1971); P. Diehl, H. Kellerhals, and E. Lustig, *NMR Basic Princ. Progr.*, **6**, 1 (1972); S. L. Manatt, *Magn. Reson. Chem.*, **40**, 317 (2002).

5

Further Topics in One-Dimensional NMR

Although the chemical shift and the coupling constant are the two fundamental measurable quantities in NMR spectroscopy, several other phenomena may be studied in a single NMR time dimension. In this chapter, we first examine the processes of spin–lattice and spin–spin relaxation, whereby a system moves toward spin equilibrium. (See Section 1-3.) Relaxation times or rates provide another important measurable quantity related to both structural and dynamic factors. Second, we explore in greater detail structural changes that occur on the NMR time scale. (See Section 1-8.) The temporal dependence of chemical shifts and coupling constants influences both line shapes and intensities and can be used to generate rate constants for reactions. Third, we describe the family of experiments that utilize a second irradiation frequency, B_2 . Double irradiation can simplify spectra, perturb intensities, and provide information about structure and rate processes. Finally, we expand on the technique of using several pulses, rather than only a single 90° pulse, sometimes separated by defined periods, to improve sensitivity, simplify spectral patterns, measure relaxation times and coupling constants, draw structural conclusions, and improve the accuracy of pulse definitions.

5-1 Spin–Lattice and Spin–Spin Relaxation

Application of the B_1 field at the resonance frequency results in energy absorption and the conversion of some $+\frac{1}{2}$ spins into $-\frac{1}{2}$ spins. Thus, magnetization in the z direction (M_z) decreases. Spin–lattice, or longitudinal, relaxation returns the system to equilibrium with time constant T_1 . Such relaxation occurs because of the presence of natural magnetic fields in the sample that fluctuate at the Larmor frequency. Because of the frequency match, excess spin energy can flow into the molecular surroundings, sometimes called the *lattice*, and $-\frac{1}{2}$ spins can return to the $+\frac{1}{2}$ state.

The major source of these magnetic fields is magnetic nuclei in motion. Like the classic model of a charge moving in a circle, a magnetic dipole in motion creates a magnetic field, whose frequency depends on the rate of motion and on the magnetic moment of the dipole. For appropriate values of these parameters, the resulting magnetic field can fluctuate at the same frequency as the resonance (Larmor) frequency of the nucleus in question, permitting energy to flow from excited spins to the lattice. Such a process is called *dipole–dipole relaxation* [$T_1(DD)$], because it involves interaction of the resonating nuclear magnetic dipole with the dipole of the nucleus in motion that causes the fluctuating field of the lattice.

The resulting relaxation time or rate (R_1) depends on nuclear properties of both resonating and moving nuclei, on the distance between them, and on the rate of motion of the moving nucleus. Mathematically, the dependence of relaxation on these factors takes the form

$$R_1(\text{DD}) = \frac{1}{T_1(\text{DD})} = n\gamma_{\text{C}}^2\gamma_{\text{H}}^2\hbar^2r_{\text{CH}}^{-6}\tau_{\text{c}} \quad (5-1a)$$

for the case of ^{13}C relaxed by protons in motion and the form

$$\frac{1}{T_1(\text{DD})} = \frac{3}{2}n\gamma_{\text{H}}^4\hbar^2r_{\text{HH}}^{-6}\tau_{\text{c}} \quad (5-1b)$$

for protons relaxed by protons. As usual, the nuclear properties are represented by the gyromagnetic ratios. The symbol n stands for the number of protons that are nearest neighbors to the resonating nucleus and hence are most effective at relaxing it. The rapid falloff with distance is indicated by the inverse of the nearest-neighbor C—H (H—H) distance r_{CH} (r_{HH}) to the sixth power. The motional properties of the protons are described by the effective correlation time τ_{c} , which is the time required for the molecule to rotate one radian and is typically in the nanosecond-to-picosecond range for organic molecules in solution. The theory of relaxation is developed more fully in Appendix 5.

Thus, carbon relaxation is faster (and the relaxation time is shorter) when there are more attached protons, when the internuclear distance is less, and when rotation in solution decreases. A quaternary carbon has a long relaxation time because it lacks an attached proton and because the distance r to other protons is large. The ratio of the carbon relaxation time of methinyl to methylene to methyl is 6:3:2 (equivalent to $1:\frac{1}{2}:\frac{1}{3}$), due to differences in the number of attached protons, other things being equal. Because the rate of molecular tumbling in solution slows as molecular size increases, larger molecules relax more rapidly (e.g., cholesteryl chloride relaxes more rapidly than phenanthrene, which relaxes more rapidly than benzene). Equation 5-1 is an approximation to a more complete equation and represents what is called the *extreme narrowing limit*. Because the frequency of motion of the moving nuclear magnet must match the resonance frequency of the excited nuclear magnet, dipolar relaxation becomes ineffective for both rapidly moving small molecules and slowly moving large molecules. Many molecules of interest to biochemists fall into the latter category, to which eq. 5-1 does not apply. Rapid internal rotation of methyl groups in small molecules also can reduce the effectiveness of dipole-dipole relaxation. The optimal correlation times (τ_{c}) for dipolar relaxation lie in the range of about 10^{-7} to 10^{-11} s (the inverse of the resonance frequency). Because the resonance frequency depends on the value of B_0 , this range also depends on B_0 .

When dipolar relaxation is slow, other mechanisms of relaxation become important. Fluctuating magnetic fields also can arise (1) from the interruption of the motion of rapidly tumbling small molecules or rapidly rotating groups within a molecule (spin rotation relaxation), (2) from the tumbling of molecules with anisotropic chemical shielding at high fields, (3) from scalar coupling constants that fluctuate through chemical exchange or through quadrupolar interactions, (4) from the tumbling of paramagnetic molecules (unpaired electrons have very large magnetic dipoles), and (5) from the tumbling of quadrupolar nuclei. In the absence of quadrupolar nuclei or paramagnetic species, these alternative mechanisms often are unimportant. A major exception is the relaxation of methyl (CH_3) and trifluoromethyl (CF_3) carbons by spin rotation. Because relaxation by dipolar interactions becomes less effective, but relaxation by spin rotation becomes more effective, at higher temperatures, these mechanisms may be distinguished by measuring T_1 at multiple temperatures. Relaxation by nondipolar mechanisms is discussed more fully in Appendix 5.

The actual value of T_1 must be known at least approximately in order to decide how long to wait between pulses for the system to return to equilibrium (the delay time). In addition, $T_1(\text{DD})$ offers both structural information, because of its dependence on r_{CH} , and

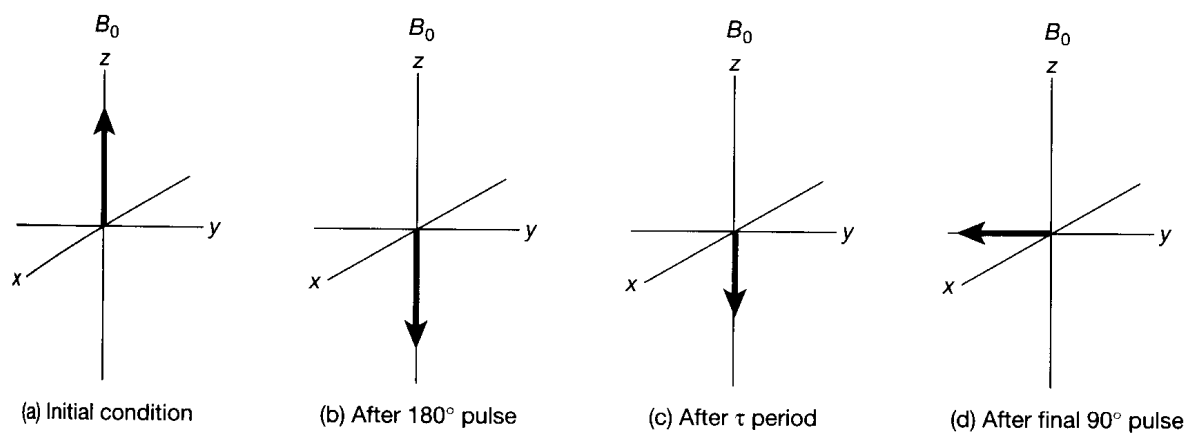


Figure 5-1 The inversion recovery experiment.

dynamic information, because of its dependence on τ_c . For these reasons, convenient methods have been developed for measuring T_1 , the commonest of which is called *inversion recovery*. The strategy is to create a nonequilibrium distribution of spins and then to follow their return to equilibrium as a first-order rate process. Inverting the spins through the application of a 180° pulse creates a maximum deviation from equilibrium. (See Figure 5-1b.) If a very short amount of time τ is allowed to pass (Figure 5-1c) and a 90° pulse is applied to move the spins into the xy plane for observation, the nuclear magnets are aligned along the $-y$ axis (Figure 5-1d) and an inverted peak is obtained. During time τ , some T_1 relaxation occurs (cf. Figures 5-1b and c). The z magnetization at the end of time τ (Figure 5-1c) is shorter than at the beginning (Figure 5-1b). Consequently, the peak produced after the 90° pulse is smaller than if the 180° and 90° pulses had been combined initially as a 270° pulse (i.e., if $\tau = 0$). The inversion recovery pulse sequence is summarized as 180°- τ -90° (acquire) and is an example of a simple multipulse sequence.

A series of such experiments with increasingly longer values of τ results in further relaxation between the 180° and 90° pulses. After the 90° pulse (Figure 5-1d), the resulting peak changes from negative through zero to positive as τ increases, until complete relaxation occurs when τ is very long. Figure 5-2 shows a stack of such experiments for the carbons of chlorobenzene. Because the carbon ipso to chlorine (C-1) has no directly attached proton, much longer values of τ are needed for the inverted peak to turn over. Relaxation for C-1 is

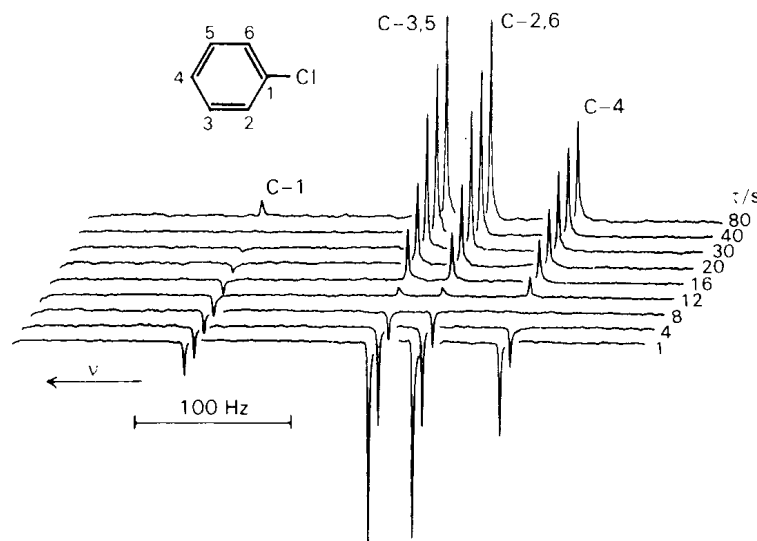


Figure 5-2 A stack plot for the inversion recovery experiment of the carbon-13 resonances of chlorobenzene at 25 MHz. The time τ in the pulse sequence 180°- τ -90° is given in seconds at the right. (From R. K. Harris, *Nuclear Magnetic Resonance Spectroscopy* Pitman Publishing, Ltd., London, 1983, p. 82. Reproduced with permission of Addison Wesley Longman, Ltd.)

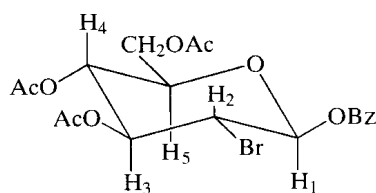
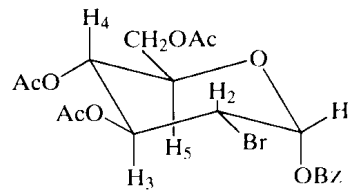
not complete even by $\tau = 80$ s. The intensity I measured at a series of times τ follows an exponential decay according to the first-order kinetics of the formula

$$I = I_0(1 - 2e^{-\tau/T_1}), \quad (5-2)$$

in which I_0 is the equilibrium intensity (measured, for example, at a very large value of τ) and the factor of two arises because magnetization recovery begins from a fully inverted condition. A plot of the natural logarithm of $(I_0 - I)$ versus τ gives a straight line with a slope of $-1/T_1$. An estimate for the spin-lattice relaxation time may be obtained through knowledge of the time τ at which the intensity passes through a null [$\tau(\text{null}) = 8$ s for C-4 in Figure 5-2]. At this time, $I = 0$, so that T_1 corresponds to $\tau(\text{null})/\ln 2$, or $1.443\tau(\text{null})$. Such an estimate might be useful, for instance, in deciding how long to wait between repetitive pulses, but it should never be considered a rigorous measurement of T_1 .

Relaxation in the xy plane, or spin-spin (transverse) relaxation (T_2), might be expected to be identical to T_1 , because movement of the magnetization from the xy plane back onto the z axis restores z magnetization at the same rate as it depletes xy magnetization. There are, however, other mechanisms of xy relaxation that do not affect z magnetization. We already saw in Section 1-3 that inhomogeneity of the B_0 magnetic field randomizes phases in the xy plane and hastens xy relaxation. As a result, T_2 is expected to be less than or equal to T_1 . In addition, xy relaxation can occur when two nuclei mutually exchange their spins, one going from $+\frac{1}{2}$ to $-\frac{1}{2}$ and the other from $-\frac{1}{2}$ to $+\frac{1}{2}$. This spin-spin, double-flip, or flip-flop mechanism is most significant in large molecules. The process can result in *spin diffusion*. The excitation of a specific proton changes the magnetization of surrounding protons as flip-flop interactions spread through the molecule. The interpretation of the spectra of large molecules such as proteins must take such a process into consideration. (For further development, see Appendix 5.)

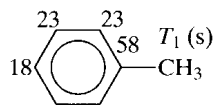
Proton relaxation times depend on the distance between the resonating nucleus and the nearest-neighbor protons. The closer the neighbors, the faster is the relaxation and the shorter is T_1 . The two isomers **5-1a** and **5-1b** [$\text{Bz} = \text{Ph}(\text{C}=\text{O})$] may be distinguished by their proton relaxation times. In **5-1a**, H_1 is axial and close to the 3 and 5 axial protons, resulting in a T_1 of 2.0 s. In **5-1b**, H_1 is equatorial and has more distant nearest neighbors,

**5-1a****5-1b**

resulting in a T_1 of 4.1 s. In this way, the structure of the anomers may be distinguished. The remaining values of T_1 may be interpreted in a similar fashion. For example, H_2 in isomer **5-1a** has only the H_4 axial proton as a nearest neighbor, so its T_1 is a relatively long 3.6 s. In **5-1b**, H_2 has not only the axial H_4 , but also the vicinal H_1 , as a nearest neighbor, so T_1 is shorter, viz., 2.1 s.

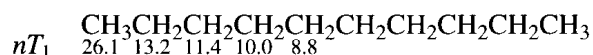
When a molecule is rigid and rotates equally well in any direction (isotropically), all the carbon relaxation times (after correction for the number of attached protons) should be nearly the same. The nonspherical shape of a molecule, however, frequently leads to preferential rotation in solution around one or more axes (anisotropic rotation). For example, toluene prefers to rotate around the long axis that includes the methyl, ipso, and para carbons, so that less mass is in motion. As a result, on average, these carbons (and their attached protons) move less in solution than do the ortho and meta carbons, because atoms on the axis of rotation remain stationary during rotation. The more rapidly moving ortho and meta carbons

thus have a shorter effective correlation time τ_c and hence, by eq. 5-1, a longer T_1 . The actual values are shown in structure 5-2. The longer value for the ipso carbon arises because it lacks a directly bonded proton and because r_{CH} in eq. 5-1a is very large.



5-2

When molecules are not rigid, the more rapidly moving pieces relax more slowly because their τ_c is shorter. Thus, in decane (5-3) the methyl carbon relaxes most slowly,



5-3

followed by the ethyl carbon, and so on, to the fifth carbon in the middle of the chain. Structure 5-3 gives the values of nT_1 (n is the number of attached protons), so that the figures may be compared for all carbons without considering any substitution patterns. These values indicate the relative rates of motion of each carbon.

The inversion recovery experiment used to measure T_1 also may be exploited to simplify spectra. In Figure 5-2, the spectrum for $\tau = 40$ s lacks a resonance for the ipso carbon (C-1). Similarly, for a τ of about 10 s, all the other ring carbons are nulled, and only the negative peak for C-1 is obtained. Such *partially relaxed spectra* can be used not only to obtain partial spectra in this fashion, but also to eliminate specific peaks. When deuterated water (D_2O) is used as the solvent, the residual HOD peak is undesirable. An inversion recovery experiment can reveal the value of τ for which the water peak is nulled. The rest of the protons will have positive or negative intensities at that τ , depending on whether they relax more rapidly or more slowly than water. The experiment may be refined by applying the 180° pulse selectively only at the resonance position of water. Selection of τ for nulling of this peak then produces a spectrum that lacks the water peak, but otherwise is quite normal for the remaining resonances. Such a procedure is an example of *peak suppression* or *solvent suppression*.

The dominant mode of spin-lattice relaxation of nuclei with spins greater than $\frac{1}{2}$ results from the quadrupolar nature of such nuclei. These nuclei are considered to have an ellipsoidal rather than a spherical shape. When $I = 1$, as in ^{14}N or ^2H , there are three stable orientations in the magnetic field: parallel, orthogonal, and antiparallel, as shown in Figure 5-3. When these ellipsoidal nuclei tumble in solution within an unsymmetrical electron cloud of the molecule, they produce a fluctuating electric field that can bring about relaxation.

The mechanism is distinguished from dipole-dipole relaxation in two ways. First, it does not require a second nucleus in motion; the quadrupolar nucleus creates its own fluctuating field by moving in the unsymmetrical electron cloud. Second, because the mechanism is extremely effective when the quadrupole moment of the nucleus is large, T_1 can become very short (milliseconds or less). In such cases, the uncertainty principle applies, whereby the product of ΔE (the spread of energies of the spin states, as measured by the line width $\Delta\nu$) and Δt (the lifetime of the spin state, as measured by the relaxation time) must remain

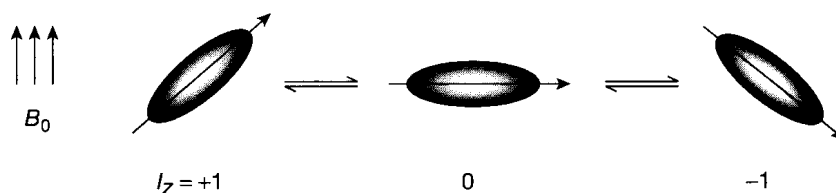


Figure 5-3 The spin states for a nucleus with $I = 1$.

constant ($\Delta E \Delta t \sim$ Planck's constant). Thus, when the relaxation time is very short, the line width becomes very large. Nuclei with large quadrupole moments often exhibit very large line widths—for example, about 20,000 Hz for the ^{35}Cl resonance of CCl_4 . The common nuclides ^{17}O and ^{14}N have smaller quadrupolar moments and exhibit sharper resonances, typically tens of Hz. The small quadrupole moment of deuterium results in quite sharp peaks, usually one or a few Hz. The line width also depends on the symmetry of the molecule, which controls how unsymmetrical the electron cloud is. π systems are more unsymmetrical and give broader lines (as in amides and pyridines for ^{14}N). Spherical or tetrahedral systems have no quadrupolar relaxation, since the electron cloud is symmetrical. Such systems exhibit very sharp line widths, like those of spin- $\frac{1}{2}$ nuclei (^{14}N in $^+\text{NH}_4$, ^{10}B in $^-\text{BH}_4$, ^{35}Cl in Cl^- or $^-\text{ClO}_4$, and ^{33}S in SO_4^{2-}).

Very important to the organic chemist is the effect of quadrupolar nuclei on the resonances of nearby protons. When quadrupolar relaxation is extremely rapid, a neighboring nucleus experiences only the average spin environment of the quadrupolar nucleus, so that no spin coupling is observed. Hence, protons in chloromethane produce a sharp singlet, even though ^{35}Cl and ^{37}Cl have spins of $\frac{3}{2}$ and exist in four spin states. Chemists have come to think of the halogens (other than fluorine) as being nonmagnetic, although they appear so only because of their rapid quadrupolar relaxation. At the other extreme, deuterium has such a weak quadrupole moment that neighboring protons exhibit normal couplings to ^2H . Thus, nitromethane with one deuterium (CH_2DNO_2) shows a 1 : 1 : 1 triplet, because the protons are influenced by the three spin states (+1, 0, and -1) of deuterium (in analogy to Figure 5-3). Nitromethane, with two deuteriums (CHD_2NO_2), shows a 1 : 2 : 3 : 2 : 1 quintet from coupling to the various combinations of the three spin states (++; +0,0+; +- ,00, -+; -0,0-; --). This quintet is often observed in deuterated solvents such as acetone- d_6 , acetonitrile- d_3 , or nitromethane- d_3 , because incomplete deuteration results in an impurity containing one proton in place of a deuterium.

The ^{14}N nucleus falls between these extremes. In highly unsymmetrical cases, such as the interior nitrogen in biuret, $\text{NH}_2(\text{CO})\text{NH}(\text{CO})\text{NH}_2$, quadrupolar relaxation is rapid enough to produce the average singlet for the attached proton. The protons of the ammonium ion, on the other hand, give a sharp 1 : 1 : 1 triplet with full coupling between ^1H and ^{14}N , since quadrupolar relaxation is absent. When relaxation is at an intermediate rate, it is possible to observe three broadened peaks, one broadened average peak, or broadening to the point of invisibility. Irradiation at the ^{14}N frequency removes the ^{14}N — ^1H interaction (Section 5-3), so that ^{14}N appears to be nonmagnetic. Figure 5-4 shows the normal spectrum of pyrrole at the bottom, containing only the AA'BB' set from the CH protons and no visible NH resonance, because the line is extremely broad. Irradiation at the ^{14}N frequency decouples the NH proton from ^{14}N and results in a quintet NH resonance from coupling to the four CH protons.

5-2 Reactions on the NMR Time Scale

NMR is an excellent tool for following the kinetics of an irreversible reaction through the disappearance or appearance of peaks over periods of minutes to hours. The spectrum is obtained repeatedly at specific intervals, and rate constants are calculated from changes in peak intensities. Thus, the procedure is a classical kinetic method, performed on the *laboratory time scale*. The molecular changes take place on a time scale much longer than the pulse or acquisition times of the NMR experiment. In addition, and more importantly, NMR has a unique capability for the study of the kinetics of reactions that occur at equilibrium and that affect line shapes, usually with activation energies in the range from 4.5 to 25 kcal mol $^{-1}$ (Section 1-8), a range that corresponds to rates in the range from 10^0 to 10^4 s $^{-1}$. This *NMR time scale* really refers to the rough equivalence of the reaction rate in s $^{-1}$ to the frequency spacing in Hz between the exchanging nuclei.

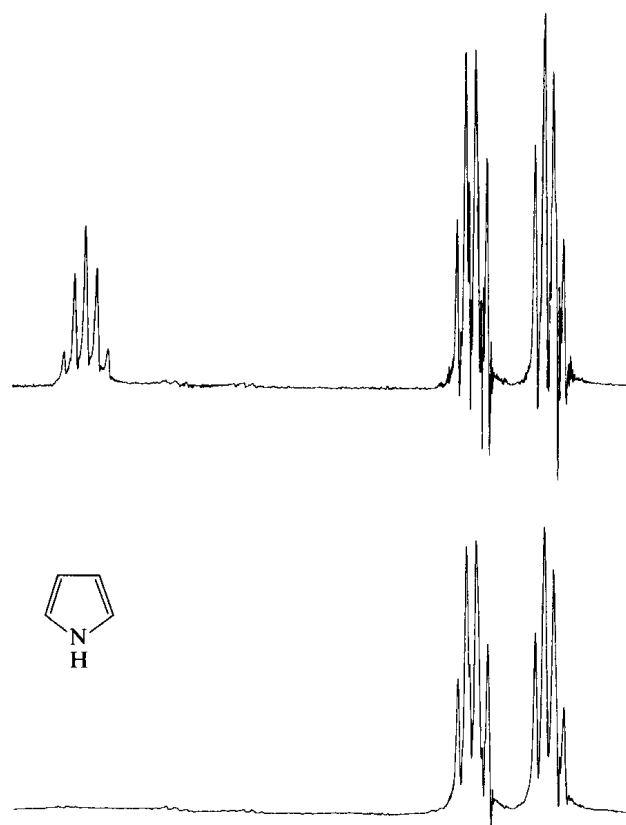
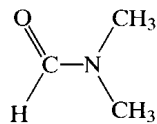


Figure 5-4 The 90 MHz proton spectrum of pyrrole with (upper) and without (lower) ^{14}N decoupling.

A series of spectra for the interchange of axial and equatorial protons in cyclohexane- d_{11} as a function of temperature is illustrated in Figure 1-31. When the interchange of two such chemical environments occurs much faster than the frequency differences between the two sites, the result is a single peak, reflecting the average environment (*fast exchange*). Keep in mind that these exchanges occur reversibly, and the system remains at equilibrium. When the interchange is slower than the frequency differences, the NMR result is two distinct peaks (*slow exchange*). When the interchange is comparable to the frequency differences, broad peaks typically result. The reaction then is said to occur on the NMR time scale. Both fast and slow exchange sometimes may be reached by altering the temperature of the experiment. Bimolecular reactions, such as the acid-catalyzed interchange of protons, also may be studied, as in the case of the hydroxy proton of methanol. (See Figure 1-30.)

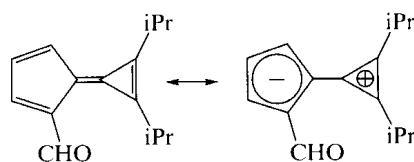
Normally, rotation around single bonds has a barrier below 5 kcal mol^{-1} and occurs faster than the NMR time scale. Rotation around the double bond of alkenes, on the other hand, has a barrier that is normally above 50 kcal mol^{-1} and is slow on the NMR time scale. There are numerous examples of intermediate bond orders, whose rotation occurs within the NMR time scale. Hindered rotation about the C—N bond in amides such as *N,N*-dimethylformamide (**5-4**) provides a classic example of site exchange. At room



5-4

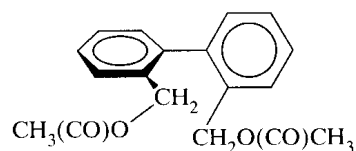
temperature, exchange is slow and two methyl resonances are observed, whereas, above 100°C , exchange is fast and a single resonance is observed. The measured barrier is about 22 kcal mol^{-1} .

Hindered rotation occurs on the NMR time scale for numerous other systems with partial double bonds, including carbamates, thioamides, enamines, nitrosamines, alkyl nitrites, diazoketones, aminoboranes, and aromatic aldehydes. Formal double bonds can exhibit free rotation when alternative resonance structures suggest partial single bonding. The calicene **5-5**, for example, has a barrier to rotation about the central bond of only 20 kcal mol^{-1} .



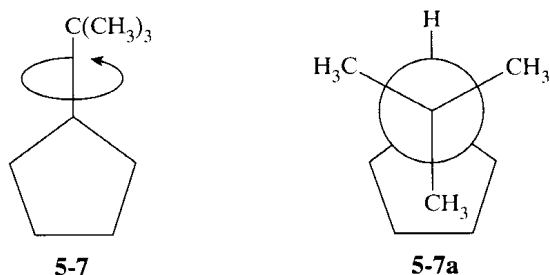
5-5

Steric congestion can raise the barrier about single bonds enough to bring it into the NMR range. Rotation about the single bond in the biphenyl **5-6** is raised to a measurable



5-6

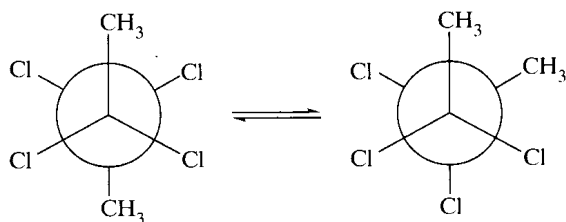
13 kcal mol^{-1} by the presence of the ortho substituents, which also provide diastereotopic methylene protons as the dynamic probe. Hindered rotation about an $\text{sp}^3\text{-sp}^3$ bond can sometimes be observed when at least one of the carbons is quaternary. Thus, at -150°C , the *tert*-butyl group in *tert*-butylcyclopentane (**5-7**) gives two resonances in the ratio of 2:1, since two of the methyl groups are different from the third (**5-7a**).



5-7

5-7a

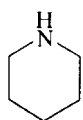
Hindered rotation has frequently been observed in halogenated alkanes. The increased barrier probably arises from a combination of steric and electrostatic interactions. 2,2,3,3-Tetrachlorobutane (**5-8**) exhibits a 2:1 doublet below -40°C from anti and gauche rotamers that are rotating slowly on the NMR time scale.



5-8

When both atoms that constitute the single bond possess nonbonding electron pairs, the barrier often is in the observable range. The high barrier may be due to electrostatic interactions or repulsions between lone pairs. For example, the barrier to rotation about the sulfur-sulfur bond in dibenzyl disulfide ($\text{C}_6\text{H}_5\text{CH}_2\text{S-SCH}_2\text{C}_6\text{H}_5$) is 7 kcal mol^{-1} . Similar high barriers have been observed in hydrazines (N-N), sulfenamides (S-N), and aminophosphines (N-P).

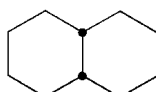
Axial–equatorial interconversion through ring reversal has been studied in a wide variety of systems in addition to cyclohexane, including heterocycles such as piperidine (**5-9**), unsaturated rings [e.g., cyclohexene (**5-10**)], fused rings like *cis*-decalin (**5-11**), and



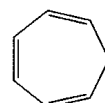
5-9



5-10

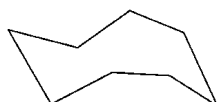


5-11



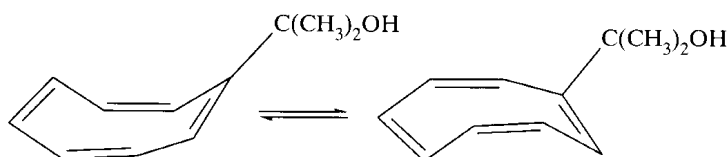
5-12

rings of other than six members, such as cycloheptatriene (**5-12**). Cyclooctane and other eight-membered rings have been examined extensively. The pentadecadeutero derivative of the parent compound exhibits dynamic behavior below -100°C , with a free energy of activation of 7.7 kcal mol^{-1} . The dominant conformation appears to be the boat–chair (**5-13**).



5-13

Cyclooctatetraene (**5-14**) undergoes a boat–boat ring reversal. The methyl groups on the side



5-14

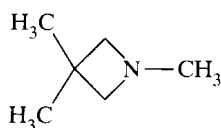
chain provide the diastereotopic probe and reveal a barrier of $14.7\text{ kcal mol}^{-1}$. The favored transition state is a planar form with alternating single and double bonds.

Trisubstituted atoms with a lone pair, such as amines, may undergo the process of pyramidal atomic inversion on the NMR time scale. The resonances of the two methyls in the aziridine **5-15** become equivalent at elevated temperatures through rapid nitrogen inversion.

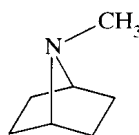


5-15

This barrier is particularly high (18 kcal mol^{-1}) because of angle strain in the three-membered ring, which is higher in the transition state than in the ground state. The effect is observed to a lesser extent in azetidines (**5-16**, 9 kcal mol^{-1}) and in strained bicyclic systems such as **5-17** (10 kcal mol^{-1}).

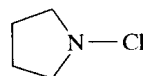


5-16



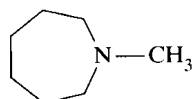
5-17

The inversion barrier may be raised when nitrogen is attached to highly electronegative elements. This substitution increases the *s* character of the ground-state lone pair. Since the transition-state lone pair must remain *p*-hybridized, the barrier is higher, as in *N*-chloropyrrolidine (**5-18**). When neither ring strain nor electronegative substituents are



5-18

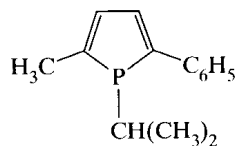
present, barriers are low, but still often measurable, as in *N*-methylazacycloheptane (**5-19**, 7 kcal mol⁻¹) and 2-(diethylamino)propane, (CH₃CH₂)₂NCH(CH₃)₂ (6.4 kcal mol⁻¹).



5-19

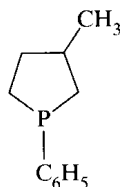
In the latter case, the barrier is considered to be a mix of nitrogen inversion and C–N bond rotation.

Inversion barriers for elements in lower rows of the periodic table generally are above the NMR range. (Chiral phosphines and sulfoxides are isolable.) Consequently, barriers are brought into the range by substitution with electropositive elements, as in the diphosphine CH₃(C₆H₅)P–P(C₆H₅)CH₃, whose barrier of 26 kcal mol⁻¹ compares with 32 kcal mol⁻¹ in CH₃(C₆H₅)(C₆H₅CH₂)P. The barrier in phosphole **5-20** is lowered because the transition



5-20

state is aromatic. Its barrier of 16 kcal mol⁻¹ compares with 36 kcal mol⁻¹ in a saturated analogue, **5-21**.



5-21

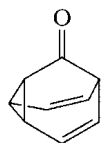
The barriers to many valence tautomerizations fall into the NMR range. A classic example is the Cope rearrangement of 3,4-homotropilidene (**5-22**). At low temperatures, the



5-22

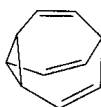
spectrum has the features expected for the five functionally distinct types of protons (disregarding diastereotopic differences). At higher temperatures, the Cope rearrangement becomes fast on the NMR time scale, and only three types of resonances are observed (14 kcal

mol^{-1} for the 1,3,5,7-tetramethyl derivative). When a third bridge is added, as in barbaralone (**5-23**), steric requirements of the rearrangement are improved, and the barrier is lowered



5-23

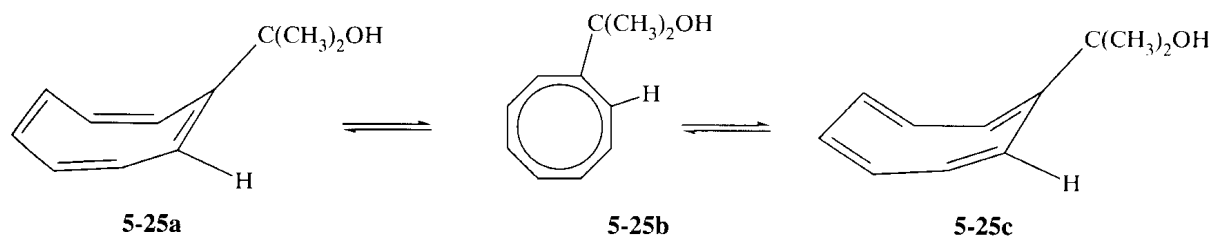
to $9.6 \text{ kcal mol}^{-1}$. When the third bridge is an ethylenic group, the molecule is bullvalene (**5-24**). All three bridges are identical, and a sequence of Cope rearrangements renders all



5-24

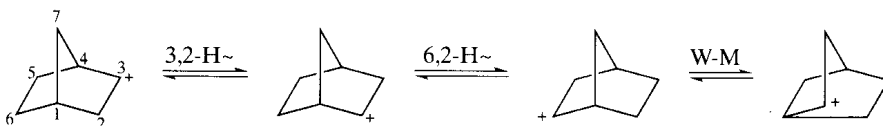
protons (or carbons) equivalent. Indeed, the complex spectrum at room temperature becomes a singlet above 180°C ($12.8 \text{ kcal mol}^{-1}$). Molecules that undergo rapid valence tautomerizations often are said to be *fluxional*.

Cyclooctatetraene offers another example of fluxional behavior. In an operation distinct from boat-boat ring reversal depicted in **5-14**, the locations of the single and double bonds are switched. Anet and co-workers used the same molecule to examine the bond-switching process, whose antiaromatic transition state is **5-25b**. (The transition state to ring reversal



has alternating single and double bonds.) The proton adjacent to the substituent is different in the bond-shift isomers **5-25a** and **5-25c**. The barrier to bond switching was determined from the conversion of the proton resonance from two peaks to one ($17.1 \text{ kcal mol}^{-1}$). The barrier to bond switching is higher than that to ring reversal because of the antiaromatic destabilization that is present in the equal-bond-length transition state **5-25b**.

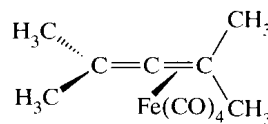
Rearrangements of carbocations also may be studied by NMR methods. The norbornyl cation (**5-26**) may undergo 3,2- and 6,2-hydride shifts, as well as Wagner-Meerwein (W-M)



5-26

rearrangements. The sum of these processes renders all protons equivalent, so that the complex spectrum below -80°C becomes a singlet at room temperature. The slowed process appears to be the 3,2-hydride shift, whose barrier was measured to be 11 kcal mol^{-1} .

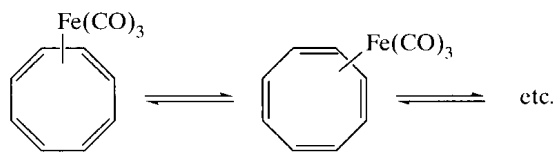
Many examples of fluxional organometallic species have been investigated. Tetramethylalleneiron tetracarbonyl (**5-27**) exhibits three distinct methyl resonances in the ratio



5-27

1 : 1 : 2 at -60°C , in agreement with the structure depicted. Above room temperature, however, the spectrum becomes a singlet (9 kcal mol^{-1}) as the $\text{Fe}(\text{CO})_4$ unit circulates about the allenic π -electron structure by moving orthogonally from one alkenic unit to the other.

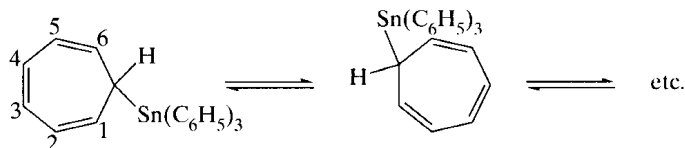
In cyclooctatetreneiron tricarbonyl (**5-28**), the spectrum below -150°C indicates four



5-28

protons on carbons bound to iron and four on carbons not bound to iron, consistent with the η^4 structure shown. Above -100°C , all the protons converge to a singlet as the iron atom moves around the ring as shown. A bond shift occurs with each 45° movement of the iron atom. Eight such operations result in complete averaging of the ring protons or carbons.

A series of 1,5-sigmatropic shifts occurs in triphenyl-(7-cycloheptatrienyl)tin (**5-29**). At 0°C , the spectrum indicates that bond shifts are slow on the NMR time scale, but at 100°C ,



5-29

all of the ring protons are equivalent. That the migration is a 1,5 shift to the 3 or 4 positions (rather than a 1,2 or 1,3 shift) was demonstrated by double-irradiation experiments (saturation transfer; see shortly).

For the simple case of two equally populated sites that do not exhibit coupling (such as cyclohexane- d_{11} in Figure 1-31 or the amide **5-4**), the rate constant (k_c) at the point of maximum peak broadening (the coalescence temperature T_c , approximately -60°C in Figure 1-31) is $\pi\Delta\nu/\sqrt{2}$, in which $\Delta\nu$ is the distance in Hz between the two peaks at slow exchange. The free energy of activation then may be calculated as $\Delta G_c^\ddagger = 2.3RT_c[10.32 + \log(T_c/k_c)]$. This result is extremely accurate and certainly easy to obtain, but the equation is limited in its application. For the two-site exchange between coupled nuclei, the rate constant at T_c is $\pi(\Delta\nu^2 + 6J^2)^{1/2}/\sqrt{2}$.

To include unequal populations, more complex coupling patterns, and more than two exchange sites, it is necessary to use computer programs such as DNMR3, which can simulate the entire line shape at several temperatures. Such a procedure generates Arrhenius plots from which enthalpic and entropic activation parameters may be obtained. The procedure is more elegant and more comprehensive, but it is more susceptible to systematic errors involving inherent line widths and peak spacings, than is the coalescence temperature method. Consequently, it is always a good idea to use both line-shape fitting and coalescence temperature methods, when possible, as an internal check.

The proportionality between k_c and $\Delta\nu$ ($k_c = \pi\Delta\nu/\sqrt{2}$) means that the rate constant is dependent on the field strength (B_0). Thus, a change in field from 300 to 600 MHz alters

the rate constant at T_c . The practical result is that T_c changes. Since the slow exchange peaks are farther apart at 600 MHz, a higher temperature is required to achieve coalescence. At a given field strength, two nuclides such as ^1H and ^{13}C have different values of $\Delta\nu$ and achieve coalescence at different temperatures. Since $\Delta\nu$ is usually larger for ^{13}C than for ^1H , the ^{13}C coalescence temperature often is much higher than the ^1H coalescence temperature [e.g., for the methyl carbons and hydrogens of *N,N*-dimethylformamide (**5-4**), even though a single rate process is involved].

Alternative procedures not requiring peak coalescence have been developed to expand the kinetic dynamic range of NMR. In many cases, coalescence and fast exchange are never attained. The system may exchange too slowly on the NMR time scale at the highest available temperatures (as determined by the temperature range of the spectrometer or the solvent or by the stability of the sample). An alternative technique, called *saturation transfer* or *magnetization transfer*, can provide rate constants without peak coalescence—that is, at the slow exchange limit. Continuous, selective irradiation of one slow-exchange peak may partially saturate the other peak. Some of the nuclei from the first site turn into nuclei of the second type by the exchange process. The intensity of the second peak then is reduced because the newly transformed nuclei already had been saturated in their previous identity. This reduction in intensity is related to the rate constant of interchange and the relaxation time. Saturation transfer is observed for rates in the range from 10^{-3} to 10^1 s^{-1} , which extends the NMR range based on line-shape coalescence (10^0 to 10^4 s^{-1}) on the slow-exchange end by about three orders of magnitude. In addition to expanding the dynamic range of NMR kinetics, this method permits the easy identification of exchanging partners. For example, in the cycloheptatrienyltin **5-29**, saturation of the 7 proton resonance (geminal to tin) at -10°C (below the coalescence temperature) brings about a decrease in the intensity of the 3,4 proton resonance, indicative of a 1,5 shift. A 1,2 shift would have saturated the 1,6 resonance, and a 1,3 shift would have saturated the 2,5 resonance. (The two-dimensional version of this experiment is termed EXSY and is discussed in Chapter 6.)

Rates that are fast on the NMR line-shape time scale (peaks fail to decoalesce at high temperatures) sometimes may be measured by observation at a different resonance frequency. Normally, nuclear spins precess around the B_0 field at their Larmor frequency. Application of the usual 90° pulse in the x direction places the spins in the xy plane, along the y axis. (See Figure 1-15a). Continuous B_1 irradiation along the y axis (not a pulse) forces magnetization to precess around that axis (called *spin locking*, as in the cross-polarization experiment of Section 1-9). The spins are said to be locked onto the y axis. Because the spins are precessing at a lower frequency (γB_1 , rather than γB_0), they are sensitive to a different range of rate processes, one corresponding to about 10^2 to 10^6 s^{-1} , which extends the NMR range on the fast-exchange end by about two orders of magnitude. Rates are obtained by comparing the relaxation time when the system is spin locked ($T_{1\rho}$) with the usual spin-lattice relaxation time (T_1) and analyzing any differences.

Through line-shape, saturation, and spin-lock methods, the entire range of rates accessible to NMR is about 10^{-3} to 10^6 s^{-1} . Thus, NMR has become an important method for studying the kinetics of reactions at equilibrium over a very large dynamic range.

5-3 Multiple Resonance

Special effects may be routinely and elegantly created by using sources of radiofrequency energy in addition to the observation frequency ($\nu_1 = \gamma B_1$) ($\gamma = \gamma/2\pi$). The technique is called *multiple irradiation* or *multiple resonance* and requires the presence of a second transmitter coil in the sample probe to provide the new irradiating frequency ($\nu_2 = \gamma B_2$). When the second frequency is applied, the experiment, which is widely available on modern spectrometers, is termed *double resonance* or *double irradiation*. Less often, a third frequency ($\nu_3 = \gamma B_3$) also is provided, to create a *triple-resonance* experiment. We already have seen several examples of multiple-irradiation experiments, including the removal of

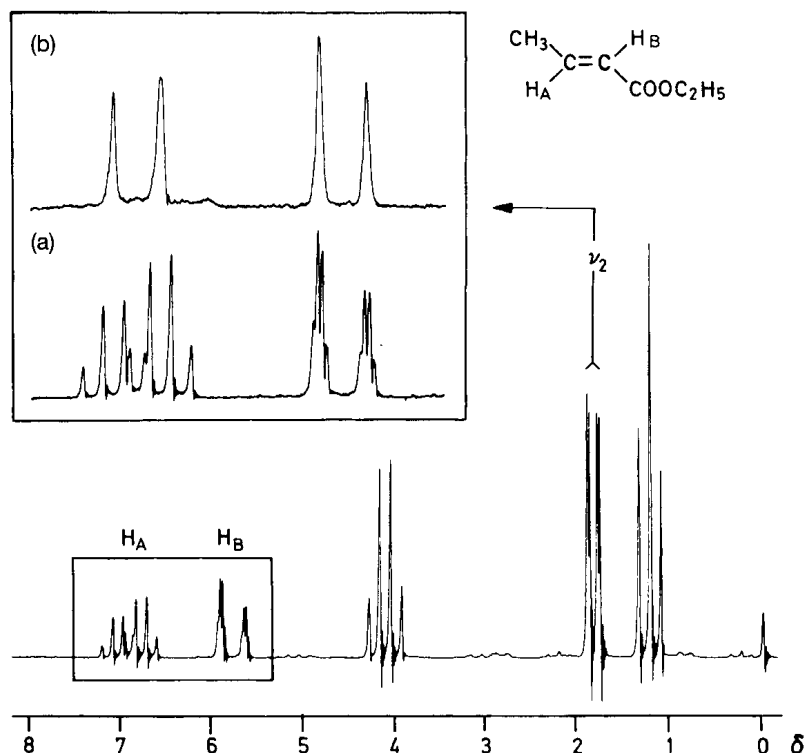
proton couplings from ^{13}C spectra, the elimination of solvent peaks by peak suppression, the sharpening of NH resonances by irradiation of ^{14}N , and the study of rate processes by saturation transfer.

One of the oldest and most generally applicable double-resonance experiments is the irradiation of one proton resonance (H_X) and observation of the effects on the AX coupling (J_{AX}) present in another proton resonance (H_A). The traditional and intuitive explanation for the resulting spectral simplification, known as *spin decoupling*, is that the irradiation shuttles the X protons between the $+\frac{1}{2}$ and $-\frac{1}{2}$ spin states so rapidly that the A protons no longer have a distinguishable independent existence. As a result, the A resonance collapses to a singlet. This explanation, however, is problematic in that it fails to account for phenomena at weak decoupling fields (spin tickling) and even some phenomena at very strong decoupling fields.

The actual experiment involves getting the coupled nuclei to precess about orthogonal axes. The magnitude of the coupling interaction between two spins is expressed by the scalar, or dot, product between their magnetic moments and is proportional to the expression $J\boldsymbol{\mu}_1 \cdot \boldsymbol{\mu}_2 = J\mu_1\mu_2 \cos \phi$. The quantity ϕ is the angle between the vectors (the axis of precession of the nucleus). So long as both sets of nuclei precess around the same (z) axis, ϕ is zero ($\cos 0^\circ = 1$) and full coupling is observed. The geometrical relationship between the spins may be altered by subjecting one of them to a B_2 field. Imagine observing ^{13}C nuclei as they precess around the z axis at the frequency B_1 . When the attached protons are subjected to a strong B_2 field along the x axis, they will precess around that axis. The angle ϕ between the ^{13}C and ^1H nuclear vectors then is 90° , as they respectively precess around the z and x axes. As a result, their spin-spin interaction goes to zero because the dot product is zero ($\cos 90^\circ = 0$). The nuclei are then said to be decoupled.

Spin decoupling has been useful in identifying coupled pairs of nuclei. Figure 5-5 provides such an example for the molecule ethyl *trans*-crotonate (ethyl *trans*-but-2-enoate). The alkenic protons split each other, and both are split by the allylic methyl group to form an ABX_3 spin system. Irradiation at the methyl resonance frequency produces the upper spectrum in the inset for the alkenic protons, which have become a simple AB quartet. A more

Figure 5-5 The ^1H spectrum of ethyl *trans*-crotonate. The inset contains an expansion of the alkenic range (a) without and (b) with decoupling of the methyl resonance at δ 1.8. (Reproduced with permission from H. Günther, *NMR Spectroscopy*, 2d ed., John Wiley & Sons, Ltd., Chichester, UK, 1992, p. 46).



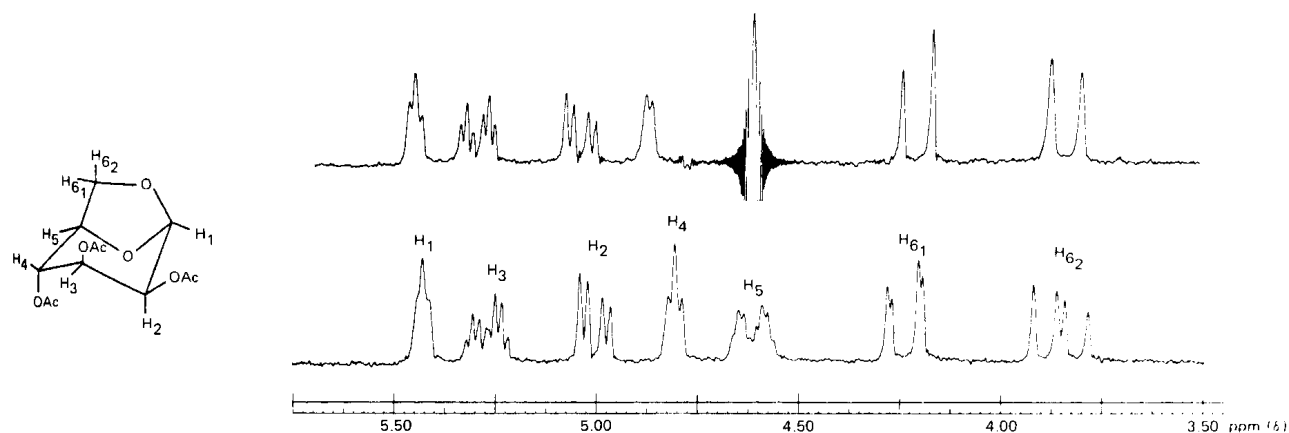


Figure 5-6 The 100 MHz ^1H spectrum of mannosan triacetate in CDCl_3 without decoupling (lower) and with double irradiation at δ 4.62 (upper). (Reproduced with the permission of Varian Associates.)

complex example is illustrated in Figure 5-6. The bicyclic sugar mannosan triacetate, whose structure is given on the left of the figure, has a nearly first-order spectrum with numerous coupling partners. Irradiation of H_5 (δ 4.62) produces simplification of the resonances of its vicinal partners H_4 , $\text{H}_{6/1}$, and $\text{H}_{6/2}$, as well as its long-range zigzag partner H_3 .

With complex molecules, it is useful to record the difference between coupled and decoupled spectra. Features that are not affected by decoupling are subtracted out and do not appear. Figure 5-7 shows the ^1H spectrum of 1-dehydrotestosterone. The complex region between δ 0.9 and 1.1 contains the resonances of four protons. A comparison of the coupled (Figure 5-7a in the inset) and decoupled (Figure 5-7b) spectra from irradiation of the 6α resonance shows little change as the result of double irradiation. The *difference decoupling spectrum* (Figure 5-7c) is the result of subtracting (a) from (b). The unaffected overlapping peaks are gone. The original resonances of the affected protons are observed as negative peaks with coupling, and the simpler decoupled resonances of the same protons are present as positive peaks. The resonances must be due to the 7α protons. The procedure provides coupling relationships when spectral overlap is a serious problem. This and other simple spin-decoupling experiments have been entirely superseded by two-dimensional experiments. (See Chapter 6.)

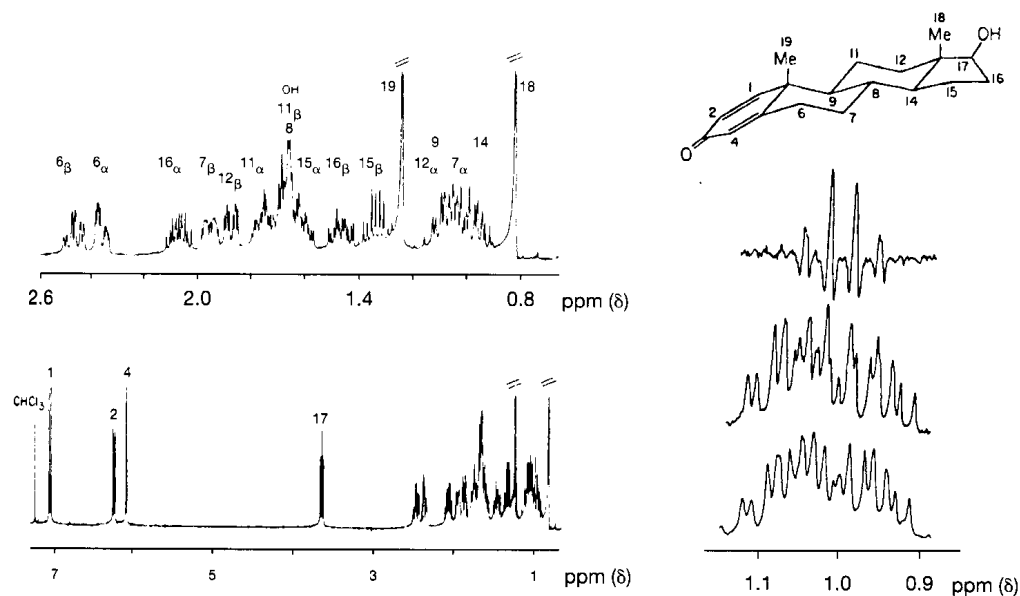


Figure 5-7 The 400 MHz ^1H spectrum of 1-dehydrotestosterone. The complete spectrum and an expansion of the low-frequency region are given on the left. On the right are shown (a) the coupled spectrum for the δ 0.9–1.1 region; (b) the same region, decoupled from the 6α proton; and (c) the difference spectrum obtained by subtracting (b) from (a). (Reproduced with permission from L. D. Hall and J. K. M. Sanders, *J. Am. Chem. Soc.*, **102**, 5703 [1980]. Copyright 1980 American Chemical Society.)

Experiments in which both the irradiated and the observed nuclei are protons are called *homonuclear double-resonance* experiments and are represented by the notation $^1\text{H}\{^1\text{H}\}$. The irradiated nucleus is denoted by braces. When the observed and irradiated nuclei are different nuclides, as in proton-decoupled ^{13}C spectra, the experiment is a *heteronuclear double-resonance* experiment and is denoted, for example, $^{13}\text{C}\{^1\text{H}\}$.

Double-resonance experiments also may be classified according to the intensity or bandwidth of the irradiating frequency. If irradiation is intended to cover only a portion of the resonance frequencies, the technique is known as *selective irradiation/decoupling*. The decoupling shown in Figures 5-5 and 5-6, the peak suppression described in Section 5-1, and the magnetization transfer discussed in Section 5-2 are three examples of selective double irradiation. In the two decoupling experiments, only couplings to the selectively irradiated proton are removed. Nonirradiated resonances can exhibit a small movement in frequency, called the *Bloch–Siegert shift*, which is related to the intensity of the B_2 field and the distance between the observed and irradiated frequencies. An examination of Figure 5-6 reveals several such shifts, found by comparing the relative positions of the resonances in the upper and lower spectra. When all frequencies of a specific nuclide are irradiated, the experiment is termed *nonselective irradiation* or *broadband decoupling*. Figure 1-25 illustrates the ^{13}C spectrum of 3-hydroxybutyric acid both with and without broadband proton double irradiation. The invention of this technique was instrumental in the development of ^{13}C NMR spectroscopy as a routine tool. The double-irradiation field B_2 was traditionally centered at about δ 5 of the ^1H range. To cover all the ^1H frequencies, B_2 was modulated with white noise, so the technique often was called *noise decoupling*.

The broadband decoupling experiment removes coupling patterns that could indicate the number of protons attached to a given carbon atom. The *off-resonance decoupling* method was developed to retain this information and still provide some of the advantages of the decoupling experiment. Irradiation above or below the usual 10-ppm range of ^1H frequencies leaves residual coupling given by the approximate formula $J_{\text{res}} = 2\pi J \Delta\nu / \gamma B_2$, in which J is the normal coupling, γ is the gyromagnetic ratio of the irradiated nucleus, and $\Delta\nu$ is the difference between the decoupler frequency and the resonance frequency of a proton coupled to a specific carbon. Because carbon multiplicities remain intact, this technique is useful for determining, with minimal peak overlap, whether carbons are methyl (quartet), methylene (triplet), methine (doublet), or quaternary (singlet). If methylene protons are diastereotopic, methylene carbons can appear as two doublets. The outer peaks of the off-resonance decoupled triplets and quartets usually are weaker than one might expect from the binomial coefficients. As a result, doublets and quartets sometimes are difficult to distinguish. Figure 5-8 shows the spectrum of vinyl acetate with full decoupling and with off-resonance decoupling. In complex molecules, peak overlap and ambiguities with regard to quartets often make assignments by this technique difficult. Therefore, it has been superseded by the editing experiments described in Section 5-5.

In early spin-decoupling experiments, the irradiation frequency was left on continuously while the experimenter observed the resonating nuclei. There are two significant problems with this method. First, the application of rf energy at the decoupling frequency generates heat. As B_0 fields increased from 100 to 800 MHz, higher decoupling intensities were required. The resulting heating was unacceptable for biological samples and for many delicate organic or inorganic samples. Second, with higher field strengths, it became increasingly more difficult for B_2 to cover the entire range of ^1H frequencies, which had been about 1000 Hz at 100 MHz, but became 5000 Hz at 500 MHz.

To overcome these problems of heteronuclear decoupling, modern methods replaced continuous irradiation with a series of pulses that eliminate the effects of coupling. In a $^{13}\text{C}\{^1\text{H}\}$ experiment (Figure 5-9 for two spins, $^{13}\text{C}-^1\text{H}$), a 90° B_1 pulse applied to the observed ^{13}C nuclei along the x direction moves magnetization from carbon coupled to either spin-up or spin-down protons into the xy plane along the y axis [(Figure 5-9a) \rightarrow (Figure 5-9b)]. The reference frequency is considered to coincide with the y axis and be midway between the

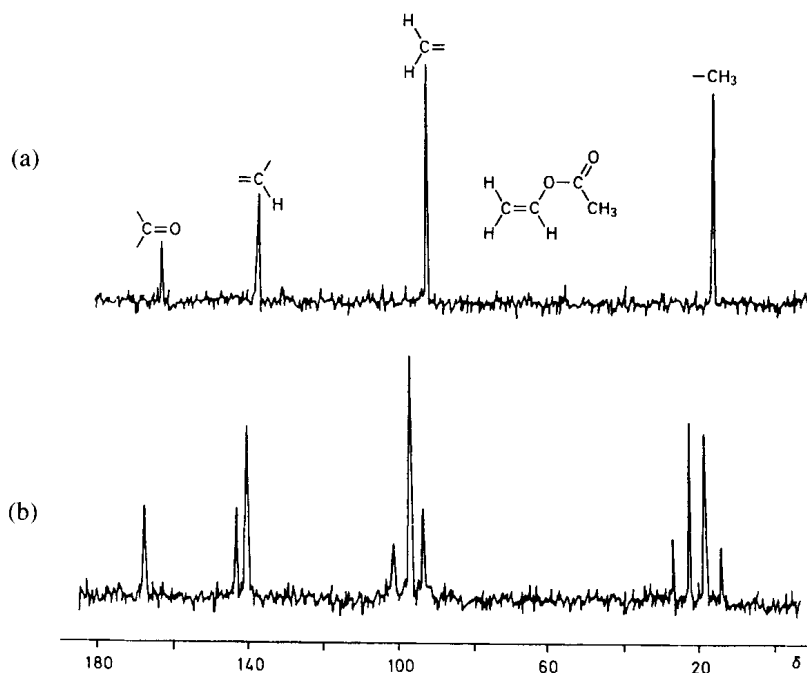


Figure 5-8 The ^{13}C spectrum of vinyl acetate (a) with complete decoupling of the protons and (b) with off-resonance decoupling of the protons. (Reproduced with permission from H. Günther, *NMR Spectroscopy*, 2d ed., John Wiley & Sons, Ltd., Chichester, UK, 1992, p. 270.)

frequencies of the carbons associated with the spin-up (β) and spin-down (α) protons. The two carbon vectors then diverge after the 90° pulse, one becoming faster and the other slower than the carrier frequency (Figure 5-9c). After time τ , a 180° proton pulse (the B_2 of the decoupling experiment) switches the locations of the vectors. The slower moving vector that was dropping behind the carrier frequency now is replaced by the faster moving vector (and the faster moving vector by the slower moving vector), so that both carbon vectors start to move back toward the y axis (Figure 5-9d). After a second period τ , the two vectors coincide on the y axis, only one frequency or peak occurs, and the coupling to the protons disappears (Figure 5-9e). The

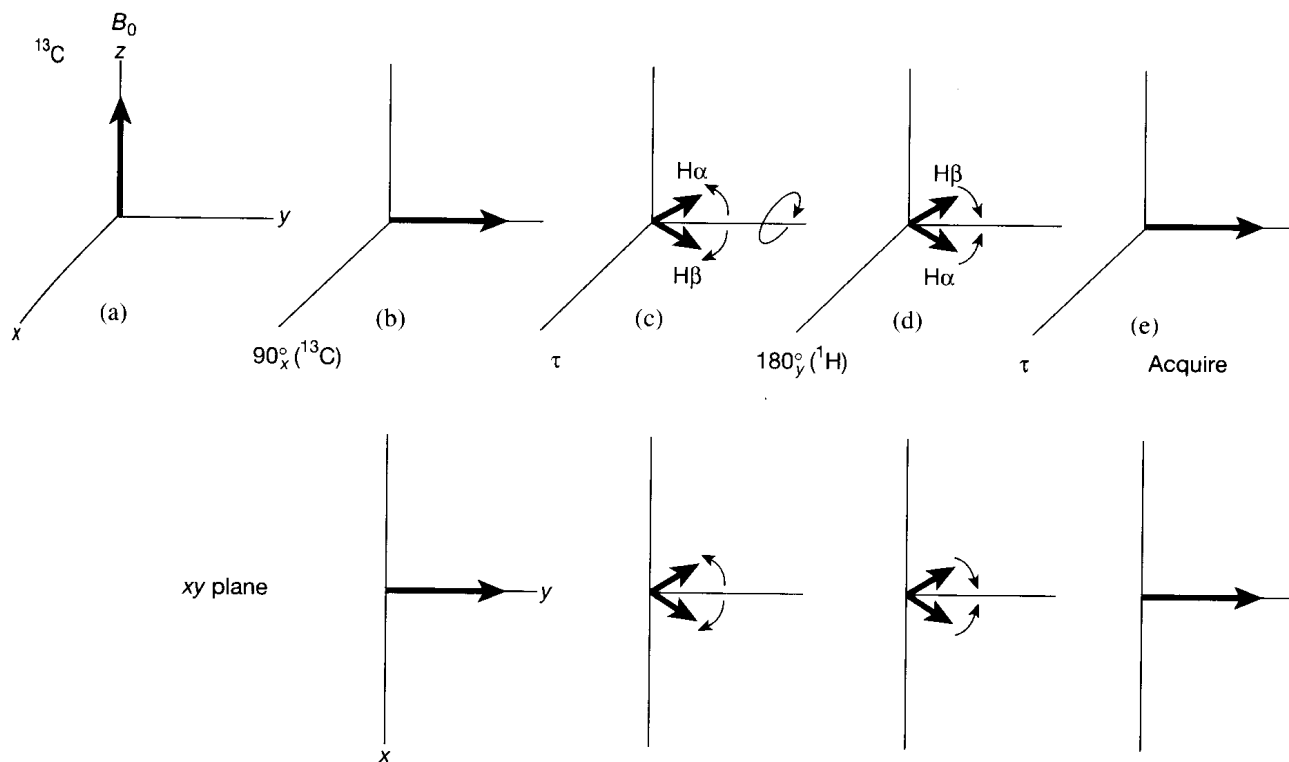


Figure 5-9 Pulse sequence to remove heteronuclear coupling.

process is repeated during acquisition at a rate (in Hz) that is faster than the coupling constant, so that the effects of coupling are removed. In this way, decoupling can be achieved with short pulses rather than with a continuous, high-intensity field. In practice, the method is limited because the 180° pulse must be very accurate or because the B_2 field is inhomogeneous. Refinements of this experiment have been achieved by replacing the 180° pulse with several pulses (*composite pulses*) and by cycling their order (*phase cycling*) so as to cancel out the inaccuracies. (See Section 5-8.) Some successful such methods include MLEV-16 and, in particular, WALTZ-16, which achieves full decoupling across a much wider range than the original continuous method and with a fraction of the power.

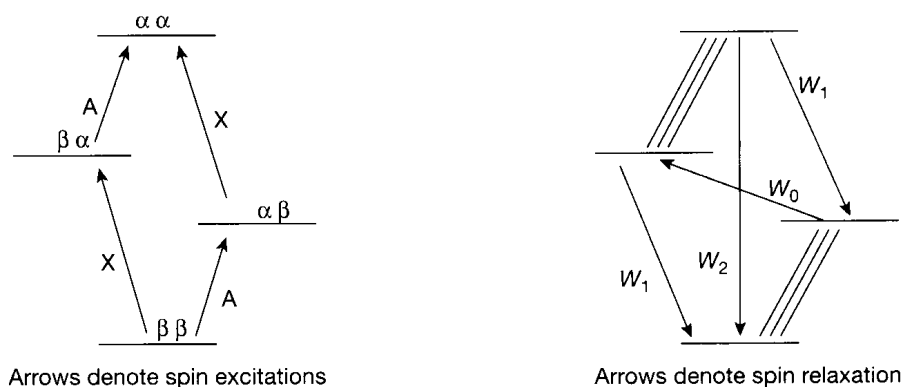
5-4 The Nuclear Overhauser Effect

Dipole–dipole relaxation occurs when two nuclei are located close together and are moving at an appropriate relative rate (Section 5-1). Irradiation of one of these nuclei with a B_2 field alters the Boltzmann population distribution of the other nucleus and therefore perturbs the intensity of its resonance. No J coupling need be present between the nuclei. The original phenomenon was discovered by Overhauser, but between nuclei and unpaired electrons. The *nuclear* Overhauser effect (when both spins are of nuclei) was observed first by Anet and Bourn and is of more interest to the chemist. It has great structural utility, because the dipole–dipole mechanism for relaxation depends on the distance between the two spins. (See eq. 5-1.)

The origin of the *Nuclear Overhauser Effect* (NOE) is illustrated in Figure 5-10. On the left are the states for two spins (A and X) in the absence of double irradiation. (The effects of J are ignored.) The diagram represents an expansion of Figure 1-4(a) for one spin, with β standing for $+\frac{1}{2}$ and α for $-\frac{1}{2}$. There are four spin states: when both spins are β , when the first (A) is β while the second (X) is α , when the first is α while the second is β , and when both are α . There are two A-type transitions (when the A spin flips from β to α)—for example, $\beta\beta$ to $\alpha\beta$ —and there are two X-type transitions—for example, $\alpha\beta$ to $\alpha\alpha$. When $J = 0$, the two A transitions coincide, as do the two X transitions. Because chemical shifts are very small in comparison with the Larmor frequency, the $\alpha\beta$ and $\beta\alpha$ states are almost degenerate. Their difference has been exaggerated enormously to emphasize the different chemical shifts.

The normal intensities of the A and X resonances are determined by the difference between the populations of the upper and lower spin states in a spin transition—for instance, between $\alpha\beta$ and $\alpha\alpha$ for one X transition. In the NOE experiment, one resonance frequency (A) is doubly irradiated, and intensity perturbations are monitored at the other resonance frequency (X). When the A resonance is irradiated, as is represented by the multiple parallel lines in the right-hand diagram of Figure 5-10, the population difference between the spin states connecting an A transition decreases through partial saturation. Compared with the normal situation on the left, the populations of $\alpha\alpha$ and $\alpha\beta$ (the upper states) have increased, while those of $\beta\alpha$ and $\beta\beta$ (the lower states) have decreased. Relaxation from $\alpha\alpha$ to $\beta\beta$, labeled W_2 in the figure, can help restore the system to equilibrium.

Figure 5-10 Left: The spin states for a normal two-spin (AX) system. Right: The spin states for an AX system when the frequency of A is doubly irradiated.



The new equilibrium present with A irradiation thus can carry spins along the route $\beta\alpha \rightarrow \alpha\alpha \rightarrow \beta\beta \rightarrow \alpha\beta$, depleting $\beta\alpha$ and augmenting $\alpha\beta$. (In a first approximation, the populations of $\alpha\alpha$ and $\beta\beta$ are constant.) Depleting $\beta\alpha$ enhances the population difference for one X transition ($\beta\beta \rightarrow \beta\alpha$), and augmenting $\alpha\beta$ enhances the population difference for the other X transition ($\alpha\beta \rightarrow \alpha\alpha$). This enhanced polarization of nuclear spin states means that the X intensity is higher in the new equilibrium during the irradiation of A. Normal relaxation of X nuclei, labeled W_1 in the figure ($\alpha\alpha \rightarrow \alpha\beta$ or $\beta\alpha \rightarrow \beta\beta$), does not alter the X intensity. These processes are unchanged from the diagram on the left and cannot generate population changes.

Relaxation from $\alpha\beta$ to $\beta\alpha$ (called W_0 in Figure 5-10) also can move the irradiated system back toward equilibrium. This relaxation mechanism actually would result in a decrease in intensity of X, since it depletes $\alpha\beta$ and augments $\beta\alpha$, the opposite of what W_2 does. For liquids and relatively small molecules, $W_0 \ll W_2$, and enhanced intensities are expected. The frequencies of W_2 are in the MHz range (represented by the large distance between the $\beta\beta$ and $\alpha\alpha$ levels in the figure), whereas those of W_0 are much smaller, in the kHz or Hz range [represented by the small (but exaggerated) distance between the $\alpha\beta$ and $\beta\alpha$ levels]. Small molecules tumbling in solution produce fields in the MHz range and hence can provide W_2 relaxation. On the other hand, large molecules tumbling in the Hz or kHz range can provide W_0 relaxation.

Double irradiation of A in molecules of molecular weight up to about a thousand thus enhances the X intensity, provided that the two nuclei are close enough for W_2 relaxation to dominate (less than about 5 Å). This circumstance corresponds to what we previously referred to as the extreme narrowing limit. For larger molecules—certainly those with molecular weights over 5,000— W_0 dominates, and reductions in peak intensity or inverse peaks occur. At some intermediate size (1,000–3,000), the effect disappears as the crossover between regimes occurs. The change in intensity [denoted by the Greek letter η (eta)] thus depends on the difference between the W_2 and W_0 relaxation rates, in comparison with the total relaxation rates, as given by the equation

$$\eta = \frac{\gamma_{\text{irr}}}{\gamma_{\text{obs}}} \left(\frac{W_2 - W_0}{W_0 + 2W_1 + W_2} \right). \quad (5-3)$$

(With two modes, W_1 is doubled). The effect is observed by comparing intensities I in the presence of double irradiation with those I_0 in its absence via the formula

$$\eta = \frac{(I - I_0)}{I_0} \quad (5-4)$$

For small molecules (the extreme narrowing limit), the maximum increment in intensity, η_{max} , is $\gamma_{\text{irr}}/2\gamma_{\text{obs}}$, so that an initial intensity of unity ($I_0 = 1.0$) increases up to $(1 + \eta_{\text{max}})$. [In our example, A was irradiated (“irr”) and X observed (“obs”).] The maximum enhanced intensity, obtained by rearrangement of eq. 5-4, is given by

$$I_{\text{max}}(\text{NOE}) = I_0 \left(1 + \frac{\gamma_{\text{irr}}}{2\gamma_{\text{obs}}} \right). \quad (5-5)$$

The increase is almost always less than the maximum, because nondipolar relaxation mechanisms are present and because the observed nucleus is relaxed by nuclei other than the irradiated nucleus.

Whenever the two nuclei are the same nuclide (e.g., both protons), the gyromagnetic ratios in eq. 5-5 cancel, η_{max} becomes 0.5, and the maximum intensity enhancement $(1 + \eta_{\text{max}})$ is a factor of 1.5, or 50%. For the common case of broadband ^1H irradiation with observation of ^{13}C , [$^{13}\text{C}\{^1\text{H}\}$] η_{max} is 1.988, so the enhancement is a factor of up to 2.988, or about 200%. Other maximum Overhauser enhancement factors $(1 + \eta_{\text{max}})$ include 2.24 for $^{31}\text{P}\{^1\text{H}\}$, 3.33 for $^{195}\text{Pt}\{^1\text{H}\}$, and 3.39 for $^{207}\text{Pb}\{^1\text{H}\}$.

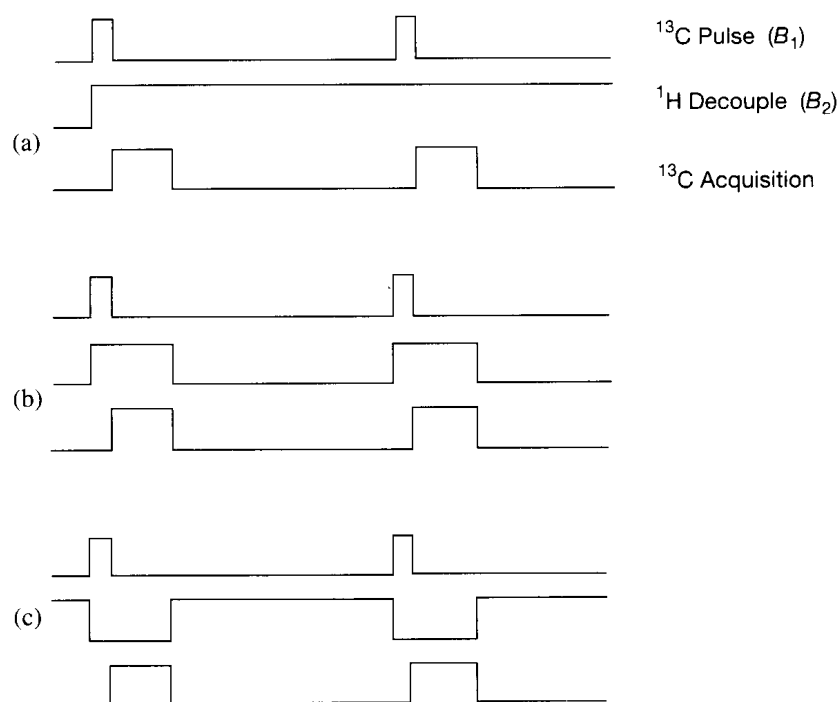
Certain nuclei have negative gyromagnetic ratios, so that η_{\max} becomes negative and a negative peak can result. For irradiation of ^1H and observation of $^{15}\text{N}\{^{15}\text{N}\{^1\text{H}\}\}$, η_{\max} is -4.94 . The maximum negative intensity is thus 3.94 times that of the original peak, or an increase of 294% $[(3.94 - 1.00) \times 100]$, but as an inverse peak. If dipolar relaxation is only partial, the $^{15}\text{N}\{^1\text{H}\}$ NOE can result in a completely nulled resonance. Silicon-29 also has a negative gyromagnetic ratio, so similar complications ensue. For the $^{29}\text{Si}\{^1\text{H}\}$ experiment, $\eta_{\max} = -2.52$. The maximum enhancement factor $(1 + \eta_{\max})$ is then -1.52 , which results in an inverted intensity with an increase of 52% over the unirradiated case. For $^{119}\text{Sn}\{^1\text{H}\}$ ($\eta_{\max} = -1.34$), there is actually a net loss in intensity. The maximum enhancement factor is -0.34 , representing a 66% loss in intensity of the negative peak, compared with the peak at the unirradiated position. The NOE is entirely independent of spectral changes that arise from the collapse of spin multiplets through spin decoupling. The NOE does not require that nuclei A and X be spin coupled—only that they be mutually relaxed through a dipolar mechanism.

Large molecules, such as proteins or nucleic acids, with molecular weights over about 5,000 are dominated by W_0 relaxation. Since the other terms (W_2 and W_1) in eq. 5-3 are small, the value of η_{\max} becomes -1 for the case of a homonuclear proton. Such a situation can result in a loss of signal. Consequently, for large molecules, transient rather than steady-state NOE's often are studied. For example, the buildup (or loss) of signal from the NOE can provide interproton distances. By observing many such relationships, the structures of large biomolecules may be determined quantitatively in a process that rivals X-ray crystallography, but applies to the liquid state (Nobel Prize, 2002).

At the crossover between the extreme narrowing and the large-molecule limits, it is possible that W_2 and W_0 are comparable in magnitude, so that, by eq. 5-3, the NOE goes to zero. The spectroscopist may improve the situation somewhat by changing the solvent or the temperature in order to alter τ_c . Viscosity, in addition to molecular size, can affect the tumbling rate and hence the rate of dipolar relaxation. Thus, viscous media can lower nuclear Overhauser enhancements.

In the traditional NOE experiment, the spectrum is recorded twice, with and without the NOE. Figure 5-11 illustrates the relative timing for the heteronuclear case of a ^{13}C pulse (B_1), a ^1H double irradiation field (B_2), and acquisition of the ^{13}C signal (not to scale) in order to carry out these two experiments. In the original experiment with continuous

Figure 5-11 (a) Observation of ^{13}C with continuous double irradiation of ^1H (decoupling and NOE). (b) Double irradiation applied during acquisition, but gated off during the wait period (decoupling, no NOE). (c) Double irradiation applied only during the wait period (NOE, no decoupling). The pulse widths are not to scale. The scheme is shown for two cycles.



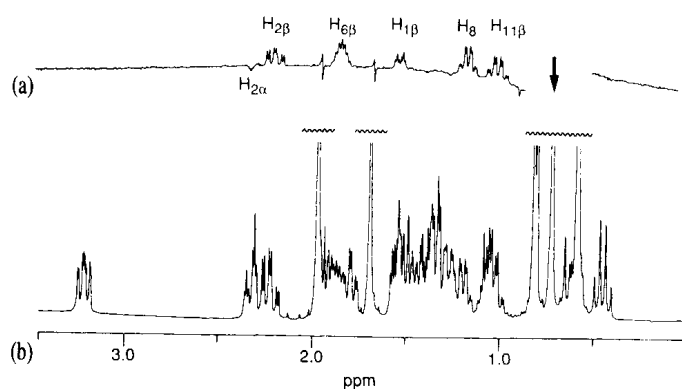
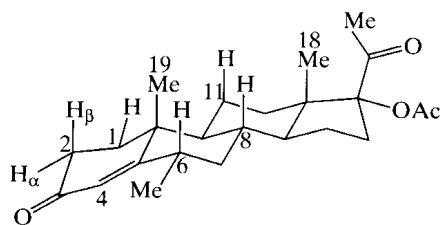


Figure 5-12 The 400 MHz ^1H spectrum (in part) of progesterone (a) without double irradiation and (b) with irradiation of the CH_3-19 resonance displayed as a difference spectrum. (Reproduced with permission from J. K. M. Sanders and B. K. Hunter, *Modern NMR Spectroscopy*, 2d ed., Oxford University Press, Oxford, UK, 1993, p. 191.)

broadband decoupling (Figure 5-11a), the B_2 field is turned on and left on. To ensure decoupling, it must be on not only during acquisition, but also during the recovery time, when relaxation occurs and the NOE builds up, although the power can be lower during times other than acquisition (*power-gated decoupling*). This experiment results in both decoupling and the Overhauser effect, providing the quantity I in eq. 5-4. By gating the decoupler off during the recovery period, as in (Figure 5-11b), but keeping it on during acquisition, the spectroscopist obtains decoupling, but no NOE, providing the quantity I_0 in eq. 5-4. Without irradiation during the recovery period, there is insufficient time for the NOE to build up, and unperturbed intensities are obtained. In practice, the double-resonance frequency is not actually turned off, but is moved far off resonance. A comparison of the intensity I in experiment (a) with the intensity I_0 in experiment (b) provides the NOE via eq. 5-4. Figure 5-11c illustrates an alternative procedure, in which the B_2 field is gated off during acquisition, but is on during the recovery period. Such an experiment provides no decoupling, but generates the NOE, so it is useful for measuring $^1\text{H}-^{13}\text{C}$ couplings with enhanced intensity.

For the homonuclear proton NOE experiment ($^1\text{H}\{^1\text{H}\}$) that parallels experiments (a) and (b) in Figure 5-11, it has traditionally been supposed that the NOE (in percentage, 100η) must exceed about 5% to be accepted as experimentally significant. The *difference NOE experiment*, however, can measure enhancements reliably to below 1%. In this procedure, spectra obtained by the methods analogous to Figure 5-11a and b are alternatively recorded and subtracted. Unaffected resonances disappear, and NOE's are signified by residual peaks.

Figure 5-12 illustrates the difference NOE spectrum for a portion of the ^1H spectrum of progesterone (5-30), in which the 19 methyl group has been irradiated (arrow). The unirradiated spectrum is given at the bottom, the difference spectrum at the top. Enhancements



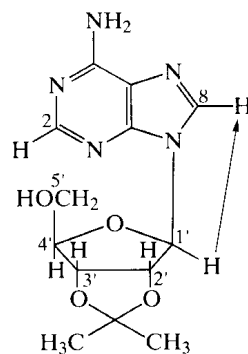
5-30

are seen by difference for five nearby protons. In general, for molecules in the extreme narrowing limit, the NOE difference experiment is preferred to the direct experiment. Proton $\text{H}_{2\alpha}$ (the equatorial 2 proton) is not close to the 19 methyl group, but its resonances show a small negative NOE. This finding is the result of a three-spin effect. (A is relaxed by B and B by C.) Irradiation at A increases the Boltzmann population for B and enhances the intensity of B. By spin diffusion (Section 5-1), this enhanced intensity of B has the opposite effect on C, decreasing the Boltzmann population and the intensity. As a result, C appears as a negative peak in the difference NOE spectrum. In this example, A is Me-19, B is $\text{H}_{2\beta}$, and C is $\text{H}_{2\alpha}$. The process occurs most commonly with very large molecules.

The NOE experiment has three distinct uses. For heteronuclear examples, the foremost use is the increase in sensitivity, which combines with the collapse of multiplets through decoupling to provide the standard ^{13}C spectrum composed of a singlet for each carbon. Because most carbons are relaxed almost entirely by their attached protons, the NOE commonly attains a maximum value of about 200%. Quaternary carbons, with more distant nearest neighbors, do not enjoy this large enhancement.

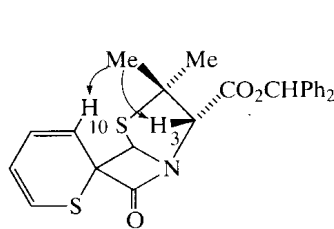
Second, interpreting ^{13}C spin-lattice relaxation routinely requires a quantitative assessment of the dipolar component, $T_1(\text{DD})$. Because the NOE results from dipolar relaxation, its size is related to the dipolar percentage of overall relaxation. If the maximum, or full, NOE for $^{13}\text{C}\{^1\text{H}\}$ of 200% is observed, then $T_1(\text{obs}) = T_1(\text{DD})$. When other relaxation mechanisms contribute to ^{13}C relaxation, the enhancement is less than 200%. The dipolar relaxation for $^{13}\text{C}\{^1\text{H}\}$ then may be calculated from the expression $T_1(\text{DD}) = \eta T_1(\text{obs})/1.988$, in which η is the observed NOE and 1.988 is the maximum NOE (η_{max}). It is possible then to discuss $T_1(\text{DD})$ in terms of structure, according to eq. 5-1.

In the third application, the dependence of the NOE on internuclear distances can be exploited to determine structure, stereochemistry, and conformation. Enhancements are expected when nuclei are close together. The adenosine derivative **5-31** (2', 3'-isopropylidene adenosine) can exist in the conformation shown with the purine ring lying over the sugar

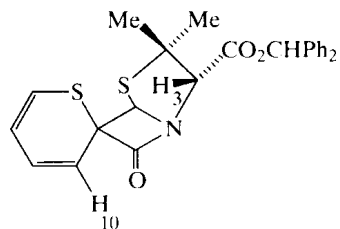


5-31

ring (syn) or in an extended form with the proton on C8 lying over the sugar ring (anti). Saturation of the H1' resonance brings about a 23% enhancement of the H8 resonance, and saturation of H2' produces an enhancement of H8 of 5% or less. Thus, H8 must be positioned most closely to H1', as in the syn form shown. Structural and stereochemical distinctions frequently are made possible by determining the relative orientations of protons. The synthetic penicillin derivative **5-32** could have the spiro sulfur heterocycle oriented either



5-32a



5-32b

as shown in (a) or with the sulfur atom and $(\text{CH})_{10}$ switched, as in (b). Irradiation of the methyl protons brings about an enhancement of H10 as well as H3 and clearly demonstrates that the stereochemistry is as shown in **5-32a**.

Despite the considerable advantages of the NOE experiment, its limitations must be appreciated. First, three-spin effects, or spin diffusion, may cause misleading intensity perturbations when the third spin is not close to the irradiated nucleus ($\text{H}_{2\alpha}$ in Figure 5-12). Second, the size of the molecule can cause NOE effects that are positive, negative, or null.

Third, nuclei with negative gyromagnetic ratios can give diminished positive peaks, no peak, or negative peaks with diminished or enhanced intensity. Fourth, chemical exchange can cause an intensity perturbation analogous to the three-spin effect. Irradiation of a nucleus can lead to intensity changes at another nucleus, which can alter its chemical identity through a dynamic exchange such as a bond rotation or valence tautomerization. The NOE can then be observed for the product nucleus—if chemical exchange is faster than relaxation of the NOE effects. Fifth, unintentional paramagnetic impurities can alter the NOE through intermolecular dipole–dipole relaxation. All these considerations must be taken into account in interpreting NOE experiments. Despite its limitations, the NOE is a very powerful tool for enhancing intensities and identifying structures.

5-5 Spectral Editing

For deducing the structure of organic molecules, one of the most useful pieces of information is a compilation of the substitution pattern of all the carbons—that is, a census of which carbons are methyl, methylene, methine, or quaternary. We have already seen (Figure 5-8) that the off-resonance decoupling procedure provides such information, although with less-than-ideal results. Through the choice of appropriate pulses and timing, the chemist may accomplish the same task by eliminating some of the resonances from the spectrum or by reversing their polarization. Such an experiment is called *spectral editing* and includes solvent suppression for example.

Most spectral editing procedures are based on the *spin echo* experiment devised by Hahn, Carr, Purcell, Meiboom, and Gill in the 1950s, largely to measure spin–spin relaxation times (T_2). An example of this experiment was given in Figure 5-9, in which a 180° pulse brought vectors from spin–spin interactions back together on the y axis as an echo. Such a procedure also refocuses dispersion in the chemical shift caused by magnetic inhomogeneity in the following fashion. As shown in Figure 5-13, in the absence of J , a resonance (Figure 5-13b) fans out over a range of frequencies (Figure 5-13c), because not every nucleus of a given type has exactly the same resonance frequency in an inhomogeneous field. The 180° pulse refocuses all the magnetization back onto the y axis after time 2τ , as in Figure 5-13e. Chemical-shift differences also may be eliminated in this fashion. Repetition of the 180° pulse every 2τ produces a train of peaks whose intensities die off with time constant T_2 . This relaxation time provides a measure of spin–spin interactions alone. (The notation T_2^* sometimes is used to denote transverse relaxation that includes the effects of inhomogeneity.)

Although developed to measure T_2 , this pulse sequence is able to improve resolution or eliminate coupling constants or chemical shifts after a single cycle. Moreover, it may be modified to achieve other effects. To obtain information about how many protons are attached to a carbon, the coupling information must be manipulated in a fashion different from that used, for example, in Figure 5-5. This is a double-resonance procedure, with pulses

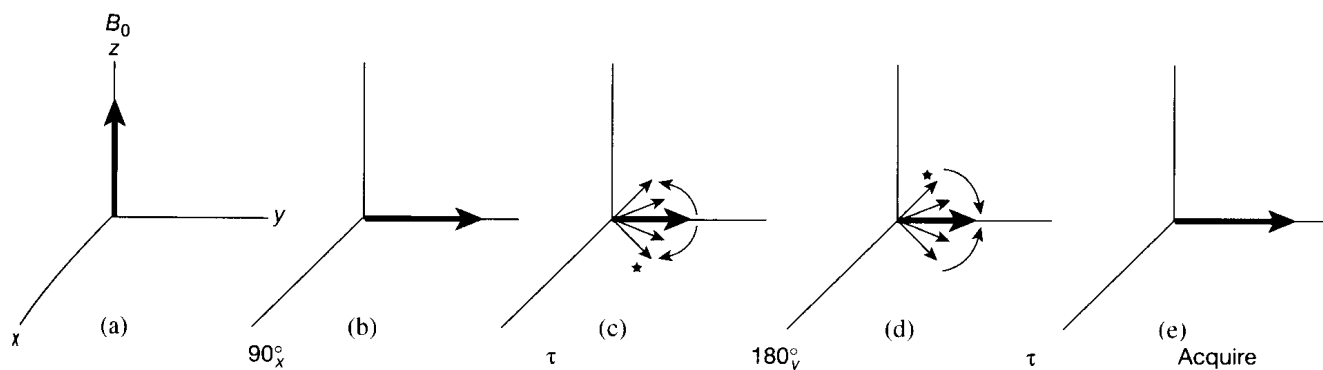


Figure 5-13 Spin echo experiment to eliminate the effects of B_1 inhomogeneity.

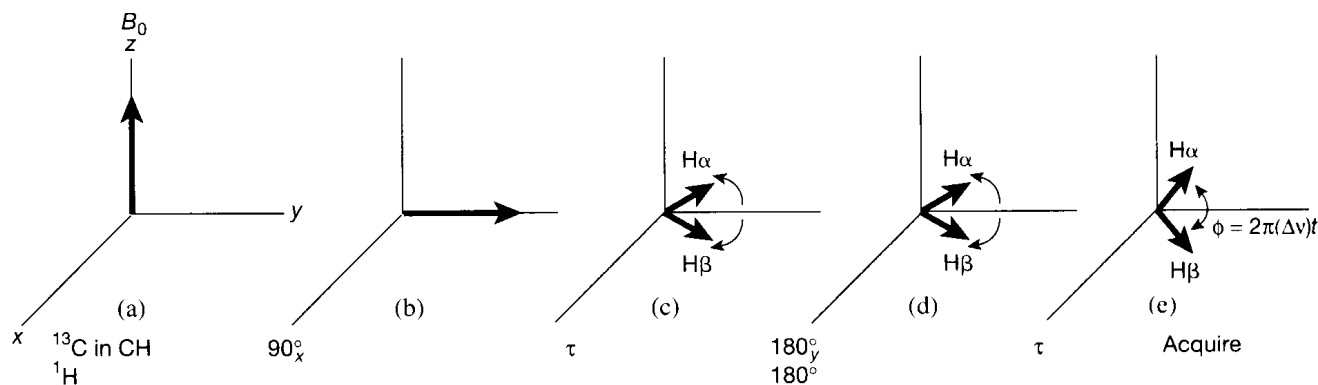


Figure 5-14 Pulse sequence that allows spin vectors to evolve to an arbitrary frequency separation ϕ .

applied at both $^{13}\text{C}(B_1)$ and $^1\text{H}(B_2)$ frequencies (Figure 5-14 for a methine group, $^{13}\text{C}\text{-}^1\text{H}$, with the reference frequency set at the ^{13}C resonance). The protons are subjected to a 180° pulse at the same time that the carbons are subjected to their 180° pulse. The two pulses cancel each other, and the vectors from spin–spin coupling continue to diverge, as in Figure 5-14d. The cancellation occurs in the following fashion. Just as the ^{13}C spins are rotated by the 180° ^{13}C pulse between (c) and (d), the signs of the ^1H spins are reversed by the 180° ^1H pulse. At point (c), the $+\frac{1}{2}$ protons are precessing around the $+z$ axis and the $-\frac{1}{2}$ protons around the $-z$ axis, as in Figure 1-10. The 180° ^1H pulse (around either the x or the y axis) switches these identities. The nuclei that were precessing around the $+z$ axis ($+\frac{1}{2}$) are now precessing around the $-z$ axis ($-\frac{1}{2}$), and vice versa. Consequently, the identities of the protons have all been switched. Consider, for example, the faster moving ^{13}C vector, which may have been associated with the $+\frac{1}{2}$ protons ($\text{H}\beta$). After the 180° ^{13}C rotation, the vector would start catching up to the y axis in the absence of the 180° ^1H pulse (as was the case in Figure 5-9d). In the presence of the pulse, however, this vector is now associated with $-\frac{1}{2}$ protons ($\text{H}\alpha$) and hence is still dropping behind the carrier frequency, as shown in Figure 5-14d. Thus, the effects of the two 180° pulses (^{13}C and ^1H) on the vectors derived from coupling cancel out, but those on inhomogeneity do not. The net effect is to achieve an improvement in homogeneity, while at the same time controlling the angle of divergence between the vectors that arise from spin–spin splitting. After the second τ period (total time $t = 2\tau$), these vectors have further diverged to an arbitrary angle ϕ , which is dependent on the difference in their frequencies ($\Delta\nu = J$) and on the total time since the initial 90° pulse; that is, $\phi = (\Delta\omega)t = 2\pi(\Delta\nu)t = 2\pi J(2\tau) = 4\pi J\tau$.

As an aside, in a homonuclear decoupling experiment such as $^1\text{H}\{^1\text{H}\}$, a 180° pulse that follows the initial 90° pulse by a time τ has the same effect as the pair of 180° pulses in Figure 5-14. The $90^\circ\text{-}\tau\text{-}180^\circ\text{-}\tau\text{-}$ acquire homonuclear sequence results in a refocusing of field inhomogeneities, but continued divergence of the two vectors. The 180° nonselective pulse not only rotates the directions of the vectors for the observed nucleus in the manner of Figure 5-14c, but also rotates all of the spins of the irradiated nucleus from above the xy plane to below it and vice versa, thus flipping the spins. For example, the pulse rotates the faster moving vector for the observed nucleus around the y axis. Because of the switch of spins of the irradiated nucleus, it becomes the more slowly moving vector and hence continues to move away from the y axis. After time 2τ , the angle between the vectors is $\phi = 2\pi(\Delta\nu)(2\tau)$.

Returning to the spectral editing experiment begun in Figure 5-14, let us set the time τ to the specific value of $(2J(^{13}\text{C}\text{-H}))^{-1}$ (J is the coupling between the carbon and hydrogen in the methine group; see Figure 5-15.) The vectors diverge during one period τ until they are 180° apart, as in Figure 5-15d, since $\phi = 2\pi J(2J)^{-1} = \pi$. After the full pulse sequence ($\tau = 2\pi$), the angle between the vectors is $4\pi J(2J)^{-1}$, or 2π , as in Figure 5-15e). If

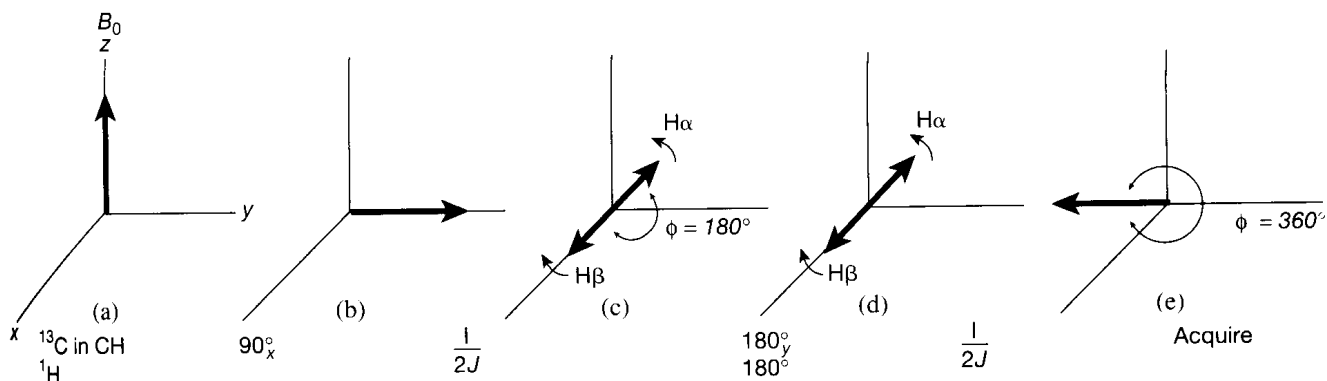


Figure 5-15 Pulse sequence for spectral editing of a methine (CH) resonance.

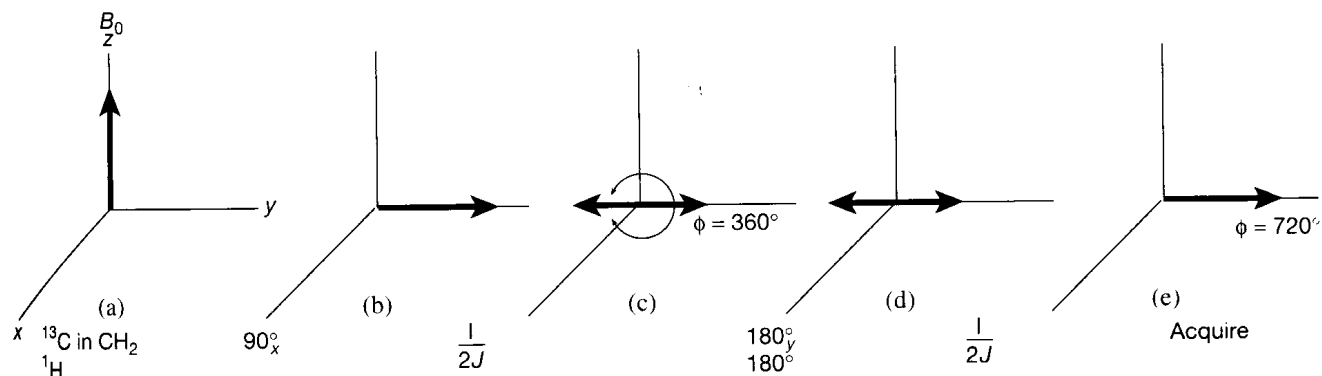


Figure 5-16 Pulse sequence for spectral editing of a methylene (CH_2) resonance.

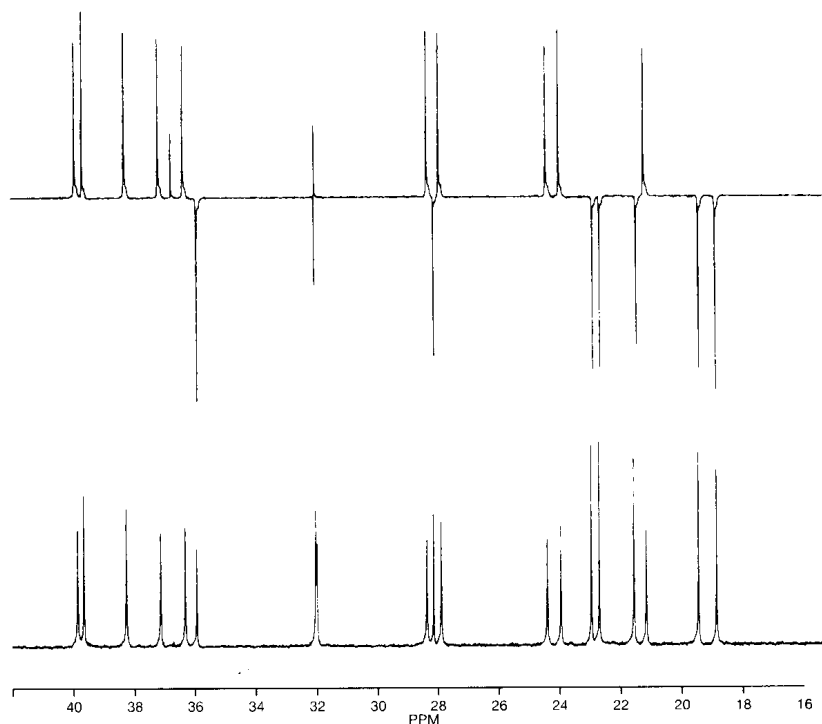
the spectrum is sampled at this time, the result is a negative singlet, because the spins are all aligned along the negative y direction.

If the same experiment is carried out for a carbon attached to two protons (CH_2 ; see Figure 5-16), the middle peak of the triplet remains on the y axis (coincident with the reference frequency, like the $+y$ vector in Figure 5-16c), and the diverging peaks now differ by $\Delta\nu = 2J$ (the distance between the outer peaks of the triplet). The value of $\phi = 2\pi(\Delta\nu)t$ after τ then is $2\pi(2J)(\tau)$, so that, for $\tau = (2J)^{-1}$, the angle is $4\pi J(2J)^{-1}$, or 2π , as for the $-y$ vector in Figure 5-16c and d. After 2τ , $\phi = 4\pi$, so that both vectors are coincident with the positive y axis, as in Figure 5-16e. Consequently, we get a positive peak for methylene carbons and a negative peak for methine protons. Quaternary carbons, of course, always give a positive peak, because, being unsplit, they remain on the positive y axis throughout these pulses. The value of $\Delta\nu$ for the four peaks of a methyl carbon is either J (the middle two peaks) or $3J$ (the outer two peaks), which results in refocusing all vectors onto the negative y axis after 2τ and hence produces a negative peak.

Figure 5-17 illustrates the result of the complete editing experiment for cholesteryl acetate, which gives negative peaks for CH and CH_3 resonances and positive peaks for C and CH_2 . Proton irradiation during acquisition provides decoupling. This experiment affords a visual identification of the substitution pattern of all carbons, and has been called *J modulation* or the *Attached Proton Test* (APT). It exists in many variants.

The procedure illustrated in Figure 5-17 does not distinguish between methine and methyl carbons, so alternative editing procedures have been developed that can provide

Figure 5-17 Lower: The normal proton-decoupled ^{13}C spectrum of cholesteryl acetate. Upper: The attached proton test (APT), phased so that CH_2 and quaternary carbons are positive and CH and CH_3 carbons are negative. (Reproduced with permission from A. E. Derome, *Modern NMR Techniques for Chemical Research*, Pergamon Press, Oxford, UK, 1987, p. 261.)



separate spectra for each substitution pattern. Figure 5-18 illustrates the full set of spectra for the trisaccharide gentamycin, using the DEPT pulse sequence (defined in greater detail in the next section). The DEPT experiment often is presented alternatively as three, rather than four, spectra: the fully decoupled spectrum with all carbons as positive singlets, a spectrum with only CH carbons as positive singlets, and a spectrum with CH_3 and CH carbons positive and CH_2 carbons negative (quaternary carbons then are identified by difference from the complete spectrum). The various DEPT experiments probably are the most commonly used experiments today for ascertaining carbon substitution patterns, because (1) they depend less on the exact value of J than does the aforementioned APT experiment, (2) they provide signal enhancement (Section 5-6), and (3) they easily distinguish CH and CH_3 groups. An edited ^{13}C spectrum is a standard, and sometimes necessary, part of the structural analysis of complex organic molecules.

5-6 Sensitivity Enhancement

Some important nuclei, including ^{13}C and ^{15}N , have low natural abundances and sensitivities. Pulse sequences have been devised to improve the observability of these nuclei when they are coupled to another nucleus of high receptivity, usually a proton. Pulses are applied in such a way that the favorable population of the sensitive nucleus S is transferred to the insensitive nucleus I . A common sequence developed by Freeman for this purpose is called INEPT, for *Insensitive Nuclei Enhanced by Polarization Transfer*, as follows:

$$\begin{array}{l} {}^1\text{H}(S) \quad 90_x^\circ - 1/4J - 180_y^\circ - 1/4J - 90_y^\circ \\ {}^{13}\text{C}(I) \quad \quad \quad 180^\circ - 1/4J - 90_x^\circ - \text{Acquire} \end{array}$$

The pulses are closely related to the spin echo experiment in Figure 5-14, with $\tau = (4J)^{-1}$ chosen to leave the ${}^1\text{H}$ and ${}^{13}\text{C}$ spin vectors 180° apart, or *antiphase*, after 2τ ($\phi = 2\pi J \cdot 2 \cdot (4J)^{-1} = \pi$). The additional 90° pulses after 2τ are necessary to place the vectors on the appropriate axes.

The results of the pulses are illustrated in Figure 5-19 for the case of two spins—for example, ${}^1\text{H}$ – ${}^{13}\text{C}$. The first set of pulses is applied to the sensitive nucleus (${}^1\text{H}$) to prepare it in

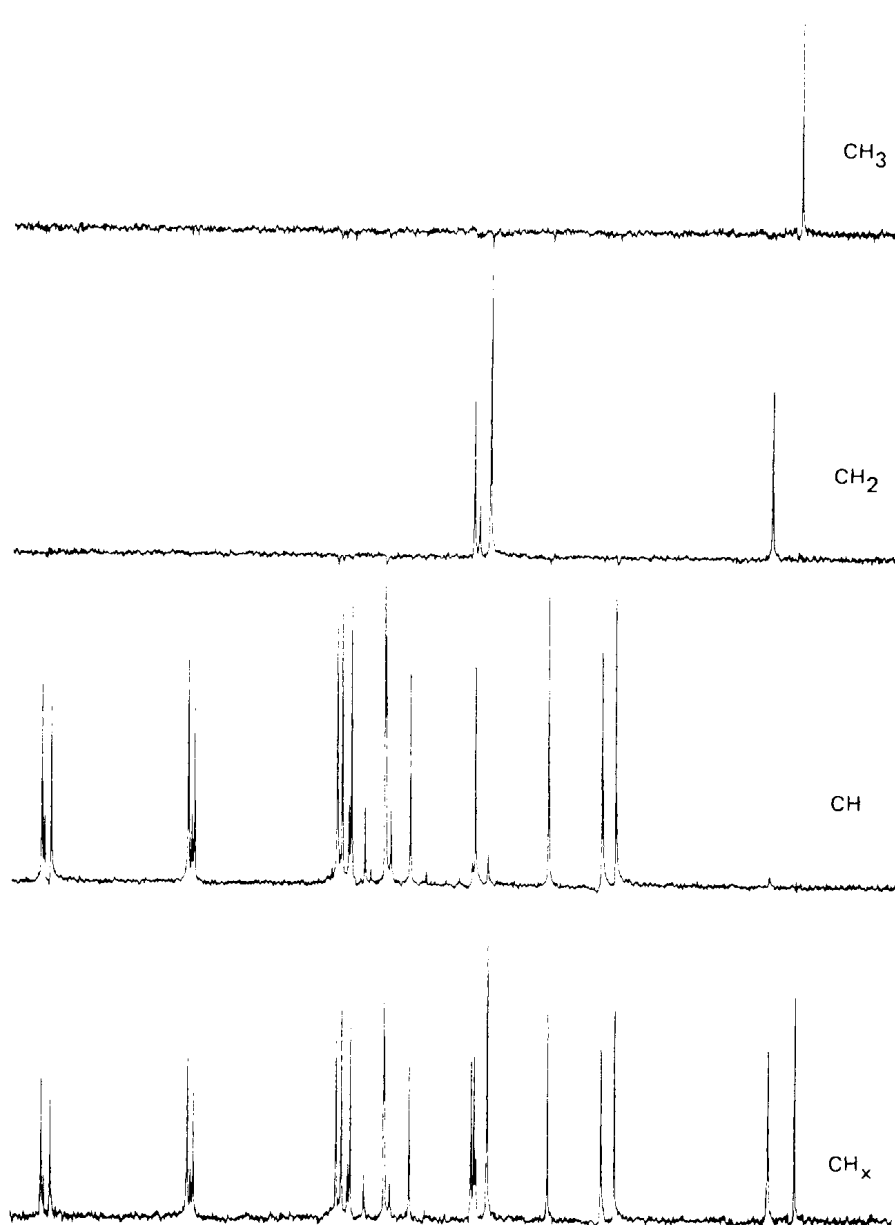


Figure 5-18 Spectral editing of the 75.6 MHz ^{13}C spectrum of the trisaccharide gentamicin by the DEPT sequence. The bottom spectrum contains resonances of all carbons with attached protons, and the ascending spectra are respectively of the methine, methylene, and methyl carbons. (Courtesy of Bruker Instruments, Inc.)

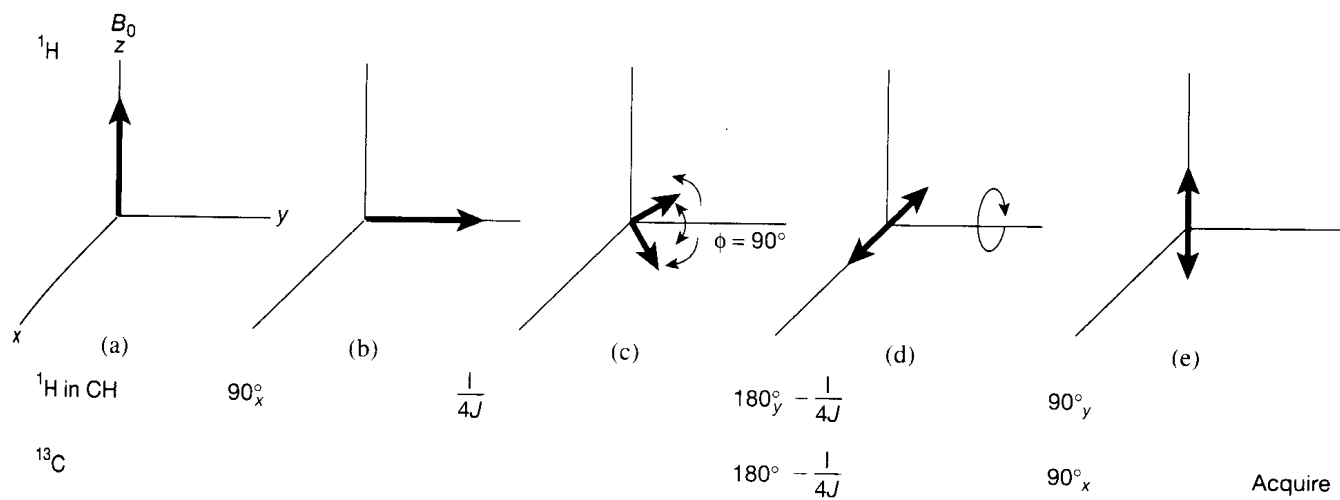


Figure 5-19 Pulse sequence for the INEPT experiment, showing the effects on the ^1H spin vectors.

the antiphase arrangement. The first 90° pulse moves the proton magnetization into the xy plane (Figure 5-19b). The simultaneous 180° pulses on both the proton and the carbon remove the effects of inhomogeneity, but allow the proton vectors to continue to diverge, as in Figure 5-14. After $(4J)^{-1}$, the protons are 90° apart (Figure 5-19c), and, after the second $(4J)^{-1}$ period, they are 180° apart (Figure 5-19d). The 90° pulse along the y direction rotates the proton vectors back onto the z axis (Figure 5-19e). Whereas in (a) the protons associated with both carbon spin up and carbon spin down are pointed in the $+z$ direction, in (b) the protons associated with carbon spin $+\frac{1}{2}$, or β , are pointed along the $+z$ direction, but the protons associated with carbon spin $-\frac{1}{2}$, or α , are pointed along the $-z$ direction (or the reverse, depending on the sign of the $^1\text{H}-^{13}\text{C}$ coupling constant). This situation is termed *antiphase*.

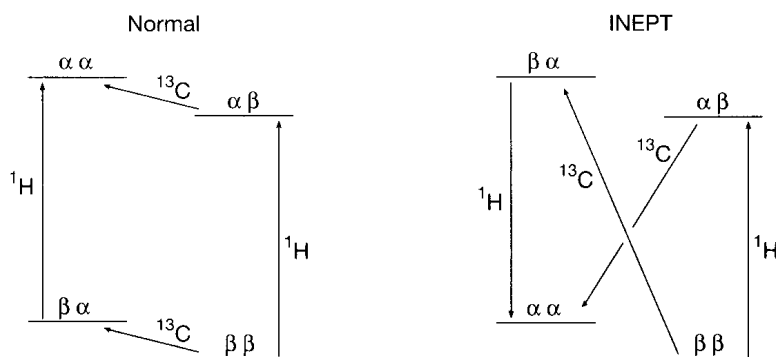
The spin energy diagram after these proton pulses is compared with that for the normal two-spin system at the beginning of the sequence in Figure 5-20. The normal diagram on the left shows that the Boltzmann distributions result in more intense ^1H resonances ($\beta\alpha \rightarrow \alpha\alpha$ and $\beta\beta \rightarrow \alpha\beta$) than ^{13}C resonances ($\alpha\beta \rightarrow \alpha\alpha$ and $\beta\beta \rightarrow \beta\alpha$), as represented by the greater vertical displacement of the arrows for the ^1H transitions than for the ^{13}C transitions. Each arrow goes from a lower to a higher state and hence represents absorption (a positive peak).

The antiphase INEPT arrangement of ^1H spin vectors on the right of Figure 5-20 means that two ^1H energy levels ($\alpha\alpha$ and $\beta\alpha$) are interchanged, so that the ^1H spin flip ($\beta\alpha \rightarrow \alpha\alpha$) gives a negative peak, while the other spin flip ($\beta\beta \rightarrow \alpha\beta$) still gives a positive peak. Thus, one ^1H signal is positive and the other is negative (antiphase). An examination of the carbon transitions in the INEPT diagram indicates that their Boltzmann distributions have increased to protonlike proportions (look at the vertical displacements of the arrows, although the representation is not proportional). In this fashion, protons have transferred polarization to carbons. According to the spin energy diagram at the right of the figure, the carbon vectors also are antiphase, since the carbon transition associated with proton spins $+\frac{1}{2}$, or β , is absorptive and must be pointed along the $+z$ direction, whereas the carbon transition associated with proton spins $-\frac{1}{2}$, or α , is emissive and must be pointed along the $-z$ direction. The situation for carbons is identical to that for protons in Figure 5-19e. The final carbon pulse, which is 90° along the x axis, places the antiphase vectors along the y direction for observation. Because of the antiphase relationship, one carbon transition ($\beta\beta$ to $\beta\alpha$) is positive (absorption) and one ($\alpha\beta$ to $\alpha\alpha$) is negative (emission).

The INEPT sequence results in enhanced signals for the insensitive I nuclei, half of which give negative and half positive peaks for a CH group, such as pyridine in Figure 5-21. For comparison, the figure includes the normal spectrum at the bottom and the spectrum in the middle, with gated irradiation, in order to obtain the NOE without decoupling. The INEPT spectrum clearly achieves a greater enhancement of sensitivity than does that produced with NOE alone. The maximum increment in intensity is $|\gamma_S/\gamma_I|$ (absolute value) for INEPT, but that for the NOE ($1 + \eta_{\max}$) is only $(1 + \gamma_S/2\gamma_I)$ (eq. 5-5) and can be positive or negative. The maximum enhanced intensity available from the INEPT experiment, analogous to that obtained from eq. 5-5 for the NOE experiment, is,

$$I_{\max}(\text{INEPT}) = I_0 \left| \frac{\gamma_{\text{irr}}}{\gamma_{\text{obs}}} \right| \quad (5-6)$$

Figure 5-20 Spin states for a two-spin ($^{13}\text{C}-^1\text{H}$) system, normally (left) and after the INEPT pulse sequence (right).



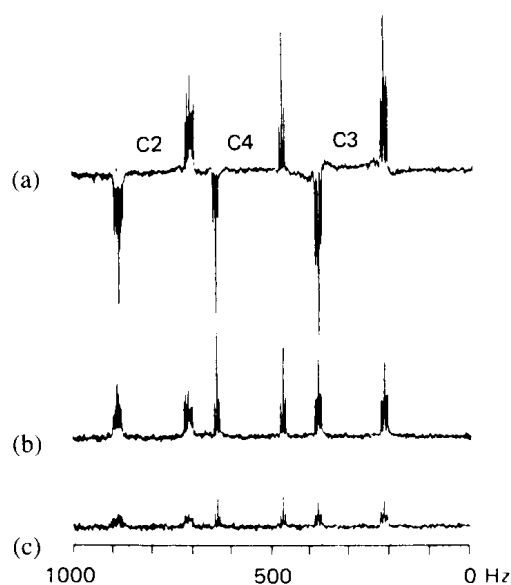
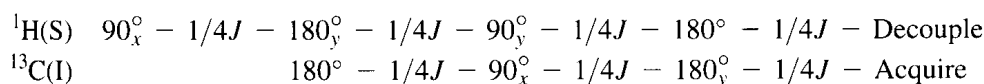


Figure 5-21 The proton-coupled ^{13}C spectrum of pyridine, (a) with INEPT, (b) with NOE only, and (c) unenhanced, all on the same scale. (Reproduced with permission from G. A. Morris and R. Freeman, *J. Am. Chem. Soc.*, **101**, 760 (1979). Copyright 1979 American Chemical Society.)

For $^{13}\text{C}\{^1\text{H}\}$, maximum increased intensities are 3.98 for INEPT and 2.99 for NOE. When the gyromagnetic ratio of the insensitive nucleus is negative, INEPT has an even greater advantage because of the subtractive factor present in the NOE expression. For $^{15}\text{N}\{^1\text{H}\}$, the INEPT and NOE factors are 9.87 and -3.94 , respectively; for $^{29}\text{Si}\{^1\text{H}\}$, 5.03 and -1.52 ; and for $^{119}\text{Sn}\{^1\text{H}\}$, 2.68 and -0.34 . Clearly, INEPT is significantly more effective in each case and is always positive.

There is one apparent drawback to the INEPT experiment. Decoupling of the $-1,1$ pattern for each CH resonance would lead to precise canceling and hence a null signal. As methylene triplets give $-1, 0, 1$ INEPT intensities and methyl quartets give $-1, -1, 1, 1$ intensities, both also would give null signals on decoupling. The *refocused* INEPT pulse sequence was designed to get around this problem and permit decoupling by repeating the INEPT pulses a second time in the following fashion:



The second refocusing period again is a spin echo in which chemical shifts are focused by the 180° pulses. The spin roles, however, are reversed in the second set, so that I magnetization is refocused back to two positive peaks for the CH case. The decoupling of protons during carbon acquisition thus does not result in the cancelation of any peaks. The spectrum that is obtained contains decoupled peaks with enhanced intensity. Figure 5-22 compares the various experiments for chloroform.

The value of $(2J)^{-1}$ for the total period between the last 90° pulse and acquisition (sometimes called Δ_2 to distinguish it from the period Δ_1 or 2τ between the first and last 90° pulses) is appropriate only for the methine fragment CH. For methylene (CH_2) and methyl (CH_3) groups, the vectors do not refocus, so that decoupling would still result in a canceled signal. Alternative values of Δ_2 , however, can lead to improved refocusing, with Δ_2 for an arbitrary CH_n fragment given by the formula

$$\Delta_2 = (1/\pi J) \sin^{-1}\left(\frac{1}{\sqrt{n}}\right). \quad (5-7)$$

The respective optimum values of Δ_2 for CH, CH_2 , and CH_3 are $(2J)^{-1}$, $(4J)^{-1}$, and $\approx(5J)^{-1}$; $\approx(3.3J)^{-1}$ represents a compromise value that yields enhanced, but not optimal, intensities for all substitution patterns under decoupling conditions. In the absence of

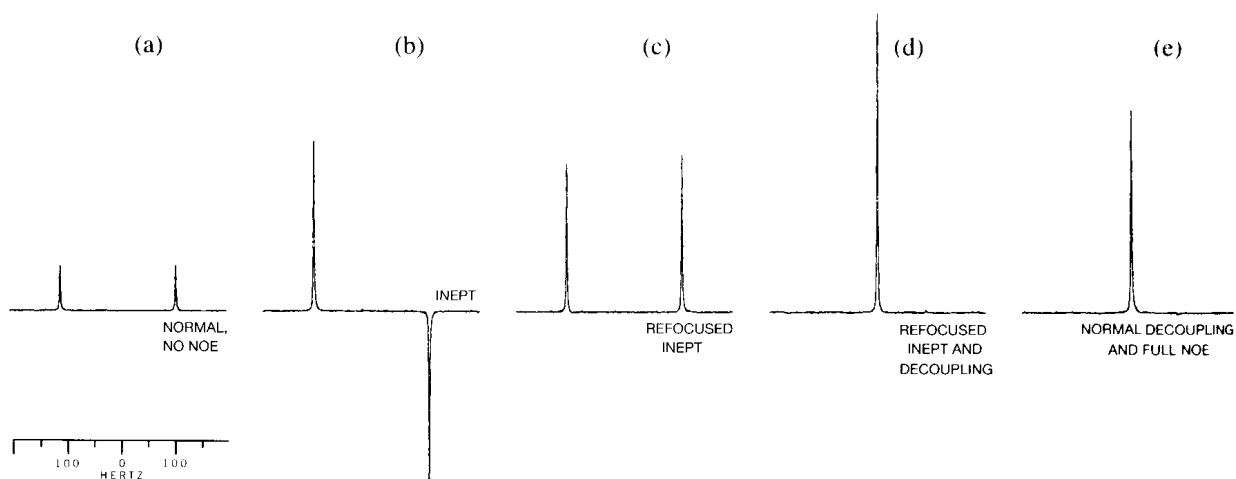
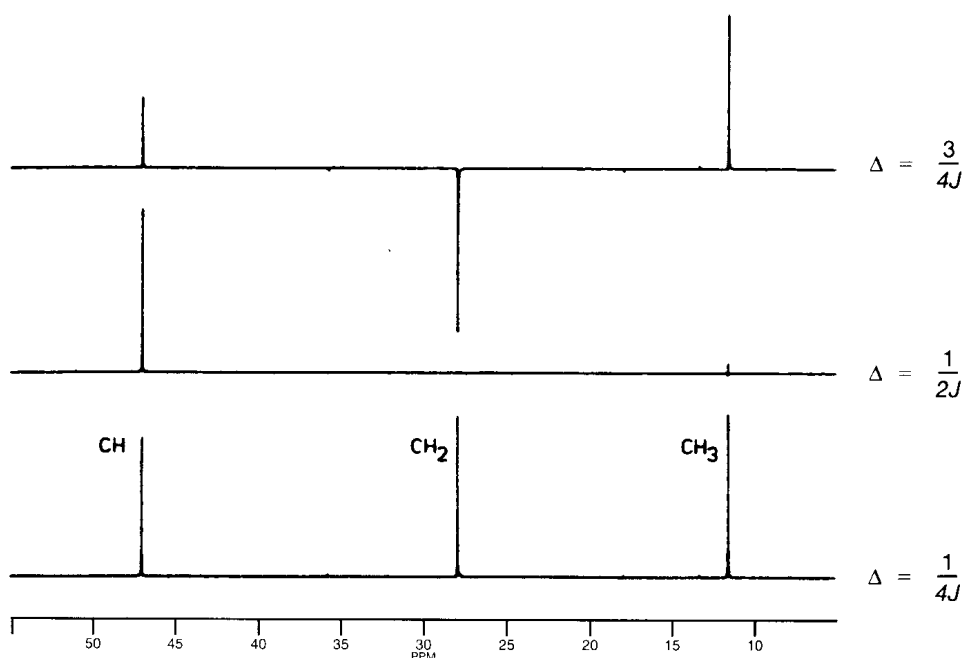


Figure 5-22 The ^{13}C spectrum of chloroform (a) without double irradiation, (b) with ^1H irradiation to achieve the INEPT enhancement, (c) with ^1H irradiation to achieve refocused INEPT enhancement, (d) with ^1H irradiation to achieve refocused INEPT enhancement and decoupling, and (e) with normal decoupling to achieve only the NOE. (Reproduced with permission from A. E. Derome, *Modern NMR Techniques for Chemistry Research*, Pergamon Press, Oxford, UK, 1987, p. 137.)

decoupling, phase differences within a collection of CH, CH_2 , and CH_3 resonances would result in peak distortions.

Because the choice of $\Delta_2 = 1/2J$ for the decoupled, refocused INEPT experiment leads to completely refocused doublets, but antiphase triplets and quartets, this particular experiment with decoupling produces a subspectrum that contains only methinyl resonances. Values of Δ_2 also can be selected to optimize the intensities of methylene and methyl resonances. The idea can be depicted graphically by defining an imaginary angle $\theta = \pi J \Delta_2$. Signal intensities then are found to be proportional to $\sin \theta$ for CH, $\sin(2\theta)$ (or $2 \sin \theta \cos \theta$) for CH_2 , and $3 \sin \theta \cos^2 \theta$ for CH_3 . Thus, when $\theta = \pi/2$ [and $\Delta_2 = (2J)^{-1}$], the CH signal is optimized and the other signals go to zero. For all other values of θ , the spectrum contains varying proportions of all substitution types. Figure 5-23 illustrates the experiment for

Figure 5-23 Intensities of the carbon resonances of an imaginary molecule containing one CH, one CH_2 , and one CH_3 under varying values of Δ_2 in the refocused INEPT experiment. (Reproduced with permission from A. E. Derome, *Modern NMR Techniques for Chemical Research*, Pergamon Press, Oxford, UK, 1987, p. 143.)



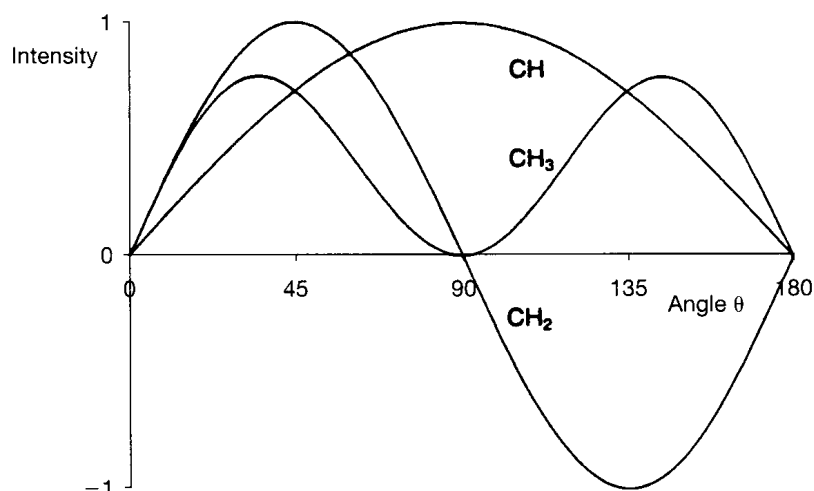


Figure 5-24 Variation of signal intensities for CH, CH₂, and CH₃ as a function of $\theta = \pi J \Delta_2$ in the refocused INEPT experiment. (Reproduced from T. D. W. Claridge, *High-Resolution NMR Techniques in Organic Chemistry*, Pergamon Press, Amsterdam, 1999, p. 138.)

three values of θ ($\pi/4$, $\pi/2$, and $3\pi/4$) that correspond to $\Delta_2 = 3/4J$, $1/2J$, and $1/4J$, respectively. Linear combinations of these spectra can lead to edited spectra that contain only methylene or only methyl resonances. Figure 5-24 is a plot of the signal intensities for the three types of carbon as a function of the angle $\theta = \pi J \Delta_2$. The spectra shown were taken as cuts at $\theta = 135^\circ$, 90° , and 45° .

A comparison of the preceding three INEPT spectra allows the multiplicity of all protonated carbon resonances to be determined, albeit with intensities that are not optimized. Section 5-5 describes the attached proton test (APT), which does not distinguish CH from CH₃. The DEPT sequence provides an editing technique that suffers from the drawbacks of neither of these other methods and moreover is less sensitive to experimental imperfections, such as the exact value of J . Already mentioned as the method of choice for spectral editing, DEPT (*Distortionless Enhancement by Polarization Transfer*) is similar to refocused INEPT. There are a pair of τ periods ($= (2J)^{-1}$) followed in the proton channel by a single variable pulse θ , an angle corresponding to that previously defined ($\pi J \Delta_2$, in which Δ_2 corresponds to two τ periods):

$$\begin{array}{l} \text{S } 90_x^\circ - 1/2J - 180_y^\circ - 1/2J - \theta_y - 1/2J - \text{Decouple} \\ \text{I } \qquad \qquad \qquad 90_x^\circ - 1/2J - 180_x^\circ - 1/2J - \text{Acquire} \end{array}$$

The DEPT and refocused INEPT sequences begin in a similar fashion, with the 90° ^1H (S) pulse generating proton magnetization that evolves under the influence of coupling to carbon. Whereas the time τ between the first and second proton pulses is $(4J)^{-1}$ for refocused INEPT, it is $(2J)^{-1}$ for DEPT, as it was for APT. The second (180°) ^1H pulse refocuses proton chemical shifts. The simultaneous initial (90°) ^{13}C pulse generates carbon magnetization and brings about a situation that cannot be followed by the vector model we have used throughout this textbook. As both proton and carbon magnetizations, linked by the C–H coupling, are evolving together, the phenomenon is termed *Multiple Quantum Coherence* (MQC), or, more specifically, *Heteronuclear Multiple Quantum Coherence* (HMQC). In essence, the proton and carbon magnetizations have become pooled. (See Appendix G for further discussion of MQC.) The MQC continues to evolve during the second $(2J)^{-1}$ period. The final proton pulse, of duration θ , transfers the MQC to single quantum carbon coherence. (Multiple quantum coherence cannot be observed, as it induces no signal in the detection coil, so it must be transformed back into *single quantum coherence*.) The final $(2J)^{-1}$ period allows the development of carbon magnetization, with a dependence on the number of attached protons (CH, CH₂, or CH₃) determined by the value of θ . As with refocused INEPT, the modulation of θ , now a pulse length, results in a series of edited spectra such as those in Figure 5-18. One of the most common sets of experiments uses the angles 45° , 90° ,

and 135° . The DEPT-45 spectrum contains resonances of all types except quaternary, DEPT-90 contains only CH, and DEPT-135 contains CH/CH₃ positive and CH₂ negative, analogous to the plot in Figure 5-24, readily permitting an assignment of each type of substitution. Spectral subtraction with some loss of signal is required to obtain the fully edited spectra illustrated in Figure 5-18. The term “distortionless” was applied because the initial set of pulses (up to the first 2τ) results, not in a combination of positive and negative peaks, but rather in positive 1:1 doublets, 1:2:1 triplets, and 1:3:3:1 quartets in the absence of decoupling.

The INEPT and DEPT sequences assume that coupling between the I and S nuclei is dominant, so that other couplings must be negligibly small. For one-bond $^{13}\text{C}-^1\text{H}$ couplings, this assumption holds, as all $^1\text{H}-^1\text{H}$ couplings are much smaller. If polarization is to be transferred from two- or three-bond $^{13}\text{C}-^1\text{H}$ couplings, however, the homonuclear couplings no longer are small in comparison. This situation is more likely to occur when attempts are being made to transfer polarization from protons to silicon, nitrogen, or phosphorus. Because Si-H, N-H, and P-H bonds are relatively uncommon (compared with C-H), recourse must be made to longer range coupling constants, with attendant difficulties.

5-7 Carbon Connectivity

The one-bond $^{13}\text{C}-^{13}\text{C}$ coupling potentially contains a wealth of structural information, as it indicates carbon-carbon linkage. Unfortunately, only 1 in about 10,000 pairs of carbon atoms contains two ^{13}C atoms and hence displays a $^{13}\text{C}-^{13}\text{C}$ coupling in the ^{13}C spectrum. These resonances can be detected as very low intensity satellites on either side of the center band that is derived from molecules containing only isolated ^{13}C atoms. For bonded pairs of ^{13}C , 1J is about 30–50 Hz, and the satellites are separated from the center band by half that amount. Coupling also may be present over two or three bonds (2J , 3J) in the range of about 0–15 Hz. Not only are these satellites low in intensity and possibly obscured by the center band, but also, spinning sidebands, impurities, and other resonances may get in the way.

The pulse sequence INADEQUATE (*Incredible Natural Abundance Double QUantum Transfer Experiment*) was developed by Freeman to suppress the usual (single-quantum) resonances and exhibit only the satellite (double-quantum) resonances. The pulse sequence is $90_x^\circ-\tau-180_y^\circ-\tau-90_x^\circ-\Delta-90_\phi^\circ$. The homonuclear 180° pulse refocuses field inhomogeneities, but allows the vectors from different $^{13}\text{C}-^{13}\text{C}$ coupling arrangements to continue to diverge. (See Section 5-5.) If the carrier frequency coincides with the center band of a carbon resonance, the center-band spins remain on the y axis after the first 90° pulse. The delay time τ is set to $(4J)^{-1}$, so that the vectors for the two satellites from the coupled $^{13}\text{C}-^{13}\text{C}$ system diverge by 180° after 2τ [$\phi = 2\pi(\Delta\nu)t = 2\pi J(2/4J) = \pi$] and lie respectively on the $+x$ and $-x$ axes. The second 90_x° pulse then rotates the center-band spins to the $-z$ axis, but leaves the satellite spins aligned along the x axis. Thus, the center band is not available for detection in the xy plane, but the satellites are.

This pulse sequence is another example of multiple quantum coherence. After the second 90° pulse, the coupled pairs of ^{13}C nuclei evolve together. (Note that each ^{13}C pair is an isolated AX system because of the natural abundance of ^{13}C .) During the period Δ , homonuclear double quantum coherence evolves as the sum of the Larmor frequencies of the two coupled spins. In the two-dimensional variant (Chapter 6), the constant period Δ becomes a variable period. The final 90° pulse reconverts multiple to single quantum coherence for observation. The phase of the final 90° pulse (90_ϕ°) is cycled through a series of directions represented by ϕ ($+x, +y, -x, -y$). The vector diagrams used throughout this book illustrate only the coherence of the spins of a single nucleus. Spins in the xy plane are said to be coherent when they have an ordered relationship between their phases, so that they all precess around one axis and can be depicted by a vector along that direction. Spins rotating with random phase in the xy plane are said to be incoherent. The simultaneous coherence of two spins, as created in the INADEQUATE experiment, is not well depicted by the vector

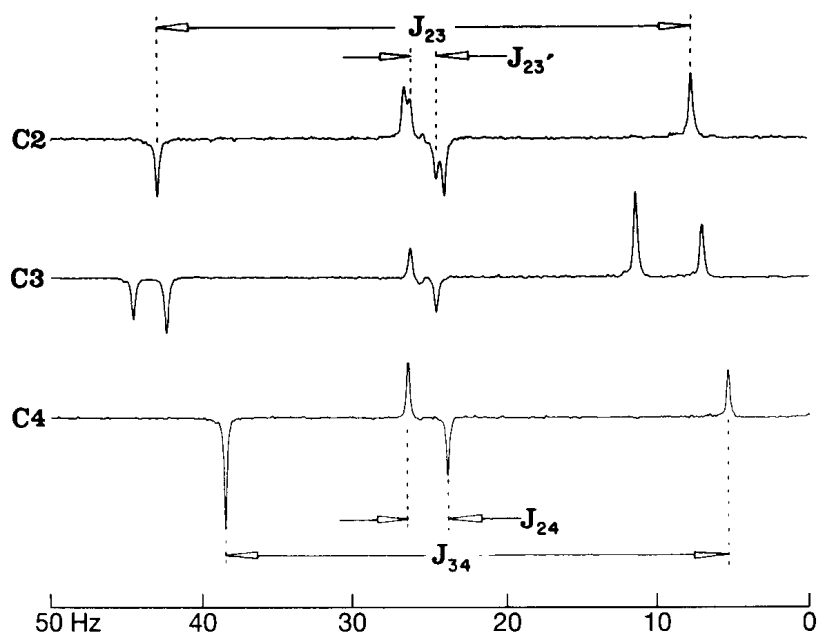


Figure 5-25 The one-dimensional INADEQUATE spectrum for the carbons of piperidine. (Reproduced with permission from A. Bax, R. Freeman, and S. P. Kempell, *J. Am. Chem. Soc.*, **102**, 4849 (1980). Copyright 1980 American Chemical Society.)

diagrams, so the reason for the final 90° pulse is not well represented. (See Appendix 6.) The special phase properties of double quantum coherence are employed in the ϕ pulse to suppress the center band (single quantum coherence).

Figure 5-25 contains the INADEQUATE spectrum for piperidine. The double-quantum (satellite) peaks are antiphase, so each ^{13}C — ^{13}C coupling constant is represented by a pair of peaks—one up, one down (+1, -1). The spectrum for C-4 of piperidine thus contains two such doublets: a large one for $^1J_{34}$ and a small one for $^2J_{24}$. For C-3, there are two large doublets, because the one-bond couplings $^1J_{23}$ and $^1J_{34}$ to the adjacent carbons are slightly different. There also is a small $^3J_{23'}$ between C-2 and the nonadjacent C-3. The spectrum for C-2 shows $^1J_{23}$, $^2J_{24}$, and $^3J_{23'}$.

Although more distant couplings are observable, the most important are the one-bond couplings, which vary slightly for every carbon-carbon bond. Thus, a match of $^1J(^{13}\text{C}$ — $^{13}\text{C})$ for any two carbons strongly suggests that they are bonded to each other. Even in complex molecules, there is sufficient variability of couplings that INADEQUATE can be used to map the complete connectivity of the carbon framework, provided that it is not broken by a heteroatom. The major drawback to the INADEQUATE experiment is its extremely low sensitivity, as it uses only 0.01% of the carbons in the molecule. The two-dimensional version is discussed in Section 6-4.

5-8 Phase Cycling, Composite Pulses, and Shaped Pulses

We have used 90° and 180° pulses extensively to carry out a variety of experiments. In each case, it is important that the length of the pulse accurately provide the desired angle of rotation. Various artifacts can arise because of imperfections in the pulses. Figure 5-26 illustrates the effect on the inversion recovery experiment ($180_x^\circ - \tau - 90_x^\circ$, Figure 5-1) used to determine T_1 , but with the initial inverting pulse not quite 180° . The magnetization after the pulse is slightly off the z axis (Figure 5-26b), so there is a small amount of transverse (xy) magnetization present at the start of the τ period. [Only the y component is shown in (Figure 5-26b).] After the period τ , the z magnetization has decreased through T_1 relaxation, and the component of magnetization in the xy plane caused by the pulse imperfection persists (Figure 5-26c). Following the final 90° pulse, the z magnetization is moved into the xy plane for detection (Figure 5-26d). The pulse imperfection in the drawing causes a reduction

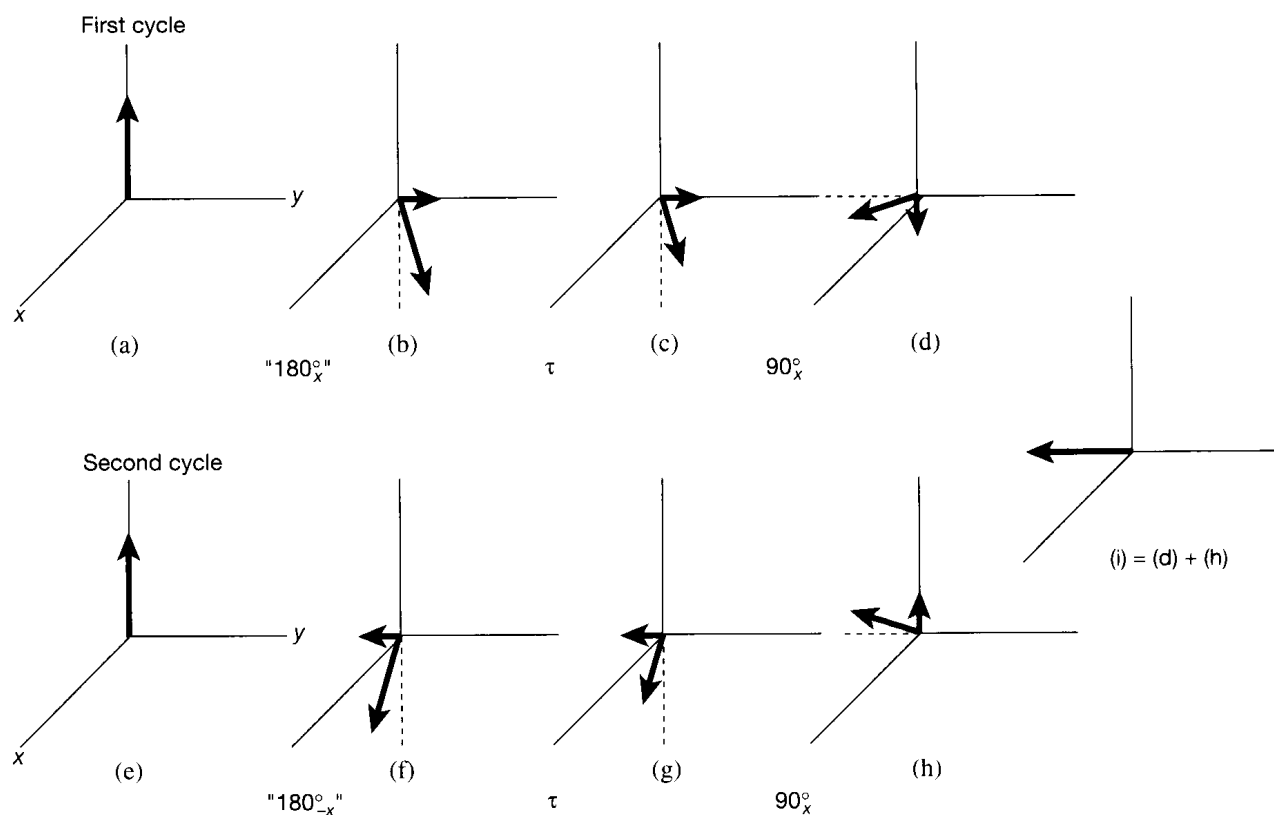


Figure 5-26 Phase cycling in the inversion recovery experiment.

in intensity, but the spectral phase also can be altered. Almost certainly, there would be errors in the 90° pulse as well, but these are not under consideration here.

Such errors may be largely eliminated by alternating the relative phase of the 180° pulse. The result of an inversion in which the 180° rotation is carried out counterclockwise instead of clockwise about the x axis ($-x$, or -180°) is illustrated in Figure 5-26f. The unwanted transverse magnetization now appears along the $-y$ axis. After time τ (Figure 5-26g) and the final 90° pulse (Figure 5-26h), the imperfection is still present, but now has the opposite effect on the z magnetization from that in (Figure 5-26d). When the two results are added, as in Figure 5-26i, the effect of the imperfection cancels out. The pulse therefore is alternated between x and $-x$. Such a procedure is called *phase cycling*, a technique that permeates modern NMR spectroscopy.

Phase cycling has improved procedures for broadband heteronuclear decoupling. As described in Section 5-3, modern methods use repeated 180° pulses rather than continuous irradiation. Imperfections in the 180° pulse, however, would accumulate and render the method unworkable. Consequently, phase-cycling procedures have been developed to cancel out the imperfections. The most successful to date is the WALTZ method of Freeman, which uses the sequence $90_x^\circ, 180_{-x}^\circ, 270_x^\circ$ in place of the 180° pulse ($90 - 180 + 270 = 180$), with significant cancellation of imperfections. The expanded WALTZ-16 sequence cycles through various orders of the simple pulses and achieves an effective decoupling result.

A third example of phase cycling is used to place the reference frequency in the middle of the spectrum, instead of off to one side. As described heretofore, the NMR experiment is sensitive only to the difference $\Delta\omega$ between a signal and the reference frequency. This situation necessitates placing the reference frequency to one side of all the resonances, so that there is no confusion of two signals that are respectively at a higher and a lower frequency than the reference frequency by the exact same amount ($+\Delta\omega$ and $-\Delta\omega$).

Such sideband detection, however, always contains signals from noise on the signal-free side of the reference. Placement of the reference in the middle of the spectrum avoids this unnecessary noise, but requires a method for distinguishing between signals with $+\Delta\omega$ and those with $-\Delta\omega$. *Quadrature detection* accomplishes this task by splitting the signal in two and detecting it twice, using reference signals with the same frequency, but 90° out of phase. Signals with the same absolute value of $\Delta\omega$, but opposite signs, are distinguished in the experiment (in terms of obtaining θ by knowing both $\sin \theta$ and $\cos \theta$, which are 90° out of phase). Systematic errors, however, can arise if the two reference frequencies are not exactly 90° out of phase. The resulting signal artifacts, called *quad images*, can appear as low intensity peaks. The CYCLOPS cycle involves four steps that move the 90° pulse and the axis of detection from $+x$ to $+y$ to $-x$ to $-y$ and change the way the two receiver channels are added, with the result that imperfections in the phase difference cancel out.

Phase cycling not only can remove artifacts from pulse or phase imperfections, but also can assist in the selection of coherence pathways. The inversion recovery experiment can be described with a slightly different vocabulary to illustrate this process. When spins are aligned entirely along the z axis, the order of coherence is said to be zero. (Phases around the xy plane are random.) An exact 90° pulse creates maximum single quantum coherence by lining the spins up along, for example, the y direction. Phase cycling in the inversion recovery experiment (Figure 5-26) removes undesired single quantum coherence (transverse or xy magnetization) and leaves coherence of order zero until the end of the τ period, at which time the final 90° pulse creates single quantum coherence. In this way, phase cycling selects the desired degree of coherence. Double quantum coherence, involving the relationship between two spins, is not well illustrated in these vector diagrams. (See Appendix 6.) The INADEQUATE experiment involves the selection of double over single quantum coherence (elimination of the center band and retention of the satellites), in part through phase cycling in the final 90° pulses, whose subscript ϕ refers to a sequence of pulses with different phases.

Imperfections in pulses also may be corrected by using *composite pulses* instead of single pulses. The 180° pulse that inverts longitudinal magnetization for the measurement of T_1 or other purposes may be replaced by the series $90_x^\circ, 180_y^\circ, 90_x^\circ$, which results in the same net 180° pulse angle, but reduces the error from as much as 20% to as little as 1%. As Figure 5-27 shows, the 180° pulse compensates for whatever imperfection existed in the 90° pulse. (Normally, 180° is taken as double the optimized 90° pulse, so errors in one are present in the other). The three components of the WALTZ-16 method ($90_x^\circ, 180_{-x}^\circ, 270_x^\circ$) also constitute a composite pulse for 180_x° .

For the most part, pulses have been generated by applying rf energy equally over the entire frequency range, with a short duration on the order of microseconds. Such excitations are sometimes referred to as *hard pulses*, in distinction to pulses that require selective excitation (i.e., excitation over a restricted frequency range). Selective excitation has been mentioned on several occasions. It is useful, for example, in the saturation transfer experiment

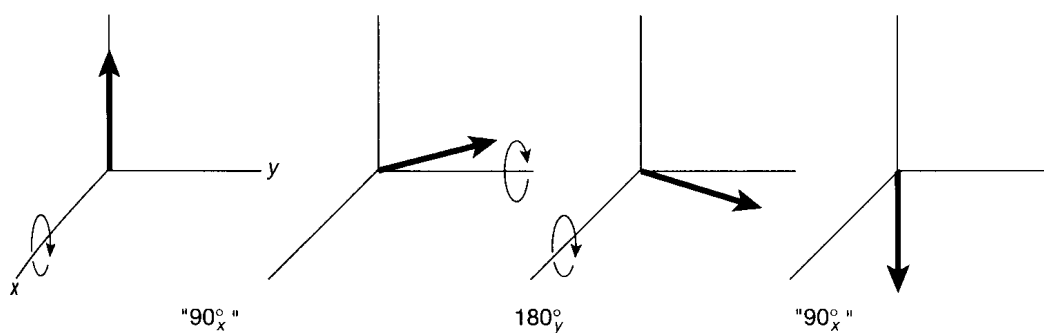
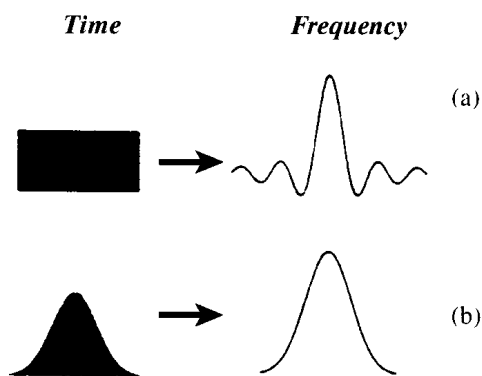


Figure 5-27 A composite pulse equivalent to a single 180° pulse.

Figure 5-28 (a) The result of Fourier transformation of a low-power rectangular pulse. (b) The result for a shaped Gaussian pulse. (Reproduced from T. D. W. Claridge, *High-Resolution NMR Techniques in Organic Chemistry*, Pergamon Press, Amsterdam, 1999, p. 349.)



(Section 5-2) and in the suppression of specific unwanted peaks (Section 5-1). Frequency selection within two-dimensional spectra (Chapter 6) results in a reduction in dimensionality, so that effects at a single frequency can be examined in detail. (A one-dimensional cut of a two-dimensional spectrum offers the twin advantages of reduced experimental time and decreased storage needs.)

The procedure for producing a selective pulse is to reduce the rf power (B_1) so that the effective frequency range also is reduced. To counter the reduction in power and still achieve the required tip angle, the duration of the pulse is increased, typically into the millisecond range. The simplest such *soft pulses* would have rectangular shapes (from zero intensity up to full intensity for a period of milliseconds and then back to zero intensity), similar to the shapes of the hard pulses in our vector diagrams. Unfortunately, such a pulse shape generates wiggles, or feet, on the signal (Figure 5-28a), much as the truncation of rectangular signals does (Section 2-5). By analogy with apodization, these wiggles may be removed by smoothing off the edges of the peaks (Figure 5-28b).

Such excitations have been called *shaped pulses*, and a considerable effort has been expended in an attempt to optimize their shapes. A simple Gaussian shape is a considerable improvement over a rectangular pulse, but is not entirely effective in achieving an optimal peak shape. The use of more elaborate mathematical functions improves the shape of the signal, although with increasing loss of intensity. The BURP (*Band selective, Uniform Response, Pure phase*) family utilizes an exponentially dependent sinusoidal series of Gaussians with considerable success in a variety of situations (EBURP for 90° , REBURP for 180°).

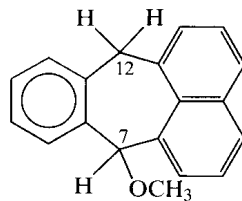
An early alternative to soft pulses was the DANTE (*Delays Alternating with Nutation for Tailored Excitation*) experiment, which used a sequence of short, hard pulses of angle $\alpha \ll 90^\circ$, followed by a fixed delay τ to achieve selective excitation. [Thus, the pulse sequence is $(\alpha-\tau)_n$]. Nuclei that are on resonance are eventually driven to the y axis and hence are selected, whereas those more removed from the frequency range are not affected. The sequence of hard pulses can achieve a result similar to that of soft pulses and even can be shaped by modulating the duration of the pulse lengths, but DANTE pulses lead to spectral artifacts not created by soft pulses, such as unwanted sidebands.

Problems

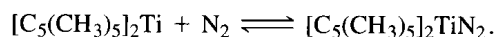
- 5.1 Give the spectral notation (AB, ABX, etc.) for the following substituted ethanes, first at slow C—C rotation, then at fast rotation:
- CH_3CCl_3
 - CH_3CHCl_2
 - $\text{CH}_3\text{CH}_2\text{Cl}$
 - $\text{CHCl}_2\text{CH}_2\text{Cl}$

Draw all stable conformations. The spectral notation for each frozen form gives the slow-rotation answer. Then imagine free rotation about the C—C bond. The identity of certain protons may average for the fast-rotation answer.

- 5.2 Ring reversal in 7-methoxy-7,12-dihydropleiadene (see accompanying figure) can be frozen out at -20°C . Two conformations are observed, in the ratio 2 : 1. When the high-frequency (low-field) part of the 12- CH_2 AB quartet in the minor isomer is doubly irradiated, the intensity of the 7-methine proton is enhanced by 27%. Double irradiation of the same proton in the major isomer has no effect on the spectrum. What are the two conformational isomers and which is more abundant?

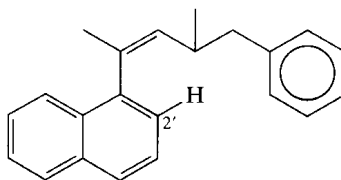


- 5.3 Permethyltitanocene reacts with an excess of nitrogen below -10°C to form a 1 : 1 complex. The reaction is



The methyl resonance of the complex is a sharp singlet above -50°C . Below -72°C , the resonance splits reversibly into two peaks of not quite the same intensity. If the nitrogen molecule is doubly labeled with ^{15}N , the ^1H -decoupled ^{15}N spectrum contains a singlet and an AX quartet ($J(^{15}\text{N}-^{15}\text{N}) = 7\text{ Hz}$) of not quite the same overall intensity at low temperatures. Explain these observations in terms of structures.

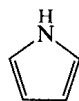
- 5.4 (a) The resonance of the methylene protons of $\text{C}_6\text{H}_5\text{CH}_2\text{SCHClC}_6\text{H}_5$ in CDCl_3 is an AB quartet at room temperature. Why?
 (b) The AB spectrum coalesces at high temperatures to an A_2 singlet with a ΔG^\ddagger of $15.5\text{ kcal mol}^{-1}$. The rate is independent of concentration in the range 0.0190–0.267 M. Explain in terms of a mechanism.
- 5.5 The ^1H spectrum of the following molecule contains resonances from two isomers at room temperature:



- (a) The spectrum of isomer A contains the resonance of H_2' at $\delta 6.42$, and that of isomer B contains the same resonance in the region $\delta 7-8$. What can you say about the conformations of A and B?
 (b) The sample crystallizes only as isomer A. Dissolution of these crystals, however, produces the spectra of both isomers, A and B. What can you say about the barrier for the equilibrium $\text{A} \rightleftharpoons \text{B}$? When CH_3 on the double bond is replaced by $-\text{CMe}_2\text{OH}$, crystallization still produces only A, but redissolution of the crystals also yields A only and none of B. What can you say about the $\text{A} \rightleftharpoons \text{B}$ barrier in this compound?
- 5.6 No coupling is observed between CH_3 and ^{14}N in acetonitrile ($\text{CH}_3-\text{C}\equiv\text{N}$), but there is a coupling in the corresponding isonitrile ($\text{CH}_3-\text{N}\equiv\text{C}$). Explain. This is not a distance effect. The phenomenon is general for nitriles and isonitriles.
- 5.7 Comment on the following ^{14}N line widths:

$^+\text{NMe}_4$ <0.5 Hz

MeNO_2 14



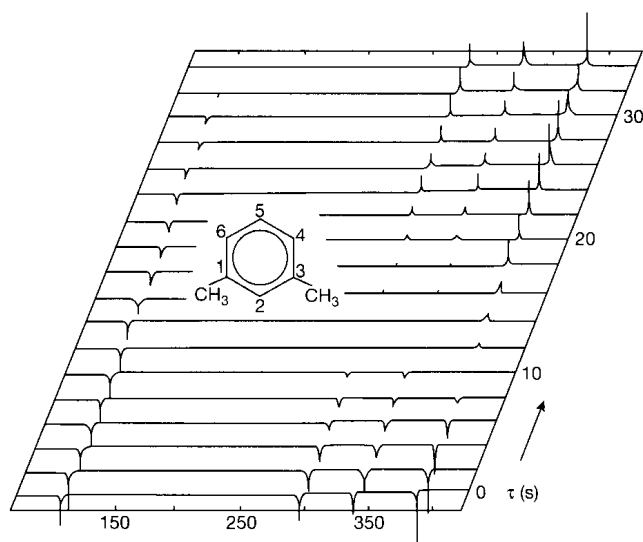
172

Me_3N 77

Aniline

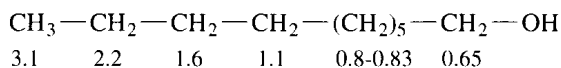
1300

5.8 The following diagram depicts the inversion recovery ($180^\circ - \tau - 90^\circ$) spectral stack* for the aromatic carbons of *m*-xylene:



Assign the resonances and explain the order of T_1 . (Look at the nulls.)

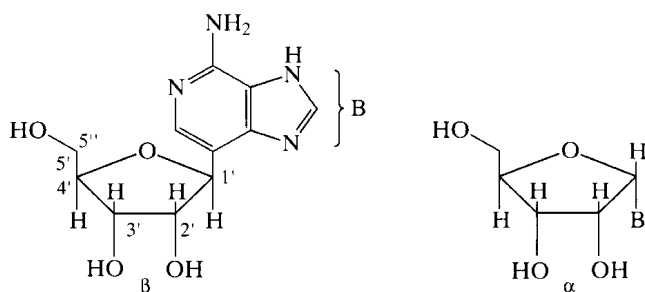
5.9 1-Decanol has the following carbon T_1 values (in s):



Explain the order.

5.10 In ribo-*C*-nucleosides, the base is attached to $C1'$ by carbon. The α and β forms ($C1'$ epimers) may be distinguished by T_1 studies.

(a) Consider the following proton T_1 (s) data:

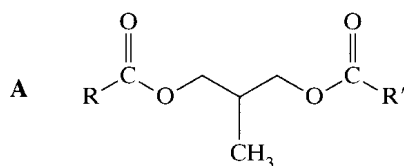


	H1'	H3'	H5'	H5''
Isomer 1	1.60	1.31	0.45	0.45
Isomer 2	3.33	1.37	0.40	0.40

Which isomer (1 or 2) is α and which is β ? Why are the $H1'$ T_1 values different for isomers 1 and 2, but the $H3'$, $H5'$, and $H5''$ values are about the same? Why is T_1 for $H5'$ and $H5''$ smaller than the other values? Use the equation for dipolar relaxation in your reasoning.

(b) Suggest another (not T_1) NMR method for distinguishing these α and β forms.

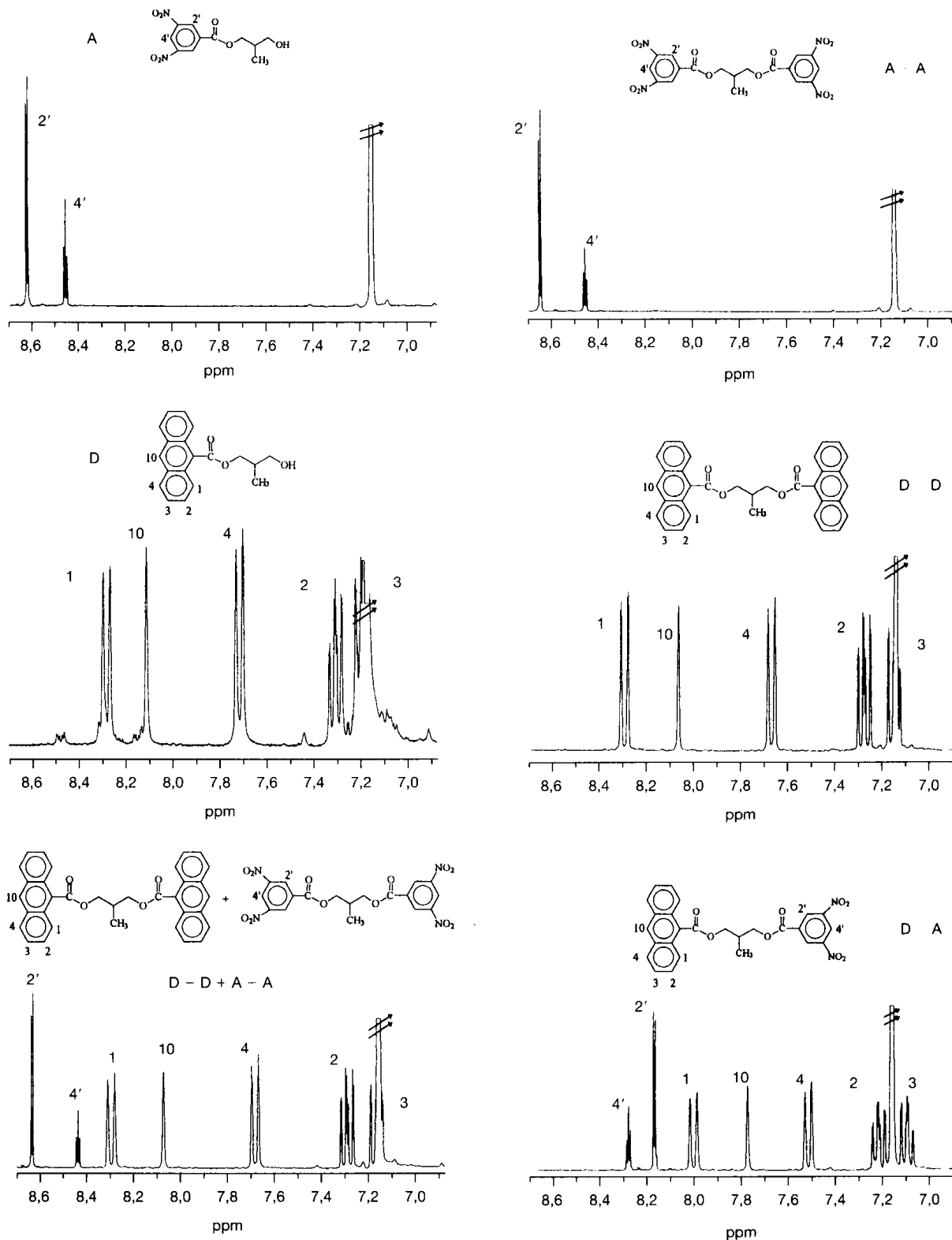
5.11 (a) Consider the following molecule A, in which rotation is rapid around all C-C bonds:



What is the spin system when $R = R'$? Are the protons within a single methylene group homotopic, enantiotopic, diastereotopic, or magnetically nonequivalent? (More than one category may apply.)

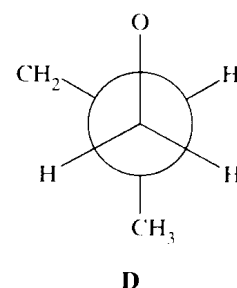
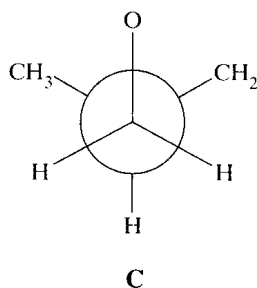
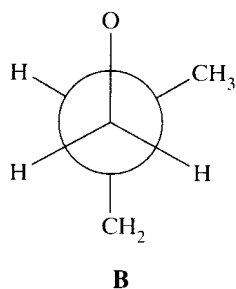
(b) Answer the same question when $R \neq R'$.

(c) The R and R' groups were chosen to be a donor (D, 9-anthracyl) or an acceptor (A, 3,5-dinitrophenyl). Three molecules can be constructed, in which both R and R' are D (D-D), both R and R' are A (A-A), and $R = D$ when $R' = A$ (D-A). The ^1H spectra of these three molecules, as well as the spectra of the model compounds containing only a single A or D and the spectrum of a solution containing equal amounts of D-D and A-A, are as follows:

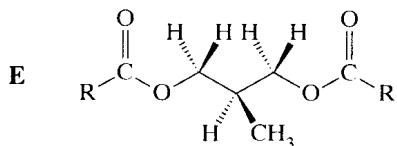


Explain the splitting patterns of the A–A molecule in spectrum (b) and of the D–D molecule in spectrum (d). All spectra were measured in C_6D_6 .

- (d) Explain why there is no difference between the aromatic resonances of A–A and of A in (a), nor between D–D and D in (c).
 (e) Explain why the spectrum of D–A in (f), however, is quite different from those of A–A, D–D, A, and D. What is the purpose of spectrum (e)? What mechanism(s) of interaction between the D and A moieties is (are) eliminated from consideration by these observations?
 (f) There are one trans (anti) (**B**) and two gauche (**C**, **D**) conformations around the C–C bonds. For the two C–C bonds, there can



be trans–trans and various gauche–trans and gauche–gauche arrangements. The trans–trans conformer, for example, resembles **E**.



The bonds labeled 1 and 2 in the following table are different for D–A, but the same for A–A or D–D:

	J(A _X), Hz	J(B _X), Hz
A–A	6.52	5.62
D–D	6.46	5.55
(A–D)-1	3.60	8.21
(A–D)-2	4.09	8.23

Rotation is fast on the NMR time scale. Couplings were measured at 298 K in C_6D_6 between CHMe (H_X) and CH_2 (H_A and H_B). What conformational conclusion may be drawn from these numbers? Explain.

- (g) NOE experiments were carried out on D–A. Irradiation of H_{10} [see spectrum in (c)] enhanced the resonances of H_4 , $H_{2'}$, and $H_{4'}$. Irradiation of $H_{4'}$ enhanced the resonances of H_1 , H_4 , and H_{10} . Explain.
- 5.12 (a) Trimethylsilylation of *N*-(triisopropylsilyl)indole gave a single product in which the 1H spectrum contained four doublets and one doublet of doublets (ignoring long-range couplings). What structures are compatible and incompatible with these observations? Explain.
- (b) Double irradiation of the trimethylsilyl 1H resonance increased the intensity of two of the doublets. Irradiation of the isopropyl septet increased the intensity of the other two doublets. What is the structure of the product? Explain.

Bibliography

Relaxation Phenomena

General

- 5.1. D. A. Wright, D. E. Axelson, and G. C. Levy, *Magn. Reson. Rev.*, **3**, 103 (1979); G. H. Weiss and J. A. Ferretti, *Progr. NMR Spectrosc.*, **20**, 317 (1988); D. J. Wink, *J. Chem. Educ.*, **66**, 810 (1989).

Carbon-13 Relaxation

- 5.2. J. R. Lyster, Jr., and G. C. Levy, *Top. Carbon-13 Spectrosc.*, **1**, 79 (1974); F. W. Wehrli, *Top. Carbon-13 Spectrosc.*, **2**, 343 (1976); D. J. Craik and G. C. Levy, *Top. Carbon-13 Spectrosc.*, **4**, 241 (1983).

Nuclear Overhauser Effect

- 5.3. J. H. Noggle and R. E. Schirmer, *The Nuclear Overhauser Effect*. New York: Academic Press, 1971; R. A. Bell and J. K. Saunders, *Top. Stereochem.*, **7**, 1 (1973); J. K. Saunders and J. W. Easton, *Determ. Org. Struct. Phys. Meth.*, **6**, 271 (1976); K. E. Kövér and G. Batta, *Progr. NMR Spectrosc.*, **19**, 223 (1987); D. Neuhaus and M. P. Williamson, *The Nuclear Overhauser Effect in Structural and Conformational Analysis*, 2d ed. New York: Wiley-VCH, 2000.

Reactions on the NMR Time Scale

General

- 5.4. G. Binsch, *Top. Stereochem.*, **3**, 97 (1968); L. M. Jackman and F. A. Cotton, eds., *Dynamic Nuclear Magnetic Resonance Spectroscopy*. New York: Academic Press, 1975; A. Steigel, *NMR Basic Princ. Progr.*, **15**, 1 (1978); J. I. Kaplan and G. Fraenkel, *NMR of Chemically Exchanging Systems*. New York: Academic Press, 1980; G. Binsch and H. Kessler, *Angew. Chem., Int. Ed. Engl.*, **19**, 411 (1980); J. Sändstrom, *Dynamic NMR Spectroscopy*. London: Academic Press, 1982; M. Ōki, ed., *Applications of Dynamic NMR Spectroscopy to Organic Chemistry*. Deerfield Beach, FL: VCH, 1985.

Carbon-13 Applications

- 5.5. *Progr. NMR Spectrosc.*, **11**, 95 (1977).

Hindered Rotation

- 5.6. H. Kessler, *Angew. Chem., Int. Ed. Engl.*, **9**, 219 (1970); W. E. Stewart and T. H. Siddall, *Chem. Rev.*, **70**, 517 (1970); M. Ōki, *Top. Stereochem.*, **14**, 1 (1983); M. L. Martin, X. Y. Sun, and G. J. Martin, *Ann. Rep. NMR Spectrosc.*, **16**, 187 (1985); C. H. Bushweller, J. B. Lambert and Y. Takeuchi, eds., in *Acyclic Organonitrogen Stereodynamics*. New York: VCH, 1992, pp. 1–55; M. Raban and D. Kost, in J. B. Lambert and Y. Takeuchi, eds., *Acyclic Organonitrogen Stereodynamics*. New York: VCH, 1992, pp. 57–88; S. F. Nelsen, in J. B. Lambert and Y. Takeuchi, eds., *Acyclic Organonitrogen Stereodynamics*. New York: VCH, 1992, pp. 89–121; B. M. Pinto, in J. B. Lambert and Y. Takeuchi, eds., *Acyclic Organonitrogen Stereodynamics*. New York: VCH, 1992, pp. 149–175.

Ring Reversal and Cyclic Systems

- 5.7. H. Booth, *Progr. NMR Spectrosc.*, **5**, 149 (1969); J. B. Lambert and S. I. Featherman, *Chem. Rev.*, **75**, 611 (1975); H. Günther and G. Jikeli, *Angew. Chem., Int. Ed. Engl.*, **16**, 599 (1977); E. L. Eliel and K. M. Pietrusiewicz, *Top. Carbon-13 Spectrosc.*, **3**, 171 (1979); F. G. Riddell, *The Conformational Analysis of Heterocyclic Compounds*. London: Academic Press, 1980; A. P. Marchand, *Stereochemical Applications of NMR Studies in Rigid Bicyclic Systems*. Deerfield Beach, FL: VCH, 1982.

Atomic Inversion

- 5.8. J. B. Lambert, *Top. Stereochem.*, **6**, 19 (1971); A. Rauk, L. C. Allen, and K. Mislow, *Angew. Chem., Int. Ed. Engl.*, **9**, 400 (1970). W. B. Jennings and D. R. Boyd, in J. B. Lambert and Y. Takeuchi, eds., *Cyclic Organonitrogen Stereodynamics*. New York: VCH, 1992, pp. 105–158; J. J. Delpuech, in J. B. Lambert and Y. Takeuchi, eds., *Cyclic Organonitrogen Stereodynamics*. New York: VCH, 1992, pp. 169–252.

Organometallics

- 5.9. K. Vrieze and P. W. N. M. Vanleeuwen, *Progr. Inorg. Chem.*, **14**, 1 (1971); B. E. Mann, *Ann. Rep. NMR Spectrosc.*, **12**, 263 (1982); K. G. Orrell and V. Šik, *Ann. Rep. NMR Spectrosc.*, **19**, 79 (1987).

Rates from Relaxation Times

- 5.10. J. B. Lambert, R. J. Nienhuis, and J. W. Keepers, *Angew. Chem., Int. Ed. Engl.*, **20**, 487 (1981).

Multiple Irradiation and One-Dimensional Multipulse Methods

General Multiple Resonance

- 5.11. R. A. Hoffman and S. Forsén, *Progr. NMR Spectrosc.*, **1**, 15 (1966); V. J. Kowalewski, *Progr. NMR Spectrosc.*, **5**, 1 (1969); W. McFarlane, *Determ. Org. Struct. Phys. Meth.*, **4**, 150 (1971); W. von Philipsborn, *Angew. Chem., Int. Ed. Engl.*, **10**, 472 (1971); W. MacFarlane, *Ann. Rep. NMR Spectrosc.*, **5A**, 353 (1972); R. L. Micher, *Magn. Reson. Rev.*, **1**, 225 (1972); L. R. Dalton, *Magn. Reson. Rev.*, **1**, 301 (1972); W. McFarlane and D. S. Rycroft, *Ann. Rep. NMR Spectrosc.*, **9**, 320 (1979); **16**, 293 (1985).

Difference Spectroscopy

- 5.12. J. K. M. Sanders and J. D. Merck, *Progr. NMR Spectrosc.*, **15**, 353 (1982).

Broadband Decoupling

- 5.13. M. H. Levitt, R. Freeman, and T. Frenkiel, *Advan. Magn. Reson.*, **11**, 47 (1983); A. J. Shaka and J. Keeler, *Progr. NMR Spectrosc.*, **19**, 47 (1987).

General Multipulse Methods

- 5.14. R. Benn and H. Günther, *Angew. Chem., Int. Ed. Engl.*, **22**, 350 (1983); C. J. Turner, *Progr. NMR Spectrosc.*, **16**, 311 (1984); G. A. Morris, *Magn. Reson. Chem.*, **24**, 371 (1986); D. L. Turner, *Ann. Rep. NMR Spectrosc.*, **21**, 161 (1989); K. Nakanishi, *One-Dimensional and Two-Dimensional NMR Spectra by Modern Pulse Techniques*. Mill Valley, CA: University Science Books, 1990; R. R. Ernst and G. Bodenhausen, *Principles of Nuclear Magnetic Resonance in One and Two Dimensions*. Oxford, UK: Oxford University Press, 1990.

Composite Pulses

- 5.15. M. H. Levitt, *Progr. NMR Spectrosc.*, **18**, 61 (1986).

6

Two-Dimensional NMR

NMR always has been multidimensional. In addition to frequency and intensity, which serve as the axes of the standard one-dimensional spectrum, reaction rates and relaxation times have provided further dimensions, often presented in the form of stacked plots. (See Figures 1-31 and 5-2.) The second dimension of modern NMR, however, refers to an additional frequency axis. This concept was first suggested in a lecture by Jeener in 1971 and reached wide application in the 1980s, when instrumentation caught up with theory. We can think of the first frequency dimension as the traditional characterization of nuclei in terms of chemical shifts and couplings. By introducing a second frequency dimension, we consider magnetic interactions between nuclei through structural connectivity, spatial proximity, or kinetic interchange.

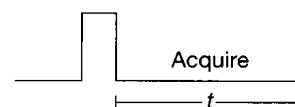
6-1 Proton-Proton Correlation Through Coupling

In the single-pulse experiments described up to this point, a 90° pulse is followed by a period during which the free-induction decay is acquired (Figure 6-1a). Fourier transformation of the time-dependent magnetic information into a frequency dimension provides the familiar spectrum of δ values, henceforth called a one-dimensional (1D) spectrum.

If the 90° pulse is preceded by another 90° pulse (Figure 6-1b), useful relationships between spins can evolve prior to acquisition. Figure 6-2 illustrates what happens in terms of magnetization vectors. Consider a sample that contains only one type of nucleus without any coupling partners—for example, the ^1H spectrum of chloroform or tetramethylsilane.

Figure 6-1 The pulse arrangements for a single cycle of one-dimensional NMR spectroscopy (top) and for two-dimensional NMR correlation spectroscopy (COSY) (bottom). In this diagram, each pulse is 90° . Data are acquired during the time t in the one-dimensional experiment and t_2 in the two-dimensional experiment.

(a) The one-dimensional experiment



(b) The two-dimensional COSY experiment



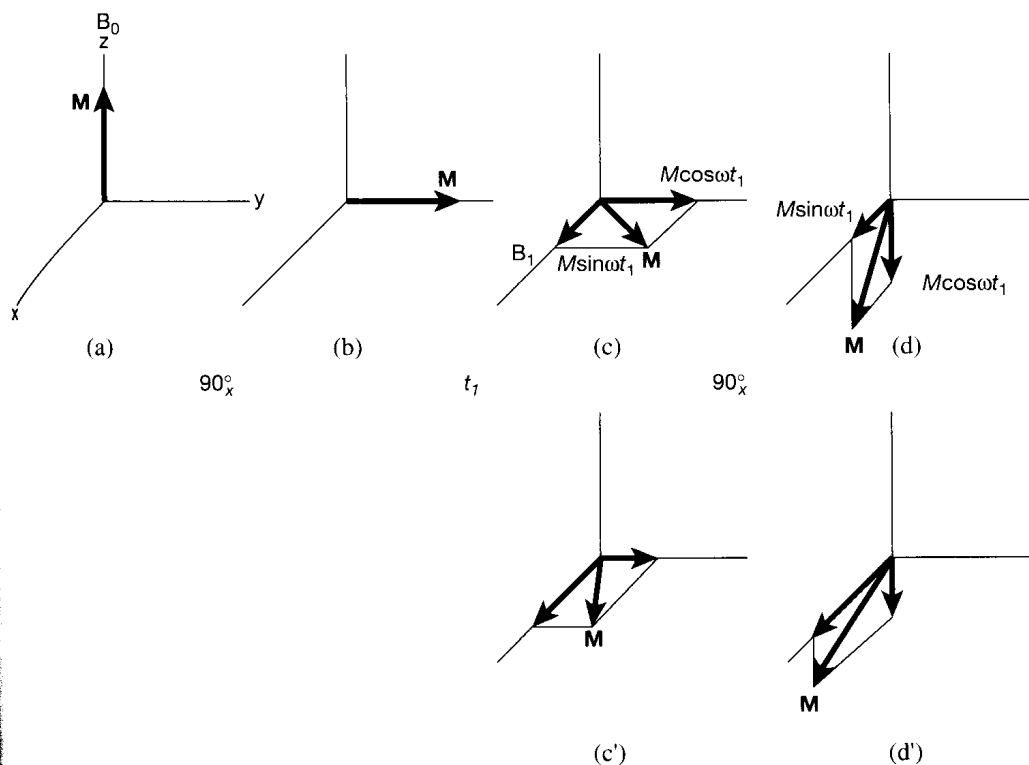


Figure 6-2 The pulse sequence for the COSY experiment. For (c'), the magnetization \mathbf{M} is allowed to evolve a longer time from (b) than for (c) before the final 90_x° pulse is applied to give (d').

Although the final result of the particular experiment we are about to describe may seem trivial or even pointless at first, it will take on fuller meaning when we introduce relationships with other nuclei. The isolated nucleus of Figure 6-2 begins with the net magnetization \mathbf{M} aligned along the z axis (Figure 6-2a) and then realigned along the y axis after application of the 90° pulse (Figure 6-2b). If the coordinate system rotates at the reference frequency and the nucleus resonates at a slightly higher frequency, the spin vector picture begins to evolve. After a short amount of time, the vector \mathbf{M} moves to a new position in the xy plane—for example, in Figure 6-2c. We ignore longitudinal relaxation (T_1) to simplify the drawings. The evolving magnetization vector may be decomposed into a y component ($M_y = M \cos \omega t_1$) and an x component ($M_x = M \sin \omega t_1$), in which ω is the difference between the frequency of the carrier and that of the resonating nucleus and t_1 is the time elapsed since the 90° pulse.

If, at this point, the second 90° pulse of Figure 6-1b is applied, again along the x axis, the result is different for the two magnetization components illustrated (Figure 6-2d). The x component is unaffected, but the y component is transferred to the negative z axis. If magnetization is detected in the xy plane, only M_x remains. This quantity appears as a free-induction decay during the time t_2 after the second pulse. Fourier transformation of the FID as a function of t_2 yields a signal at the resonance frequency (ν_A). The intensity of this signal is determined by the quantity $M \sin \omega t_1$. (The subscripts are necessary to distinguish the evolution period t_1 from the acquisition period t_2 ; see Figure 6-1b.) If t_1 is relatively short, $M_x (= M \sin \omega t_1)$ is small, little x magnetization has developed (Figure 6-2d), and the resulting peak is small. A slightly longer value of t_1 yields a larger x component (Figure 6-2c' and d') as $M \sin \omega t_1$ grows. Note that the spin population (the z , or longitudinal, magnetization) is inverted in Figure 6-2d and d'.

Figure 6-3 shows the result of a whole series of such experiments, with a buildup of $M_x (= M \sin \omega t_1)$ as t_1 increases, reaching a maximum when the spin vector \mathbf{M} is lined up along the x axis. The peak height then decreases as the vector moves to the left of the x axis, reaching zero intensity when it is lined up along the negative y axis. As it passes behind the

Figure 6-3 The solid line slanting upwards at frequency ν_A on the horizontal axis serves as the baseline for a series of ^1H spectra of chloroform, according to the COSY pulse sequence for a series of values of t_1 . Each peak results from one cycle of $90^\circ-t_1-90^\circ$ followed by Fourier transformation during t_2 of Figure 6-1 to give frequency ν_A on the axis labeled ν_2 (corresponding to the time domain t_2). The period t_1 is ramped up after each cycle. Fourier transformation in the t_1 dimension has not been carried out.

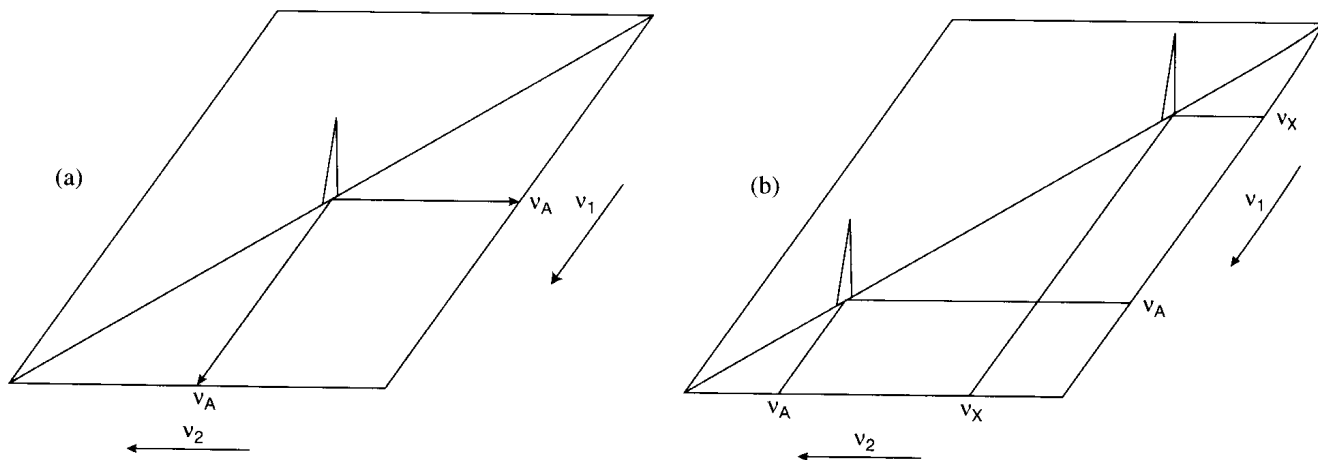
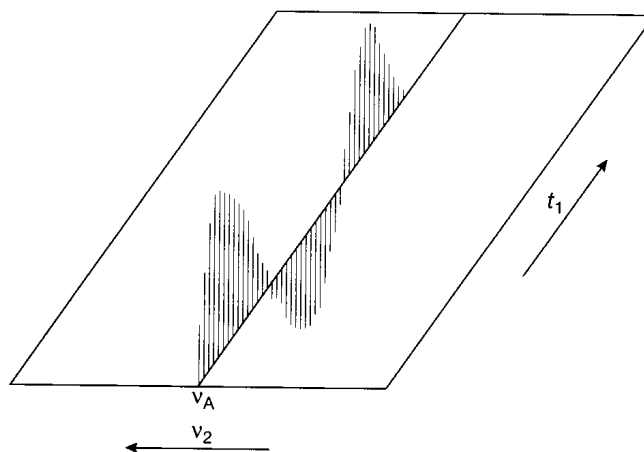


Figure 6-4 (a) The result of the COSY experiment after double Fourier transformation for a single isolated nucleus such as that in Figure 6-3. (b) The result of the COSY experiment for two uncoupled nuclei.

y axis, the intensity becomes negative, attaining a negative maximum when the vector is aligned along the $-x$ axis. This negative maximum would be slightly smaller than the initial positive maximum, because of T_2 relaxation. It is clear from the figure that this family of experiments generates a sine curve when M_x is plotted as a function of t_1 . Frequency (obtained from the Fourier transformation of t_2 to give ν_2) is along the horizontal dimension, and time t_1 is along the vertical dimension. The set of data generated from stepping t_1 in this fashion in fact constitutes a free-induction decay that also may be Fourier transformed. Because the frequency ω represented by the sine curve in t_1 is the same as the frequency from the initial Fourier transformation in t_2 , the result of the second Fourier transformation is a single peak at the coordinates (ν_A, ν_A) when plotted in two frequency dimensions (Figure 6-4a). This is the trivial result previously alluded to.

The utility of the experiment just discussed becomes evident when two coupled nuclei are treated in the indicated fashion. Two uncoupled nuclei yield the trivial result of two peaks, at (ν_A, ν_A) and (ν_X, ν_X) , respectively, as in Figure 6-4b. These peaks are necessarily on the diagonal of the two-dimensional representation. Satisfying complications arise when the two nuclei are coupled. Figure 6-5 illustrates the possible spin states for nuclei A and X,

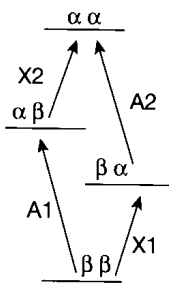


Figure 6-5 The energy diagram for an AX spin system.

as for example the alkenic protons in β -chloroacrylic acid, $\text{ClCH}=\text{CHCO}_2\text{H}$. The 1D AX spectrum contains four peaks, due to scalar (J) coupling. The diagram is intended to indicate the four different frequencies, from the highest (A1) to the lowest (X2). It is useful first to consider population perturbations during an old-style, 1D selective-decoupling CW experiment. Irradiation, for example, of only transition A1 tends to bring the $\alpha\beta$ and $\beta\beta$ states closer together in population. Consequently, there is a direct effect on the intensities of the connected transitions X1 and X2, which propagates as a secondary effect on the intensity of the A2 transition. With respect to A1, X2 is called a *progressive transition* (a transition that goes on to a higher spin state), X1 is called a *regressive transition*, and A2 is called a *parallel transition*.

In the pulse experiment, energy absorption at frequency A1 has similar effects, which bring about magnetization or population transfer. The first 90° pulse serves to label all the magnetization with the 1D frequencies during period t_1 : A1, A2, X1, and X2. The second 90° pulse results in a population inversion for any given transition (Figure 6-2d). This perturbation causes population changes in all connected transitions of the resonances to which the nucleus is coupled, as well as changes secondarily to parallel transitions. Part of the magnetization at frequency A1, for example, is transferred to each of the other three transitions by the second pulse during period t_2 . This transferred magnetization has a new frequency. Such transfers occur from all four of the transitions to each of the other three. Thus, the magnetization observed at frequency A1 during t_2 contains components modulated at frequencies A2, X1, and X2. That portion of the magnetization, for example, that has frequency A1 during t_1 , but frequency X2 during t_2 , is observed as a peak off of the diagonal, at frequency (ν_{A1}, ν_{X2}) . In the absence of J couplings, the A and X transitions of Figure 6-5 are not connected, and magnetization is not transferred.

Figures 6-6 and 6-7 are two representations of the two-dimensional (2D) experiment for β -chloroacrylic acid. In Figure 6-6, the *stacked representation* contains several hundred complete 1D experiments, whose closely packed horizontal lines are barely distinguishable. On the diagonal from the lower left to the upper right (as drawn into the plots in Figure 6-4) are the four peaks that arise directly from resonance without magnetization transfer, that is, the components of magnetization that possess the same frequency in t_1

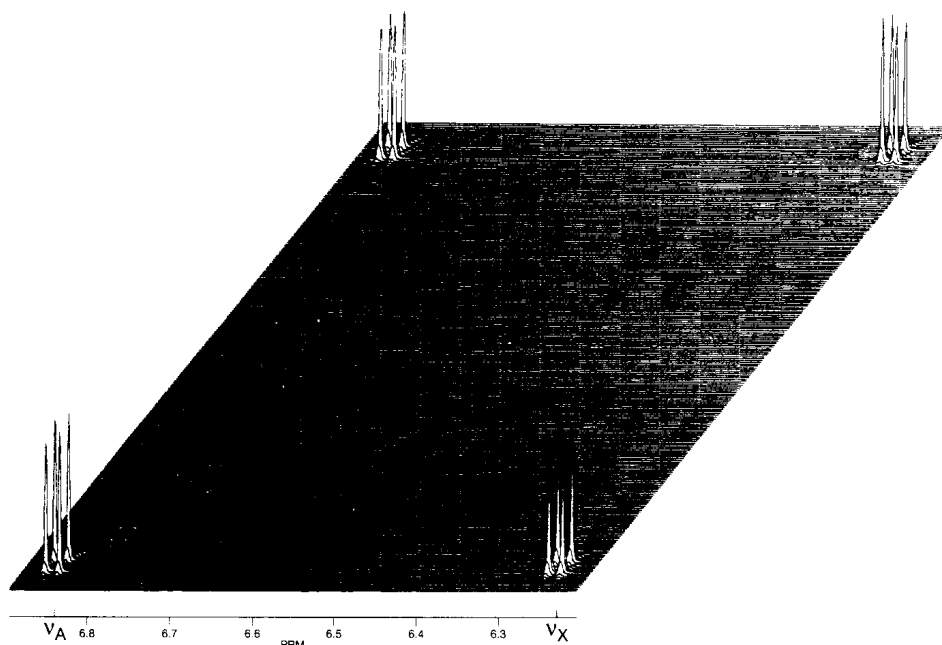
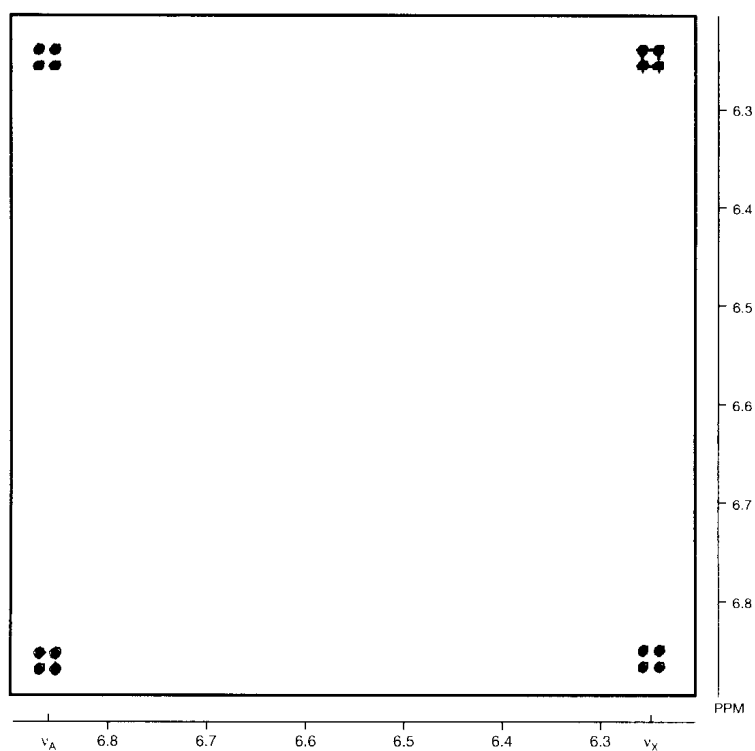


Figure 6-6 The stacked representation of the COSY experiment for the two coupled nuclei of β -chloroacetic acid. (Reproduced from A. E. Derome, *Modern NMR Techniques for Chemistry Research*, Pergamon Press, Oxford, UK, 1987, p. 189.)

Figure 6-7 The contour representation of the COSY experiment for two coupled nuclei of β -chloroacetic acid. (Reproduced from A. E. Derome, *Modern NMR Techniques for Chemistry Research*, Pergamon Press, Oxford, UK, 1987, p. 191.)



and t_2 . These four peaks constitute the normal four-peak 1D spectrum. All the peaks off of the diagonal represent magnetization transfer by scalar (J) coupling. For example, a transfer between the parallel transitions A1 and A2 is found as symmetrical peaks just above and below the diagonal at the lower left. One peak represents a transfer from A1 to A2, the other from A2 to A1. Because of this reciprocal relationship, all off-diagonal peaks appear in pairs reflected across the diagonal. Normally, the off-diagonal peaks between parallel transitions are more of a nuisance than useful, and they can be reduced or deleted by special techniques. The important information results from magnetization transfer between the A and the X nuclei, whose peaks are the clusters in the upper left and lower right of Figure 6-6, representing all the possible transfers between the A and X transitions: A1 to X1, X2 to A1, and so on—eight in total, including the mirror-image pairs (A to X and X to A) on either side of the diagonal.

Figure 6-7 is the alternative *contour representation* of the same data, in which the distracting baselines are removed and only the peak bases remain, as if the spectator is viewing the spectrum from directly above it. By convention, the original diagonal usually is from lower left to upper right. The Jeener experiment commonly is given the quasi acronym COSY, for *CORrelation Spectroscopy*. Since most 2D experiments involve spectral correlations, the name is not apt. Alternative terms, such as 90° COSY, COSY90, H,H-COSY, or homonuclear H COSY, have gone by the wayside through public acceptance of the general term COSY. The experiment itself has become an essential part of the analysis of complex proton spectra.

Figure 6-8 is the COSY experiment for the indicated annulene, from the work of H. Günther. The 1D spectrum is shown along both the horizontal and the vertical axes, and the resonances are labeled α , β , and A through F. The aromatic protons that are ortho and meta to the ring fusion provide an isolated spin system, and their coupling is represented by the off-diagonal (or cross) peak labeled α,β . The presence of a cross peak normally indicates that the protons giving the connected resonances on the diagonal are geminally or vicinally

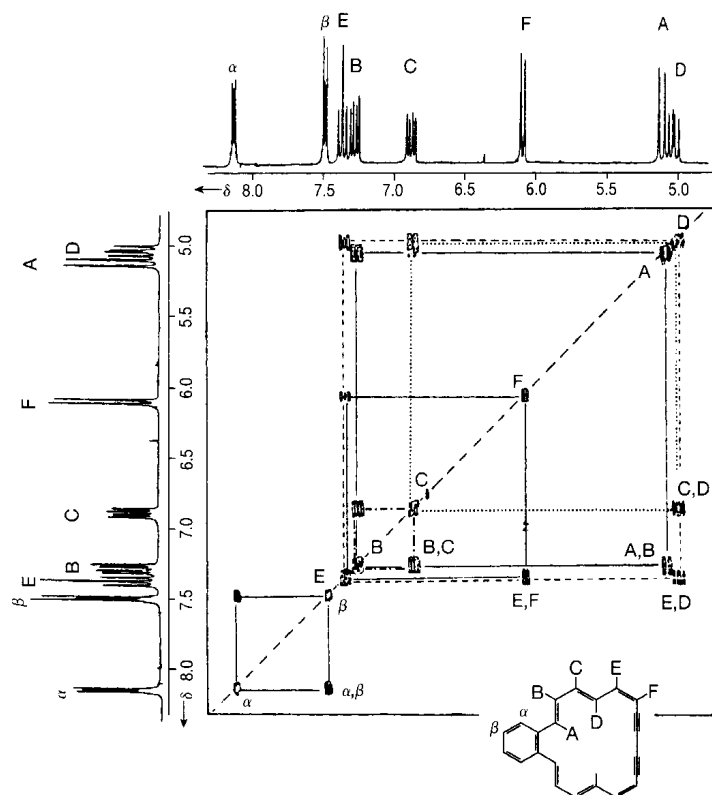


Figure 6-8 The COSY experiment for the illustrated annulene. (Reproduced from R. Benn and H. Günther, *Angew. Chem., Int. Ed. Engl.*, **22**, 350 [1983]).

coupled. Long-range couplings do not usually provide significant cross peaks. Exceptions, however, can be expected, since long-range couplings can be large.

The COSY analysis of the remainder of the spectrum in Figure 6-8 provides the peak assignments and confirms the structure. Protons A and F are the only ones split by a single neighbor. The coupling of A with B is trans and should be larger than the cis coupling between E and F. The two doublets then may be assigned as F (the smaller coupling) at δ 6.1 and A (the larger coupling) at δ 5.2. It usually is essential in a COSY analysis to be able to make an initial assignment through traditional considerations of chemical shifts and coupling constants. (See Chapters 3 and 4.) The COSY analysis then consists of moving from the known diagonal peak, to a cross peak, and back to the diagonal for the assignment of a new peak. Only A and F have single cross peaks (one coupling partner). All remaining resonances in the large ring have two cross peaks, which provide the means for assignment. We can start with either A or F. Dropping down from A leads to the cross peak A,B, and horizontal movement to the left leads to a diagonal peak and the assignment of proton B. The horizontal path passes through another cross peak, which must be between B and its other coupling partner, C. Moving up from B,C then leads to a diagonal peak and the assignment of proton C. Horizontal movement to the right leads to the cross peak C,D and returning upward to the diagonal assigns proton D. Dropping back down from D and passing through C,D leads to the other cross peak from D, labeled E,D. Returning to the diagonal to the left assigns proton E and passes through the other cross peak from E, labeled E,F. Returning upward from E,F to the diagonal completes the assignment with proton F.

A group at IBM has provided a useful example of a more complex COSY analysis with the tripeptide Pro-Leu-Gly (**6-1**). The three carbonyl groups disrupt vicinal connectivities, so the molecule consists of four independent spin systems: proline, leucine, glycine, and the

The top spectrum of Figure 6-10 completes the COSY analysis of the Leu portion and confirms the fact that the NH at δ 8.1 is part of Leu rather than Pro. The expected Leu connectivity is $\text{NH} \rightarrow \text{CH} \rightarrow \text{CH}_2 \rightarrow \text{CH} \rightarrow \text{CH}_3$. Cross peaks with the following connectivities (starting with NH) are observed: δ 8.1 \rightarrow 4.3 (q or dd) \rightarrow 1.5 (m) \rightarrow 0.9 (dd). Apparently, two of the proton resonances coincide, most likely those from CH_2 and the isopropyl CH. The CH_3 resonance, as expected, is at the lowest frequency and cannot be from any Pro group. Its higher multiplicity (dd, Figure 6-9, top) arises because the two methyl groups are diastereotopic due to the chiral center to which the butyl group is attached.

The lower spectrum of Figure 6-10 shows the Pro connectivity. The highest-frequency resonance (δ 3.7) should be from the CH group adjacent (α) to the carbonyl group. The

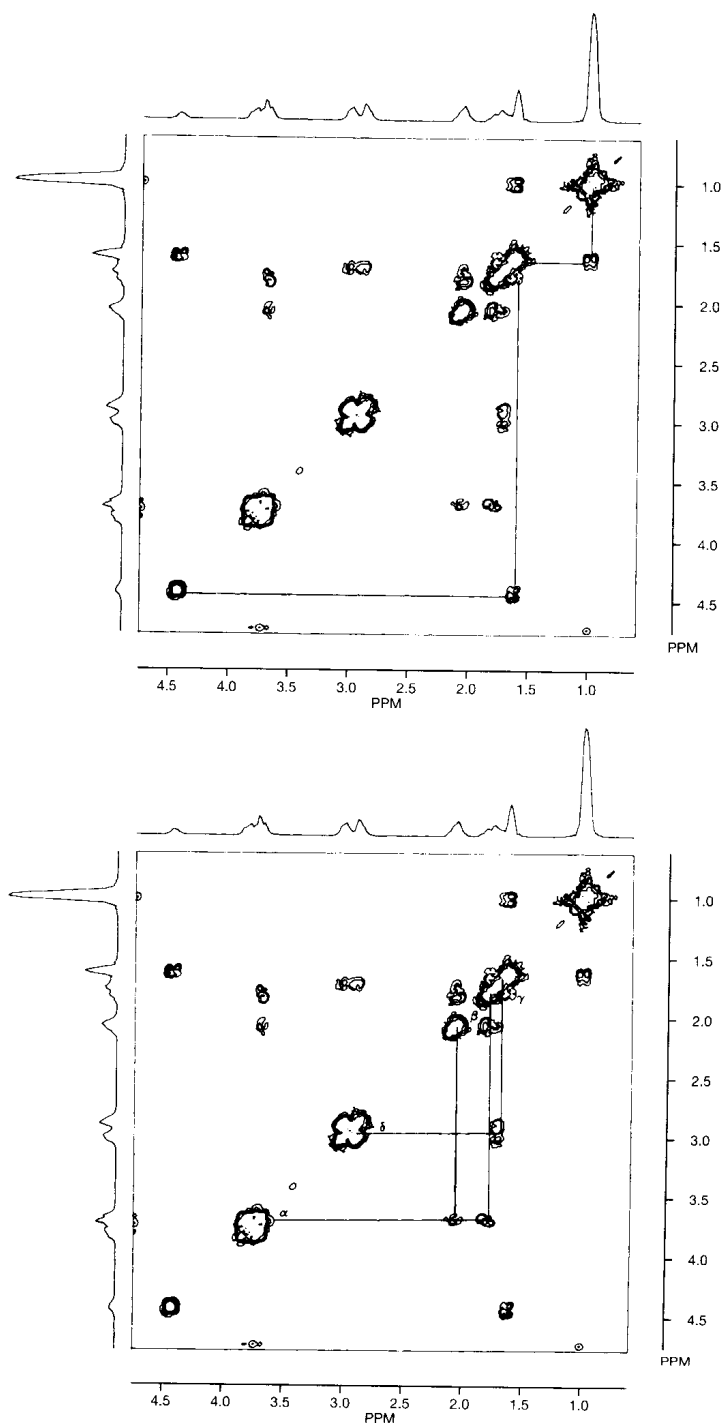


Figure 6-10
Top: Connectivity within the leucine portion of Pro-Leu-Gly by COSY.
Bottom: Connectivity within the proline portion of Pro-Leu-Gly by COSY.
(Courtesy of IBM Instruments, Inc.)

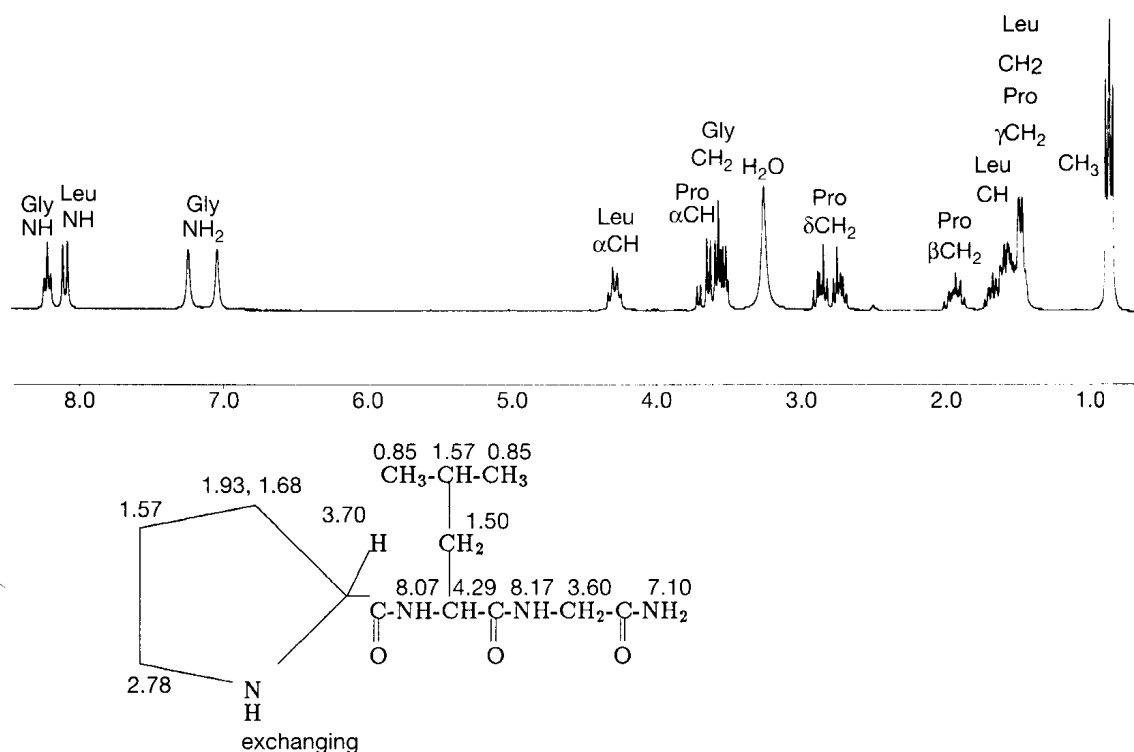


Figure 6-11 The fully assigned ^1H spectrum of Pro-Leu-Gly. (Courtesy of IBM Instruments, Inc.)

resonance at δ 3.7 actually is an overlap of this Pro CH (the higher frequency portion) with the Gly CH_2 (the lower frequency portion). The Pro CH has two cross peaks with the diastereotopic β protons, at δ 1.7 and 1.9, which are mutually coupled and have their own cross peak. Unfortunately, the γ protons are nearby (δ 1.6), but their cross peak with the δ protons at δ 2.8 completes the assignment of the spectrum. The fully assigned 1D spectrum and structure are given in Figure 6-11.

False peaks and a lack of symmetry around the diagonal are common in the COSY experiment and can arise for several reasons. First, differences in digital resolution in the two periods, t_1 and t_2 , may prevent perfect symmetry. Second, incorrect pulse lengths or, third, incomplete transverse relaxation during the delay time can create false cross peaks. Fourth, there may be effects from longitudinal relaxation. Any magnetization in the z direction does not precess during t_1 and therefore is rotated by the second 90° pulse into the position recognized as $\nu_1 = 0$ (the position of the reference frequency). Signals thus occur at $\nu_1 = 0$ and at any value of ν_2 associated with a resonance, resulting in a stream of lines, called *axial peaks* or *t_1 noise*, in the 2D plot. Fifth and finally, folding can occur in two dimensions and can give rise to off-position diagonal peaks and even cross peaks. All these artifacts may be minimized by optimizing pulse lengths, by allowing sufficient time for transverse relaxation, by using phase cycling, or by employing symmetrization. Axial peaks may be suppressed largely by alternating $+90^\circ$ and -90° for the second pulse, thus canceling z magnetization. The more complex CYCLOPS procedure suppresses axial peaks and eliminates other artifacts, such as quad images. (See Section 5-8.) *Symmetrization* is a procedure for imposing bilateral symmetry around the diagonal. Most artifacts are conveniently eliminated by this procedure, but not all. For example, if two resonances have streams of t_1 noise, a point on one stream can occur at the precise mirror position (with respect to the diagonal) of a point on the other stream. Although the streams are largely eliminated, the two peaks at the symmetrical positions are retained and appear as handsome cross peaks. Usually common sense can reject them. Experimental procedures for optimizing the COSY experiment are discussed in Chapter 7.

There are many variants of the standard COSY experiment that either improve on its basic aims or provide new information. We shall consider several of them without appreciable attention to the details of the pulse sequences.

COSY45. The large size of diagonal peaks sometimes can be a deterrent to understanding the significance of nearby cross peaks. The problem is aggravated by the presence of cross peaks from parallel transitions. (See Figure 6-5.) The COSY45 experiment reduces the intensities of both the diagonal peaks and the cross peaks from parallel transitions. Figure 6-12 compares the COSY90 and COSY45 experiments for 2,3-dibromopropionic acid ($\text{CH}_2\text{BrCHBrCO}_2\text{H}$). The COSY45 experiment clarifies cluttered regions close to the diagonal and also provides information on the signs of coupling constants. The name derives from alteration of the second pulse length: $90^\circ-t_1-45^\circ-t_2(\text{acquire})$. The use of the smaller tip angle restricts the magnetization transfer between nuclei, but the effect is larger for the directly connected parallel transitions than for the more remotely connected progressive and regressive transitions. It is for this reason that the diagonal peaks are clarified. Inevitably, however, there is a loss of signal. A tip angle of 60° (COSY60) may be used as a compromise, but any gains in sensitivity occur at the expense of clarification of the diagonal.

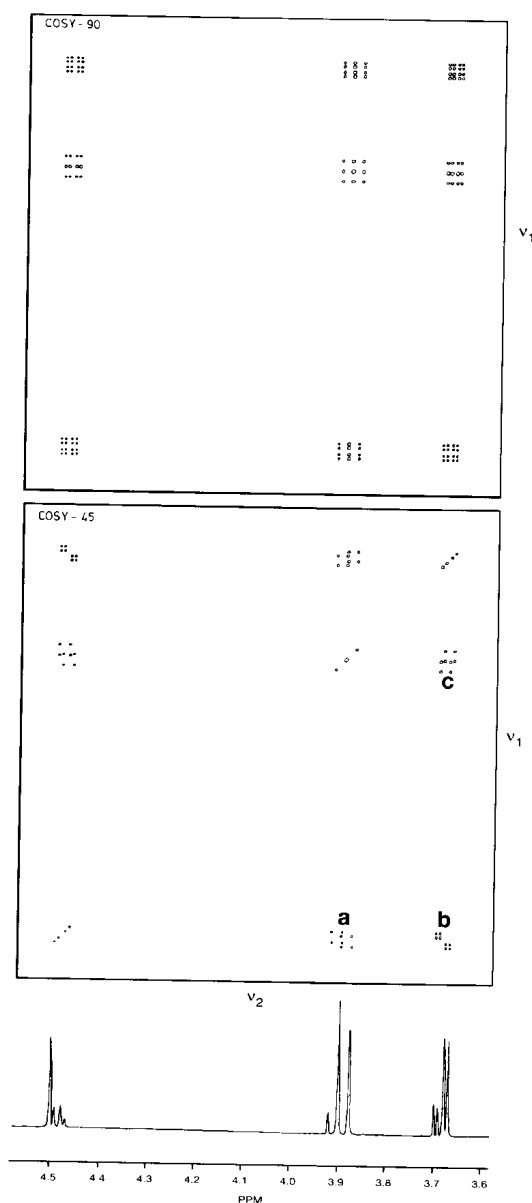


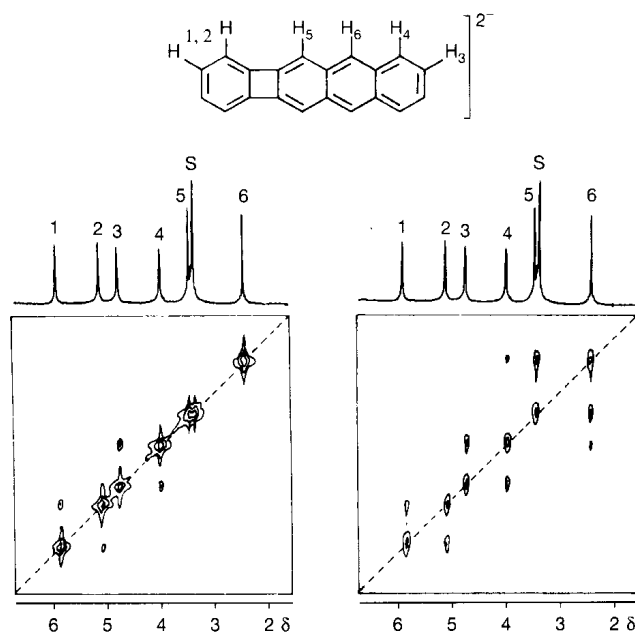
Figure 6-12 The COSY90 (top) and COSY45 (bottom) spectra of 2,3-dibromopropionic acid. The 1D spectrum at the bottom is a cross section through the COSY45 spectrum. (Reproduced from A. E. Derome, *Modern NMR Techniques for Chemistry Research*, Pergamon Press, Oxford, UK, 1987, p. 228.)

An examination of the cross peaks in the COSY45 spectrum of Figure 6-12 reveals overall appearances different from those in normal COSY spectra. Rather than possessing the usual squarish or rectangular shape, many of the cross peaks have taken on a decided tilt. The direction of tilt is related to the relative signs of coupling constants. In an AMX system, for example, the A,M off-diagonal peak is caused by magnetization transfer through J_{AM} , referred to as the *active coupling*. Its tilt, however, depends on whether couplings of A and M with the third nucleus, X, have the same or opposite signs. A tilt with a positive slope (parallel to the diagonal), for example, results if the two *passive couplings*, J_{AX} and J_{MX} , have the same sign; a tilt with a negative slope (orthogonal to the diagonal) results if they have opposite signs.

COSY cross peaks are caused predominantly by both geminal (HCH) and vicinal (HCCH) couplings. Because connectivity inferences are based largely on vicinal couplings, it would be useful to be able to distinguish these two classes. As described in Chapter 4, vicinal couplings are, in general, positive, and geminal couplings (at least on saturated carbons) are negative. Consequently, the two classes can, in principle, be distinguished by the slope of the tilt in the COSY45 spectrum, as illustrated in Figure 6-12. This spectrum is closer to ABX than AMX, but nonetheless shows the expected off-diagonal COSY peaks. The resonances of the diastereotopic CH₂ protons are found at δ 3.67 and 3.89, and the resonance of the methine proton is at δ 4.49, shifted to a higher frequency (lower field) by attachment of the carbon to two electron-withdrawing substituents (Br and CO₂H). The off-diagonal peaks that have been labeled **a** and **b** result from the active coupling of either methylene proton with the methine proton: a positive, vicinal coupling. The passive couplings for these cross peaks are the geminal coupling to the diastereotopic partner and the vicinal coupling to the other methylene proton. As these couplings have opposite sign, the tilt has a negative slope. The off-diagonal peak labeled **c** results from active coupling between the diastereotopic methylene protons. The passive couplings for this cross peak are the two vicinal couplings between the diastereotopic protons and their vicinal neighbor. Because both passive couplings are positive, the tilt has a positive slope. In this fashion, **c** is spotted as a cross peak between geminal protons.

Long-Range COSY (LRCOSY or delayed COSY). The normal assumption in the COSY experiment is that two- or three-bond (geminal or vicinal) couplings provide the dominant magnetization transfer to create cross peaks. Information from longer range couplings, however, also can be useful. Introducing a fixed delay Δ during the evolution and detection periods [$90^\circ - t_1 - \Delta - 90^\circ - \Delta - t_2(\text{acquire})$] enhances magnetization transfer from small couplings at the expense of large couplings. Figure 6-13 compares the COSY and

Figure 6-13 The 400 MHz COSY (left) and LRCOSY (right) spectra of naphthobiphenylene dianion. (The signal S is from solvent.) (Reproduced from H. Günther, *NMR Spectroscopy*, 2d ed. John Wiley & Sons, Ltd., Chichester, UK, 1995, p. 300.)



LRCOSY experiments for a polynuclear aromatic compound. In the COSY spectrum, cross peaks occur only between ortho neighbors (1,2 and 3,4). In the LRCOSY spectrum, additional cross peaks arise between peri neighbors (5,6 and 4,6). Information on the connectivity between fused aromatic rings thus becomes available in the LRCOSY case.

Phase-Sensitive COSY (ϕ -COSY). Fourier transformation involves building up a signal from the sum of sine and cosine curves. Every point in the spectrum has both sine and cosine contributions, which are 90° out of phase. These contributions sometimes are called the imaginary and real terms and lead mathematically to the *dispersion-mode* and *absorption-mode* spectra. (See Appendix 2.) An in-phase, or absorption, signal has the familiar form of a positive peak. A dispersion signal, commonly used for electron spin resonance spectra, has a sideways S shape with a portion below and a portion above the baseline. (See Figure 2-11.) Such a signal produces both negative and positive maxima for a given peak and a value of zero at the resonance frequency as the sign changes. NMR experiments normally are tuned to the absorption mode by the process of phasing, but the two signals also may be combined mathematically to produce what is called a *magnitude*, or *absolute-value*, spectrum.

Many of the COSY experiments we have examined thus far used magnitude representations because of phase differences between various peaks in the pure modes. Both magnetization that is not transferred (and thus appears on the diagonal) and magnetization that is transferred to parallel transitions undergo no phase shift. Cross peaks, however, exhibit phase shifts. A transfer between progressive transitions (A1 to X2 in Figure 6-5) shifts the phase -90° , and a transfer between regressive transitions (A1 to X1) shifts it $+90^\circ$. Because absorption and dispersion modes differ by 90° , phasing the diagonal peak to absorption results in dispersive cross peaks, or vice versa. Moreover, cross peaks from progressive and regressive transitions are always out of phase by 180° . (If one represents positive absorption, the other represents negative absorption; or if one begins a dispersive signal negatively, the other begins positively.) The magnitude, or absolute-value, mode is used to eliminate all phase differences and produce absorptionlike peaks. The resulting peaks tend to be broad and often are distorted. In small molecules with little peak overlap, there may be no problem with the use of magnitude spectra, but larger molecules such as proteins, polysaccharides, or polynucleotides may produce unacceptable overlap. The phase-sensitive COSY experiment then can tune the cross peaks to a pure absorption (real) mode. This experiment not only provides enhanced resolution, but also enables coupling constants to be read more easily from the cross peaks when the data are highly digitized.

Because the 2D method involves two time domains, the transformations in both t_1 and t_2 generate real and imaginary components. As a result, the phase-sensitive 2D signal has four modes rather than two. These phase modes, or quadrants, correspond to both frequency signals being real, both being imaginary, or one being real while the other is imaginary. Figure 6-14 illustrates the four modes. The real-real (RR) mode produces the familiar peak with a contour shaped like a four-pointed star at the base. Figure 6-15 illustrates what the COSY spectrum for two spins looks like when the diagonal and parallel components are tuned dispersively (both imaginary) and the progressive and regressive cross peaks are tuned absorptively (both RR, but 180° out of phase). This common phase-sensitive representation provides straightforward identification of the cross peaks derived from coupling and hence determines J .

Multiple Quantum Filtration. The one-dimensional INADEQUATE pulse sequence suppresses the center-band singlet in order to measure ^{13}C - ^{13}C couplings from the satellites. (See Section 5-7.) The procedure involves creating double quantum coherences. (See Section 5-8.) A similar procedure may be used in two-dimensional ^1H spectra to suppress singlets, which are single quantum coherences. Such singlets may arise from solvent or from uncoupled methyl resonances, both of which can constitute major impediments in locating highly split resonances in a complex spectrum. In a *Double Quantum Filtered COSY* (DQF-COSY) experiment, an extra 90° pulse is added after the second 90° COSY pulse,

Figure 6-14 The four types of 2D phase quadrants, corresponding to frequency modes that are real–real (RR), imaginary–real (IR), real–imaginary (RI), and imaginary–imaginary (II). (Reproduced from A. E. Derome, *Modern NMR Techniques for Chemistry Research*, Pergamon Press, Oxford, UK, 1987, p. 207.)

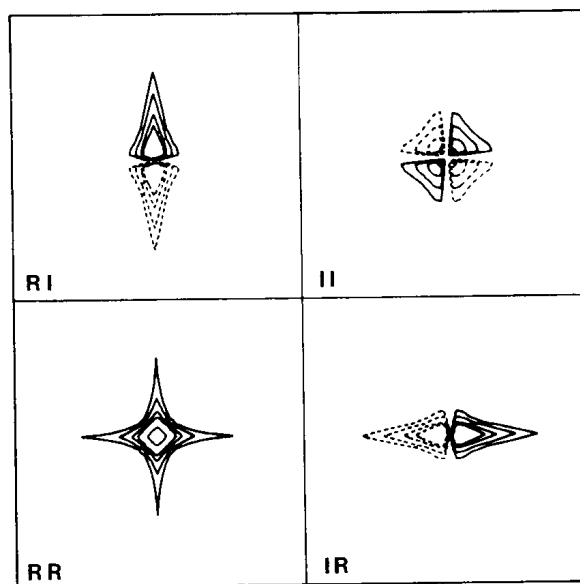
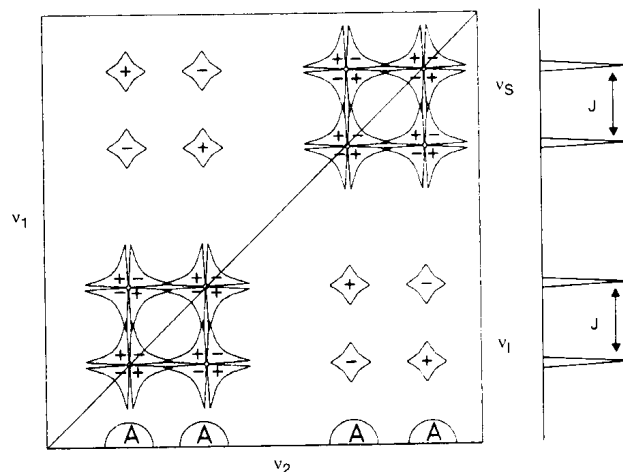
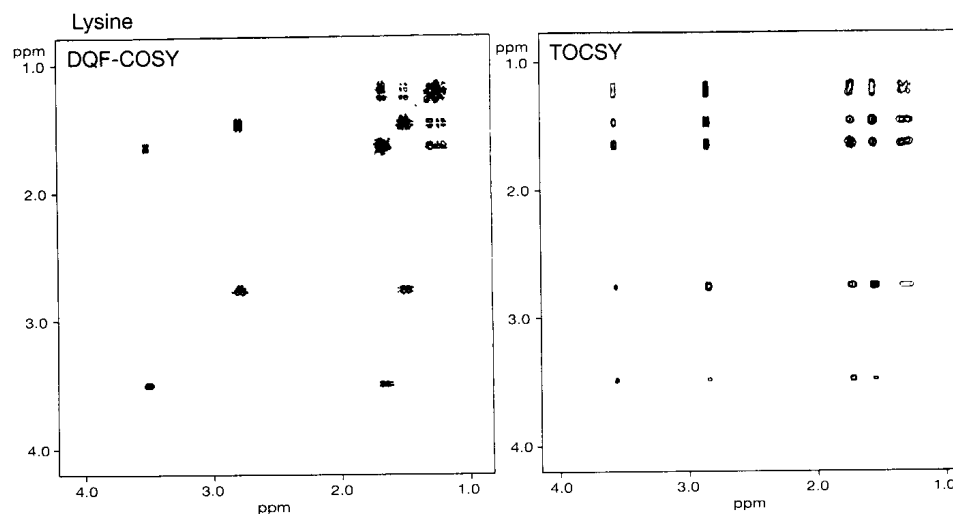


Figure 6-15 Phase-sensitive COSY diagram for two spins, with the diagonal peaks in dispersion mode and the cross peaks in antiphase absorption mode. The 1D spectrum is on the right. (Reproduced from F. J. M. van de Ven, *Multidimensional NMR in Liquids*, VCH, New York, 1995, p. 171.)



and phase cycling converts multiple quantum coherences into observable magnetizations. The resulting 2D spectrum lacks all singlets along the diagonal. For example, the left spectrum of lysine, $^+NH_3CH(CH_2CH_2CH_2CH_2NH_2)CO_2^-$, in Figure 6-16 has no solvent (HOD) peak. An important feature of the phase-sensitive DQF-COSY experiment is that

Figure 6-16 The DQF-COSY and TOCSY spectra of lysine. (Reproduced from J. N. S. Evans, *Biomolecular NMR Spectroscopy*, Oxford University Press, Oxford, UK, 1995, p. 428.)



double quantum filtration allows both diagonal and cross peaks to be tuned into pure absorption at the same time. This feature reduces the size of all the diagonal signals and permits cross peaks close to the diagonal to be analyzed. The only disadvantage of DQF-COSY is a reduction in sensitivity by a factor of two. The *Triple Quantum Filtered COSY* (TQF-COSY) experiment removes both singlets and AB or AX quartets, providing greater spectral simplification. It is rarely used because of a concomitant increased loss of sensitivity.

Total Correlation Spectroscopy (TOCSY). In the standard COSY experiment, the connectivity within an entire spin system, such as that in a butyl group ($\text{CH}_3\text{CH}_2\text{CH}_2\text{CH}_2-$), must be mapped out from proton to proton via a series of cross peaks. By spin locking the protons during the second COSY pulse, the chemical shifts of all the protons may be brought essentially into equivalence. Recall that resonance frequencies of protons and carbons are made equal through cross polarization for solids by achieving the Hartmann-Hahn condition. (See Section 1-9.) In the 2D variant of this experiment, the initial 90° pulse and the period t_1 occur as usual, but the second pulse locks the magnetization along the y axis so that all protons have the spin lock frequency. All coupled spins within a spin system then become closely coupled to each other, and magnetization is transferred from one spin to all the other members. The right spectrum of Figure 6-16 shows the result for lysine. The methylene group at the lowest frequency (upper right corner) exhibits four TOCSY cross peaks, one with each of the other three methylene groups and one with the methine proton. The TOCSY experiment, a variation of which is called the *HOmonuclear HArtmann-HAhn* or HOHAHA, experiment, has particular advantages for large molecules, including enhanced sensitivity and, if desired, the phasing of both diagonal and cross peaks to the absorption mode. The process of identifying resonances within specific amino acid or nucleotide residues is considerably simplified by this procedure. Each residue can be expected to exhibit cross peaks among all its protons and none with protons of other residues.

Relayed COSY. An alternative, but less general, method for displaying extended levels of connectivity is provided by *Relayed Coherence Transfer* (RCT). The typical COSY experiment for an AMX system with $J_{AX} = 0$ produces cross peaks between A and M and between M and X. It is not unusual for the key diagonal peak for M to be coincident with a resonance from another spin system, making it difficult to follow the connectivity path. (Recall, for example, the Leu portion of the COSY spectrum of Pro-Leu-Gly in Figure 6-10.) The RCT experiment generates a cross peak between the A,M and M,X cross peaks, eliminating the ambiguity. The RCT pulse sequence is $90^\circ-t_1-90^\circ-\tau-180^\circ-\tau-90^\circ-t_2(\text{acquire})$, in which the sequence after the second 90° pulse permits coherence to be relayed to the next spin. The result is shown diagrammatically in Figure 6-17 for AMX and $A'M'X'$ systems whose M and M' resonances coincide. The COSY experiment contains the expected four cross peaks. The RCT experiment contains two additional cross peaks, connecting the cross

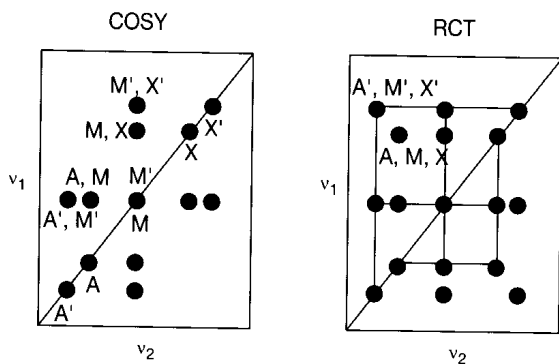


Figure 6-17 Diagram of COSY and relayed coherence transfer (RCT) experiments for two three-spin systems (AMX and $A'M'X'$) whose M and M' portions overlap. (Adapted from F. J. M. van de Ven, *Multidimensional NMR in Liquids*, VCH, New York, 1995, p. 233.)

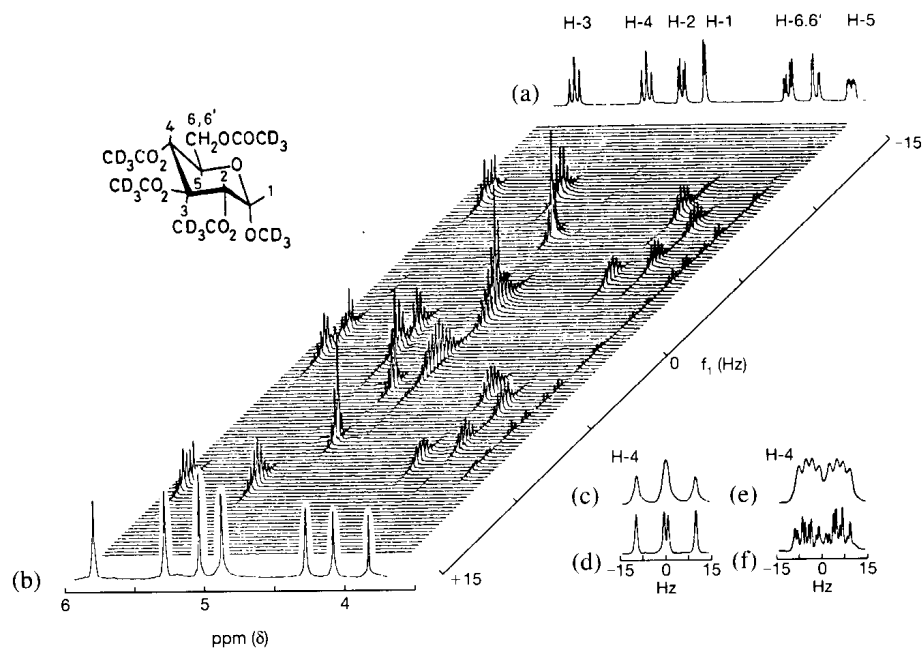
peaks of the individual spin systems. The two new cross peaks are labeled (A, M, X) and (A', M', X'). The connectivity of AMX and of A'M'X' is then rendered unambiguous.

J-Resolved Spectroscopy. In Chapter 5, we saw how the spin echo experiment can isolate or remove characteristics of chemical shifts or coupling constants. Spin echoes may be used in two dimensions to generate one frequency dimension representing chemical shifts and another representing coupling constants. The sequence $90^\circ - \frac{1}{2}t_1 - 180^\circ - \frac{1}{2}t_1 - t_2$, for example, uses the 180° pulse to refocus chemical shifts during t_1 . The result for a glucose derivative is shown in Figure 6-18. The ^1H frequencies are found on the horizontal axis (ν_2 , in δ), with the normal 1D spectrum displayed at the top (Figure 6-18a). The vertical axis ("f₁" = ν_1) contains only proton-proton coupled multiplets, each centered about a zero frequency point (i.e., all multiplets occur at the same chemical shift in $\nu_1 = 0$). Thus, the multiplet at the highest frequency (lowest field) from H-3 is a quartet, seen with further splitting when viewed from the vertical axis. By taking a projection at an angle (45°) that causes each of the members of the individual multiplets to overlap when viewed from the horizontal axis, as at the bottom (b), a display is obtained that, in essence, is a proton-proton decoupled proton spectrum. Resonances devoid of any couplings are present at each frequency. This projection is a novel way to examine ^1H spectra, although it has not seen widespread use because it reveals no connectivities.

The pulse sequence, as a variant of the spin echo experiment, also refocuses the spread of frequencies caused by field inhomogeneity, so that some improvement in resolution is obtained. The inset at the lower right of Figure 6-18 shows the normal 1D spectra of H-4 and H-5 at the top (Figure 6-18c and e) and the unrotated projection of the 2D *J*-resolved spectra at the bottom [Figure 6-18d and f, extracted from the projected spectrum (Figure 6-18a) at the top of the 2D display]. The much higher resolution of the 2D resonances is clearly evident. Thus, the procedure is an effective way to measure *J* accurately, particularly when *J* is poorly resolved in the 1D spectrum. The experiment fails for closely coupled nuclei (second-order spectra).

In addition to resolving small couplings that may be absent in the 1D spectrum, the *J*-resolved procedure can be used to distinguish homonuclear from heteronuclear couplings. The vertical axis in the figure displays couplings only between spins that were affected by the 180° pulse. Hence, only $^1\text{H}-^1\text{H}$ couplings appear on that axis. Couplings to heteronuclei

Figure 6-18 The 270 MHz 2D *J*-resolved ^1H spectrum of 2,3,4,6-tetrakis-*O*-trideuterioacetyl- α -D-glucopyranoside. (Reproduced from L. D. Hall, S. Sukumar, and G. R. Sullivan, *J. Chem. Soc., Chem. Commun.*, 292 [1979]).



are not phase modulated and, consequently, appear as spacings along the horizontal axis. In this way, $^1\text{H}-^{19}\text{F}$ and $^1\text{H}-^{31}\text{P}$ couplings may be distinguished from $^1\text{H}-^1\text{H}$ couplings, which are removed in the rotated spectrum such as that shown in (b) at the bottom of the figure.

COSY for other Nuclides. The basic COSY experiment can be carried out for any spin- $\frac{1}{2}$ nucleus that is 100% abundant. In addition to $^1\text{H}-^1\text{H}$, the procedure thus is applicable to $^{19}\text{F}-^{19}\text{F}$ (F,F-COSY) and $^{31}\text{P}-^{31}\text{P}$ (P,P-COSY), respectively, in organofluorine and organophosphorus compounds. When the nuclide is less than 100% abundant, the uncoupled center band must be separated from the coupled satellites, usually by the 2D INADEQUATE procedure (Section 6-4).

6-2 Proton-Heteronucleus Correlation

Cross peaks in the standard COSY experiment are generated through magnetization transfer that arises from scalar (J) coupling between protons. Coupling from a proton to a different nuclide, such as carbon-13, should be able to generate a similar response. Analogous cross peaks then would provide very useful information about which carbons are bonded to which protons. Thus, the assignment of a proton resonance would automatically lead to the assignment of the resonance of the carbon to which it is bonded, and vice versa. This field has seen considerable development recently, and there now are several pulse sequences commonly used to explore connectivity between protons and carbon or other heteronucleides.

HETCOR. The simplest extension of the COSY sequence that includes magnetization transfer to carbon takes the form given in Figure 6-19. The pulse sequence is reminiscent of the one-dimensional INEPT sequence, and the manipulation of magnetization is much the same. (CF. Figure 5-19, but ignore the 180° pulse.) The initial 90° ^1H pulse generates y magnetization. For the simplest case, one carbon bonded to one proton (as in CHCl_3), ^1H magnetization evolves during the period t_1 according to its Larmor frequency. Two ^1H vectors diverge due to coupling with ^{13}C . The second 90° ^1H pulse generates nonequilibrium z magnetization that is transferred to ^{13}C in the manner of the INEPT experiment of Figure 5-19. The single 90° ^{13}C pulse then provides the ^{13}C free-induction decay that is acquired during t_2 . The 2D spectrum then has one axis in ^1H frequencies (ν_1) and one in ^{13}C frequencies (ν_2).

For the simple AX case, the 2D spectrum contains two peaks when it is projected onto either the ^1H or the ^{13}C axis (the A and X portions, respectively, of the AX spectrum), as in the INEPT experiment. Thus, the ^1H resonances that are detected actually correspond to the ^{13}C satellites of the usual ^1H spectrum. The 2D display contains four peaks: two along a diagonal and two symmetrically off the diagonal. Moreover, the peaks are in antiphase for each nuclide, since the INEPT spectrum without decoupling generates one peak up and one peak down. Decoupling would result in summing the peaks algebraically to zero.

To bring about decoupling, another pulse and two fixed periods are added (Figure 6-20). The first (90_x°) ^1H pulse allows chemical shifts and coupling constants to evolve during t_1 . The 180° ^{13}C pulse refocuses the H-C coupling constants in the ^1H dimension. (^1H then is decoupled from ^{13}C .) The fixed time Δ_1 allows the ^1H vectors to obtain the antiphase (180° out of phase) relationship illustrated in Figure 5-19e. The second (90_y°) ^1H pulse moves the vectors in antiphase relationship onto the z axis and enables polarization to be transferred to ^{13}C , also in the antiphase

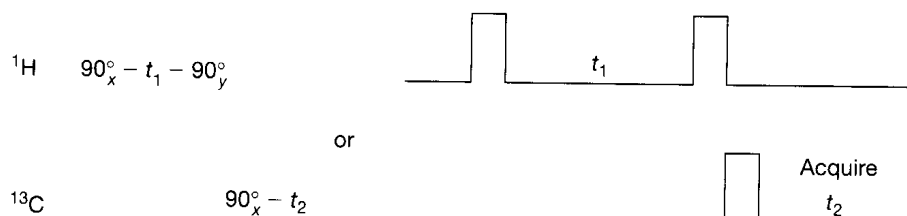
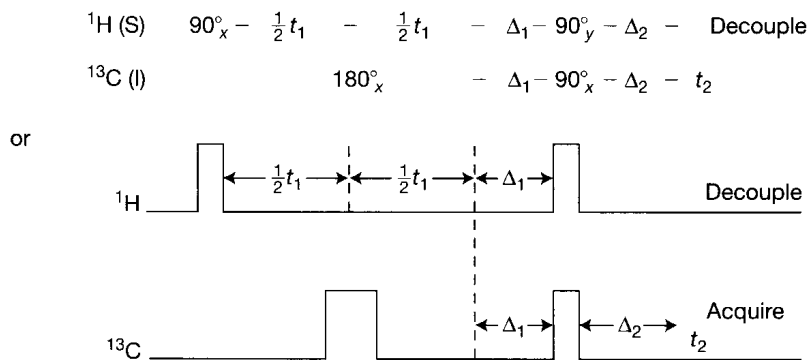


Figure 6-19 The pulse sequence for the HETCOR experiment.

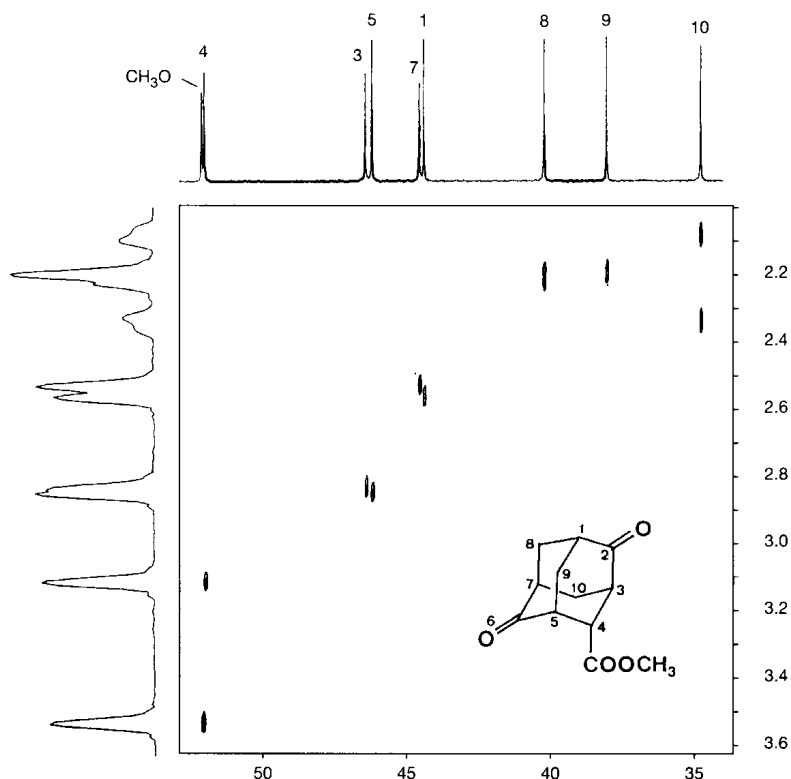
Figure 6-20 The pulse sequence for the HETCOR experiment with decoupling.



relationship. The 90° ^{13}C pulse is for observation. The second fixed time, Δ_2 , restores phase alignment and permits ^{13}C to be decoupled from ^1H during ^{13}C acquisition.

Figure 6-21 illustrates this procedure for an adamantane derivative. The ^1H frequencies are on the vertical axis and the ^{13}C frequencies are on the horizontal axis. The respective spectra are illustrated on the left and at the top. The 2D spectrum is composed only of cross peaks, each one relating a carbon to its directly bonded proton(s). There are no diagonal peaks (and no mirror symmetry associated with a diagonal), because two different nuclides are represented on the frequency dimensions. Quaternary carbons are invisible to the technique, as the fixed times Δ_1 and Δ_2 normally are set to values for one-bond couplings. This experiment often is a necessary component in the complete assignment of ^1H and ^{13}C resonances. Its name, *HET*eroneuclear chemical-shift *COR*relation, usually is abbreviated as HETCOR, but other acronyms (e.g., HSC, for *H*eteroneuclear *S*hift *C*orrelation, and H, C-COSY, also are used. The method may be applied to protons coupled to many other nuclei, such as ^{15}N , ^{29}Si , and ^{31}P , as well as ^{13}C .

Figure 6-21 The HETCOR spectrum of 4-(methoxycarbonyl)adamantane-2,6-dione. (Reproduced from H. Duddeck and W. Dietrich, *Structure Elucidation by Modern NMR*, Steinkopff Verlag, Darmstadt, Germany, 1989, p. 22.)



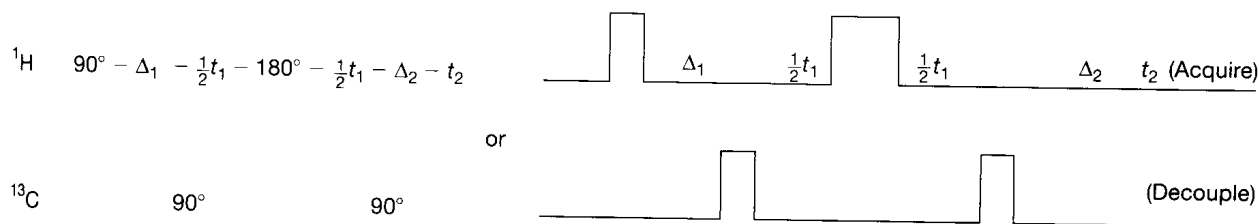


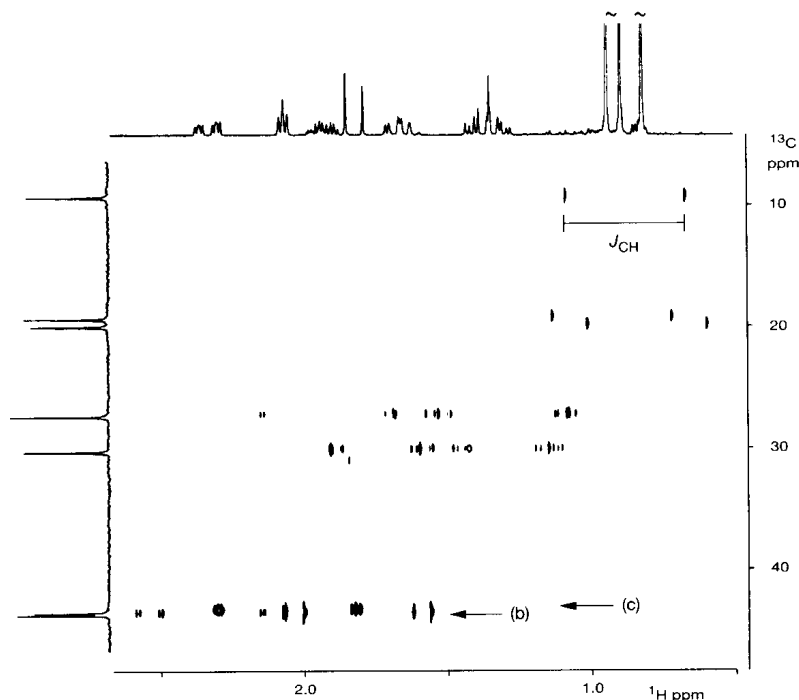
Figure 6-22 The pulse sequence for the HMQC experiment.

Figure 6-21 illustrates several advantages of the HETCOR experiment: (1) The correlation between protons and carbons means that spectral assignment at one frequency automatically leads to spectral assignment at the other. Thus, ^{13}C assignments can assist in ^1H assignments, and vice versa. (2) Overlapping proton resonances often can be dispersed in the carbon dimension. Even at very high fields, proton resonances can overlap; consider, for example, those of H8 and H9, which coincide at δ 2.2 in the figure. The presence of the two cross peaks from C8 (δ 40) and C9 (δ 38) reveals the spectral overlap in the proton dimension. Similar considerations apply to H3 and H5. (3) COSY cross peaks can arise from either geminal (HCH) or vicinal (HCCH) connectivities, so that ambiguities can be present. Geminally related protons that are diastereotopic are attached to a common carbon and hence have HETCOR connectivities to a single ^{13}C frequency, whereas vicinally related protons are attached to different carbons and thus have HETCOR connectivities to two different ^{13}C frequencies. This advantage is not illustrated in the figure, but is useful for distinguishing geminal from vicinal relationships in COSY spectra.

HMQC. A major drawback to the HETCOR experiment is the low sensitivity that results from detection of the X nucleus (usually ^{13}C). The HMQC (*Heteronuclear correlation through Multiple Quantum Coherence*) experiment uses *inverse detection*, whereby ^{13}C responses are observed in the ^1H spectrum. The pulse sequence is given in Figure 6-22 and represents a transfer of coherence rather than polarization. The initial ^1H magnetization from the 90° pulse becomes antiphase during the fixed period Δ_1 through the ^1H - ^{13}C coupling constant. Multiple quantum coherence then is created by the first ^{13}C pulse. The remainder of the sequence is designed to select double or higher quantum coherence (the ^{13}C satellites in the ^1H spectrum) over single quantum coherence (the ^1H center bands), in a process similar to the 1D INADEQUATE experiment in Section 5-7. The 2D representation, as shown in Figure 6-23 for camphor, still includes the ^1H - ^{13}C coupling information in the ^1H dimension, although ^{13}C irradiation can be applied during the ^1H t_2 acquisition period to provide decoupling. The major difference between HETCOR and HMQC is that the acquisition period t_2 is at ^{13}C frequencies in the former experiment (Figure 6-20), but at ^1H frequencies in the latter (Figure 6-22). Consequently, the HMQC experiment is much more sensitive. Like HETCOR, HMQC can be used with heteronuclei other than ^{13}C , of which the experiment involving ^{15}N is the most common.

BIRD-HMQC. The most difficult aspect of implementing the HMQC experiment is the suppression of signals from protons attached to ^{12}C (the center-band or single quantum coherences) in favor of the protons attached to ^{13}C (the satellites or double quantum coherences). The use of pulse field gradients (PFG, Section 6-6) is the most effective technique, but relatively few spectrometers are equipped with the hardware required for their generation. Fortunately, there is an effective alternative for the suppression of center bands by means of the BIRD (*BI*linear *R*otation *D*ecoupling) sequence, which is outlined by the vector

Figure 6-23 The HMQC spectrum of camphor, with ^1H - ^{13}C couplings retained in the ^1H dimension. (Reproduced from J. K. M. Sanders and B. K. Hunter, *Modern NMR Spectroscopy*, 2d ed., Oxford University Press, Oxford, UK, 1993, p. 111.)



notation in Figure 6-24. Two sets of vectors are followed, one for the protons attached to ^{12}C and one for the protons attached to ^{13}C . The initial 90° proton pulse (Figure 6-24a and a') along the x direction moves all magnetization onto the y axis (Figure 6-24b and b'); keep in mind that eventually the inverse detection HMQC pulses will be applied, with ultimate detection in the proton channel). Protons on a ^{12}C are unsplit, so their magnetization evolves as depicted in the upper set of vector diagrams. After the delay period $(2J)^{-1}$, these vectors have reached some arbitrary angle with respect to the y axis (Figure 6-24c), according to their individual Larmor frequencies. (Only one such frequency is illustrated.) By contrast, protons on a ^{13}C evolve as two vectors (Figure 6-24c'), separated by the frequency of the one-bond coupling constant ($\Delta\omega = 2\pi\Delta\nu = 2\pi J$), as illustrated in the lower set of vector diagrams. (The center of the diagrams is maintained on the y axis for viewing simplicity, but the chemical shifts of the vectors evolve according to their Larmor frequencies.) After the delay period $(2J)^{-1}$, these vectors are separated by a 180° angle (Figure 6-24c'; Section 5-5, $\phi = 2\pi(\Delta\nu)t = 2\pi J(2J)^{-1} = \pi$). At this time, a 180° pulse is applied to the ^1H channel and a 180° pulse is applied to the ^{13}C channel. The ^1H pulse rotates the vector for the protons attached to ^{12}C about the y axis (Figure 6-24d), so that, after another period $(2J)^{-1}$, that vector converges onto the y axis to create a spin echo (Figure 6-24e). The simultaneous ^{13}C pulse, however, switches the spin identities of the coupled partners for the protons attached to ^{13}C , so that the vectors continue to diverge, as was discussed with regard to Figure 5-14. After the second period $(2J)^{-1}$, these vectors converge onto the $-y$ axis (e' , $\phi = 360^\circ$). Application of the second 90° pulse along the x axis moves all the proton magnetization back to the z axis. Because they had opposite phases in Figure 6-24e and e', the protons attached to ^{12}C now point along the $-z$ axis (Figure 6-24f), whereas the protons attached to ^{13}C point along the $+z$ axis (Figure 6-24f'). The experiment then requires a delay time τ for relaxation. The protons attached to ^{13}C are already essentially at equilibrium and remain unaffected (Figure 6-24g'), but those attached to ^{12}C are upside down and hence begin to relax back to equilibrium. The HMQC pulses are applied after a time τ that brings the magnetization for the protons attached to ^{12}C exactly to zero (Figure 6-24g). At this point, BIRD has suppressed the single quantum coherences (Figure 6-24g) and selected the multiple quantum coherences (Figure 6-24g').

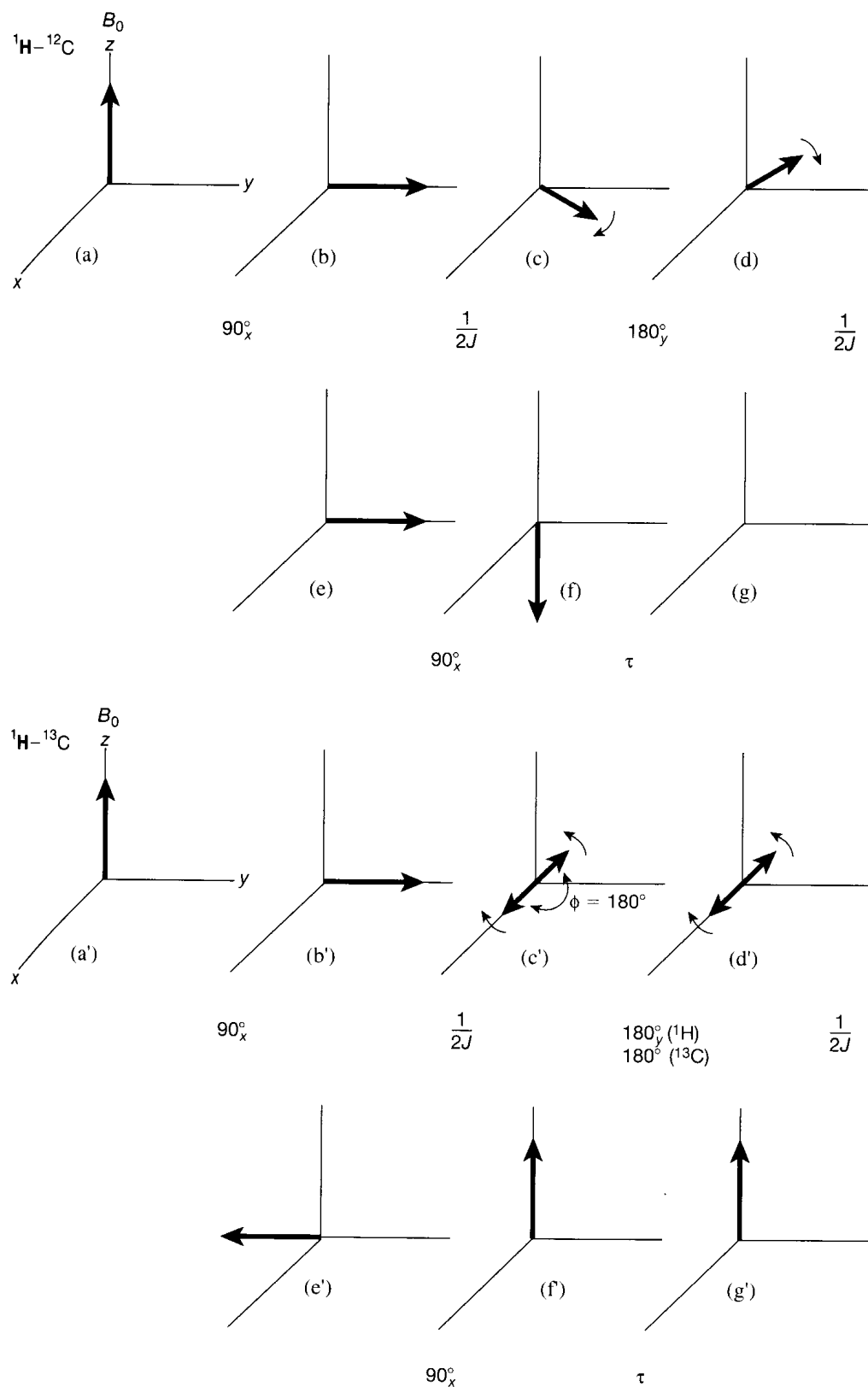


Figure 6-24 The BIRD sequence for the selection of signals from protons attached to ${}^{13}\text{C}$ over those from protons attached to ${}^{12}\text{C}$.

The overall experiment thus becomes BIRD- τ -HMQC-DT, in which τ is chosen to null the single quantum coherences and DT is the normal delay time between pulse repetitions, which includes the time taken to acquire the signal, as well as a recycle time during which the signal is regenerated through relaxation. The details of the experiment require

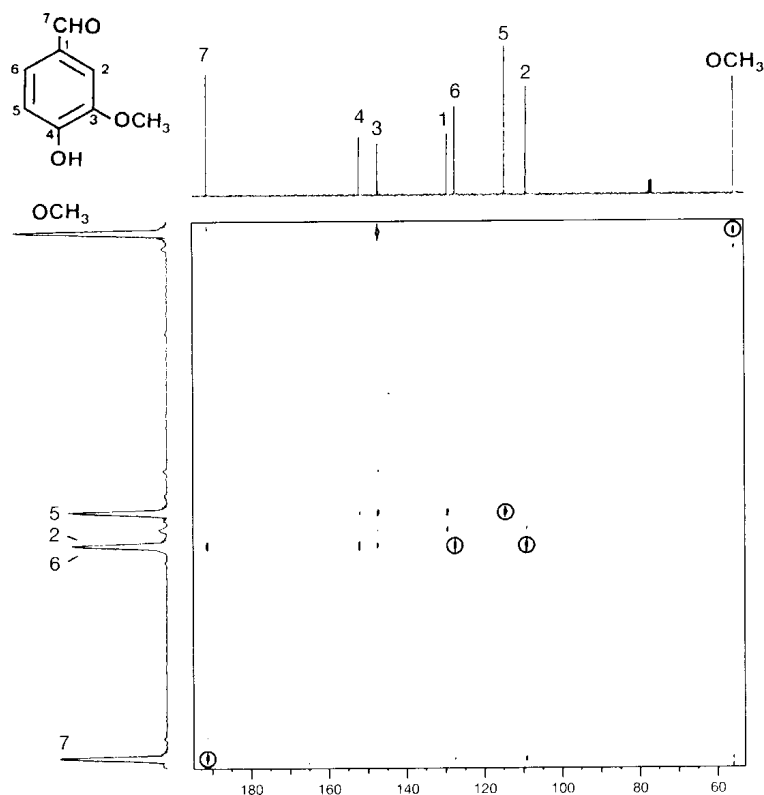
some knowledge of the relaxation times T_1 and an appropriate choice of the intervals τ and DT . The optimized result can provide effective suppression of the unwanted signals for small molecules. Larger molecules can undergo a negative nuclear Overhauser effect (Section 6-3) from the inverted signals, with loss of sensitivity.

HSQC. The *Heteronuclear Single Quantum Correlation* (HSQC) experiment is an alternative to HMQC that accomplishes a similar objective. The experiment generates, via an INEPT sequence, single quantum ^{13}C (or ^{15}N) coherence, which evolves and then is transferred back to the proton frequency by a second INEPT sequence, this time in reverse. The main difference from the HMQC result is that HSQC spectra do not contain ^1H - ^1H couplings in the ^{13}C (ν_1) dimension. As a result, HSQC cross peaks tend to have improved resolution over analogous HMQC cross peaks. HSQC is preferred when there is considerable spectral overlap.

COLOC. To focus on longer range H-C couplings, the fixed times Δ_1 and Δ_2 of HETCOR can be lengthened accordingly. A loss of magnetization due to transverse relaxation then reduces sensitivity significantly. The COLOC pulse sequence (*CO*relation *sp*ectroscopy *vi*a *LO*ng-range *C*oupling) avoids this problem by incorporating the ^1H evolution period t_1 inside the Δ_1 delay period. Figure 6-25 shows a COLOC spectrum for vanillin. The circled cross peaks are residues from one-bond couplings. The only long-range coupling of the methoxy group is with C-3, which indicates that methoxy is connected at that point. Other long-range couplings, however, also are seen—for example, between C-1 and H-5, C-3 and H-5, and C-2 and H-7.

The principal disadvantage of the COLOC sequence lies in the fixed nature of the evolution period. In such a pulse sequence, C-H correlations are diminished or even absent when two- and three-bond ^1H - ^{13}C couplings are of a magnitude similar to that of ^1H - ^1H couplings within a molecular fragment. This situation occurs quite commonly (Chapter 4). The FLOCK sequence (so named because it contains three BIRD sequences; see Figure 6-24) contains a variable evolution time, in which t_1 becomes progressively larger.

Figure 6-25 The COLOC spectrum of vanillin.
(Reproduced from H. Duddeck and W. Dietrich, *Structure Elucidation by Modern NMR*, Steinkopff Verlag, Darmstadt, Germany, 1989, p. 24.)



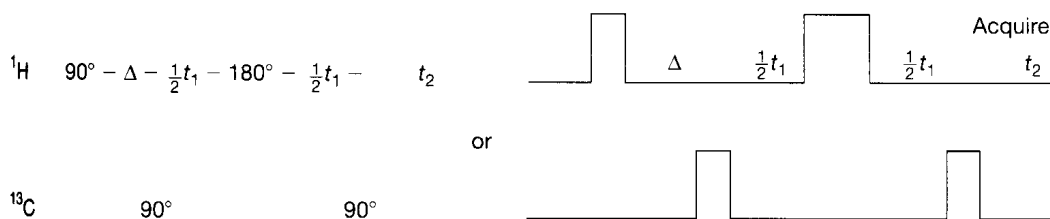


Figure 6-26 The pulse sequence for the HMBC experiment.

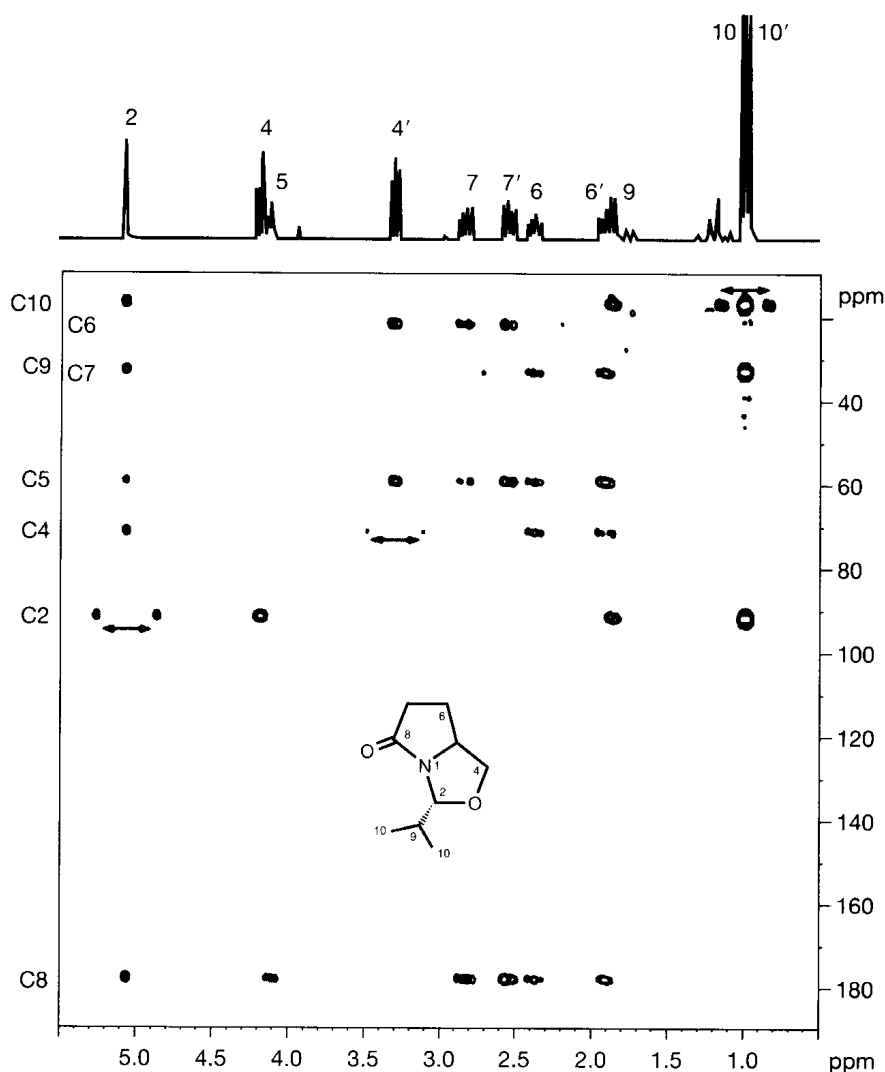
and avoids the potential loss of C–H correlations. Although the experiment detects carbon, it is quite useful when there is signal overlap in the ^1H spectrum.

HMBC. Correlations through longer range H–C couplings offer at least a couple of potential advantages. (1) Heteronuclei that lack an attached proton are invisible to the HETCOR–HMQC–HSQC family of experiments. Thus, carbonyl groups and tetrasubstituted carbons cannot be studied. Such carbons, however, are likely to show coupling to protons two or more bonds away. (2) A single carbon can be correlated with several neighboring protons. Hence, connectivities over heteroatoms or carbonyl groups can help define larger groupings of atoms, thereby complementing information from COSY. The COLOC and FLOCK sequences, however, suffer from the same drawback as HETCOR, namely, low sensitivity arising from direct observation of a nuclide (^{13}C , ^{15}N , and so on) with a low gyromagnetic ratio.

Proton-detected *Heteronuclear Multiple Bond Correlation* (HMBC) is designed to provide correlations between protons and heteronuclei such as carbon or nitrogen by a pulse sequence similar to that used in HMQC (Figure 6-26). The second delay time (Δ_2) is no longer necessary, because H–C couplings are not intended to be removed. The major difference from HMQC is the duration of the initial delay time Δ , which is lengthened in order to select for the smaller couplings over two or more bonds. These couplings are usually in the range 0–15 Hz. [See Section 4-4 for $^2J(\text{HCC})$ and Section 4-5 for $^3J(\text{HCCC})$.] A typical delay Δ of $(2J)^{-1}$ then corresponds to the range 60–200 ms ($J = 2.5\text{--}8.3\text{ Hz}$), in comparison with 2–4 ms for HMQC. Shorter delay times tend to improve sensitivity (there is less loss of signal through relaxation), but longer times may be entirely acceptable for small molecules with relatively long relaxation times. Longer delay times occasionally may permit the observation of connectivities through four-bond couplings [e.g., $^4J(\text{HCCCC})$] or even five. (See Section 4-6.) Interpreting the magnitudes of H–C couplings over two to five bonds entails all the subtleties of analogously interpreting H–H couplings and includes inductive effects, zigzag pathways, π bonding, Karplus stereochemical considerations, and so on. Methyl groups often exhibit the most intense HMBC correlations, because of the multiplicative effect of simultaneous detection by three protons and because free rotation provides almost no stereochemical restrictions that can reduce couplings.

Figure 6-27 provides the HMBC spectrum of the illustrated heterocycle. As with HETCOR, the spectrum contains only cross peaks. For example, the carbonyl carbon C8 apparently couples with H2, H5, H6, H6', H7, and H7', as it exhibits cross peaks with all these protons, representing all possible two- and three-bond couplings. Three further points are worth noting. First, the protons on C4, C6, and C7 respectively are diastereotopic. Separate peaks are observed for each such connectivity (e.g., that between C8–H7 and C8–H7'). Second, some one-bond couplings break through the selection process, because of accidental phase coincidence. Such couplings show up as doublets (the one-bond H–C coupling survives because HMBC does not include carbon irradiation during t_2) and are noted in the spectrum by doubly headed arrows. The cross peaks are obvious, because of the large magnitude of $^1J(^{13}\text{C}\text{--}^1\text{H})$ and because they appear at the coincidence of C and H chemical shifts for the CH fragment, such as C2/H2. They can be filtered out by a more complex pulse

Figure 6-27 The HMBC spectrum of the illustrated heterocycle. The 1D ^1H spectrum is given at the top. The vertical axis corresponds to ^{13}C frequencies, the horizontal axis to ^1H frequencies. One-bond correlations are indicated by peaks connected by doubly headed arrows. (Reproduced from T. D. W. Claridge, *High-Resolution NMR Techniques in Organic Chemistry*, Pergamon Press, Oxford, UK, 1999, p. 245.)



scheme. Third, suppression of the single coherence ($^1\text{H}-^{12}\text{C}$) signals is the primary task of the experiment, and the process is significantly enhanced by the use of pulsed field gradients (Section 6-6).

Heteronuclear Relay Coherence Transfer. The relay COSY experiment (RCT) may be adapted to the HETCOR context. The result of such an experiment is illustrated in Figure 6-28 for the illustrated acetal of acrolein, along with the normal HETCOR experiment ("HSC" in the figure). The following HETCOR cross peaks are present: $\text{H}_\text{C}/\text{C}_2$ at the bottom left, $\text{H}_\text{B}/\text{C}_1$ and $\text{H}_\text{A}/\text{C}_1$ in the middle, and $\text{H}_\text{D}/\text{C}_3$ at the upper right. This experiment shows that C_3 is bonded to H_D , C_2 to H_C , and C_1 to H_A and H_B . The H-H-C relay coherence transfer experiment is depicted at the upper right. In a general fragment $\text{H}_\text{X}-\text{C}_\text{X}-\text{C}_\text{Y}-\text{H}_\text{Y}$, off-diagonal HETCOR peaks occur for $\text{H}_\text{X}/\text{C}_\text{X}$ and $\text{H}_\text{Y}/\text{C}_\text{Y}$, respectively, defining $\text{H}_\text{X}-\text{C}_\text{X}$ and $\text{H}_\text{Y}-\text{C}_\text{Y}$ fragments. In the RCT experiment, off-diagonal peaks also occur for $\text{H}_\text{X}/\text{C}_\text{Y}$ and $\text{H}_\text{Y}-\text{C}_\text{X}$, thereby defining the larger $\text{H}_\text{X}-\text{C}_\text{X}-\text{C}_\text{Y}-\text{H}_\text{Y}$ moiety. The normal HETCOR cross peaks are labeled N. (That for $\text{H}_\text{C}/\text{C}_2$ is missing.) The additional cross peaks resulting from relayed connectivity between given CH pieces are labeled R. Thus, the relayed (R) peak at the upper left indicates that the $\text{H}_\text{D}/\text{C}_3$ and $\text{H}_\text{C}/\text{C}_2$ pairs are connected ($\text{H}_\text{D}-\text{C}_3-\text{C}_2-\text{H}_\text{C}$). The relayed peak in the middle left indicates that the $\text{H}_\text{A}/\text{B}/\text{C}_1$ and $\text{H}_\text{C}/\text{C}_2$ pairs are connected ($\text{H}_\text{A}/\text{B}-\text{C}_1-\text{C}_2-\text{H}_\text{C}$). The other two peaks

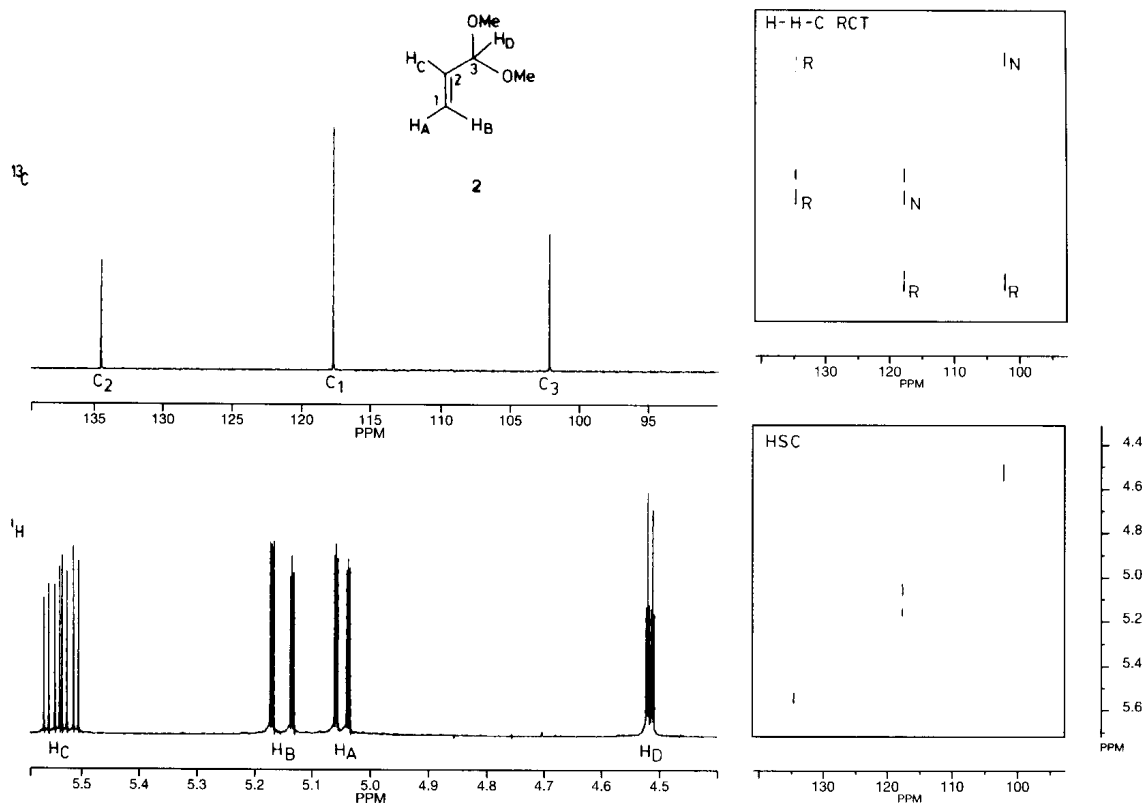


Figure 6-28 Left: The ^{13}C and ^1H spectra of the dimethyl acetal of acrolein. Right: The normal HETCOR (called HSC, bottom) and the H-H-C relay coherence transfer (top) experiments for the same molecule. (Reproduced from A. E. Derome, *Modern NMR Techniques for Chemistry Research*, Pergamon Press, Oxford, UK, 1987, p. 257.)

labeled R (bottom middle and right) are mirror images of the former relayed peaks across the diagonal, as relay occurs symmetrically ($\text{H}_\text{D}/\text{C}_3 \longrightarrow \text{H}_\text{C}/\text{C}_2$ or $\text{H}_\text{C}/\text{C}_2 \longrightarrow \text{H}_\text{D}/\text{C}_3$). This particular experiment is called H-H-C RCT because the pulses involve ^1H signals twice and ^{13}C signals once, in that order. Other heteronuclear relay experiments can involve a different order (H-C-H) or different nuclei (H-H-N).

6-3 Proton-Proton Correlation Through Space or Chemical Exchange

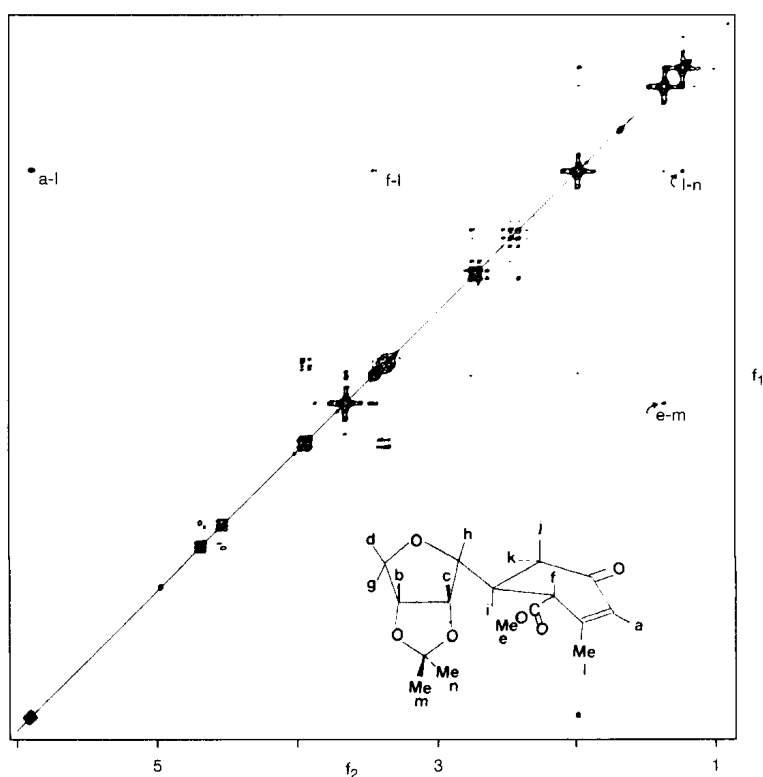
In the original depiction of the two-dimensional experiment in Figure 6-2, the magnetization vector was resolved into sine and cosine components during t_1 . The sine component was followed through the second 90° pulse and into the t_2 domain to create the COSY sequence. We ignored the cosine component, which was placed along the $-z$ axis after the second 90° pulse and hence was unobservable. There are mechanisms other than scalar coupling for transferring magnetization, and these methods can affect z magnetization and hence the cosine component. Irradiation at the frequency of one proton can transfer magnetization to nearby protons through dipolar interactions (the nuclear Overhauser effect). The clear effect of this technique on z magnetization is reflected in spectral intensity perturbations in one dimension. (See Section 5-4.) In addition, altering the chemical identity of a nucleus through chemical exchange affects z magnetization. A nucleus resonating at one frequency becomes a nucleus resonating at a different frequency. (See Section 5-2.) The population (z magnetization) thus decreases at the first frequency and increases at the second.

After the second 90° pulse in Figure 6-2d, both the NOE and the chemical exchange mechanisms can modulate the cosine component of the magnetization along the z axis. The frequency of modulation is the frequency of the magnetization transfer partner, either from dipolar relaxation or chemical exchange. After a suitable fixed period of time, during which this modulation is optimized (τ_m , the mixing period), the cosine component may be moved to the xy plane by a third 90° pulse and may be detected along the y axis during a t_2 acquisition period. Thus, the complete experiment is $90^\circ-t_1-90^\circ-\tau_m-90^\circ-t_2(\text{acquire})$. Because the frequency of magnetization during t_1 moves to another value during τ_m and is observed at the new frequency during t_2 , the two-dimensional representation of this experiment exhibits cross peaks. When the cross peaks derive from magnetization transfer through dipolar relaxation, the 2D experiment is called NOESY (*NOE SpectroscopY*). When they derive from chemical exchange, the experiment is called EXSY (*EXchange SpectroscopY*).

The duration of the fixed time τ_m depends on the relaxation time T_1 , the rate of chemical exchange, and the rate of NOE buildup. In the case of the NOESY experiment, valuable information can be ascertained about the distance between various protons within a molecule. Figure 6-29 illustrates the NOESY spectrum for a complex heterocycle. As with COSY, the 1D spectrum is found along the diagonal, and off-diagonal or cross peaks occur when two protons are close to each other. Thus, methyl group **l** shows an expected cross peak with the adjacent alkenic proton **a** (upper left). Additional cross peaks of methyl **l** indicate its closeness to the methinyl proton **f** and the acetal methyl **n**. The ester methyl **e** is close to the other acetal methyl **m**. The NOESY experiment can provide both structural and conformational information. In practice, cross peaks become unobservable when the proton-proton distance exceeds about 5 \AA .

At least three factors complicate the analysis of NOESY spectra. First, COSY signals may be present from scalar couplings and may interfere with interpretations intended to be based entirely on interproton distances. (Vicinal couplings, for example, are largest when the coupled nuclei are farthest apart, a condition that obtains in the antiperiplanar geometry.) Such unwanted spectral features are called *artifacts*. COSY signals may be reduced through

Figure 6-29 The ^1H NOESY spectrum for the indicated compound. (Courtesy of Bruker Instruments, Inc.)



phase cycling or by a statistical variation of τ_m by about 20%. (The NOESY signals grow monotonically, but the COSY signals are sinusoidal and cancel out.) In the phase-sensitive NOESY experiment, NOESY cross peaks due to positive NOE's may be distinguished from COSY cross peaks because they have opposite phases. Weak NOESY cross peaks, however, may be canceled in this experiment when breakthrough COSY cross peaks happen to be of similar intensity. Also, COSY signals are not distinguished from NOESY signals that are due to negative NOE's.

Second, in small molecules, the NOE builds up slowly and attains a theoretical maximum of only 50%, as noted earlier in the 1D context. (See Section 5-4 and Appendix 5.) Because a single proton may be relaxed by several neighboring protons, the actual maximum normally is much less than 50%. (Of course, the same problem exists in the 1D NOE experiment.) Moreover, as the molecular size increases and behavior departs from the extreme narrowing limit, the maximum NOE decreases to zero and becomes negative. Thus, particularly for medium-sized molecules, the NOESY experiment may fail. For larger molecules, whose relaxation is dominated by the W_0 term, not only is the maximum NOE -100% rather than $+50\%$, but also the NOE buildup occurs more rapidly. The NOESY experiment thus has been of particular utility in the analysis of the structure and conformation of large molecules such as proteins and polynucleotides.

Third, in addition to its transfer directly from one proton to an adjacent proton, magnetization may be transferred by spin diffusion. In this mechanism, already described in the 1D experiment (see Section 5-4 and Appendix 5), magnetization is transferred through the NOE from one spin to a nearby second spin and then from the second to a third spin that is close to the second spin, but not necessarily to the first one. These multistep transfers can produce NOESY cross peaks between protons that are not close together. Spin diffusion can even occur through two or more intermediate spins, but the process becomes increasingly less efficient. The direct transfer of magnetization and its transfer by spin diffusion sometimes may be distinguished by examining the NOE buildup rate, as illustrated in Figure 6-30. In this hypothetical plot of the NOE intensity as a function of the mixing time τ_m for the system D—A—B—C, AA is the intensity of the diagonal peak, and the other lines represent intensities of cross peaks. The NOE between two close protons (A and B, separated by 2 Å in the model) rises most rapidly. Protons A and D are 4 Å apart and show a very small NOE. Protons A and C also are 4 Å apart (2 Å between A and B and another 2 Å between B and C), but the intensity of the AC cross peak rises steadily through spin diffusion with B as the intermediary. The model shows that spin diffusion provides the major contribution to the AC cross peak for a distance of 4 Å, but, for the AB cross peak, the buildup is slower than for the direct transfer.

The rotating-frame NOESY experiment (ROESY) provides some advantages for small and medium-sized, as well as large, molecules. The pulse sequence for ROESY (previously

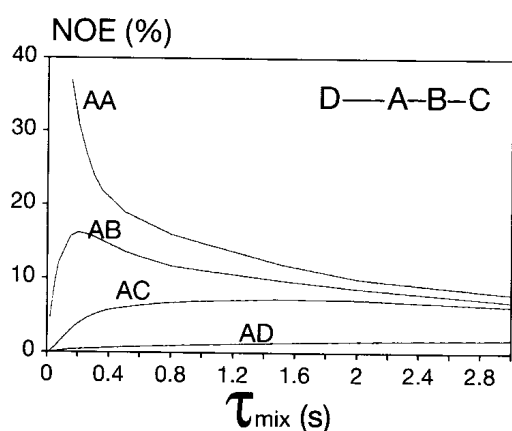
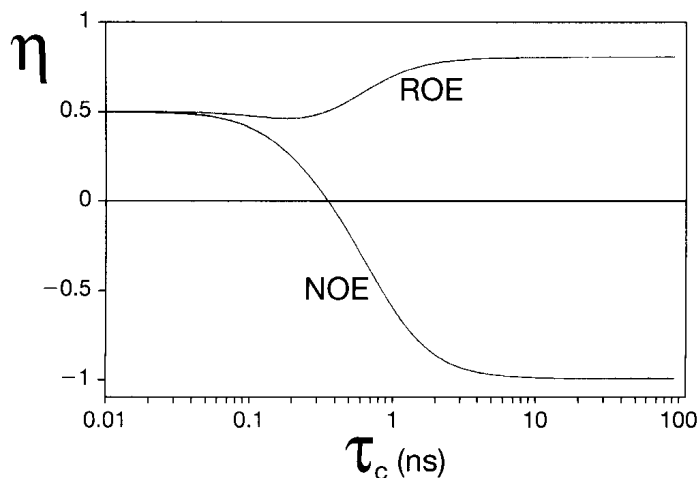


Figure 6-30. Peak intensities calculated for a hypothetical NOESY experiment involving four nuclei, D—A—B—C, with D 4 Å from A and B 2 Å from A and C. The curve labeled AA is for the diagonal peak, and the remaining curves are for the various cross peaks. (Reproduced from F. J. M. van de Ven, *Multidimensional NMR in Liquids*, VCH, New York, 1995, p. 188.)

Figure 6-31 The enhancement factor η as a function of the effective correlation time τ_c for the standard nuclear Overhauser experiment (NOE) and for the spin-lock, or rotating-coordinate, (ROE) variant. The curves were calculated for an interproton distance of 2.0 Å and a spectrometer frequency of 500 MHz. (Reproduced from F. J. M. van de Ven, *Multidimensional NMR in Liquids*, VCH, New York, 1995, p. 251.)



called CAMELSPIN) is similar to TOCSY or HOHAHA, although the period of spin locking is chosen to optimize magnetization transfer through the NOE (via dipolar interactions) rather than through scalar couplings. Whereas the NOE decreases to zero and becomes negative as the mean correlation time τ_c for molecular rotation increases (larger molecules move more slowly), in the rotating frame the maximum NOE remains positive and even increases from 50% to 67.5% (Figure 6-31). In addition to enhancing the signal, the ROESY experiment decreases spin diffusion, offering advantages for large molecules. Just as COSY artifacts may be present in the NOESY spectrum, however, so can TOCSY artifacts be present in the ROESY spectrum. Steps must be taken to remove them, as they are in the T-ROESY variant. The use of a weak static spin-lock pulse can reduce the TOCSY peaks. Positive ROESY cross peaks also can be easily distinguished from negative TOCSY peaks in a phase-sensitive ROESY experiment. As with COSY/NOESY, there is the possibility of canceling signals if TOCSY artifacts have intensities similar to those of the desired ROESY cross peaks.

When magnetization is transferred via chemical exchange in the EXSY experiment, it may be necessary to perform several preliminary experiments to optimize the value of τ_m , which should be approximately $1/k$. Figure 6-32 illustrates the EXSY experiment from an early example by Ernst, in which the diagonal peaks run nontraditionally from upper left to lower right. At fast exchange, the 1D ^1H spectrum of the heptamethylbenzenium ion contains only one methyl resonance, as the methyl group moves around the ring. At slow exchange, there are distinct resonances for the four types of methyls labeled on the left in the

Figure 6-32 The ^1H EXSY spectrum for the heptamethylbenzenium ion. (Reproduced with permission from R. H. Meier and R. R. Ernst, *J. Am. Chem. Soc.*, **101**, 6441 [1979]. Copyright 1979 American Chemical Society.)

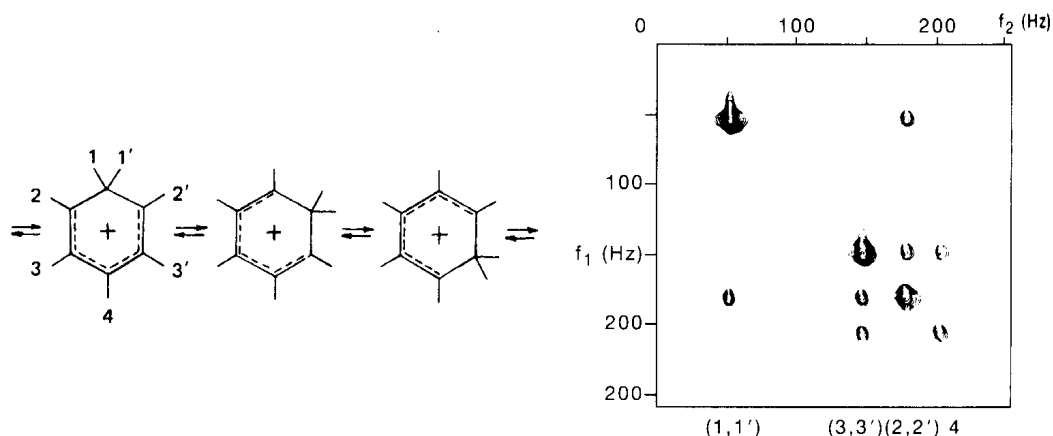


figure. The EXSY experiment shows which methyls interchange with which. One can imagine 1,2, 1,3 or 1,4 shifts, but the EXSY experiment agrees only with the 1,2 mechanism. Each off-diagonal peak indicates magnetization transfer between two diagonal peaks. Thus, the 1 methyls have a cross peak only with (and hence exchange only with) the 2 methyls, the 2 methyls exchange with the 1 and 3 methyls, the 3 methyls exchange with the 2 and 4 methyls, and the 4 methyls exchange only with the 3 methyls. This is the pattern expected for 1,2 shifts.

The intensities of the cross peaks depend on the rate constant for exchange. For the case of exchange between equally populated sites lacking spin–spin coupling [e.g., the two methyls of *N,N*-dimethylformamide, $\text{H}(\text{CO})\text{N}(\text{CH}_3)_2$], the rate constant k is related to the mixing time τ_m , the intensity of the cross peak I_c , and the intensity of the diagonal peaks I_d by the formula

$$\frac{I_d}{I_c} \sim \frac{(1 - k\tau_m)}{k\tau_m}, \quad (6-1)$$

in which

$$k \sim \frac{1}{[\tau_m(I_d/I_c + 1)]}. \quad (6-2)$$

Since the pulse sequence is the same for EXSY and NOESY, NOESY (or ROESY) cross peaks might be mistaken for EXSY cross peaks. They can be distinguished in the phase-sensitive experiment, since EXSY and ROESY peaks have opposite phases, as do EXSY and NOESY peaks in the fast motion regime. For example, two resolved OH or NH resonances may exhibit EXSY cross peaks from slow proton exchange. These peaks could be mistakenly taken to be NOESY peaks and interpreted incorrectly in terms of stereochemistry.

6-4 Carbon–Carbon Correlation

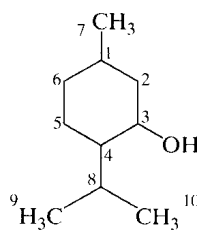
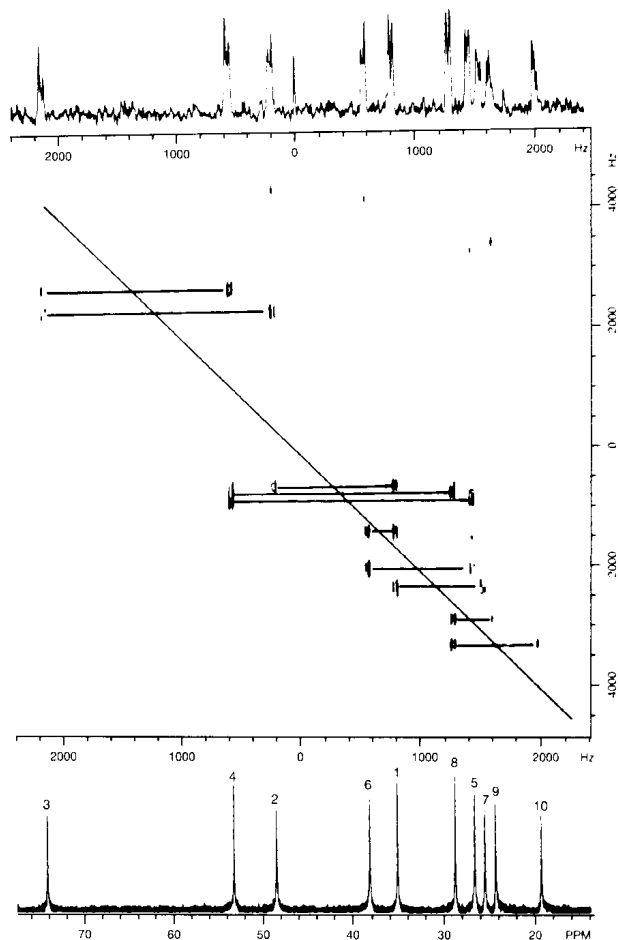
The 1D INADEQUATE experiment provides a method for measuring ^{13}C – ^{13}C coupling constants and for determining carbon–carbon connectivity by establishing coupling magnitudes that are common to two carbon atoms. (See Section 5-7.) In practice, the application of the method to solving connectivity problems is complicated not only by the inherently low sensitivity of detecting two dilute nuclei but also by the similarity of many ^{13}C – ^{13}C couplings. Duddeck and Dietrich have pointed out that all the one-bond carbon–carbon couplings in cyclooctanol fall into the narrow region from 34.2 to 34.5 Hz, except for C_1 – C_2 , which is 37.5 Hz. The second problem may be largely alleviated by translating the experiment into two dimensions. The original INADEQUATE experiment (see Section 5-7) can be adapted directly to two dimensions by incrementing the fixed time Δ as the t_1 domain: $90_x^\circ - 1/4J_{\text{CC}} - 180_y^\circ - 1/4J_{\text{CC}} - 90_x^\circ - t_1 - 90_\phi^\circ - t_2$ (acquire).

The period t_1 is used to encode the double quantum frequency domain. The resulting 2D display contains a horizontal axis in ν_2 (the normal ^{13}C frequencies) and a vertical axis that is a double quantum domain represented by the sum of the frequencies of coupled ^{13}C nuclei ($\nu_2 = \nu_A + \nu_X$). The latter frequencies are referenced to a transmitter frequency at zero.

Figure 6-33 illustrates the 2D INADEQUATE spectrum of menthol (6-2). The experiment also has been called C–C–COSY, as the cross peaks represent connectivity between two carbons. There are no diagonal peaks (which would arise from ^{13}C nuclei with ^{12}C neighbors), because the experiment removes single quantum signals. The diagonal usually is drawn in, as in the figure. The normal proton-decoupled ^{13}C spectrum is shown at the bottom. At the top, the 2D procedure permits recovery of the carbon-coupled ^{13}C spectrum through a projection of the ν_2 dimension.

To obtain connectivity from a 2D INADEQUATE experiment, a single assignment is made and the remainder of the structure is mapped. Only a gap caused by the presence of a heteroatom, C–X–C, prevents mapping the entire skeleton. For menthol, the

Figure 6-33 The 2D INADEQUATE spectrum of menthol, with the ^1H -decoupled ^{13}C spectrum. (Reproduced from G. E. Martin and A. S. Zehtzer, *Two-Dimensional NMR Methods for Establishing Molecular Connectivities*, VCH, New York, 1988, p. 362.)



6-2

oxygen-substituted C-3 resonates at the highest frequency (far left). Horizontal lines are drawn between coupled carbons in the 2D spectrum, passing through the diagonal at their midpoints. There are two cross peaks at the C-3 frequency, corresponding to connectivities to C-2 and to C-4. Of these, the secondary C-2 should be at a lower frequency (higher field). The connectivity then may be followed: C-2 \longrightarrow C-1 \longrightarrow C-6 (and from C-1 to the C-7 methyl) \longrightarrow C-5 \longrightarrow C-4 \longrightarrow C-8 (and from C-4 to the original C-3) \longrightarrow C-9 and C-10. The 2D INADEQUATE procedure also is applicable to concatenations of other coupled nuclides, such as $^{29}\text{Si}/^{29}\text{Si}$, $^{11}\text{B}/^{11}\text{B}$, and $^6\text{Li}/^6\text{Li}$ in organosilicon, organoboron, and organolithium systems, respectively.

The major disadvantage to this experiment is its extremely low sensitivity. An alternative is INEPT-INADEQUATE (sometimes called ADEQUATE), which uses proton observation and pulsed field gradients over pathways such as H-C-C. The resulting spectrum resembles that of 2D INADEQUATE, but can contain peaks only when at least one of the paired carbons has an attached proton. Although such technical refinements ameliorate the problem of sensitivity, this family of experiments has not been widely used.

6-5 Higher Dimensions

The enormous complexity of spectra of large biomolecules such as proteins, polynucleotides, and polysaccharides has led to the development of three- and four-dimensional experiments. Two independently incremented evolution periods (t_1 and t_2), in conjunction with three separate Fourier transformations of them and of the acquisition period t_3 , result in a cube of data with three frequency coordinates.

Figure 6-34, from a study by van de Ven, illustrates the complexity of the 2D NOESY spectrum of a DNA-binding protein of phage Pf3, consisting of 78 amino acids. The vertical line at δ 9.35 highlights the problems at a single resonance position in the NH region. The NH proton in a given peptide unit $-\text{CHR}'-\text{CO}-\text{NH}-\text{CHR}-\text{CO}-$ could have one cross peak with its own CHR proton and another with the neighboring CHR' protein, but the NOESY spectrum contains more than a dozen cross peaks at the one frequency of δ 9.35. Thus, more than one NH must be generating cross peaks at that frequency.

The nitrogen HMQC experiment provides information about the connectivity of nitrogens and their attached protons. For proteins, the use of HMQC normally requires isotopic enrichment of ^{15}N , which is obtained by growing an organism in a medium containing a single nitrogen source, such as $^{15}\text{NH}_4\text{Cl}$. (Similarly, ^{13}C enrichment may be obtained from a medium containing ^{13}C -labeled glucose.) The normal 2D HMQC spectrum (^{15}N vs. ^1H) for this same protein is given in Figure 6-35, and two connectivities are seen at the ^1H frequency of δ 9.35 (vertical line). Accordingly, there are two NH resonances (or more if there are coincidences) at δ 9.35.

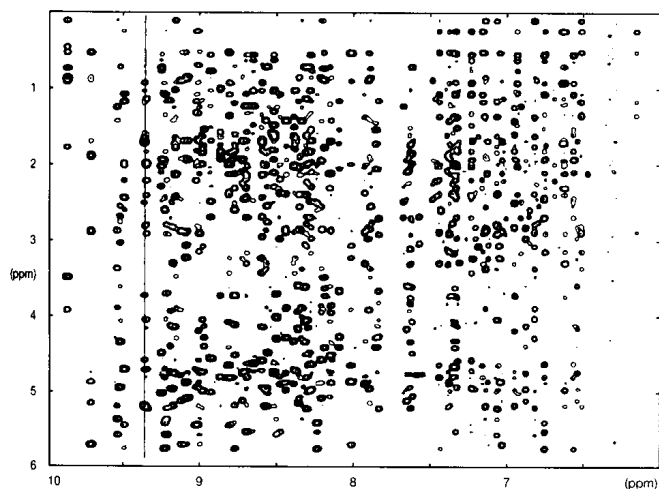


Figure 6-34 A portion of the NOESY spectrum of a DNA-binding protein of phage Pf3 containing cross peaks between NH and aliphatic protons. (Reproduced from F. J. M. van de Ven, *Multidimensional NMR in Liquids*, VCH, New York, 1995, p. 296.)

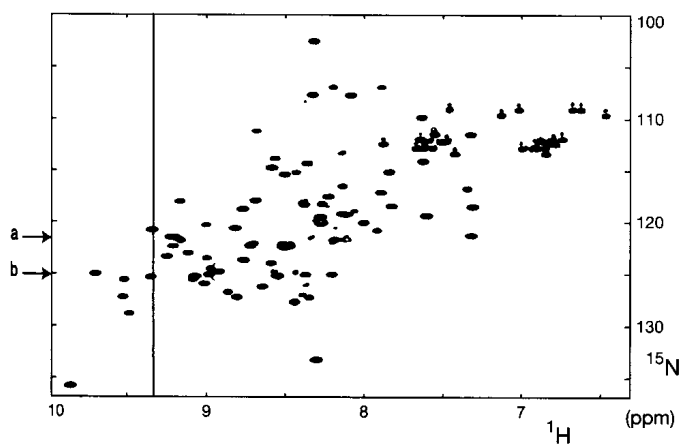


Figure 6-35 The ^1H , ^{15}N HMQC spectrum of ^{15}N -labeled Pf3. The arrows are explained in Figure 6-38. (Reproduced from F. J. M. van de Ven, *Multidimensional NMR in Liquids*, VCH, New York, 1995, p. 297.)

Figure 6-36 The pulse sequence for the three-dimensional NOESY/HMQC experiment.

^1H	$90^\circ - t_1 - 90^\circ - \tau_m - 90^\circ$	—	180°	—	t_3 (Acquire)
^{15}N	180°	—	$\Delta - 90^\circ - t_2 - 90^\circ - \Delta$	—	Decouple

The 3D experiment takes the 2D experiments in Figures 6-34 and 6-35 into an additional dimension. The 3D procedure illustrated in Figure 6-36 labels each NOESY peak with the ^{15}N frequency through the HMQC method, thus combining NOESY and HMQC data. The pulses and time delays constitute the standard ^1H NOESY sequence through the third 90° ^1H pulse. The pulses and delays thereafter make up the standard HMQC sequence, which ends with the inverse detection of ^{15}N at the ^1H frequencies in t_3 . The totality of data requires a cube for its representation, as illustrated diagrammatically in Figure 6-37, in which the flat dimensions are the NOESY data in ^1H frequencies and the vertical axis provides the ^{15}N frequencies from HMQC. In practice, horizontal planes (single ^{15}N frequencies) are selected for analysis, as in Figure 6-38 for δ 120.7 and 124.9. (See the arrows labeled a and b in Figure 6-35.) The vertical lines at δ 9.35 each show two dominant cross peaks for the NH NOE's to the inter- and intraresidue CHR. Note that both ^{15}N frequencies show a cross peak for δ 9.35 at a CHR frequency of δ 5.2, so that, indeed, there is overlap in Figure 6-35.

This type of heteronuclear 3D experiment is called NOESY-HMQC. (In Figure 6-37, there are two ^1H dimensions and one ^{15}N dimension.) Most 3D experiments use high-sensitivity methods and displays that are particularly effective for large molecules. Thus, COSY is not often used, but TOCSY-HMQC is a useful method for separating ^1H - ^1H coupling connectivities into a ^{13}C or ^{15}N dimension. The homonuclear 3D experiment NOESY-TOCSY (all three dimensions are ^1H) separates through-space connectivities from

Figure 6-37 Diagram of the 3D NOESY-($^1\text{H}/^{15}\text{N}$)HMQC spectrum of Pf3 in three frequency dimensions: F_1 , F_2 , and F_3 (ν_1 , ν_2 , and ν_3). (Reproduced from F. J. M. van de Ven, *Multidimensional NMR in Liquids*, VCH, New York, 1995, p. 299.)

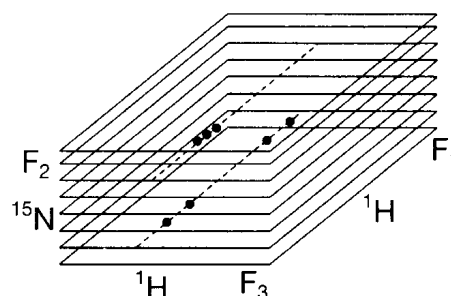
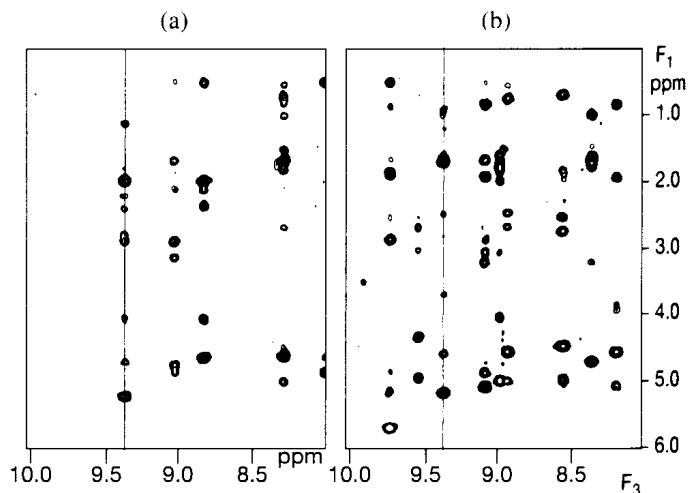


Figure 6-38 Two ν_1 - ν_3 (F_1 - F_3) planes taken from the 3D NOESY-($^1\text{H}/^{15}\text{N}$)HMQC spectrum of Pf3, corresponding to the frequencies indicated by arrows in Figure 6-35. (Reproduced from F. J. M. van de Ven, *Multidimensional NMR in Liquids*, VCH, New York, 1995, p. 300.)



coupling connectivities by the simple pulse sequence $90^\circ-t_1-90^\circ-\tau_m-t_2-(\text{spin lock})-t_3(\text{acquire})$. The three dimensions may each represent a different nuclide, as in $^1\text{H}/^{13}\text{C}/^{15}\text{N}$, and are considered as variants of the HETCOR experiment. The nuclides usually are selected to explore specific connectivities in biomolecules. The H-N-CO experiment looks at the connection $^1\text{H}-^{15}\text{N}-(\text{C})-^{13}\text{C}=\text{O}$ in the peptide unit $-\text{NH}-\text{CHR}-\text{CO}-$ and requires double labeling of ^{15}N and ^{13}C to provide sufficient sensitivity in proteins. The 3D cross peaks connect the HN proton in the first dimension, the HN nitrogen in the second, and the intraresidue carbonyl carbon in the third. An analogue in nucleotide analysis is the H-C-P experiment, in which the third dimension is ^{31}P . Numerous variations of these triple resonance experiments exist. In particularly complex cases, a fourth time domain t_4 may be introduced to produce 4D experiments.

When through-bond connectivity experiments are combined with the spatial information from buildup rates of NOESY cross peaks, proton-proton distances can be obtained by comparison with known bond lengths. The result can be a complete three-dimensional structure of biomolecules. Such solution-phase structures complement solid-phase information from X-ray crystallography. In this way, NMR spectroscopy has become a structural tool for obtaining detailed molecular geometries of complex molecules in solution.

6-6 Pulsed Field Gradients

Field inhomogeneity has been mentioned as the primary contributor to transverse (xy) relaxation (T_2) (Sections 1-3 and 5-1). Transverse magnetization arises because the phases of individual magnetic vectors become coherent (Figure 1-10) rather than random (Figure 1-11). In a perfectly homogeneous field, this coherence would relax only through spin-spin interactions. In an inhomogeneous field, however, the existence of slightly unequal Larmor frequencies permits vectors to move faster or more slowly than the average, thereby randomizing their phases and destroying transverse magnetization, as described in Section 1-3.

There are several situations in which transverse magnetization is unwanted and may be eliminated by the application of a *Pulsed Field Gradient* (PFG; also called a *gradient pulse*). An example of a PFG is presented in Figure 6-39. The gradient is along the direction (z) of the B_0 field. When a PFG is applied, nuclei with different positions in the sample (different z coordinates) resonate at different frequencies. Such spatial encoding of frequency information is the fundamental principle of *Magnetic Resonance Imaging* (MRI). In the present context, MRI may be viewed as a method for inducing transverse relaxation very quickly by a rapid dephasing of the spins. In a typical 2D pulse sequence, a delay time is necessary between repetitions of the pulse sequence in order for relaxation to occur. If repetition occurs before transverse magnetization has relaxed to zero, sensitivity is reduced and artifacts may occur in the 2D spectrum. Consequently, the application of a PFG at the beginning of the sequence reduces or avoids these problems.

For the NOESY experiment, the following pulse sequence may be used: $G1-90^\circ-t_1-90^\circ-\tau_m, G2-90^\circ-t_2(\text{acquire})$. The first PFG ($G1$) destroys residual transverse

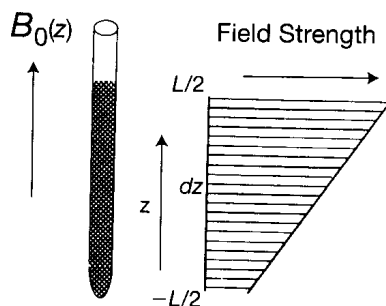


Figure 6-39 Diagram of a B_0 field gradient along the z direction. (Reproduced from F. J. M. van de Ven, *Multidimensional NMR in Liquids*, VCH, New York, 1995, p. 212.)

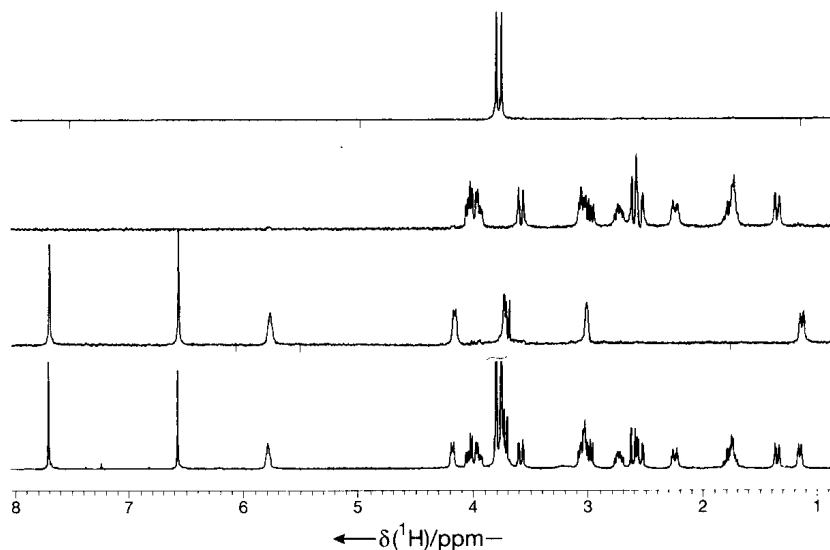
magnetization from previous pulses by dephasing the magnetic vectors. A second PFG (G_2) is applied during the mixing period τ_m . Only the effects on longitudinal (z) magnetization are of interest during this period. The PFG helps to eliminate false cross peaks that can arise from transverse magnetization.

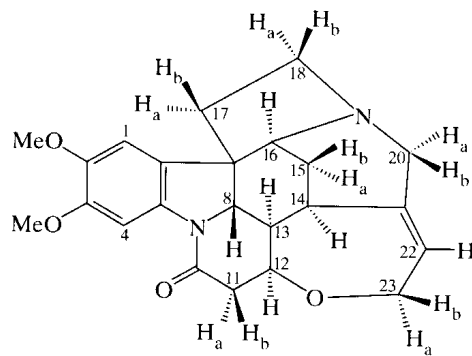
PFG's may be used to remove unwanted resonances. One of the most successful methods for solvent suppression destroys solvent magnetization by a PFG, but retains all other resonances through the sequence $G-S-G-t$ (acquire), which is reminiscent of solvent suppression through partial relaxation (Section 5-1). In this sequence (called WATERGATE for **WATER** suppression by **GrAdient-Tailored Excitation**), the S pulse is chosen to invert all resonances except the solvent peak, which is left at zero magnetization, as in partially relaxed spectra. The two identical gradients provide a spin-echo process, whereby the dephasing of the first PFG is undone by the second PFG. Normally, the result would be a *gradient echo*. Such an echo occurs for all resonances except solvent. Because the middle pulse eliminates solvent magnetization, the final PFG serves only to dephase solvent, while all other resonances are rephasing.

In addition to dephasing transverse magnetization, PFGs are used to select a coherence order. The use of phase cycling to select a coherence order inevitably involves multiple scans, by which pulse sequences move through 4, 16, or 64 variations with switching, for example, of x , $-x$, y , and $-y$. A full exploitation of phase cycling thus is time consuming. The development of zero, single, or double quantum coherence depends on the rate of various dephasing processes. Proper use of PFG's permits the selection of a coherence order without the repetitive scans of phase cycling. For example, in the inverse-detection HMQC experiment, the single quantum coherence signal for protons attached to ^{12}C (or ^{14}N) must be suppressed while selecting the multiple quantum coherence signal for protons attached to ^{13}C (or ^{15}N). Through phase cycling, this selection is achieved by measuring the difference between two strong signals. The PFG method selects and measures the small signal directly in a single scan.

PFG procedures have been developed to implement most of the 1D and 2D experiments discussed in Chapters 5 and 6. The procedures may be used for INADEQUATE, all common 2D experiments, and spectral editing. A PFG combination of DEPT and HMQC results in editing of proton spectra according to carbon substitution patterns. A PFG-based multiple quantum filtration leads to evolution of double, triple, or quadruple quantum coherence providing proton spectra containing only CH , CH_2 , or CH_3 resonances, respectively. Broadband decoupling removes coupling to ^{13}C , while proton-proton couplings remain. Figure 6-40 illustrates the result for brucine (**6-3**).

Figure 6-40 Editing of the ^1H spectrum of brucine (**6-3**) into subspectra for CH_3 , CH_2 , and CH (top to bottom). The complete ^1H spectrum is given at the bottom. (Reproduced with permission from T. Parella, F. Sánchez-Ferrando, and A. Virgili, *J. Magn. Reson. A*, **117**, 80 [1995]).





6-3

PFG's may be used to optimize the NOE experiment. Although the two-dimensional NOESY experiment is useful in analyzing spatial relationships in large molecules such as proteins, the enhancements are weaker for smaller molecules. The one-dimensional NOE experiment thus may be more appropriate for small molecules. The difference experiment described in Section 5-4 was instrumental in lowering the limit for ^1H NOE's from about 5% to about 1%. The experiment, however, suffers from problems arising from incomplete subtraction between the irradiated and unirradiated spectra. Such *subtraction artifacts* limit the difference NOE method. The use of pairs of PFG's can yield Overhauser enhancements without difference methods. This procedure has been called *excitation sculpting* and involves a pulse sequence of the general type $G1-S-G1-G2-S-G2$, in which S represents a selective inversion pulse or sequence of pulses (to produce, for example, the NOE). For the selected spins, the identical G1 pulses act in opposition and hence refocus the magnetization to produce a gradient echo. Spins outside the selected frequency range absorb the cumulative effect of $G1 + G1$ and are fully dephased. Hence, after a single gradient echo, all resonances have been eliminated, except those in the selected range of the pulse S. Because S may not have ideal phase properties, the gradient echo is repeated a second time ($G2/G2$) with a gradient of different magnitude, to avoid accidental refocusing of unwanted dephased magnetization. The resulting sequence has been called the *Double PFG Spin Echo* (DPFGSE) experiment. In practice, the sequence is preceded by a nonselective 90° pulse. All nuclei move into the xy plane, and the gradient pulses then dephase all resonances except those selected by the S pulse.

If the double PFG's are followed by a mixing time τ_m that permits the development of the NOE's that arise due to irradiation by the pulse S, the only resonances that develop are those coming from the NOE. All others have been dephased. The sequence then continues with another PFG to eliminate transverse magnetization and finishes with a 90° pulse for acquisition. The complete pulse sequence is thus $90^\circ-G1-S-G1-G2-S-G2-90^\circ-\tau_m-G3-90^\circ-t(\text{acquire})$, in which all 90° pulses are along the x axis, S is a selective pulse for the target (irradiated) nucleus, τ_m is set to optimize the NOE's, and G3 eliminates transverse magnetization. Figure 6-41 shows the results of this experiment with 11β -hydroxyprogesterone. (Cf. Figure 5-12.) The bottom spectrum (a) contains the unirradiated spectrum, and the ascending spectra contain the DPFGE NOE experiments on a series of target nuclei. These spectra are taken directly, not by a difference technique. Only Overhauser-enhanced resonances result. The technique easily extends the limit for ^1H NOE's to 0.1% and has been used to observe enhancements as small as 0.02%.

Excitation sculpting also can be used for solvent suppression in the DPFGE version of WATERGATE [$G1-S-G1-G2-S-G2-t(\text{acquire})$], in which the solvent peak is selected for dephasing during S and all other resonances are refocused. Figure 6-42 illustrates the removal of the solvent resonance for 2-mM sucrose in 9:1 $\text{H}_2\text{O}/\text{D}_2\text{O}$.

Figure 6-41 The double pulse field gradient spin echo (DPFGSE) NOE experiment with 11 β -hydroxyprogesterone: (a) the unirradiated spectrum; (b)–(g) spectra with irradiation at selected frequencies. (Reproduced with permission from K. Stott, J. Keeler, Q. N. Van, and A. J. Shaka, *J. Magn. Reson. A*, **125**, 322 (1997).

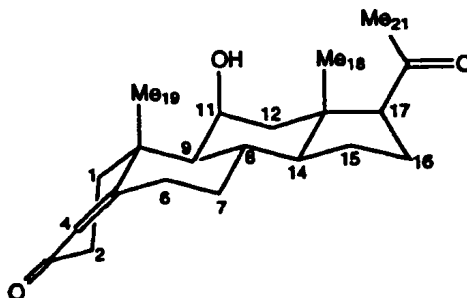
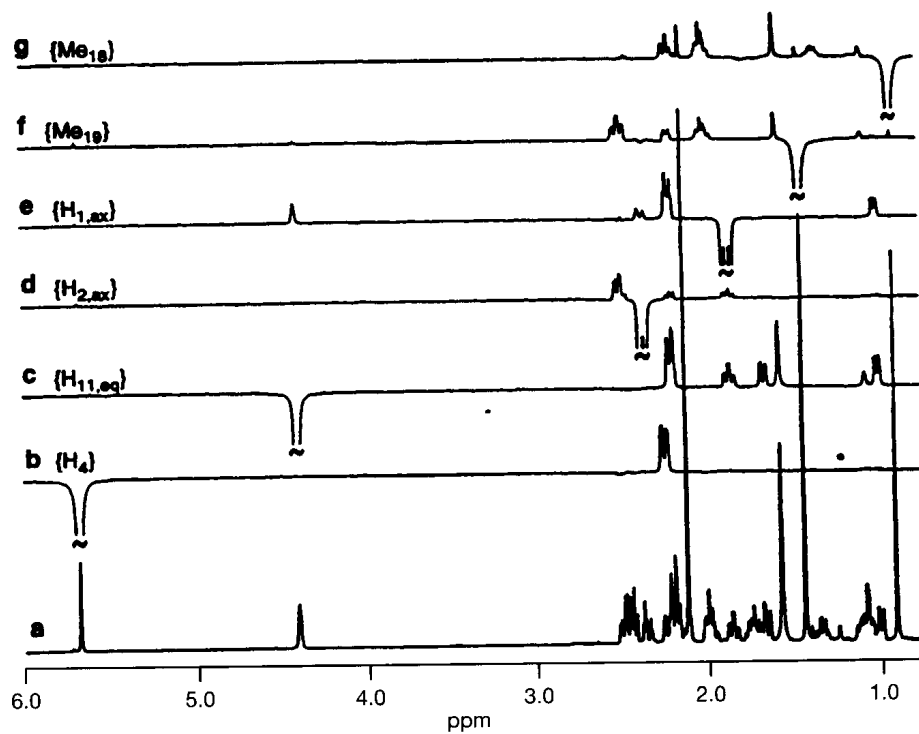
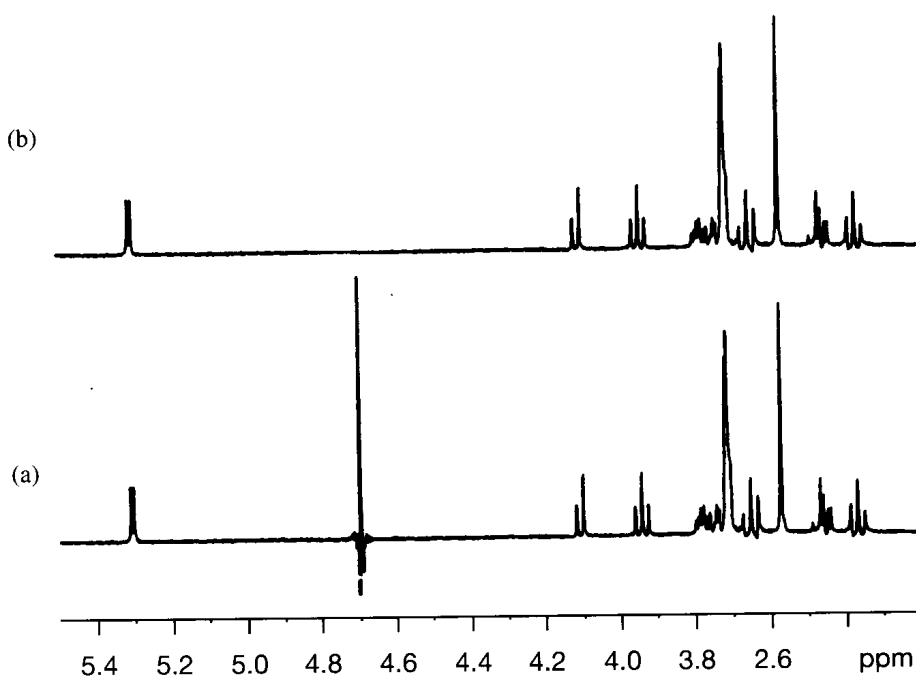


Figure 6-42 (a) Water suppression with excitation sculpting on 2-mM sucrose in 9:1 H₂O/D₂O. (b) The residual solvent peak has been eliminated by further processing. (Reproduced from T. D. W. Claridge, *High-Resolution NMR Techniques in Organic Chemistry*, Pergamon Press, Amsterdam, 1999, p. 365.)



6-7 Summary of Two-Dimensional Methods

A bewildering array of two-dimensional methods is available to the NMR spectroscopist today. This chapter has described a number of the most widely used experiments. A routine structural assignment begins with recording the one-dimensional ^1H and ^{13}C spectra. Many resonances may be assigned according to the principles outlined in Chapters 3 and 4 on chemical shifts and coupling constants. Normally, recourse is made to 2D methods only if this traditional approach is insufficient. Some type of spectral editing for determining the number of protons attached to each carbon, such as DEPT, is helpful in completing the ^{13}C assignments (Section 5-5). The HETCOR or HMQC experiment then provides correlations between the ^{13}C and ^1H resonances, possibly with completion of the ^1H assignments.

Further 2D methods are necessary if the structure is not learned in the process of making spectral assignments for hypothetical or expected structures. The COSY experiment lays the groundwork for identifying structure through ^1H – ^1H connectivities based on J couplings. For small molecules, there may not be enough vicinal or geminal couplings for the method to be useful. For molecules of medium complexity, COSY may be sufficient to provide the entire structure by confirming expected ^1H – ^1H connectivities based on vicinal and geminal couplings. The analogous experiment based on long-range couplings (LRCOSY) may be necessary to assign connections between molecular pieces that do not involve vicinal protons—for example, between two rings, for substituents on a ring, or over a heteroatom or carbonyl group.

Additional 2D experiments may be necessary for larger molecules. As peaks accumulate along the diagonal, the COSY45 or DQF-COSY experiment may be used to simplify that region and uncover cross peaks that are close to the diagonal. For even larger molecules, the TOCSY or relayed COSY experiments may be necessary. Further connectivities between protons and carbons may be explored through longer range couplings (HMBC) in order to define structural regions around quaternary carbons. If ^1H – ^1H couplings need to be measured, either the J -resolved method or DQF-COSY may be carried out.

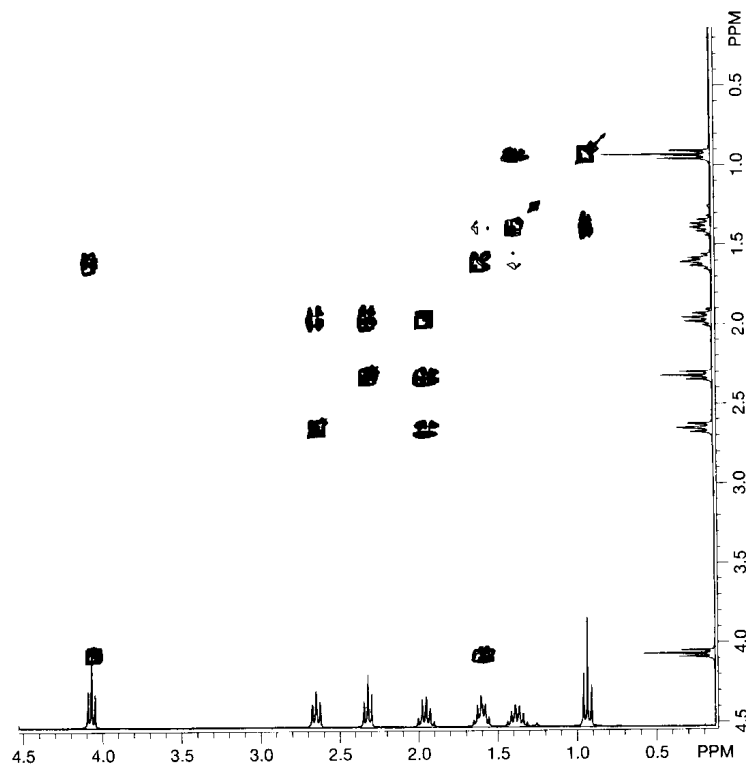
The NOESY experiment provides information about the proximity of protons and hence is used primarily for distinguishing structures that have clear stereochemical differences. For larger molecules, the ROESY experiment may offer some advantages because of its lower tendency to exhibit spin diffusion. The related EXSY experiment is used only when chemical exchange is being investigated.

The 2D INADEQUATE or INEPT–INADEQUATE experiment requires additional spectrometer time. It is usually an experiment of last resort, although specific structures may be particularly amenable to this technique—for example, when there are several quaternary carbons that prevent COSY analysis.

Problems

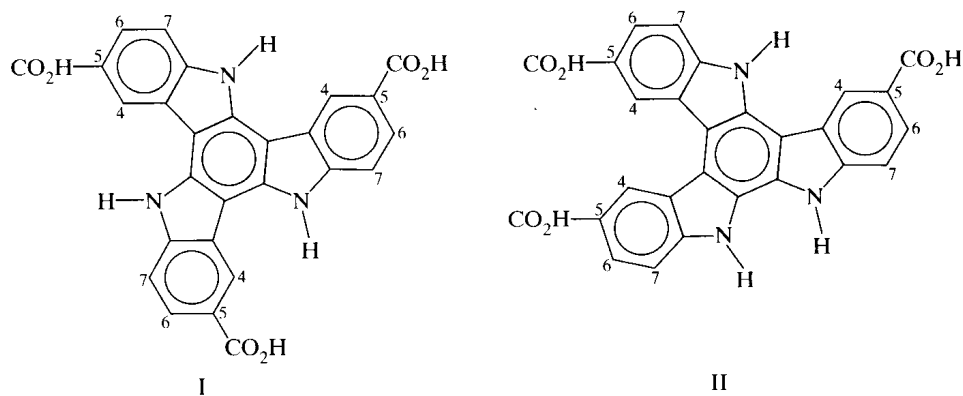
For a large selection of relatively straightforward 2D spectra, see Problem 6-12. The remaining problems involve molecules of medium to high complexity, although none is so complex as to require 3D methods.

6.1 The following is the 300 MHz COSY spectrum* of a molecule with the formula $C_{14}H_{20}O_2$:

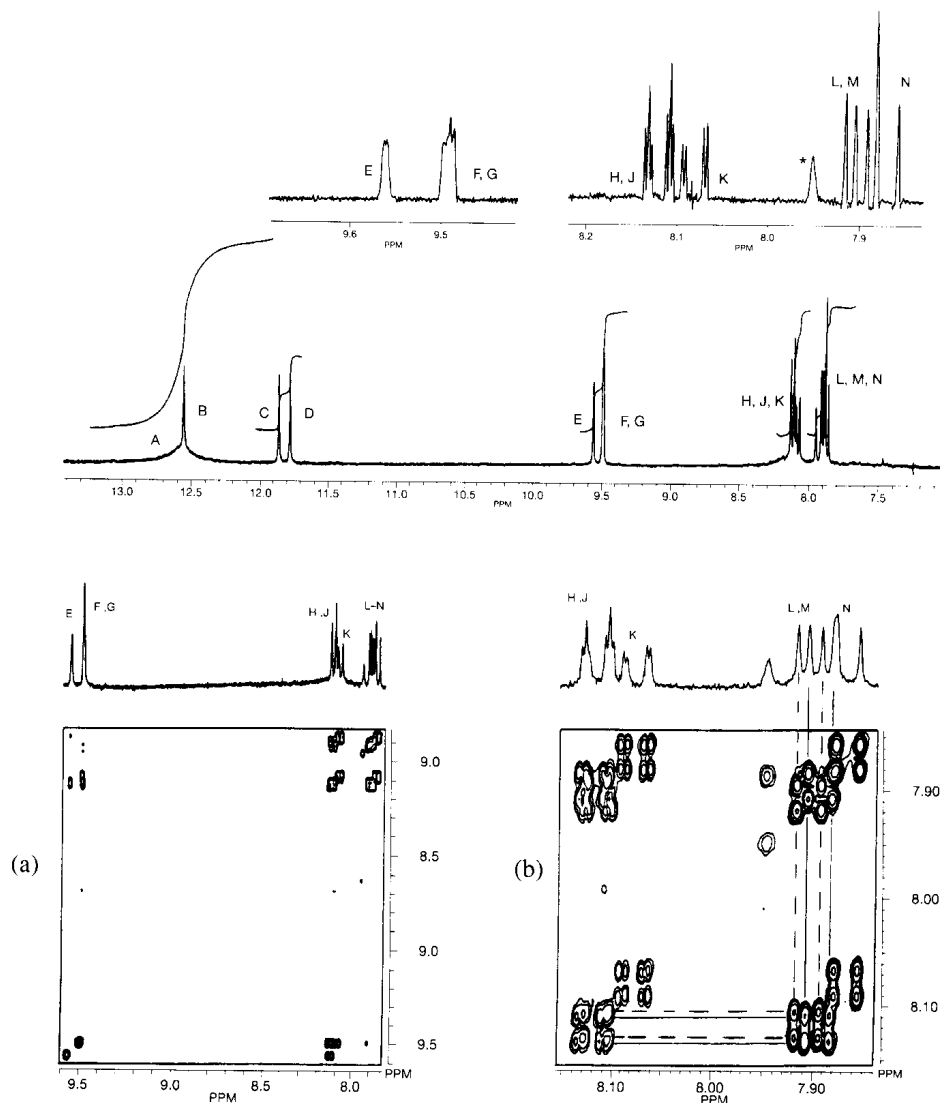


The 1D spectrum is given on either edge. In addition to the illustrated resonances, the 1H spectrum contains a broad singlet at δ 7.3 with integral 5. What is the structure? Show your reasoning.

6.2 The trimerization of indole-5-carboxylic acid gives one of the following two isomers:



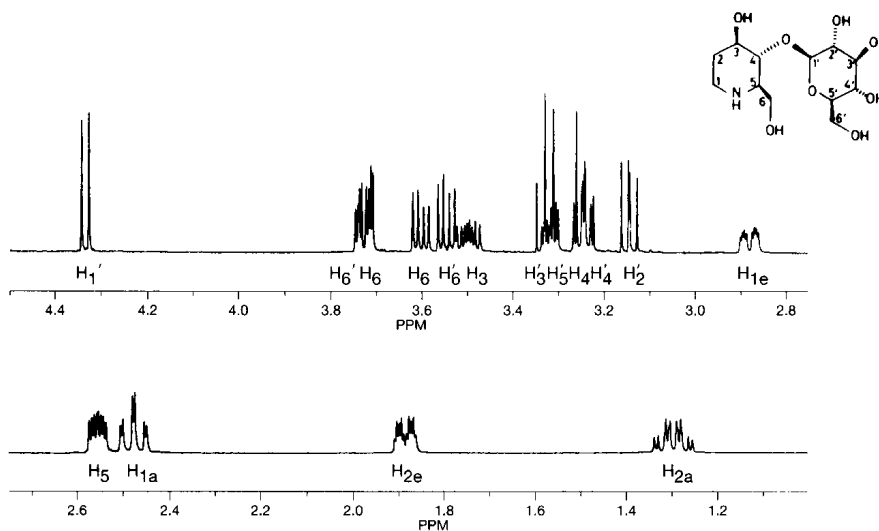
Shown below are the 360.1 MHz ^1H spectrum* of the product and the COSY spectrum (with a blowup of the δ 7.8–8.2 region) in $\text{DMSO}-d_6$:



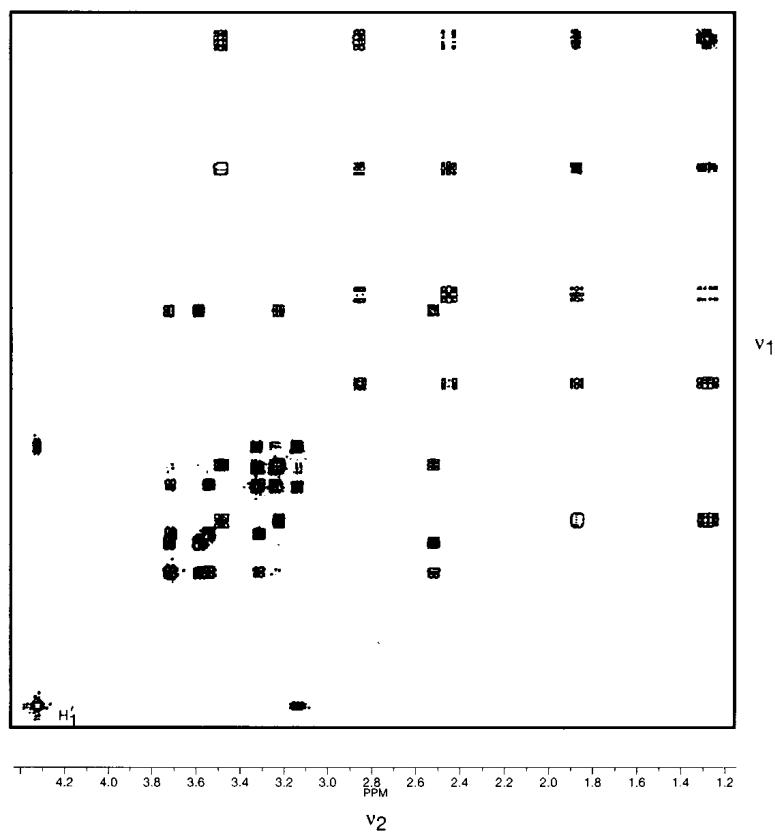
The signal marked with an asterisk is an impurity. The ^1H signals are labeled A through N. Signals A to D were removed with the addition of D_2O . Signal A is a broad peak at the base of B. In the 1D NOE experiment, irradiation of B affected F/G and N, irradiation of C and D affected M and L, respectively, and irradiation of F/G affected B.

- From the overall appearance of the spectrum, is the trimer I or II? Explain.
- Using peak multiplicities, the NOE experiments, and the COSY spectrum, assign all the resonances. Discuss your reasoning in a step-by-step fashion. You should end up with an assignment of peaks A through N to specific protons.

6.3 The 500 MHz ^1H spectrum of a sugar derivative (extracted from a bean) is as follows, aside from hydroxy resonances:



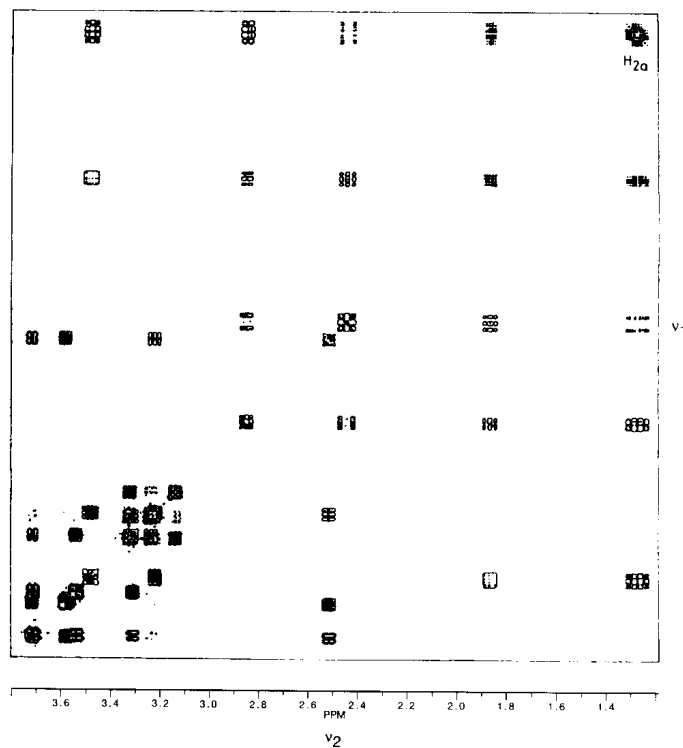
(a) The complete COSY spectrum,* with the assignment of one resonance, is as follows:



Complete the assignment for protons in the sugar ring.

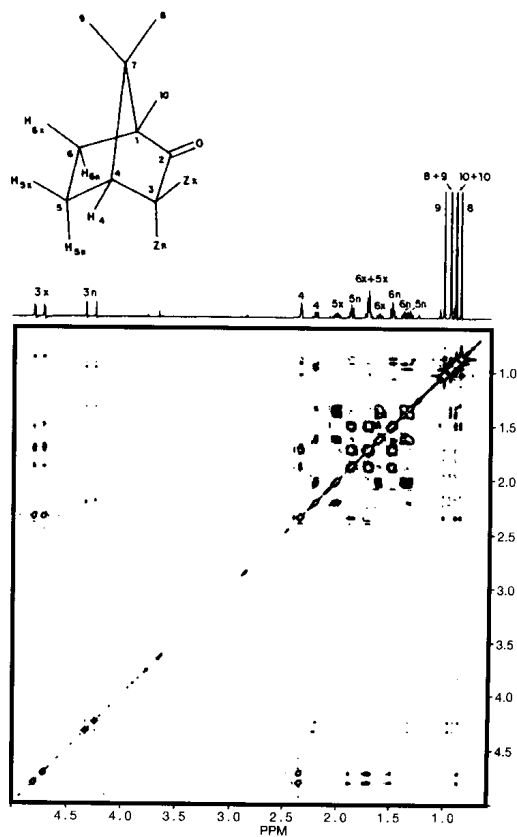
*A. E. Derome, *Modern NMR Techniques for Chemistry Research*, Pergamon Press, Oxford, UK, 1987, p. 257.)

- (b) The following is a slightly expanded version of the low-frequency portion of the COSY spectrum, again with the assignment of one resonance:



Complete the assignment for the protons of the piperidine ring. First, it is advisable to draw out the chair conformation.

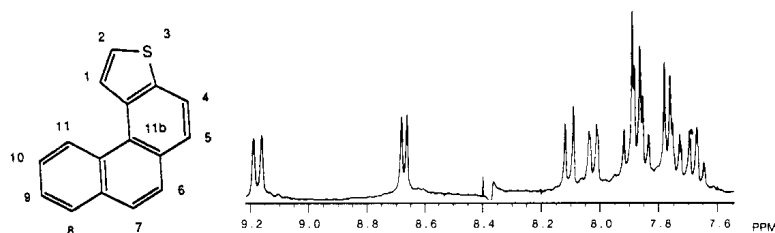
- 6.4 The following is the 600 MHz COSY45 spectrum* for a mixture of 3-*endo*- and 3-*exo*-fluorocamphor:



*C. R. Kaiser, R. Rittner, and E. A. Basso, *Magn. Reson. Chem.*, **32**, 503–508 (1994). Reproduced with permission of John Wiley & Sons, Ltd.

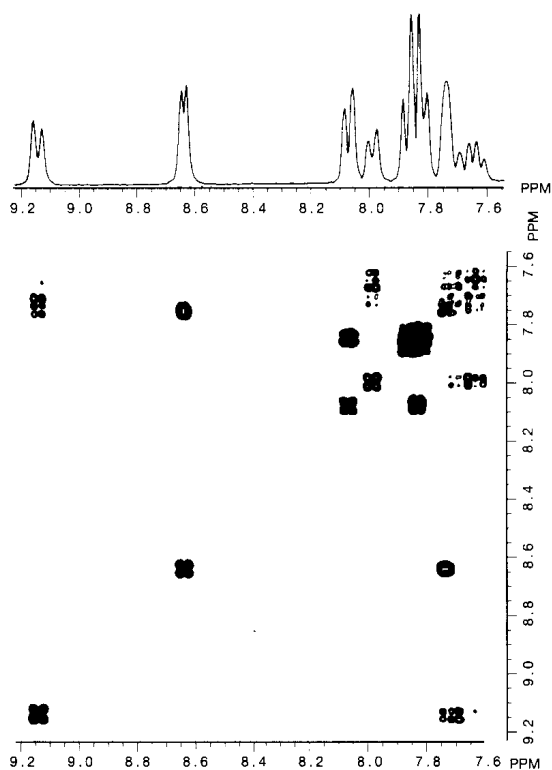
The two high-frequency peaks are from the 3 protons on the exo-F isomer ("3n," an endo proton) and the endo-F isomer ("3x," an exo proton), respectively. The remaining protons have been assigned to positions but not to the isomer. Using the COSY45 spectrum, indicate which peaks come from the exo and which from the endo isomer. Show your reasoning by drawing lines on the spectrum.

- 6.5 (a) From the following 300 MHz ^1H spectrum* of phenanthro[3,4-b]thiophene, identify the resonances of H-1 and H-11, as a pair:



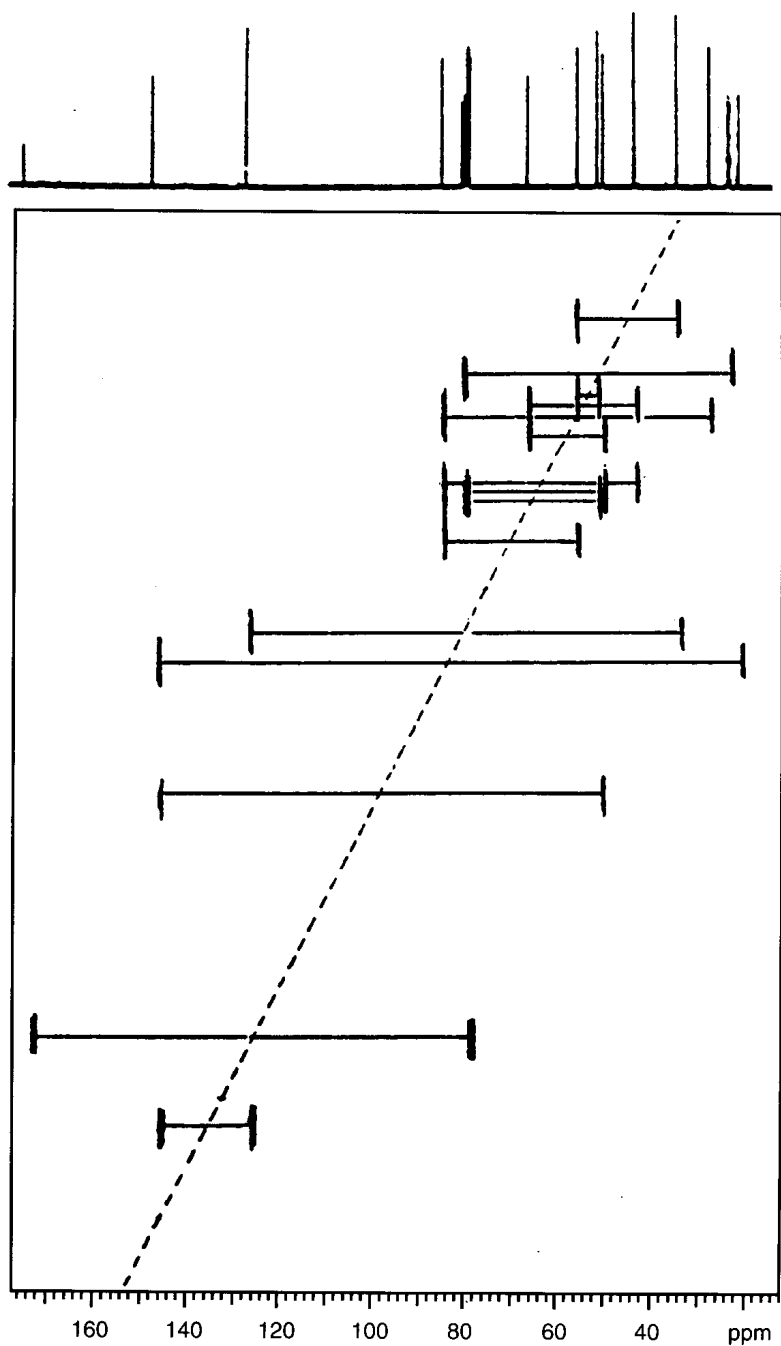
How are these resonances distinguished from the remaining ones?

- (b) From the following 300 MHz COSY spectrum, how would you distinguish H-1 and H-11?



Assign resonances to H-2, H-8, H-9, and H-10.

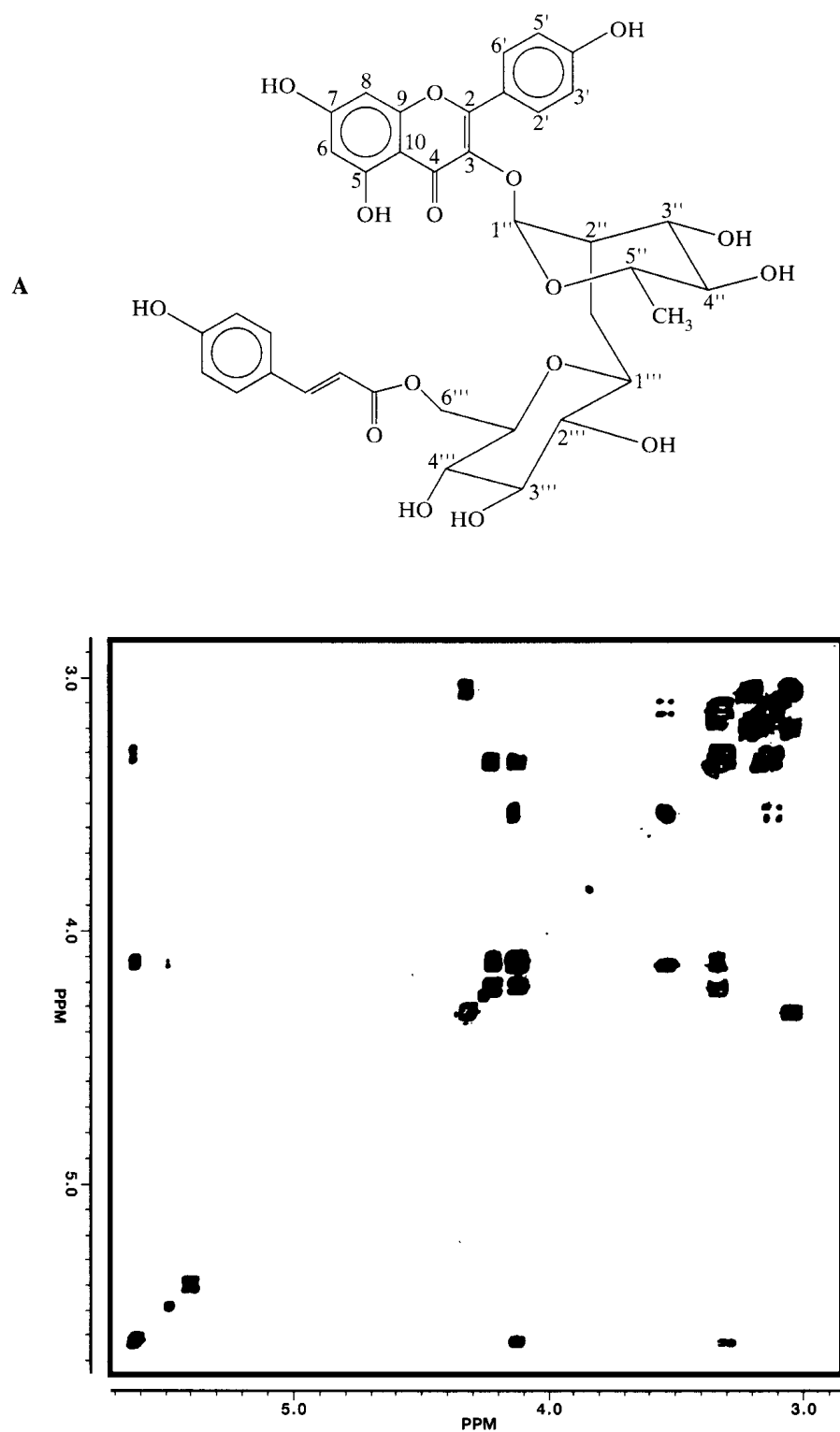
6.6 With only the following 2D INADEQUATE spectrum,* derive the structure for the skeleton of isomontanolide:



There are two overlapping resonances at δ 78, so you must work around ambiguities at that chemical shift. Also, there are substituents on the carbons in the range δ 60–80 that are not defined by the experiment.

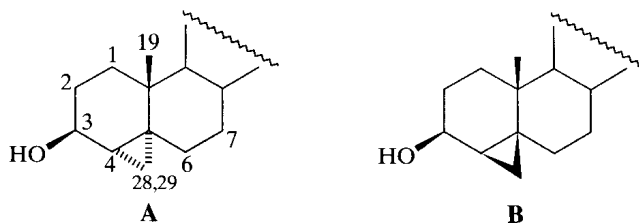
*Liberalized from, and with the permission of, M. Budesinsky and D. Saman, *Ann. Rev. NMR Spectrosc.*, **30**, 231–475 (1995).

6.7 The following molecule with the structure **A** gave the DQF-COSY spectrum illustrated after it (sugar portion only) in DMSO- d_6 :

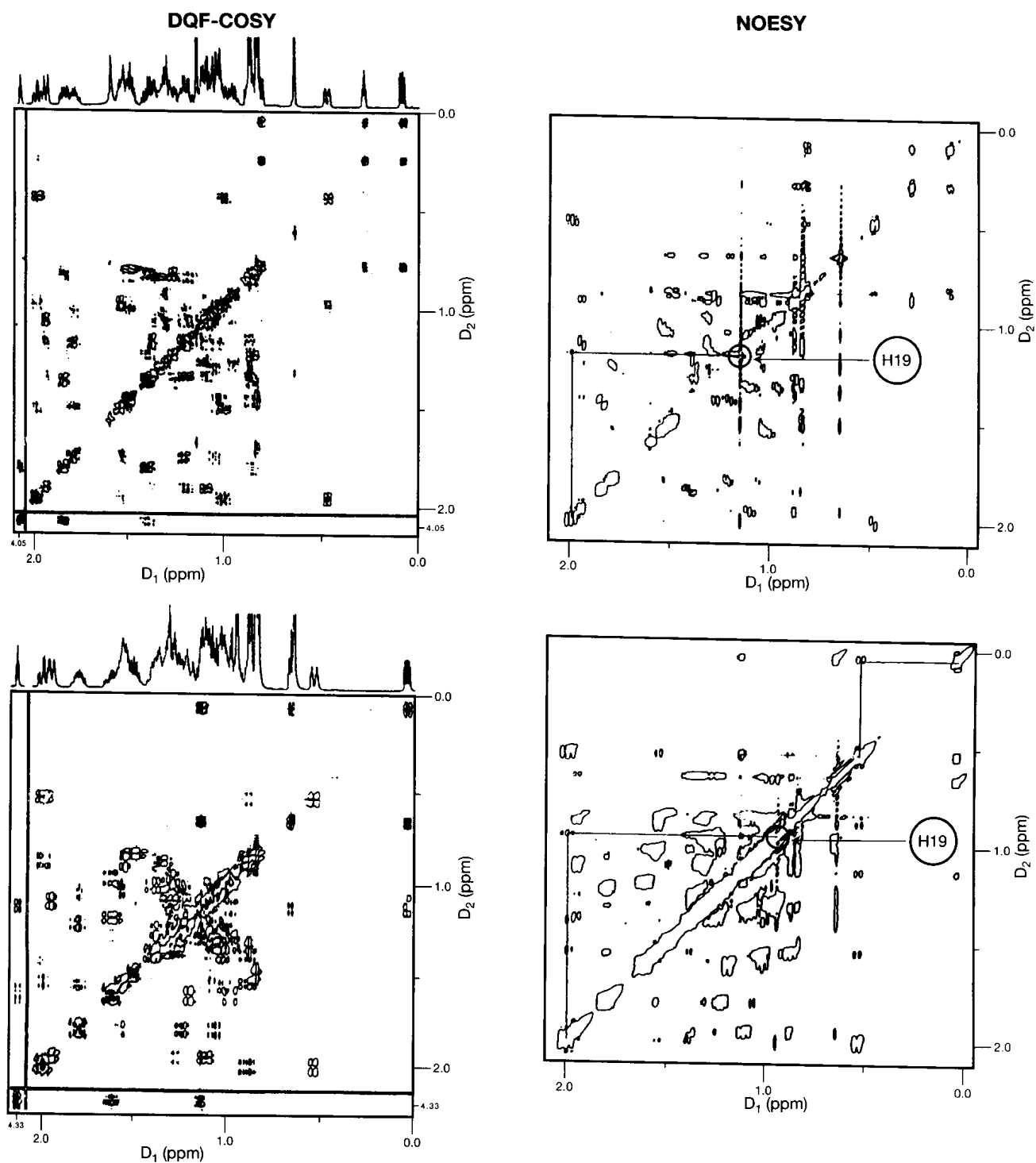


- Assign the sugar protons as fully as possible, and explain their positions.
- Assign the ^1H resonance at δ 12.56, and explain its high-frequency position.
- The ^1H spectrum exhibited vicinal couplings of $^3J = 9.4$ Hz for H-O-C(3''')-H and of $^3J = 3.1$ for H-O-C(2''')-H. Explain in terms of medium effects and conformations.

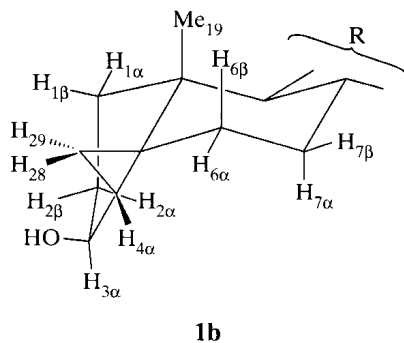
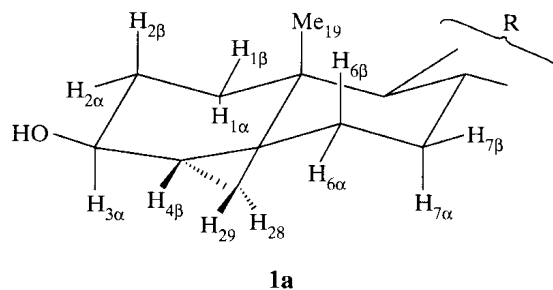
- 6.8 The 4,5-cyclopropanocholestan-3-ols are expected to be inhibitors of cholesterol oxidase. There are two isomers, shown in part A and B. (Protons pointing up are labeled β and protons pointing down are α .) The remainder of the structure is the cholestane skeleton and is not relevant to this problem. The DFQ-COSY and NOESY spectra for both isomers are



as follows:

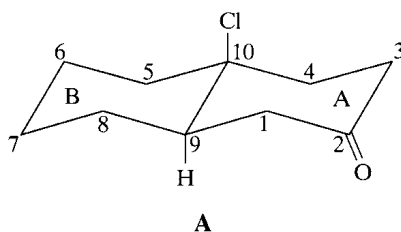


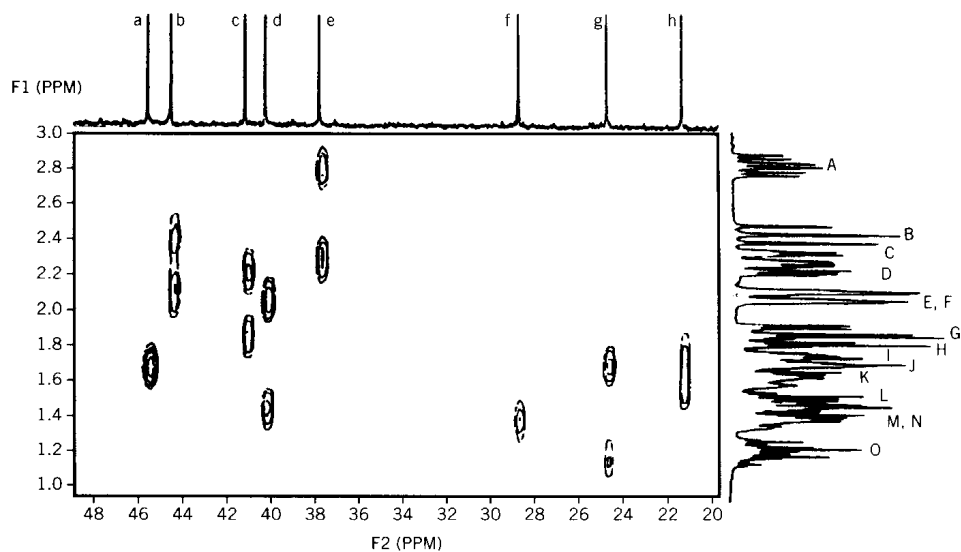
- (a) Starting with H(3 α) in the DQF-COSY spectrum of one isomer, assign the cyclopropane protons (H4, H28, H29). [This approach works only for one isomer; see part (b).] Note the discontinuity in the DQF-COSY axes between δ 2 and 4. Assign cross peaks for H4/H28, H4/H29, and H28/H29.
- (b) The approach fails for the other isomer. Why? By analogy with your assignments in (a), assign the cyclopropane resonances and cross peaks anyway.
- (c) In both isomers, there is a third low-frequency peak in addition to the cyclopropane resonances (δ 0.5). It has a large $J = 13.5$ Hz, with a partner at about δ 2 in both isomers. Identify the DFQ-COSY cross peak between the $J = 13.5$ Hz partners in both isomers. Assign these resonances and explain the low-frequency position for the one partner.
- (d) The NOESY spectra for both isomers reveal that H19 (the methyl group) is close to the δ 2 proton, from (c). The proton to which the δ 2 proton is coupled ($J = 13.5$ Hz) shows a NOESY cross peak with one of the other low-frequency cyclopropane protons in only one isomer. These cross peaks are indicated on the spectra. With your peak assignments and these NOESY data, assign the isomers to the spectra. The expected conformations are as follows.



Show the NOESY relationships.

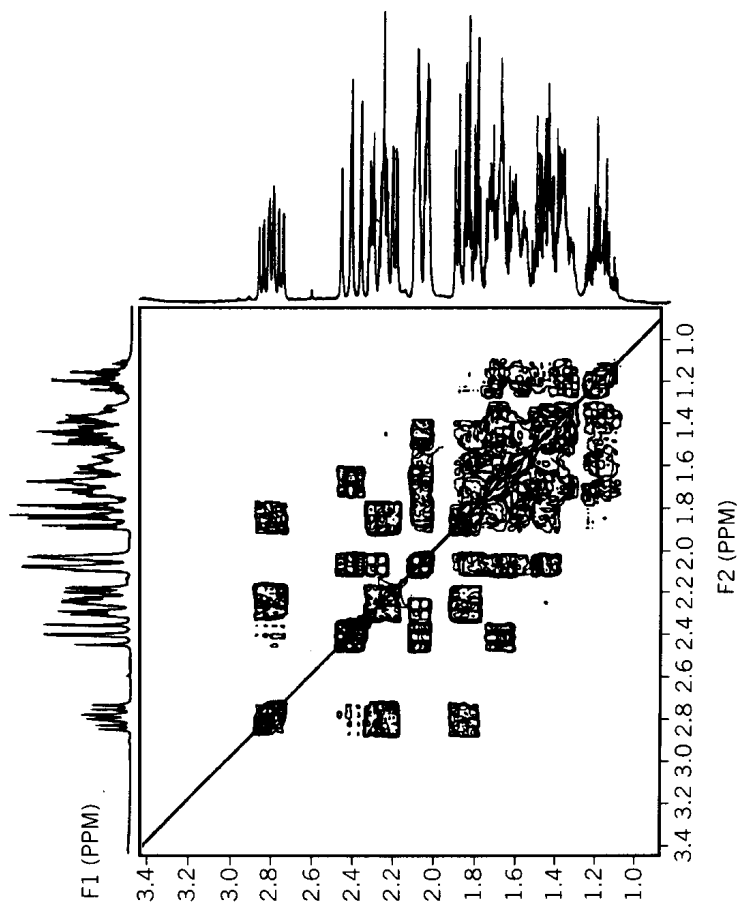
- 6.9 (a) The ^1H and ^{13}C spectra of *trans*-10-chlorodecal-2-one (A) are given in the HETCOR representation on the next page:





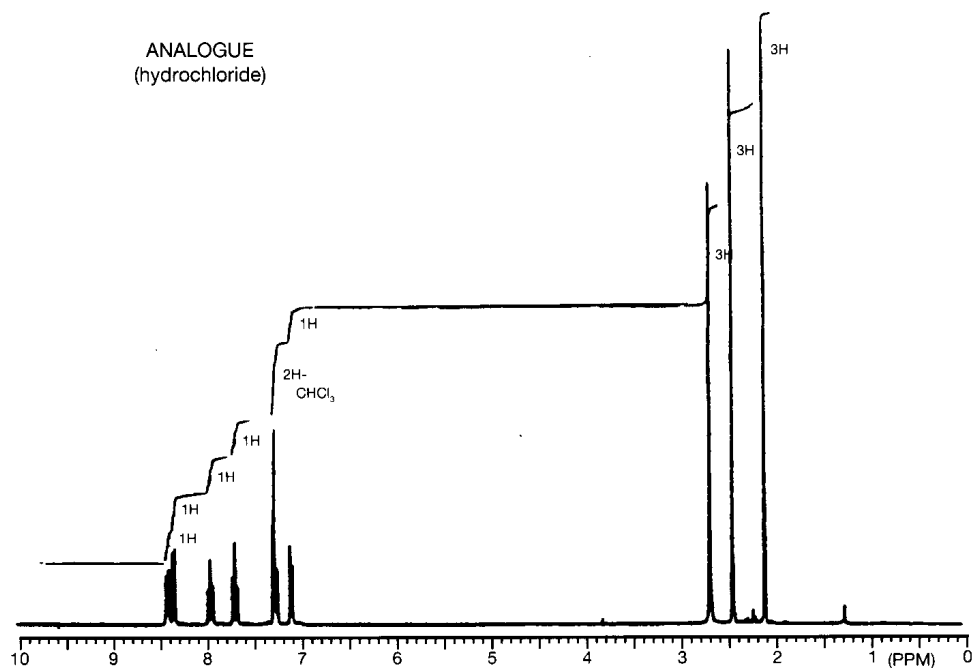
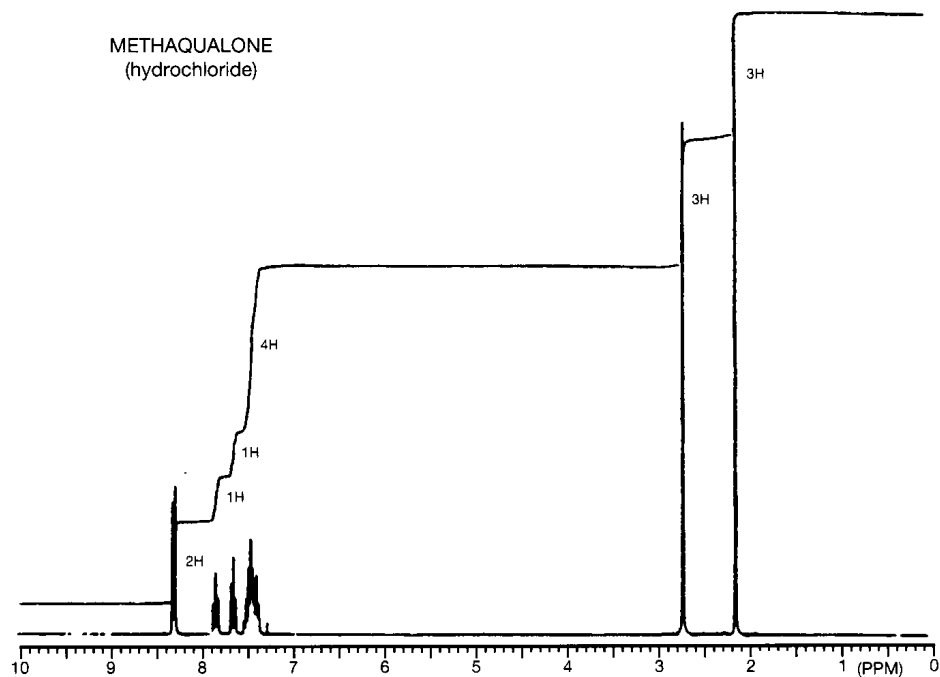
The conformation is rigid, so each geminal proton pair exhibits distinct axial and equatorial resonances. Identify the C6, C7, and C8 resonances *as a group*, and explain.

- Now assign H9 and C9. Explain your logic.
- What ^1H signals are expected to occur at the highest frequency (lowest field)? Explain.
- From the following COSY spectrum and the previous HETCOR spectrum, assign all the protons and carbons in the A ring:



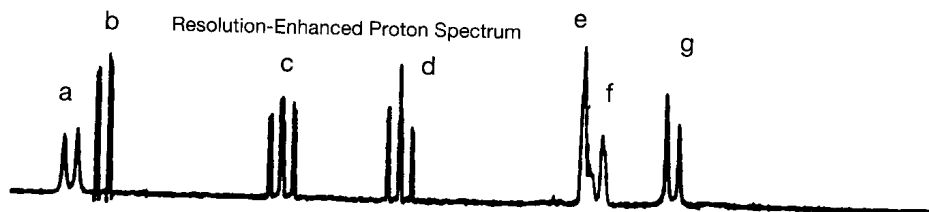
Caution! In this spectrum, the normal axial–equatorial relationship is reversed, as H1a and H3a respectively occur at a *higher* frequency than H1e and H3e.

- 6.10 (a) The controlled substance methaqualone has the formula $C_{16}H_{14}N_2O$ (MW 250). A closely related analogue with MW 264 started to appear as a replacement in the illegal drug market. From their infrared spectra, both molecules contain a carbonyl group ($C=O$, at 1705 cm^{-1}). The 300 MHz ^1H spectra of methaqualone and its analogue are as follows:

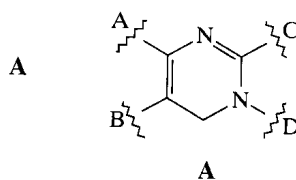


What structural fragments can you deduce from these spectra?

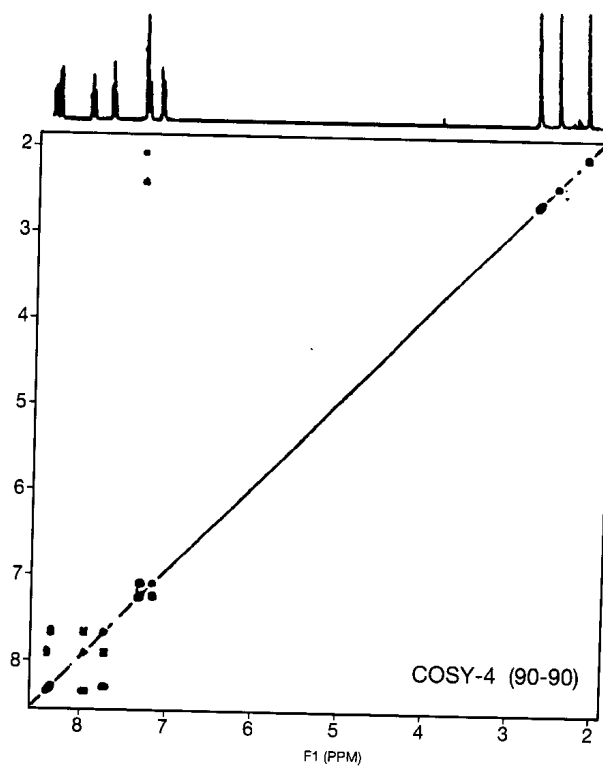
- (b) From the expansion of the high-frequency portion of the spectrum of the analogue, deduce the substructures responsible for these resonances:



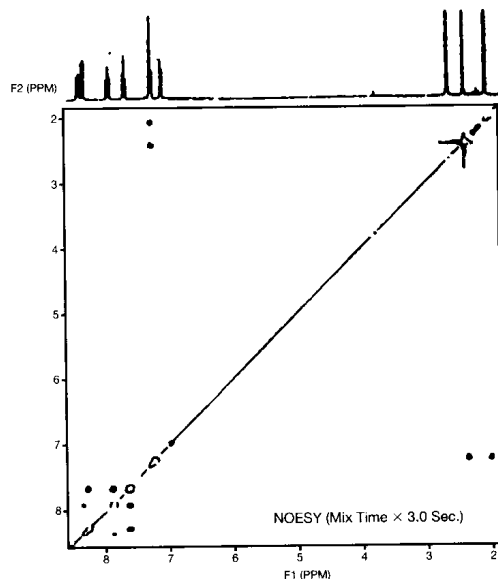
- (c) Both the parent and the analogue contain a pyrimidine ring (A) that is unsaturated and substituted at all positions. Now assemble the entire analogue molecule.



- (d) Assign all the COSY cross peaks for the analogue molecule.



(e) From the following NOESY spectrum, complete any unresolved aspects of the structure of the analogue molecule:

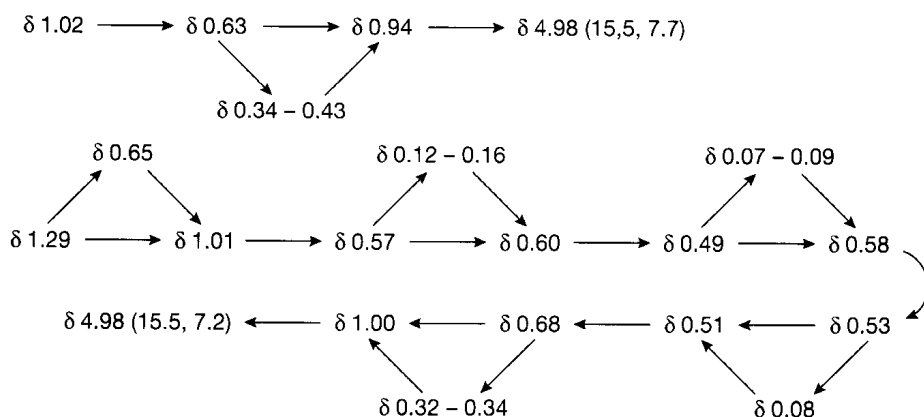


(f) From the structure of the analogue molecule and earlier spectral data, deduce the structure of methaqualone.

- 6.11 Upjohn scientists isolated a potent inhibitor of the cholesteryl ester transfer protein U-106305. The high-resolution mass spectrum indicated that the formula was $C_{28}H_{41}NO$, and the ^{13}C spectrum had 27 distinct resonances (including one pair of equivalent carbons at δ 20.02). DEPT spectra indicated the multiplicities given in the following table:

^{13}C Chemical Shift and Multiplicities	1H Chemical Shift and Coupling Constants	^{13}C Chemical Shift and Multiplicities	1H Chemical Shift and Coupling Constants
7.6 (T)	0.07, 0.09 (dt: 8.43, 4.85)	20.0 (D)	1.00 (m)
7.6 (T)	0.12, 0.16 (dt: 8.39, 4.90)	20.02 (Q)	0.90 (d: 6.8)
8.0 (T)	0.08 (not first order)	20.7 (D)	1.29 (m)
11.4 (T)	0.32, 0.34 (dt: 8.20, 4.77)	21.8 (D)	0.68 (m)
13.4 (T)	0.65 (dt: 8.59, 4.87)	22.4 (D)	0.94 (m)
14.8 (T)	0.34, 0.43 (dt: 8.33, 4.60)	24.0 (D)	1.01 (m)
14.8 (D)	0.63 (m)	28.5 (D)	1.77 (h: 6.8)
17.9 (D)	0.57 (dq: 13.27, 4.93)	46.7 (T)	3.20 (d: 6.8)
18.0 (D)	0.58 (m)	120.0 (D)	5.91 (d: 15.2)
18.2 (D)	0.49 (m)	130.4 (D)	4.98 (dd: 15.5, 7.2)
18.2 (D)	0.51 (m)	131.0 (D)	4.98 (dd: 15.5, 7.7)
18.4 (D)	0.53 (m)	148.8 (D)	6.24 (dd: 15.2, 9.8)
18.41 (Q)	1.02 (d: 6.0)	166.0 (S)	
18.8 (D)	0.60 (m)		

- (a) The infrared spectrum showed intense bands at 1630 and 1558 cm^{-1} . What functional group is suggested? What NMR peak confirms this assignment?
- (b) What substructures are suggested by the ^{13}C peaks at δ 120–150?
- (c) The HETCOR spectrum gave full ^1H assignments. (See preceding table.) From the ^1H resonance correlated with the δ 120–150 ^{13}C peaks, what else can you tell about the substructures from (b)? Use the magnitudes of J (values in parentheses), the values of the four ^1H and ^{13}C chemical shifts, and the proton multiplicities. In particular, note that δ 120 is d rather than dd.
- (d) The UV–vis spectrum showed a strong band at 215 nm. Using the functional groups you have already deduced, what is the chromophore?
- (e) Examine the six low-frequency ^{13}C triplets. Each is correlated with a very low frequency (high field) pair of protons ($\delta < 0.7$). What grouping is suggested here that is present six times?
- (f) Now count up your unsaturations. You should have accounted for them all. Enumerate them.
- (g) The DQF-COSY spectrum was given by the authors for one substructure as follows: the integral-6 ^1H resonance at δ 0.90 (d: 6.8) was linked to the integral-1 resonance at 1.77 (heptet: 6.8), which was linked to the integral-2 resonance at δ 3.20 (d: 6.8). What substructure is suggested by this 2D evidence?
- (h) How is this substructure linked to a previously determined functionality? Look at the chemical shifts.
- (i) You actually have almost all the structure now. The remaining unassigned ^{13}C resonances are 12 doublets and one quartet. Locate these carbons (without specific assignment) on your previous substructures, and comment on the chemical shifts of the attached protons.
- (j) These protons are all found in the DQF-COSY spectrum, except for the δ 1.29 resonance. Even at 600 MHz, there is severe overlap, so here are the connectivities derived from this experiment:

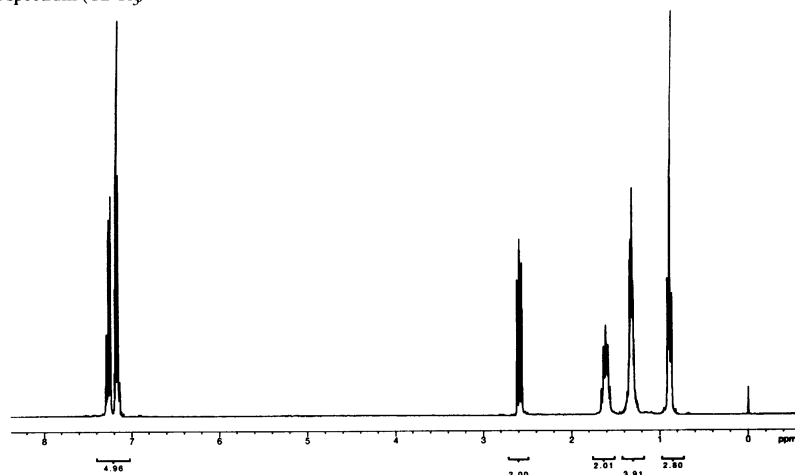


Write out the entire structure. (Some stereochemistries are not set.)

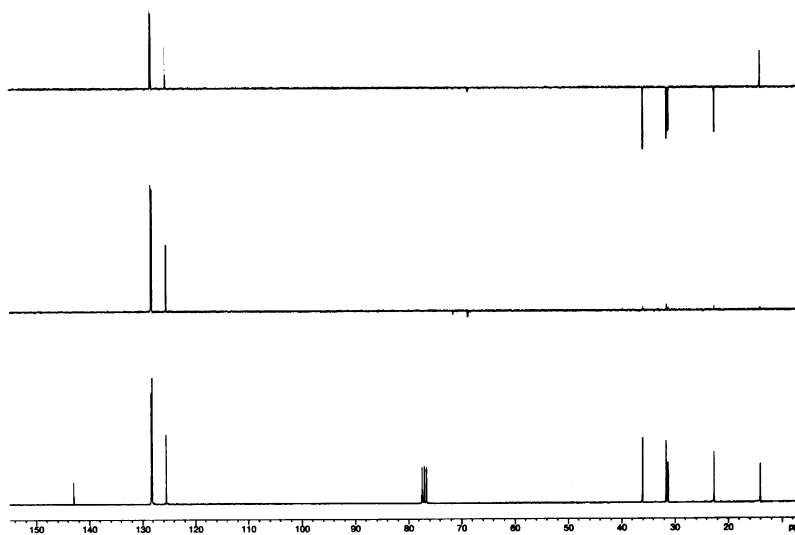
- (k) Look at the available multiplicities and J values for the protons associated with the six high-frequency triplets. (All are dt with J either ~ 8.4 or ~ 4.8 Hz.) This information sets the final stereochemistries. Give the full structure.
- 6.12 The spectra shown in this problem provide relatively routine practice. In the DEPT spectra, the methine and methyl carbons give positive peaks and methylene carbons negative peaks at the top. Only methine carbons are in the middle, and a full spectrum of all carbons is at the bottom. The ^1H spectra were recorded at 300 MHz and the ^{13}C spectra at 75 MHz. The spectra are as follows:

(a) $C_{11}H_{16}$

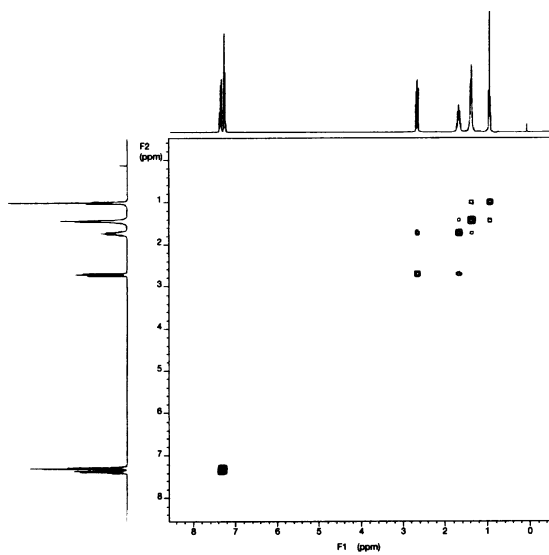
Proton NMR spectrum ($CDCl_3$)



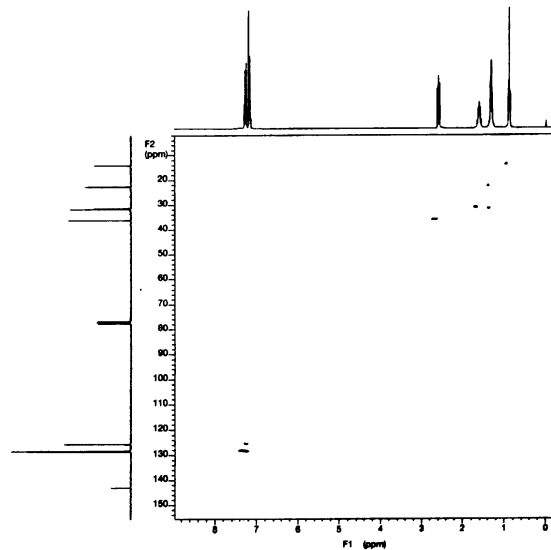
DEPT spectra

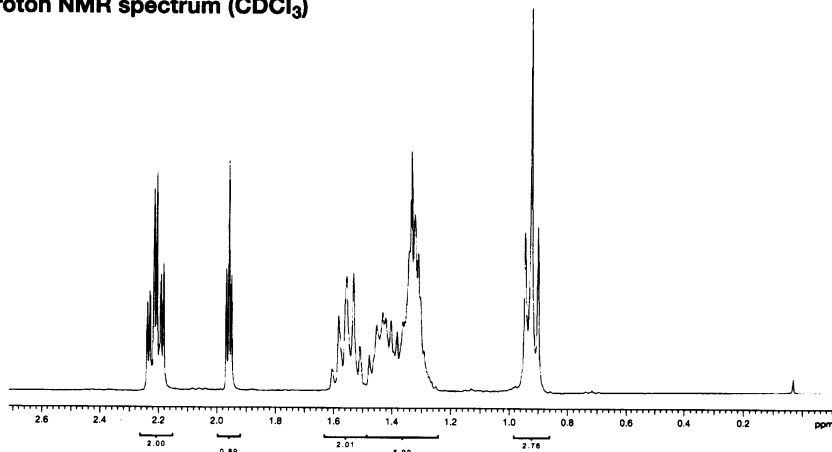


COSY spectrum

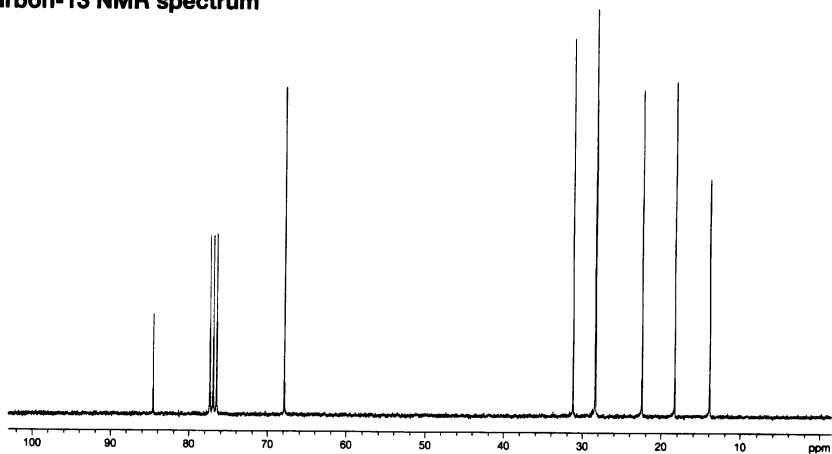


HETCOR spectrum

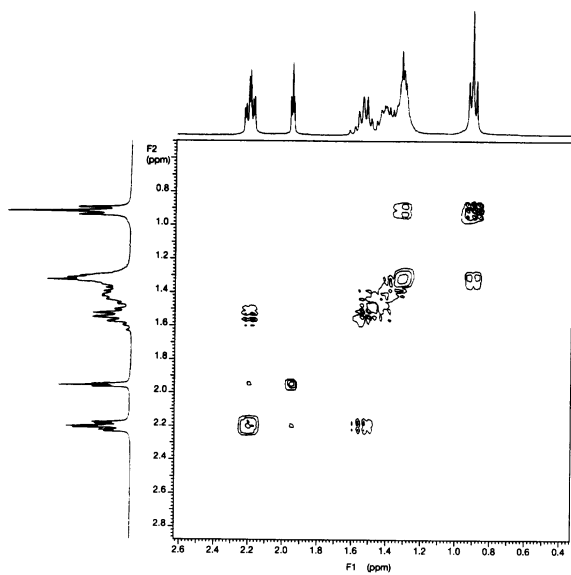


(b) C_8H_{14} Proton NMR spectrum ($CDCl_3$)

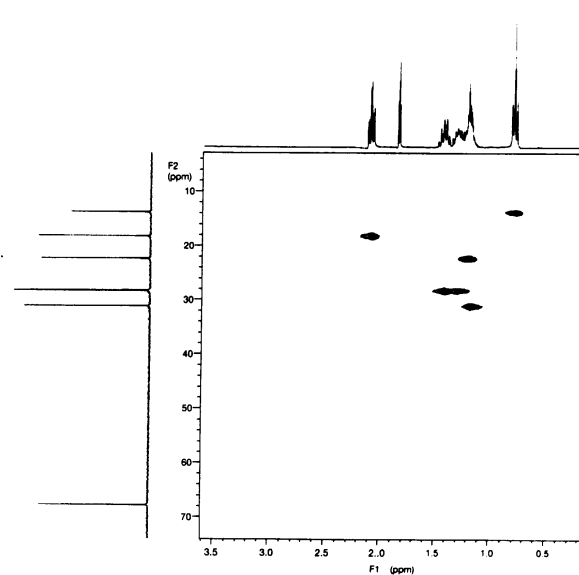
Carbon-13 NMR spectrum



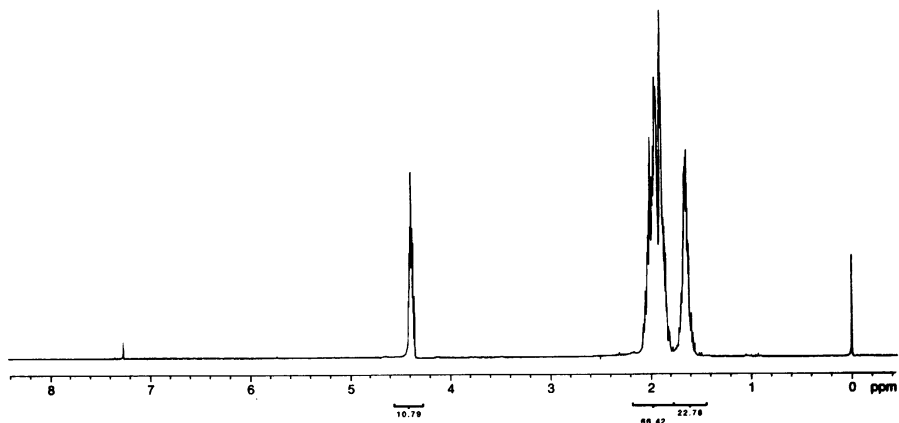
COSY spectrum



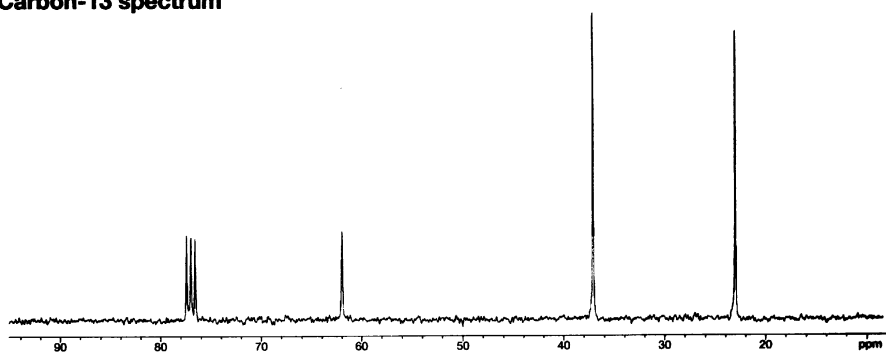
HETCOR spectrum



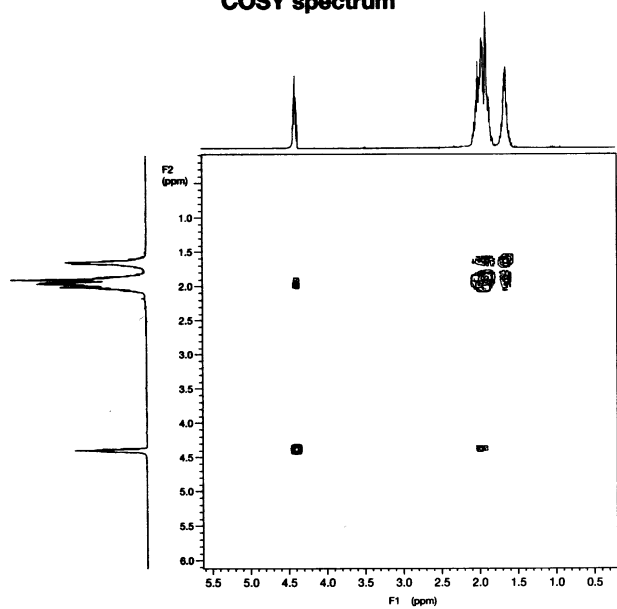
(c) C_5H_9Cl Proton NMR spectrum ($CDCl_3$)



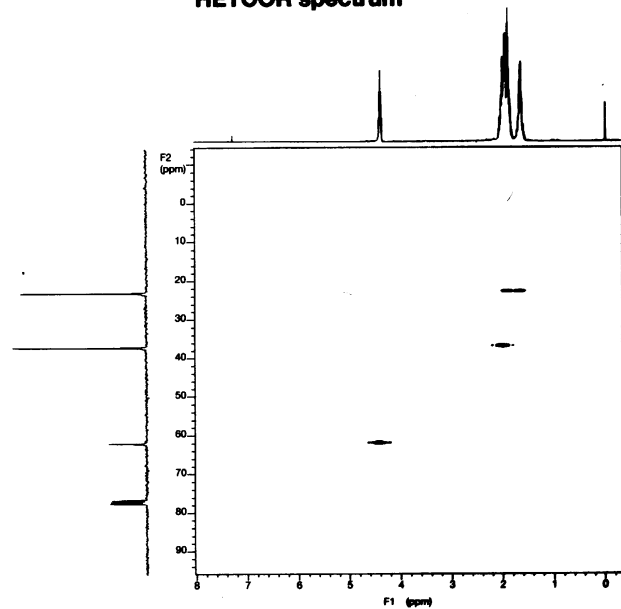
Carbon-13 spectrum

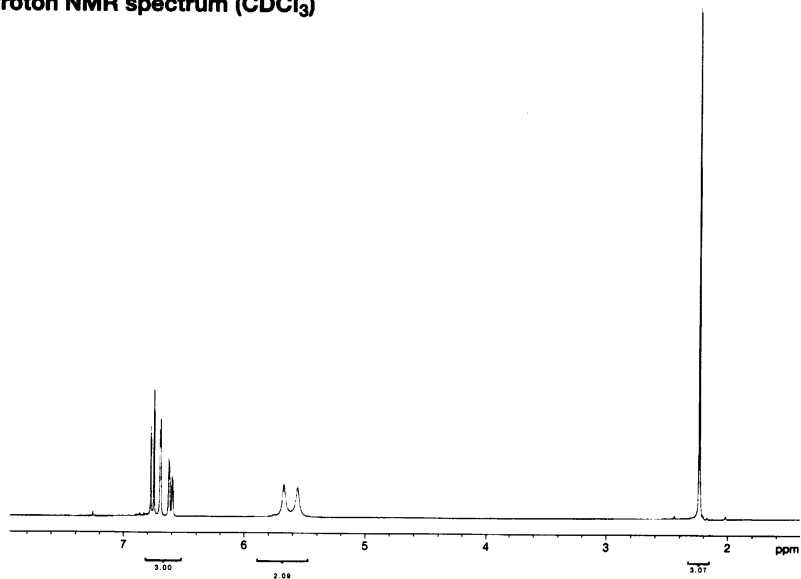
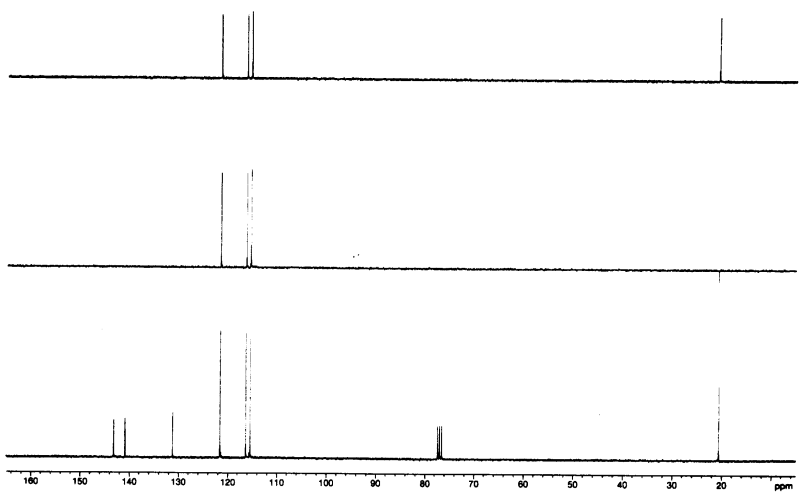
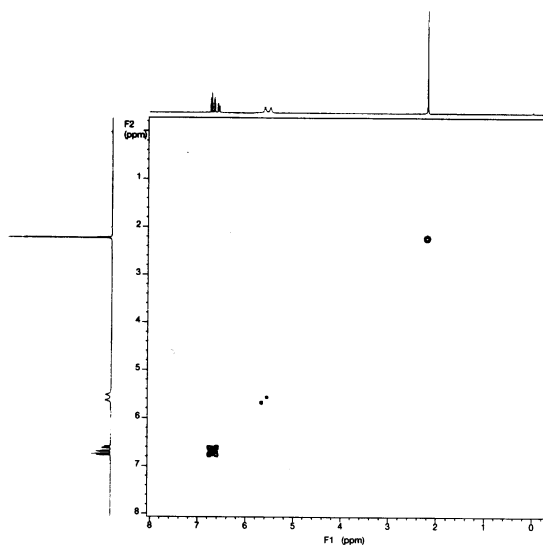
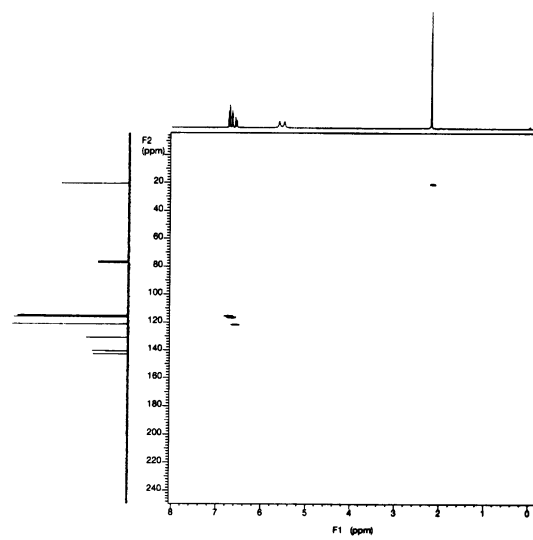


COSY spectrum



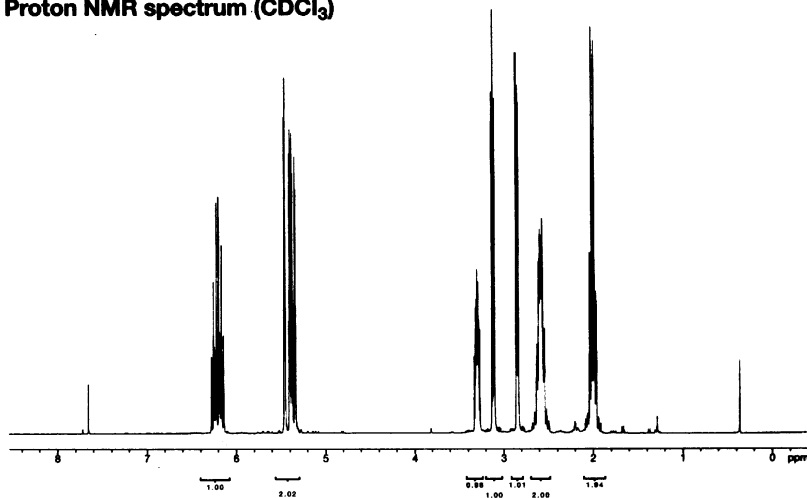
HETCOR spectrum



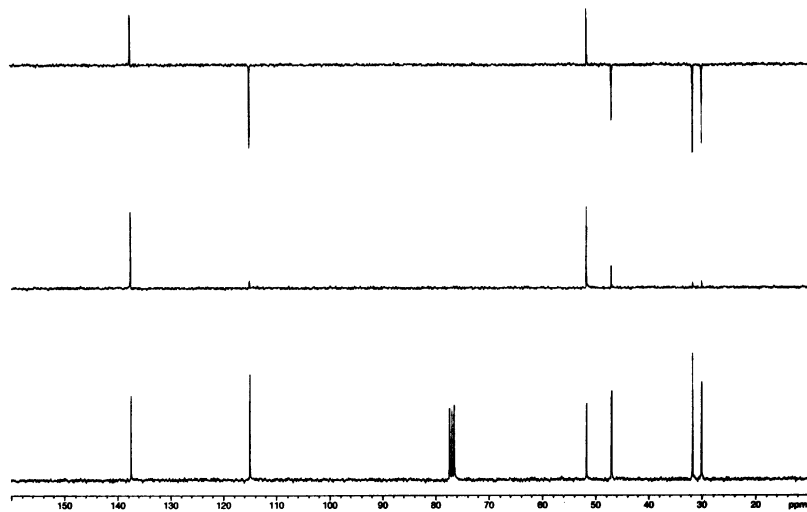
(d) $C_7H_8O_2$ **Proton NMR spectrum ($CDCl_3$)****DEPT spectra****COSY spectrum****HETCOR spectrum**

(e) $C_6H_{10}O$

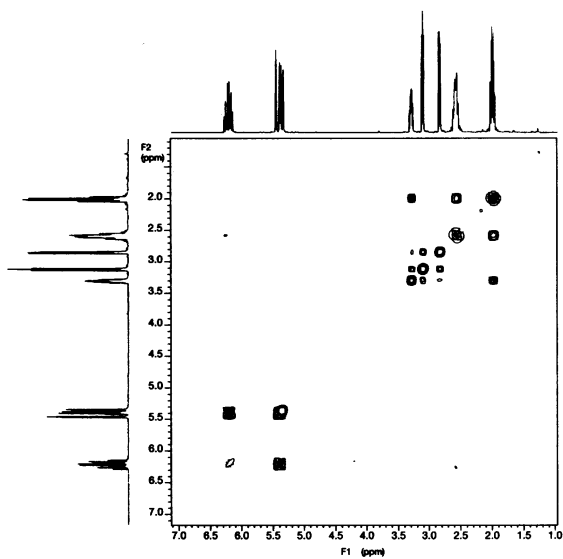
Proton NMR spectrum ($CDCl_3$)



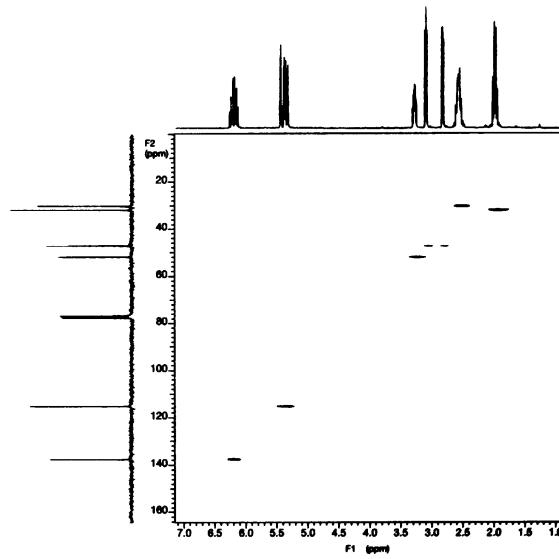
DEPT spectra

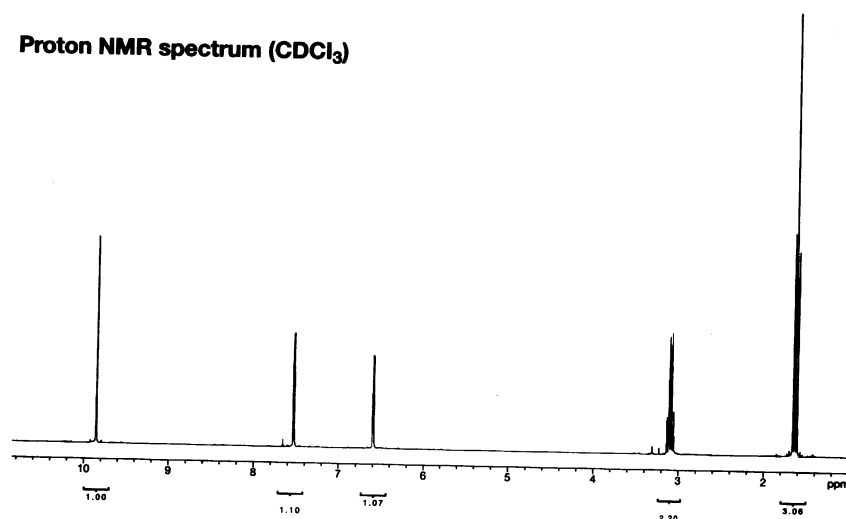
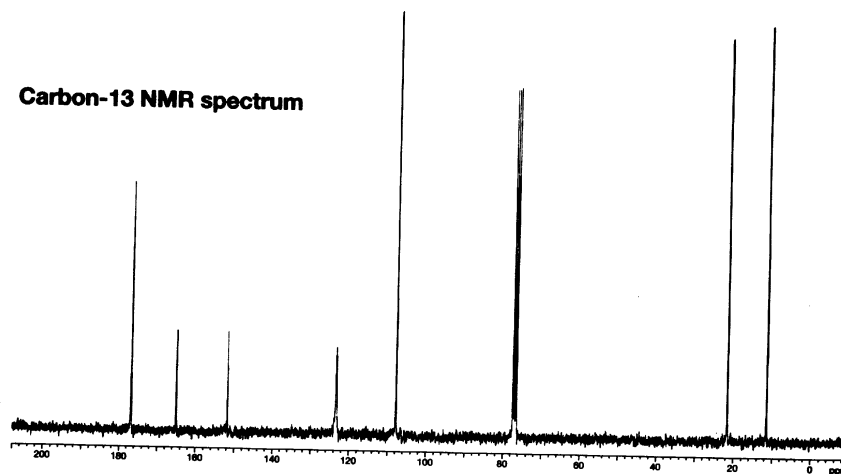
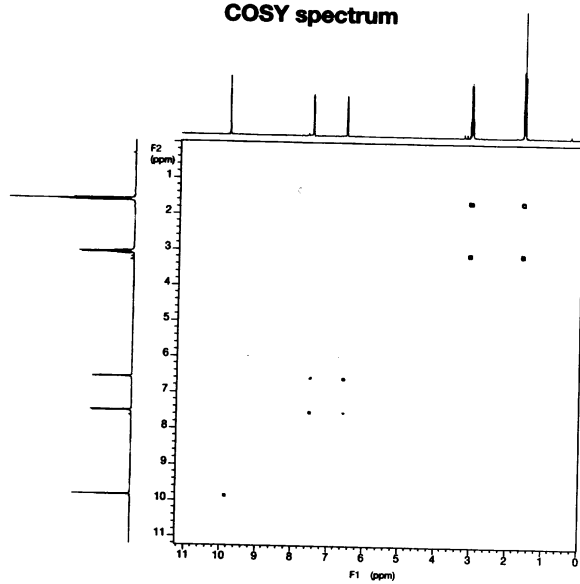
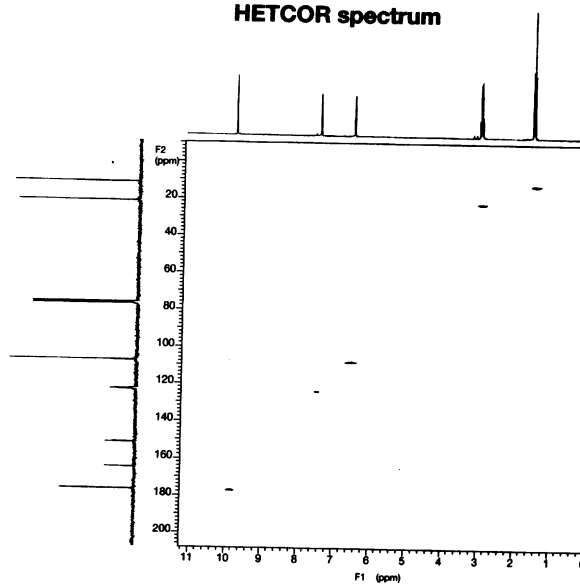


COSY spectrum



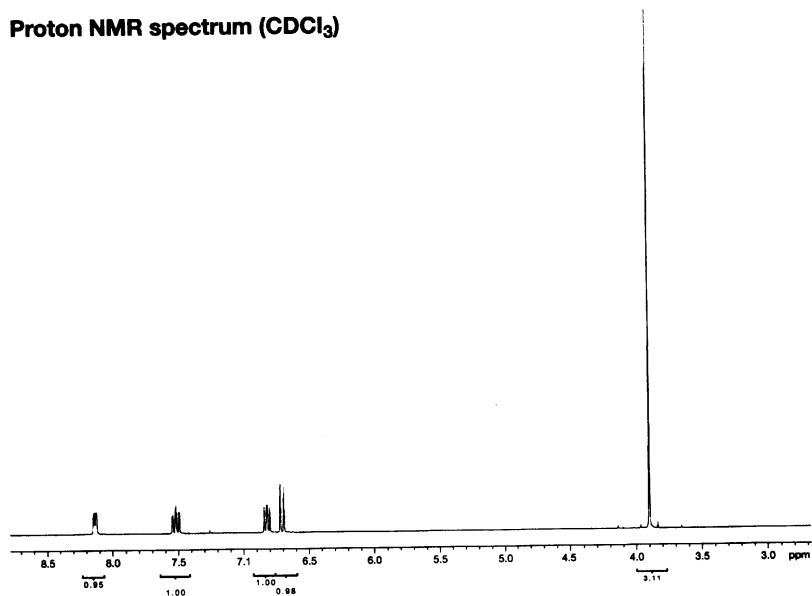
HETCOR spectrum



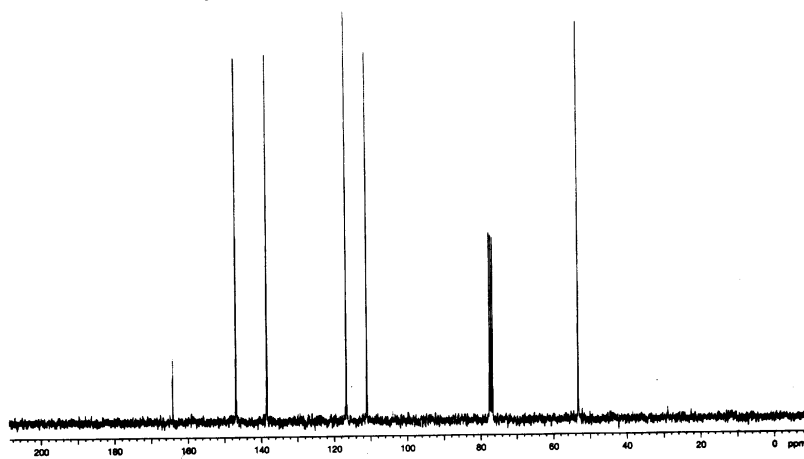
(f) $C_7H_8O_2$ **Proton NMR spectrum ($CDCl_3$)****Carbon-13 NMR spectrum****COSY spectrum****HETCOR spectrum**

(g) C_6H_7NO

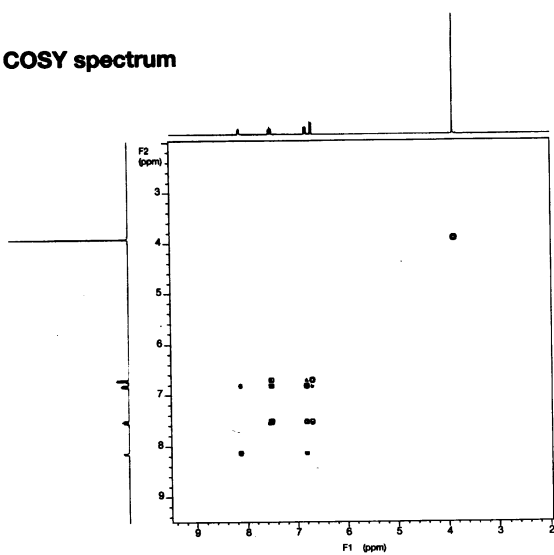
Proton NMR spectrum ($CDCl_3$)



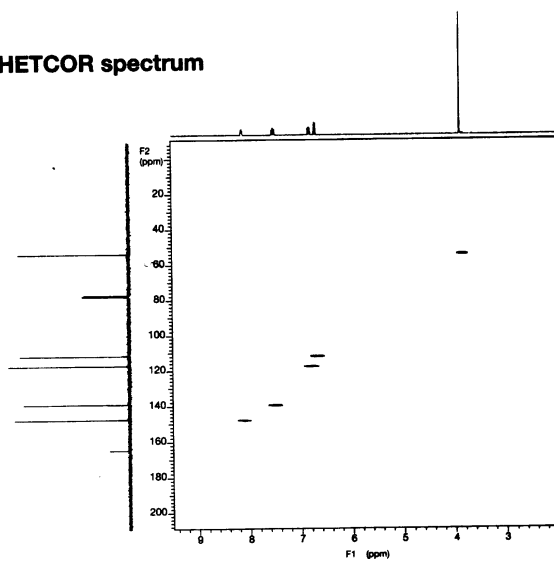
Carbon-13 NMR spectrum



COSY spectrum

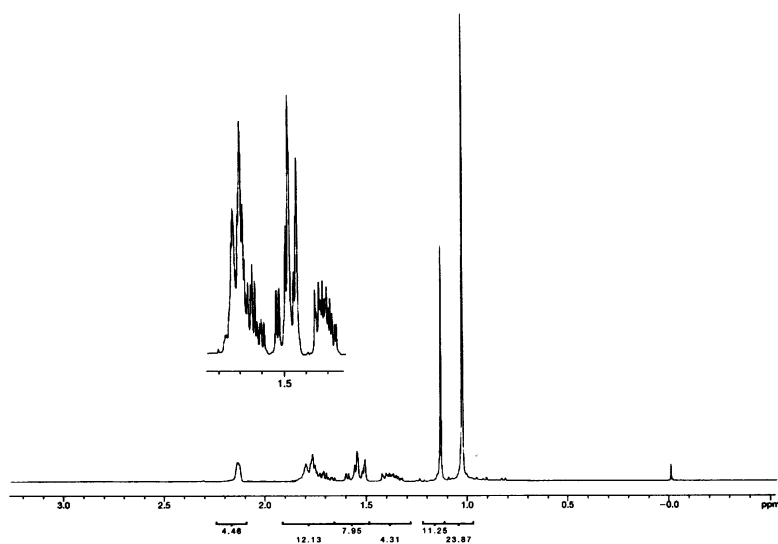


HETCOR spectrum

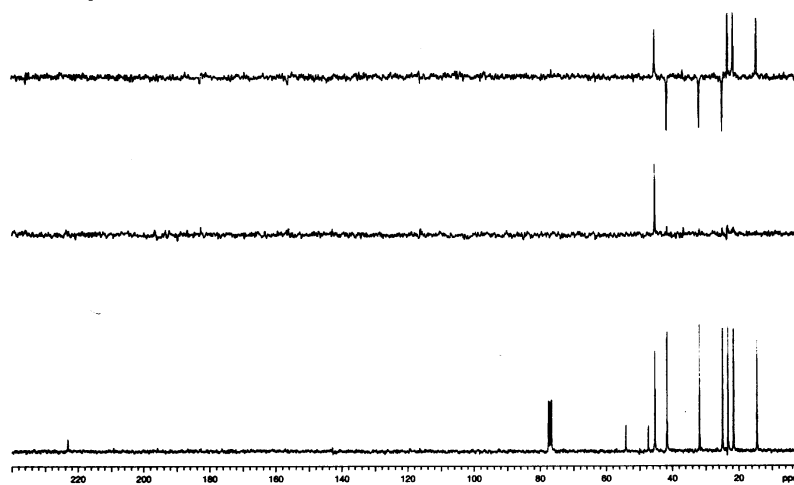


(h) $C_{10}H_{16}O$

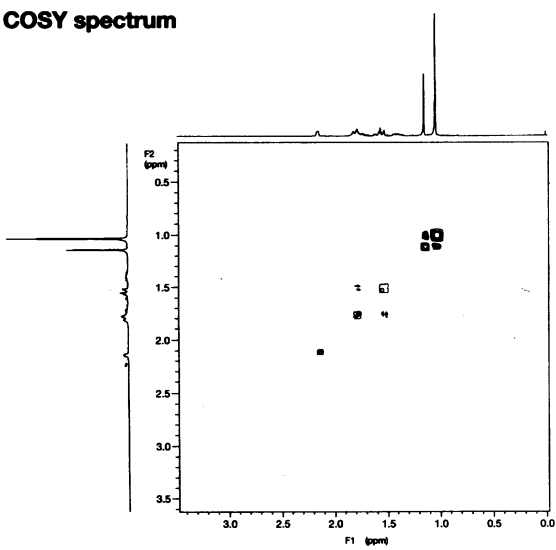
Proton NMR spectrum with expansion ($CDCl_3$)



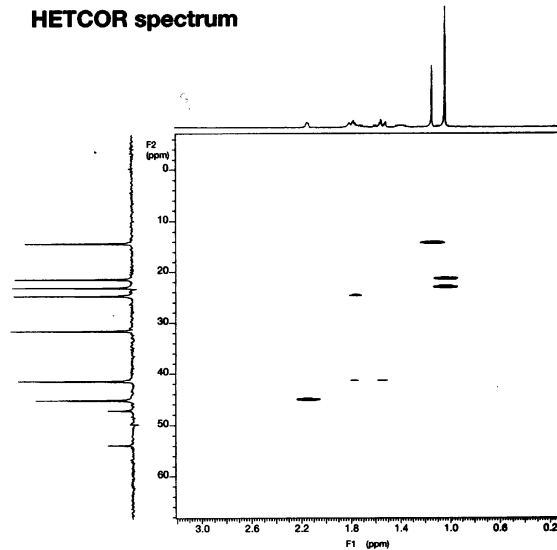
DEPT spectra



COSY spectrum

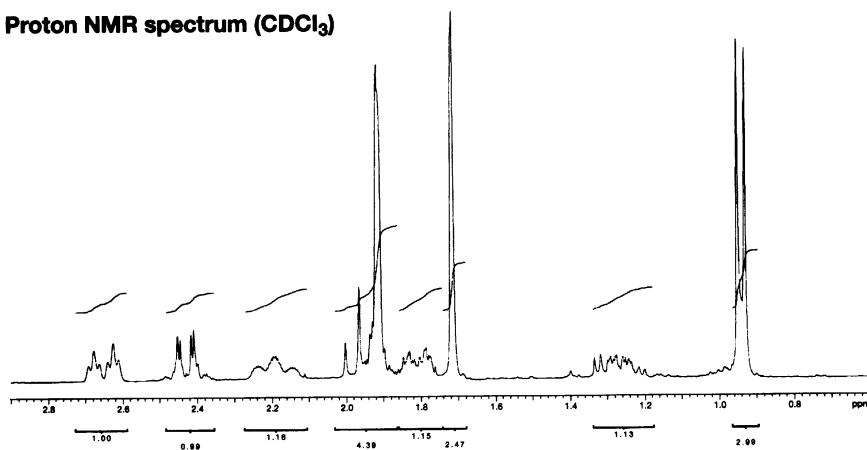


HETCOR spectrum

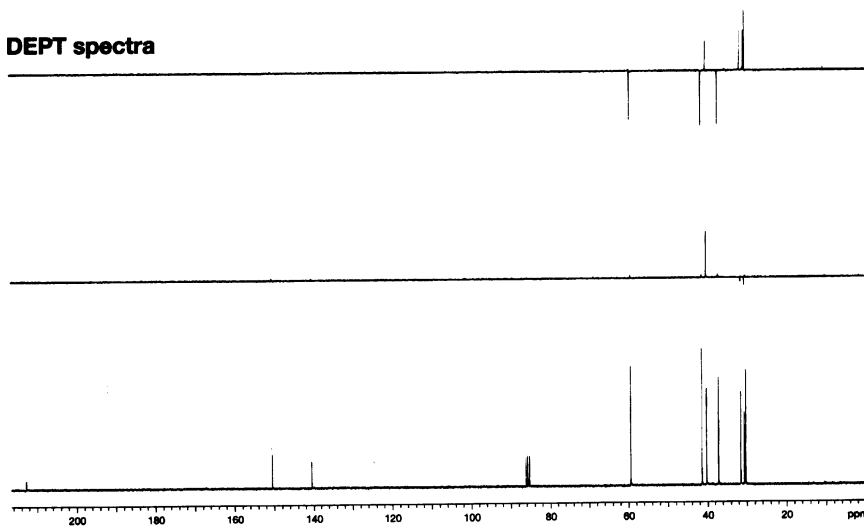


(i) $C_{10}H_{16}O$

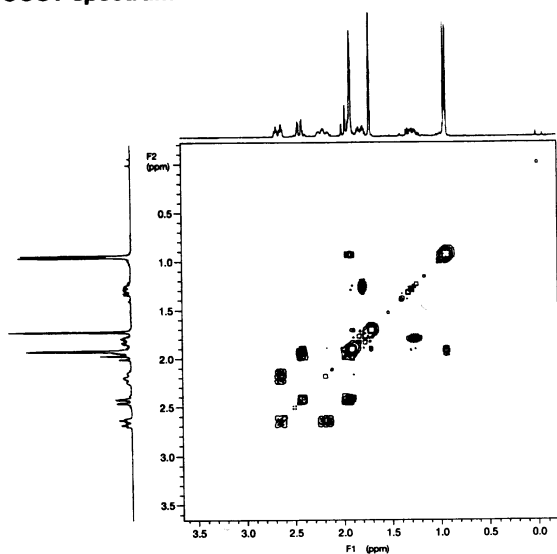
Proton NMR spectrum ($CDCl_3$)



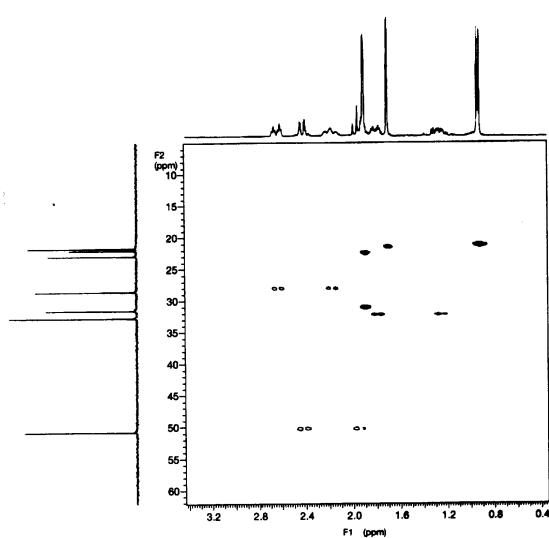
DEPT spectra



COSY spectrum

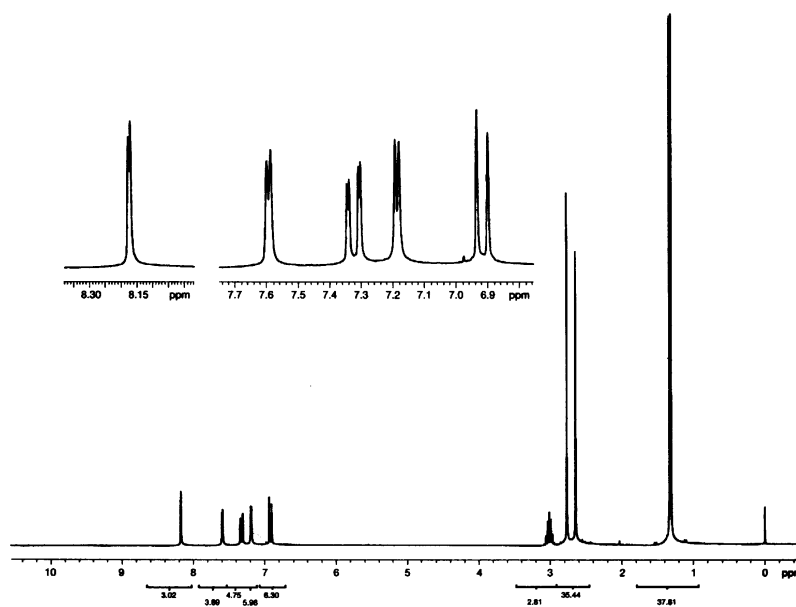


HETCOR spectrum

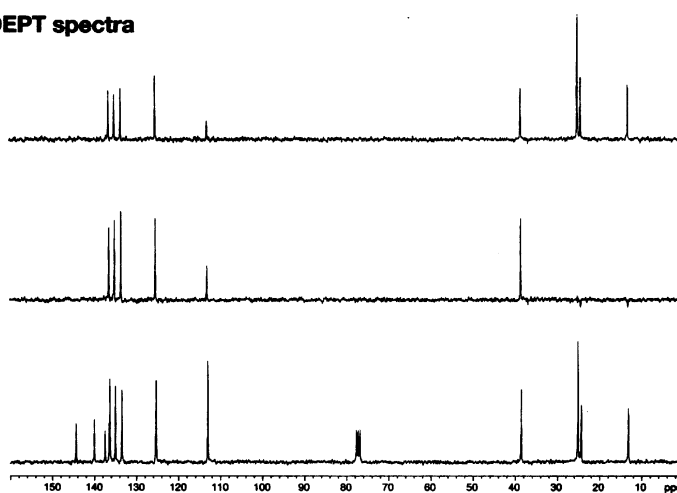


(j) $C_{15}H_{18}$

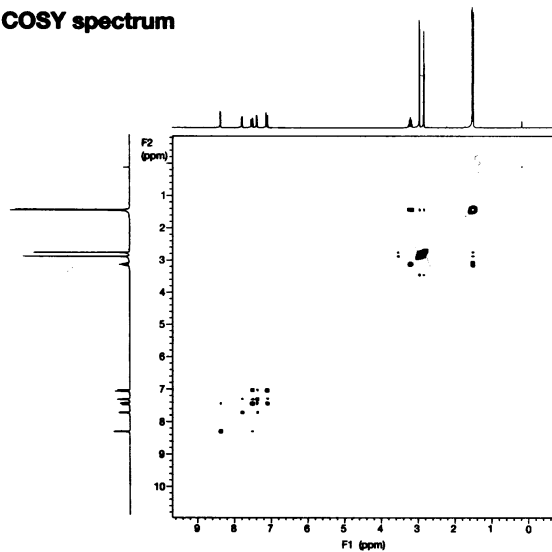
Proton NMR spectrum with expansion ($CDCl_3$)



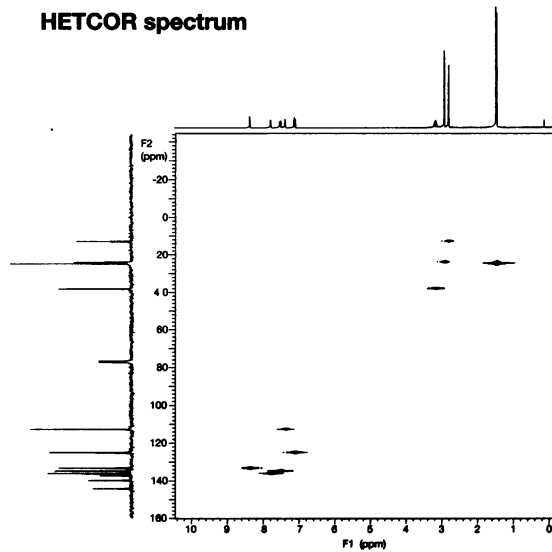
DEPT spectra



COSY spectrum



HETCOR spectrum



Bibliography

See also general texts referenced in previous chapters.

- 6.1. R. R. Ernst, G. Bodenhausen, and A. Wokaun, *Principles of Nuclear Magnetic Resonance in One and Two Dimensions*. Oxford, UK: Oxford University Press, 1987.
 - 6.2. G. E. Martin and A. S. Zektzer, *Two-Dimensional NMR Methods for Establishing Molecular Connectivity*. New York: VCH, 1988.
 - 6.3. K. Nakanishi, *One-Dimensional and Two-Dimensional NMR Spectra by Modern Pulse Techniques*. Mill Valley, CA: University Science Books, 1990.
 - 6.4. R. R. Croasmun and R. M. K. Carlson, eds., *Two-Dimensional NMR Spectroscopy*. 1st and 2d eds. New York: VCH, 1987, 1994.
 - 6.5. H. Friebolin, *Basic One- and Two-Dimensional NMR Spectroscopy*. Weinheim, Germany: VCH, 1993.
 - 6.6. F. J. M. van de Ven, *Multidimensional NMR in Liquids*. New York: VCH, 1995.
 - 6.7. J. N. S. Evans, *Biomolecular NMR Spectroscopy*. Oxford, UK: Oxford University Press, 1995.
 - 6.8. Atta-ur-Rahman and M. I. Choudhary, *Solving Problems with NMR Spectroscopy*. San Diego: Academic Press, 1996.
 - 6.9. A. Kumar, *Bull. Magn. Reson.*, **10**, 96–118 (1988).
- COSY**
- Long-range HETCOR**
- 6.10. G. E. Martin and A. S. Zektzer, *Magn. Reson. Chem.*, **26**, 631–652 (1990).
- EXSY**
- 6.11. R. Willen, *Progr. NMR Spectrosc.*, **20**, 1–94 (1987); C. L. Perrin and T. J. Dwyer, *Chem. Rev.*, **90**, 935–967 (1990).
- 2D INADEQUATE**
- 6.12. J. Buddrus and J. Lambert, *Magn. Reson. Chem.*, **40**, 3–23 (2002).
- Multiple quantum methods**
- 6.13. T. J. Norwood, *Progr. NMR Spectrosc.*, **24**, 295–375 (1992).
- Pulsed field gradients**
- 6.14. W. S. Price, *Ann. Rev. NMR Spectrosc.*, **32**, 51–142 (1996); T. Parella, *Magn. Reson. Chem.*, **34**, 329–347 (1996); K. Stott, J. Keeler, Q.-N. Yan, and A. J. Shaka, *J. Magn. Reson. A*, **125**, 302–324 (1997).

7

Advanced Experimental Methods

Part A. One-Dimensional Techniques

Introductory experimental methods for ^1H and ^{13}C NMR were presented in Chapter 2. The experiments described there provide information on the number of protons, garnered from the integrals (Section 2-6c), and on general characterizations of protons and carbons, obtained from the chemical shifts (Chapter 3). In addition, an analysis of ^1H - ^1H coupling constants can reveal much regarding a particular proton's neighbors (Chapter 4). In the case of relatively simple organic molecules, this information, together with mass spectral and infrared spectroscopic data, can be sufficient to elucidate the structures of those molecules. In most cases, however, considerably more information is required, and the techniques set forth in Chapters 5 and 6 are useful in that regard. The current chapter describes procedures for the performance of additional one-dimensional experiments that allow one to determine (i) the spin-lattice relaxation times (T_1) of protons (Section 5-1), (ii) the number of each type of carbon (e.g., methyl, methylene, etc.; Section 5-5), and (iii) the spatial relationships that exist between protons (via the NOE; Section 5-4).

7-1 T_1 Measurements

In virtually every NMR experiment, the nucleus of choice is pulsed more than once. Such multipulse experiments require either knowledge, or at least an approximation, of the spin-lattice relaxation times (T_1) of the nuclei under investigation (Section 2-4f). For economy of space, we will use the term T_1 throughout the text when we are really referring to the *effective* T_1 , because, among other things, the relaxation effects of paramagnetic substances, such as molecular oxygen, are not rigorously excluded by, for example, sample degassing.

Moreover, if a particular compound is going to be more than routinely examined, it is worth investing the time to measure its ^1H T_1 's, because these values are especially helpful in determining the appropriate repetition times to be used in two-dimensional NMR experiments (Section 7-4g). Knowledge of ^{13}C T_1 's also is desirable, but the time required to determine these values usually is deemed to be too long to make the information gained worthwhile. This statement is especially true today, since the relaxation delays of the most important 2D NMR experiments are dependent on ^1H , rather than ^{13}C , T_1 's.

The most commonly used experiment for the measurement of T_1 's is the inversion-recovery method (Section 5-1): ($DT-180^\circ-\tau-90^\circ-t_a$). The importance of a complete reestablishment of z magnetization was previously encountered in Section 2-7a concerning $90^\circ t_p$ determinations. Again, failure of z magnetization to recover fully between pulses results in signal amplitudes that are decreased from their true intensities and T_1 values that are in error. Practically speaking, this means that $t_a + DT > 5T_1$. This relationship can be confirmed by using Eq. 5-2 to calculate the amount of recovered z magnetization (I_t/I_0) for various multiples of T_1 . The resulting values are given in Table 7-1.

Table 7-1 Recovered Magnetization for Various Values of T_1

nT_1	I_t/I_0
1	0.264
2	0.729
3	0.900
4	0.963
5	0.987
6	0.995

Owing to the uncertainty of most ^1H T_1 values, the first run through the experiment is an approximation (like the first $90^\circ t_p$ calibration attempt). A small number of τ values can be used, ranging from 0.1 to 10 s (e.g., 0.004, 0.02, 0.1, 0.5, 2.5, and 10), with DT set to 10 s (for $T_1 \sim 2$ s). The resulting stack plot appears in the absolute-intensity mode and should look something like Figure 5-2. Some signals, with relatively short T_1 's, quickly become positive and then plateau at longer τ values, while others, with relatively long T_1 's, do not reach maximum intensity even at the largest τ values. Most modern spectrometers have programs that automatically calculate T_1 's from the available data. (Note that these T_1 's may be greatly in error if the data are far from optimal.) This preliminary experiment quickly reveals whether the range of τ values selected and DT are too small (with relatively few positive signals and little or none of maximum amplitude) or too large (with most of the resonances near or at the maximum amplitude) for the T_1 's of the compound in question.

In order to determine T_1 's with reasonable accuracy, a plot similar to that shown in Figure 7-1 should be obtained for each nucleus. Because of the spread of T_1 values in most compounds, however, the inversion-recovery experiment necessarily has to be stretched to accommodate whatever nucleus has the longest T_1 . With a better idea of the longest T_1 , the experiment can then be rerun with an appropriate range of τ values and a suitable DT . Again, modern spectrometers have T_1 programs that automatically select a range of τ values for an estimated T_1 and a $DT = 5T_1$. For the example shown in Figure 7-1 (where T_1 was previously determined to be about 1 s), $DT = 10$ s and the range of τ 's is 0.05, 0.55, 1.05, 1.55, 2.05, 2.55, 3.05, 3.55, 4.05, and 4.55 s.

7-2 ^{13}C Spectral Editing Experiments

After preliminary ^1H and ^{13}C NMR experiments have been performed in a nonroutine analysis, an important piece of information concerns sorting the carbons in terms of the number of directly bonded hydrogens (i.e., methyl, methylene, methine, and quaternary). This knowledge can be gained from both one- and two-dimensional experiments. The principal sources of such information, however, are the one-dimensional APT and DEPT experiments (Section 5-5).

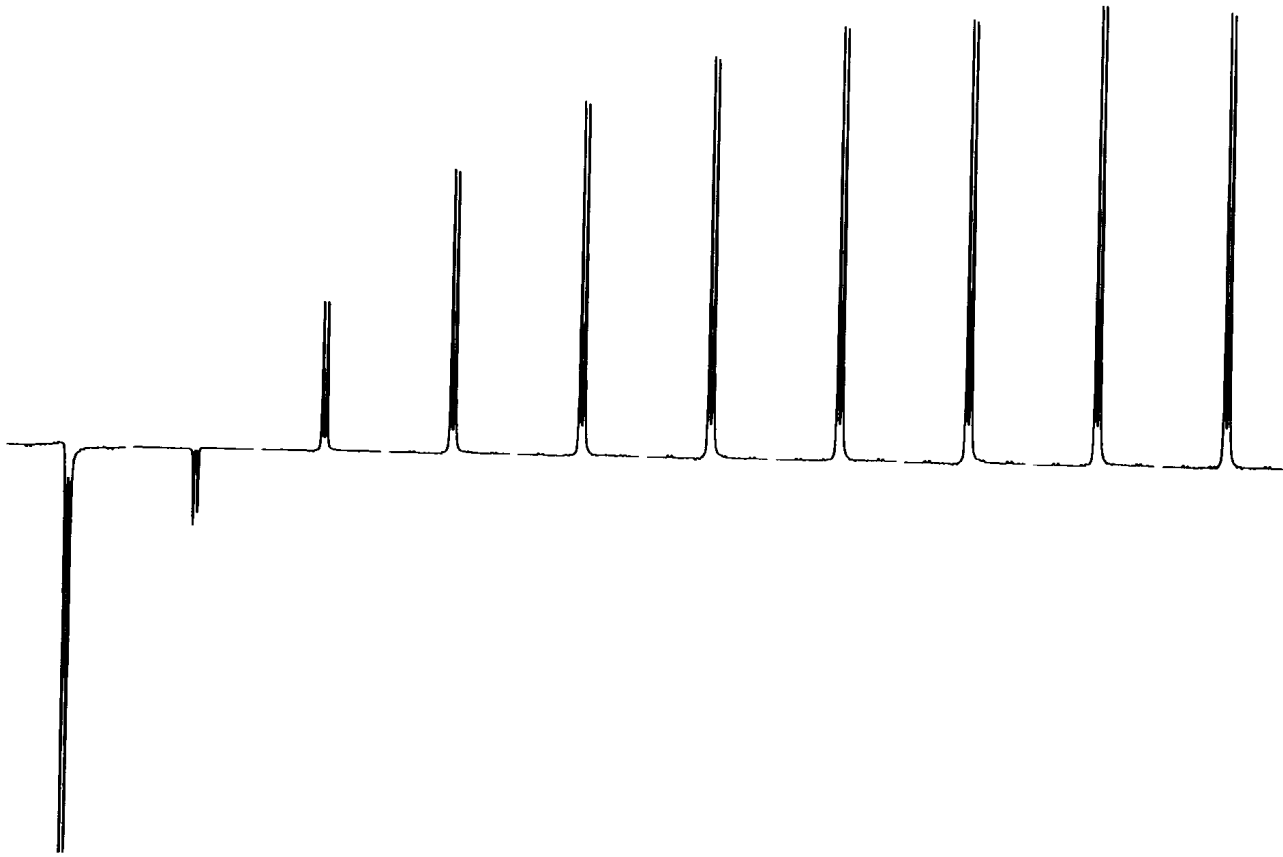


Figure 7-1 An inversion-recovery experiment. Signal intensities are shown as a function of τ .

7-2a The APT Experiment

The behavior of the four types of CH_n units in the APT experiment is illustrated for $n = 1$ and 3 in Figure 5-15 and for $n = 0$ and 2 in Figure 5-16. There are several versions of the APT pulse sequence, and one of the more popular is shown in Figure 7-2. Similar to the standard ^{13}C NMR experiment, the APT experiment is commonly performed in either of two ways. In one way, the initial pulse (θ) can be set to 90° , and a relaxation delay (DT, Section 2-4f) of approximately 1 s employed. We saw in Section 2-4f, however, that the most efficient way to collect NMR data is to pulse continuously, without a DT and with $\alpha \neq 90^\circ$.

In order to pulse rapidly without a DT, it is necessary to locate any residual magnetization along the $+z$ axis, where it can relax rapidly to its equilibrium value. This goal can be achieved by setting $\theta = \alpha + 90^\circ$ (i.e., $90^\circ < \theta < 180^\circ$). A value of α is selected as it would be in an ordinary ^{13}C NMR experiment, and 90° is added to that number. Residual z magnetization, therefore, starts along the $-z$ axis and is driven back to the $+z$ axis by the 180° pulse.

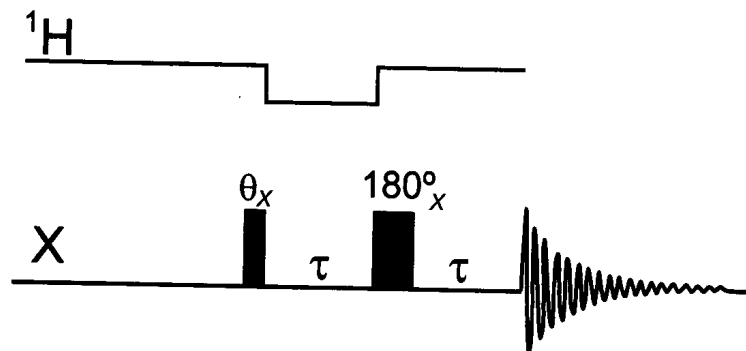


Figure 7-2 An APT pulse sequence.

The final parameter to be selected is the delay time τ , which governs refocusing of the carbon vectors. Two factors that slightly complicate matters are (i) the normal variation of one-bond C–H couplings present in typical molecules and (ii) the dependence of the behavior of C–H fragments on hybridization of the carbon atom. To compensate for the former, τ is set to a value near the midpoint of the expected range of one-bond C–H coupling constants. The latter difficulty arises because vectors of sp^2 hybridized carbons dephase and refocus at different rates (faster) than do those of sp^3 carbons. For a compound whose carbons are all sp^3 hybridized, then $^1J_{CH} \sim 125$ Hz (Table 4-1), and τ is set to $(J)^{-1} = 8$ ms. Likewise, if the carbons are all sp^2 hybridized, $^1J_{CH} \sim 160$ Hz and τ becomes 6 ms. When both types of carbons are present, a compromise value of 7 ms is used, corresponding to $^1J_{CH} = 140$ Hz.

In the full editing APT spectrum [$\tau = (J)^{-1}$] shown in Figure 5-17, carbons with an odd number of attached protons (CH and CH_3) are easily distinguished from those with an even number (CH_2 and quaternary, as zero is considered to be an even number). If it is necessary to differentiate carbons within either of these two groups, the APT experiment can be rerun with different values of τ . For $\tau = (2J)^{-1}$, methylene and quaternary carbons can be distinguished, because the former are nulled while the latter have full intensity. Differentiating between methyl and methine carbons is less definitive. For $\tau = 2/3J$, methyl signals have approximately one-third of the intensity of the methine resonances.

The drawbacks to APT are its dependence on the magnitude of one-bond C–H couplings and its inability to distinguish methyl from methine carbons unambiguously. If one already has a ^{13}C NMR spectrum and is interested only in determining the multiplicities of protonated carbons, then a full editing experiment [$\tau = (J)^{-1}$], can be carried out relatively rapidly (usually, with just half the number of scans of the parent ^{13}C NMR experiment) and is useful for characterizing compounds of known structure. Both of the foregoing limitations are absent in the DEPT experiment.

7-2b The DEPT Experiment

The DEPT experiment, whose pulse sequence is given in Section 5-5, has now become the method of choice in editing procedures. The method gives spectra of only protonated carbons that can be edited to contain just methyl, methylene, or methine carbons (Figure 5-18). The delay time $\tau = (2J)^{-1}$ and is set with similar carbon hybridization considerations as in the APT experiment (i.e., 4 ms for sp^3 hybridized carbons, 3 ms for sp^2 carbons, and 3.6 ms for both). The main feature of the DEPT experiment is the variable θ pulse, which gives editing results that are somewhat reminiscent of those produced by varying the delay time (τ) in the APT experiment. It is, however, this dependence upon an *angle* rather than a *delay time* that makes DEPT less sensitive than APT to variations in $^1J_{CH}$. The types of carbon observed with various θ values are as follows:

1. $\theta = 45^\circ$: all protonated carbons
2. $\theta = 90^\circ$: primarily methine carbons, with possible small breakthroughs of some other signals
3. $\theta = 45^\circ, 90^\circ$, and 135° : full spectral editing (CH and CH_3 , positively phased; CH_2 , negatively phased)

Because DEPT is a polarization transfer experiment, the relaxation delay times are a function of the 1H -, and not the X-nucleus', T_1 's. The following are additional suggested spectral parameters:

1. DT = 0.5–1.5 s, which is 1–3 $^1H T_1(\max)$
2. steady-state scans = minimum of 8
3. number of scans = multiple of 4 (for phase-cycling purposes)

It is also recommended that data accumulation be interleaved in blocks of 32 scans. Interleaving, which is common for stability purposes in lengthy experiments, operates in the following manner. For a full spectral editing experiment, instead of acquiring each of the spectra with different θ angles in turn, one determines 32 scans for $\theta = 45^\circ$, then 32 scans for $\theta = 90^\circ$ (this segment is done twice to get the same S/N ratio as in the other two experiments), and, finally, 32 scans for $\theta = 135^\circ$. This four-step cycle is repeated until sufficient scans are accumulated to produce four spectra with acceptable S/N ratios. These spectra are then added and subtracted in an appropriate manner to produce the subspectra illustrated in Figure 5-18.

A disadvantage of DEPT is that it is a *subtraction* experiment and, therefore, much more sensitive to certain problems than are typical one-dimensional techniques. One remedy that is used in many experiments that suffer from stability problems is the employment of *steady-state*, or dummy, scans (parameter 2 in the foregoing list; Section 2-4i). Poor signal cancellation is generally the result of difficulties in one or more of the following areas:

1. *lock stability*: keep the lock power just below saturation and the lock gain in the 30% range.
2. *temperature of the sample*: perform experiments at a constant temperature.
3. *pulse calibration*: calibration of the ^{13}C 90° and 180° pulses is critical.
4. *incomplete cancelation in spectral subtractions*: steady-state scans are critical.

A modified DEPT experiment, DEPTQ, recently was developed that permits the detection and display of nonprotonated nuclei, such as quaternary carbons, and that possesses the editing features and polarization transfer sensitivity advantages of the DEPT sequence. The DEPTQ experiment promises to become an important method for the determination molecular structures.

7-3 NOE Experiments

The nuclear Overhauser effect provides information on the spatial proximity of nuclei (Section 5-4). NOE determinations are usually homonuclear, in the case of protons, but also can be heteronuclear, with ^1H signals irradiated and those of heteronuclei observed. NOE's occupy both an intermediary and a final position in the overall progression of structural determination. In most cases, NOE's afford information on the three-dimensional structure of a molecule after its two-dimensional structure has been determined. NOE's, however, also can be used earlier in the structural elucidation process, to provide answers to questions concerning stereochemistry in systems containing double bonds or rings.

Classical steady-state NOE determinations involved irradiating a particular (target) signal and measuring the integrated intensities of other signals whose nuclei were believed to be spatially proximate to that nucleus whose signal was saturated (the *on-resonance* part of the experiment). Control experiments also were performed in which the irradiating frequency was positioned in a blank region of the spectrum and the integration(s) repeated (the *off-resonance* part). Some of today's NOE experiments are still carried out with on- and off-resonance components to provide difference spectra, while others are selective and do not require subtraction.

Because NOE enhancements are a function of competitive relaxation processes, they are highly dependent on the internuclear distances between the relaxed nucleus in question and nonirradiated neighbors that also can participate, as competing agents, in the overall relaxation process. For this reason, the two enhancements ($A\{B\}$ and $B\{A\}$) are seldom identical and can be quite different. The contrast is particularly apropos of $\text{CH}_3\text{-H}$ systems, for which very different results are obtained, depending on which way the NOE experiment is performed. Due to their close spatial proximity, methyl protons are highly

efficient at relaxing one another. In addition, since they possess three dipoles, they are generally very effective relaxing agents for nearby protons. Because of their efficient, self-relaxing nature, methyl protons themselves are thus relaxed very little by neighboring protons. Relatively large enhancements can, therefore, be observed in neighboring protons when methyl groups are irradiated, but the reverse experiment yields enhancements that are very small to nil.

7-3a The NOE Difference Experiment

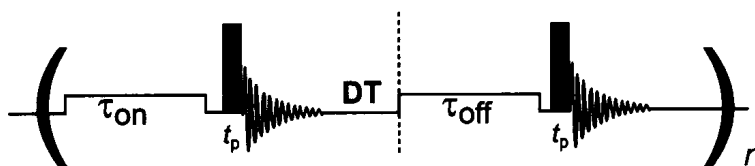
Almost all nongradient NOE experiments today are performed in the difference mode. On- and off-resonance experiments are conducted in much the same way as before, with the pulse sequence shown in Figure 7-3. On- and off-resonance spectra, or FID's when there are very strong signals like that of water, are stored separately in the computer memory and then subtracted to yield a spectrum that, in theory, shows signals only from those nuclei which are spatially proximate to the target proton. Typical acquisition parameters for small and intermediate-sized molecules ($MW < 750$) are $\alpha = 90^\circ$ and $\tau = 5T_1$ (generally, 3–5 s). Sufficiently long presaturation times (τ in the figure) are important, so that all of the NOE's—and especially the small ones—have enough time to develop fully. In addition, while complete saturation of the target signal (and its subsequent inversion, after subtraction of the off-resonance spectrum or FID, in the spectrum) is ideal, it is not always realistic in crowded spectra. A 50–75% decrease in intensity of the target signal generally indicates that a sufficient saturating power level has been attained.

NOE difference experiments are extremely sensitive to stability problems and are plagued by poor signal cancelation. These problems arise, in part, from the fact that the two spectra being subtracted are frequently both near full intensity. Any residual signals resulting from incomplete subtraction can, therefore, easily obscure the small NOE's typically present in small molecules. Nevertheless, NOE's can be measured in about the 0.1% range, which represents approximately an order-of-magnitude improvement on minimum NOE's that can be determined by the older steady-state method. (Steady-state scans are used here as they were in Section 7-2b with the DEPT experiment.) The following experimental conditions have been found to minimize subtraction problems:

1. Use eight steady-state scans.
2. Perform experiments with a nonspinning sample.
3. Perform experiments at a constant temperature.
4. Keep the lock power just below saturation and the lock gain at approximately 20% of maximum for optimum lock stability.
5. Interleave on- and off-resonance irradiation, using a block size of four to eight scans.
6. A moderate line broadening (< 2 Hz, not enough to cause signal overlap) reduces spectral noise.
7. Use identical phasing for the on- and off-resonance spectra or the FID's.

When the target signal is a multiplet, modern spectrometers have programs that irradiate each individual line of the multiplet. For stability purposes, four scans per resonance line can be taken per cycle before moving to the off-resonance part of the sequence. The NOE difference spectrum for the sesquiterpene T-2 toxin (7-1) is shown in Figure 7-4a. The centrally located methyl-14 at $\delta 0.77$ is irradiated and appears as a large negative signal.

Figure 7-3 The NOE difference pulse sequence.



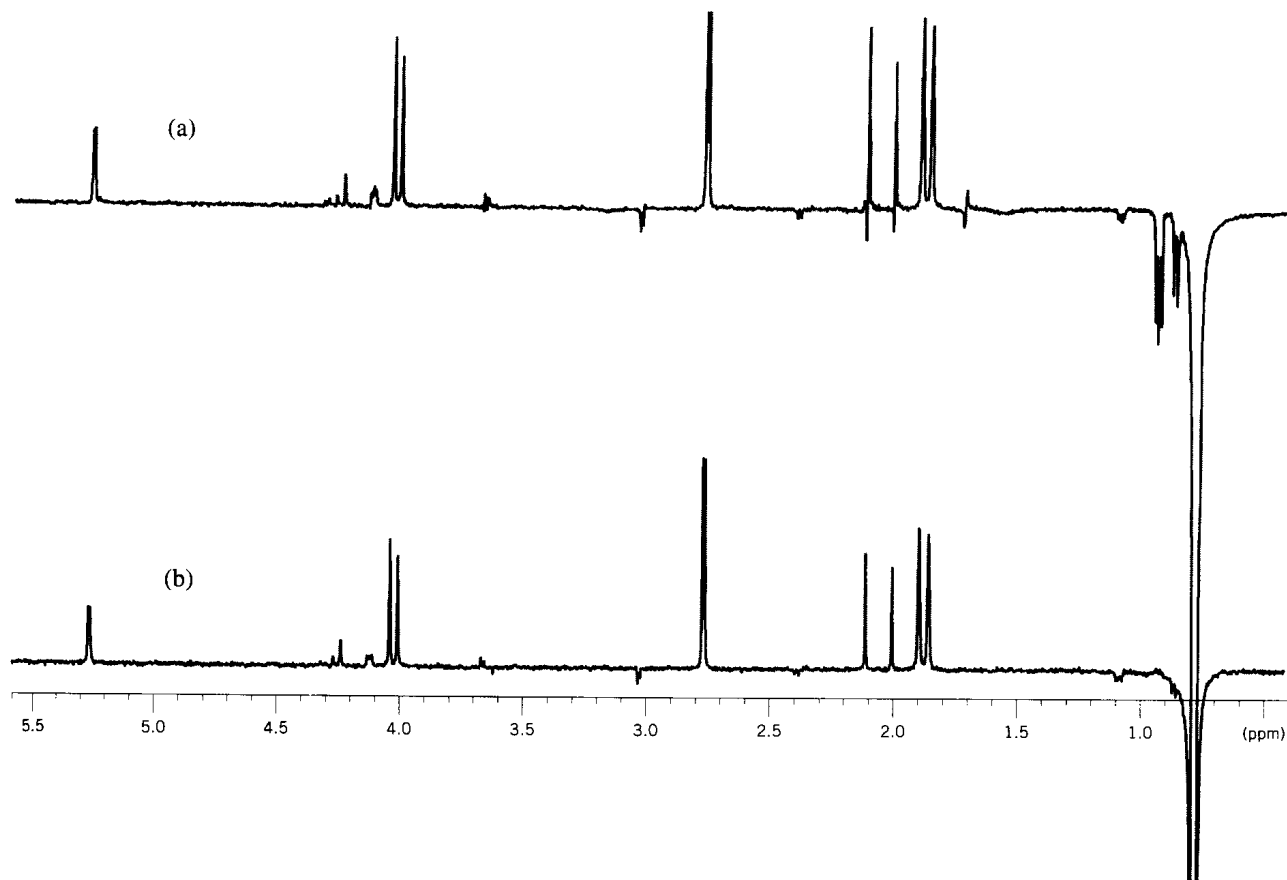
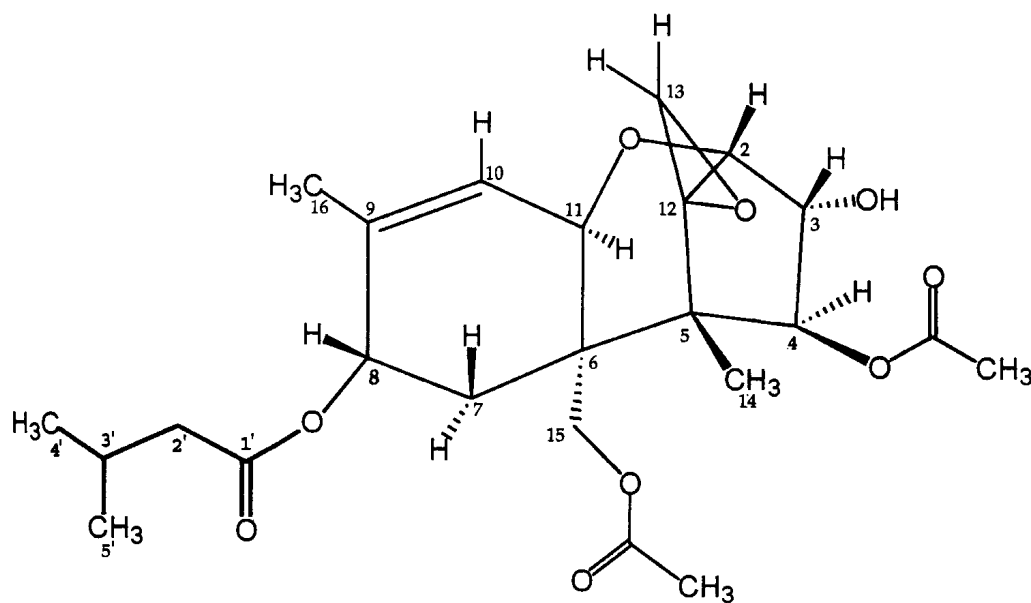


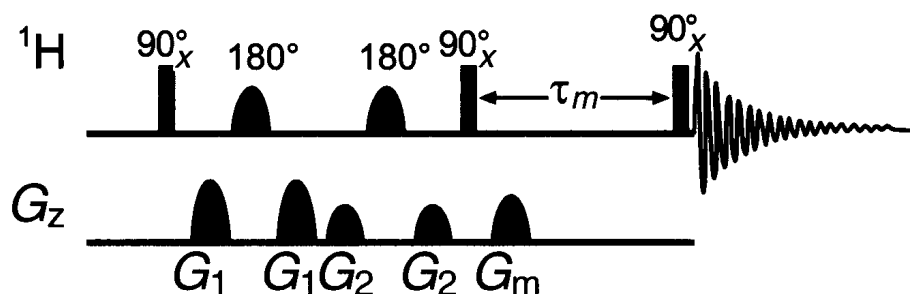
Figure 7-4 (a) NOE difference; (b) Double pulsed field gradient spin echo-NOE for T-2 toxin.



7-1

Signals indicative of (i) relatively large NOE's are seen for H-7B (δ 1.87) and H-13B (δ 2.77), (ii) medium-sized NOE's for H-15B (δ 4.02) and H-8 (δ 5.30), (iii) a small NOE for H-15A (δ 4.27), and a very small NOE for H-3 (δ 4.14). In addition, medium-sized signals are observed for the acyl methyls at δ 2.05 and 2.15. These resonances might appear

Figure 7-5 The double pulsed field gradient spin echo-NOE pulse sequence. The relative strengths of gradients G_1 , G_2 , and G_m are 16, 7, and 13 G cm^{-1} , respectively. The mixing time is 650 ms.



to be indicative of moderate enhancements, but it must be remembered that they correspond to the largest signals in the normal proton spectrum and instead represent very weak NOE's. The subtraction problems just discussed are avoided with a relatively new NOE pulse sequence, described in the next section.

7-3b The Double Pulsed Field Gradient Spin Echo-NOE Experiment

The double pulsed field gradient spin echo-NOE (DPFGSE-NOE) sequence devised by Shaka and Keeler represents a marked improvement on the NOE difference experiment and is shown in Figure 7-5. The experiment produces spectral results that look like those of a subtraction experiment, but neither spectral nor FID subtraction is involved. Critical to the DPGSE-NOE pulse sequence is the pair of *shaped pulses* and pulsed field gradients (Section 6-6). Modern, research-grade NMR spectrometers are able to produce finely defined pulses that are capable of irradiating extremely specific regions of a spectrum. Care should be taken, however, not to make the irradiated spectral region too narrow, since the pulse then becomes too long. [The pulse width (in s) and spectral width (in Hz) are inversely related.] Practically speaking, pulse widths should be less than about 70 ms. If the pulses become too long, considerably less than the full target signal may be inverted, a result that should be avoided because there is a direct relationship between the degree of inversion of the target signal at the start of the mixing time and the size of the NOE. If insufficient scans are taken, it could appear that there are fewer NOE's—or even none—from the target proton.

After a nonselective 90° pulse places the magnetization of all of the ^1H spins in the xy plane, magnetization of the target spin alone is refocused in that plane with a pair of selective 180° pulses, each flanked by a pair of gradients of equal strength and duration. The target magnetization then is moved to the $-z$ axis by a second nonselective 90° pulse, and NOE's develop from this z magnetization.

A DPGSE-NOE spectrum for T-2 toxin is presented in Figure 7-4b. Methyl-14 is again the target and appears as a large negative signal. It is immediately obvious that the DPGSE-NOE spectrum is considerably superior to the NOE difference spectrum in Figure 7-4a. NOE's as small as approximately 0.02% can be reliably determined by this method, which represents another order-of-magnitude improvement over the NOE difference method.

The following parameters are appropriate for DPGSE-NOE experiments:

1. steady-state scans = 8
2. RT ~ 5 s
3. line broadening ~ 0.5 Hz
4. selective 180° pulse width < 70 ms.

Part B. Two-Dimensional Techniques

The experimental methods presented in Part A permit us to determine the number of each type of carbon present in a molecule and the spatial relationships between protons, which are critical to the elucidation of the two- and, perhaps, three-dimensional structure of that molecule. As we have seen, this new information, combined with that obtained from chemical shifts, coupling constants, and other spectroscopic methods, might be sufficient to determine

a molecular structure. In most cases, however, the situation requires that still more spectral data be acquired. In Part B, we will become acquainted with the performance of two-dimensional (2D) NMR experiments, which provide information on *direct* ^1H - ^1H and ^1H - ^{13}C connectivities, *longer range* ^1H - ^{13}C connectivities, and ^1H - ^1H spatial proximities.

7-4 Two-Dimensional NMR Data-Acquisition Parameters

Data acquisition is approached very differently in 2D, compared with 1D, NMR experiments. The reason is that we are now dealing with, at minimum, a one-dimensional data matrix (for 2D NMR) and, perhaps, two or three matrices (for 3D and 4D NMR, respectively) for complex biological molecules.

7-4a Number of Data Points

To keep experimental times and data storage requirements reasonable, far fewer data points are used in each dimension in 2D experiments than with typical 1D experiments. Reasonable digital resolution can be obtained in the *detected* dimension (ν_2) for ^1H , homonuclear correlation (e.g., COSY) and ^1H -detected, heteronuclear correlation (e.g., HMQC) spectra by using 1,024 or 2,048 data points. Due to their greater spectral widths, however, heteronuclear-detected correlation (e.g., HETCOR) spectra require 2,048, or even 4,096, data points in ν_2 . 2D experiments are commonly performed with 2,048 data points in each dimension.

7-4b Number of Time Increments

The number of time increments employed to create the nondetected second dimension (ν_1 , Section 6-1) is just one of the factors that influence the number of data points used to describe the ν_1 domain. In an analogous manner to the quadrature phase detection of signals in 1D NMR experiments (Section 2-4b), phase-sensitive spectral data can be acquired either with two signal detectors differing in phase by 90° (the "States" method which uses a hypercomplex FT) or with a single detector with the phase incremented by 90° on successive data acquisitions (time-proportional phase incrementation, or TPPI). For the States method with phase-sensitive data, a value of 128–256 increments represents a good compromise between time and resolution. While that number doubles to 256–512 for the TPPI method, the t_1 increments are only half as large and thus result in the same total acquisition time t_1 .

Digital resolution in the ν_1 dimension (DR_1), analogous to ν_2 , is a function of the number of increments (n_i) and the spectral width (sw_1). Its calculation is less straightforward and is considered in Section 7-5c. Unlike DR_2 , however, DR_1 is somewhat vexing because, whereas sw_1 is reduced as is sw_2 (the two are identical for homonuclear correlation experiments), increasing n_i increases the time required to conduct the 2D experiment much more than would a corresponding increase in n_{p_2} (which has essentially no effect). If, for example, n_i is increased by a factor of two, the time of the experiment is doubled. To make matters worse, collecting 2,048 increments might very well not result in better *observable* ν_1 resolution. Unless the sample is highly concentrated, such a large n_i might effectively accomplish little more than several levels of zero filling ($n - 1$ of which do nothing to improve DR_1 ; Section 2-5b). The reason is that, as the incremented time (t_1) increases, vector phase coherence (and thus xy magnetization) is lost due to magnetic field homogeneity effects and T_2 relaxation (T_2^*). Thus, there can be little xy magnetization left to be transferred between coupled nuclei and little left to be detected by the receiver. The last thousand or so increments may, therefore, have essentially zero intensity. The solution to this dilemma is forward *linear prediction*, which is discussed in Section 7-5d. In addition, optimum resolution is achieved by similarly reducing sw_1 as much as possible from its value in the parent ^1H or ^{13}C spectrum.

7-4c Spectral Widths

In homonuclear correlation experiments, sw_1 is almost always set equal to sw_2 . In addition, *reduced* spectral widths are used in both dimensions to improve digital resolution. The reduced sw 's are set equal to the distance between the highest- and lowest-frequency signals,

plus approximately 20% of that distance (about 10% added to each end of the *reduced sw*), to avoid artifacts along both the horizontal and vertical edges of the 2D spectra.

7-4d Acquisition Time

Because np_2 is so much smaller than the number of points in an ordinary 1D spectrum, whereas sw_2 is not commensurately smaller than common 1D spectral widths, two-dimensional acquisition times typically are in the 100–300-ms range for ^1H -detected, and less than 100 ms for heteronuclear-detected, 2D experiments. Remember that, as in 1D experiments, sw_2 (in Hz) depends on the magnetic-field strength and, therefore, affects the value of t_a . Similarly, t_a is normally set by the spectrometer after np_2 and sw_2 have been selected.

7-4e Transmitter Offset

When sw is reduced, modern spectrometer programs have a series of commands, called “macros,” which automatically move the transmitter offset so that it is in the middle of the reduced sw_2 . The operator can verify that the transmitter has moved by noting the offset values for the original and reduced sw 's.

7-4f Flip Angle

Flip angles are determined by the specific 2D experiment being conducted, and Ernst angle considerations are not an issue. The COSY family of experiments has a variety of final pulses (Section 6-1), and they are considered in Section 7-7a. Moreover, the final pulse before t_a that is delivered to the detected nucleus is known as the *read pulse*.

7-4g Relaxation Delay and Repetition Times

Almost all of the experiments described in this chapter, and certainly all 2D experiments, require some time between scans during which the spin systems that have been irradiated or otherwise perturbed can return to equilibrium. There are two times during which relaxation processes occur: (i) the relaxation delay time (DT), which is the period between the end of the acquisition of the signal (t_a) and the first pulse of the pulse sequence being used; and (ii) the repetition time (RT), which is the sum of $DT + t_a$. Since relaxation occurs during t_a as well as DT, especially for ^1H -detected pulse sequences, it is important to consider RT, and not just DT, when deciding on experimental delay times between pulses. If, for example, it is determined that RT ought to be about 1 s and $t_a \sim 200$ ms, then DT should be set to approximately 800 ms.

Many operators, unfortunately, consider only DT, and the values that they employ are too long for their experiments. For ^1H -detected experiments, proton T_1 's determine the choice of RT. Recommended RT's in textbooks and spectrometer manuals are on the order of $1-2T_1$, with those geared toward optimum sensitivity (using 90° pulses) being approximately $1.3T_1$. Of course, in a typical molecule, chemists are confronted with a range of T_1 values that are dependent on the magnetic-field strength (Section 5-1). It is for this reason that the suggestion was made in Section 7-1 to determine the ^1H T_1 's of nonroutine samples. Fortunately, even without such T_1 measurements, reasonable estimates can be made for RT values.

For *very small* molecules, RT's closer to the $3T_1$ range are appropriate. Molecules of this size, however, are not usually encountered, except in textbooks. In addition, RT's should be in the range of 0.8–1.2 s ($\sim 1.3T_1$) for *small* molecules (MW $\sim 400-450$) and 0.6–0.8 s for *intermediate-size* molecules (MW $\sim 500-750$). Exceptions are found for two groups of experiments. The first includes ^1H -detected, heteronuclear chemical-shift correlation experiments, such as HMQC and HSQC, in which broadband ^{13}C decoupling is carried out during t_a . In these experiments, sample heating can be a problem, especially for high-dielectric solutions, if t_a is too large a portion of the overall RT. The second group includes NOESY

and ROESY experiments, in which RT's should be at least two times the average T_1 value and mixing times about the average T_1 value.

The foregoing range of RT's for small molecules corresponds to a ^1H T_1 range of 0.5–1s and might appear to be too small. Considering an entire range of T_1 values, however, to determine the RT for a ^1H -detected experiment is misleading. Recall that methyl protons, which tend to have longer T_1 's than methines and methylenes, should generally be ignored in RT deliberations, because their signals are usually much larger than those of methine and methylene protons. They can, therefore, afford to lose some intensity due to incomplete relaxation. Typically, t_a is small, but if it exceeds 400 ms, due to a small sw, then DT can be reduced commensurately.

For the heteronucleus-detected FLOCK experiment, longer RT's are appropriate since the signals of nonprotonated nuclei are being recorded.

7-4h Receiver Gain

The receiver gain cannot necessarily be set in 2D experiments in the manner described for 1D experiments in Section 2-4g. For gradient, ^1H -detected, ^1H - ^{13}C correlation sequences, the gain can usually be increased by at least 10 dB because ^1H - ^{12}C magnetization is eliminated directly in each FID acquisition rather than by phase cycling. One way to determine a reasonable receiver gain setting is to perform the first few increments of a particular 2D experiment several times, with the number of scans set to unity. The gain is then increased until a receiver-overflow warning is observed, after which it is decreased to the next-lower setting.

7-4i Number of Scans per Time Increment

In order to minimize the overall time of a 2D experiment, one wishes to keep the number of scans per increment (ns/i) at a value that is sufficient to observe the spectrum of that particular increment. For heteronucleus detection, this number usually is large, but for protons, adequate detection can often be accomplished in 1 to 4 scans. The minimum ns/i , however, is determined by the phase cycle (Section 5-8) of the pulse sequence used and may be anywhere from 4 to 64 scans. As a general rule, 8 scans/ i is a minimum value for ^1H -detected experiments. Longer experiments that require a large ns/i , such as the study of dilute solutions (proton detection) or heteronucleus detection, can make good use of interleaved acquisition with a suitable block size (as described in the discussion of the DEPT experiment in Section 7-2b).

In recent years, gradient versions of many of the basic 2D NMR experiments have become very popular. One of the main reasons is that the use of gradients eliminates the need for phase cycling in the selection of a coherence pathway. Experiments involving ^1H detection can, therefore, often be performed with one to two transients per increment.

7-4j Steady-State Scans

Steady-state scans (Section 2-4i) are used before the start of essentially all 2D experiments. They are particularly important in a number of pulse sequences in order to compensate for spin-lock (Sections 7-7b and 7-10b) and decoupler (Section 7-8) heating effects. Larger numbers of steady-state scans are employed in experiments that have either particularly long spin-lock times or X-nucleus decoupling over especially wide spectral widths.

7-5 Two-Dimensional NMR Data-Processing Parameters

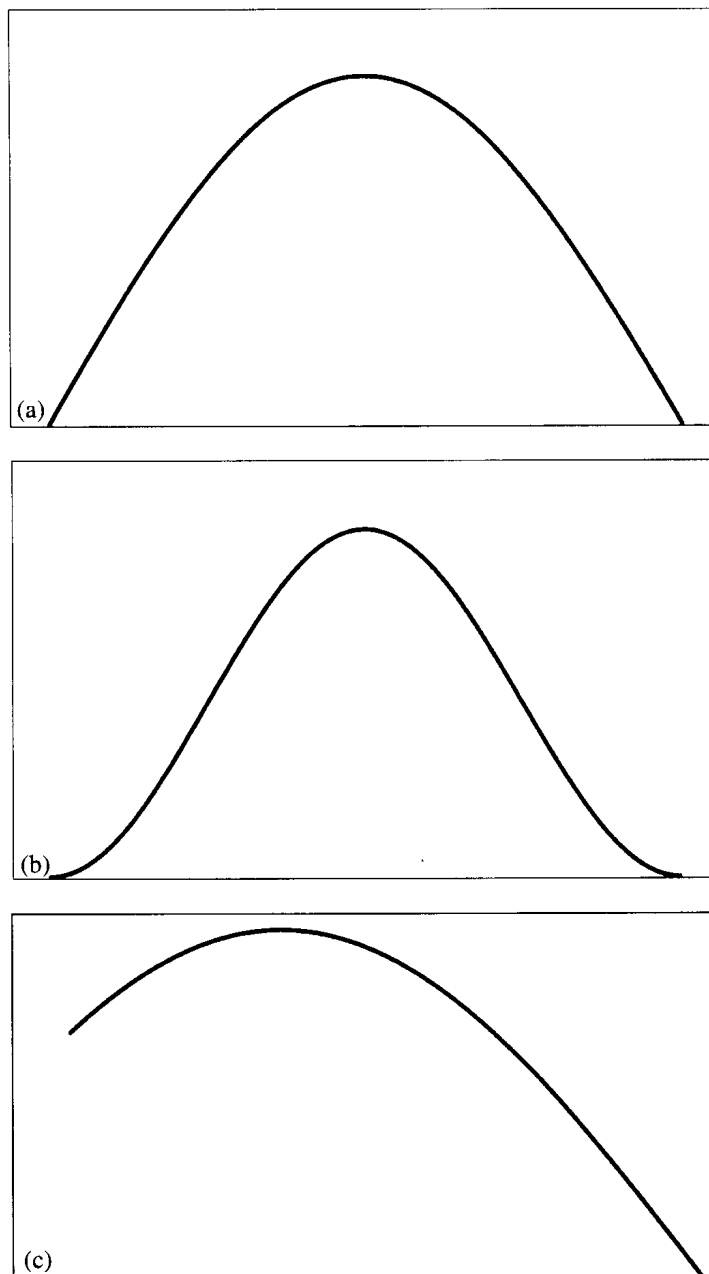
Like acquisition, data processing is performed differently in 2D, compared with 1D, NMR experiments. The principal reason is that signal truncation is a much more serious problem in 2D than 1D experiments. Zero filling also is used in 2D experiments, as is the relatively new technique of linear prediction.

7-5a Weighting Functions

It should not be surprising that signal (FID) truncation is a problem in the detected (t_2) domain, given the short t_a 's (<300 ms) in that dimension. In the nondetected (t_1) domain, we are dealing with *interferograms* (due to the individual signals of each incremented spectrum at a particular chemical shift) rather than with true FID's, but their behavior with respect to truncation is similar. Because of relaxation effects, the signals at the end of an interferogram are smaller than those at its beginning, but unless n_1 is unduly large, the individual interferograms have not decayed to zero by the last increment. A variety of weighting functions, which have been developed so that apodization can be carried out in both the t_1 and t_2 dimensions, is pictured in Figure 7-6.

The choice of weighting function depends largely on whether the 2D data are presented in the absolute-value (magnitude) or phase-sensitive mode (Section 6-1). Absolute-value data require rather severe discrimination against both the beginning and end parts of the FID's; they are, therefore, usually processed with a *sine bell* function in order to suppress

Figure 7-6 Weighting functions. (a) Sine bell. (b) Squared sine bell. (c) Shifted sine bell.



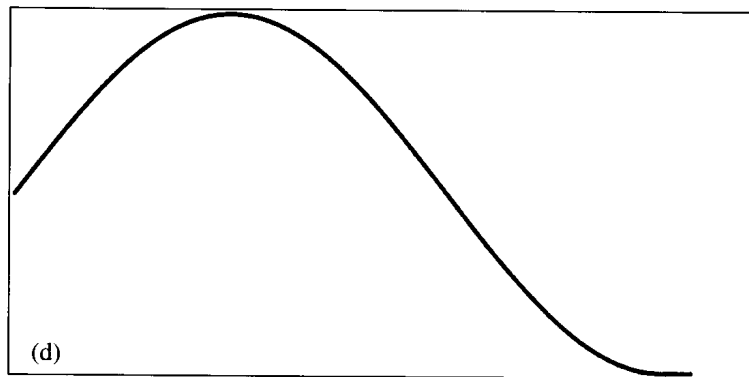
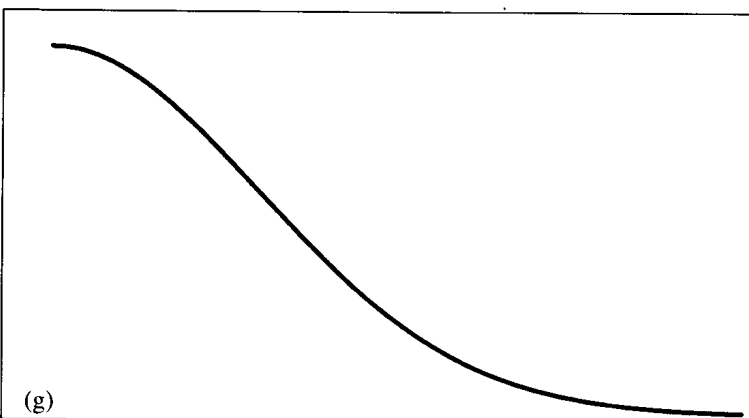
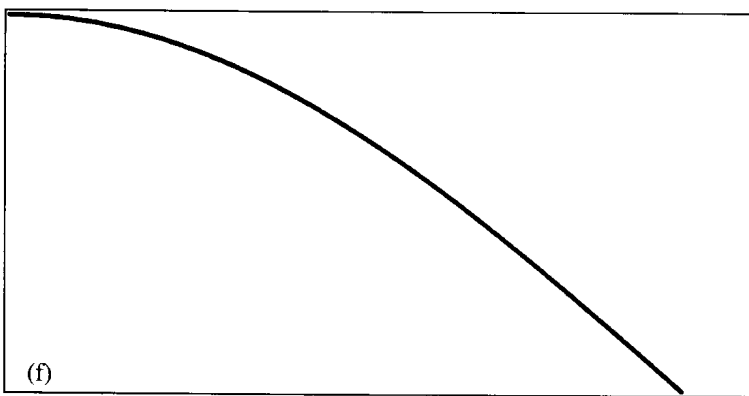
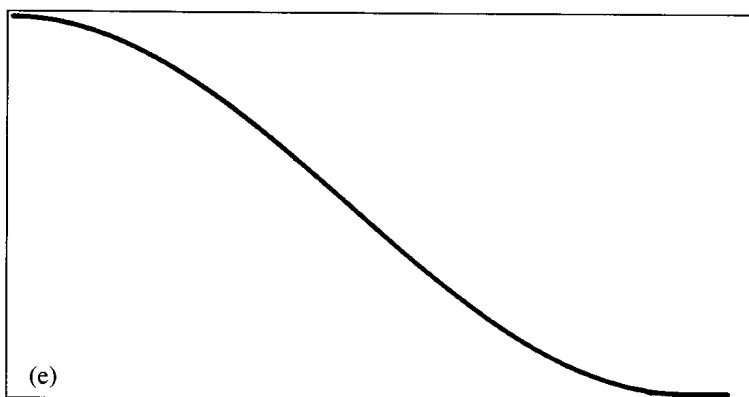


Figure 7-6 (cont.)
(d) Shifted squared sine bell.
(e) Gaussian. (f) Cosine (90° shifted sine bell). (g) Squared cosine (90° shifted squared sine bell).



the dispersive tails from the phase-twisted line shapes. Two other choices are the *pseudo-echo* and *squared sine bell* functions, which are nearly identical to each other and give results similar to those obtained from sine bell weighting. These two functions emphasize the middle part of the FID a little more and discriminate somewhat more against its beginning and end, relative to the sine bell function. If sensitivity is an issue, a *shifted sine bell* function can be used in the following manner.

Most modern spectrometers have interactive software that permits the operator to vary a particular weighting parameter and immediately observe the effect of this change on the final spectrum. The first increment generally is selected to see what the effects of weighting parameters are on the t_2 data. With the first FID displayed, the operator can then shift the midpoint of the sine bell function toward the S/N (left) part of the FID, until the best compromise is reached between sensitivity and resolution. It is important for the operator to remember that the weighting function must have a zero value at the right end of the FID so that it drives the FID to zero intensity at the end of (i) t_a in t_2 and (ii) the effective t_a (ni/sw_1) in t_1 .

Data (interferograms) in the t_1 -domain are handled in much the same manner as those in t_2 . Appropriate weighting and Fourier transformation of the t_2 -domain data result in a (ν_2, t_1) data matrix that consists of rows of interferograms at the chemical shifts in the vertical dimension. A row showing a good S/N ratio is selected and interactively weighted as just described for the first increment in t_2 .

Phase-sensitive data do not have the dispersive-tail problem and can be processed with more gentle apodization functions. They are most frequently processed with a *Gaussian* function, but other possibilities are the 90° *shifted sine bell (cosine)* and the 90° *shifted squared sine bell (squared cosine)* functions, the latter of which is functionally similar to a simple Gaussian function. If the operator has a series of compounds to be investigated, it might be worthwhile to apply interactive weighting with all three functions to determine whether there is a clear advantage to any one of them. (To avoid confusion of terminology, note that, in this text, the expression “Gaussian function” refers to sensitivity-enhancing multiplication, shown in Fig. 7-6e, and not the resolution-enhancing function described in Fig. 2-7b.)

Most modern spectrometers have macros that automatically set sine bell and Gaussian weighting functions on the basis of the acquisition parameters. Shift values for the various *shifted functions* are entered interactively, and the function is then readjusted so that it goes to zero at the end of the t_a 's in t_2 and t_1 .

7-5b Zero Filling

After appropriate weighting is carried out in the t_2 and t_1 domains, both data sets should be zero filled by at least a factor of two (one level).

7-5c Digital Resolution

We saw in Section 2-5d that a proper number of data points is important in 1D spectra for the complete separation of spectral lines. In that section, we also learned that a resolution smaller than 1 Hz required a DR of $(\Delta\nu)/2$, or $J/2 \sim 0.5$ Hz/point. Digital resolution likewise is an important concept in 2D NMR. The concern now, however, is the relationship between the resolution and the magnitude of couplings that can be observed as cross peaks in 2D spectra. The cross peaks of DQF-COSY spectra, for instance, have positive-negative (or up-down) character (Section 6-1 and Figures 7-11b and 7-11c). The intensities of the inner parts of these cross peaks decrease markedly when the *active* coupling constant (the distance between adjacent positive and negative cross peaks—e.g., 4 Hz) is less than the digital resolution (e.g., 8 Hz/point), due to signal cancelation. The outer edges of the cross peaks, however, do maintain their intensities. Similarly, for absolute-value COSY spectra, the maximum cross-peak intensity occurs for coupling constants that are equal to or greater than the digital resolution. Significant cross-peak intensity, however, can be detected for couplings that are only about 20% of the digital resolution value. If, for example, one wishes to observe COSY correlations from couplings of less than 1 Hz, digital resolution in the ν_1 and ν_2 dimensions must be approximately 4 Hz/point.

Digital resolution in the ν_2 domain is a function of the number of data points (np_2) and the spectral width (sw_2) and is calculated in the same manner as for 1D experiments (i.e., the acquisition of $2N$ data points results in N real points, after Fourier transformation) that describe spectra in the ν_2 dimension (Section 2-5d). If $sw_2 = 2,100$ Hz and $np_2 = 1,024$, then, after the FT, $DR_2 = sw_2/(np_2/2) = 2,100 \text{ Hz}/(1,024/2) = 4.1 \text{ Hz/point}$. Again as with 1D experiments, one level of zero filling should be performed for optimum DR. If this is done, then $np_2 = 2,048$. Using the real points obtained after the FT operation results in $DR_2 = 2,100 \text{ Hz}/(2,048/2) = 2.1 \text{ Hz/point}$.

As stated in Section 7-4b, digital resolution in the ν_1 domain is a function of the number of increments (ni) and the spectral width (sw_1). Spectral data describing the ν_1 dimension can be acquired in either the phase-sensitive or the absolute-value mode. Real and imaginary ν_1 -domain data sets exist for both types of acquisition, but are treated differently. The imaginary data are discarded in phase-sensitive acquisition, just as with the ν_2 dimension data previously described. By contrast, with absolute-value data, both the absorptive (real) and dispersive (imaginary) components of the ν_1 domain are used to describe the spectrum. The important point is that, for both kinds of data, the acquisition of $2M$ increments yields M points, after Fourier transformation, to characterize spectra in the ν_1 dimension. Therefore, if $sw_1 = 2,100$ Hz and $ni = 512$, then $DR_1 = sw_1/(ni/2) = 2,100 \text{ Hz}/(512/2) = 8.2 \text{ Hz/point}$. If one level of zero filling is carried out, then the effective $ni = 1,024$ and it follows that $DR_1 = 2,100 \text{ Hz}/(1,024/2) = 4.1 \text{ Hz/point}$.

Optimum resolution is thus achieved by reducing sw_2 and sw_1 as much as possible from their values in the parent ^1H and, perhaps, ^{13}C spectra and by zero filling np_2 and ni by a factor of two.

7-5d Linear Prediction

We have mentioned repeatedly that NMR spectroscopists are engaged in a seemingly never-ending conflict between sensitivity, on the one hand, and both time and resolution, on the other. Nowhere are these problems more acute than in the t_1 dimension of 2D experiments. There must, of course, be a sufficient number of scans per time increment to observe a spectrum, but there must also be enough increments to resolve closely situated signals. Both requirements take precious spectrometer time, and spectroscopists are forced to compromise between sensitivity and resolution in a number of 2D experiments.

Forward linear prediction (LP) represents an elegant solution to the t_1 -domain sensitivity–resolution–time dilemma. While the mathematical implementation of LP is not trivial, its underlying principle is surprisingly simple. LP can be likened to an ideal automobile race in which the vehicles travel at a constant rate of speed. If their relative positions after 256 laps are noted, a very good estimate can be made as to what their positions will be after 1,024 laps.

Since LP is employed predominantly for data in the t_1 dimension, our discussion of its use will be limited to that domain. The interferograms, or pseudo FID's, of the t_1 dimension can be considered to be composed of a series of exponentially decaying cosine (real) and sine (imaginary) functions, where each interferogram corresponds to a chemical shift in the ν_2 dimension. It is possible to extend these interferograms mathematically by using information from previous data points (the incremented spectra already collected) and thus very accurately predict what the pseudo FID's would look like if more incremented spectra had been taken. The interferograms are typically extended two to four times and result in considerably sharper signals, and narrower cross peaks, in the ν_1 domain.

In a time sequence of data points, the value of a particular data point, d_m , can be estimated from a linear combination (hence the name *linear prediction*) of the data points that immediately precede it (Hoch and Stern, 1996), as shown in the following equation, in which a_1, a_2, a_3, \dots are the LP *coefficients* (also called the LP *prediction filter*):

$$d_m = d_{m-1}a_1 + d_{m-2}a_2 + d_{m-3}a_3 + \dots \quad (7-1)$$

The number of coefficients used in the LP process is known as the *order* of the LP. The number of coefficients corresponds to the number of data points that are used to predict the value of the next data point in the series.

The critical requirement for the employment of LP is that the interferograms must have sufficient S/N so that an accurate estimation can be made of the coefficients. This requirement presents a problem for both heteronucleus-detected 2D experiments and very dilute solutions in proton-detected experiments. LP, however, is less important for the former, in which protons, with their much smaller chemical-shift range, and hence intrinsically better data point resolution, constitute the ν_1 dimension. Another important requirement is that the number of coefficients used in LP should be *larger* than the number of signals that make up each FID being extended. *How much* larger depends on the manufacturer of the spectrometer.

Linear predictions are commonly performed on instruments of one manufacturer with 8 coefficients while another manufacturer recommends that anywhere from 16 to 32 coefficients be used for its systems. It is important that the correct number of coefficients be employed. Too few will fail to make accurate predictions, and the resulting spectra will, at best, look as if no LP has been performed and, at worst, have even poorer resolution. In contrast, too many coefficients will result in artifacts along the ν_1 axis that resemble t_1 noise, and the calculations will take an inordinate amount of time or cause the system to shut down.

It is also important that LP not be abused. A sufficient number of increments must be taken from which the FID's can confidently be extended. A total of 64 increments has, for example, been found to be insufficient, while LP's have successfully been carried out with 96 increments. A good practice is to acquire at least 128 increments for accurate prediction. A second concern is that LP not be extended too far (e.g., 128 points predicted to 4,096). W. F. Reynolds (2002) has found that, as a general rule, data presented in the phase-sensitive mode can be predicted fourfold (e.g., 256 data points can be predicted to 1,024), while absolute-value data can be extended twofold, 256 points to 512. A significant exception to the fourfold rule for phase-sensitive experiments concerns the ^1H -detected, heteronuclear chemical-shift correlation experiments. In marked contrast to COSY and HMBC spectra, for which the interferograms are frequently composed of many signals, those of HMQC and HSQC spectra constitute only one (due to the directly attached ^{13}C). LP's up to sixteen-fold can be performed in these experiments (Sections 7-8a and 7-8b).

Because of the requirement that the number of coefficients be larger (or even very much larger) than the number of signals constituting the FID's, LP is usually not appropriate for either 1D data or the summed FID's that eventually form the ν_2 dimension. It is ideally suited, as previously noted, for operating on data in the t_1 domain, for several reasons. First and foremost is digital resolution. If, for example, the number of increments needs to be doubled because of considerations relating to the resolution of the ν_1 dimension, the total time of the experiment will, likewise, be doubled. This situation might require an inordinate amount of spectrometer time and might even ultimately prove unsuccessful because of T_2^* effects. For instance, as t_1 of a COSY experiment becomes increasingly larger, T_2^* relaxation correspondingly reduces the amount of evolving xy magnetization. If the number of increments is too large, there may be little or no signal remaining to be detected. An interesting exception to the rule that LP is restricted to ν_1 -domain data is seen with the HSQMBC experiment [the single-quantum analog of the HMBC experiment (Section 6-2)], which is used to determine longer range, heteronuclear coupling constants (i.e., $^nJ_{\text{XH}} > 1$). In this experiment, LP is performed on data in both dimensions, where the data are generally twofold predicted in the ν_2 domain (e.g., 4,096 data points predicted to 8,192).

A second reason for restricting LP to the t_1 dimension of 2D experiments concerns spectral resolution. In most instances, the signals of spectra in the final time increments have nonzero intensities. If a strong weighting function is not used to drive interferograms to zero intensity, truncation wiggles are produced upon Fourier transformation (Section 2-5c). Such apodization, however, results in line broadening and is not really an ideal solution. LP allows more gentle apodization functions to be employed, thereby improving spectral resolution and

greatly reducing truncation errors. In addition, since t_1 interferograms are generally composed of many fewer signals than are typical t_2 FID's, the LP requirement that the number of signals be smaller than the number of coefficients generally is not violated.

It is important to realize that zero filling is complementary, and not an alternative, to LP. Both techniques effectively increase t_a , thereby increasing digital resolution (Section 2-5d). LP, however, provides a much greater enhancement because it extends an FID that would otherwise be truncated, while zero filling just adds zeros to an already apodized FID. This difference can be demonstrated by calculating DR for phase-sensitive data in the ν_1 dimension with and without LP. If $sw_1 = 2,100$ Hz, $ni = 256$, and one level of zero filling (256 points) is carried out for a total of 512 points, then $DR_1 = 2,100 \text{ Hz}/(512/2) = 8.2 \text{ Hz/point}$. Now, if those same 256 time increments are subjected to fourfold LP (768 points), for a total of 1,024 points, and then are zero filled to 2,048 points, $DR_1 = 2,100 \text{ Hz}/(2,048/2) = 2.1 \text{ Hz/point}$ (a fourfold improvement).

Like zero filling, LP can be employed as a data-processing method after the fact. The maximum benefits of LP, however, are realized if the operator plans for its use when setting up the experimental acquisition parameters. In this approach, only one-fourth to one-half of the number of time increments that would be sufficient for resolution requirements are actually taken. The interferograms in t_1 are then subjected to a two- or fourfold LP, zero filled to a factor of two, and processed in the normal fashion. The resulting 2D spectra have the same digital resolution in the ν_1 dimension as if 2 to 4 ni had been used and have been obtained in one-fourth to one-half the time. If both sensitivity and resolution are problems, then, for a given length of spectrometer time, a *reduced* ni with LP can be used for resolution and an *increased* number of scans per increment for sensitivity. Linear prediction is the most important 2D experimental timesaving technique available to NMR spectroscopists. If it is not being used regularly for processing at least phase-sensitive 2D data, valuable spectrometer time is being wasted. A good example of the resolution-enhancing ability of LP is illustrated in Figure 7-7, which shows HSQC spectra of the natural product T-2 toxin, with and without LP.

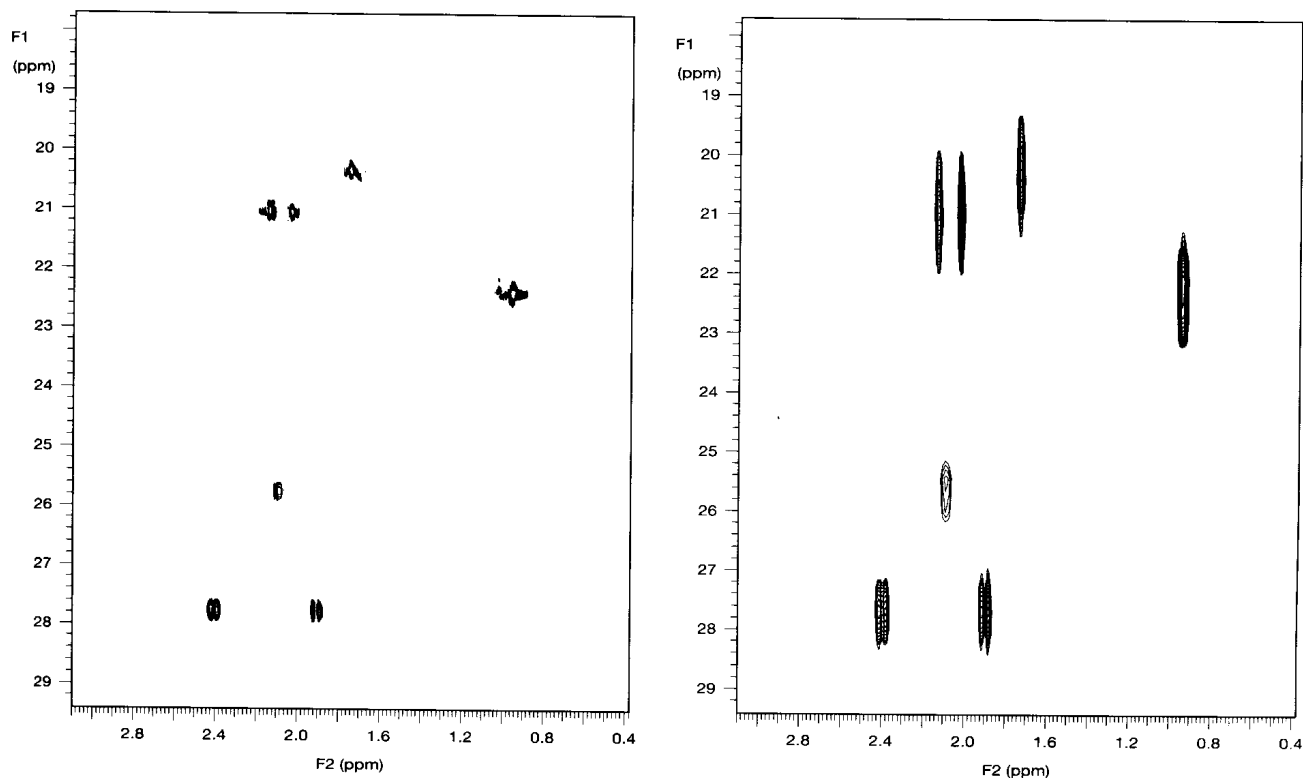


Figure 7-7 Expanded HSQC spectra with sixteenfold linear prediction (left) and no linear prediction (right).

In addition, *backward* LP can be utilized for a completely different purpose. The first few data points at the beginning of the FID occasionally become corrupted if acquisition of the signal starts before pulse ringdown has faded to an acceptable level. In such a situation, a large baseline roll appears in the spectrum and renders it essentially useless. This result is especially disheartening when it occurs in a ^{13}C spectrum accumulated over a weekend. Still, the problem can easily be solved by replacing the first 5–10 data points with predicted points. Reweighting and a second FT result in an undistorted spectrum.

A new mathematical technique for processing 2D data, known as the filter diagonalization method (FDM), was recently developed by A. J. Shaka. The technique accomplishes goals similar to those aimed at in LP. In this method, even fewer time-incremented spectra, namely, two to four increments for an HMQC or HSQC experiment, are collected than with LP. FDM appears to be best suited for those heteronuclear chemical-shift-correlated experiments for which there are a limited number of ν_1 signals for any particular frequency ν_2 [e.g., for HMQC or HSQC spectra when the maximum number of ν_1 (^{13}C) signals per ν_2 (^1H) frequency is unity].

7-6 Two-Dimensional NMR Data Display

7-6a Phasing and Zero Referencing

2D experiments are almost always presented as contour, rather than stacked, plots (Section 6-1). If the 1D spectra, from which the spectra in the ν_2 dimension are derived, are phased and zero referenced properly, both the phase and zero reference of diagonal and cross peaks along the ν_2 axis should be very close to correct. If they are not, then a horizontal cross section through a signal in the upper right corner of the contour plot is zero-order phase corrected and checked for correct zero referencing at the same time. A second cross section through a signal in the lower left corner is then first-order phase corrected. One such cycle is often sufficient to phase the signals in the ν_2 domain. If major phase adjustments are required, however, several zero-order–first-order cycles may be necessary.

To correct the phase and zero reference of diagonal and cross peaks along the ν_1 axis, the contour plot is rotated by 90° so that ν_1 is the horizontal axis. Signals at each end of the ν_1 axis then are selected, phased, and checked for zero referencing, as was done for ν_2 . Finally, by convention, contour plots are presented so that the detected (ν_2) dimension is along the horizontal axis and the nondetected (ν_1) dimension is along the vertical axis.

7-6b Symmetrization

Symmetrization is commonly employed in the display of homonuclear, absolute-value, 2D NMR data to preserve true cross peaks and to discard unsymmetrical artifacts. A particularly troublesome type of artifact known as t_1 noise is manifested as streams of signals, or ridges (Section 6–1). Associated with strong signals in a contour plot, these ridges run parallel to the ν_1 axis and are found at their chemical shifts along the ν_2 axis. They can seriously interfere with the observation of real cross peaks from the signals in question. Critical to the symmetrization operation is the requirement that digital resolution be equal in *both* the ν_1 and ν_2 dimensions. Thus, symmetrization is not generally suitable for phase-sensitive data, because of the potential introduction of distortions in the cross peaks. Symmetrization must, therefore, be undertaken with caution and is best used in comparison with the unsymmetrized data.

7-6c Use of Cross Sections in Analysis

The procedure for establishing atomic connectivities in contour plots is relatively straightforward. It should be remembered, however, that these plots can be deceiving. Threshold values, which are essential for removing baseline noise from contour plots, may be sufficiently high also to eliminate smaller cross peaks. For this reason, it is recommended that cross sections through the individual frequencies of specific resonances be examined on the

monitor and either tabulated or plotted directly. This recommendation is especially true for the longer range, proton-heteronucleus, chemical-shift correlation experiments such as HMBC and FLOCK. Further, cross sections through the frequencies of both protons and the X nuclei should be analyzed in these two experiments. In the case of unknown compounds, homo- and heteronuclear, cross-sectional examinations are critical, since dihedral angles close to 90° often result in a number of very small cross peaks.

Part C. Two-Dimensional Techniques: The Experiments

There are many ways to approach the acquisition, processing, display, and even interpretation of 2D NMR experiments. The sections that follow describe many of the 2D experiments that have been discussed thus far and provide guidelines for their performance using the States method of detection. For the best results, 2D experiments should be performed at constant temperature (ideally, just above room temperature, in order to minimize evaporation of the solvent and degradation of the sample) and with a nonspinning sample.

If computer speed and memory permit, 2D NMR experiments generally are planned so that at least a 2K (2,048-point) FT is carried out in each dimension. In this approach, np_2 should be 1,024 and zero filled by one level, to 2,048, prior to the FT2. In addition, n_1 should then be linear predicted two- to fourfold, to 1,024, and zero filled by one level, to 2,048, before FT1. RT's of 0.8–1.2 s are generally sufficient, and most experiments call for the use of steady-state scans.

Most of the 2D NMR experiments described in Part C have been adapted for the use of z-axis gradients. For the HSQC experiment, for which the gradient and nongradient versions differ by more than the obvious inclusion of gradients in the former, the differences between the two pulse sequences are noted in the text. The principal advantage of these gradient-selected sequences over the corresponding nongradient versions is that the need for phase cycling (Section 5-8) is largely, or completely, eliminated. This difference represents a significant timesaving benefit for high-sensitivity, ^1H -detected experiments. A second significant advantage is realized in ^1H -detected heteronuclear, chemical-shift correlation experiments for which gradients are used to suppress the strong signals of solvent protons and of protons (the majority) attached to ^{12}C nuclei. A third, less important, benefit of gradients concerns relaxation delay times (DT's), which can sometimes be reduced without the attendant generation of artifacts.

There is, in fact, one disadvantage associated with acquiring a signal by means of gradients: gradient versions of various 2D experiments exhibit a $2^{1/2}$ decrease in sensitivity with respect to their nongradient counterparts. This is, however, seldom a serious problem, especially with the proliferation of ^1H -detected, 2D NMR experiments.

A number of 2D spectra of the sesquiterpene natural product T-2 toxin (**7-1**) are collected in Part C to illustrate certain 2D experiments and the critical differences between them.

7-7 Homonuclear Chemical-Shift Correlation Experiments Via Scalar Coupling

Experiments that correlate the chemical shifts of two nuclei of the same type (homonuclear correlation) on the basis of the scalar (or spin-spin) coupling that exists between them are the most frequently performed of all the 2D experiments. Most of these experiments are adaptations of the basic COSY sequence. Another COSY-type experiment, TOCSY, is useful for observing correlations of individual protons with most, or all, of the other protons in an entire spin system.

Homonuclear contour plots are symmetric with respect to both spectral widths, and data point resolutions are almost always identical. Linear prediction can help greatly in making DR_1 equal to DR_2 by keeping the data accumulation time within acceptable limits.

7-7a The COSY Family of Experiments

Basic COSY The COSY-90 experiment (which is referred to simply as COSY; Section 6-1 and Figure 6-1) has been described as being nearly foolproof in that fairly decent results can be obtained even when the 90° pulses are not well calibrated. COSY is one of a very few 2D experiments that is better performed in the absolute-value, rather than the phase-sensitive, mode, because of the mixed-phase line shape that arises in phase-sensitive contour plots. If the cross peaks are phased to appear as absorptive signals, then the diagonal peaks are phased dispersively. Strong diagonal signals can, in turn, have long, dispersive tails (Section 7-5a), which easily can obscure cross peaks located near the diagonal. Compared with other COSY experiments, phase-sensitive COSY has a multitude of disadvantages and should not be used.

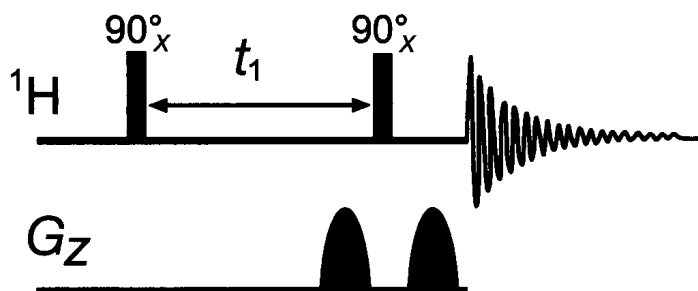
COSY experiments also have benefited greatly from the adaptation of gradients, and the gradient COSY pulse sequence is shown in Figure 7-8. The use of gradients is important chiefly because, in nongradient, ^1H -detected experiments, more scans per time increment are often required to satisfy a phase cycle (4–16 steps, Section 5-8) than to acquire a spectrum. Gradient COSY (gCOSY) spectra are, on the other hand, routinely taken with one to two scans per increment. Another advantage of gCOSY experiments is that much shorter relaxation delay times are required relative to the nongradient versions. The reason is that artifacts are generated with the latter if RT is too short, and especially if ns/i is less than the optimum number required for the phase cycle. Thus, when combined with LP methods, gCOSY experiments can be carried out in a matter of minutes. The gCOSY pulse sequence is like the COSY sequence, with a pair of z gradients flanking the second 90° (read) pulse (Figure 7-8). The gradient and nongradient COSY spectra of T-2 toxin are not compared here because the only substantial difference between the two is the time required to accumulate spectra with equivalent S/N ratios.

In addition to some of the general parameters presented in Part B and at the beginning of this section, the following parameters are appropriate for COSY experiments:

1. steady-state scans = 16 (with gradients) or 8 (for basic, nongradient versions)
2. $ns/i = 1-2$ (with gradients) or 8 or 16 (better) for nongradient experiments
3. $ni = 512$
4. LP = 512
5. pseudo-echo, sine bell, or squared sine bell weighting

COSY45 The COSY45 experiment (Section 6-1 and Figure 6-12) is essentially identical to the basic COSY experiment, except that the final pulse is 45° rather than 90° . The COSY45 experiment is superior to the standard COSY experiment for two reasons. (1) An approximately 15% loss of sensitivity relative to COSY is more than compensated for by COSY45's suppression of both diagonal signals and cross peaks resulting from parallel transitions (which are very close to the diagonal). (2) The diminution in intensity of these signals permits the observation of more interesting cross peaks due to progressive and regressive

Figure 7-8 The gradient COSY pulse sequence.



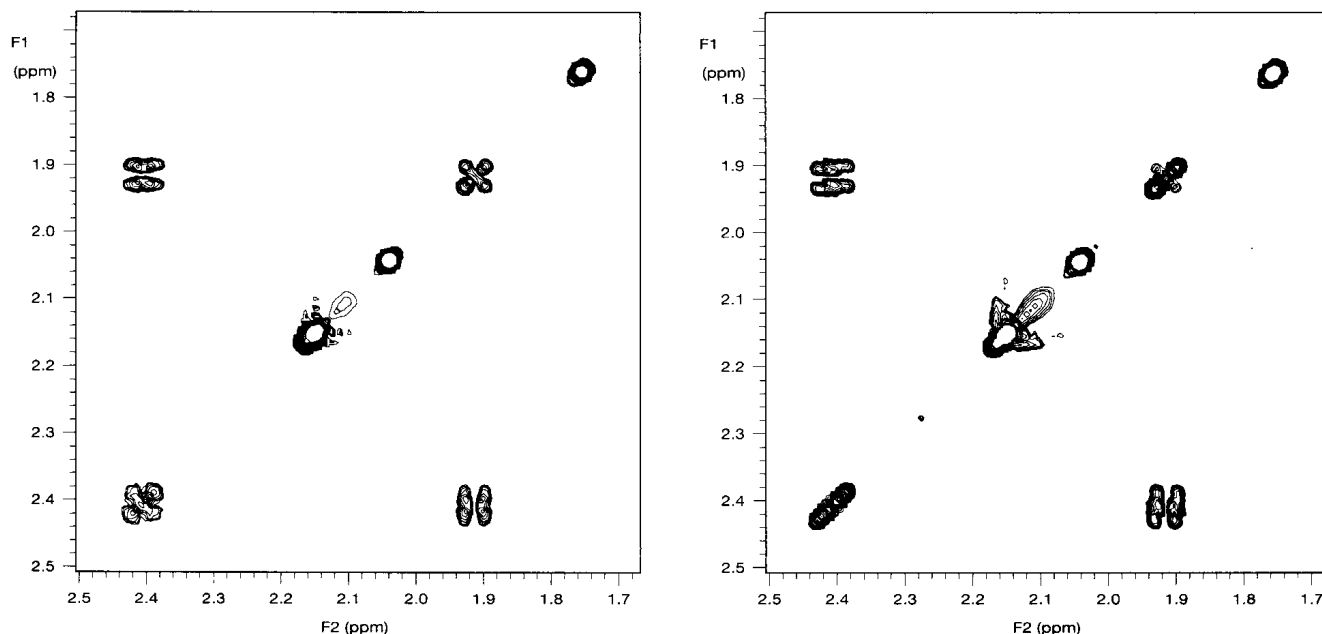


Figure 7-9 Expansions: COSY spectrum (left) and COSY45 spectrum (right) of T-2 toxin.

transitions, which happen to be located close to the diagonal. The simplified diagonal signals and tilted cross peaks of the COSY45 spectrum of T-2 toxin (7-1) are clearly visible when that spectrum is compared with the standard COSY spectrum in Figure 7-9.

Long-Range COSY The long-range COSY (LRCOSY, Section 6-1 and Figure 6-13) experiment is, likewise, virtually identical to COSY. Two constant-time delays τ , equal to approximately 200 ms, are inserted into the COSY sequence after t_1 and flanking the read pulse, making the pulse sequence $90^\circ-t_1-\tau-90^\circ-\tau-t_2$ (acquire) and enhancing correlations due to small couplings. Considerable digital resolution, however, is now available in the COSY family of experiments, through increased computer memory size (larger t_1 and t_2 data sets). This enhanced DR makes possible the observation of $^1\text{H}-^1\text{H}$ correlations that are due to very small coupling constants. Many long-range correlations are, in fact, detected along with the stronger vicinal and geminal correlations in regular COSY experiments. LRCOSY is, therefore, less of a necessity than it was years ago.

High- and low-resolution COSY spectra of T-2 toxin (7-1), with and without long-range correlations, respectively, are compared in Figure 7-10. The high-resolution COSY experiment used 512 time increments linearly predicted to 1,024, while the low-resolution COSY employed only 128 increments linearly predicted to 256. It is important to realize that the former is considered a high-resolution experiment because it contains not only more increments (1,024 vs. 256, for greater digital resolution), but also a longer amount of time between the two 90° pulses, in these final 768 increments, for those long-range correlations to develop.

In addition to the obviously poorer resolution in Figure 7-10 (right), long-range cross peaks due to (i) four-bond W coupling between H-11 and H-7B (δ 4.4, 1.9) and H-8 and Me-16 (δ 5.3, 1.7) and (ii) homoallylic coupling between H-11 and Me-16 (δ 4.4, 1.7) are clearly visible in Figure 7-10 (left), but are noticeably absent in Figure 7-10 (right).

Double Quantum Filtered COSY The double quantum filtered COSY experiment (DQF-COSY, Section 6-1 and Figure 6-16) is similar to COSY, with three 90° pulses in the sequence $90^\circ-t_1-90^\circ-\tau-90^\circ-t_2$ (acquire). The DQF-COSY experiment is performed in the phase-sensitive mode, but, unlike the situation in the phase-sensitive COSY experiment, in the DQF-COSY both diagonal and cross peaks can be phased as absorptive signals. This difference not

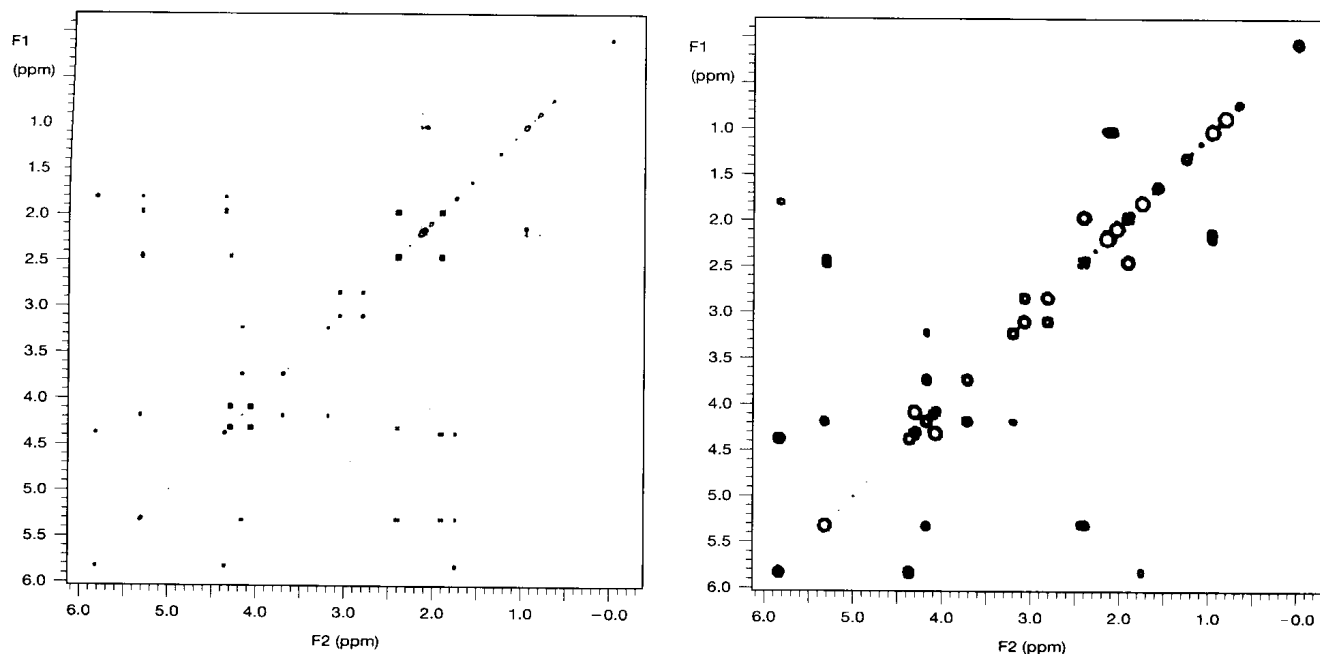


Figure 7-10 COSY spectra: high-resolution spectrum (left) and low-resolution spectrum (right) for T-2 toxin.

only allows cross peaks close to the diagonal (such as in COSY45) to be observed, but also permits the analysis of cross peaks to determine the coupling constants that give rise to their multiplet structures. It should be remembered that the observation of positive and negative signals requires that the *active* coupling constant (the distance between cross peaks of *opposite* sign) be *greater* than the digital resolution (Section 7-5c). In addition, the nature of the pulse sequence eliminates *singlet* signals from methyl groups and solvents (Section 6-1).

The use of gradients with DQF-COSY is, however, less important than with the other COSY experiments, for two reasons. First, the relative intensity of DQF-COSY cross peaks is only about 40% of that of corresponding COSY signals. This reduction in sensitivity necessarily results in more scans being required per increment compared with other COSY experiments. Phase cycles of even 16 steps are, therefore, not so wasteful of time. Second, rapid pulsing (one of the advantages of the gCOSY experiments) should be avoided in DQF-COSY because pulsing too rapidly can produce artifacts.

The lower overall sensitivity of the DQF-COSY experiment and the phase sensitivity of selected cross peaks of **7-1** are illustrated in Figures 7-11a and 7-11b, respectively. (*Closed* peaks indicate positive signals; *open* peaks denote negative signals.) Figure 7-11c shows the cross peak between H-7A and H-8. The spectrum illustrates how the active 5.5-Hz coupling ($J_{7A,8}$) and the *passive* 14-Hz coupling ($J_{7A,7B}$, between signals of the *same* sign) can readily be observed in the DQF-COSY spectrum (right), but are totally obscured in the corresponding COSY spectrum (left). Note, too, the absence of diagonal peaks due to singlet signals arising from the two acetate (δ 2.03 and 2.16) methyl groups in the DQF-COSY spectrum in Figure 7-11b.

Since DQF-COSY data are usually presented in the phase-sensitive mode and generally are not symmetrized (Section 7-6b), DQF-COSY experiments are inherently more sensitive to artifacts than are absolute-value COSY experiments. Therefore, t_1 noise arising from strong signals (other than singlets, which, of course, are absent) can be a problem in the former experiments. The difficulty, however, can be minimized by carefully calibrating the 90° pulse. Pulsing too rapidly also can be avoided by setting RT more conservatively toward $3T_1$ when $T_1(\text{max})$ is not known. DQF-COSY is, therefore, not an experiment to be used regularly, like COSY, but rather is to be employed in those instances when certain coupling constants have to be determined or when strong singlet signals are obscuring important cross peaks.

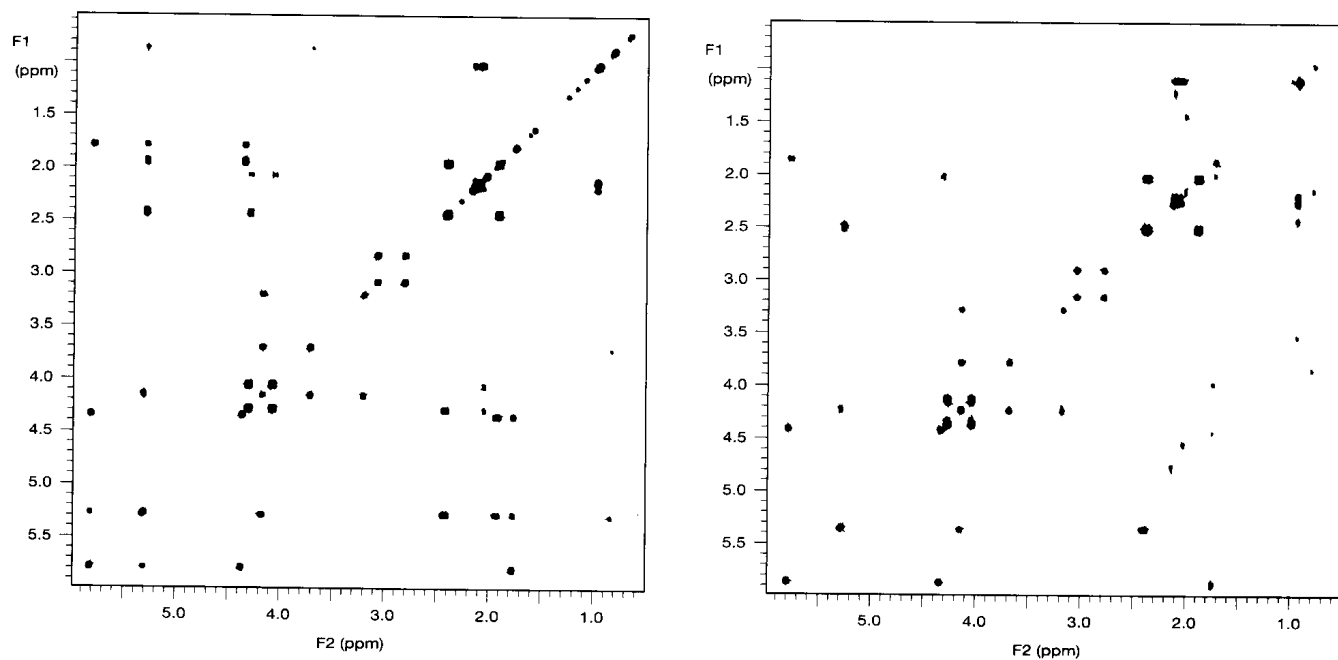


Figure 7-11a (a) COSY spectrum (left) and DQF-COSY spectrum (right). (b) Expansions for $J_{7A,7B}$: COSY spectrum (left) and DQF-COSY spectrum (right). (c) Further expansions for $J_{7A,8}$: COSY spectrum (left) and DQF-COSY spectrum (right) for T-2 toxin.

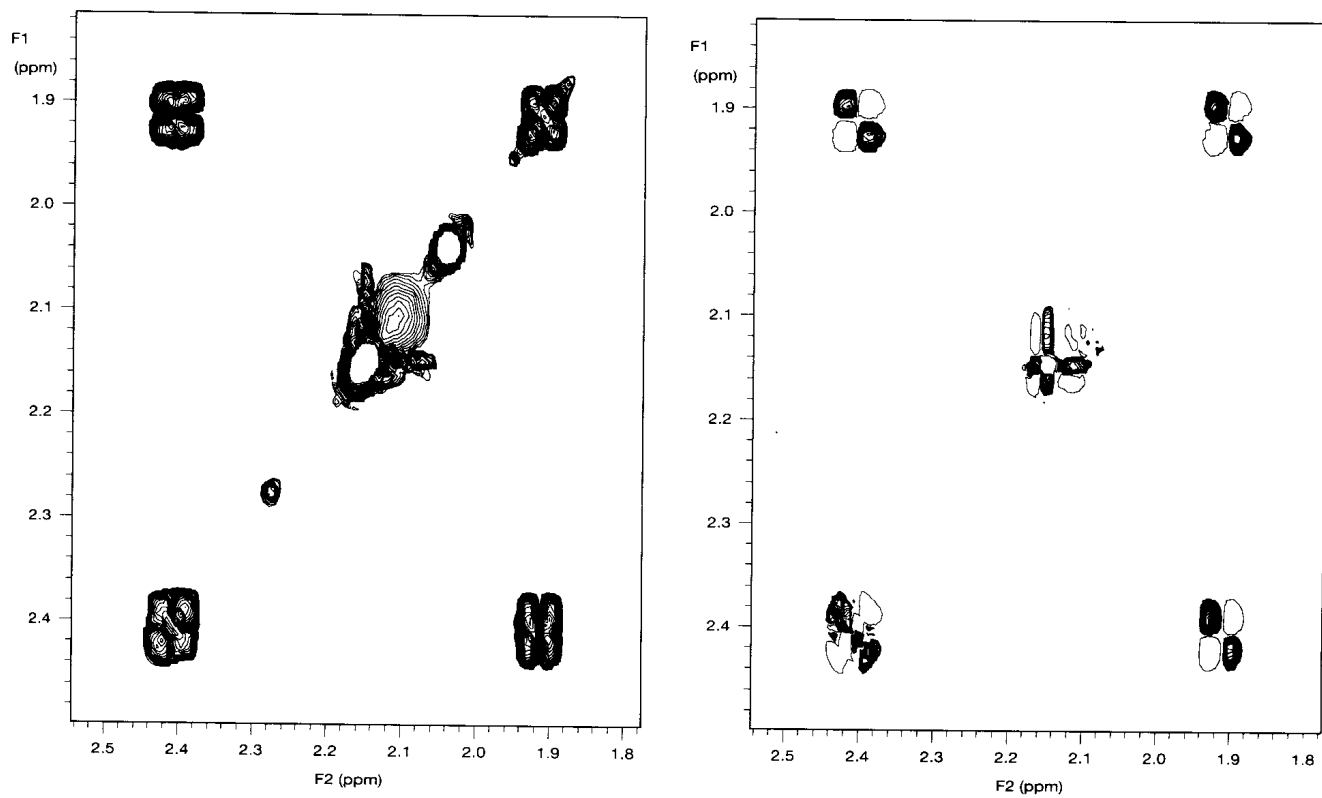


Figure 7-11b

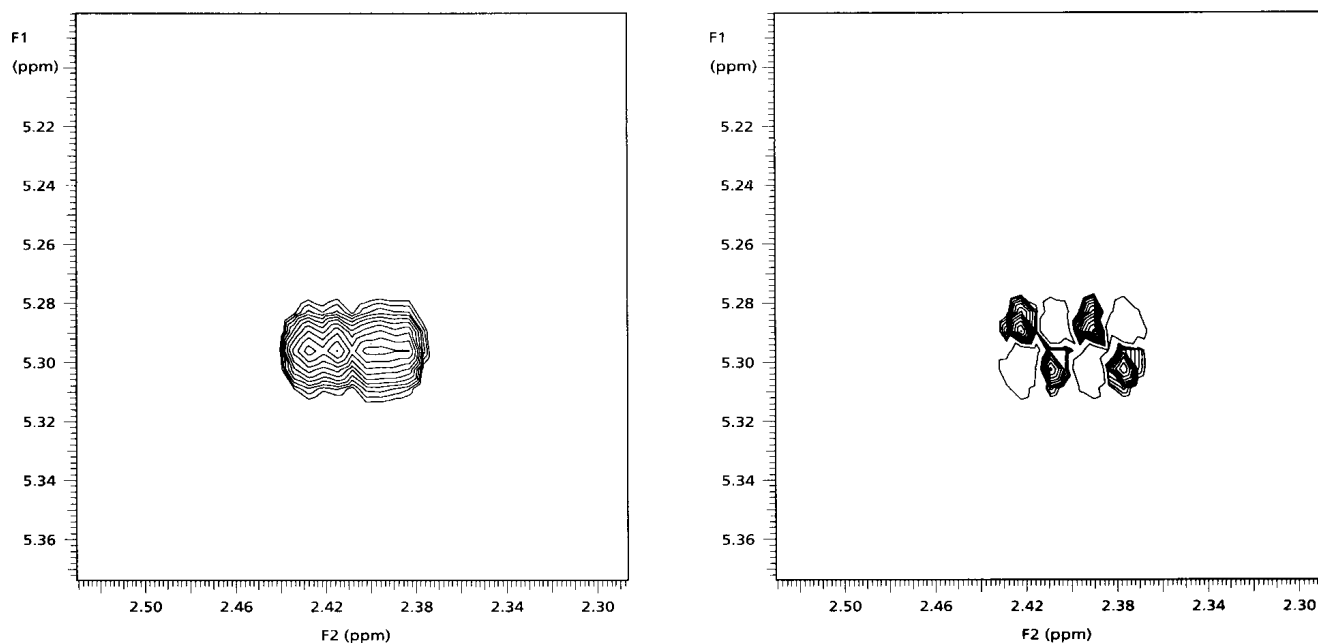


Figure 7-11c

The following parameters are appropriate for DQF-COSY experiments:

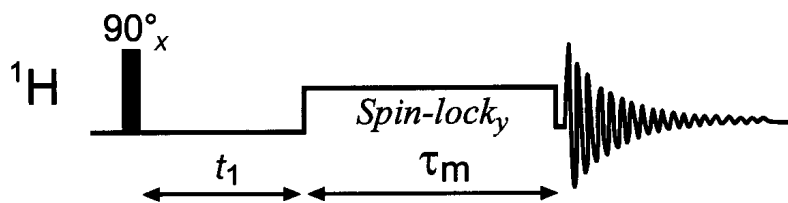
1. $\tau = 4 \mu\text{s}$ or an appropriate delay to allow for pulse rise and fall times
2. steady-state scans = 32 (with gradients) or 8 (for nongradient versions)
3. $ns/i = 1-2$ (with gradients) or 8 or 16 (better) for nongradient experiments
4. $ni = 256$
5. $LP = 768$
6. Gaussian, cosine, or squared cosine weighting

7-7b The TOCSY Experiment

The TOCSY experiment (Section 6-1 and Figure 6-16) gives information similar to that afforded by relayed COSY and is well suited for large molecules. It is performed in the phase-sensitive mode, and, as with DQF-COSY, both the diagonal and the cross peaks can be phased as absorptive signals. The TOCSY pulse sequence is given in Figure 7-12, and the isotropic mixing sequence can be WALTZ-16, MLEV-17, or DIPSI-2, the last being particularly good for magnetization transfer.

TOCSY and COSY spectra for T-2 toxin (7-1) are pictured in Figure 7-13. The greater number of cross peaks in the TOCSY spectrum illustrates the further relaying of coupling information. For example, H-2 (δ 3.70) shows connectivity to H-3 (δ 4.16) in the COSY spectrum and relayed connectivity to OH-3 (δ 3.20) and to H-4 (δ 5.31) in the TOCSY spectrum.

Figure 7-12 The TOCSY pulse sequence.



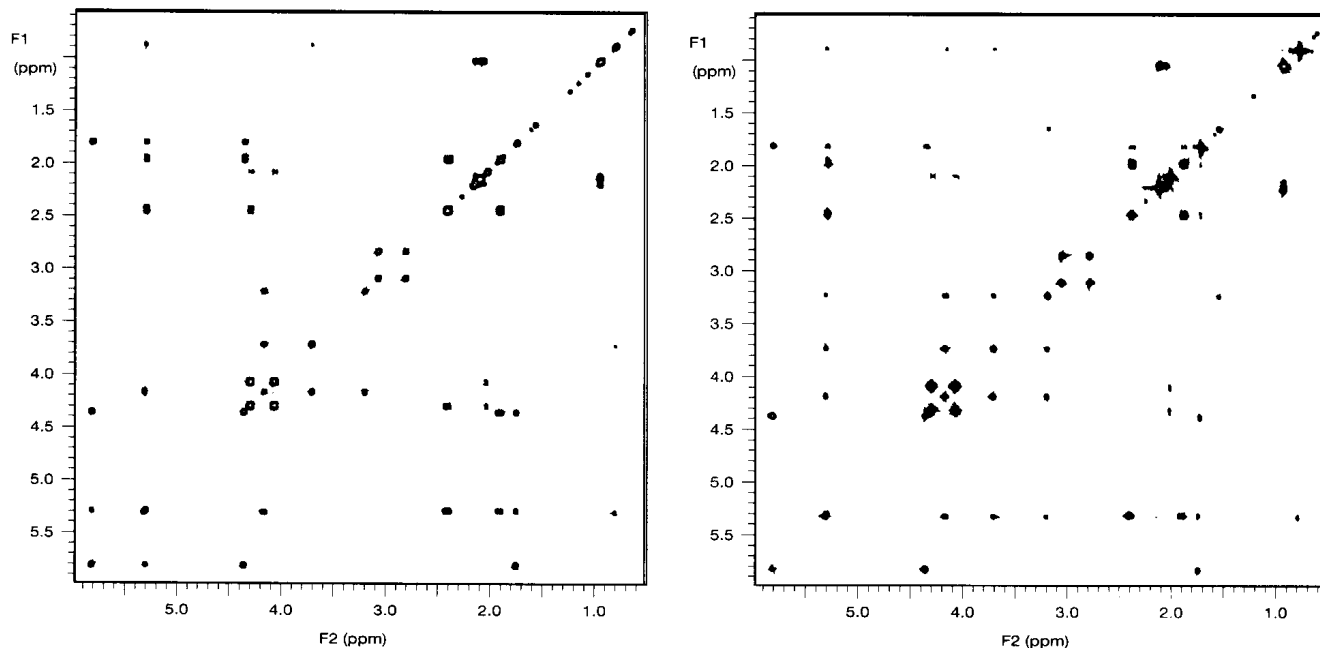


Figure 7-13 COSY spectrum (left) and TOCSY spectrum (right) of T-2 toxin. The TOCSY mixing time is 80 ms.

The degree to which a particular proton in a spin system perturbs its more remote neighbors increases with the length of the spin-lock mixing time. For small molecules, for example, mixing times of 20–50 ms produce a COSY-like spectrum with few relays, those in the range of 50–90 ms extend the correlations by one or two additional protons, and mixing times of 100–150 ms largely transfer magnetization throughout an entire spin system. TOCSY, like DQF-COSY, is an experiment with inherently lower sensitivity, requiring more scans per increment. The gradient experiment is, likewise, less advantageous with respect to the nongradient version than is the case for COSY.

The following parameters are appropriate for 2D TOCSY experiments:

1. spin-lock mixing time range = 20–150 ms
2. steady-state scans = 32, or 64 for long mixing times
3. $ns/i = 8$ minimum (or a greater multiple of 4)
4. $n_i = 256$
5. LP = 768
6. Gaussian, cosine, or squared cosine weighting

The 1D version of this experiment is especially useful and is considered in Section 7-11.

7-8 Direct Heteronuclear Chemical-Shift Correlation Via Scalar Coupling

Heteronuclear chemical-shift correlation experiments usually involve protons as one of the nuclei and can be performed by detecting either protons or the X nuclei (the most common being ^{13}C ; Section 6-2). The principal advantage of ^1H -detected experiments is their sensitivity, which is a function of the gyromagnetic ratios: $(\gamma_{\text{H}}/\gamma_{\text{X}})^{3/2}$. In terms of the ratios of Larmor frequencies (instead of γ 's) at, say, 400 MHz for ^1H and 100 MHz for ^{13}C , the benefit of detecting ^1H rather than ^{13}C is $(400/100)^{3/2} = 8$.

X-nucleus-detected experiments, however, have an advantage that can become important. In heteronuclear, chemical-shift correlation experiments, it is, as a rule, better to detect the nucleus with the more congested spectrum, which is almost always protons. On occasion, however, X-nucleus spectra are more crowded than their ^1H counterparts. In this situation, it could be better (if sensitivity permits) to carry out an experiment that detects the X nuclei.

The two principal ^1H -detected, direct, heteronuclear chemical-shift correlation experiments are HMQC and HSQC. The X-nucleus-detected counterpart is HETCOR. The ^1H and X-nucleus spectral widths are reduced in each of these experiments. It is important to remember that the latter should be decreased to contain only the signals of *protonated* X nuclei. Quaternary carbons, for example, do not participate in these experiments, and their signals should not be included in the reduced spectral windows.

Since the X nucleus in HMQC and HSQC experiments is usually carbon, X refers to ^{13}C in the discussions that follow.

7-8a The HMQC Experiment

HMQC (Section 6-2 and Figure 6-22) is the more commonly used ^1H -X correlation experiment and is a relatively robust sequence. The delay time Δ governs both the initial defocusing of the ^{13}C -bonded ^1H vectors and the final refocusing of these vectors. It is selected in a compromise manner, as is τ in the APT experiment (Section 7-2a). Carbon decoupling also can be performed as the ^1H signal is acquired. Decoupling is accomplished with the GARP or WURST sequences, which are similar, but superior, to WALTZ decoupling sequences (Section 5-8). Since decoupling can result in heating of the sample, especially with aqueous solutions, it is often recommended to keep the relaxation delay time (DT) equal to about $5t_a$.

A major difficulty with HMQC is that protons which are directly bonded to ^{13}C are being detected in the presence of an overwhelming number of protons (99%) bonded to ^{12}C . Solving this problem of interfering ^1H - ^{12}C magnetization can be approached in two ways. As pointed out in Section 6-2, the HMQC sequence can begin with a BIRD pulse, which is selective for protons directly bonded to ^{12}C , and a nulling delay τ ; alternatively, gradients can be employed to refocus ^1H - ^{13}C magnetization selectively while leaving ^1H - ^{12}C magnetization defocused and, therefore, undetected.

The gradient version of HMQC is performed in the absolute-value mode, whereas the nongradient experiment is conducted in the phase-sensitive mode. While the use of gradients does result in a $2^{1/2}$ decrease in sensitivity with respect to the nongradient version (Part C, introduction), this decrease is seldom important, because HMQC is inherently a relatively sensitive experiment. Sensitivity is, however, critical in other experiments, as will be seen in Section 7-9a.

Since the signal of any particular proton can be modulated by only its directly bonded carbon, the HMQC experiment is ideal for linear prediction. We saw in Section 7-5d that one of the factors that influences LP is the number of signals constituting the interferogram. The number of coefficients used in the LP process should be larger than the number of resonances that make up each FID that is being extended. Since the number of ^{13}C signals contributing to each ^1H interferogram is unity, relatively few coefficients have to be used in the LP. This characteristic, in turn, suggests that LP can be extended beyond the normal fourfold limit.

The following parameters are appropriate for phase-sensitive HMQC experiments:

1. $\tau = 0.3\text{--}0.6$ s if a BIRD pulse is used
2. $\Delta = (2^1J_{\text{CH}})^{-1} \sim 1/(2 \times 140 \text{ Hz}) = 3.6$ ms
3. steady-state scans = 32 (gradient and nongradient versions)
4. $ns/i =$ multiple of 8
5. $ni = 256$

6. LP = 768 (recommended minimum), but can be up to 3,840 (sixteenfold)
7. Gaussian, cosine, or squared cosine weighting

7-8b The HSQC Experiment

Although the HSQC experiment (Section 6-2) is superior to HMQC in several respects, it is used much less often. The disfavor may be due, in part, to the fact that the sequence contains more than twice as many pulses as the basic HMQC experiment and is more susceptible to artifacts. Probe tuning and calibration of the two ^{13}C 180° pulses are very important. In addition, a larger phase-cycling scheme is required to reduce artifacts. HSQC's principal advantage over HMQC is that it has considerably better ^{13}C resolution along the ν_1 -axis. The reason is that HMQC cross peaks exhibit ^1H multiplet structure from ^1H - ^1H coupling along both the ν_1 - (^{13}C)- and ν_2 - (^1H)-axes, while HSQC cross peaks are singlet in nature along ν_1 . The ν_1 resolution advantage is even more important for lower field spectrometers, because ^1H multiplet widths are independent of magnetic-field strength while chemical-shift differences (expressed in Hz) are proportional to the field strength. This difference may not be apparent in the full HMQC and HSQC spectra of Figure 7-14a, but it can be clearly seen along the vertical dimensions of the expansion spectra of Figure 7-14b.

Like the COSY and HMQC experiments, HSQC benefits greatly from the use of gradients. Fewer scans need to be taken per time increment, and the more extensive phase cycle problem is obviated. Notably absent in the gradient HSQC spectrum of T-2 toxin, shown in Figure 7-15, are the t_1 noise artifacts observed in the nongradient HSQC spectrum at the chemical shifts of the strong methyl signals (δ 0.8 and ~ 2). HSQC is performed in the phase-sensitive mode and can incorporate a BIRD pulse and nulling delay τ to suppress ^1H - ^{12}C magnetization if the gradient version is not being used. The double INEPT pulse sequence of HSQC is shown in Figure 7-16. The gradient version of HSQC differs from the nongradient version by the inclusion of an additional 180° pulse on the X nucleus, after t_1 , flanked by two δ times.

As in HMQC, a delay time Δ governs both the initial defocusing of the ^{13}C -bonded ^1H vectors and the final refocusing of these vectors and is, likewise, selected in a compromise manner. Carbon decoupling also can be performed with the GARP or WURST sequences as

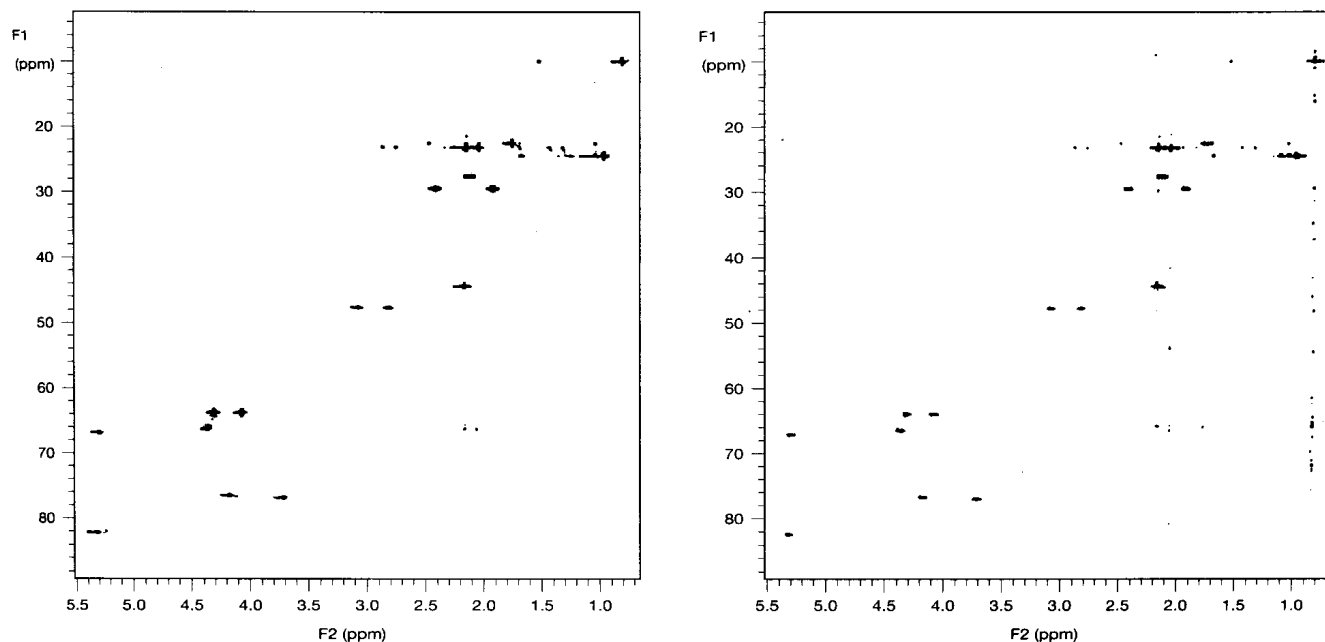


Figure 7-14a (a) HMQC spectrum (left) and HSQC spectrum (right). (b) Expansions: HMQC spectrum (left) and HSQC spectrum (right) of T-2 toxin.

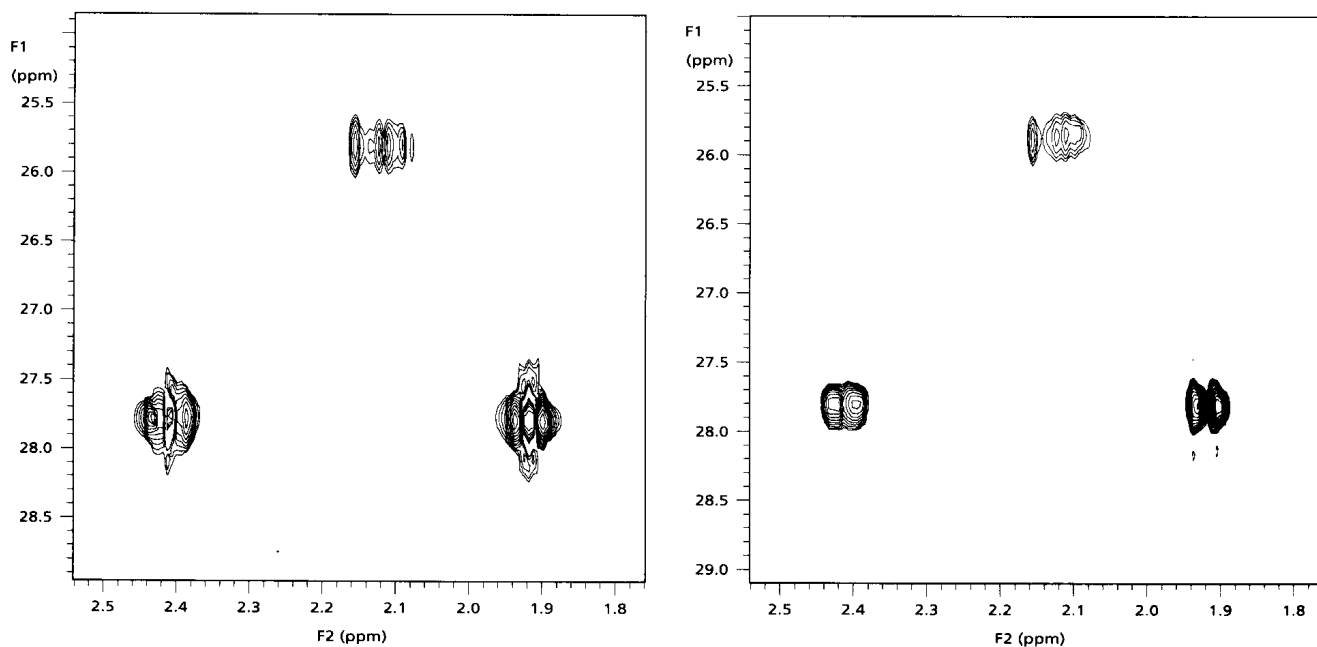


Figure 7-14b

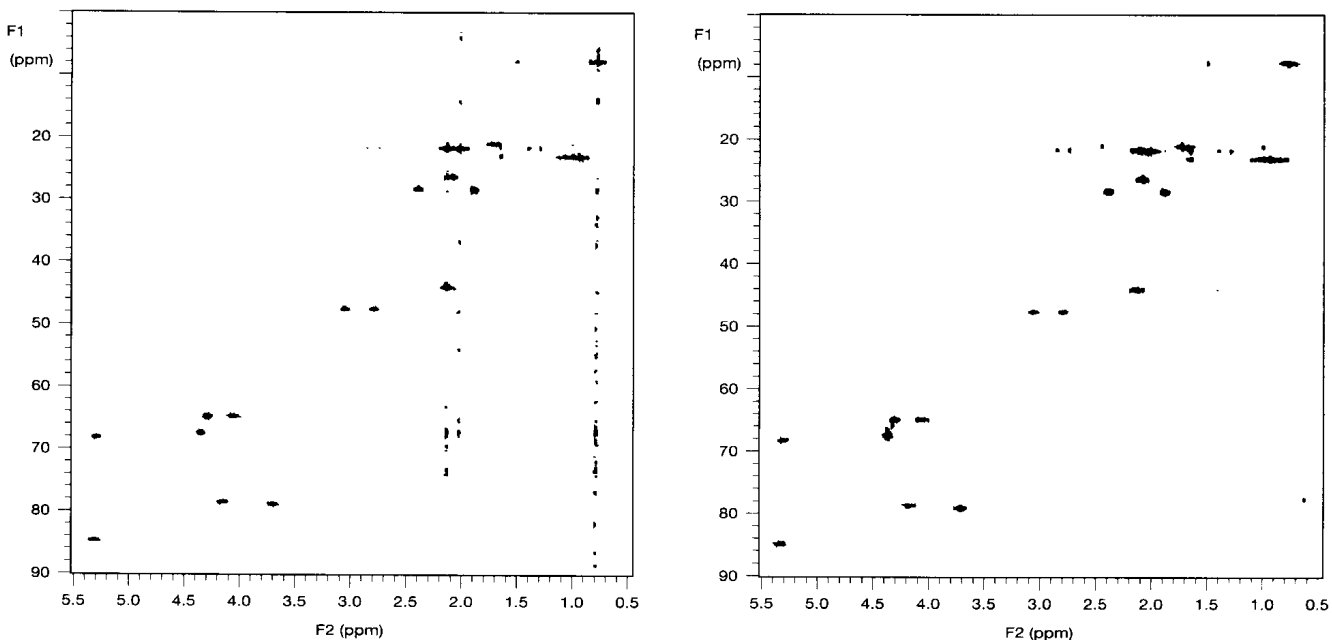


Figure 7-15 HSQC spectrum (left) and gradient HSQC spectrum (right) of T-2 toxin.

the ^1H signal is acquired, and similar sample-heating precautions ($DT \sim 5t_a$) are in order. The same considerations for linear prediction that were discussed for HMQC experiments (Section 7-8a) are even more pertinent to HSQC, because of its greater resolution in the ν_1 dimension. Remarkably, up to sixteenfold LP of ^{13}C chemical shifts can be carried out. It is recommended that HSQC be used, rather than HMQC, unless instrumental instabilities dictate otherwise.

A decision as to whether to employ HSQC or gHSQC may be reached in the following manner. For a relatively concentrated sample that displays strong signals in its ^1H NMR spectrum, where t_1 noise ridges could be a problem, gHSQC is preferred, because t_1 ridges are

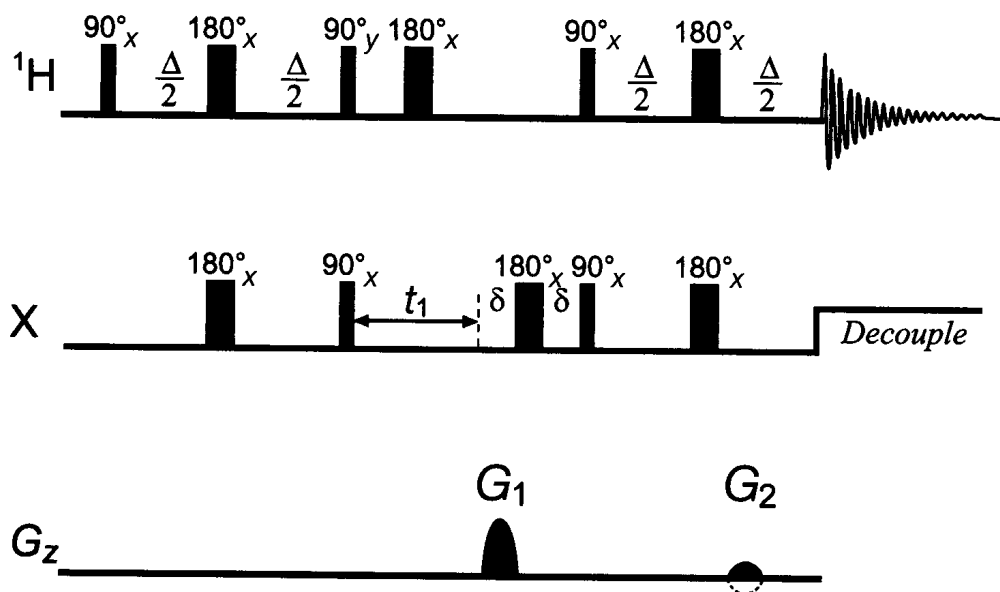


Figure 7-16 The gradient HSQC pulse sequence. The relative strengths of gradients G_1 and G_2 are 4 and 1 G cm^{-1} , respectively, as shown, when $X = {}^{13}\text{C}$.

virtually eliminated in this experiment. By contrast, the nongradient HSQC experiment does *not* eliminate t_1 ridges, even with a BIRD pulse during the relaxation delay. Still, nongradient sequences are inherently more sensitive than their gradient counterparts (Part C, introduction), so nongradient HSQC might be the experiment of choice with a more dilute sample.

The following parameters are appropriate for HSQC experiments:

1. $\tau = 0.3\text{--}0.6$ s if a BIRD pulse is used
2. $\Delta/2 = (4 {}^1J_{\text{CH}})^{-1} \sim 1/(4 \times 140 \text{ Hz}) = 1.8$ ms
3. steady-state scans = 32 (gradient and nongradient versions)
4. ns/i = multiple of 8
5. ni = 256
6. LP = 768 (recommended minimum), but can be up to 1,792 (eightfold) with gradients and 3,840 (sixteenfold) for nongradient versions
7. Gaussian, cosine, or squared cosine weighting

7-8c The HETCOR Experiment

HETCOR (Section 6-2 and Figure 6-20) is an X-nucleus-detected experiment and is now the least used of the ${}^1\text{H}\text{--}X$ correlation experiments. It remains, however, a useful experiment when ultrahigh resolution (~ 0.01 ppm) is required along both the ${}^1\text{H}$ and ${}^{13}\text{C}$ axes. In addition, two factors reduce the sensitivity advantage of gradient HSQC over nongradient HETCOR to closer to approximately 3.5:1, rather than the theoretical 8:1 value: (i) the insertion of a BIRD pulse at the midpoint of t_1 in the HETCOR sequence improves the experiment's sensitivity by collapsing ${}^1\text{H}$ multiplets to singlets (methine protons) or doublets (diastereotopic methylene protons), and (ii) there is a $2^{1/2}$ gain in sensitivity associated with nongradient experiments relative to their gradient counterparts (Part C, introduction).

Like COSY, HETCOR is a relatively robust sequence. Unlike COSY, it can be performed reasonably in either the absolute-value or phase-sensitive mode, although the latter gives better resolution. Since it is relatively immune to artifacts (if pulsing is not too rapid), a gradient version is largely unnecessary. Because HETCOR is a polarization transfer experiment, the relaxation delay times are a function of the ${}^1\text{H}$ -, and not the X-nucleus, T_1 's.

There are two important delay times in the HETCOR experiment. Δ_1 governs the defocusing of the ^{13}C -bonded ^1H vectors and is set in the same compromise manner that we have seen in the APT, DEPT, and HMQC experiments. The selection of Δ_2 , which controls the final refocusing of the ^1H -bonded ^{13}C vectors, however, is not so straightforward. A problem arises from the fact that both methyl and methine carbon vectors refocus at a time of $(2\ ^1J_{\text{CH}})^{-1}$, whereas methylene vectors do so at $(4\ ^1J_{\text{CH}})^{-1}$. The latter value is commonly chosen for Δ_2 and does represent a good compromise, for the following reason. Methyl and methine carbons can have just one ^1H cross peak, but methylene carbons can have two when they are attached to diastereotopic protons. The intensity of these methylene cross peaks is thus halved. This loss is partially compensated for by optimizing the refocusing time for methylene carbons. In addition, a common artifact in HETCOR experiments is the appearance of small signals halfway between the correlations of diastereotopic protons bonded to the same carbon.

^1H decoupling with the WALTZ sequence (Section 5-8) for HETCOR typically is performed as the ^{13}C signal is being acquired.

The following parameters are appropriate for absolute-value HETCOR experiments:

1. $\Delta_1 = (2\ ^1J_{\text{CH}})^{-1} \sim 1/(2 \times 140\ \text{Hz}) = 3.6\ \text{ms}$
2. $\Delta_2 = (4\ ^1J_{\text{CH}})^{-1} \sim 1/(4 \times 140\ \text{Hz}) = 1.8\ \text{ms}$
3. $\text{RT} = 1.3T_1$ of ^1H for an optimal pulse rate
4. steady-state scans = 32 (with gradients) or 8 (for nongradient versions)
5. $\text{ns}/i = 8$ minimum (or a greater multiple of 4)
6. $\text{ni} = 512$
7. $\text{LP} = 512$
8. pseudo-echo, sine bell, or squared sine bell weighting (all left shifted to improve sensitivity)

7-9 Indirect Heteronuclear Chemical-Shift Correlation Via Scalar Coupling

Heteronuclear chemical-shift correlation experiments can be performed by detecting either protons or the X nuclei (Section 7-8). All of the comments that were made there for the *direct*, heteronuclear chemical-shift correlation experiments apply equally well to their *indirect* (or longer range—e.g., two- and three-bond correlation) counterparts.

The two best longer range, heteronuclear chemical-shift correlation experiments are HMBC and FLOCK. Not surprisingly, HMBC (^1H detection) is more commonly used than the FLOCK experiment (X-nucleus detection) because of its much greater sensitivity. Since the X nucleus in these experiments is overwhelmingly carbon, X refers to ^{13}C in the sections that follow.

7-9a The HMBC Experiment

The HMBC experiment (Section 6-2 and Figure 6-26) is similar to the HMQC experiment from which it was derived. The delay time Δ governs the defocusing of the longer range (usually 2–3 bonds) ^{13}C -bonded ^1H vectors and is much longer than the corresponding delay in HMQC. Since the range of multiple-bond C–H couplings is approximately 2–15 Hz, the Δ value of HMBC is, likewise, selected in a compromise manner and generally set to about 60 ms, which corresponds to $^nJ_{\text{CH}} \sim 8\ \text{Hz}$.

One of the problems with HMBC involves the suppression of the signals of the protons that are directly bonded to ^{13}C . This interfering ^1H – ^{13}C magnetization can be dealt with in the following way. A ^{13}C 90° pulse (known as a *J*-filter) is inserted into the pulse sequence at a time equal to $(2\ ^1J_{\text{CH}})^{-1}$ after the initial ^1H 90° pulse (i.e., during the longer range delay

time Δ). First, the ${}^1J_{\text{CH}}$ delay time allows the directly ${}^{13}\text{C}$ -bonded ${}^1\text{H}$ vectors to move to an antiphase orientation. Then, the ${}^{13}\text{C}$ 90° pulse is applied to produce ${}^1J_{\text{CH}}$ multiple quantum coherence. This coherence is unobservable and is allowed to dissipate.

The greatest problem associated with HMBC involves the very large signals of the protons that are bonded to ${}^{12}\text{C}$ nuclei. When this ${}^1\text{H}$ - ${}^{12}\text{C}$ magnetization is incompletely canceled, t_1 noise ridges are produced that can greatly interfere with the analysis of HMBC spectra. A BIRD pulse cannot be used here, as in HMQC, because it would also suppress the longer range ${}^{13}\text{C}$ -bonded ${}^1\text{H}$ vectors we wish to observe. This interfering ${}^1\text{H}$ - ${}^{12}\text{C}$ magnetization was dealt with, until recently, by phase cycling. A much better solution is the incorporation of gradients to refocus longer range ${}^1\text{H}$ - ${}^{13}\text{C}$ magnetization selectively while leaving both direct ${}^1\text{H}$ - ${}^{13}\text{C}$ and ${}^1\text{H}$ - ${}^{12}\text{C}$ magnetization defocused and, thus, undetected. The gradient HMBC (gHMBC) pulse sequence is illustrated in Figure 7-17.

Nongradient HMBC occupies a unique position among 2D NMR experiments. Its incremented spectra are acquired in the phase-sensitive mode, whereas those of gHMBC are usually obtained in the absolute-value mode. Moreover, the developer of the HMBC experiment, Ad Bax, has recommended that nongradient HMBC data be processed in the mixed mode (i.e., by using the absolute-value mode in the t_2 dimension and the phase-sensitive mode in t_1). This method results in a $2^{1/2}$ gain in sensitivity relative to gHMBC data, which are acquired and processed in the absolute-value mode in both domains. Mixed-mode processing also gives rise to an increase in ${}^{13}\text{C}$ resolution, for the following reason. The individual resonances of absolute-value spectra are composed of a combination of both absorption and dispersion signals (Section 7-5c) such as those shown in Figure 2-11; while the resulting composite signals have a greater intensity than that of either their real or imaginary components alone, they are also broader and thus exhibit poorer resolution.

These two approaches to data processing (i.e., mixed mode and absolute value) are related to another interesting feature of the HMBC experiment. As remarkable as the use of gradients is in 2D experiments, they are not always the method of choice. Gradient-selected sequences involve a $2^{1/2}$ loss of sensitivity (Part C, introduction). A potential twofold increase in sensitivity, therefore, results for nongradient HMBC spectra that are acquired in the phase-sensitive mode and processed in the mixed mode ($2^{1/2} \times 2^{1/2} = 2$), relative to absolute-value gHMBC spectra. In addition, since phase-sensitive spectra can usually be linearly predicted fourfold, versus only twofold for absolute-value spectra (Section 7-5d), an additional sensitivity advantage is realized for nongradient experiments.

Choosing between HMBC and gHMBC may be approached as follows. If a sample is fairly concentrated and displays strong signals in its ${}^1\text{H}$ NMR spectrum, then t_1 noise ridges

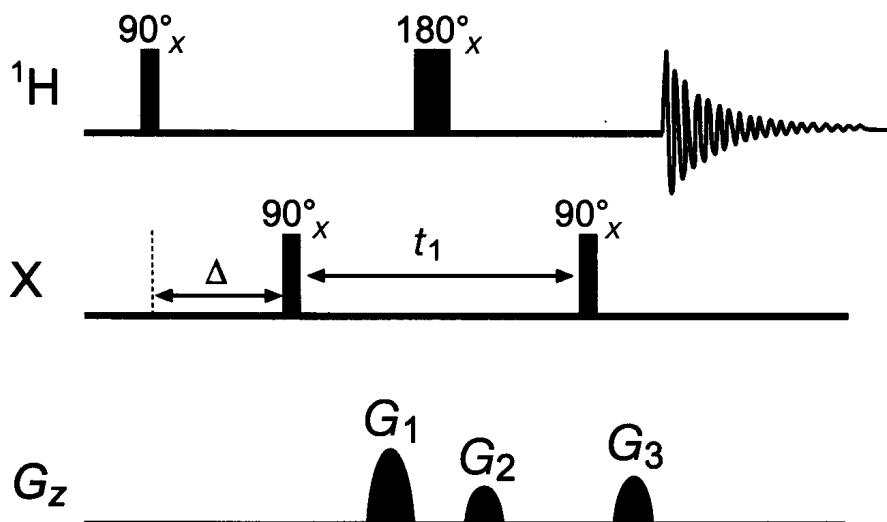


Figure 7-17 The gradient HMBC pulse sequence. The relative strengths of gradients G_1 , G_2 , and G_3 are 5, 3, and 4 G cm^{-1} , respectively, as shown, when $X = {}^{13}\text{C}$.

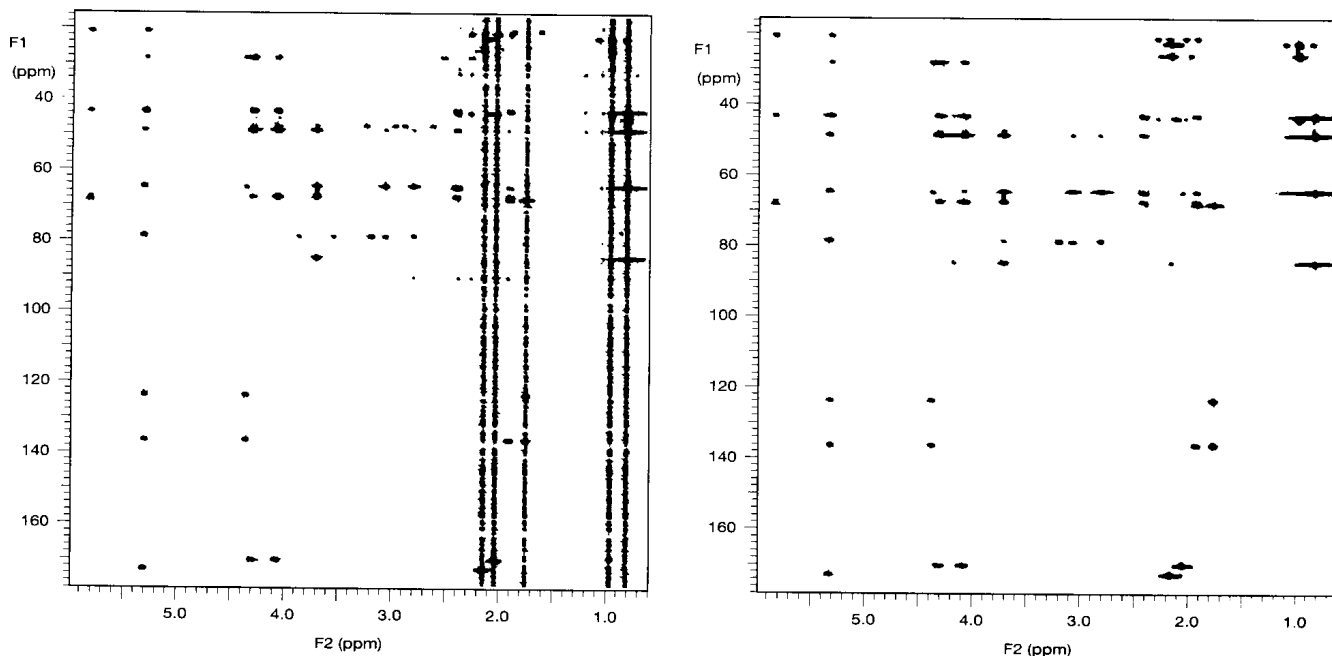


Figure 7-18 HMBC spectrum (left) and gradient HMBC spectrum (right) of T-2 toxin.

could be a major problem. If this is the case, gHMBC would certainly be the method of choice. If the opposite is true, however, then sensitivity, and not t_1 noise, is the major issue. In this case, a nongradient HMBC might be the preferred experimental method. Figure 7-18 of T-2 toxin (7-1) compares these two sequences for the first case, in which t_1 noise due to strong methyl signals in the δ 1–2 region is an obvious problem.

Since the time Δ of HMBC is so much larger than that of either HMQC or HSQC (~ 60 ms vs. 3.6 ms), the refocusing delays with accompanying ^{13}C decoupling of the latter experiments are not used, for reasons of sensitivity. Too much signal would be lost through relaxation processes in the approximately 60 ms that it would take the antiphase ^1H vectors to refocus prior to detection (Section 6-2).

Because of the uncertainty concerning both the location and intensity of correlations in HMBC contour plots, cross sections should be taken through individual chemical shifts on both the ^1H and ^{13}C axes.

The following parameters are appropriate for HMBC experiments:

1. $\Delta = \text{average}(2^n J_{\text{CH}})^{-1} \sim 1/(2 \times 8 \text{ Hz}) = 60 \text{ ms}$
2. steady-state scans = 32 (with gradients) or 8 (for nongradient versions)
3. $ns/i =$ multiple of 8 recommended
4. $ni = 256$ (with phase-sensitive data) or 512 (with absolute-value data)
5. $LP = 768$ (with phase-sensitive data) or 512 (with absolute-value data)
6. pseudo-echo, sine bell, or squared sine bell weighting (all of which can be left shifted to improve sensitivity) in the t_2 domain
7. Gaussian, cosine, or squared cosine weighting in t_1 (with phase-sensitive data) or pseudo-echo, sine bell, or squared sine bell weighting in t_1 (with absolute-value data)

7-9b The FLOCK Experiment

The FLOCK experiment (Section 6-2) is an X-nucleus-detected experiment which, despite its lower sensitivity compared with that of HMBC, is still very useful in certain circumstances. Another longer range ^1H -X chemical-shift correlation experiment is COLOC, and the X nucleus for both experiments is ^{13}C .

The principal disadvantage of the COLOC sequence derives from the fact that it is a *fixed-evolution-time* experiment (i.e., t_1 is incorporated into the delay time Δ_1). The major limitation with fixed- t_1 pulse sequences is that C–H correlations are considerably diminished, or completely absent, when the two- and three-bond ^1H – ^{13}C coupling constants of a C–H fragment are similar in magnitude to the ^1H – ^1H couplings of the same fragment. As can be seen from the compilations of coupling constants in Chapter 4, the latter situation is the rule rather than the exception. To minimize losing C–H correlations when ${}^nJ_{\text{CH}} \sim {}^nJ_{\text{HH}}$, people using COLOC have typically conducted the experiment twice: once with ${}^nJ_{\text{CH}}$ optimized for, perhaps, 5-Hz coupling constants and again with ${}^nJ_{\text{CH}}$ optimized for 10-Hz coupling constants.

The FLOCK sequence (so named because it contains three BIRD pulses) of Reynolds is similar to the rest of the pulse sequences that have been discussed in that it is a *variable-evolution-time* experiment (t_1 becomes progressively larger). FLOCK thus avoids the potential absence of C–H correlations. Its pulse sequence is given in Figure 7-19.

The FLOCK pulse sequence is reminiscent of the HETCOR sequence with its refocusing of desired vectors during t_1 , dephasing during Δ_1 , polarization transfer at the end of Δ_1 , and refocusing during Δ_2 . The three BIRD pulses in the FLOCK experiment act in the following way. The first is selective for ${}^1J_{\text{CH}}$ vectors during t_1 and permits the separation of their effect from that of ${}^nJ_{\text{CH}}$ vectors by appropriate phase cycling. The chemical shifts of protons directly bonded to ^{13}C are rotated through a *constant* angle and thus are not modulated. Similarly, ${}^1J_{\text{CH}}$ vectors are dephased through a variable angle that suppresses one-bond polarization transfer. In contrast, the chemical shifts of protons that are indirectly bonded to ^{13}C are rotated through a *variable* angle and, therefore, are modulated. Likewise, ${}^nJ_{\text{CH}}$ vectors are refocused and thus are set up to participate in longer range polarization transfer.

The second BIRD pulse is selective for ${}^nJ_{\text{CH}}$ vectors during Δ_1 and acts as a simple ^{13}C 180° pulse for ${}^1J_{\text{CH}}$ vectors, which tend to refocus. Nonetheless, there may be some one-bond polarization transfer. The ${}^nJ_{\text{CH}}$ vectors, however, move to antiphase for maximum polarization transfer. In addition, the BIRD pulse refocuses magnetic-field inhomogeneities for protons that are indirectly bonded to ^{13}C and refocuses the individual ${}^nJ_{\text{CH}}$ vector components (which themselves are defocusing) prior to polarization transfer.

The third BIRD pulse, during Δ_2 , also is selective for ${}^nJ_{\text{CH}}$ vectors, which are focused from an antiphase orientation. ^{13}C nuclei that are directly bonded to protons behave in either of two ways. On the one hand, the ${}^1J_{\text{CH}}$ vectors of the majority of ^{13}C nuclei, which have not undergone any polarization transfer, remain focused, but are eliminated by phase-cycling subtraction. On the other hand, the minority of ^{13}C nuclei that have undergone some polarization transfer remain at antiphase and are not observed.

In addition to a variable t_1 , FLOCK has four fixed delay times. The first delay time (for relaxation) is a function of the ^1H -, not the X-nucleus, T_1 's because, like HETCOR, FLOCK is a polarization transfer experiment. The second (τ , the delay in the BIRD pulses) is a

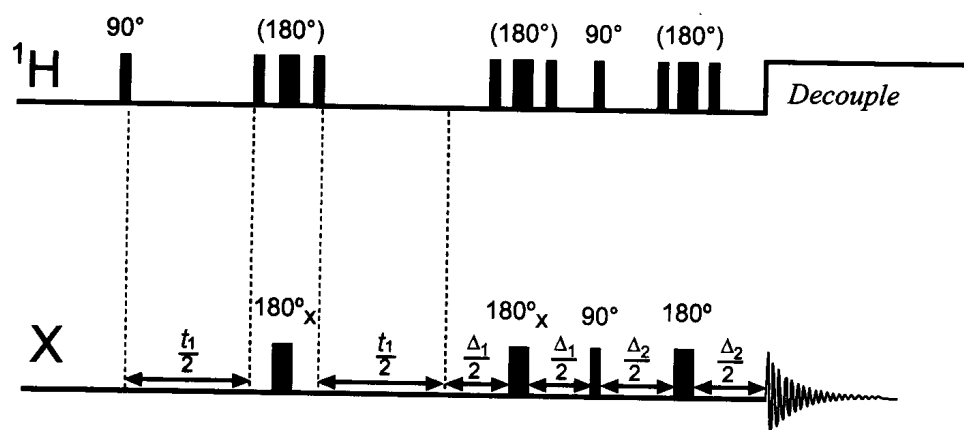


Figure 7-19 The FLOCK pulse sequence. The 180° ^1H pulses in parentheses are BIRD pulses ($90^\circ - \tau - 180^\circ - \tau - 90^\circ$) with $\tau = (2J_{\text{CH}})^{-1}$. The relative phases of the three pulses are $x, y, -x$ for the first BIRD pulse and $x, x, -x$ for the second and third BIRD pulses.

function of the one-bond C–H coupling and is usually optimized for 140 Hz. The third and fourth, Δ_1 and Δ_2 , are functions of ${}^nJ_{\text{CH}}$. They are set in the same compromise fashion as HMBC-for ${}^nJ_{\text{CH}} \sim 8$ Hz. In addition, they function like the delays in HETCOR, with Δ_1 optimized for ${}^1\text{H}$ defocusing and Δ_2 optimized for ${}^{13}\text{C}$ refocusing. Note that, because of the compromise value of Δ_2 (${}^nJ_{\text{CH}} = 2\text{--}15$ Hz), the sensitivity advantage of HMBC over FLOCK or COLOC is greater than the 8 : 1 predicted by theory (Section 7-8).

${}^1\text{H}$ decoupling for FLOCK typically is performed as the ${}^{13}\text{C}$ signal is acquired and is accomplished with the WALTZ sequence (Section 5-8). FLOCK data are presented in either the phase-sensitive or the absolute-value mode. Because of uncertainty concerning both the location and intensity of correlations in FLOCK contour plots, cross sections should be taken through individual chemical shifts on both the ${}^1\text{H}$ and ${}^{13}\text{C}$ axes, as with HMBC spectra.

As stated in Section 7-8, on those occasions when (i) the ${}^{13}\text{C}$ spectrum is more congested than the ${}^1\text{H}$ spectrum and (ii) a sufficient amount of the sample (~ 20 mg for MW $\sim 400\text{--}750$) can be dissolved to obtain ${}^{13}\text{C}$ spectra in reasonable time, FLOCK spectra can be indispensable in the elucidation of molecular structures and the assignment of chemical shifts.

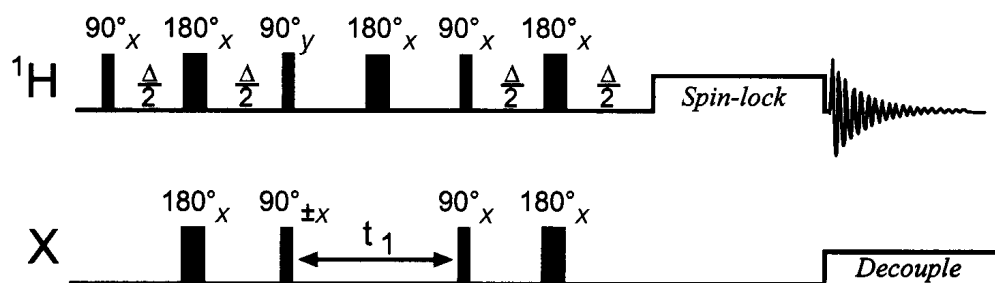
The following parameters are appropriate for FLOCK experiments:

1. $\Delta_1 = (2 {}^nJ_{\text{CH}})^{-1} \sim 1/(2 \times 8 \text{ Hz}) = 60 \text{ ms}$
2. $\Delta_2 = (4 {}^nJ_{\text{CH}})^{-1} \sim 1/(4 \times 8 \text{ Hz}) = 30 \text{ ms}$
3. $\tau = (2 {}^1J_{\text{CH}})^{-1} \sim 1/(2 \times 140 \text{ Hz}) = 3.6 \text{ ms}$
4. RT = $1 - 2T_1$ of ${}^1\text{H}$ (0.8 s for MW $\sim 400\text{--}450$, 0.5 s for MW $\sim 500\text{--}750$)
5. steady-state scans = 2
6. ns/i = multiple of 32
7. ni = 256 (with phase-sensitive data) or 512 (with absolute-value data)
8. LP = 768 (with phase-sensitive data) or 512 (with absolute-value data)
9. Gaussian, cosine, or squared cosine weighting (with phase-sensitive data) or pseudo-echo, sine bell, or squared sine bell weighting (with absolute-value data), all left shifted to improve sensitivity

7-9c The HSQC-TOCSY Experiment

The HSQC-TOCSY experiment gives essentially the same information as TOCSY, but has the important advantage of *spectral dispersion*. When considerable spectral overlap exists in a ${}^1\text{H}$ NMR spectrum, subsequent TOCSY spectra may be of limited utility in establishing ${}^1\text{H}$ spin systems. The X-nucleus spectrum, however, possesses much greater spectral dispersion, owing to its larger range of chemical shifts. It is this increased chemical-shift range that is critical to the utility of the HSQC-TOCSY experiment. Rather than being correlated with the chemical shifts of other, possibly overlapping, protons, the ${}^1\text{H}$ signals are correlated with the chemical shifts of directly bonded X nuclei, which are far less likely to suffer similar overlap. In the HSQC-TOCSY experiment for protons and carbons, for example, magnetization is transferred from a ${}^1\text{H}$ to its directly bonded ${}^{13}\text{C}$, just as in a regular HSQC experiment. A TOCSY spin-lock mixing scheme, however, is placed where acquisition normally would occur. The HSQC-TOCSY pulse sequence is pictured in Figure 7-20.

Figure 7-20 The HSQC-TOCSY pulse sequence.



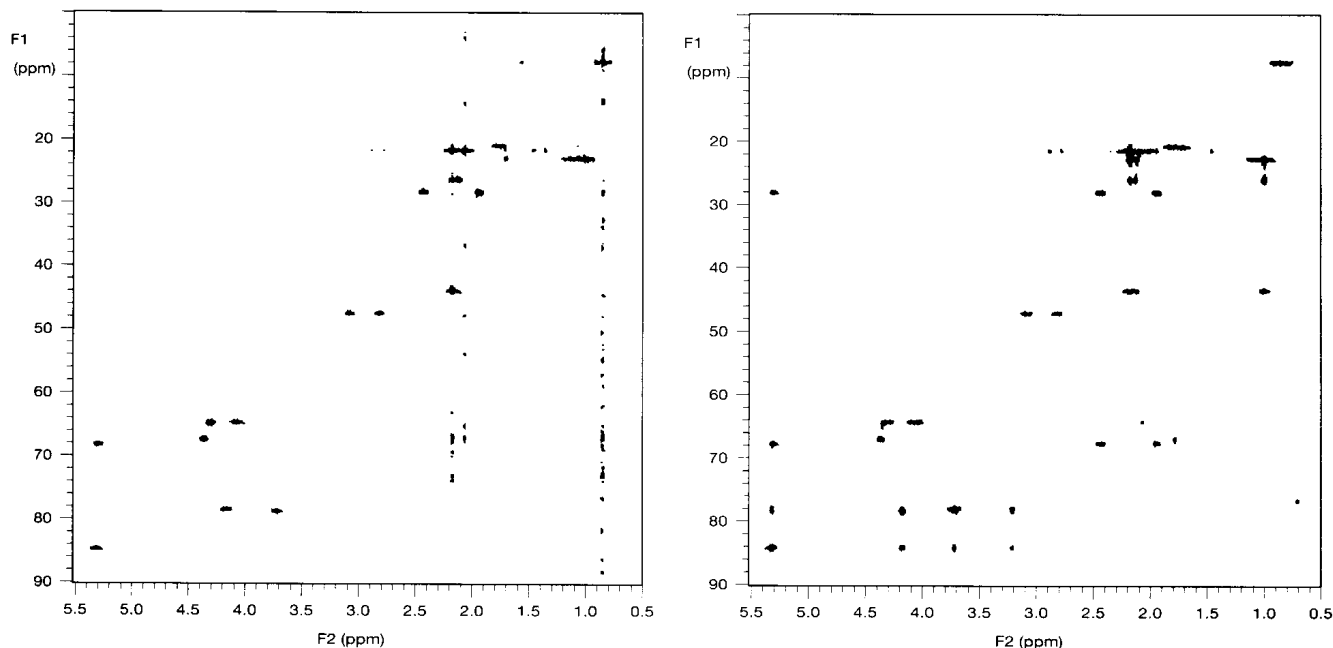


Figure 7-21 HSQC spectrum (left) and HSQC-TOCSY spectrum (right) of T-2 toxin.

After the HSQC part of the experiment, ^1H magnetization is transferred to other protons in the spin system and is detected, at various mixing times, in the TOCSY part of the experiment. If a mixing time of approximately 12 ms is used, a spectrum is produced that exhibits correlations between carbons and only their directly attached protons. Longer mixing times are thus required for the transfer of magnetization to more remote protons. The process also demonstrates a limitation of the HSQC-TOCSY experiment with respect to HMBC: correlations are observed only for *protonated* X nuclei. Quaternary carbons do not participate in HSQC-TOCSY. In addition, HSQC-TOCSY is less sensitive, by at least a factor of two, than the corresponding HSQC experiment, because magnetization arising from a single ^1H - ^{13}C system is spread out over several proton signals.

A comparison of HSQC and HSQC-TOCSY spectra in Figure 7-21 for T-2 toxin shows the same extended coupling as that of the COSY and TOCSY spectra in Figure 7-13. For example, C-4 (δ 84.5) shows connectivity to H-4 (δ 5.31) in both the HSQC and HSQC-TOCSY spectra, as well as relayed connectivity to H-3 (δ 4.16), H-2 (δ 3.70), and OH-3 (δ 3.20) in the HSQC-TOCSY spectrum (see 7-1 for numbering scheme).

Parameters for the HSQC-TOCSY experiment are the same as for the component HSQC and TOCSY experiments.

7-10 Homonuclear Chemical-Shift Correlation Via Dipolar Coupling

Nuclei that undergo mutual relaxation via dipolar coupling are said to be *dipolar coupled* and give rise to the nuclear Overhauser effect. Whether the nuclei in question also may be scalar (or spin) coupled is not pertinent to the discussion (Section 5-4). NOE experiments can be either homonuclear or heteronuclear in nature, although the former, involving protons, are much more common. One-dimensional homonuclear Overhauser experiments are discussed in Section 7-3; their 2D versions, NOESY and ROESY, are treated in this section.

Similar to the COSY experiments, contour plots for NOESY and ROESY are symmetric, with both the spectral widths and the data point resolutions almost always identical. Linear prediction can, again, help greatly in making DR_1 equal to DR_2 by keeping the data

accumulation time within acceptable limits. Because of the lengthy-buildup nature of the NOE, the experimental times required for NOESY and ROESY experiments tend to be much longer than those of 2D experiments showing spin-coupling correlations.

It should also be remembered that the results of 2D NOE experiments are averaged (i.e., an AB cross peak represents the average of the enhancement of H_B when H_A is irradiated, and vice versa). As we saw in Section 7-3, the two enhancements ($A\{B\}$ and $B\{A\}$) usually are different, sometimes very much so. The resulting averaged cross peaks can thus be small and difficult to detect.

The apparent absence of NOE cross peaks must, therefore, be interpreted with caution. In situations in which the presence, or especially the absence, of NOE's are critical to stereochemical decisions (e.g., determining whether substituents on a carbon-carbon double bond are cis or trans to each other) and when the existence of cross peaks is uncertain, selective 1D NOE experiments, such as DPGSE-NOE, should always be performed.

7-10a The NOESY Experiment

The NOESY experiment (Section 6-3) is an extension of the basic COSY experiment with a mixing time and third 90° read pulse following the original two-pulse sequence. NOESY experiments should be performed in the phase-sensitive mode in order to distinguish cross peaks due to *positive* NOE's (i.e., those enhancements which would be positive in 1D experiments and whose cross peaks are phased positively in these 2D experiments) from both COSY artifacts and EXSY cross peaks, which may be present in the spectrum, but will appear as negatively phased signals. Cross peaks due to *negative* NOE's (negative enhancements in 1D experiments) and diagonal signals also appear as negative signals. Fortunately, COSY artifacts in NOESY spectra are *not* common. While they can be easily distinguished from positive NOESY cross peaks by their opposite phase, their greatest threat to the NOESY experiment lies in the cancelation, complete or nearly so, of real, positive cross peaks.

If signal cancelation due to COSY artifacts is suspected, selective 1D NOE experiments such as those just discussed should be conducted. These require little additional time and can prevent confusion due to misinterpretation of apparent NOE results. The presence of COSY-induced signal cancelation can be tested for, albeit not rapidly, by rerunning the NOESY experiment at a lower temperature or a lower field strength. Decreases in temperature and field strength increase the NOE's of small molecules by increasing the dipole-dipole contribution to overall relaxation (Sections 5-1 and 5-4, Appendix 5) and decreasing T_1 's (Section 5-1 and Appendix 5), respectively. COSY artifacts, which might be present, will not be affected to the same degree as real NOESY cross peaks.

The likelihood of signal cancelation due to EXSY artifacts is rather remote. If such nulling is believed to be occurring, the same remedies as those given for COSY artifacts are applicable. In addition to their aforementioned effects on NOE's, decreases in temperature reduce the EXSY cross peaks of small molecules by decreasing exchange rates.

The successful observation of NOESY correlations can depend critically on the choice of two parameters: the mixing (τ_m) and repetition times, both of which depend on the spread of $^1H T_1$'s in a molecule. Recommended RT's are about $2T_1$ for small to intermediate-sized molecules. They should be set to 1.2–1.8 s for small molecules (MW ~ 400 –450), 0.9–1.2 s for intermediate-sized molecules (MW ~ 500 –750), and, more conservatively, to 2–3 s when the T_1 's are unknown. The choice of mixing times also is important, because if τ_m is too short, NOE enhancements do not have a chance to develop to detectable intensities, and NOESY cross peaks are not observed. On the other hand, if τ_m is too long, the NOE enhancements disappear because of relaxation, and, again, cross peaks are absent. Compromise mixing times should be about the average T_1 value and can be set to 0.3–0.6 s for MW ~ 400 –750 and 1–2 s for very small molecules.

Another reason for the careful selection of RT is that NOESY spectra are susceptible to artifacts from pulsing too rapidly. Problems also occur for molecules (MW ~ 750 –2,000) in the crossover region in which NOESY cross-peak intensities approach zero for even

spatially proximate protons (Section 6-3 and Figure 6-31). The latter complication is absent in the ROESY experiment, which is discussed in the next section.

Chemical and conformational exchange effects are observed in NOESY spectra, but they are not usually troublesome if the experiment is performed in the phase-sensitive mode. If these exchange processes occur on the same time scales that have been discussed here, the same NOESY parameters can be used for EXSY experiments, but τ_m now is the average time of the exchange process under investigation. The following parameters are appropriate for NOESY experiments:

1. $\tau_m = 0.3\text{--}0.6$ s (for average-sized or small molecules)
2. RT $\sim 0.9\text{--}1.8$ s (see preceding discussion), or 2–3 s for very small molecules
3. steady-state scans = 8
4. $ns/i =$ multiple of 8
5. $n_i = 256$
6. LP = 768
7. Gaussian, cosine, or squared cosine weighting

An alternative solution to the problem of NOE's that occur in the zero-intensity crossover region is the use of lower field magnets. NOE's that are absent at 500 MHz can sometimes be observed at, for example, 300 MHz.

7-10b The ROESY Experiment

The ROESY experiment (Section 6-3) is basically the same as TOCSY, except for the values of two important parameters: (i) the spin-lock mixing time is generally 100–500 ms, compared with 20–150 ms for TOCSY, and (ii) the spin-lock power is considerably lower than that of TOCSY. Since ROE enhancement factors do not go through zero intensity for molecules of MW $\sim 750\text{--}2,000$ as NOE enhancements do, all ROESY cross peaks are of the same sign, and ROESY is used especially for intermediate-sized molecules. The ROESY experiment is performed in the phase-sensitive mode in order to distinguish real ROESY cross peaks (phased positively) from both TOCSY artifacts and EXSY cross peaks, which, if present in the spectrum, are displayed as negative signals. Diagonal signals also are observed as negative resonances.

TOCSY artifacts are to be expected in ROESY spectra to some degree, particularly when the ROESY mixing time is close to the upper limit of the TOCSY range (>100 ms). While the two types of cross peaks can be easily distinguished from each other by their opposite phase, the problem with TOCSY signals in ROESY spectra (as it is with COSY signals in NOESY spectra, but more so) is cross-peak cancelation. TOCSY signals, however, are greatly suppressed in the transverse-ROESY (or T-ROESY) experiment. A comparison of NOESY and T-ROESY spectra of T-2 toxin (Figure 7-22) shows essentially no difference between the two experiments for this molecule.

The same considerations that are relevant for the selection of mixing times and relaxation delay times for NOESY experiments also apply to ROESY [i.e., suggested RT's are about $2T_1$ for small to intermediate-sized molecules (MW $\sim 400\text{--}750$) and should generally be in the 0.9–1.8-s range (Section 7-10a)]. Spin-lock mixing times are in the 100–500-ms range—closer to 100 ms for larger molecules and 400–500 ms for smaller molecules.

By analogy with NOESY experiments, ROESY parameters can be used for EXSY experiments. The following parameters are appropriate for ROESY experiments:

1. spin-lock mixing time = 100–500 ms
2. RT = 0.9–1.8 s, or 2–3 s for very small molecules
3. steady-state scans = 32, or 64 for long mixing times

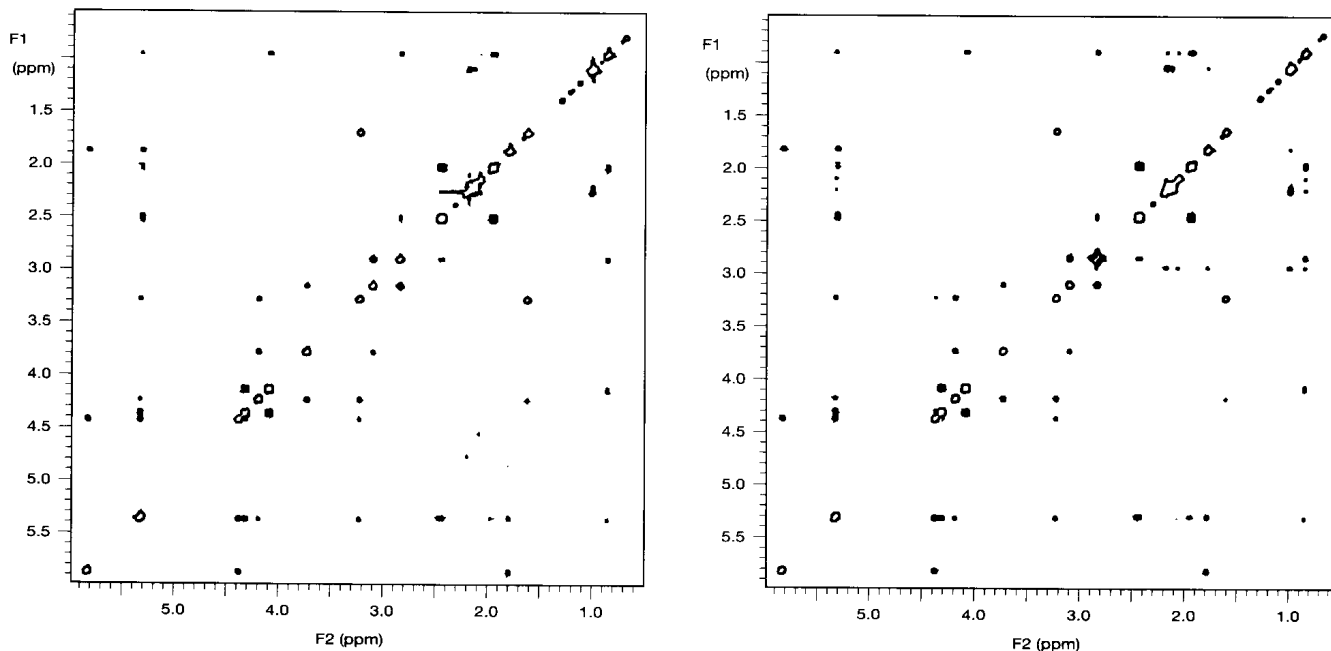


Figure 7-22 NOESY spectrum (left) and T-ROESY spectrum (right) of T-2 toxin.

4. $ns/i = \text{multiple of } 8$
5. $n_i = 256$
6. $LP = 768$
7. Gaussian, cosine, or squared cosine weighting

7-11 Miscellaneous 1D and 2D Experiments

7-11a The 1D TOCSY Experiment

As mentioned in Section 7-7b, the 1D version of the TOCSY experiment is especially useful for larger molecules that possess complicated and overlapping ^1H spin systems. The 2D TOCSY spectra of classes of molecules such as oligosaccharides can be very difficult to interpret. 1D TOCSY experiments, however, permit the mapping of entire spin systems when the chemical shift of just one member of the system is distinct. An example is the anomeric (H-1) protons of oligosaccharides, which are situated at higher frequency (downfield) from the carbinol protons.

The single most important factor that has enabled 1D TOCSY experiments to become such a powerful tool is the extraordinary selectivity of modern shaped pulses (Section 5-8). These pulses can selectively irradiate a middle signal for which the adjacent resonances are remarkably close. Three 1D TOCSY spectra that do not even begin to test the selectivity of the technique are shown in Figure 7-23 for a four-spin system of T-2 toxin (7-1) composed of H-2 (δ 3.70), H-3 (δ 4.16), OH-3 (δ 3.20), and H-4 (δ 5.31). H-2 has been irradiated selectively, and the spectra are for (a) zero, (b) 120 ms, and (c) 300 ms. No magnetization is transferred for a mixing time of zero, and, as expected, only H-2 is found in (a). After 120 ms, magnetization has been transferred to the vicinal coupling partner (H-3), and its signal is detected. After 300 ms, magnetization has been further transferred from H-3 to OH-3 and H-4 (i.e., throughout the entire spin system), and the resonances of all four protons are observed. Figure 7-24 illustrates the results of taking horizontal traces through the chemical shift of (i) H-2 (δ 3.70) for 1D (bottom; see Figure 7-23) and 2D TOCSY (middle; see Figure 7-13) spectra and (ii) C-2 (δ 79.2) for the HSQC-TOCSY spectrum (top; see Figure 7-21) of T-2

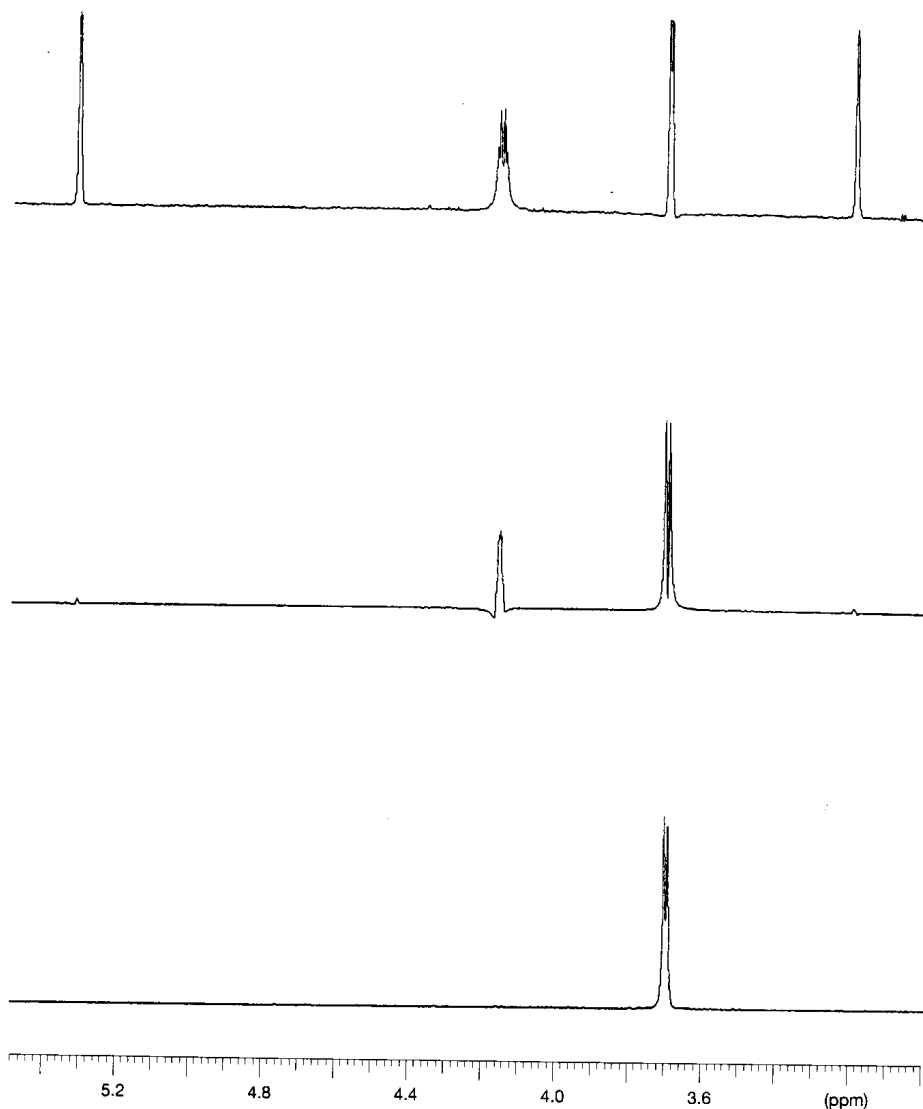


Figure 7-23 1D-TOCSY spectra for a four-spin system of T-2 toxin for mixing times: 0 ms (bottom), 120 ms (middle), and 300 ms (top).

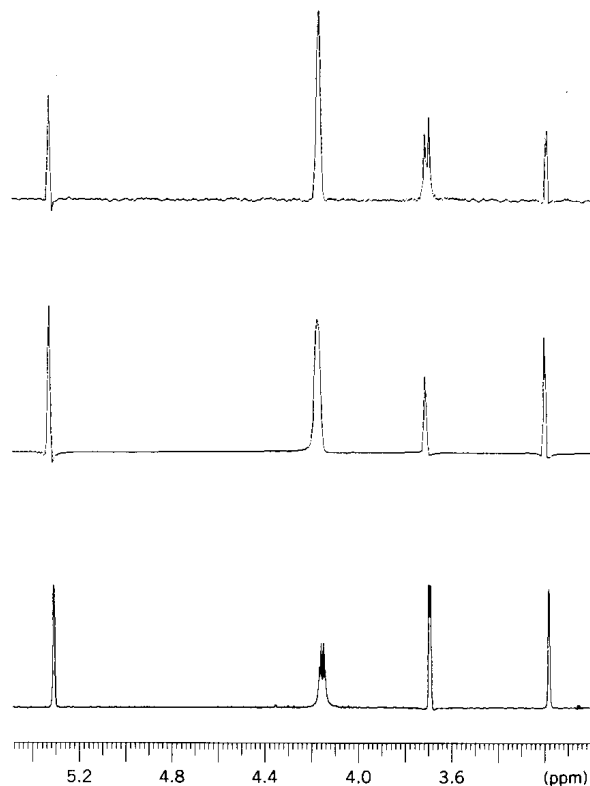
toxin. The resolution is clearly best in the 1D TOCSY trace, but is largely equivalent in the other two.

The 1D TOCSY experiment is essentially the same as the 2D version, but with the parameters being those of a 1D, rather than a 2D, experiment. The initial, hard 90° pulse is replaced by either a selective, soft 90° pulse or, still better, a DPGSE sequence such as that shown in Figure 7-5 (the initial 90° pulse and the pair of 180° pulses with their attendant sets of gradients).

7-11b The Multiplicity-Edited HSQC Experiment

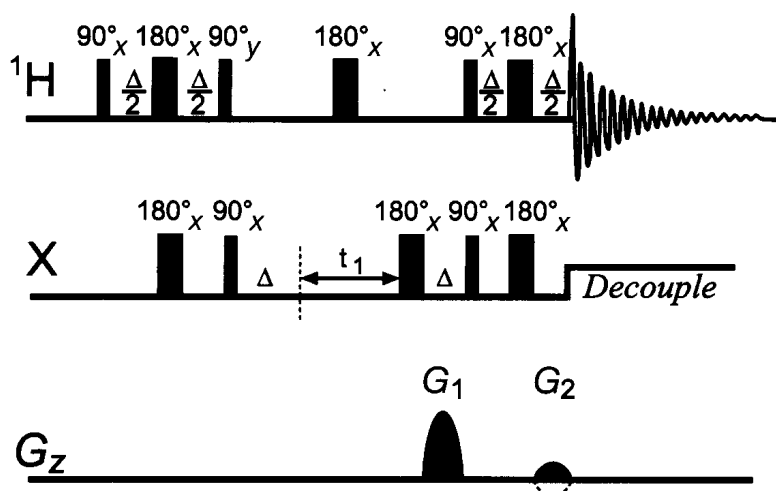
In dealing with any compound that contains an appreciable number of carbons, it is highly recommended that one obtain a ^{13}C NMR spectrum. The information that can thereby be learned is especially important when some degree of uncertainty exists concerning the structure of the compound in question. It is further recommended to record both DEPT and HSQC (again, particularly for unknowns), so that each experiment can serve as a check on the other and better reveal spectral anomalies such as overlapping signals and, more importantly, any cancelation of signals. If a sample is very limited, however, there might not be enough material to determine a ^{13}C NMR spectrum or an edited ^{13}C spectrum. In that case, the multiplicity-edited HSQC experiment can be especially useful.

Figure 7-24 Comparison spectra: Selective 1D-TOCSY (bottom), 2D-TOCSY trace (middle), and HSQC-TOCSY trace (top).



The gradient-selected, spin-echo HSQC experiment (cf. Section 6-6: DEPT-HMQC) permits one to obtain a multiplicity-edited HSQC spectrum, in which XH and XH₃ groups are phased in one direction (typically positive) and XH₂ groups are phased oppositely (negatively). This experiment suffers two disadvantages: (i) a 15–25% decrease in sensitivity compared with the corresponding HSQC sequence, with larger molecules that have shorter T_1 's exhibiting the greater reductions, and (ii) potential cancelation of closely situated negative methylene and positive methine or methyl signals. The experiment, however, largely eliminates the need to carry out a DEPT experiment, except in the case of complete unknowns. The multiplicity-edited HSQC experiment is basically an HSQC pulse sequence in which two additional delay times (Δ) and a 180° X-pulse are inserted around t_1 , as in Figure 7-25.

Figure 7-25 The multiplicity-edited gradient HSQC pulse sequence. The relative strengths of gradients G_1 and G_2 are 4 and 1 G cm⁻¹, respectively as shown, when X = ¹³C.



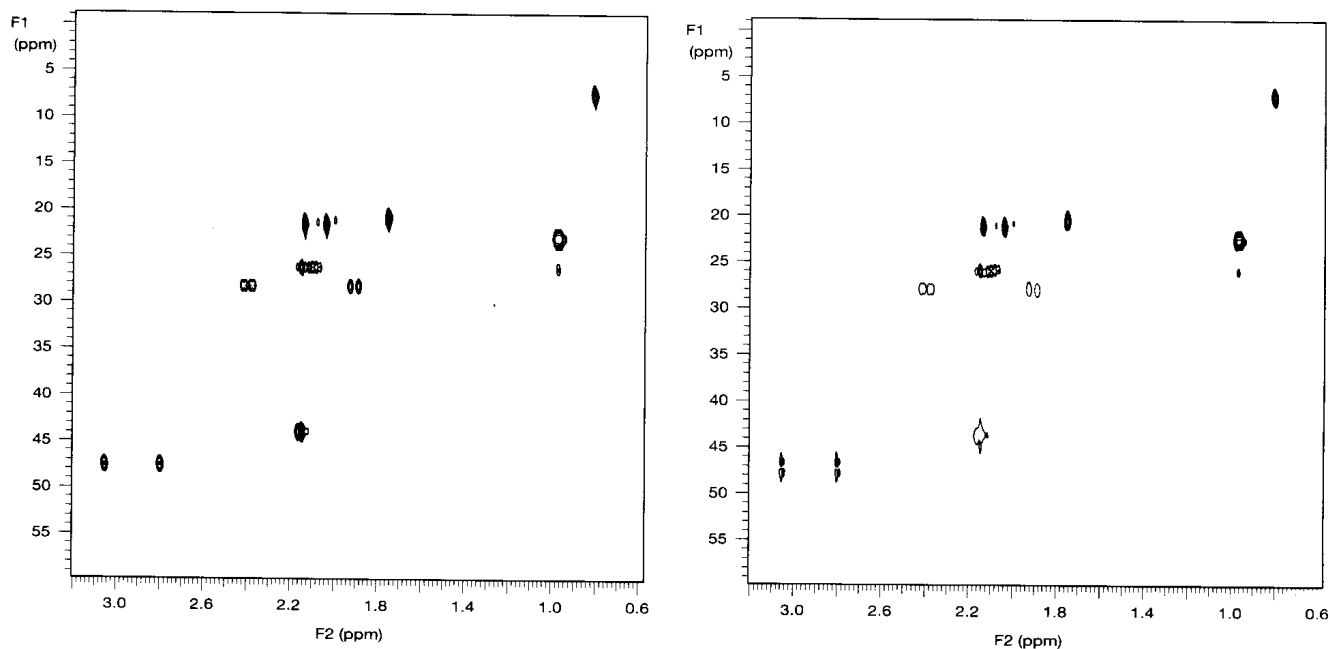


Figure 7-26 Expansions: HSQC spectrum (left) and multiplicity-edited HSQC spectrum (right) of T-2 toxin.

Comparison HSQC spectra of T-2 toxin (**7-1**) are given in Figure 7-26. In the edited HSQC spectrum, CH and CH₃ cross peaks are shown as closed contours and CH₂ cross peaks as open signals. Cross peaks arising from three methylene groups appear at the following C/H coordinates: δ 27.9/ δ 2.41, 1.91 (7), δ 43.8/ δ 2.17 (2'), and δ 47.4/ δ 3.06, 2.80 (13). Open contours clearly differentiate the cross peaks due to methylenes 2' and 7 from the others, but those of methylene-13 look like dispersive signals (Figure 2-11). The reason for their unusual appearance is that one-bond C–H coupling constants for epoxides are about 175 Hz and thus approximately 40 Hz different from the average value of 140 Hz used for $^1J_{\text{CH}}$'s. By comparison, the $^1J_{\text{CH}}$ values for the sp³ carbons are much closer to 140 Hz, ranging from 125–130 Hz.

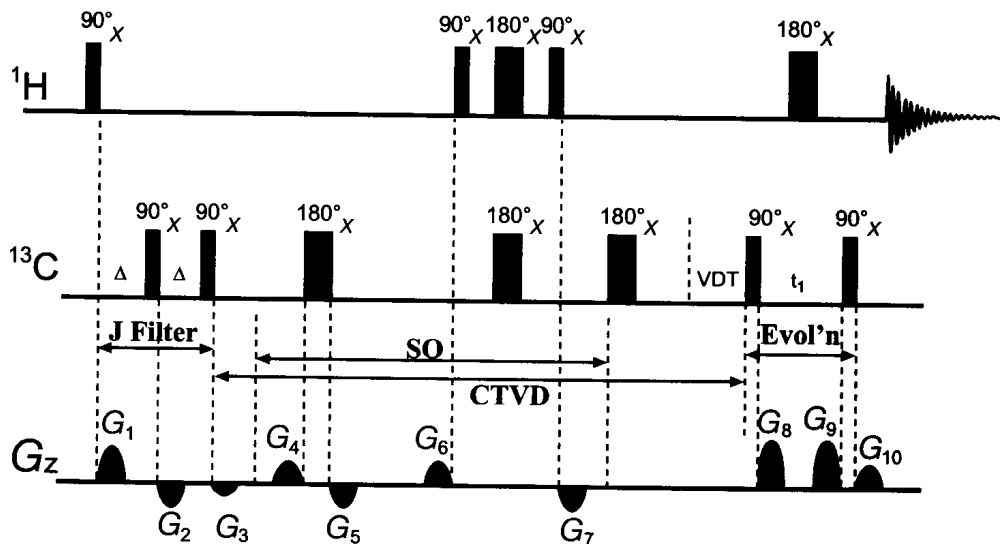
The following parameters are appropriate for edited HSQC experiments:

1. $\Delta/2 = (4 \ ^1J_{\text{CH}})^{-1} \sim 1/(4 \times 140 \text{ Hz}) = 1.8 \text{ ms}$
2. steady-state scans = 32
3. ns/i = multiple of 8
4. ni = 256
5. LP = 768 (recommended), but can be up to sixteenfold
6. Gaussian, cosine, or squared cosine weighting

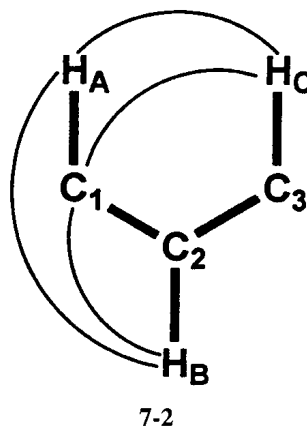
7-11c The 2J , 3J -HMBC Experiment

In Section 7-9a, we saw that the critical delay time Δ in the HMBC experiment is set to approximately 8 Hz, which is an average value of $(2^n J_{\text{CH}})^{-1}$, with n usually equal to 2 or 3. Implicit in this relationship is the fact that the HMBC experiment cannot differentiate two-bond from three-bond (and occasionally greater) X–H couplings. This is an unfortunate shortcoming, especially with regard to problems involving structural elucidation (Chapter 8).

Figure 7-27 The ${}^2J, {}^3J$ -HMBC pulse sequence. The relative strengths of the 10 gradients are as follows: (i) dual-stage, low-pass J -filter (G_1 – G_3) 10, –6.63, –3.37; (ii) STAR operator (G_4 – G_7) 20, –20, 20, –20; (iii) coherence selection (G_8 – G_{10}) 5, 5, 2.52 G cm^{-1} , respectively.



Recently, however, Krishnamurthy and Martin, developed a variation of the HMBC experiment—the ${}^2J, {}^3J$ -HMBC pulse sequence shown in Figure 7-27—that can distinguish between two-bond and three-bond (or greater) X–H couplings for *protonated* carbons or nitrogens. In this regard, the ${}^2J, {}^3J$ -HMBC experiment is somewhat analogous to the ${}^{13}\text{C}$ -detected, longer range C–H correlation XCORFE experiment of Reynolds. The basis of the two- and three-bond differentiation lies in the modulation of two-bond X–H couplings by three-bond H–H couplings and is illustrated for C–H couplings in 7-2. If we examine the coupling between H_A and H_B , on the one hand, and H_A and H_C , on the other, we see that H_A



can be three-bond (vicinally) coupled to H_B , but only weakly four-bond (${}^4J_{\text{HH}} \sim 0$), if at all, to H_C (Chapter 4). If we next consider the two-bond coupling between C_1 and H_B and the three-bond coupling between C_1 and H_C , we conclude that H_A can modulate the coupling of C_1 to H_B , but not that of C_1 to H_C .

The experimental consequence of this H–H modulation of C–H couplings is that cross peaks due to two-bond C–H couplings are tilted and look somewhat like COSY45 cross peaks (with the tilting being, however, all in the same direction). Cross peaks arising from C–H couplings of three or more bonds are not similarly modulated and thus exhibit no tilting. A ${}^2J, {}^3J$ -HMBC spectrum of T-2 toxin (7-1) is given in Figure 7-28.

Several features can be observed in the two spectra shown. First, the tilting of two-bond cross peaks appearing at the coordinates $\delta 26.0/\delta 2.17$ ($\text{C}3', \text{H}2'$) and $\delta 26.0/\delta 0.96$ and

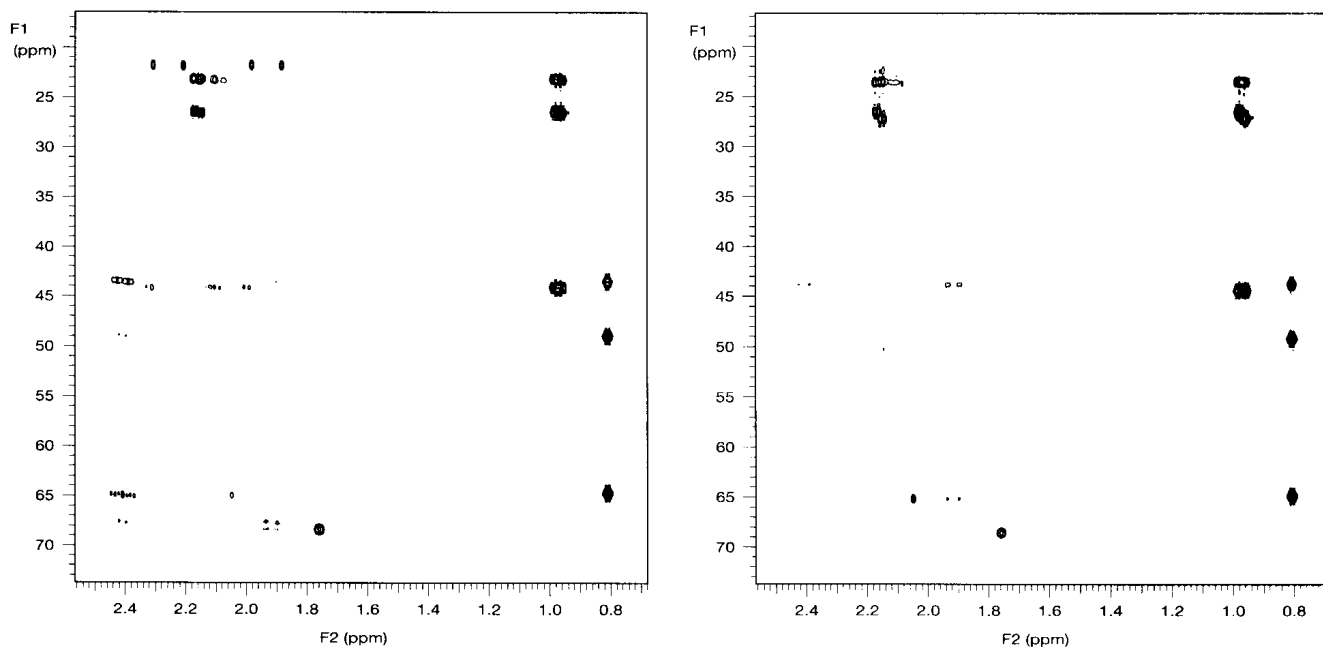


Figure 7-28 Expansions: HMBC spectrum (left) and ${}^2J, {}^3J$ -HMBC spectrum (right) of T-2 toxin.

0.98 (C3', H4' and H5') is obvious. Second, the lower sensitivity of the ${}^2J, {}^3J$ -HMBC experiment becomes evident when one realizes that, while both HMBC experiments were performed with the same number of increments and the same number of transients per increment, the ${}^2J, {}^3J$ -HMBC spectrum is shown at a vertical scale three times that of the HMBC spectrum. A third and not-so-obvious feature of these spectra is the absence of tilting of three-bond cross peaks in the ${}^2J, {}^3J$ -HMBC spectrum, compared with the normal HMBC spectrum. General tilting of cross peaks is present in HMBC spectra due to homonuclear coupling modulation, although insufficient digital resolution in the ν_1 domain often renders such tilting unobservable. This tilting can be seen for most of the cross peaks in the lower left quadrant of the HMBC spectrum in the figure. Most of the corresponding cross peaks are not as visible in the ${}^2J, {}^3J$ -HMBC spectrum, but careful inspection of those cross peaks that are visible reveals that they lie parallel to the ν_2 axis and are not tilted.

In addition to discriminating between two- and three-bond X-H couplings, the ${}^2J, {}^3J$ -HMBC experiment makes use of what is known as *accordion excitation*. In this technique, critical vector dephasing and refocusing times are varied so that the experiment is optimized for a range of two- and three-bond X-H couplings and not for just an average ${}^nJ_{XH}$.

In performing the ${}^2J, {}^3J$ -HMBC experiment, the chemist must be mindful of several things. First, the experiment is applicable only to protonated nuclei and should be performed in addition to the normal HMBC experiment. Like the COSY and DQF-COSY experiments, HMBC and ${}^2J, {}^3J$ -HMBC are complementary, not supplementary. Second, discrimination of two- and three-bond X-H couplings relies on the presence of adequate vicinal (three-bond) H-H coupling. When the coupling constants involved are either very small or absent, the resulting cross peaks arising from two-bond X-H couplings may exhibit negligible, or no, tilting, respectively. Third, the degree of cross-peak tilting can be adjusted by the operator. The greater the desired tilting, however, the longer are the required delay times. This result, in turn, decreases the sensitivity of the experiment. Nevertheless, if properly used, the ${}^2J, {}^3J$ -HMBC experiment promises to become a crucial method for those who determine molecular structures.

The following parameters are appropriate for 2J , 3J -HMBC experiments:

1. $^nJ_{\min} = 4$ Hz and $^nJ_{\max} = 8$ Hz
2. steady-state scans = 32
3. ni = 512
4. LP = 512 (absolute-value data)
5. pseudo-echo, sine bell, or squared sine bell weighting (all of which can be left shifted to improve sensitivity)

Bibliography

- 7.1. J. C. Hoch and A. S. Stern, *NMR Data Processing*. New York: Wiley-Liss, 1996.
- 7.2. W. F. Reynolds and R. G. Enriquez, *J. Nat. Prod.*, **65**, 221 (2002).
- 7.3. C. Griesinger, H. Schwalbe, J. Schleucher, and M. Sattler, in W. R. Croasmun and R. M. K. Carlson, eds., *Two Dimensional NMR Spectroscopy: Applications for Chemists and Biochemists*, 2d ed. New York: VCH, 1994, p. 514.

8

Structural Elucidation: An Example

A considerable number of NMR experiments have been introduced and discussed in this book. In order to illustrate how a series of such experiments is used in practice, we will take the reader through a complete structural elucidation of the compound T-2 toxin, many of whose 2D spectra were encountered in Chapter 7. If we had no knowledge of the compound's structure, our study would begin with the determination of its infrared, ^1H NMR, ^{13}C NMR, and high-resolution mass spectra. T-2 toxin is a white solid that is soluble in chloroform.

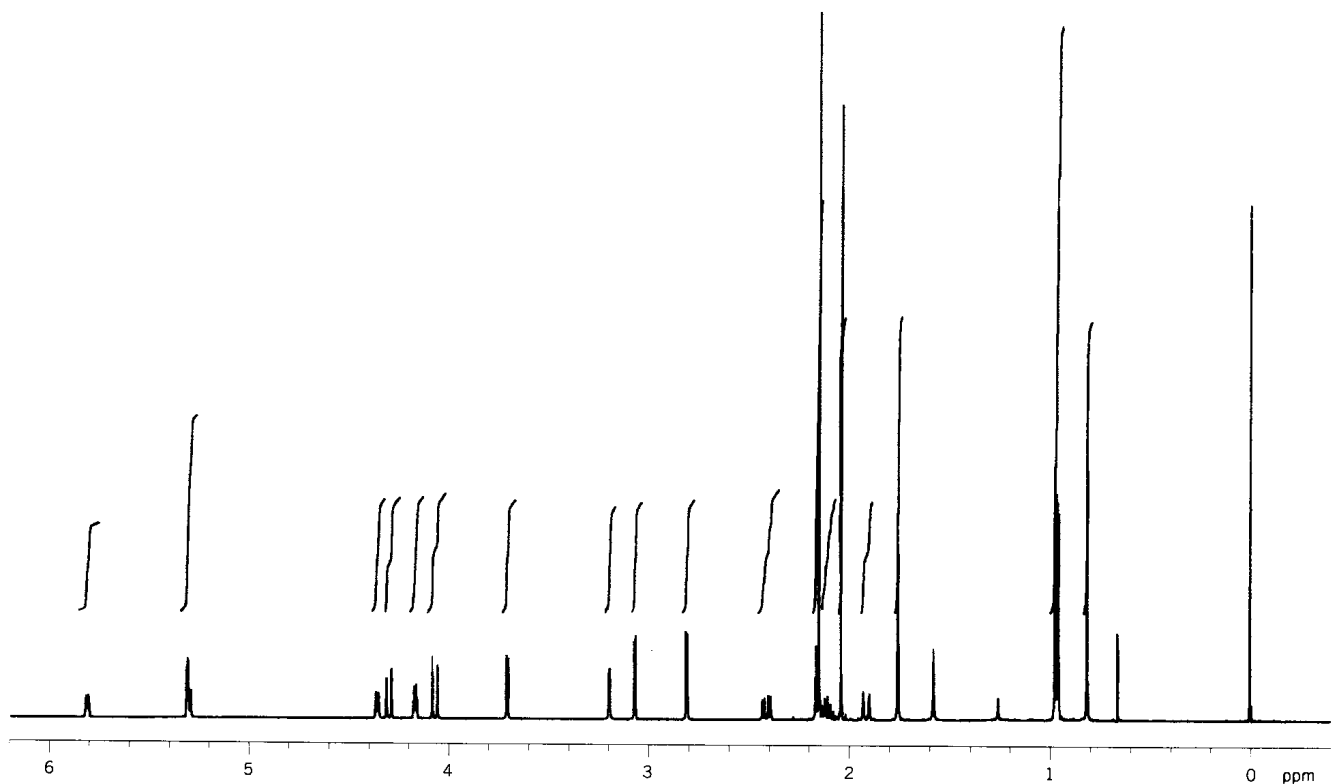
The high-resolution mass spectrum ($\text{MW} = 466.5573$) gives us several pieces of information about the compound. The even molecular weight (466) indicates that the unknown contains an even number of nitrogen atoms and probably none at all. (Zero, as in the APT experiment, is considered to be an even number.) If we make the preliminary, and usually justified, assumption that the unknown compound contains only carbon, hydrogen, and oxygen, the high-resolution, mass spectral-determined molecular weight supports a molecular formula of $\text{C}_{24}\text{H}_{34}\text{O}_9$. This formula, in turn, indicates the presence of eight units of unsaturation. While that unsaturation number is compatible with the presence of an aromatic compound, the H-to-C ratio appreciably greater than unity suggests that the unknown compound is likely composed primarily of aliphatic carbons. The presumptive molecular formula also indicates that T-2 toxin is heavily oxygenated.

Strong infrared absorptions centered at $1,740$ and $1,100\text{--}1,300\text{ cm}^{-1}$ suggest the presence of two or more carbonyl groups, which more likely are ester functionalities than ketone groups. Moreover, the occurrence of 9 oxygens in the molecular formula supports the inference that the carbonyl absorptions are probably due to ester, rather than ketone, groups.

8-1 ^1H NMR Data

The $500\text{ MHz } ^1\text{H}$ NMR spectrum of a 15-mg sample of the unknown compound is shown in Figure 8-1. The ^1H signals are designated by letters (skipping "H" to avoid confusion) in decreasing chemical-shift order from A to V. The chemical shifts of the signals, any coupling data, and integrations are given in Table 8-1. Chemical shifts, coupling constants, and integrals can be measured with considerable accuracy from expansions of Figure 8-1.

Integration of ^1H spectra is especially important for unknown materials. The presence of six signals, each of which integrates to three protons, indicates that this unknown contains

Figure 8-1 The 500 MHz ^1H NMR spectrum of T-2 toxin.**Table 8-1** ^1H NMR Data of T-2 Toxin

Designation	Chemical Shift ^a	Coupling Constants (Hz)	Integration (^1H)
A	5.81 d	5.0	1
B	5.31 d	2.4	1
C	5.28 d	5.5	1
D	4.34 d	5.0	1
E	4.28 d	12.6	1
F	4.16 ddd	5.0, 2.4, 2.4	1
G	4.06 d	12.6	1
I	3.70 d	5.0	1
J	3.20 d	2.4	1
K	3.06 d	4.0	1
L	2.80 d	4.0	1
M	2.41 dd	14.0, 5.5	1
N	2.17 d	6.3	2
O	2.16 s	—	3
P	2.11 m	6.4, 6.3	1
Q	2.03 s	—	3
R	1.91 d	14.0	1
S	1.75 s	—	3
T	0.98 d	6.4	3
U	0.96 d	6.4	3
V	0.81 s	—	3

^aMultiplicities: d = doublet, m = multiplet, s = singlet.

six methyl groups. The only real difficulty in integration arises with regard to the signals centered at δ 2.17, 2.16, and 2.11. Those at δ 2.17 and 2.16 cannot be integrated separately and total five protons. Since the signal at δ 2.16 (O) is a sharp singlet, however, it must, in all likelihood, be a methyl group. Two protons remain for the signal at δ 2.17 (N), which appears to be a methylene doublet whose low-frequency (high-field) signal is obscured by the sharp methyl singlet at δ 2.16 (O). The fact that these methylene protons exhibit just one coupling (6.3 Hz) means that they are enantiotopic and likely are located on a side chain. If they were incorporated into a ring, they would almost certainly be diastereotopic. The signal at δ 2.11 (between the methyl signals at δ 2.16 and 2.03) is a complex multiplet, but integrates cleanly to one proton.

The integrals sum to 34, which is the number of protons required by the high-resolution mass spectrum. Moreover, according to the tabulated coupling-constant data, the protons whose signals appear at δ 4.28 and 4.06 (both with $J = 12.6$ Hz) and at δ 2.41 and 1.91 (both exhibiting $J = 14$ Hz) appear to be geminal pairs. Other couplings that are similar and even identical are observed, but the establishment of additional spin systems is better deferred until the COSY spectrum is recorded.

A quick look at the data in Table 8-1 confirms the earlier inference that few of the protons in the unknown compound can be attached to alkenic or aromatic carbons (Section 3-2 and Figure 3-9).

8-2 ^{13}C NMR Data

The ^1H -decoupled ^{13}C NMR spectrum of a 50-mg sample of the unknown compound is shown in Figure 8-2. The ^{13}C signals are designated by number in decreasing chemical-shift order, from 1 to 24. Their chemical shifts and the number of attached protons are given in Table 8-2. A list of chemical shifts is printed by the spectrometer for those ^{13}C signals which exceed a threshold value that is selected to include likely signals and exceed the height of the noise. Quaternary carbons give rise to the smallest signals in the ^{13}C spectrum, and the intensities of the highest-frequency (lowest-field) resonances are generally what determine the threshold level. Since very small signals (those with small NOE's or unusually long T_1 's) sometimes barely exceed the noise, threshold levels must be set with caution and with the realization that real resonances may be missed in the signal-listing process.

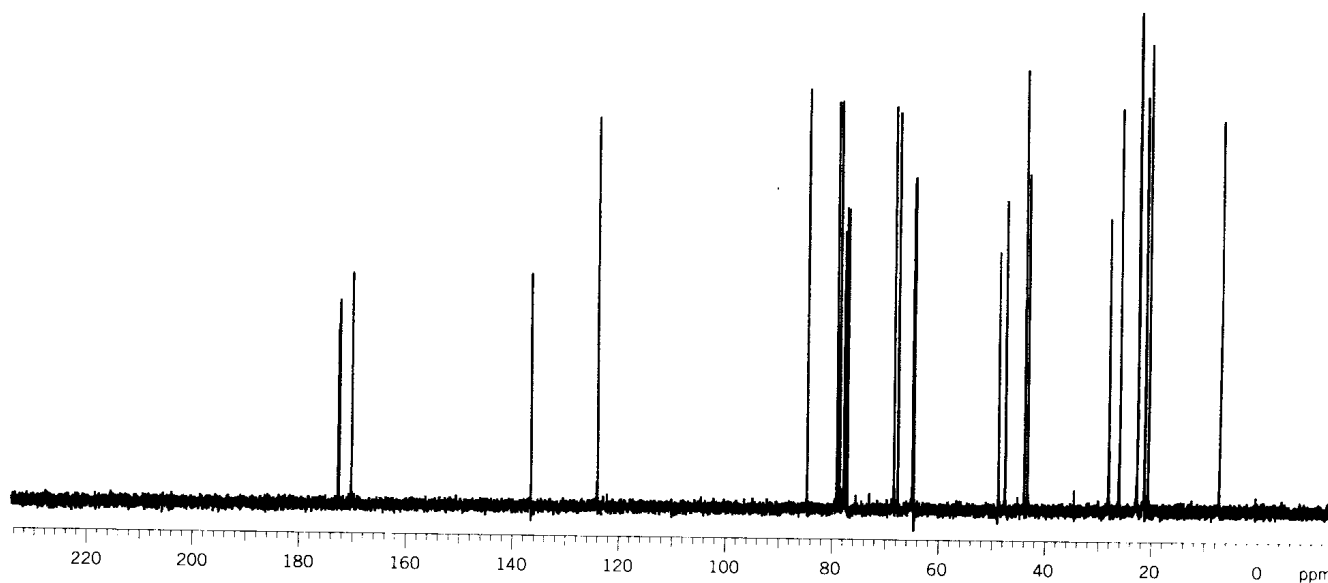


Figure 8-2 The 125 MHz ^{13}C NMR spectrum of T-2 toxin.

Table 8-2 ^{13}C NMR Data of T-2 Toxin

Designation	Chemical Shift	n^a	Directly Attached Hydrogen(s)
1	173.0	0	—
2	172.8	0	—
3	170.5	0	—
4	136.6	0	—
5	124.2	1	A
6	84.5	1	B
7	79.2	1	I
8	78.5	1	F
9	68.3	1	C
10	67.6	1	D
11	64.9	2	E, G
12	64.6	0	—
13	48.8	0	—
14	47.4	2	K, L
15	43.8	2	N
16	43.3	0	—
17	27.9	2	M, R
18	26.0	1	P
19	22.5	3	T
20	22.4	3	U
21	21.1	3	O
22	21.0	3	Q
23	20.3	3	S
24	7.0	3	V

^aNumber of attached protons.

Especially small resonances can sometimes be differentiated from noise spikes by their line widths, which tend to be very thin. Missing signals must always be a concern with unknown compounds if the number of observed ^{13}C signals cannot be confirmed by a high-resolution mass spectrum. While molecular weight data from such mass spectra can reveal the occurrence of absent resonances, the spectroscopist has to be cautious because molecular symmetry can result in fewer observed ^{13}C (and ^1H) signals than are required by the mass spectral data. Keep in mind that the ^{13}C peak intensities (in contrast to ^1H intensities) are not necessarily a good measure of the relative numbers of contributing carbon atoms. In the case of T-2 toxin, however, the number of carbon resonances is 24, the same number of carbons as required by the high-resolution mass spectrum.

A cursory examination of the data in Table 8-2 also supports the assumption that the unknown compound is essentially aliphatic in nature (Section 3-5 and Figure 3-11). The three highest-frequency (downfield) signals (carbons 1–3) are in the ester carbonyl range (Section 3-5c), while carbons 4 and 5 appear to be alkenic and require the presence of a mono-substituted, carbon–carbon double bond (Section 3-5b). The resonances corresponding to carbons 6–12 are in the chemical-shift range for aliphatic carbons that are attached to oxygen (Section 3-5a).

8-3 The DEPT Experiment

For unknown compounds, the number of attached protons per carbon is best determined by the DEPT experiment (Section 7-2b). The DEPT spectrum of the 50-mg sample of T-2 toxin is shown in Figure 8-3. It reveals the presence of six methyl, four methylene, and seven

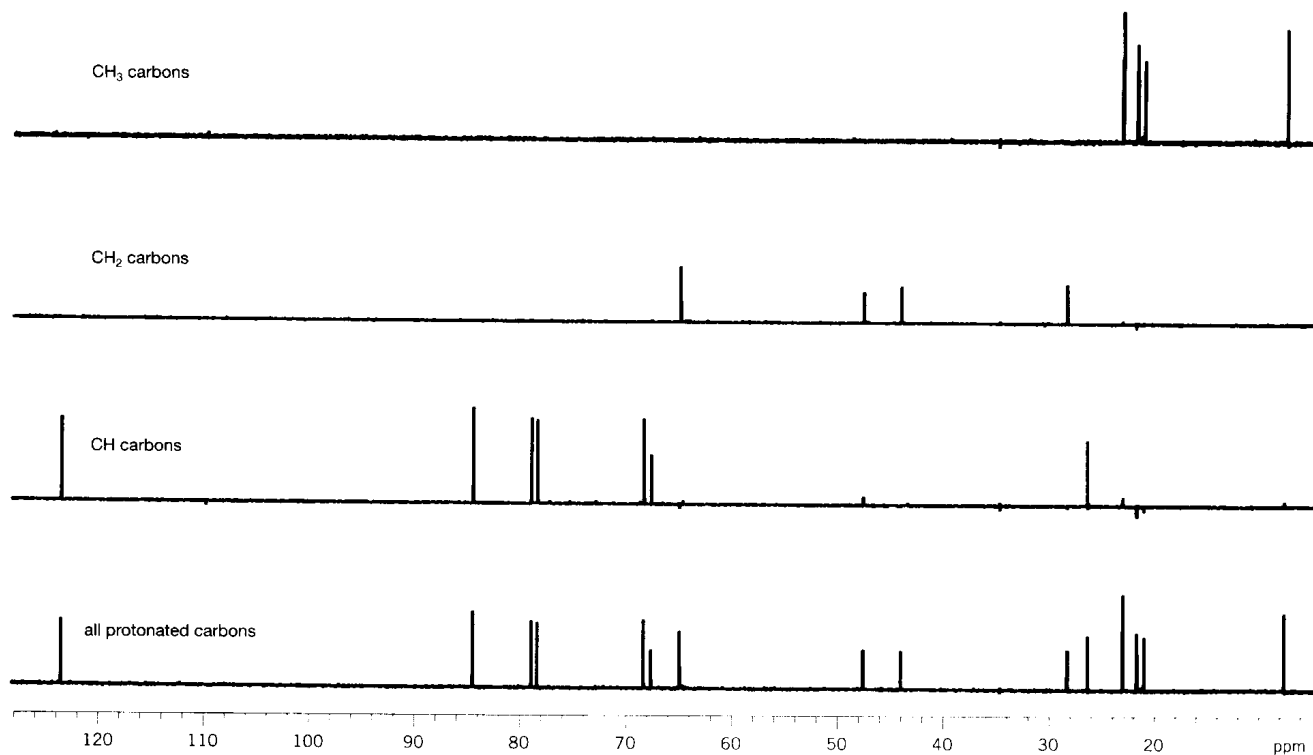


Figure 8-3 DEPT subspectra of T-2 toxin.

methine carbons. Subtracting these 17 protonated carbons from 24 identifies the remaining 7 quaternary carbons. The DEPT data are listed in the third column of Table 8-2. In addition, summing the 18 methyl, 8 methylene, and 7 methine signals accounts for 33 protons. The molecular formula and the integrals in Table 8-1 require 34, so the final proton must be attached to oxygen (OH).

8-4 The HSQC Experiment

At this point in a structural elucidation exercise, some NMR spectroscopists prefer to begin assembling ^1H NMR spin systems by means of COSY experiments. COSY correlations, however, can be difficult to interpret in unknown compounds, since protons that are several bonds removed may exhibit spin coupling. In addition, vicinal couplings cannot always be distinguished from geminal couplings in congested spectra, even if COSY-45 experiments are performed (Section 6-1). It is useful, therefore, to ascertain initially which protons are directly attached to specific carbons by a $^1\text{H}/^{13}\text{C}$ correlation experiment (Sections 7-8a and 7-8b, respectively, as well as Section 6-2). Standard and gradient HSQC spectra of the 15-mg sample of the unknown compound are shown in Figure 7-15 for all of the protonated carbons except the signal at δ 124.2. Both of the full spectra, moreover, reveal that this carbon is directly bonded to the proton at δ 5.81.

The HSQC data are presented in the fourth column of Table 8-2. Thus, we see that H_A is attached to C-5, H_B to C-6, ..., H_E and H_G to C-11, ..., H_S to C-23, and H_V to C-24. The seven quaternary carbons, of course, exhibit no direct proton connectivities, while H_J displays no carbon connectivity. Hence, H_J must be the proton attached to oxygen. The HSQC data confirm that protons E and G and protons M and R are geminal pairs, as is expected from their coupling constants (12.6 and 14 Hz, respectively). These data, however, also demonstrate that protons K and L constitute a third geminal system. They might easily have been mistaken for a vicinal pair because of their unusually small 4-Hz coupling (Section 4-5). In addition, the doublet at δ 2.17 (N) with integral 2 is found to represent a fourth geminal pair of protons. The

partial redundancy found in the DEPT and HSQC experiments is quite helpful with unknowns, because it serves as a built-in check of the consistency of spectral interpretations.

8-5 The COSY Experiment

The construction of proton spin-coupling networks is achieved by a variety of COSY experiments (Section 7-7). Standard COSY and DQF-COSY spectra of the 15-mg sample of the unknown compound are shown in Figure 7-11a, and the data from these contour plots are summarized in Table 8-3. Coupling constants, which have been measured in the ^1H NMR spectrum, correspond to cross peaks, and are given in parentheses in the table.

Four ^1H spin systems are observed in the COSY contour plots, three of which are illustrated in Figure 8-4. The first, and simplest, is the K,L pair, which also was identified in the ^1H spectrum. This group is isolated from the other spin systems. The second group comprises H_P , protons N, and the methyl groups T and U. H_P is coupled to protons N and to methyls T and U, suggesting an isopropyl array with H_P in the middle. With the inclusion of N, the entire group is isobutyl: $(\text{CH}_3)_2\text{CHCH}_2-$. The third system is composed of protons B, F, I, and J. H_F is coupled to the other three members of this group, but there is no coupling among protons B, I, and J. Because C_6 , C_7 , and C_8 are methinyl, an array with the structure $\text{C}_7\text{H}_\text{I}-\text{C}_8\text{H}_\text{F}-\text{C}_6\text{H}_\text{B}$ is indicated. Coupling is not expected between I and B. The placement of OH_J remains to be finalized. The fourth and largest network includes protons A, C, D, E, G, M, R, and methyl S. In addition to the geminal pairs of protons already identified in this system (E and G, and M and R), H_A and H_D constitute a vicinal pair, as do H_C and H_M . The structure of this large system requires further discussion.

Weaker cross peaks are observed between (i) methyl S and protons A, C, and D, (ii) H_D and protons G and R, (iii) H_E and H_M , and (iv) H_C and H_R . Since H_A is attached to an sp^2 -hybridized carbon (5), and methyl S, from its chemical shift, might be likewise (Section 3-2a), couplings between H_A and its vicinal partner (H_D) to methyl S (allylic and homoallylic, respectively, Section 4-6) are not unreasonable. Moreover, protons C, M, and R

Table 8-3 COSY NMR Data of T-2 Toxin

Designation	Spin-Coupling Partners ^a
A	C, D (5.0), S
B	F (2.4)
C	A, M (5.5), R, S
D	A (5.0), G, R, S
E	G (12.6), M
F	B (2.4), I (5.0), J (2.4)
G	D, E (12.6)
I	F (5)
J	F (2.4)
K	L (4.0)
L	K (4.0)
M	C (5.5), E, R (14.0)
N	P (6.3)
P	N (6.3), T (6.4), U (6.4)
R	C, D, M (14.0)
S	A, C, D
T	P (6.4)
U	P (6.4)

^aCoupling constants from the ^1H spectrum are in parentheses.

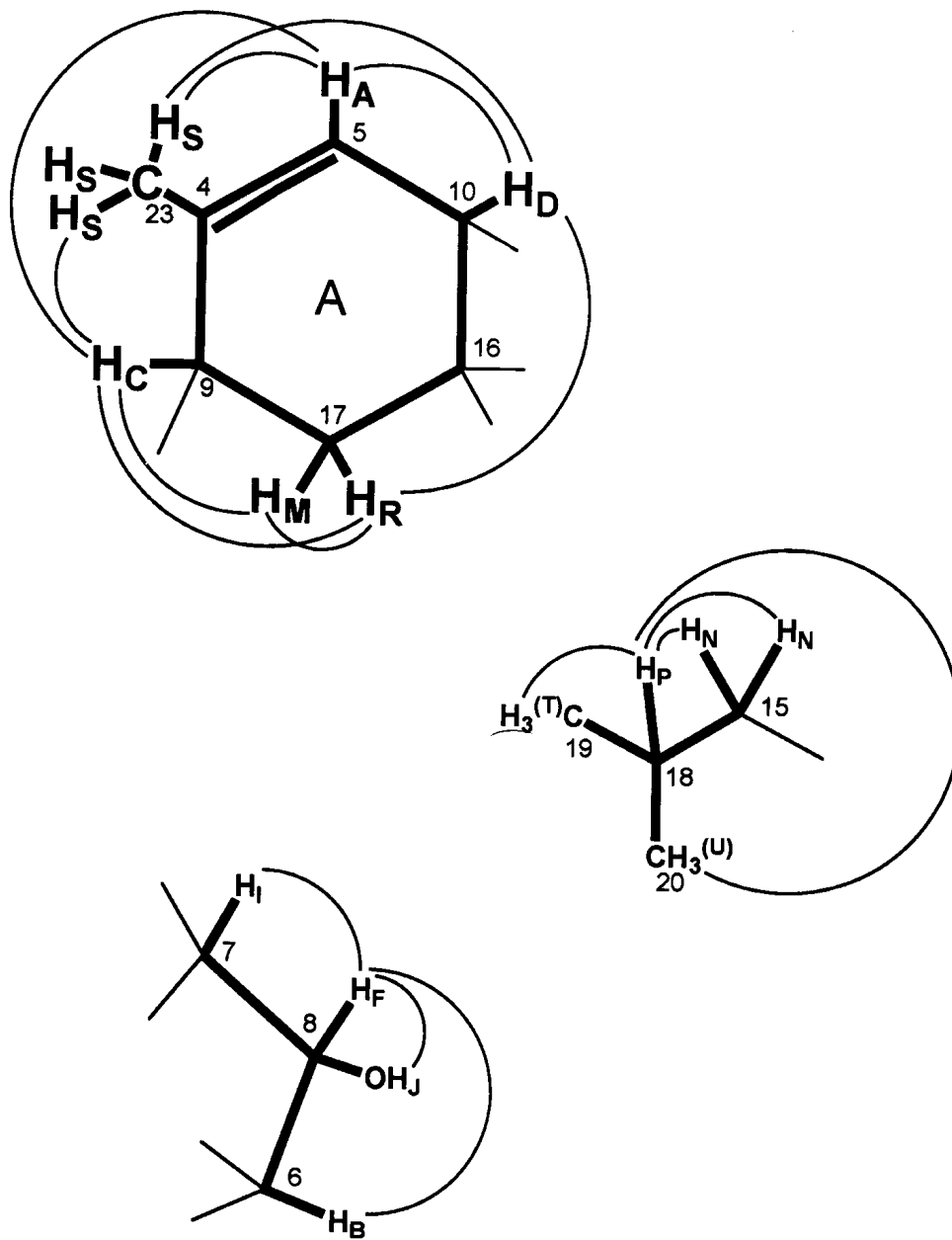


Figure 8-4 Molecular fragments established by COSY correlations.

form a three-spin subsystem with ${}^3J_{CM} = 5.5$ Hz. Since ${}^3J_{CR}$ is present as a small cross peak in the COSY spectrum, but does not appear in the ${}^1\text{H}$ NMR spectrum, the $\text{H}_C\text{-C}_9\text{-C}_{17}\text{-H}_R$ dihedral angle must be close to 90° . This subsystem is an excellent example of the way in which small vicinal and long-range couplings can give rise to COSY cross peaks that are similar in appearance. Weak cross peaks between H_C and methyl S and between H_D and H_R serve to link the $\text{H}_C\text{-H}_M\text{-H}_R$ and $\text{H}_D\text{-H}_A\text{-methyl S}$ subsystems. The substructure given in Figure 8-4 is thus suggested, although the connection through C_{16} is not yet demonstrated.

A TOCSY experiment is not employed in this structural determination exercise despite the fact that the extended proton spin network A, C, D, E, G, M, R, and methyl S would appear to take advantage of relayed connectivity. As a general rule, however, only those spin systems in which there is *appreciable* coupling between each member of the system and both the preceding and following protons are appropriate for TOCSY experiments. If there are very small couplings at certain points in the chain, relaying tends to stop there. It can be readily seen in Figure 7-11a and Table 8-1 that 7 of the 11 correlations in this extended system

are so small that they appear only in the COSY contour plots. A TOCSY experiment would, in all likelihood, add little information to that inferred from one of the COSY experiments.

In addition, on the basis of their chemical shifts (δ 67.6–84.5), carbons 6, 7, 8, 9, and 10 are almost certainly attached to oxygen atoms (Section 3-5a). The three molecular fragments shown in Figure 8-4 can tentatively be constructed from the COSY correlations described. If they are verified, these fragments would account for over half of the carbons and hydrogens in the unknown compound and two units of unsaturation.

8-6 The HMBC Experiment

Since the ^{13}C NMR spectrum of the unknown compound is not more congested than its ^1H spectrum, HMBC is the experiment of choice to establish the longer range C–H correlation networks. Standard and gradient HMBC spectra of the 15-mg sample of the unknown compound are shown in Figure 7-18, and the data from these contour plots are summarized in Table 8-4.

8-7 General Molecular Assembly Strategy

Of the many techniques available to the NMR spectroscopist in structural elucidations, none is so valuable as the indirect chemical-shift correlation experiment, such as HMBC, TOCSY (both homo- and heteronuclear varieties), and FLOCK. Once molecular fragments have been identified by the COSY and HSQC experiments, the spectroscopist attempts to combine these fragments by means of the preceding techniques. As indispensable as these methods have become to NMR spectroscopists, they nonetheless suffer a common

Table 8-4 HMBC NMR Data of T-2 Toxin

Designation of Carbons	Chemical Shift	Longer Range Attached Hydrogens
1	173.0	C, N
2	172.8	B, C(H _O) ₃
3	170.5	E, G, C(H _Q) ₃
4	136.6	C, D, R, C(H _S) ₃
5	124.2	C, D, C(H _S) ₃
6	84.5	F, I, C(H _V) ₃
7	79.2	B, J, K
8	78.5	B, I, J
9	68.3	A, D, R, C(H _S) ₃
10	67.6	A, E, G, I, R, C(H _S) ₃
11	64.9	M, R
12	64.6	B, I, K, L, C(H _V) ₃
13	48.8	B, D, E, G, I, C(H _V) ₃
14	47.4	(none)
15	43.8	C(H _T) ₃ , C(H _U) ₃
16	43.3	B, C, D, E, G, M, R, C(H _V) ₃
17	27.9	C, D, E, G
18	26.0	N, C(H _T) ₃ , C(H _U) ₃
19	22.5	N, C(H _U) ₃
20	22.4	N, C(H _T) ₃
21	21.1	(none)
22	21.0	(none)
23	20.3	A
24	7.0	(none)

limitation: two-bond C–H couplings cannot generally be distinguished from three-bond C–H couplings. The *occasional* observation of four- and five-bond C–H couplings complicates matters further. Unfortunately, there is no overall solution to this uncertainty concerning the number of bonds over which C–H coupling is being detected.

The process of molecular assembly can be approached in the following manner. If possible, a carbon atom is selected, from which the remainder of the molecular skeleton can be built in just *one* direction. Methyl groups are excellent starting points. Adjacent (vicinal) protons, if any, can be identified from a COSY contour plot, and the carbon to which they are directly attached can be identified from an HSQC or HMQC plot. The HMBC or FLOCK spectra can then be scanned, using either the contour plot (for uncongested spectra) or methyl–proton or methyl–carbon traces (whichever is less congested) if spectral congestion or weak cross peaks are a problem. Cross peaks may be found for the adjacent carbon (if methyl–proton traces are viewed) or protons (if methyl–carbon traces are observed). In either case, the cross peaks represent two-bond couplings. Cross peaks may also be found for other carbons or protons; if so, they are indicative of three-bond couplings. (Keep in mind, however, that one, or more, members of the second group could be due to ${}^nJ_{\text{CH}} > 3$.) The fortunate redundancy of these 2D experiments is seen, whereby an adjacent carbon may be identified by a combination of COSY (${}^3J_{\text{HH}}$) and HSQC/HMQC (${}^1J_{\text{CH}}$) connectivities and also by HMBC/FLOCK (${}^2J_{\text{CH}}$) correlations.

The second carbon atom in the fragment (adjacent to the original methyl group) likely shows two-bond couplings with one or more directly attached protons, if present, both backward to the original methyl carbon and forward to the third carbon in the series. Carbon atom connectivities can thus be built up by using two-bond C–H couplings to confirm previously determined C–C connectivities generally and then employing three-bond H–H and C–H couplings to extend the developing molecular structure. These forward- and backward-looking two- and three-bond C–H coupling networks are illustrated in Figure 8-5, in which the number and letter designations are generic and do not correspond to those developed for T-2 toxin. To avoid confusion from too many lines, the corresponding H–H couplings are not shown.

Alternatively, when a methyl ${}^1\text{H}$ signal is nothing more than a broadened singlet, the COSY spectrum (either the contour plot or the methyl trace) can be scanned for cross peaks from longer range coupling. As before, either the contour plot or the methyl ${}^1\text{H}$ trace of the HMBC or FLOCK spectrum can be scanned for cross peaks from (i) two-bond coupling to adjacent (quaternary) carbons and (ii) three-bond coupling to farther removed carbons (with the usual caveat that ${}^nJ_{\text{CH}} > 3$). Finally, we express a note of caution. Like NOE's, three-bond C–H correlations are not necessarily symmetrical (e.g., in the 4-carbon fragment pictured in Figure 8-5, a strong cross peak may be observed between H_A and C_3 , while a weak one or none at all is seen between H_C and C_1). The main reason for these weak or missing correlations is the dependence of vicinal couplings on the $\text{H}_\text{A}\text{--}\text{C}_1\text{--}\text{C}_2\text{--}\text{C}_3$ and $\text{H}_\text{C}\text{--}\text{C}_3\text{--}\text{C}_2\text{--}\text{C}_1$ dihedral angles (Karplus relationship, Section 4-5), which are seldom identical. Since similar considerations are largely absent for two-bond couplings, cross peaks should be detected between H_A and C_2 and also between H_B and C_1 . Extensive redundancy

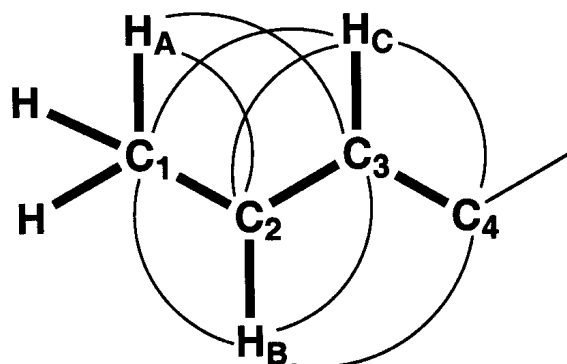


Figure 8-5 Generalized two- and three-bond C–H couplings.

of the type described is in fact observed for vicinal C–H correlations and is invaluable in the construction of molecular structures.

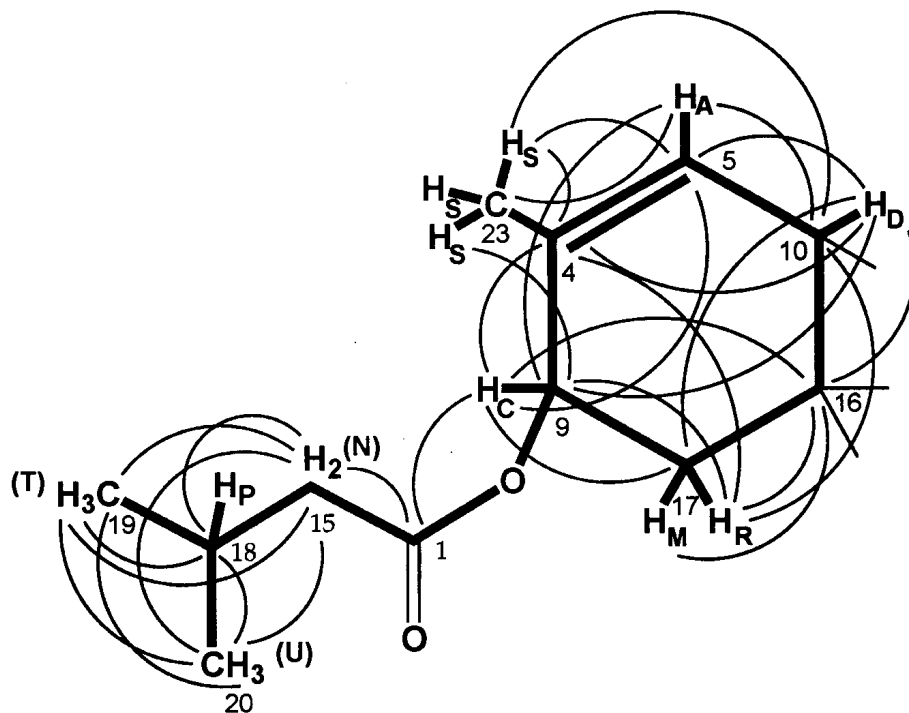
The same factors that influence vicinal H–H couplings (e.g., dihedral angle dependence, substituent electronegativity, and bond lengths and order; Chapter 4) apply to vicinal C–H couplings. As a general rule, C–H coupling constants are approximately two-thirds the value of the corresponding H–H couplings. In alkenes, for example, average *cis* and *trans* H–H couplings are approximately 11 and 18 Hz, respectively, while the corresponding C–H coupling constants are about 7 and 12 Hz, respectively.

8-8 A Specific Molecular Assembly Procedure

Upon examination of the three fragments of Figure 8-4 as possible starting points for the structural elucidation of the unknown compound, it becomes clear that the isobutyl group is an attractive choice if, of course, additional connections can be made to carbons and protons elsewhere in the molecule. If such connections cannot be made, the methyl protons (S) of the putative cyclohexene system provide another possible starting point.

The HMBC data (Table 8-4) confirm the isobutyl structure. An examination of the methyl group protons (T and U) shows HMBC correlations to both C₁₈ and C₁₅. In addition, methyl protons T exhibit a connectivity to C₂₀, while the methyl protons U likewise do to C₁₉. Correlations due to H_P are obscured because of the proximity of its signal to those of methyls O and Q. Connectivities, however, are found from the methylene protons N to carbons 18, 19, and 20, thus confirming the presence of the isobutyl group.

A fourth HMBC correlation is detected between the methylene protons N and the most deshielded carbon. That carbon (C₁) appears to be an ester carbonyl from its chemical shift (δ 173.0, Section 3-5c) and exhibits a second connectivity to H_C. This correlation is crucial because it is the only one that connects C₁ indirectly to C₉ (via an oxygen as an isovaleryl ester group) of the presumptive cyclohexene fragment. If the connection is confirmed, the molecular fragment **8-1** (with HMBC connectivities shown) accounts for three units of unsaturation and 12 carbons (including the previously surmised carbon-carbon double bond), 17 hydrogens, and 2 oxygens.



8-1

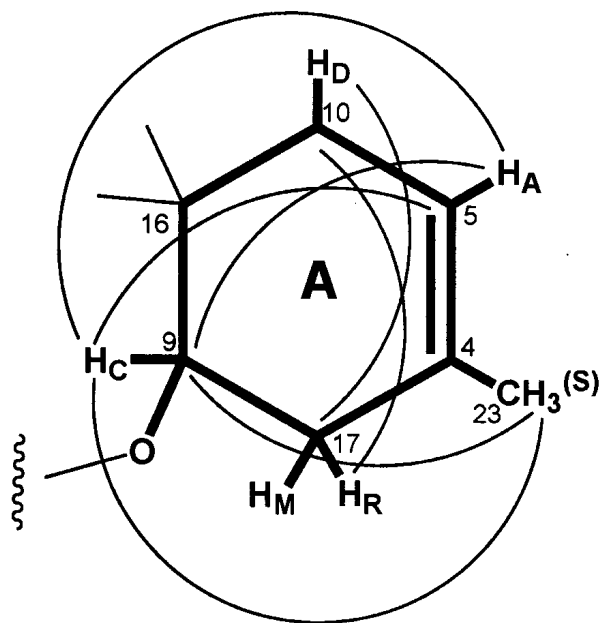
The next step in this structural determination is the confirmation of the proposed cyclohexene (A) ring of Figure 8-4. Several COSY and HMBC correlations provide this confirmation. The $H_C C_9$ fragment is central to the issue, and vicinal coupling between H_C and H_M previously established that C_9 is attached to the $C_{17}H_M H_R$ fragment. Confirmatory HMBC connectivities between H_C and C_{17} and between H_R and C_9 also are observed, as are COSY cross peaks between H_C and H_R . In addition, C_9 displays HMBC connectivities to H_A , H_D , and the methyl protons S, while H_C exhibits HMBC correlations to C_4 , C_5 , and C_{16} .

Since H_A and H_D also display vicinal coupling, their directly attached carbons (5 and 10) must be adjacent, and confirmatory HMBC connectivities between H_A and C_{10} and between H_D and C_5 are observed. Furthermore, inspection of the ^{13}C NMR data indicates that these are the only two noncarbonyl, sp^2 carbons, and it is logical to pair them as C_4 and C_5 . H_C and H_D each exhibit HMBC connectivities to both carbons 4 and 5, confirming the 4,5-double bond. These data also demonstrate that C_5 is located between C_4 and C_{10} .

Several COSY and HMBC correlations suggest that methyl 23 be positioned at C_4 and that it, in turn, be attached to C_9 . First, COSY cross peaks between the methyl protons S and H_A and H_C and HMBC connectivities between (i) the methyl protons S and C_4 , C_5 , and C_9 and (ii) H_A and methyl C_{23} argue that methyl 23 be located at C_4 . Second, these correlations, plus (i) that (COSY) between H_A and H_C and (ii) those (HMBC) between H_A and C_9 and between H_C and C_4 , require that C_4 be joined to C_9 .

Finally, the HMBC connectivities that C_{16} displays to H_C , H_D , H_M , and H_R suggest that C_{16} be situated between C_{10} and C_{17} to complete the six-membered A ring. HMBC correlations between H_D and C_{17} and H_R and C_{10} support this placement. The 4,5-double bond and A ring account for the second and third units of unsaturation.

Two allylic C-H connectivities thus are observed in the A ring (H_D to C_9 and the methyl protons S to C_{10}), underscoring the warning that HMBC cross peaks are not restricted just to two- and three-bond correlations. Unsaturated ring systems pose special problems for structural analysis via HMBC experiments because of long-range connectivities from allylic and homoallylic C-H couplings that can be mistaken for low-intensity cross peaks from small vicinal coupling constants. This situation can be illustrated by alternatively assembling the A ring as shown in structure 8-2.

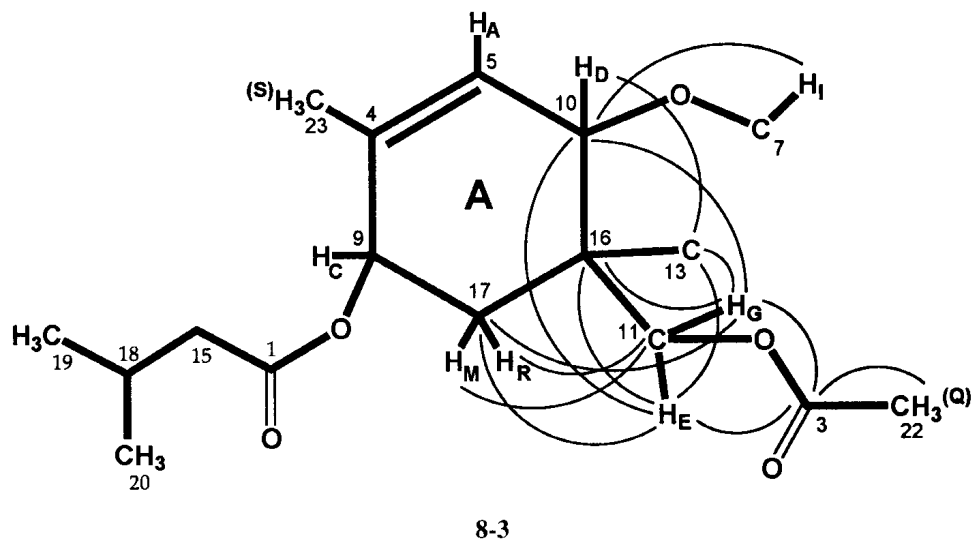


8-2

Most of the HMBC correlations used to derive the A ring are *possible* for the rearranged ring. A problem, however, arises with their intensities. Where there were two allylic couplings in **8-1** (H_D to C_9 and methyl S to C_{10}), there must now be three allylic couplings (H_A to C_9 , H_D to C_{17} , and H_R to C_{10}), one W-type coupling (methyl S to C_9 ; Section 4-6) and one nondescript four-bond coupling between H_C and C_5 in **8-2**. Even if these couplings did exist, their cross-peak intensities in the HMBC spectrum would not be expected to be anywhere nearly so great as those of the corresponding couplings in **8-1**.

Another problem with the arrangement of **8-2** concerns the observed COSY cross peaks between H_A and H_C and between H_C and the methyl protons S. These represent allylic and W-type couplings, respectively, in **8-1**, but would have to be nondescript five-bond couplings in **8-2**. Substructure **8-2** is, therefore, rejected as a likely possibility.

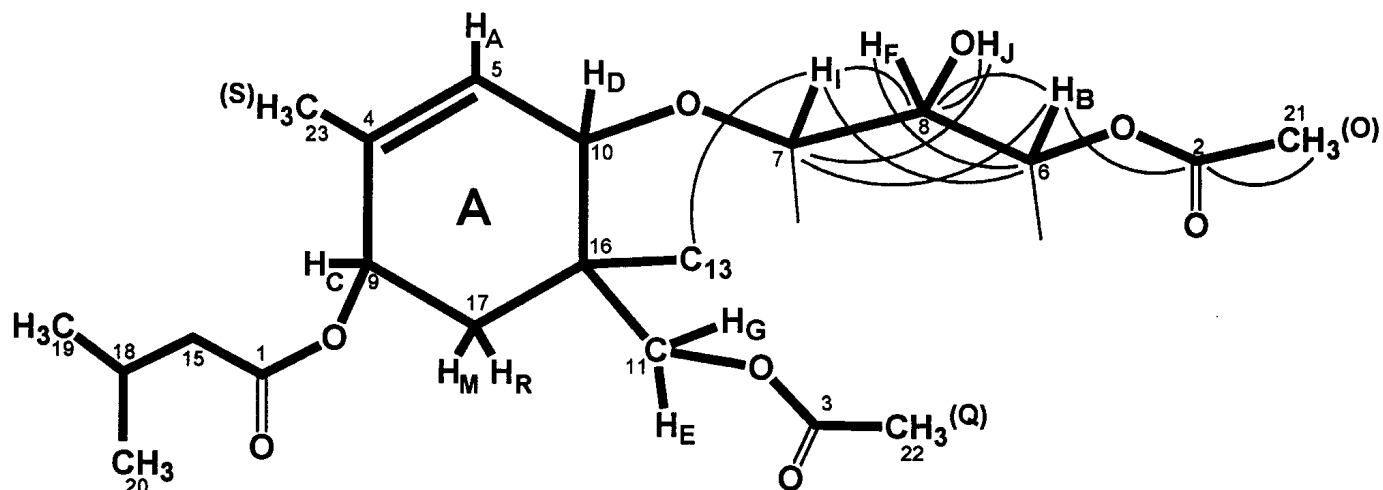
In addition to the connectivities noted, C_{16} displays two more from the geminal protons E and G, and this methylene pair also shows correlations with both C_{10} and C_{17} . Furthermore, three-bond connectivities are seen from C_{11} to protons M and R. These correlations are illustrated in the lower right-side portion of substructure **8-3** and necessitate that C_{11} be attached directly to C_{16} .



The considerably high-frequency (low-field) chemical shifts of H_E (δ 4.28) and H_G (δ 4.06) suggest both that they are carbinol protons and that the oxygen, to which their directly bonded carbon is attached, is part of an ester group (Section 3-2a). Protons E and G also exhibit connectivities to C_3 , which, in turn, displays correlations with methyl protons Q. These connectivities require that the acetate group, $(H_Q)_3C_{22}(O)O$, be attached to C_{11} . H_D and methylene protons E and G also show a three-bond correlation with C_{13} and thus necessitate that it be attached to C_{16} .

The chemical shift of C_{10} (δ 67.6) indicates that it is bonded to an oxygen atom (Section 3-5a). In addition, it exhibits what must be a three-bond connectivity from H_I . The chemical shift of C_7 (δ 79.2), to which H_I is directly attached, suggests that it, too, is bonded to oxygen. The connection of C_{10} and C_7 by an oxygen atom is consistent with the chemical shift and with the HMBC data, thereby completing substructure **8-3**, which accounts for a fourth unit of unsaturation and a total of 17 carbons, 23 hydrogens, and 5 oxygens.

The extension of the developing structure to C_7 is especially important, because it unites substructure **8-3** with the third molecular fragment (comprising $C_7-C_8-C_6$) shown in Figure 8-4, to produce substructure **8-4**.



8-4

Similar to our approach to the cyclohexene system, the next step in this structural determination is to confirm the structure of the third fragment. Unlike the former subunit, the latter is well defined by its COSY and 1D spin-coupling data. Nevertheless, the HMBC data are checked for consistency. H_I displays two- and three-bond correlations with C_8 and C_6 , respectively, while C_7 exhibits connectivities to H_B and the hydroxyl proton J . In addition, two-bond correlations are shown by H_B and H_F with C_8 and C_6 , respectively. The middle carbon (8) exhibits the aforementioned connectivities and another (two-bond) connectivity from OH_J .

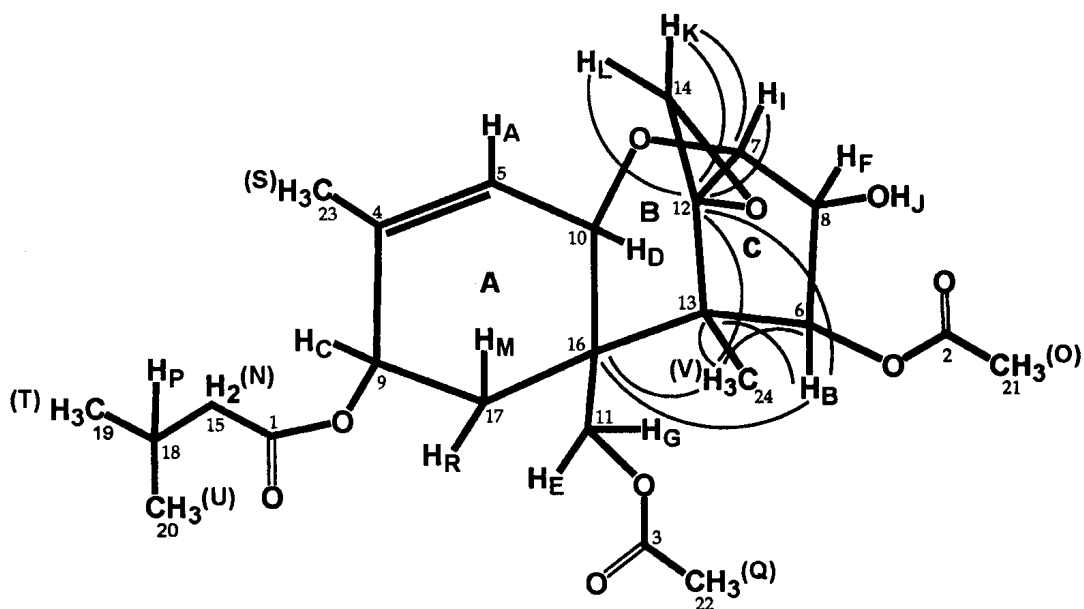
H_B displays an HMBC correlation to C_2 , which, in turn, displays connectivities to the methyl protons O . These correlations require that the acetate group, $(H_O)_3C_{21}(O)O$, be attached to C_6 . Substructure 8-4 accounts for a fifth unit of unsaturation and a total of 21 carbons, 29 hydrogens, and 8 oxygens. At this point, 3 carbons, 5 hydrogens, 1 oxygen, and three units of unsaturation remain undetermined.

The carbons remaining to be added to substructure 8-4 are the following: quaternary C_{12} , the methylene fragment $C_{14}H_KH_L$, and the methyl group $C_{24}(H_V)_3$. In addition, carbons 6 and 7 each need to be connected to one more atom, and quaternary C_{13} requires three. Furthermore, since only 1 oxygen and no sp^2 carbons remain unaccounted for, the remaining three units of unsaturation must be due to ring systems, rather than carbon-carbon or carbon-oxygen double bonds.

The methyl protons V exhibit connectivities to C_{16} and C_{13} , which have been placed in the structure, and to C_6 and C_{12} , which have not. These correlations necessitate that C_{12} and $C_{24}(H_V)_3$ also be attached to C_{13} . They account for the methyl group and are illustrated in structure 8-5.

In addition to its already noted connectivities to C_7 and C_8 , H_B shows correlations with C_{12} , C_{13} , and C_{16} . The last one is particularly strong and suggests that it is a three-bond, rather than some type of longer range, coupling. If this assumption is correct, then C_6 must be connected to C_{13} as part of the three-bond coupling pathways of H_B to C_{12} and C_{16} .

The chemical shift of C_{12} (δ 64.6) indicates that it is bonded to the remaining oxygen. Moreover, the chemical shift of C_7 (δ 79.2) requires that it be attached to only 1 oxygen (Section 3-5a), as illustrated in substructure 8-4, and that its last unassigned bond be to another carbon (12 or 14). With C_{12} already connected to C_{13} , its remaining two bonds must, therefore, be to C_7 and C_{14} . This arrangement requires that the last unassigned bond of C_{14} be to the same oxygen that is bonded to C_{12} to form an epoxide. At this point, all of the carbons, hydrogens, and oxygens are accounted for. In addition, the complete structure of the unknown compound, shown in structure 8-5, satisfies the required eight units of unsaturation.



8-5

The final HMBC connectivities support structure 8-5. C₁₂, for example, displays correlations with H_B, H_I, H_K, and H_L, while C₇ shows a correlation with H_K. The directly attached carbon (14) of H_K and H_L is somewhat isolated, in that it displays no proton connectivities. These last correlations illustrate the difficulties in determining the substructures of ring compounds in which junction carbons display many HMBC connectivities that cannot be differentiated as two- or three-bond correlations.

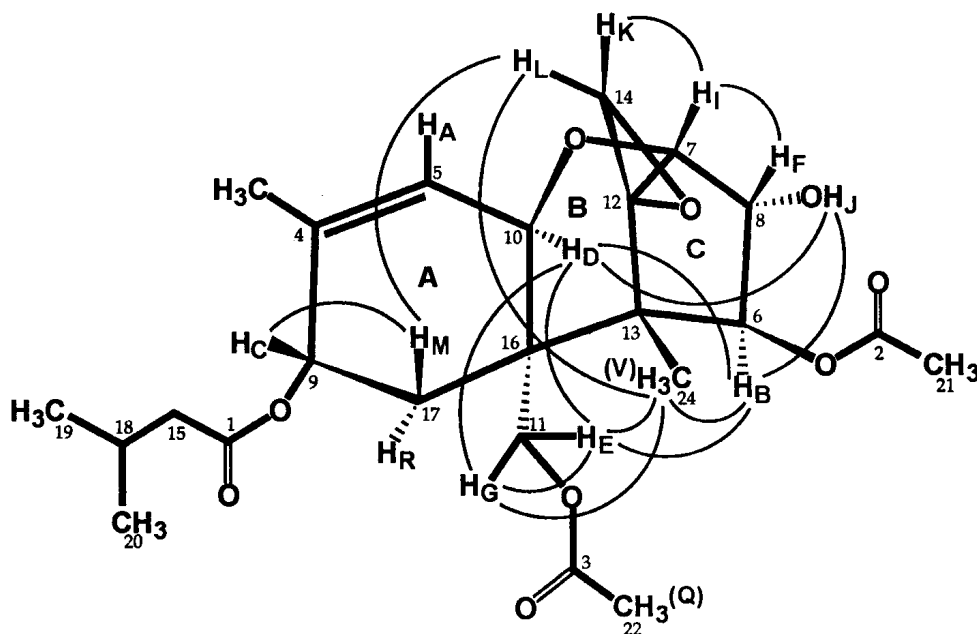
8-9 The NOESY Experiment

With the completion of the two-dimensional structural elucidation of the unknown compound, questions arise concerning its three-dimensional shape [i.e., the relative orientations of substituents (e.g., H_M or methyl 24) at various carbons]. For a molecule with MW = 466, the NOESY experiment can provide a wealth of such stereochemical information. The NOESY spectrum of the 15-mg sample of the compound is shown in Figure 7-22. The data from these contour plots are summarized in Table 8-5 and illustrated, in part, in structure 8-6.

Table 8-5 NOESY NMR Data of T-2 Toxin

Designation of Hydrogens	NOE Enhancements ^a	Designation of Hydrogens	NOE Enhancements ^a
A	s D, S	M	C, w L, s R
B	s D, E, w F, J, O, V	N	w Q, T, U (P obscured)
C	M, w Q, w R, S	O	B, w E, w F
D	A, s B, E, w G, w J	P	T, U (N obscured)
E	B, D, s G, w O, w V	Q	w C, w N
F	w B, s I, J, w O	R	w C, G, s M, s V
G	w D, s E, R, s V	S	A, C
I	s F, w K	T	P
J	B, w D, F	U	P
K	w I, s L	V	B, w E, s G, s L, s R
L	s K, w M, s V		

^as = strong, w = weak.



8-6

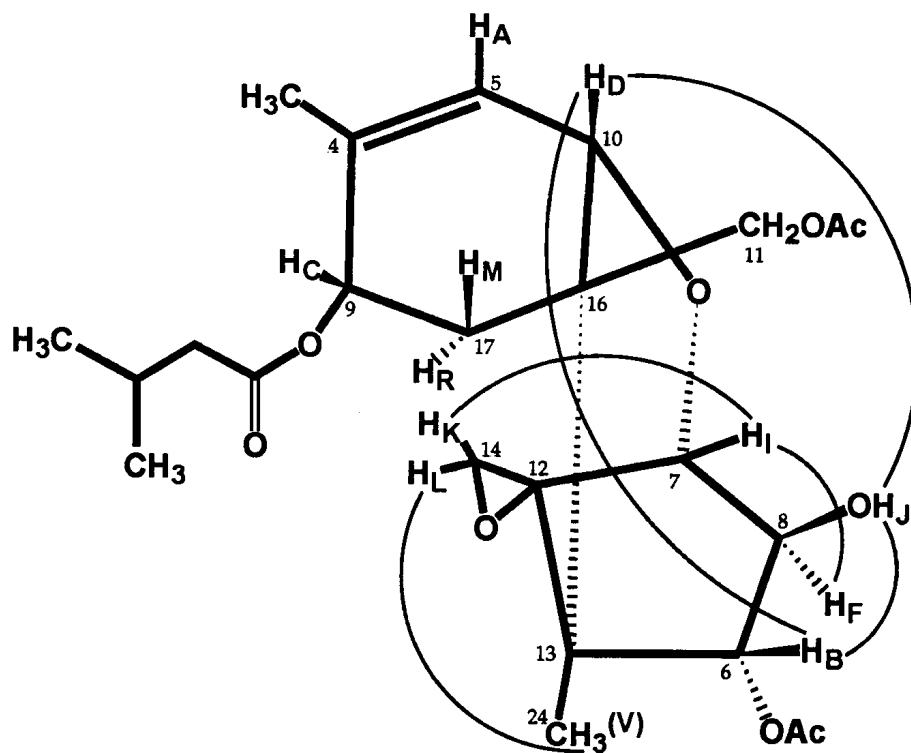
A number of NOESY cross peaks are critical in identifying the overall stereochemistry of T-2 toxin. NOE's, for example, demonstrate that protons B, D, E, G, and J are located in one region of the molecule, protons C, L, and M in another, and protons F, I, and K in a third. In addition, C₂₄(H_V)₃ and H_L are spatially proximate.

The A ring must exist in a half-chair conformation, because of the 4,5-double bond. Moreover, COSY and ¹H NMR coupling data require that H_C bisect the H_M-C₁₇-H_R angle unequally (i.e., the H_C-C₉-C₁₇-H_M dihedral angle must be about 20°, while that between H_C and H_R must be approximately 90° (Sections 4-5 and 8-5). This arrangement can be achieved by having C₁₇ puckered up while C₁₆ is puckered down. A reversed orientation keeps the approximately 20° dihedral angle between H_C and H_M, but the H_C-C₉-C₁₇-H_R dihedral angle would open up to about 180°. This arrangement would result in three large and easily detected couplings between H_C, H_M, and H_R, contrary to observation.

The NOESY correlations between H_D, H_E, and H_G are crucial in establishing how the six-membered B ring is attached to ring A. A trans AB ring junction is eliminated from consideration because it requires that H_D and C₁₁H_EH_G be on *opposite* sides of the AB ring plane, and NOE's between H_D and both H_E and H_G are impossible in this orientation.

Two cis AB ring systems can be fashioned in the following way: (i) C₁₃ of the B ring can be attached at the equatorial position of C₁₆ and the ether oxygen at the pseudoaxial site of C₁₀ (both with respect to the A ring), as shown in substructure 8-6, or (ii) C₁₃ can occupy the axial position of C₁₆ and the ether oxygen the pseudoequatorial site of C₁₀, given in substructure 8-7.

While both substructures accommodate the NOESY connectivities between H_L and C₂₄(H_V)₃, H_K and H_I, H_I and H_F, and among H_B, H_D, and OH_J, that between H_M and H_L is reconciled only by 8-6. Substructure 8-7 is, therefore, rejected because it places H_M and the epoxy group on *opposite* sides of the A ring (this arrangement may be hard to visualize in the drawing, but can be seen easily with a Dreiding model), where the strong NOESY enhancement exhibited by H_M and H_L is impossible. The B ring thus exists in a chair conformation in which C₁₃ is puckered down, the ether oxygen is puckered up, and carbons 7, 12, 10, and 16 lie in a common plane.

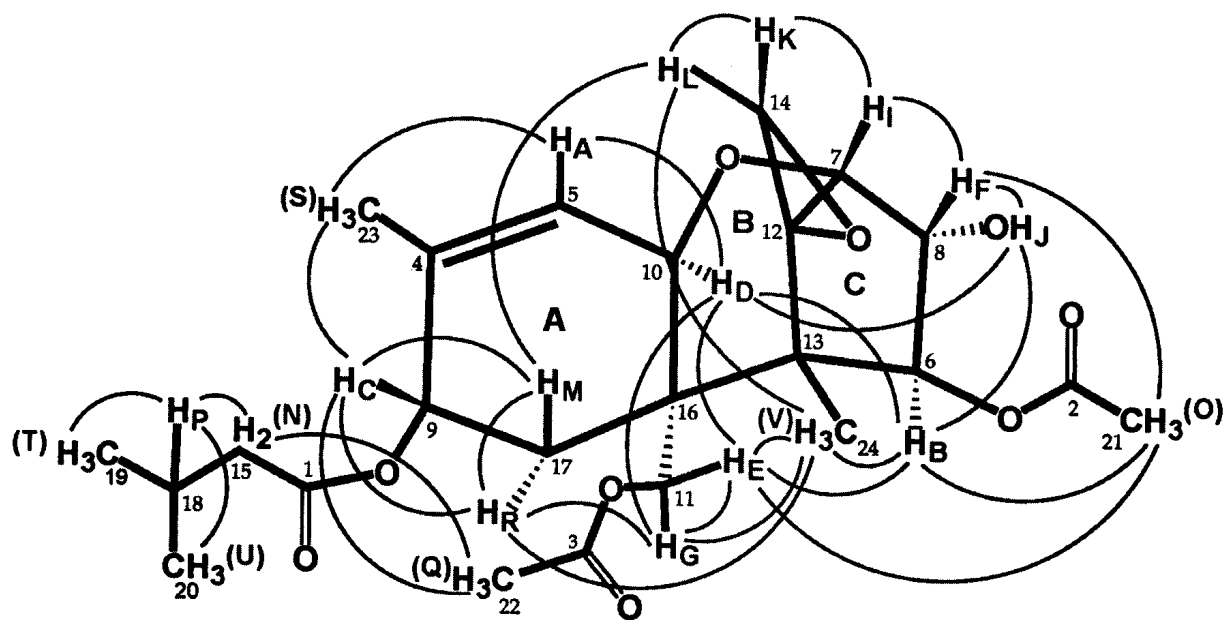


8-7

Furthermore, in this representation, H_D is pseudoequatorial and the $C_{11}H_EH_GOAc$ group is axial (again, both with respect to ring A). The five-membered C ring is nearly perpendicular to ring B, with C_7 , C_8 , C_6 , and C_{13} residing in a common plane and C_{12} puckered up. (These puckers cannot all be illustrated in any one drawing.) In addition, if the A ring is positioned in the plane of the paper, the epoxide group at C_{12} projects outward toward the reader, as in substructure 8-6. Note that the epoxy oxygen points toward the acetoxy group at C_6 , and H_L is oriented toward H_M to accommodate the H_L/H_M NOESY correlation.

The $C_{11}H_EH_GOAc$ group is interesting because it can, in principle, rotate to some degree about the $C_{11}-C_{16}$ bond. In addition to both the NOESY connectivities that H_E and H_G display with each other and their aforementioned correlation with H_D , they both exhibit a connectivity to $C_{24}(H_V)_3$. The NOE of H_E , however, is much stronger to H_D , while that of H_G to $C_{24}(H_V)_3$ is more intense. Further, H_E exhibits correlations with H_B and $C_{21}(H_O)_3$ while H_G does so with H_R . Moreover, $(H_Q)_3C_{22}C_3(O)O$ displays connectivities to H_C and the methylene protons N. When the A ring is placed in the plane of the paper, these NOESY correlations (shown in structure 8-8) suggest that the $C_{11}H_EH_GOC_3(O)C_{22}(H_Q)_3$ group orients itself so that H_G is pointing toward the reader, H_E is pointing back toward C_8 and somewhat parallel to the $C_{16}-C_{17}$ bond, and $(H_Q)_3C_{22}C_3(O)O$ is positioned back toward methyl 23, where it participates in relaxation of the protons N and H_C .

Structure 8-8 is, to a reasonable approximation, a complete three-dimensional representation of T-2 toxin. It can readily be seen that there is no molecular plane in this molecule. What is more, the meaning of stereochemical descriptors like α and β is, to a certain degree, indefinite. Nevertheless, with ring A positioned horizontally, a final description of the relative orientation of the remaining substituents is as follows. The isovaleryl ester group at C_9 is α and axial, H_M is β and axial, and H_R is α and equatorial. Substituents at the AB ring junction cannot be described easily as axial or equatorial, because these descriptors depend on whether the A or B ring is used as a reference point. A better choice is to label both H_D and the $C_{11}H_EH_GOAc$ moieties as α . At the BC ring junction, both H_I and methyl 24 are β .



8-8

In the C ring, several lines of reasoning support the inference that H_B and OH_J are α . First, such an arrangement puts both hydrogens in close proximity to H_D, and NOESY enhancements are observed between all three nuclei. Both groups would be oriented away from H_D if they were β . Second, OH_J must be α (and H_F necessarily β), due to the 5-Hz coupling observed between H_I and H_F. Since the H_I-C₇-C₈-R _{β} dihedral angle is approximately 20° and the H_I-C₇-C₈-R _{α} dihedral angle is about 90°, if H_F were not β , it would be only slightly, if at all, coupled to H_I (Section 4-5).

In the epoxide group, NOESY connectivities between H_I and H_K and between H_L and both H_M and C₂₄(H_V)₃ indicate that H_K is β and pointed toward H_I while H_L is α and oriented toward methyl 24. With the interpretation of these final NOESY correlations, the two- and three-dimensional structural elucidation of T-2 toxin is complete.

APPENDIX 1

Derivation of the NMR Equation

The magnitude of the magnetic moment μ_N of a nucleus N is directly proportional to its spin angular momentum \mathbf{J} , with the constant of proportionality defined as the gyromagnetic ratio (γ_N). That is,

$$\mu_N = \gamma_N \mathbf{J}. \quad (\text{A1-1})$$

Physicists and chemists have preferred to discuss these concepts in terms of a dimensionless spin \mathbf{I} ($\mathbf{J} = \hbar \mathbf{I}$, in which \hbar is Planck's constant divided by 2π). Eq. A1-1 then becomes

$$\mu_N = \gamma_N \hbar \mathbf{I}. \quad (\text{A1-2})$$

Spin is quantized (i.e., it takes on only certain values). The magnitude \mathbf{I} has values of 0 (^{12}C , ^{16}O), $\frac{1}{2}$ (^1H , ^{13}C), 1 (^2H , ^{14}N), $\frac{3}{2}$ (^7Li , ^{35}Cl), and so on in increments of $\frac{1}{2}$. The spin in the direction (z) of the external magnetic field (B_0) can have $2I + 1$ values, varying from $-I$ to $+I$ in unity increments (e.g., $I_z = -\frac{1}{2}$ and $+\frac{1}{2}$ for $I = \frac{1}{2}$, $I_z = -1, 0,$ and $+1$ for $I = 1$, etc.).

In the absence of B_0 , all orientations of the nuclear magnets in space have the same energy. The B_0 field, however, interacts with the nuclear magnets to alter their energies as a function of I_z . Because energy is a scalar quantity, it is obtained by the scalar or dot product of the magnetic moment and the external magnetic field; that is,

$$\text{energy} = \boldsymbol{\mu} \cdot \mathbf{B}. \quad (\text{A1-3})$$

Equation A1-2 for the nuclear magnet may be substituted into eq. A1-3 to give

$$\text{energy} = \gamma \hbar \mathbf{I} \cdot \mathbf{B}, \quad (\text{A1-4})$$

in which the subscript N has been dropped. Expansion of this expression in the usual fashion ($\mathbf{I} \cdot \mathbf{B} = I_x B_x + I_y B_y + I_z B_z$) is simplified because there are no x or y components of the magnetic field and B_z is represented by B_0 . The energy thus is expressed by

$$\text{energy} = \gamma \hbar I_z B_0, \quad (\text{A1-5})$$

in which I_z can assume only the two values $I_z = -\frac{1}{2}$ and $+\frac{1}{2}$. Two states result, whose energies are given respectively by

$$E_1(I_z = -\frac{1}{2}) = -\frac{1}{2} \gamma \hbar B_0 \quad (\text{A1-5a})$$

and

$$E_2(I_z = \frac{1}{2}) = \frac{1}{2} \gamma \hbar B_0. \quad (\text{A1-5b})$$

This splitting into multiple states has been called the *Zeeman effect*. By convention, we shall assign the lower energy E_1 to the state with $I_z = -\frac{1}{2}$. The difference in energy between the two spin states then is given by

$$\Delta E = E_2 - E_1 = h\nu_0 = \gamma \hbar B_0. \quad (\text{A1-6})$$

By the Planck equation ($\Delta E = h\nu_0$), this quantity corresponds to the energy of an electromagnetic wave with frequency ν_0 . The cancelation of Planck's constant in the two expressions in the rightmost equality of eq. A1-6 leads to

$$\nu_0 = \frac{\gamma B_0}{2\pi} \quad (\text{A1-7})$$

in linear frequency or to

$$\omega_0 = \gamma B_0 \quad (\text{A1-8})$$

in angular frequency ($\omega = 2\pi\nu$). The quantities ν_0 and ω_0 are called the *Larmor frequency*.

APPENDIX 2

The Bloch Equations

The Bloch equations provide a mathematical expression for the magnetization based on classical vector mechanics. The overall magnetization \mathbf{M} is the sum of three Cartesian components:

$$\mathbf{M} = \mathbf{i}M_x + \mathbf{j}M_y + \mathbf{k}M_z. \quad (\text{A2-1})$$

The magnetic field B_0 that gives rise to the Zeeman splitting is in the z direction, and the applied magnetic field B_1 operates in the xy plane.

When perturbed from equilibrium in the z direction, the system returns to equilibrium in a first-order rate process with a time constant T_1 : the spin-lattice, or longitudinal, relaxation time. Consequently, the rate of return from a perturbed value M_z to the equilibrium value M_0 is given by

$$\frac{dM_z}{dt} = \frac{1}{T_1}(M_0 - M_z). \quad (\text{A2-2})$$

Similarly, relaxation processes in the xy plane are controlled by the spin-spin, or transverse, relaxation time T_2 , so that the equations

$$\frac{dM_x}{dt} = -\frac{M_x}{T_2} \quad (\text{A2-3})$$

and

$$\frac{dM_y}{dt} = -\frac{M_y}{T_2} \quad (\text{A2-4})$$

describe the rates of return from perturbed values M_x and M_y to the equilibrium values of zero.

The various magnetization components are influenced by the magnetic fields B_0 and B_1 . The forces between the \mathbf{M} and \mathbf{B} vectors provide the mechanism to move the magnetization out of equilibrium. Eqs. A2-2, A2-3, and A2-4 describe only the return to equilibrium. To include the interaction of the magnetic fields on \mathbf{M} , Bloch followed a purely phenomenological

approach rather than one based on theory. The overall effect of all magnetic fields \mathbf{B} on a single nuclear magnet $\boldsymbol{\mu}$ is given by the vector cross product, as in the case for the force (or moment or torque) between any two vectors. In classical mechanics, the moment is the same thing as the rate of change of angular momentum \mathbf{J} with time; that is,

$$\frac{d\mathbf{J}}{dt} = \boldsymbol{\mu} \times \mathbf{B}. \tag{A2-5}$$

(For example, see *The Feynman Lectures on Physics*, Vol. 1, eqs. 20.11–20.13.) From eq. A1-2 ($\boldsymbol{\mu} = \gamma\hbar\mathbf{I}$) and from the definition of dimensionless spin ($\mathbf{J} = \hbar\mathbf{I}$), eq. A2-5 can be recast as

$$\frac{d\mathbf{I}}{dt} = \gamma\mathbf{I} \times \mathbf{B}. \tag{A2-6}$$

Since \mathbf{M} is the sum of all spins ($\mathbf{M} = \Sigma\mathbf{I}$), the rate of change of magnetization, perturbed by the magnetic fields, is given by

$$\frac{d\mathbf{M}}{dt} = \gamma\mathbf{M} \times \mathbf{B} = \gamma \begin{vmatrix} \mathbf{i} & \mathbf{j} & \mathbf{k} \\ M_x & M_y & M_z \\ B_x & B_y & B_z \end{vmatrix}, \tag{A2-7}$$

which we see expanded into matrix form for the vector cross product.

Our eventual aim is to obtain simple, closed expressions for the three magnetization components. We can derive the contribution from the force of \mathbf{B} on \mathbf{M} by matrix expansion of eq. A2-7 to give the formulas

$$\frac{dM_z}{dt} = \gamma M_x B_y - \gamma M_y B_x, \tag{A2-8}$$

$$\frac{dM_x}{dt} = \gamma M_y B_z - \gamma M_z B_y, \tag{A2-9}$$

and

$$\frac{dM_y}{dt} = -\gamma M_x B_z + \gamma M_z B_x. \tag{A2-10}$$

Although we can substitute $B_0 = B_z$, we still need expressions for B_x and B_y in terms of B_1 . As depicted in Figure A2-1, the linear oscillation of B_1 along the x direction is equivalent to a circular sweep. More rigorously, the linear vector is equivalent to two vectors rotating circularly in opposite directions. The x components of two circular vectors sum to give the linear vector along the x direction, whereas the y components (directed up and down) cancel out. At any time, the components of the clockwise vector are $B_x = B_1 \cos \omega t$ and $B_y = -B_1 \sin \omega t$, and those of the counterclockwise vector are $B_x = B_1 \cos \omega t$ and $B_y = B_1 \sin \omega t$. By convention, the clockwise vector is used to describe the B_1 field.

Substituting these values into eqs. A2-8, A2-9, and A2-10 and combining those equations with eqs. A2-2, A2-3, and A2-4 leads to the expressions

$$\frac{dM_z}{dt} = -\gamma M_x B_1 \sin \omega t - \gamma M_y B_1 \cos \omega t + \frac{(M_0 - M_z)}{T_1}, \tag{A2-11}$$

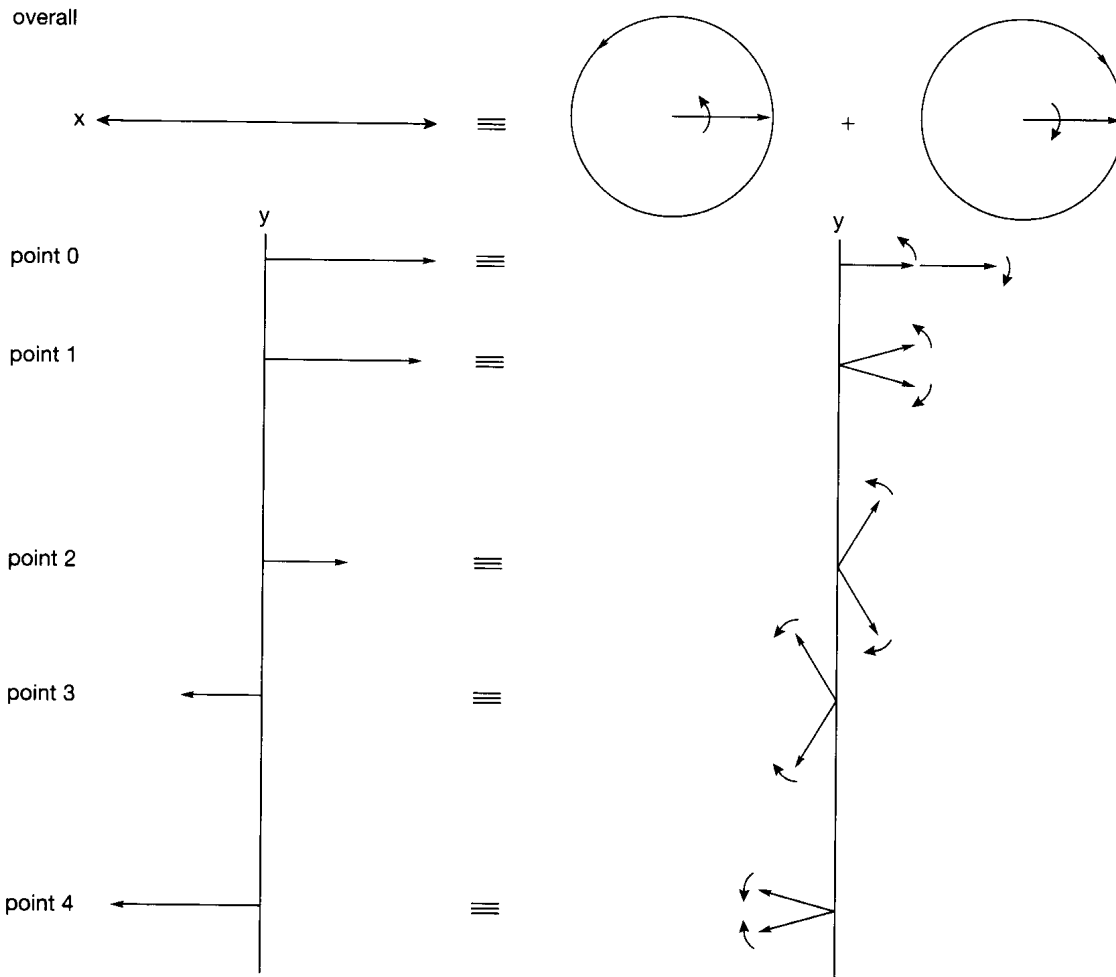


Figure A2-1 The equivalence of a linearly oscillating frequency to two circularly oscillating frequencies.

$$\frac{dM_x}{dt} = \gamma M_y B_0 + \gamma M_z B_1 \sin \omega t - \frac{M_x}{T_2}, \quad (\text{A2-12})$$

and

$$\frac{dM_y}{dt} = -\gamma M_x B_0 + \gamma M_z B_1 \cos \omega t - \frac{M_y}{T_2}. \quad (\text{A2-13})$$

These expressions may be simplified before they are solved by a change in coordinates that corresponds to the use of a *rotating coordinate system*. There is no change along the z direction, but a set of coordinates rotating around z at rate ω replaces x and y . The new coordinate x' rotates along (in phase) with B_1 , and the new coordinate y' rotates 90° behind x' (out of phase). Thus, the magnetization in the xy plane can be expressed as real u and imaginary v components of a complex number $M_{xy} = u + iv$ (u is the same as $M_{x'}$ and v as $M_{y'}$). The equations

$$M_x = u \cos \omega t - v \sin \omega t \quad (\text{A2-14})$$

and

$$M_y = -u \sin \omega t - v \cos \omega t \quad (\text{A2-15})$$

fully define the change in coordinates. Substitution of these quantities into eqs. A2-11, A2-12, and A2-13, leads, after considerable algebra and trigonometry, to the new differential equations

$$\frac{dM_z}{dt} = \gamma B_1 v + \frac{(M_0 - M_z)}{T_1}, \quad (\text{A2-16})$$

$$\frac{du}{dt} = -(\omega_0 - \omega)v - \frac{u}{T_2}, \quad (\text{A2-17})$$

and

$$\frac{dv}{dt} = (\omega_0 - \omega)u - \frac{v}{T_2} - \gamma B_1 M_z \quad (\text{A2-18})$$

(with the additional substitution of ω_0 for γB_0 , the resonance condition).

At the equilibrium condition of slow adiabatic passage, all three of these time variations are small and may be set equal to zero. We then have three equations in three unknowns (u , v , and M_z). These equations may be solved algebraically to give

$$u = M_0 \frac{\gamma B_1 T_2^2 (\omega_0 - \omega)}{1 + T_2^2 (\omega_0 - \omega)^2 + \gamma^2 B_1^2 T_1 T_2}, \quad (\text{A2-19})$$

$$v = -M_0 \frac{\gamma B_1 T_2}{1 + T_2^2 (\omega_0 - \omega)^2 + \gamma^2 B_1^2 T_1 T_2}, \quad (\text{A2-20})$$

and

$$M_z = M_0 \frac{1 + T_2^2 (\omega_0 - \omega)^2}{1 + T_2^2 (\omega_0 - \omega)^2 + \gamma^2 B_1^2 T_1 T_2}. \quad (\text{A2-21})$$

Although either u or v could be detected, normally the component (v or M_y') that is out of phase with respect to the B_1 field is detected and observed. This component is called the *absorption mode*, and the component u or M_x' that is in phase with B_1 is called the *dispersion mode*. Whereas the dispersion-mode signal goes to zero at resonance, when $\omega = \omega_0$ (and is used in electron spin resonance), the absorption mode goes to $-M_0 \gamma B_1 T_2 / (1 + \gamma^2 B_1^2 T_1 T_2)$, which has the familiar maximum value at $\omega = \omega_0$.

The phase relationship between u and v is best seen from the equations

$$u = M_x \cos \omega t - M_y \sin \omega t \quad (\text{A2-22})$$

and

$$v = -M_x \sin \omega t - M_y \cos \omega t \quad (\text{A2-23})$$

for the reverse coordinate transformation. If there is no x magnetization, then u is a sine function, v is a cosine function, and the two are 90° out of phase. Similarly, if there is no y magnetization, then u is a cosine function, v is a sine function, and, again, the two are 90°

out of phase. The linear sums of x and y magnetization then also are 90° out of phase. The phase relationships are illustrated in Figure A2-2. When the magnetization is lined up along the y axis of the rotating coordinate system (called y'), the resulting signal is *positive absorption* (Figure A2-2a). When the magnetization is lined up along the $-y$ axis, the signal is *negative absorption* (Figure A2-2b). When the signal is lined up along the x axis (and hence is in phase with B_1), the signal is *negative dispersion* (Figure A2-2c). Finally, when the signal is lined up along the $-x$ axis, the signal is *positive dispersion* (Figure A2-2d).

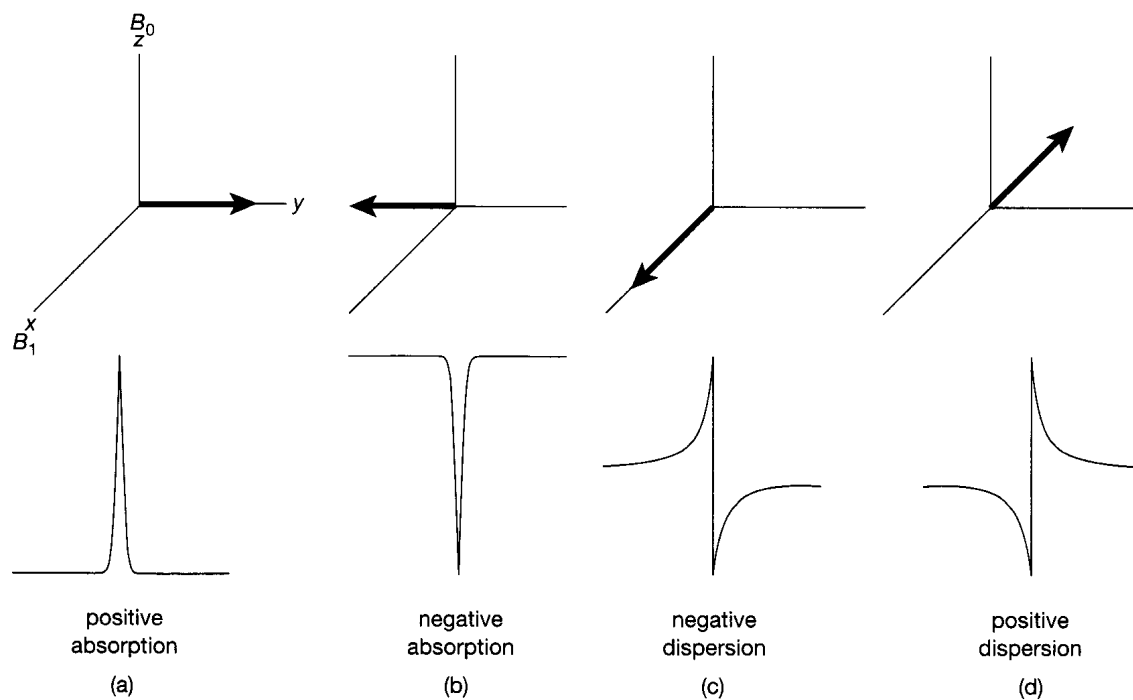


Figure A2-2 Phase relationships and the shape of the NMR signal. (Reproduced from T. D. W. Claridge, *High-Resolution NMR Techniques in Organic Chemistry*, Pergamon Press, Amsterdam, 1999, p. 19.)

APPENDIX 3

Quantum Mechanical Treatment of the Two-Spin System

Modern spectral analysis has largely lost track of the quantum mechanical foundation of NMR spectroscopy. As a result, many common NMR phenomena must be taken on faith. Without knowledge of the quantum mechanical treatment, however, one cannot answer common questions such as the following:

- Where does the coupling constant J come from?
- Why do equivalent or isochronous nuclei not split each other, even when they couple?
- What do the terms *closely coupled* and *second order* mean in terms of spin states?
- How are second-order intensities determined?
- What does the sign of the coupling constant signify?
- How is the chemical-shift difference measured in an AB spectrum?

To answer these and other questions, in this appendix we describe the quantum mechanical treatment for two spins. The description provides one of the few examples of an exact solution of the Schrödinger equation.

Schrödinger's wave equation,

$$\mathcal{H}\Psi = E\Psi, \quad (\text{A3-1})$$

provides a process whereby the energies of wave functions may be obtained. Whereas, in molecular science, wave functions are used to describe molecules, as regards NMR they describe spin states $(+\frac{1}{2}, -\frac{1}{2})$. The Hamiltonian operator \mathcal{H} provides the instruction to be executed on the wave function whereby the energy is obtained according to eq. A3-1. Our objective in this presentation is fourfold: (1) to describe wave functions for spin systems, (2) to obtain the energies of the wave functions from the Schrödinger equation, (3) to derive the frequencies of individual transitions between spin states, and (4) to evaluate the intensities of the resulting NMR absorptions. This information provides all the parameters needed to define the NMR spectrum, except the relaxation time, which controls the spectral line width.

The Hamiltonian operator for NMR is composed of a series of terms, the most important of which define the chemical shift and the coupling constant. Since we are dealing with the scalar energies of the interactions between vectors (between the magnetic moment μ

and the magnetic field \mathbf{B} for the chemical shift and between two spins \mathbf{I} for the coupling constant), the Hamiltonian operators are vector dot products. We have

$$\text{chemical shift:} \quad \mathcal{H}^0 = \sum_i \boldsymbol{\mu}_i \cdot \mathbf{B}; \quad (\text{A3-2a})$$

$$\text{coupling constant:} \quad \mathcal{H}^1 = \sum_i \sum_j J_{ij} \mathbf{I}(i) \cdot \mathbf{I}(j). \quad (\text{A3-2b})$$

The superscript on the Hamiltonian signifies that the chemical shift is considered to be the zeroth-order Hamiltonian (\mathcal{H}^0) and the coupling constant the first-order Hamiltonian (\mathcal{H}^1). The familiar coupling constant J is seen to be the proportionality constant between the Hamiltonian operator and the dot product of the spins and signifies quantitatively how strongly the spins interact. The summation over i in \mathcal{H}^0 allows the inclusion of all nuclei, and the double summation over i and j ($i < j$) in \mathcal{H}^1 assures that interactions between all spins are included, but only once.

In Appendix A1, we saw how the expression $\boldsymbol{\mu} \cdot \mathbf{B}$ can be expanded. Substitution into eq. A3-2a gives $\mathcal{H}^0 = \gamma \hbar \mathbf{I} \cdot \mathbf{B}$, which corresponds to $\gamma \hbar I_z B_0$ (eq. A1-5) in the presence of only B_0 . By eqs. A1-6 and A1-7, the Hamiltonian operator for the chemical shift becomes $\hbar \nu_0 I_z$, or, in units of frequency (Hz), $\nu_0 I_z$. The full Hamiltonian operator then is given by

$$\mathcal{H} = \mathcal{H}^0 + \mathcal{H}^1 = \sum_i \nu_i I_z(i) + \sum_i \sum_j J_{ij} \mathbf{I}(i) \cdot \mathbf{I}(j). \quad (\text{A3-3})$$

In order to apply the Schrödinger equation, we need to define spin wave functions. For a single spin with $I = \frac{1}{2}$, the wave function for the $I_z = -\frac{1}{2}$ state is simply called β , and that for the $I_z = +\frac{1}{2}$ state is called α . To construct wave functions for systems containing multiple spins, products of these wave functions are used as a basis, or beginning, set. Thus, for two spins, the basis set comprises the products $\beta(1)\beta(2)$, $\alpha(1)\beta(2)$, $\beta(1)\alpha(2)$, and $\alpha(1)\alpha(2)$. It is always understood that the first character represents nucleus one, and so on, so the parentheses may be dropped, giving $\beta\beta$, $\alpha\beta$, $\beta\alpha$, and $\alpha\alpha$. For larger spin systems, this process is carried out in logical fashion (for three spins, $\beta\beta\beta$, $\beta\beta\alpha$, $\beta\alpha\beta$, $\alpha\beta\beta$, and so on). The basis wave functions are orthonormal; that is, the projection of a wave function onto itself gives unity (normality) and that of one wave function onto another gives zero (orthogonality). In the following equations, the shorthand Dirac quantum mechanical notation for integration is used:

$$\langle \alpha | \alpha \rangle = 1, \quad \langle \beta | \beta \rangle = 1, \quad (\text{A3-4a})$$

$$\langle \alpha | \beta \rangle = 0, \quad \text{and} \quad \langle \beta | \alpha \rangle = 0. \quad (\text{A3-4b})$$

Thus, $\langle \alpha | \alpha \rangle = \int \alpha \alpha \, dv$, in which the integration is over a spatial element v . The extension of these equations to two spins thus implies that $\langle \alpha\alpha | \alpha\alpha \rangle$ and so on are unity and $\langle \alpha\alpha | \alpha\beta \rangle$ and so on are zero.

The complete wave function for a spin system is constructed by linearly combining the various basis-set wave functions, as in the formula

$$\Phi_q = \sum_m a_{qm} \Psi_m, \quad (\text{A3-5})$$

in which Φ_q is the complete function for the q th spin state, Ψ_m is the set of m basis functions, and a_{qm} is the mixing coefficient for each of the m basis functions. In a first-order, two-spin system (AX rather than AB), by definition there is no mixing between the spin states, so the basis functions also are the final, or stationary-state, wave functions. This is the quantum mechanical meaning of first order. Table A3-1 provides a list of the first-order wave functions Φ_q . The quantity S_z is the sum of the constituent I_z states. Thus, for $\alpha\alpha$,

Table A3-1 Two-Spin, First-Order (AX) Parameters without Coupling ($J = 0$) and with Coupling ($J \neq 0$)

q	Φ_q	S_z	$E_q(J = 0)$	$E_q(J \neq 0)$
1	$\alpha\alpha$	+1	$\frac{1}{2}(v_A + v_X)$	$\frac{1}{2}(v_A + v_X) + \frac{1}{4}J$
2	$\alpha\beta$	0	$\frac{1}{2}(v_A - v_X)$	$\frac{1}{2}(v_A - v_X) - \frac{1}{4}J$
3	$\beta\alpha$	0	$-\frac{1}{2}(v_A - v_X)$	$-\frac{1}{2}(v_A - v_X) - \frac{1}{4}J$
4	$\beta\beta$	-1	$-\frac{1}{2}(v_A + v_X)$	$-\frac{1}{2}(v_A + v_X) + \frac{1}{4}J$

$S_z = (\frac{1}{2} + \frac{1}{2}) = 1$; for $\alpha\beta$ and $\beta\alpha$, $S_z = (-\frac{1}{2} + \frac{1}{2}) = 0$; and for $\beta\beta$, $S_z = (-\frac{1}{2} - \frac{1}{2}) = -1$. The energies of a given state are obtained from the Hamiltonian matrix, whose component values are $H_{mn} = \langle \Phi_m | \mathcal{H} | \Phi_n \rangle$. With orthonormal wave functions, this matrix is diagonalized in the first-order case, so $H_{mn}(m \neq n) = 0$ and

$$H_{nn} = \langle \Phi_n | \mathcal{H} | \Phi_n \rangle = E_n \langle \Phi_n | \Phi_n \rangle = E_n. \quad (\text{A3-6})$$

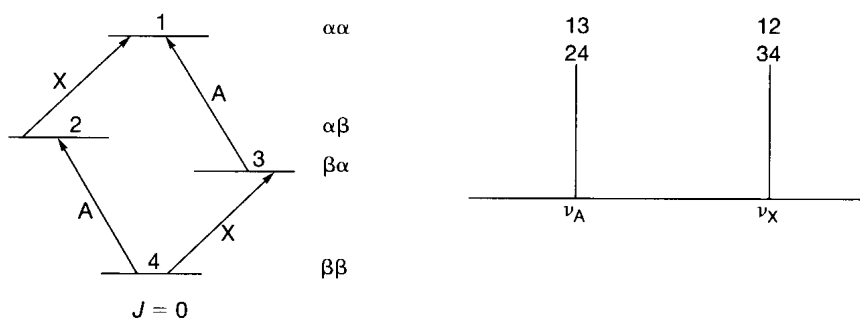
Thus, the energies of the spin states are the diagonal elements of the diagonalized Hamiltonian matrix. In the first-order case, the off-diagonal elements are zero (there is no mixing), so the energies are calculated directly from the diagonal elements (eq. A3-6).

When $J = 0$, the Hamiltonian operator is given by

$$\mathcal{H} = \mathcal{H}^0 = \sum_i v_i I_z(i). \quad (\text{A3-7})$$

For example, for $\alpha\alpha$, I_z is $+\frac{1}{2}$ for both nuclei, so $\mathcal{H} = \frac{1}{2}v_A + \frac{1}{2}v_X$, as recorded in the fourth column of Table A3-1. The other three values are calculated analogously. Figure A3-1 illustrates the order of spin states in what is called an *energy-level diagram*. Resonance corresponds to transitions between any two of the levels shown. Only transitions between adjacent values of S_z , however, are allowed; that is, there is a selection rule of $\Delta S_z = 1$. The forbidden transitions are $4 \rightarrow 1$ and $3 \rightarrow 2$, which respectively are called double ($\Delta S_z = 2$) or zero ($\Delta S_z = 0$) quantum transitions and occasionally can be seen as very weak peaks. There are two allowed transitions of A nuclei ("A-type transitions"): from 3 to 1 (13) and from 4 to 2 (24). There are also two allowed transitions of X nuclei ("X-type transactions"): from 2 to 1 (12) and from 4 to 3 (34). Table A3-1 shows that, when the subtractions are carried out, $\Delta E_{13} = \Delta E_{24} = v_A$ and $\Delta E_{12} = \Delta E_{34} = v_X$. These are the resonance frequencies of the four allowed transitions. The spectrum, illustrated diagrammatically at the right of Figure A3-1, thus is composed of two singlets, respectively at v_A and v_X ($v_A > v_X$, arbitrarily), each composed of two coincident transitions. The position of the double quantum transition can be obtained by equating $2h\nu$ to ΔE_{14} . The resulting frequency occurs at $\frac{1}{2}(v_A + v_X)$, the midpoint of the spectrum.

Figure A3-1 The energy level diagram and the transitions for a first order, two spin system (AX) with $J = 0$.



In order to describe the coupled AX spectrum ($J \neq 0$), it is necessary to evaluate the \mathcal{H}^1 part of the Hamiltonian matrix and add it to \mathcal{H}^0 . The simple results already are given in the last column of Table A3-1, where it is seen that the term from \mathcal{H}^0 is modulated by a term related to the coupling constant J from \mathcal{H}^1 (eq. A3-3). The integral to be evaluated is of the type $\langle \Phi_n | \mathcal{H}^1 | \Phi_m \rangle = J_{ij} \langle \Phi_n | \mathbf{I}(i) \cdot \mathbf{I}(j) | \Phi_m \rangle$. Evaluation of this integral requires a specification of the effects of the operator \mathbf{I} on the wave functions, as follows:

$$\begin{aligned} I_x \alpha &= \frac{1}{2} \beta, & I_x \beta &= \frac{1}{2} \alpha, \\ I_y \alpha &= \frac{1}{2} i \beta, & I_y \beta &= -\frac{1}{2} i \alpha, \\ I_z \alpha &= \frac{1}{2} \alpha, & \text{and } I_z \beta &= -\frac{1}{2} \beta. \end{aligned} \quad (\text{A3-8})$$

Here, $i = \sqrt{-1}$.

Since the system is first order, the H_{nm} terms are zero and the energy is given by H_{nn} in eq. A3-6. Figure A3-2 illustrates the evaluation of \mathcal{H}^1 for E_1 . In this way, the energies are obtained for $J \neq 0$ in Table A3-1. The energies illustrated in Figure A3-1 thus are nudged up (for $\alpha\alpha$ and $\beta\beta$) and down (for $\alpha\beta$ and $\beta\alpha$) by $\frac{1}{4}J$, as indicated by the arrows beside the energy levels in the leftmost diagram of Figure A3-3. When the subtractions are carried out between the energies E_q ($J \neq 0$) in Table A3-1, the transition energies, which are the differences, are found to be $\Delta E_{13} = \nu_A + \frac{1}{2}J$, $\Delta E_{24} = \nu_A - \frac{1}{2}J$, $\Delta E_{12} = \nu_X + \frac{1}{2}J$, and $\Delta E_{34} = \nu_X - \frac{1}{2}J$. Now each allowed transition has a different energy, and the spectrum is composed of four peaks. The pairs of peaks are centered respectively about ν_A and ν_X . The spacings within each pair are the coupling constant J : $[(\nu_A + \frac{1}{2}J) - (\nu_A - \frac{1}{2}J) = J]$ and $[(\nu_X + \frac{1}{2}J) - (\nu_X - \frac{1}{2}J) = J]$.

$$\begin{aligned} E_1^1 &= H_{11}^1 = \langle \alpha\alpha | \mathcal{H}^1 | \alpha\alpha \rangle \\ &= J \langle \alpha\alpha | \mathbf{I}(1) \cdot \mathbf{I}(2) | \alpha\alpha \rangle \\ &= J \langle \alpha\alpha | (I_x I_x + I_y I_y + I_z I_z) | \alpha\alpha \rangle \\ &= J (\langle \alpha\alpha | I_x I_x | \alpha\alpha \rangle + \langle \alpha\alpha | I_y I_y | \alpha\alpha \rangle + \langle \alpha\alpha | I_z I_z | \alpha\alpha \rangle). \end{aligned}$$

Figure A3-2 Evaluation of the diagonal elements of the Hamiltonian for scalar coupling in a first-order, two-spin system (AX).

Separate into terms for the individual spins:

$$\begin{aligned} E_1^1 &= J (\langle \alpha(1) | I_x(1) | \alpha(1) \rangle \langle \alpha(2) | I_x(2) | \alpha(2) \rangle + \\ &\quad \langle \alpha(1) | I_y(1) | \alpha(1) \rangle \langle \alpha(2) | I_y(2) | \alpha(2) \rangle + \\ &\quad \langle \alpha(1) | I_z(1) | \alpha(1) \rangle \langle \alpha(2) | I_z(2) | \alpha(2) \rangle). \end{aligned}$$

Spins 1 and 2 are equivalent:

$$E_1^1 = J (\langle \alpha | I_x | \alpha \rangle^2 + \langle \alpha | I_y | \alpha \rangle^2 + \langle \alpha | I_z | \alpha \rangle^2).$$

The integrals are evaluated by eq. A3-8:

$$\begin{aligned} E_1^1 &= J (\langle \alpha | \frac{1}{2} \beta \rangle^2 + \langle \alpha | \frac{1}{2} i \beta \rangle^2 + \langle \alpha | \frac{1}{2} \alpha \rangle^2) \\ &= J (0 + 0 + \frac{1}{4}) \\ &= \frac{1}{4} J. \end{aligned}$$

Similarly,

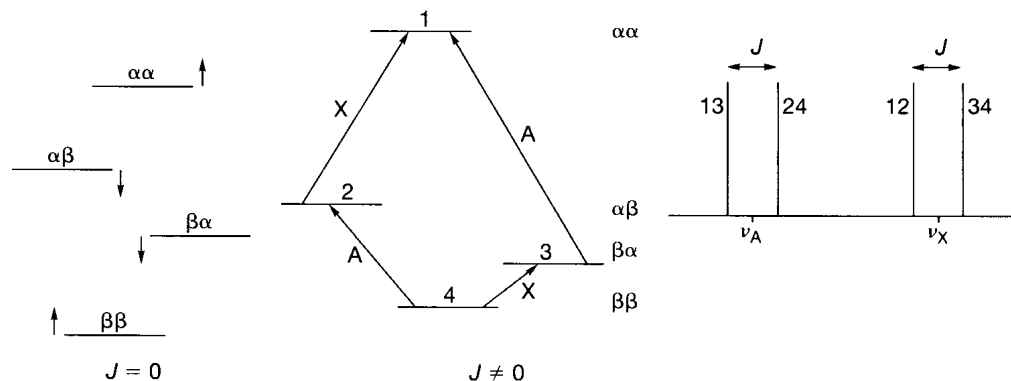
$$E_2^1 = J \langle \alpha\beta | \mathbf{I} \cdot \mathbf{I} | \alpha\beta \rangle = -\frac{1}{4} J,$$

$$E_3^1 = J \langle \beta\alpha | \mathbf{I} \cdot \mathbf{I} | \beta\alpha \rangle = -\frac{1}{4} J,$$

and

$$E_4^1 = J \langle \beta\beta | \mathbf{I} \cdot \mathbf{I} | \beta\beta \rangle = \frac{1}{4} J.$$

Figure A3-3 The energy-level diagram and the transitions for a first-order, two-spin system (AX) with $J \neq 0$.



As the A and X chemical shifts move closer together, mixing occurs between some of the basic wave functions, the off-diagonal matrix elements can no longer be ignored, and the spectrum is said to be second order. Only wave functions with the same S_z can mix. Thus, $\alpha\alpha$ and $\beta\beta$, the sole representatives for $S_z = +1$ and $S_z = -1$, respectively, do not mix with any other wave functions and continue to be stationary-state wave functions. The $S_z = 0$ states ($\alpha\beta$ and $\beta\alpha$), however, do mix.

It is easiest first to examine the extreme at which the chemical shifts coincide—that is, the case of A_2 . We can construct the stationary-state wave functions with the knowledge that contributions from each spin must be equivalent, a condition that is possible only with equal mixing coefficients: $(\alpha\beta + \beta\alpha)$ and $(\alpha\beta - \beta\alpha)$. In order to make the wave functions orthonormal, mixing coefficients of $1/\sqrt{2}$ must be used—that is, $(\alpha\beta + \beta\alpha)/\sqrt{2}$ and $(\alpha\beta - \beta\alpha)/\sqrt{2}$, as can be seen by evaluating the integrals $\langle(\alpha\beta + \beta\alpha)/\sqrt{2} | (\alpha\beta + \beta\alpha)/\sqrt{2}\rangle$ and $\langle(\alpha\beta - \beta\alpha)/\sqrt{2} | (\alpha\beta - \beta\alpha)/\sqrt{2}\rangle$.

These wave functions have important symmetry properties. For $\alpha\alpha$, $\beta\beta$, and $(\alpha\beta + \beta\alpha)/\sqrt{2}$, the two A nuclei may be interchanged to give the identical initial wave functions back. Such wave functions are said to be *symmetric*. In contrast, interchanging nuclei in $(\alpha\beta - \beta\alpha)/\sqrt{2}$ gives $(\beta\alpha - \alpha\beta)/\sqrt{2}$, which is the negative of the original wave function. Such wave functions are said to be *antisymmetric*. There is a second selection rule when wave functions have these properties, namely, that transitions are allowed only between wave functions of the same symmetry. By contrast, transitions are forbidden between symmetric and antisymmetric wave functions.

This second selection rule can be rationalized by introducing two new operators: the raising operator F_+ , which can raise β to α , but cannot operate on α , and the lowering operator, which can lower α to β , but cannot operate on β . (We will need to use only the raising operator.) The operation rules are as follows:

$$\begin{aligned} F_+|\beta\rangle &= |\alpha\rangle; & F_+|\alpha\rangle &= 0; \\ F_-|\beta\rangle &= 0; & F_-|\alpha\rangle &= |\beta\rangle. \end{aligned} \quad (\text{A3-9})$$

A transition probability is thus the squared integral $\langle\Phi_n|F_+|\Phi_m\rangle^2$, which evaluates the probability of raising Φ_m to Φ_n . Figure A3-4 evaluates two of these integrals and confirms the symmetry selection rule. Note that the operation of F_+ on $\beta\beta$ gives $(\alpha\beta + \beta\alpha)$, because F_+ must operate separately on each spin [i.e., $F_+ = F_{1+} + F_{2+}$, in which F_{1+} operates on the first spin ($\beta\beta \rightarrow \alpha\beta$) and F_{2+} operates on the second spin ($\beta\beta \rightarrow \beta\alpha$)]. The result is zero for transitions between states of unlike symmetry and 2 for transitions between states of like symmetry. The significance of the value 2 is noted presently.

Table A3-2 contains the parameters for the case of A_2 . The wave functions have been sorted according to symmetry. Let us first consider the case for which $J = 0$. The E^0 term is

$$\begin{aligned}
 & \text{Probability of transition from } \beta\beta \text{ to } (\alpha\beta + \beta\alpha)/\sqrt{2} \\
 &= \langle (\alpha\beta + \beta\alpha)/\sqrt{2} | F_+ | \beta\beta \rangle^2 \\
 &= \frac{1}{2} \langle (\alpha\beta + \beta\alpha) | (\alpha\beta + \beta\alpha) \rangle^2 \\
 &= \frac{1}{2} (\langle \alpha\beta | \alpha\beta \rangle + \langle \alpha\beta | \beta\alpha \rangle + \langle \beta\alpha | \alpha\beta \rangle + \langle \beta\alpha | \beta\alpha \rangle)^2 \\
 &= \frac{1}{2} (1 + 0 + 0 + 1)^2 \\
 &= 2.
 \end{aligned}$$

Figure A3-4 Evaluation of the transition probabilities in a two-spin system with identical chemical shifts (A_2).

$$\begin{aligned}
 & \text{Probability of transition from } \beta\beta \text{ to } (\alpha\beta - \beta\alpha)/\sqrt{2} \\
 &= \langle (\alpha\beta - \beta\alpha)/\sqrt{2} | F_+ | \beta\beta \rangle^2 \\
 &= \frac{1}{2} \langle (\alpha\beta - \beta\alpha) | (\alpha\beta + \beta\alpha) \rangle^2 \\
 &= \frac{1}{2} (\langle \alpha\beta | \alpha\beta \rangle + \langle \alpha\beta | \beta\alpha \rangle - \langle \beta\alpha | \alpha\beta \rangle - \langle \beta\alpha | \beta\alpha \rangle)^2 \\
 &= \frac{1}{2} (1 + 0 - 0 - 1) \\
 &= 0.
 \end{aligned}$$

Table A3-2 Parameters for Two Equivalent Spins without Coupling ($J = 0$) and with Coupling ($J \neq 0$)

q	Φ_q	S_z	$E_q(J = 0)$	$E_q(J \neq 0)$
S_1	$\alpha\alpha$	+1	ν_A	$\nu_A + \frac{1}{4}J$
S_0	$(\alpha\beta + \beta\alpha)/\sqrt{2}$	0	0	$\frac{1}{4}J$
S_{-1}	$\beta\beta$	-1	$-\nu_A$	$-\nu_A + \frac{1}{4}J$
A_0	$(\alpha\beta - \beta\alpha)/\sqrt{2}$	0	0	$-\frac{3}{4}J$

evaluated from $\sum_i \nu_i I_z(i)$ (eq. A3-7) and the Hamiltonian component H_{nm} (eq. A3-6). The results for $\alpha\alpha$ and $\beta\beta$ must be the same as in Table A3-1 when $\nu_A = \nu_X$. The results for $(\alpha\beta \pm \beta\alpha)/\sqrt{2}$ are interesting in that the resonance frequency cancels out as follows:

$$E^0(S_0) = \frac{[E^0(\alpha\beta) + E^0(\beta\alpha)]}{\sqrt{2}} = \frac{[\frac{1}{2}(\nu_A - \nu_A) + \frac{1}{2}(-\nu_A + \nu_A)]}{\sqrt{2}} = 0; \quad (\text{A3-10a})$$

$$E^0(A_0) = \frac{[E^0(\alpha\beta) - E^0(\beta\alpha)]}{\sqrt{2}} = \frac{[\frac{1}{2}(\nu_A - \nu_A) - \frac{1}{2}(-\nu_A + \nu_A)]}{\sqrt{2}} = 0. \quad (\text{A3-10b})$$

Thus, the E^0 term is zero for the S_0 and A_0 states, which is the same thing as saying that the B_0 field does not interact with those states.

Figure A3-5 shows the energy-level diagram. Subtraction of the energies for allowed transitions between spin states indicates that resonances occur at $\Delta E(S_0 \rightarrow S_1) = \nu_A$ and at $\Delta E(S_{-1} \rightarrow S_0) = \nu_A$. Thus, two transitions occur at the same position, and the result is a singlet at ν_A . Although there are four spin states, only two of these can make upward transitions. These transitions, however, have a probability of 2 (Figure A3-4), so that the average probability for all four states is $\frac{1}{4}(0 + 0 + 2 + 2)$, or unity.

When $J \neq 0$, the values for \mathcal{H}^1 are evaluated as in Figure A3-2. The symmetric states are raised in energy by $\frac{1}{4}J$, and the antisymmetric state is lowered by $-\frac{1}{4}J$, as illustrated in Figure A3-6. Again, the arrows beside the energy levels in the leftmost diagram indicate the

Figure A3-5 The energy-level diagram and the transitions for the two-spin system with identical chemical shifts (A_2) with $J = 0$.

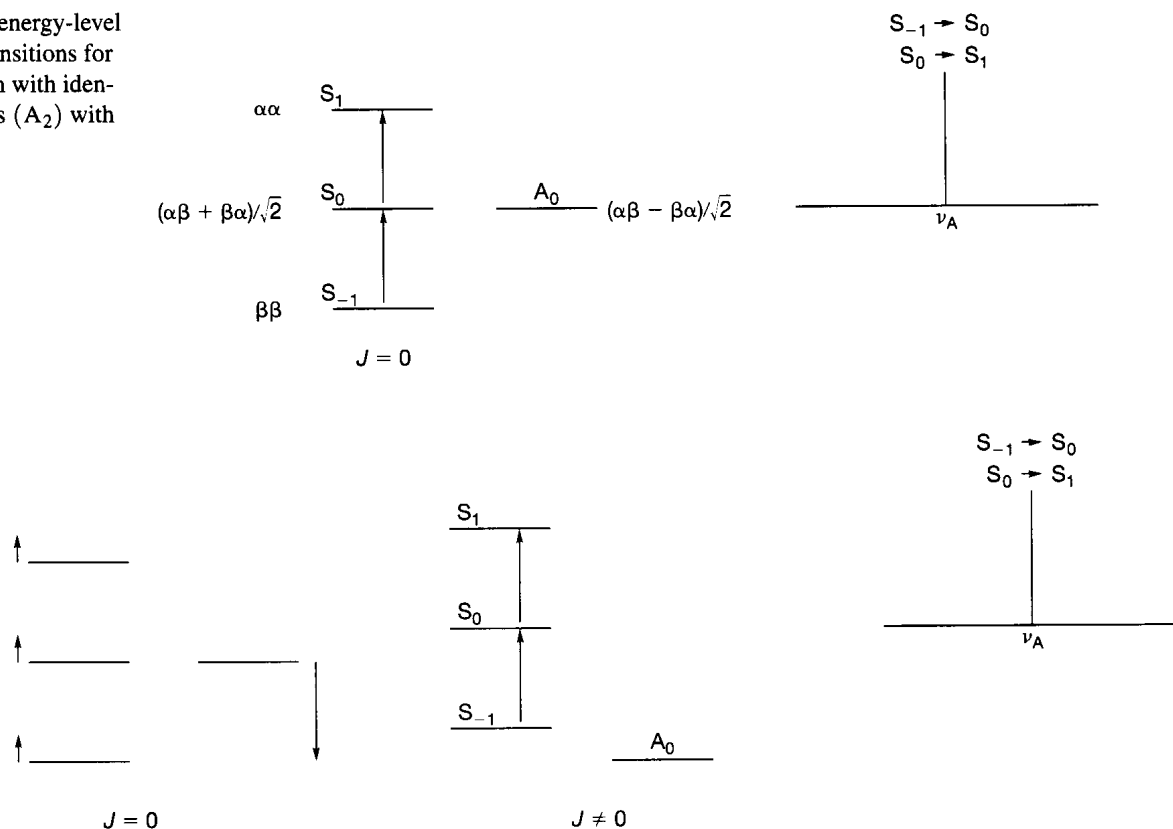


Figure A3-6 The energy-level diagram and the transitions for the two-spin system with identical chemical shifts (A_2) with $J \neq 0$.

direction of the change in energy. Because the symmetric states are perturbed by identical amounts, the transition energies remain unchanged: $\Delta E(S_0 \rightarrow S_1) = \Delta E(S_{-1} \rightarrow S_0) = \nu_A$. Again, the two transitions occur at the same position, and the result is a singlet at ν_A . Hence, the explanation as to why equivalent nuclei do not split each other is subtle. First, transitions between symmetric and antisymmetric states are forbidden, so different perturbations of these families are irrelevant. Second, each symmetric state is perturbed by the same amount, so the coupling drops out of the difference between states. It even drops out of the forbidden double quantum transition from S_{-1} to S_1 , which would occur with low intensity at ν_A ($2h\nu = 2\nu_A$).

When two nuclei have similar, but nonidentical, chemical shifts ($\Delta\nu/J \lesssim 10$), the AX system becomes AB. The $\alpha\alpha$ and $\beta\beta$ states still are stationary-state wave functions, but now $\alpha\beta$ and $\beta\alpha$ are mixed to an unknown, unequal extent. The general wave function is $[a(\alpha\beta) + b(\beta\alpha)]$, with two pairs of values for a and b . We need to obtain these values to evaluate the energies of the spin states, to calculate the frequencies of the resonances, and to determine the intensities of the resonances.

The energies are determined from the Hamiltonian matrix, and those for $\alpha\alpha$ and $\beta\beta$ are the same as in Table A3-1. The Hamiltonian matrix is then reduced to a 2×2 determinant. The off-diagonal elements (H_{23} and H_{32}) represent the extent of mixing. This determinant must be diagonalized by subtracting the variable from the diagonal elements, setting the results equal to zero, and working out the algebra. The process is carried out in Figure A3-7. The diagonal elements, H_{22} and H_{33} , are the same as in Table A3-1. The off-diagonal elements—for example, H_{23} —are calculated from $\langle \Psi_m | \mathcal{H} | \Psi_n \rangle$. The E^0 components are obtained from Table A3-1, with ν_B substituted for ν_X . The E^1 components are calculated from $\langle \alpha\beta | \mathcal{H}^1 | \beta\alpha \rangle$ and $\langle \beta\alpha | \mathcal{H}^1 | \alpha\beta \rangle$ and are found to be $\frac{1}{2}J$, by the method illustrated in Figure A3-2.

$$\mathbf{H}_{mn} = \begin{vmatrix} H_{22} & H_{32} \\ H_{23} & H_{33} \end{vmatrix}$$

$$\begin{vmatrix} H_{22} - E & H_{32} \\ H_{23} & H_{33} - E \end{vmatrix} = 0.$$

$$\begin{vmatrix} \frac{1}{2}(\nu_A - \nu_B) - \frac{1}{4}J - E & \frac{1}{2}J \\ \frac{1}{2}J & -\frac{1}{2}(\nu_A - \nu_B) - \frac{1}{4}J - E \end{vmatrix} = 0.$$

$$\left[\left(\frac{1}{2}(\nu_A - \nu_B) - \frac{1}{4}J - E \right) \left(-\frac{1}{2}(\nu_A - \nu_B) - \frac{1}{4}J - E \right) - \frac{1}{4}J^2 \right] = 0;$$

$$-\frac{1}{4}(\nu_A - \nu_B)^2 + \frac{1}{16}J^2 + \frac{1}{2}JE + E^2 - \frac{1}{4}J^2 = 0;$$

$$(E + \frac{1}{4}J)^2 = \frac{1}{4}[(\nu_A - \nu_B)^2 + J^2];$$

$$E_{\pm} = \pm \frac{1}{2}[(\nu_A - \nu_B)^2 + J^2]^{\frac{1}{2}} - \frac{1}{4}J;$$

$$E_{\pm} = \pm C - \frac{1}{4}J.$$

Note:

$$2C = [(\nu_A - \nu_B)^2 + J^2]^{\frac{1}{2}};$$

$$4C^2 = (\nu_A - \nu_B)^2 + J^2;$$

$$\nu_A - \nu_B = (4C^2 - J^2)^{\frac{1}{2}}.$$

Figure A3-7 Diagonalization of the $S_z = 0$ Hamiltonian matrix for the second-order, two-spin system (AB) and evaluation of the spin state energies.

A new parameter, C , is defined in Figure A3-7. The chemical-shift differences $(\nu_A - \nu_B)$ can be calculated if J and C are known. Table A3-3 summarizes the results. After C is inserted, and when the chemical-shift difference is much greater than the coupling constant $[(\nu_A - \nu_B) \gg J]$, the values of E_q are the same as those for the first-order case in Table A3-1.

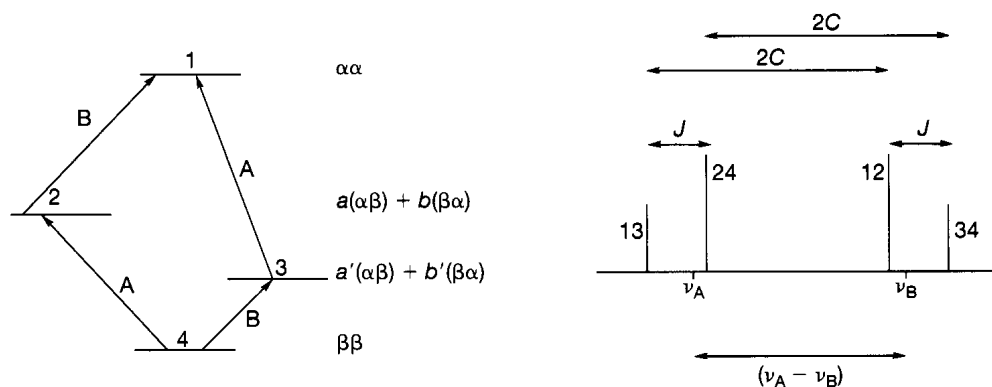
Figure A3-8 illustrates the energy levels and transitions. Subtraction of the energies leads to four transition frequencies. By convention, the center of the spectrum is given zero frequency, so that $\frac{1}{2}(\nu_A + \nu_B) = 0$. Consequently, the four transition frequencies are $(-C + \frac{1}{2}J)$ for $2 \rightarrow 1$ (12), $(-C - \frac{1}{2}J)$ for $4 \rightarrow 3$ (34), $(C + \frac{1}{2}J)$ for $3 \rightarrow 1$ (13), and $(C - \frac{1}{2}J)$ for $4 \rightarrow 2$ (24) with respect to the center point. The value of J thus corresponds to the difference between the first (13) and second (24) or between the third (12) and fourth (34) peaks, and the value of C corresponds to one-half the difference between the first and third or between the second and fourth peaks, as illustrated in the figure. The chemical-shift difference comes from these two quantities: $(\nu_A - \nu_B) = (4C^2 - J^2)^{\frac{1}{2}}$. When $J = 0$, the spectrum collapses to the two-line form seen in Figure A3-1.

Table A3-3 Two-Spin, Second-Order (AB) Parameters

q	Φ_q	S_z	E_q
1	$\alpha\alpha$	+1	$\frac{1}{2}(\nu_A + \nu_B) + \frac{1}{4}J$
2	$a(\alpha\beta) + b(\beta\alpha)$	0	$C - \frac{1}{4}J$
3	$a'(\alpha\beta) + b'(\beta\alpha)$	0	$-C - \frac{1}{4}J$
4	$\beta\beta$	-1	$-\frac{1}{2}(\nu_A + \nu_B) + \frac{1}{4}J$

$$C = \frac{1}{2}[(\nu_A - \nu_B)^2 + J^2]^{\frac{1}{2}}$$

Figure A3-8 The energy-level diagram and the transitions for the second-order, two-spin system (AB).



What remains is to evaluate the coefficients in the stationary-state wave function for $S_z = 0$ and to determine the relative intensities of the inner and outer peaks, which are seen to be unequal in Figure A3-8. One method of determining the coefficients is to recognize that their ratio corresponds to the ratio of their matrix cofactors. (The cofactor of a particular matrix element is obtained by deleting the top row and the column in which it resides). With reference to Figure A3-7, the cofactor for $\alpha\beta$ (H_{22}) is $[-\frac{1}{2}(\nu_A - \nu_B) - \frac{1}{4}J - E]$ and the cofactor for $\beta\alpha$ (H_{33}) is $\frac{1}{2}J$. The formula

$$\frac{a}{b} = \frac{1}{J} [-(\nu_A - \nu_B) \pm 2C] \quad (\text{A3-11})$$

gives the coefficient ratio when the values of E_+ and E_- from Figure A3-7 are substituted for E in the cofactor for $\alpha\beta$. In order to obtain normalized wave functions, we also require that $(a^2 + b^2) = 1$. The coefficients a and b are thus two unknowns to be obtained from two equations. A simplification results when one defines an angle (with no physical significance) from $\sin 2\theta = J/2C$. When this substitution is made, it is found that $a = \cos \theta$ when $b = \sin \theta$ and $a = \sin \theta$ when $b = -\cos \theta$. [Note that $(\sin^2 \theta + \cos^2 \theta) = 1$, corresponding to $(a^2 + b^2) = 1$.] The stationary-state wave functions then are given by the two equations

$$\phi_2 = \cos \theta(\alpha\beta) + \sin \theta(\beta\alpha) \quad (\text{A3-12})$$

and

$$\phi_3 = \sin \theta(\alpha\beta) - \cos \theta(\beta\alpha).$$

When $\theta = 0$, ϕ_2 becomes $\alpha\beta$ and ϕ_3 becomes $\beta\alpha$, which are the stationary-state wave functions for the first-order (AX) case. When $\theta = 45^\circ$, ϕ_2 becomes $(\alpha\beta + \beta\alpha)/\sqrt{2}$ and ϕ_3 becomes $(\alpha\beta - \beta\alpha)/\sqrt{2}$, which are the stationary-state wave functions for the case of A_2 .

The intensities or transition probabilities are obtained with the use of the raising operators, as shown in Figure A3-9. The intensity ratio (inner \div outer) thus is seen to be $(1 + 2ab)/(1 - 2ab)$, which may be manipulated algebraically to $(a + b)^2/(a - b)^2$, or $(1 + ab)^2/(1 - ab)^2$. The ratio a/b from eq. A3-11 is inserted into the latter expression, yielding the intensity ratio from J , C , and $(\nu_A - \nu_B)$. The intensity ratio may be obtained more directly by inserting the definition $2ab = J/2C = \sin 2\theta = 2 \sin \theta \cos \theta$ into the probability expressions in Figure A3-9. The intensities of transitions 24 and 12 are thus

Probability of $4 \rightarrow 2$:

$$\begin{aligned}
 & \{ \langle [a(\alpha\beta) + b(\beta\alpha)] | F_+ | \beta\beta \rangle \}^2 \\
 &= \{ \langle [a(\alpha\beta) + b(\beta\alpha)] | (\alpha\beta + \beta\alpha) \rangle \}^2 \\
 &= \{ \langle [a(\alpha\beta|\alpha\beta) + b(\beta\alpha|\alpha\beta) + a(\alpha\beta|\beta\alpha) + b(\beta\alpha|\beta\alpha)] \rangle \}^2 \\
 &= [a(1) + b(0) + a(0) + b(1)]^2 \\
 &= (a + b)^2 \\
 &= 1 + 2ab.
 \end{aligned}$$

Probability of $3 \rightarrow 1$:

$$\begin{aligned}
 & \{ \langle [\alpha\alpha | F_+ | [a'(\alpha\beta)] + b'(\beta\alpha)] \rangle \}^2 \\
 &= \{ \langle \alpha\alpha | F_+ | [b(\alpha\beta) - a(\beta\alpha)] \rangle \}^2 \quad (\text{From eq. A3-12}) \\
 &= (b - a)^2 \\
 &= 1 - 2ab.
 \end{aligned}$$

Figure A3-9 Evaluation of the transition probabilities in the second-order, two-spin system (AB).

$1 + J/2C$ and of transitions 13 and 34 are $1 - J/2C$. Their ratio becomes $(1 + J/2C)/(1 - J/2C)$, or $(2C + J)/(2C - J)$, which is the same as $(\nu_{13} - \nu_{34})/(\nu_{24} - \nu_{12})$. The intensity ratio thus corresponds to the ratio of the distances between the outer and the inner peaks.

Expressions for three-spin systems or higher can be developed in the same fashion, but with increasingly larger matrix elements to evaluate.



APPENDIX 4

Analysis of Second-Order, Three- and Four-Spin Systems by Inspection

The analysis of the second-order, two-spin (AB) system by inspection is given in Section 4-7 and is explained in Appendix 3. A few other second-order systems may be analyzed without recourse to computer methods. Analyzing a three-spin systems ranges from the trivial (AX_2 , AMX) to the impossible (many ABC systems). As the AX chemical-shift difference in the AX_2 system decreases, degeneracies are lifted, intensities change, and a new peak can appear (Figure A4-1). In the AB_2 extreme, a total of nine peaks can be observed. Four of these peaks result from spin flips of A protons, four from spin flips of B protons, and one from simultaneous spin flips of both A and B protons. The ninth peak, called a combination line, is forbidden in the first-order case (AX_2) and is rarely observed even in the AB_2 extreme. The combination line is seen only in the most closely coupled case at the top, as a very low intensity peak at the far right.

When eight peaks are observed, the AB_2 spectrum may be analyzed by inspection. By convention, the peaks are numbered from the A to the B nuclei, from left to right in Figure A4-1. The spectrum in Figure A4-1e is nearly first order, and peaks 2/3, 5/6, and 7/8 are degenerate pairs giving the triplet and doublet (five peaks) expected of AX_2 . In Figure A4-1d, the degeneracy of 2/3 is lifted to give a total of six peaks, and, in Figures A4-1b and A4-1c, all degeneracies are lifted to give the full complement of eight peaks. In Figure A4-1a, peaks 5/6 are degenerate again, and the combination line 9 is barely visible. Intensities increase toward the middle of the spectrum as the chemical-shift difference approaches zero for the A_3 extreme. The chemical shift of the A proton always corresponds to the position of the third peak; that is,

$$\nu_A = \nu_3. \quad (\text{A4-1})$$

The chemical shift of the B proton occurs at the average of the fifth and seventh peaks, or

$$\nu_B = \frac{1}{2}(\nu_5 + \nu_7), \quad (\text{A4-2})$$

and the AB coupling constant is obtained from a linear combination of four peak positions, or

$$J_{AB} = \frac{1}{3}(\nu_1 - \nu_4 + \nu_6 - \nu_8). \quad (\text{A4-3})$$

Thus, the entire spectrum may be analyzed without reference to the combination line. When not all eight of the remaining peaks are distinct, as in Figures A4-1a and A4-1d, care must be taken to recognize which peaks overlap. Recourse to computer methods then may be necessary.

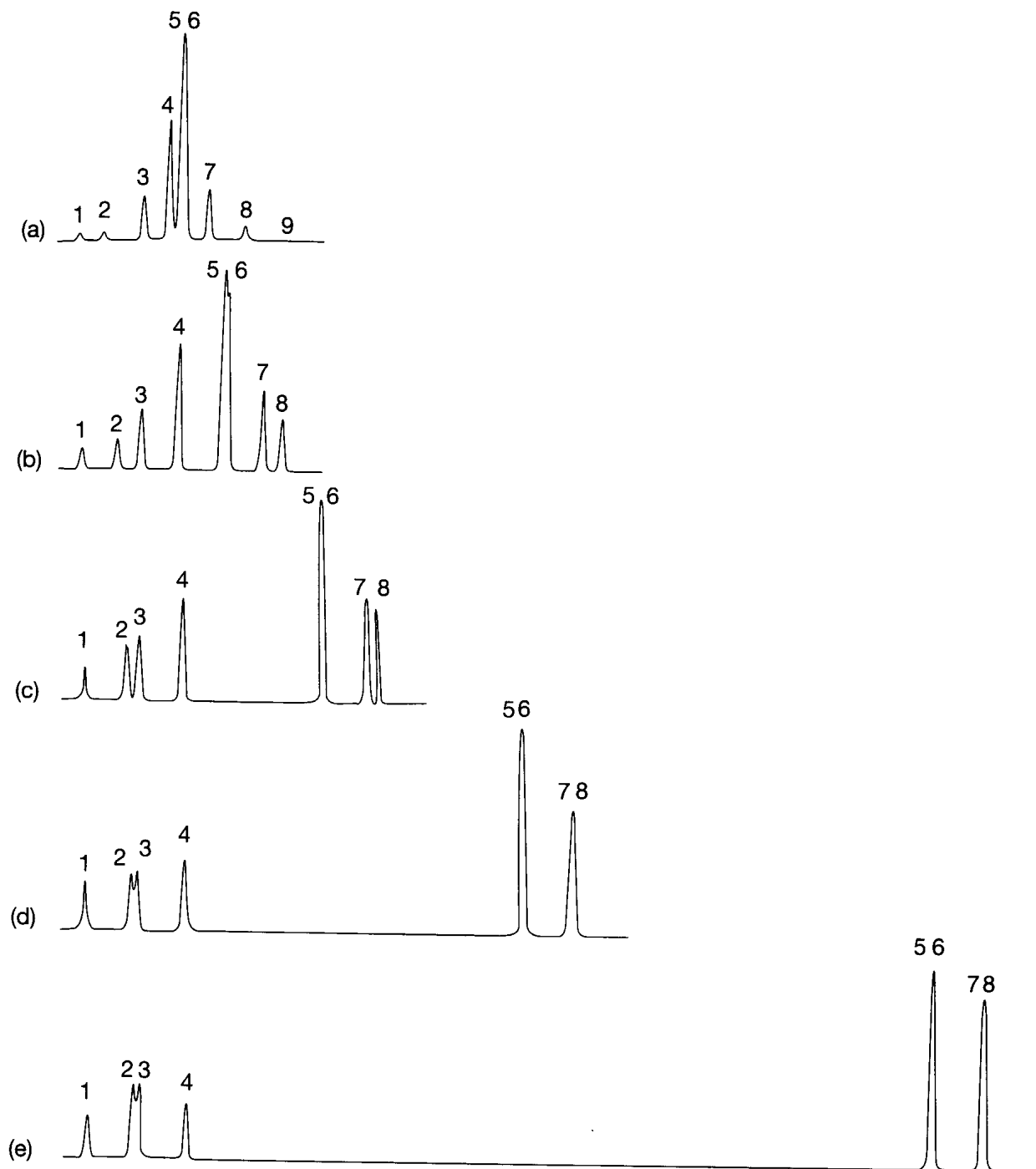
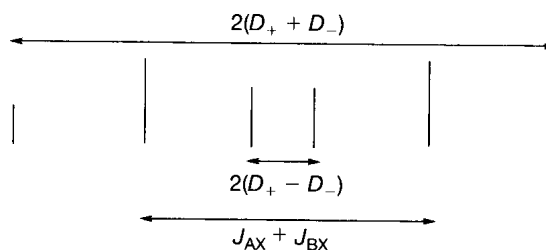


Figure A4-1 The transition from first order (AX_2 , bottom) to second order (AB_2 , top), with J_{AB} held at 10 Hz and $\Delta\nu_{AB}$ ($\Delta\nu_{AX}$) varied: 10 (top), 20, 40, 80, and 160 Hz.

The next level of spectral complexity is the case in which all three nuclei have different chemical shifts, but one of the resonances is well removed from the other two (ABX). This spectrum is determined by six parameters: ν_A , ν_B , ν_X , J_{AB} , J_{AX} , and J_{BX} . The X resonance of an ABX spectrum generally has six lines (two overlapping triplets), with ν_X at the midpoint (Figure A4-2). The distance between the two tallest peaks is equal to the sum of J_{AX} and J_{BX} . The separation between the outermost lines is twice the sum of a pair of important quantities, which have been designated D_+ and D_- , and the separation of the innermost

Figure A4-2 The X portion of an ABX spectrum.



peaks is twice the difference of these two quantities. Thus, D_+ and D_- , which are defined by the formula

$$D_{\pm} = \frac{1}{2} \left\{ \left[(\nu_A - \nu_B) \pm \frac{1}{2} (J_{AX} - J_{BX}) \right]^2 + J_{AB}^2 \right\}^{1/2}, \quad (\text{A4-4})$$

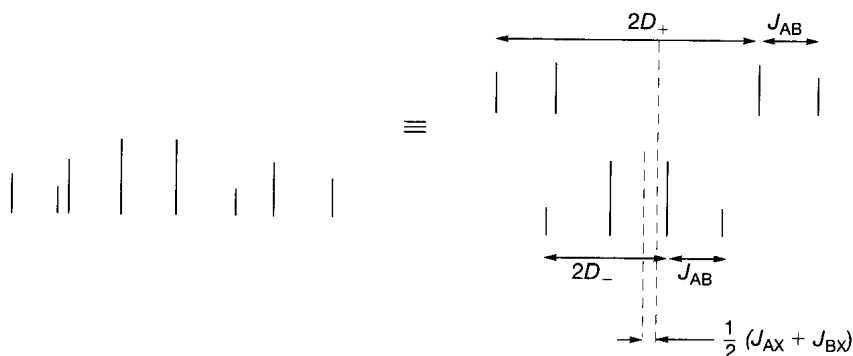
may be derived from the X resonance. The value of J_{AB} is obtained from the AB part of the spectrum, as described shortly. With the knowledge of D_+ , D_- , and J_{AB} , the pair of eqs. A4-4 give values for $(\nu_A - \nu_B)$ and $(J_{AX} - J_{BX})$. Since $J_{AX} + J_{BX}$ is known from the X part, the individual values for J_{AX} and J_{BX} may be calculated. Two solutions, however, are possible, depending on whether these two coupling constants have the same sign (either both plus or both minus) or opposite signs (one plus and one minus). The two possibilities may be distinguished by examining the AB portion of the spectrum.

The AB part of the ABX spectrum is made up of two overlapping quartets (Figure A4-3). The doublet separation between the first and second and between the third and fourth peaks in both quartets gives four independent measurements of J_{AB} . (No absolute or relative information about the sign is obtained.) The separation of alternate peaks (first and third or second and fourth) provides redundant determinations of D_+ and D_- . The separation of the midpoints of the two quartets gives an additional measurement of $\frac{1}{2}(J_{AX} + J_{BX})$. All of these spacings are illustrated in the figure.

If the arithmetic for a particular ABX spectrum is followed through, the exact values of ν_X , $(\nu_A - \nu_B)$, and J_{AB} may be obtained, but two sets of J_{AX} and J_{BX} are produced, with either like or unlike signs. Although both of these solutions correctly reproduce all the peak positions, only one gives the X portion with the proper intensities. The most straightforward method of differentiating the two sets therefore is to use computer methods to calculate the spectrum corresponding to each. Most modern spectrometers have simple programs for calculating spectra from an input of all the chemical shifts and coupling constants. The correct set of parameters reproduces the experimental X intensities.

The ABC spectrum, in which all three nuclei are closely coupled, contains up to 15 lines (four A-type, four B-type, four C-type, and three combination lines), but analysis by inspection is very difficult. Accordingly, recourse must be made to a general computer method, such as LAOCN3 or DAVINS, or to Castellano and Waugh's EXAN II program, which was designed specifically for ABC spectra and is successful in more than 90% of cases.

Figure A4-3 The AB portion of an ABX spectrum.



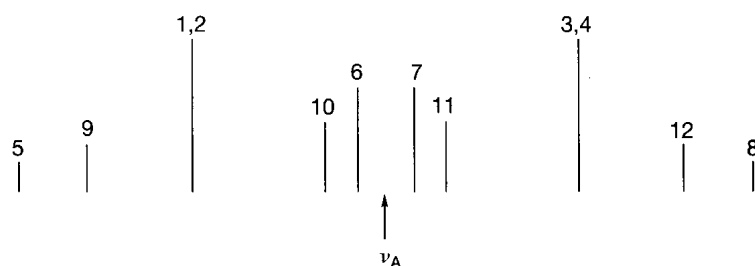


Figure A4-4 The A part of an AA'XX' spectrum.

Arithmetic analysis of four spin systems is very limited. First-order spectra (AX_3 , A_2X_2) provide no difficulty. Of the second-order spectra, however ($AA'XX'$, $AA'BB'$, $ABXY$, $ABCX$, $ABCD$, etc.), only the $AA'XX'$ can be analyzed readily. This common pattern, which is second order only because of magnetic nonequivalence, is determined by six parameters: ν_A , ν_X , $J_{AA'}$, $J_{XX'}$, J_{AX} ($= J_{A'X'}$), and $J_{AX'}$ ($= J_{A'X}$). Note that such a spectrum is dependent on the coupling between chemically equivalent nuclei ($J_{AA'}$ and $J_{XX'}$). The A and X parts of the spectrum are identical, and the chemical shifts (ν_A and ν_X) are readily obtained from their respective midpoints. Figure A4-4 gives a diagrammatic representation of the A part of an $AA'XX'$ spectrum with mirror symmetry about ν_A . As $(\nu_A - \nu_X)$ gets smaller, this symmetry is lost, and the spectrum becomes $AA'BB'$.

As the following equations show, the $AA'XX'$ spectrum is dependent primarily on the sums and differences of coupling constants, rather than on the couplings themselves:

$$K = J_{AA'} + J_{XX'}; \quad L = J_{AX} - J_{AX'}; \quad M = J_{AA'} - J_{XX'}; \quad N = J_{AX} + J_{AX'}. \quad (\text{A4-5})$$

The distance between the two dominant peaks ($\nu_{1,2} - \nu_{3,4}$), each of which is a degenerate pair of peaks, corresponds to N , the sum of J_{AX} and $J_{AX'}$. The remainder of the spectrum corresponds to two AB-like quartets (ν_{5-8} and ν_{9-12}). The separation of adjacent outer peaks in a given quartet corresponds to K [$(\nu_5 - \nu_6)$ and $(\nu_7 - \nu_8)$] and M [$(\nu_9 - \nu_{10})$ and $(\nu_{11} - \nu_{12})$]. Finally, L may be obtained from K , M , and the separation between alternate peaks in either quartet via the relations

$$\nu_5 - \nu_7 = (K^2 + L^2)^{1/2} \quad (\text{A4-6A})$$

and

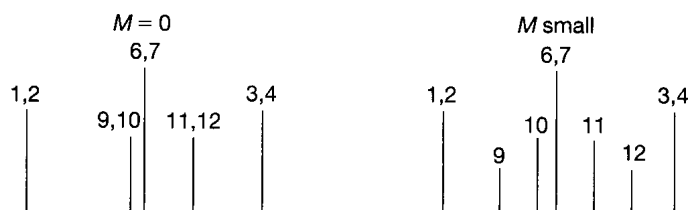
$$\nu_9 - \nu_{11} = (M^2 + L^2)^{1/2}. \quad (\text{A4-6B})$$

If all 10 peaks are observed, the analysis of the $AA'XX'$ spectrum is quite straightforward, as could be done, for example, with the spectrum of 1,1-difluoroethene in Figure 4-2. When fewer peaks are observed, as in the spectrum of 1,2-dichlorobenzene (which is $AA'BB'$ rather than $AA'XX'$) (Figure 4-3), the analysis is more difficult and normally requires the use of computer programs. Often, such spectra are termed *deceptively simple*. The analysis does not distinguish $J_{AA'}$ from $J_{XX'}$ or J_{AX} from $J_{AX'}$.

A common example of the $AA'XX'$ spectrum occurs in the bismethylene fragment ($-\text{CH}_2-\text{CH}_2-$) of both acyclic and cyclic compounds. The $J_{AA'}$ and $J_{XX'}$ are geminal couplings, and the J_{AX} and $J_{AX'}$ are vicinal couplings. Because geminal couplings are usually about -12 Hz in such situations, K is quite large. As a result, ν_5 and ν_8 are well removed and of very small intensity, and ν_6 and ν_7 become degenerate. Because $J_{AA'}$ and $J_{XX'}$ usually have similar values and often are identical, the separation (M) between ν_9 and ν_{10} and between ν_{11} and ν_{12} is small or zero, so that ν_9 and ν_{11} are drawn inside the two large peaks ($\nu_{1,2}$ and $\nu_{3,4}$) that give the sum of the vicinal couplings (N). If M is zero, then the difference between the vicinal couplings (L) is given by the separation between $\nu_{9,10}$ and $\nu_{11,12}$

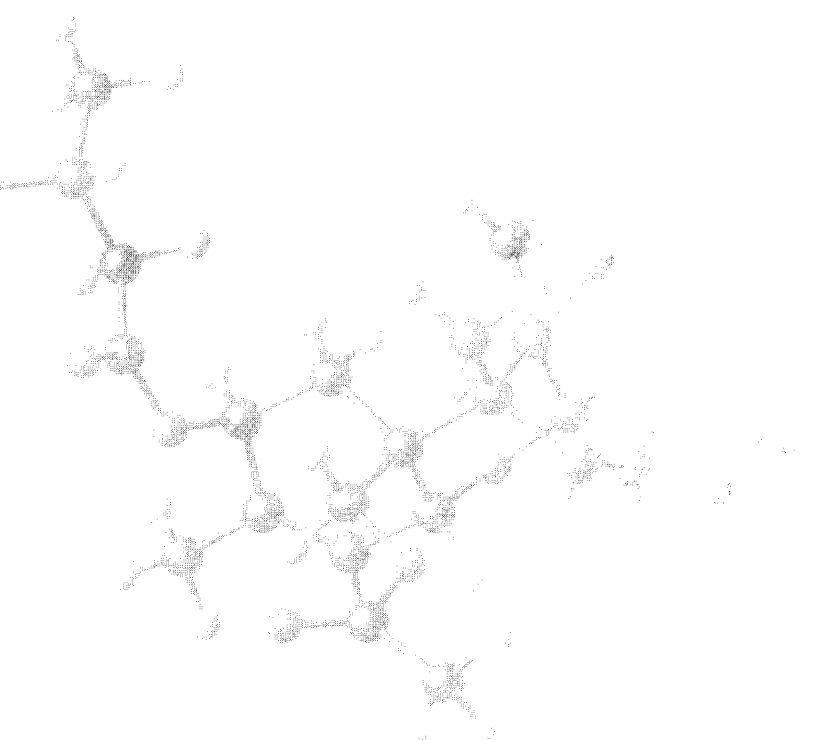
(Figure A4-5, left). Otherwise, L is obtained from M and eq. A4-6b (Figure A4-5, right). This spectrum thus readily gives J_{AX} , $J_{AX'}$, and $(J_{AA'} - J_{XX'})$, but not $(J_{AA'} + J_{XX'})$. The spectrum of 2-chloroethanol in Figure 4-4 is $AA'BB'$, but provides an example close to that on the left in Figure A4-5, in which peaks 9/10 fall on top of 6/7 to give the large central peak in each half and peaks 11/12 appear as a small peak on the side of the central one.

Figure A4-5 Two examples of the special case of $AA'XX'$ spectra (A part) for a $-\text{CH}_2\text{CH}_2-$ fragment in a cyclic compound: (left) when $M = 0$ and (right) when M is small.



APPENDIX 5

Relaxation

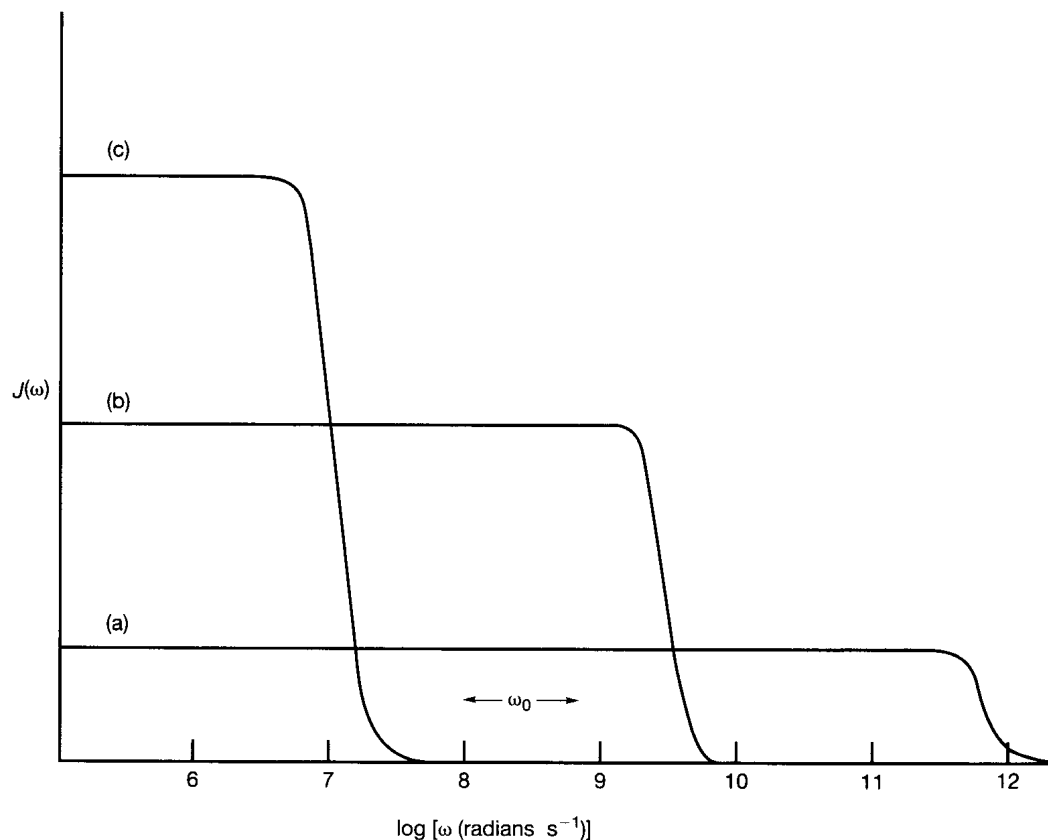


Spin–lattice relaxation occurs by the interaction of an excited nucleus with a magnetic field fluctuating in the approximate frequency range 10^8 – 10^9 s^{-1} . Energy passes from the excited nucleus to the source of the magnetic field in the surrounding lattice. Since molecular tumbling is the primary cause of the fluctuating magnetic field, the frequency is most appropriately expressed as ω in units of radians per second. The time constant for this process (the average time to rotate through one radian) is the effective correlation time τ_c , with units of seconds. Note that ω is an instantaneous rate, but τ_c is an average period. Thus, τ_c is only roughly equivalent to the inverse of the tumbling rate. The effective correlation time depends on a number of factors, including the size of the molecule, the viscosity of the solution, the temperature of the experiment, hydrogen bonding interactions of both solvent and solute, and even the pH. It is not the same for every atom in the molecule, as segmental motion can cause some groups in a molecule (methyl, in particular) to rotate more rapidly than other components. Relaxation is most efficient when $1/\tau_c$ and the resonance (Larmor) frequency ω_0 are comparable in magnitude, (i.e., $\omega_0\tau_c \approx 1$).

The most common source of the fluctuating field is tumbling of a nearby magnetic dipole. Such a dipole is supplied by a magnetic nucleus, usually a proton (called the S nucleus). Relaxation of a resonating proton (called the I nucleus) occurs by interaction with fields from nearby tumbling protons, which are geminal in methylene (CH_2) or methyl groups (CH_3) and vicinal or more distant for methinyl protons (CH). Carbon or nitrogen relaxation usually occurs by interaction with fields from attached protons, if present, or more distant protons, if not. Eq. 5-1 (in Chapter 5) shows the distance dependence of this dipolar interaction.

Tumbling of a very small molecule such as methanol can occur at a rate ω as high as 10^{12} s^{-1} . Not all molecules in a given sample are tumbling at this rate, however. Molecules collide with each other and with the walls of the vessel, so that their tumbling rate can drop to zero and then accelerate back to the maximum value of 10^{12} s^{-1} . The existence of a range of tumbling rates within a sample means that there also is a range of magnetic fields that they generate. The concentration of fields at a particular frequency ω (or the fraction of time the molecule tumbles at frequency ω) is called the *spectral density*, $J(\omega)$. The value of the spectral density at the resonance frequency, $J(\omega_0)$, is critical for relaxation to be efficient. Because small molecules tumble at rates around 10^{12} s^{-1} , their spectral density at the desirable range, 10^8 – 10^9 s^{-1} , is low ($1/\tau_c \gg \omega_0$) and falls to zero above 10^{12} . The situation is

Figure A5-1 Plot of spectral density vs. logarithm of tumbling frequency.



illustrated in Figure A5-1a. Relaxation rates increase with larger molecules, as the tumbling rate slows ($\omega_0\tau_c \approx 1$), as in Figure A5-1b. The spectral density now is sufficiently high at the Larmor frequency to provide efficient relaxation. For very large, slowly tumbling molecules, the plot, as in Figure A5-1c, backs off further and has a very low value at the Larmor frequency ($1/\tau_c \ll \omega_0$).

The following equation describes the spectral density in terms of the tumbling frequency and the correlation time:

$$J(\omega) = 2\tau_c / (1 + \omega^2\tau_c^2). \quad (\text{A5-1})$$

It is noteworthy that the spectral density is constant from zero up to the maximum rate and then rapidly drops to zero (Figure A5-1). The long, flat portion of the curve corresponds to the region in which $1/\tau_c$ is much greater than ω , so that $\omega^2\tau_c^2 \ll 1$ and $J(\omega) = 2\tau_c$ (a constant). This is the *extreme narrowing condition*. (Under this condition, any dipolar line broadening is completely averaged out, so narrowing is at its extreme). For liquid samples of molecules with molecular weights up to a few thousand, the extreme-narrowing condition normally holds.

The size of the dipolar interaction depends primarily on the distance and orientation between the two dipoles, not on the correlation time. By contrast, the *rate of change* of the dipolar interactions depends on τ_c and hence is relevant to the efficiency of relaxation. The total amount of fluctuating fields is independent of τ_c , although τ_c determines the upper limit of the frequencies of the fields. The three curves in Figure A5-1 must enclose the same area, but their upper limits vary. In curve (a), molecular tumbling is very rapid and the spectral density is low. In curves (b) and (c), the upper limit of frequencies decreases with the lengthening of τ_c , so the spectral density increases proportionately to maintain a constant area.

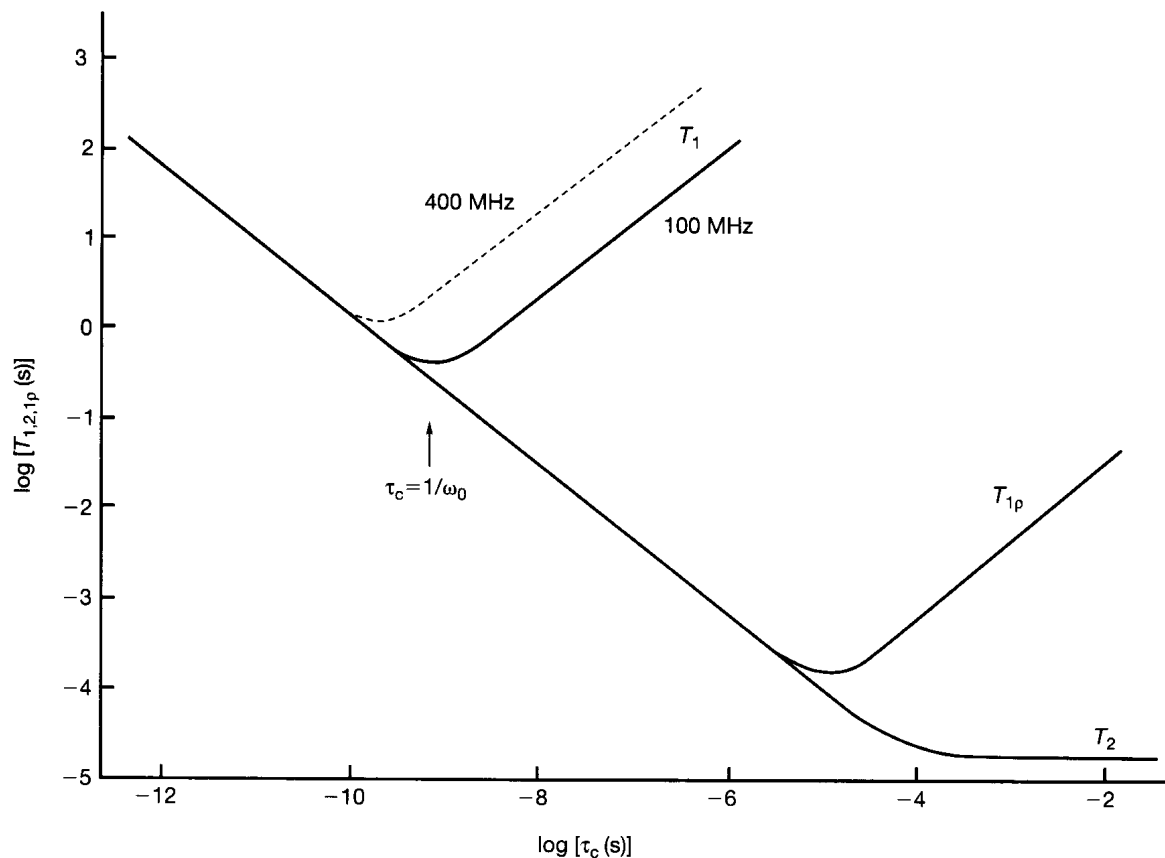


Figure A5-2 Logarithmic plot of relaxation times vs. the effective correlation time.

Since relaxation is most efficient when $\omega_0\tau_c \approx 1$ ($1/\tau_c$ is on the order of ω_0), the relaxation time goes through a minimum when plotted against the correlation time (Figure A5-2). Equation A5-1 can be transformed into the following expression for the relaxation rate (the reciprocal of the relaxation time):

$$T_1^{-1} = \gamma^2 [B_{xL}^0]^2 \left[\frac{2\tau_c}{(1 + \omega_0^2\tau_c^2)} \right]. \quad (\text{A5-2})$$

In this expression, γ is the gyromagnetic ratio and B_{xL}^0 is the root-mean-square average of the x component of the fluctuating local field. Note that ω_0 replaces ω in the expression for the relaxation time, which, under the extreme-narrowing condition, becomes $2\gamma^2 [B_{xL}^0]^2 \tau_c$. Thus, the relaxation time T_1 decreases as τ_c increases (i.e., as mobility decreases with, for example, larger molecules or lower temperatures). This regime is depicted for T_1 at the left of Figure A5-2; note that T_1 is independent of the resonance frequency ω_0 here.

When $\tau_c = 1/\omega_0$, the relaxation time attains its minimum (the relaxation rate achieves its maximum), at $1/T_1 = \gamma^2 [B_{xL}^0]^2 / \omega_0$. The minimum is dependent on the resonance frequency. Since T_1 is directly proportional to ω_0 , the minimum occurs at longer T_1 for a higher frequency. This situation is illustrated in Figure A5-2 by the dashed line. (For example, the solid line represents 100 MHz and the dashed line 400 MHz.) The T_1 minimum occurs as the spectral density moves off the long, flat region and quickly drops to zero. The minimum for spin-lock relaxation, or relaxation in the rotating frame, $T_{1\rho}$, occurs at a much shorter T_1 because the effective resonance frequency (the spin-lock frequency) is very low—approximately 40 kHz.

When $1/\tau_c$ is even shorter, as with macromolecules, $\omega_0^2\tau_c^2 \gg 1$. The denominator of eq. A5-2 then becomes $\omega_0^2\tau_c^2$, and $1/T_1 = \gamma^2 [B_{xL}^0]^2 [2/(\omega_0^2\tau_c)]$. In this regime, T_1 and the correlation time are directly proportional. Thus, T_1 increases as τ_c increases (i.e., as the

mobility decreases), the opposite to the extreme-narrowing condition. Such a situation is illustrated with the continuations of the solid and dashed lines in the figure. This segment is clearly dependent on the resonance frequency, so the dashed and solid lines do not coincide.

Transverse, or spin–spin, relaxation is influenced not only by the effects of fluctuating magnetic fields, but also by direct interactions between spins. The mutual exchange of two spins occurs without energy transfer to the lattice (adiabatically) and without altering the net magnetization in the z direction. Thus spin–spin interactions alter T_2 without affecting T_1 . In the absence of the adiabatic term, the two relaxation times are approximately equal. As T_1 increases (signifying a slower relaxation rate) with decreased mobility outside the extreme-narrowing limit in Figure A5-2, the adiabatic term does not respond in the same way to reduced mobility, but instead continues to decrease monotonically until the lattice becomes rigid at very long τ_c . (Spins dephase without relaxation.) When τ_c is longer than T_2 , T_2 reaches an asymptotic limit (the rigid-lattice value).

Spin–lattice relaxation can occur by several mechanisms, in addition to dipolar interactions:

1. *Chemical shielding anisotropy.* Because shielding at the nucleus varies with the orientation of the molecule with respect to the B_0 field, the magnetic field acting on the nucleus varies (except for extremely symmetrical molecules). Molecular tumbling therefore modulates the local field and provides a mechanism for relaxation. This tumbling process is identical to that for dipolar relaxation, so both mechanisms have the same correlation time τ_c . Consequently, in the extreme-narrowing limit, both mechanisms respond in the same way to a change in temperature (i.e., decreasing at lower temperatures). This mechanism becomes more important at higher fields. (Its magnitude varies with the square of B_0 .) Because many instruments operate at extremely high fields today, line broadening can arise when relaxation by chemical shielding anisotropy causes very short relaxation times.
2. *Spin rotation.* Coherent molecular rotations (or rotations of molecular segments) generate a magnetic field. These rotations are interrupted by molecular collisions, causing the magnetic field to fluctuate. The correlation time for this mechanism, τ_{sr} , depends on the time between collisions and therefore is different from τ_c . Because τ_{sr} decreases with increased temperature, relaxation by spin rotation is faster at higher temperatures (T_1 decreases), the opposite of relaxation by dipolar interactions in the extreme-narrowing regime. This mechanism is important for very small molecules for which τ_c is too short for effective dipolar relaxation (Figure A5-1a). It also is important for rapidly rotating groups within a molecule, so that a terminal methyl carbon may have an important component from spin rotation, whereas the internal methylene carbons, rotating more slowly, do not. The trifluoromethyl carbon (CF_3) almost always relaxes by spin rotation. A plot of T_1 vs. $1/T$ exhibits a maximum as dipolar relaxation at lower temperatures changes over to relaxation by spin rotation at higher temperatures. At the maximum of the plot, the contributions from the two mechanisms are equal. Curved temperature dependencies are an indication of a mixture of these mechanisms.
3. *Scalar coupling.* The J coupling constant can be varied by two mechanisms: (i) If the molecule is engaged in molecular exchange between two forms by a dynamic process, differences between magnitudes of the J values in the two forms can provide a time dependence of J , which in turn can modulate the local magnetic field and cause relaxation. This mechanism has been called *scalar relaxation of the first kind* and is relatively rare. Its correlation time is the correlation time for the exchange process. (ii) When the excited nucleus (I) is coupled to a quadrupolar nucleus (S), the value of the coupling can depend on the relaxation rate of S. For example, we usually think of bromine as being a nonmagnetic nucleus, but, of course, the spin of both ^{79}Br and ^{81}Br is $\frac{3}{2}$. Rapid quadrupolar relaxation interconverts the bromine spin states, so that a

neighboring ^1H or ^{13}C is affected only by the average and appears uncoupled. The interaction, however, is dependent on the rate of quadrupolar relaxation of the I nucleus. Modulation of the value of J hence can provide a fluctuating magnetic field and a mechanism for relaxation. For example, carbons directly bonded to bromine may undergo additional relaxation from scalar coupling and hence exhibit broadened peaks. This effect is largest when the Larmor frequencies of the coupled nuclei are similar, as is the case for ^{13}C and ^{79}Br . The time constant for the mechanism is the time constant for relaxation of the I nucleus.

4. *Quadrupole*. This mechanism of relaxation applies only to quadrupolar nuclei and has been discussed in detail in Section 5-1.
5. *Unpaired electrons*. The electron has a magnetic moment more than three orders of magnitude greater than that of the proton. Consequently, dipolar interactions between an excited nucleus (I) and an electron (S) are extremely strong, and the resulting fluctuating magnetic fields are quite effective at producing relaxation. Thus, paramagnetic impurities can shorten relaxation times to the point that uncertain broadening occurs and line widths are increased, sometimes significantly. For the measurement of T_1 , samples are routinely degassed, so that unwanted dissolved oxygen does not contribute to the relaxation time. Unpaired spins within a molecule can have the same effect, resulting in contact shifts as well as the broadening of peaks. Relaxation agents containing unpaired spins sometimes are introduced intentionally at trace levels in order to shorten relaxation times and allow shorter times between pulses.

When multiple mechanisms contribute to relaxation, the rate is the sum of all contributions; that is,

$$T_1^{-1} = T_1^{-1}(\text{dipolar}) + T_1^{-1}(\text{shielding anisotropy}) + \dots \quad (\text{A5-3})$$

In addition to utilizing these intramolecular mechanisms, relaxation can occur intermolecularly (as has been noted already for dissolved oxygen). Intermolecular dipolar relaxation can occur, particularly with solvent, but the contributions usually are small.

The nuclear Overhauser effect (NOE) requires dipolar relaxation of the I nucleus by the S nucleus. As illustrated in Figure 5-10, W_2 relaxation provides a mechanism whereby the intensity of the I nucleus is enhanced. This mechanism applies to relatively small molecules in the extreme-narrowing limit, since motional frequencies are fast enough to correspond to W_2 . The maximum intensity change is +50% when I and S are both protons and is $100\gamma_S/2\gamma_I$ (in %) when the nuclei are different. When $\omega_0^2\tau_c^2 \gg 1$, as is the case with extremely large molecules, motional frequencies correspond to W_0 , and relaxation by W_1 and W_2 is inefficient. In this regime, the maximum intensity change is -100% when I and S are both protons. Thus, for macromolecules, the NOE can be expected to be negative and twice as large as for molecules in the extreme-narrowing condition. The W_0 mechanism of relaxation occurs without any change in the net z magnetization, as the I and S nuclei interchange their spins. In this fashion, spin disturbances can propagate beyond the nucleus that originally received the perturbation, in a process called *spin diffusion*. The regime in which $\omega_0^2\tau_c^2 \gg 1$ sometimes is called the *spin-diffusion limit*. For example, spin saturation can propagate throughout the sample and suppress macromolecular signals. With spin diffusion, the distance specificity of the NOE is lost. When the I nucleus has a low gyromagnetic ratio, as with ^{13}C or ^{15}N , there is essentially no change in the signal for slowly tumbling molecules, in contrast to the very important enhancement of the signal obtained for ^{13}C in the extreme-narrowing limit. This result follows from the small perturbation on I spin populations by W_0 relaxation. The situation can be advantageous when one is examining samples containing both small and large molecules (e.g., cells), as carbons in the small molecules will experience the normal, large NOE. The effects of spin diffusion can be limited by truncating the NOE experiment. If the irradiation time is shortened, for example, distance specificity can be restored.

APPENDIX 6

Product-Operator Formalism and Coherence-Level Diagrams

The Bloch equations (Appendix 2) describe the magnetization that results from the effects of the external magnetic field B_0 and the applied magnetic field B_1 . In order to include the effects of coupling between nuclei, it was necessary to apply quantum mechanical methods (Appendix 3), which permitted the calculation of the energies of spin states and the probabilities of transitions between them. These approaches were developed during the age of continuous-wave experiments. The use of pulses and pulse sequences, however, emphasizes the importance of the evolution of magnetic phenomena over time. A new formalism therefore is necessary to understand the effects of pulses, relaxation during pulse sequences, interactions between spins, and multiple time domains. *Product-operator formalism* was introduced by Ernst and others to provide a more straightforward theory than that offered by the more complete density matrix theory of quantum mechanics.

Appendix 3 used spin operators in calculating the effects of coupling. The overall Hamiltonian operator for the NMR experiment (eq. A3-3) is repeated here:

$$\mathcal{H} = \mathcal{H}^0 + \mathcal{H}^1 = \sum_i \nu_i I_z(i) + \sum_i \sum_j J_{ij} \mathbf{I}(i) \cdot \mathbf{I}(j). \quad (\text{A6-1})$$

The frequency quantities in this equation (ν, J) are expressed in units of Hz, and it is necessary at this point to move into angular frequencies ($\omega = 2\pi\nu$) through multiplication by 2π . Accordingly, eq. A6-1 becomes

$$\mathcal{H} = \mathcal{H}^0 + \mathcal{H}^1 = \sum_i \omega_i I_z(i) + \sum_i \sum_j 2\pi J_{ij} I_z(i) I_z(j). \quad (\text{A6-2})$$

In this equation, the effects of coupling are expressed only for the z axis, as initially there is no magnetization in the xy plane. In Appendix 3, the effects of the spin operator \mathbf{I} were examined and evaluated along each axis (eq. A3-8). The product-operator formalism expands upon this approach by exploring the effects of adding a time factor to the Hamiltonian. In this fashion, we can evaluate the evolution of magnetization over time.

The effects of three general phenomena over time must be explored: (1) pulses, (2) chemical shifts, and (3) spin-spin coupling. To express the effect of a $90^\circ (\pi/2)$ pulse along the x axis on magnetization that exists initially along the z axis, we use the formalism

$$I_z \xrightarrow{90^\circ I_x} I_y. \quad (\text{A6-3})$$

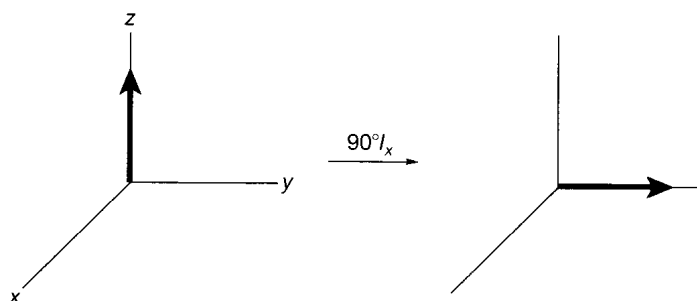


Figure A6-1 The vector representation of a 90° pulse in the x direction.

This expression indicates that a $90^\circ I_x$ pulse transforms I_z (z magnetization) into I_y (y magnetization), as illustrated in Figure A6-1 by the familiar vector picture. Equation A6-3 and Figure A6-1 represent the same phenomenon. Other pulses could be similarly represented; for example, the expression

$$I_z \xrightarrow{90^\circ I_y} -I_x \quad (\text{A6-4})$$

represents the effect of a 90° pulse along the y axis on z magnetization, the expression

$$I_z \xrightarrow{90^\circ(-I_x)} -I_y \quad (\text{A6-5})$$

represents the effect of a 90° pulse along the $-x$ axis on z magnetization, the expression

$$I_y \xrightarrow{90^\circ I_x} -I_z \quad (\text{A6-6})$$

represents the effect of a 90° pulse along the x axis on y magnetization, and, finally,

$$I_x \xrightarrow{90^\circ I_x} I_x \quad (\text{A6-7})$$

represents the effect of a 90° pulse along the x axis on x magnetization. Note that in the last case a parallel pulse has no effect on magnetization, as was mentioned earlier. These equations introduce an operator formalism that is equivalent to the vector diagrams. For a general pulse angle θ , the effect is described, for example, by the notation

$$I_z \xrightarrow{\theta I_x} I_z \cos \theta + I_y \sin \theta. \quad (\text{A6-8})$$

In the vector formalism of Figure A6-2, the effect of chemical shifts (differences in Larmor frequencies) is represented by the rotation of a vector in the xy plane from a position on the y axis (not shown) to one ahead of it. The coordinate system is rotating around the z axis at the reference frequency ω_r , so that the frequency of the magnetization vector moves away from the axis at a rate $\Delta\omega = (\omega - \omega_r)$, subtending an angle of $(\Delta\omega)t$ with the y axis. For simplicity, we will drop the Δ and refer both to the frequency of the nucleus and its difference from the reference frequency as ω , as in eq. A6-2 (corresponding actually to the special case of $\omega_r = 0$). In the product operator formalism, the effect of chemical shifts is represented by the operation of the Hamiltonian term \mathcal{H}^0 on magnetization, illustrated for the three Cartesian coordinates by the expressions

$$I_x \xrightarrow{\omega I_z} I_x \cos \omega t - I_y \sin \omega t, \quad (\text{A6-9})$$

$$I_y \xrightarrow{\omega I_z} I_y \cos \omega t + I_x \sin \omega t, \quad (\text{A6-10})$$

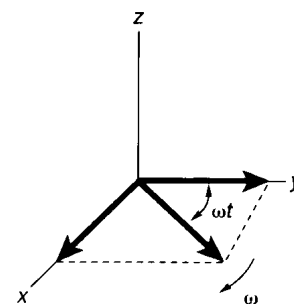


Figure A6-2 Evolution of an uncoupled ($J = 0$) spin vector with frequency ω over time t in the xy plane.

and

$$I_z \xrightarrow{\omega t I_z} I_z. \quad (\text{A6-11})$$

As mentioned earlier, the operator has been multiplied by time t in order to include the evolution of the chemical shift with time and to convert the operator to the unit of angles (radians).

There is no evolution of the chemical shift along the z axis (eq. A6-11), and its evolution in the xy plane occurs as the sum of sine and cosine components. For example, in Figure A6-2, magnetization begins ($t = 0$) aligned along the y axis (represented by the left side of equation A6-10), but then, under the influence of the chemical shift (the symbols over the arrow), evolves into a cosine component along the y axis (starting at unity) and into a sine component along the x axis (starting at zero). The result is represented by the right side of eq. A6-10. Fourier transformation of the trigonometric components yields the Larmor frequency as $\pm\omega$. The experiment cannot distinguish between signals that are equally spaced on either side of the reference frequency. Quadrature detection then performs this selection. In the absence of coupling, the expression

$$I_z \xrightarrow{90^\circ I_x} I_y \xrightarrow{\omega t I_z} I_y \cos \omega t + I_x \sin \omega t \quad (\text{A6-12})$$

describes a typical NMR experiment in the product-operator formalism: initial condition with only longitudinal magnetization, application of a 90° pulse to create transverse magnetization, and evolution of the chemical shift during the detection period, corresponding to the vector diagrams illustrated, for example, in Figure A6-1 and A6-2.

Scalar coupling during the continuous-wave era was primarily a tool for assigning multiplicities of neighboring protons and for determining stereochemistry through Karplus considerations. In complex pulse sequences, the coupling constant often is the engine that produces spectral modifications resulting from structural connectivities. In terms of the product-operator formalism, the coupling-constant term of the Hamiltonian (eq. A6-2, multiplied by time t) is given, for nucleus i coupled to nucleus j , by

$$I_x(i) \xrightarrow{2\pi J_{ij} I_z(i) I_z(j) t} I_x(i) \cos(\pi J_{ij} t) - 2I_y(i) I_z(j) \sin(\pi J_{ij} t) \quad (\text{A6-13})$$

and

$$I_y(i) \xrightarrow{2\pi J_{ij} I_z(i) I_z(j) t} I_y(i) \cos(\pi J_{ij} t) + 2I_x(i) I_z(j) \sin(\pi J_{ij} t) \quad (\text{A6-14})$$

on the x and y axes, respectively. The vector description of the evolution of coupling for one member of a two-spin system is illustrated in Figure 5-9a–c. The reference frequency of the rotating coordinate system is set at the Larmor frequency so that the two vectors of nucleus i that result from coupling to nucleus j move in the plus and minus directions away from the y axis at equal velocities ($J/2$ from the axis, or J from each other). Figure A6-3a picks up from Figure 5-9c. The two vectors are projected onto the xy plane in Figure A6-3b, one vector representing coupling to the α vector of the j nucleus and the other to the β vector. Each of these vectors can be resolved into x and y components, as depicted in Figure A6-3c. The in-phase component along the y axis starts off large and decreases as the vectors fan out, so it is modulated by a cosine function and is given mathematically by the first term in eq. A6-14: $I_y(i) \cos(\pi J_{ij} t)$. This is the signal that is detected and Fourier transformed in the experiment to produce the spectrum.

The out-of-phase (or *antiphase*) x component is made up of mutually canceling terms along the $+x$ and $-x$ axes (Figure A6-3c; the term moving counterclockwise in the xy plane is exactly canceled by the term moving clockwise). The antiphase x component is not detected, as the cancelation process leads to zero macroscopic magnetization. This component

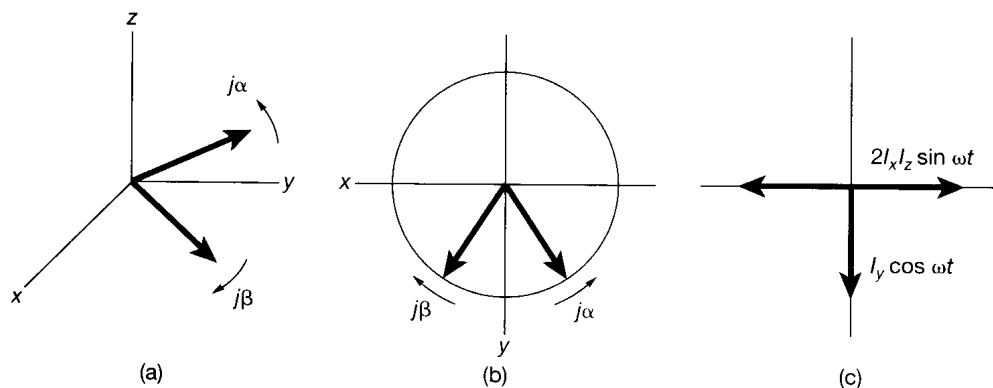


Figure A6-3 Evolution of the two vectors from scalar coupling (J) in the xy plane from two perspectives (a) and (b) and resolved into components along the x and y axes (c).

can be described as $I_x(i)[I_\beta(j) - I_\alpha(j)]$ if one says that the β spin of nucleus j points to $+x$ and the α spin to $-x$. (The convention is arbitrary and depends on the sign of the coupling constant between i and j .) The difference in population $[I_\beta(j) - I_\alpha(j)]$ between the α and β levels corresponds to $2I_z$, so that the x component is expressed mathematically as $I_x(i)[2I_z(j)]$. This quantity is modulated by a sine function over time and becomes the second term in eq. A6-14, which, then, describes the evolution of the two vectors illustrated in Figures 5-9c, A6-3a, and elsewhere, expressed as distinct components, respectively, along the y and x axes.

The second (antiphase) term in eq. A6-14 contains the product of *two* operators, $I_x(i)I_z(j)$, for the first time. Coupling thus can be considered to create a new operator through the process $I_y \rightarrow 2I_xI_z$, whereby one operator is transformed into the product of two. It is worth considering a particular case when the amount of time t is set to a constant value, as has been done in numerous examples in Chapters 5 and 6. If t is set equal to $(2J)^{-1}$, then the transformation of eq. A6-14 takes the form

$$I_y(i) \xrightarrow{\pi I_z(i)I_z(j)} 2I_x(i)I_z(j), \quad (\text{A6-15})$$

since $\cos(\pi/2) = 0$ and $\sin(\pi/2) = 1$. At this time, there is no in-phase component, and the only magnetization is the antiphase component. Selection for antiphase magnetization occurs in this way, for example, in the INEPT sequence (Section 5-6). If one allows precession to continue under the influence of the same coupling constant, the antiphase component is transformed in a fashion parallel to that of eq. A6-14, with a reversal of roles, so that the antiphase component is multiplied by a cosine term and the in-phase component by a sine term, giving

$$2I_x(i)I_z(j) \xrightarrow{2\pi J_{ij}I_z(i)I_z(j)t} 2I_x(i)I_z(j) \cos(\pi J_{ij}t) - I_y(i) \sin(\pi J_{ij}t). \quad (\text{A6-16})$$

When another period $t = (2J)^{-1}$ passes, this expression becomes

$$2I_x(i)I_z(j) \xrightarrow{\pi I_z(i)I_z(j)} -I_y(i). \quad (\text{A6-17})$$

Magnetization thus is refocused as an echo along the negative y axis, as we saw in Section 5-6. The second stage of this sequence involves the annihilation of an operator through the process $2I_xI_z \rightarrow I_y$. Thus, the operation of coupling can serve both to create and annihilate operators. In this way, coherence is said to be transferred. It is useful to include the relationship

$$2I_y(i)I_z(j) \xrightarrow{2\pi J_{ij}I_z(i)I_z(j)t} 2I_y(i)I_z(j) \cos(\pi J_{ij}t) + I_x(i) \sin(\pi J_{ij}t) \quad (\text{A6-18})$$

for the transformation of antiphase magnetization along the y axis as a complement to eq. A6-16.

A two-spin system has a total of 16 product operators, three each for the Cartesian coordinates of the two spins: $I_x(i), I_y(i), I_z(i), I_x(j), I_y(j),$ and $I_z(j)$. By eqs. A6-3 through A6-14, these six operators transform according to the various effects of pulses, chemical shifts, and coupling constants. The effects of chemical shifts and coupling constants occur simultaneously. In the absence of strong coupling (i.e., the first-order condition), they may be depicted as occurring sequentially, since the operators commute. Not all possible equations are given, but the others may be derived by analogy. There also is an identity or unity operator that always operates without changing the function, and there are nine product operators that involve two spins. We have already seen the four antiphase spin magnetizations— $2I_x(i)I_z(j), 2I_y(i)I_z(j), 2I_z(i)I_x(j),$ and $2I_z(i)I_y(j)$ —whose transformations through coupling are given by eqs. A6-16 and A6-18 or analogous ones. The operator $2I_z(i)I_z(j)$ is said to have longitudinal two-spin order and refers to certain spin perturbations that do not lead to any net spin polarization. The remaining four operators— $2I_x(i)I_x(j), 2I_y(i)I_y(j), 2I_x(i)I_y(j),$ and $2I_y(i)I_x(j)$ —describe two-spin coherence, which requires further explanation.

Coherence refers to a connection between the states of two spins via a spin flip. The initial condition of the NMR experiment, at which all spins are precessing randomly about the z axis, is incoherent with respect to phase (Figure 1-10). As magnetization moves into the xy plane through simple spin flips, z magnetization decreases, xy magnetization appears, and phases become coherent rather than random (Figure 1-11). The term *coherence* has taken on more complex meanings within the realm of pulse NMR phenomena. A simple spin flip, involving a β spin becoming an α spin in a one-spin system, implies a connection between two adjacent spin levels. The difference in their spin quantum numbers, $\Delta m = \left[\frac{1}{2} - \left(-\frac{1}{2}\right)\right]$, is unity. The sign of Δm corresponds to absorption or emission and is not important at this stage. The number Δm now is defined as the *coherence order* p , so that a simple spin flip is said to have unity order ($p = \pm 1$) and constitute *single quantum coherence*. In more complex systems, with coupling, the phenomenon carries over, so that, for example, the transition from $\beta\beta$ to $\alpha\beta$ involves a single spin flip and constitutes single quantum coherence.

Previously, we described transitions that simultaneously involve two spin flips as being forbidden and hence inherently of low probability. Although this statement is true, the phenomena can be realized by pulse processes. When two spins flip at the same time, the net change in magnetization, Δm , can be either 0 or 2. For example, the transition from $\beta\beta$ to $\alpha\alpha$, $\Delta m = 2$, is referred to as *double quantum coherence* ($p = \pm 2$), and the transition $\beta\alpha$ to $\alpha\beta$, $\Delta m = 0$, is referred to as *zero quantum coherence* ($p = 0$). During pulse sequences, such coherences may be created, exploited, and annihilated, so that it no longer is a simple question of looking for low-intensity double or zero quantum transitions. We will not be concerned with coherences involving more than two states.

Only single quantum coherences can be observed. (This assertion is equivalent to saying that only single spin flips are observable.) In the product-operator formalism, these are represented by symbols such as $I_y(i)$, denoting the observation of nucleus i along the y axis, as in eq. A6-3. Two-spin coherences (double spin flips), such as $2I_x(i)I_x(j)$ and $2I_y(i)I_x(j)$, are not observable. Antiphase coherences, such as $2I_x(i)I_z(j)$, may be transformed into single quantum coherence and can be observed when coupling is present between i and j by processes analogous to those represented in eq. A6-17. Antiphase coherences are recognized as having exactly one transverse component (I_x or I_y) (corresponding to a single spin flip) and any number of longitudinal components (I_z). Longitudinal magnetization by itself, of course, is not observable. Thus, an ensemble of nuclei can pass through multiple or zero quantum states during a pulse sequence, but must end up as either I_x or I_y for detection.

Transformations can occur between any of the various operators. For example, the expressions

$$2I_y(i)I_z(j) \xrightarrow{90^\circ[I_x(i)+I_x(j)]} -2I_z(i)I_y(j) \quad (\text{A6-19})$$

and

$$2I_x(i)I_z(j) \xrightarrow{90^\circ[I_x(i)+I_x(j)]} 2I_x(i)I_y(j) \quad (\text{A6-20})$$

illustrate, respectively, the transformation of antiphase i magnetization into antiphase j magnetization and the transformation of antiphase i magnetization into two-spin coherence. These relationships require that product operators carry out their transformations independently. There are sign conventions that we will not go into, but are discussed, for example, in Freeman (1987), who also presents a complete table of all possible operations in a two-spin system.

Pulse sequences have been portrayed herein in a number of different ways: (1) as a listing of pulse angles and time periods [e.g., $90^\circ(\text{acquire})$ for the single pulse and $180^\circ-\tau-90^\circ(\text{acquire})$ for the inversion recovery sequence]; (2) as a series of blocks connected by continuous lines, as in Figure A6-1 for the single pulse and for the COSY experiment; and (3) as vectors moving in a three-dimensional Cartesian coordinate system, as in Figure 1-15 for the single pulse and Figure A6-2 for the COSY experiment. These representations successfully treat the movement of incoherent magnetization (I_z) into single quantum coherences (I_y) or into antiphase arrangements [$2I_x(i)I_z(j)$], but there is no way for them to depict zero or multiple quantum coherences [e.g., $2I_x(i)I_x(j)$ or $2I_y(i)I_x(j)$]. To fill in this gap, Ernst, Bodenhausen, Bain, and others developed a fourth method of depicting NMR experiments — a method that emphasizes the coherence order.

Figure A6-4 illustrates the changes in coherence for the single 1D 90° pulse followed by acquisition. The experiment begins with spins randomly precessing about the z axis, depicted by the thick horizontal line with zero coherence ($p = 0$). When the 90° pulse is applied, the vector moves to the y axis in the rotating coordinate system, and single quantum coherence develops, represented by the movement of the thick horizontal line to $p = 1$. This signal may be thought of either as a frequency oscillating along the y axis or as two signals rotating respectively clockwise and counterclockwise in the xy plane (analogous to Figure 1-12 and A2-1). The signals with either $+\omega$ or $-\omega$ are respectively labeled $p = +1$ and -1 (the difference in sign is an arbitrary distinction that is not used consistently in the literature), and these two possibilities are represented in parts (a) and (b) of the figure. Quadrature detection is tuned to receive one or the other of the two signals, which are 90° out of phase from each other. This sort of depiction is called a *coherence-level diagram*.

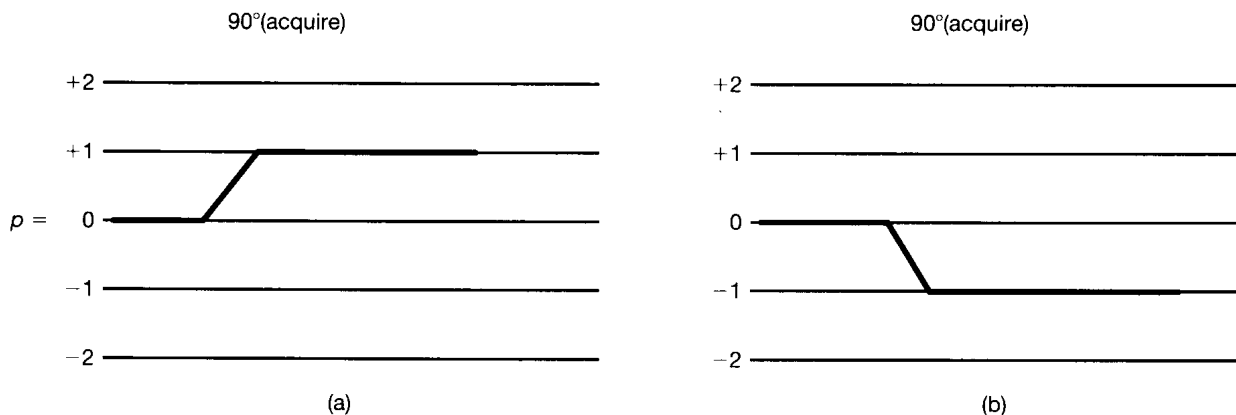
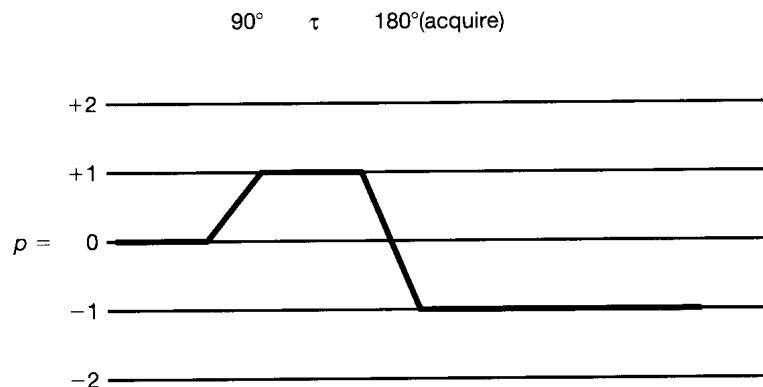


Figure A6-4 Coherence-level diagram for a 90° pulse.

Figure A6-5 Coherence-level diagram for the inversion recovery experiment.



The effect of a 180° pulse in such a diagram depends on what has gone before it. In the inversion recovery experiment, the 180° pulse inverts incoherent spins. There is no change in coherence order, so the pulse does not alter the horizontal line. The coherence-level diagram for the inversion recovery experiment [$180^\circ-\tau-90^\circ$ (acquire)] differs from those in Figure A6-4 only in that the change in the thick line at 90° (acquire) is preceded by the constant period τ . If a 90° pulse, however, has initially moved the coherence order to $+1$, the effect of the 180° pulse is to change it to -1 , as in the simple spin echo experiment, $90^\circ-\tau-180^\circ-\tau$ (acquire), with no coupling. (See Figure 5-13 for the vector diagram and Figure A6-5 for the coherence-level diagram, in which only the $p = +1$ component is shown; the refocusing of chemical shifts is not evident in the latter depiction.)

Now let us examine the most fundamental 2D experiment, COSY, in terms of the product-operator formalism. Most of the relationships developed in the earlier equations will be utilized. The pulse sequence (Figure A6-1) involves two pulses separated by a period t_1 and followed by a second period t_2 : $90^\circ-t_1-90^\circ-t_2$ (acquire). The effects of chemical shifts and coupling constants are expressed during both periods. The theory may be understood by examining a two-spin coupled system (nuclei i and j). The expression

$$I_z(i) \xrightarrow{90^\circ I_x} I_y(i) \xrightarrow{\omega_i I_z(i) t_1} I_y \cos \omega_i t_1 + I_x \sin \omega_i t_1 \quad (\text{A6-21a})$$

includes the product operator for the effects of the initial 90° pulse and the evolution of the chemical shift on nucleus i . An analogous equation would apply for nucleus j . Magnetization moves onto the y axis and evolves during period t_1 according to the Larmor frequency ω_i . This result follows from eqs. A6-3 and A6-10. The relationship

$$\begin{aligned} &\xrightarrow{2\pi J_{ij} I_z(i) I_z(j) t_1} [I_y(i) \cos \omega_i t_1 + I_x(i) \sin \omega_i t_1] \cos(\pi J_{ij} t_1) \\ &+ [2I_x(i) I_z(j) \cos \omega_i t_1 - 2I_y(i) I_z(j) \sin \omega_i t_1] \sin(\pi J_{ij} t_1) \end{aligned} \quad (\text{A6-21b})$$

then gives the transformation arising from the effects of the coupling constant J_{ij} . There are two terms in this transformation: the cosine term, which corresponds to the in-phase signal, and the sine term, which represents the antiphase signal. This result follows from eqs. A6-13 and A6-14.

At this stage, the second 90° pulse is applied along the x axis. Each of the terms in eq. A6-21b is transformed appropriately: the first in-phase term according to eq. A6-6, the second in-phase term by eq. A6-7, the first antiphase term by eq. A6-20 (the transformation of antiphase i into multiple quantum coherence), and the second antiphase term in accordance with eq. A6-19 (the transformation of antiphase i magnetization into antiphase j magnetization). The overall result is given by the expression

$$\begin{aligned} &\xrightarrow{90^\circ [I_x(i) + I_x(j)]} [-I_z(i) \cos \omega_i t_1 + I_x(i) \sin \omega_i t_1] \cos(\pi J_{ij} t_1) \\ &+ [2I_x(i) I_y(j) \cos \omega_i t_1 + 2I_z(i) I_y(j) \sin \omega_i t_1] \sin(\pi J_{ij} t_1). \end{aligned} \quad (\text{A6-21c})$$

During the new period t_2 , magnetization evolves according to the values of the chemical shifts and coupling constants during the detection period. Only the second and fourth terms of eq. A6-21c result in detectable signals, as the first term is longitudinal and the third term contains two transverse components. Thus, eq. A6-21c simplifies to

$$\xrightarrow{90^\circ[I_x(i)+I_x(j)]} I_x(i) \sin \omega_i t_1 \cos(\pi J_{ij} t_1) + 2I_z(i)I_y(j) \sin \omega_i t_1 \sin(\pi J_{ij} t_1) \quad (\text{A6-21d})$$

during the detection period t_2 .

Let us now consider the two terms of this equation separately for their evolution during t_2 . The operation of the chemical shift of nucleus i on the in-phase term of eq. A6-21d gives

$$\begin{aligned} I_x(i) \sin \omega_i t_1 \cos(\pi J_{ij} t_1) &\xrightarrow{\omega_i I_z(i) t_2} I_x(i) \sin \omega_i t_1 \cos(\pi J_{ij} t_1) \cos \omega_i t_2 \\ &- I_y(i) \sin \omega_i t_1 \cos(\pi J_{ij} t_1) \sin \omega_i t_2 \end{aligned} \quad (\text{A6-21e})$$

according to the result of eq. A6-9. The operation of coupling (eqs. A6-13 and A6-14) on eq. A6-21e in turn leads to

$$\begin{aligned} &\xrightarrow[\text{(in-phase terms)}]{2\pi J_{ij} I_z(i) I_z(j) t_2} I_x(i) \sin \omega_i t_1 \cos(\pi J_{ij} t_1) \cos \omega_i t_2 \cos(\pi J_{ij} t_2) \\ &- I_y(i) \sin \omega_i t_1 \cos(\pi J_{ij} t_1) \sin \omega_i t_2 \cos(\pi J_{ij} t_2), \end{aligned} \quad (\text{A6-21f})$$

which is simplified because we need include only the in-phase terms of eqs. A6-13 and A6-14. The antiphase terms introduce unobservable multiple quantum states, and it must be kept in mind that t_2 is the detection period. The observable quantity along the y axis in eq. A6-21f (the second term) has the frequency of nucleus i (ω_i) during both the t_1 evolution and the t_2 detection periods, so that in a two-dimensional plot this detected magnetization falls on the diagonal. Because the signal is modulated by the cosine of the coupling term in t_2 , it is in phase. (Recall the definition of *in phase* from Figure A6-3c.) The first term of eq. A6-21d therefore leads to the diagonal signals in the 2D experiment.

From eq. A6-10, the operation of the chemical shift on the second term of eq. A6-21d leads to the expression

$$\begin{aligned} 2I_z(i)I_y(j) \sin \omega_i t_1 \sin(\pi J_{ij} t_1) &\xrightarrow{\omega_i I_z(j) t_2} 2I_z(i)I_y(j) \sin \omega_i t_1 \sin(\pi J_{ij} t_1) \cos \omega_j t_2 \\ &+ 2I_z(i)I_x(j) \sin \omega_i t_1 \sin(\pi J_{ij} t_1) \sin \omega_j t_2, \end{aligned} \quad (\text{A6-21g})$$

and, from eqs. A6-13 and A6-14, the operation of coupling leads to

$$\begin{aligned} &\xrightarrow{2\pi J_{ij} I_z(i) I_z(j) t_2} 2I_z(i)I_y(j) \sin \omega_i t_1 \sin(\pi J_{ij} t_1) \cos \omega_j t_2 \cos(\pi J_{ij} t_2) \\ &+ I_x(j) \sin \omega_i t_1 \sin(\pi J_{ij} t_1) \cos \omega_j t_2 \sin(\pi J_{ij} t_2) \\ &+ 2I_z(i)I_x(j) \sin \omega_i t_1 \sin(\pi J_{ij} t_1) \sin \omega_j t_2 \cos(\pi J_{ij} t_2) \\ &- I_y(j) \sin \omega_i t_1 \sin(\pi J_{ij} t_1) \sin \omega_j t_2 \sin(\pi J_{ij} t_2). \end{aligned} \quad (\text{A6-21h})$$

In this case, we must include both in-phase and antiphase terms of eqs. A6-13 and A6-14. The first and third terms derive from the in-phase term of the coupling operation, whereby the two terms in eq. A6-21g are modulated by the cosine term of eqs. A6-13 and A6-14. In the final expression, these terms are antiphase and hence undetectable, so they may be ignored. The second and fourth terms began as the antiphase term of the coupling operation.

The second application of the coupling operator, however, annihilates an operator. The operations are best taken from the table in Freeman. [The operation of $I_z(i)I_z(j)$ on $2I_z(i)I_y(j)$ gives $I_x(j)$, and the operation of the same operator on $2I_z(i)I_x(j)$ gives $-I_y(j)$.] The operations also may be worked out, with the additional fact that $I_z(i)I_z(i) = \frac{1}{4}$, which cancels the factor of 2. The second and fourth terms in eq. A6-21h are the detectable signals. Note that, for the signals in these terms, the chemical shift during t_1 was ω_i , but during t_2 was ω_j . Thus, the signals constitute cross peaks at different frequencies in the two frequency domains after Fourier transformation. These terms are modulated by the sine of the coupling term in t_2 and hence differ in phase from the diagonal peaks by 90° . When the diagonal peaks are dispersive, for example, the cross peaks are absorptive, and vice versa.

It is worthwhile to streamline the analysis of these equations, in order to avoid getting lost in the trigonometry. The expression

$$\begin{aligned}
 I_z(i) &\xrightarrow{90^\circ I_x} I_y(i) \xrightarrow{\omega} I_x(i) \sin \omega_i t_1 \\
 &\xrightarrow[\text{(in-phase term)}]{J} I_x(i) \sin \omega_i t_1 \cos(\pi J_{ij} t_1) \xrightarrow[\text{(in-phase term)}]{90^\circ I_x} \\
 &I_x(i) \sin \omega_i t_1 (\cos \pi J_{ij} t_1) \xrightarrow{\omega} I_y(i) \sin \omega_i t_1 \cos(\pi J_{ij} t_1) \sin \omega_i t_2 \\
 &\xrightarrow{J} I_y(i) \sin \omega_i t_1 \cos(\pi J_{ij} t_1) \sin \omega_j t_2 \cos(\pi J_{ij} t_2) \quad (\text{A6-22})
 \end{aligned}$$

gives each of the steps in the 2D experiment that leads to the observed diagonal signal for nucleus i . The initial longitudinal magnetization of nucleus i moves to the y axis when the 90° pulse is applied along the x axis and, during the period t_1 , is subject to the effects of nucleus i 's chemical shift and coupling to nucleus j . In this abbreviated version, only magnetization along the x axis has been retained, as it ultimately leads to the detected y magnetization. The second 90° pulse has no effect on the in-phase x magnetization, which then evolves during the period t_2 according to the aforesaid chemical shift and coupling constant to give the term describing the observed magnetization. This term, which contains the same frequency ω_i in both time domains, so that the observed signal falls on the diagonal of the 2D plot, is modulated by the cosine of the coupling term during the detection period. Hence, the signal is in phase.

The expression

$$\begin{aligned}
 I_z(i) &\xrightarrow{90^\circ I_x} I_y(i) \xrightarrow{\omega} I_x(i) \sin \omega_i t_1 \xrightarrow[\text{(antiphase term)}]{J} 2I_y(i)I_z(j) \sin \omega_i t_1 \sin(\pi J_{ij} t_1) \\
 &\xrightarrow[\text{(antiphase term)}]{90^\circ I_x} 2I_z(i)I_y(j) \sin \omega_i t_1 \sin(\pi J_{ij} t_1) \xrightarrow{\omega} \\
 &2I_z(i)I_x(j) \sin \omega_i t_1 \sin(\pi J_{ij} t_1) \sin \omega_j t_2 \xrightarrow{J} \\
 &I_y(j) \sin \omega_i t_1 \sin(\pi J_{ij} t_1) \sin \omega_j t_2 \sin(\pi J_{ij} t_2) \quad (\text{A6-23})
 \end{aligned}$$

gives each of the steps in the 2D experiment that leads to the observed off-diagonal peaks for nucleus i . The initial steps are the same as in eq. A6-22 for the diagonal signal, until the antiphase term is selected during the evolution of coupling in t_1 . After the second 90° pulse, the term that came from antiphase i magnetization evolves during the second period t_2 according to the relevant chemical shift and coupling constant. We select the term from the chemical-shift operation that eventually produces y magnetization. The coupling operation now serves to annihilate an operator, producing single quantum coherence along the y axis. Signs have been omitted for simplicity in this streamlined depiction. The final signal exhibits ω_i during t_1 and ω_j during t_2 , so it appears as a cross peak. Because it is modulated by

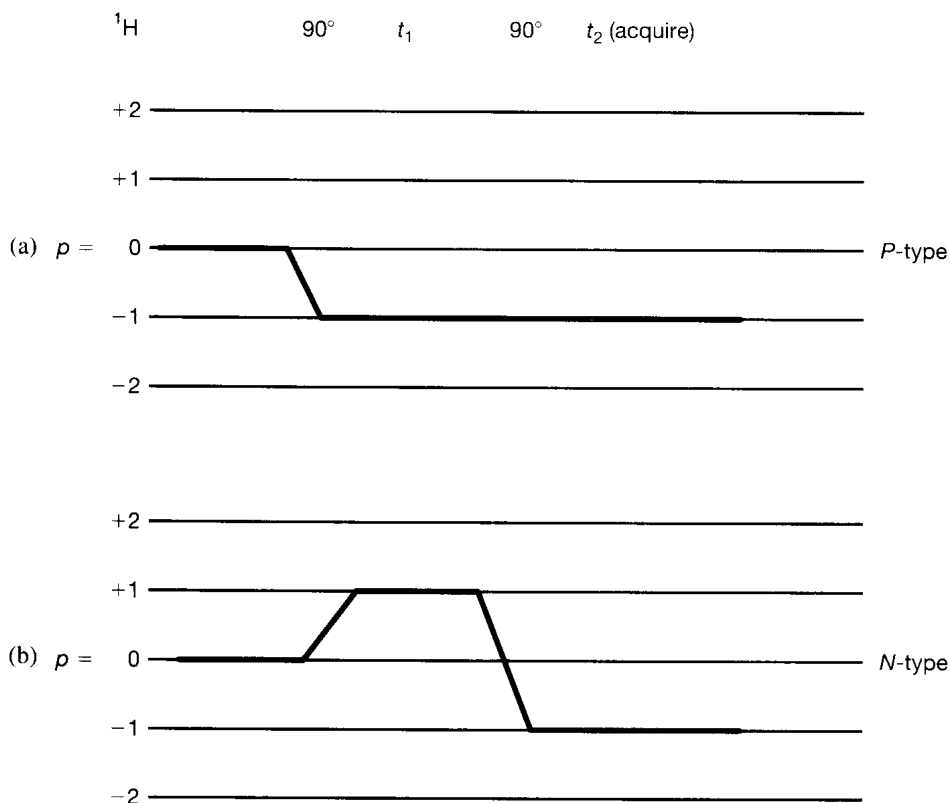


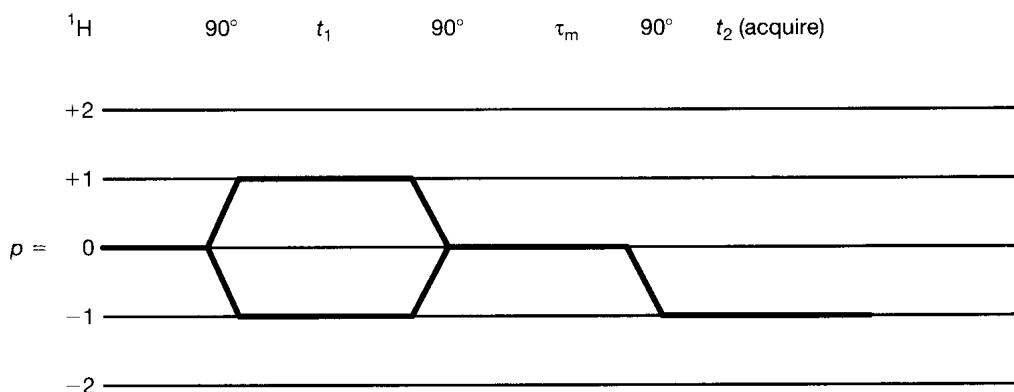
Figure A6-6 Coherence-level diagram for the COSY experiment.

the sine of the coupling term during the period t_2 , this signal is 90° out of phase with the signals along the diagonal.

The coherence-level diagram for the COSY experiment is illustrated in Figure A6-6. The initial 90° pulse generates y magnetization, which may precess either clockwise or counterclockwise, corresponding to the coherence modes $p = \pm 1$ in Figure A6-4. Phase cycling selects the type of coherence to be detected at the end of the experiment—for example, $p = -1$. When the initial and detected coherences have the same coherence number, as in Figure A6-6a, the experiment is called a P-type (or antiecho) experiment, and when the initial and detected coherences have opposite coherence numbers, as in Figure A6-6b, the experiment is called an N-type (or echo) experiment. They differ only in the sense of precession ($\pm\omega$) of the original signal. The second 90° pulse changes the coherence number p from $+1$ to -1 in the N-type experiment, but has no effect on the P-type experiment (as the result of the antiphase shift caused by the coupling operator). In the phase-sensitive COSY experiment, both ± 1 pathways must be retained during t_1 .

As discussed in Section 6-3, the NOESY and EXSY experiments exploit the residual longitudinal magnetization left after the second 90° pulse in the COSY experiment. This longitudinal magnetization is allowed to develop during the mixing time τ_m , when intensities are modulated either through dipolar relaxation that generates the NOE or through chemical exchange that alters nuclear identities. A third 90° pulse then moves the altered longitudinal magnetization into the xy plane for detection. Figure A6-7 shows the coherence-level diagram for the NOESY and EXSY experiments. In terms of coherence orders, the initial 90° pulse generates single quantum coherence (both $+\omega$ and $-\omega$ are shown), which evolves according to chemical shifts during t_1 . The magnetization that is returned to the z axis by the second 90° pulse (which generates zero quantum coherence) then is perturbed by dipolar relaxation or chemical exchange during τ_m . Since the COSY signal, which includes both single and double quantum coherence, also is present, the experiment must select the zero quantum signal and convert it to $p = -1$ by the third 90° pulse for observation.

Figure A6-7 Coherence-level diagram for the NOESY or EXSY experiment.

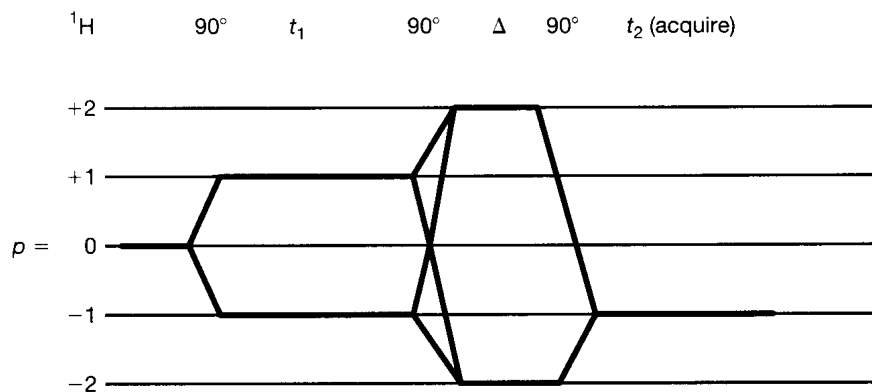


This process was described in Section 6-3 as a simple 90° pulse that left unwanted signals along the z axis. In practice, coherence numbers are selected either by phase cycles or by pulsed field gradients. The process of phase cycling, described in Section 5-8, can select a particular phase coherence by exploiting differences between phases. Pulsed field gradients generally perform the operation more efficiently. (See Section 6-6.)

The double-quantum-filtered COSY experiment (DQF-COSY) was described in Section 6-1 as a method that produces a COSY spectrum lacking signals from nuclei with no homonuclear coupling partner. The COSY experiment generates double quantum coherences (the third term in eq. A6-21c), which we ignored as unobservable. Figure A6-8 shows the development of these coherences during the DQF-COSY experiment. Zero (the first term in eq. A6-21c) and single quantum coherences (the second and fourth terms) also are present, but are not shown in the figure. Phase cycling or pulse field gradients are used to select the double quantum coherences and convert them to observable single quantum coherences. A comparison of Figures A6-7 and A6-8 indicates a strong similarity between the NOESY and the DQF-COSY experiments, which differ only in the length of the mixing time that follows the second 90° pulse. This time is selected for dipolar relaxation, on the one hand, or homonuclear coupling, on the other. In addition, phase cycling of the third 90° pulse differs, depending upon the coherence selection.

Finally, let us reexamine the 2D INADEQUATE experiment (Section 6-4) in terms of its coherence-level diagram (Figure A6-9). This experiment utilizes pulses only at the frequency of the insensitive nucleus, such as ^{13}C . The initial 90° pulse generates single quantum coherence, and the periods τ are selected to produce an antiphase disposition of ^{13}C nuclei with ^{13}C coupling partners. The center-band signal from ^{13}C nuclei lacking adjacent ^{13}C nuclei is left on the z axis. During the period t_1 , double quantum coherences develop by processes similar to the DQF-COSY experiment. These coherences evolve as the sums of

Figure A6-8 Coherence-level diagram for the DQF-COSY experiment.



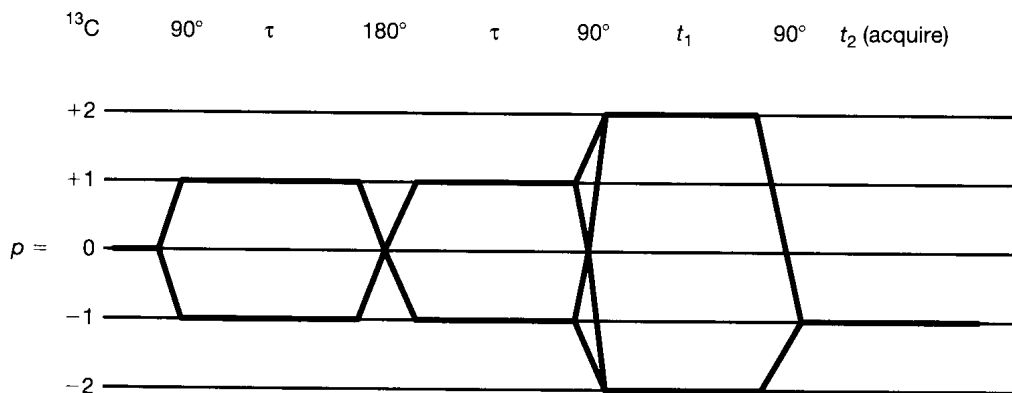


Figure A6-9 Coherence-level diagram for the 2D INADE-QUATE experiment.

the Larmor frequencies $\omega_i + \omega_j$ in the notation of eq. A6-21 and are selected by phase cycling of the final 90° pulse. The signals that are observed during t_2 appear as cross peaks at $\omega_i + \omega_j$ on the ν_1 axis and at the positions of ω_i and ω_j on the ν_2 axis, as, for example, in Figures 6-33. There are no diagonal peaks, because they have been selected out. This experiment is usually accompanied by heteronuclear decoupling to suppress $^1\text{H}-^{13}\text{C}$ coupling and to exploit possible heteronuclear NOE's.

Bibliography

- A6.1. R. Freeman, *A Handbook of Nuclear Magnetic Resonance*. Essex, England: Longman Scientific & Technical, 1987.

APPENDIX 7

Stereochemical Considerations

In Section 4-2, the terms *isochrony*, *equivalence*, and *topicity* were introduced to describe nuclei that are of interest in NMR spectroscopy. *Isochronous* nuclei, or groups, were seen to be chemically (symmetry) equivalent. *Magnetic equivalence* was, however, found to be a more strict requirement than *chemical equivalence*, as it is determined by the coupling constant(s) of each nucleus in a group of chemically equivalent nuclei. Finally, *topicity* was seen to be dependent on the nature of symmetry operations that interchange chemically equivalent nuclei or groups.

The particular type of organization that has to do with *prochiral* groups (the “a” ligands in CaabCxyz systems) remains a source of confusion in NMR spectroscopy. Typical examples are the R-CH₂-R' and R-C(CH₃)₂-R' arrangements of, for example, ethylbenzene and isopropylbenzene, respectively. With the presence of a chiral center in either the R or R' group, a common misconception is that the geminal protons or methyl groups of these systems are equivalent (the term is usually not defined, but, from the context, generally refers to magnetic equivalence by the chemical-shift criterion; Section 4-2) under suitable conditions. Moreover, it is often expected that the methylene protons are magnetically equivalent by the coupling-constant criterion (Section 4-2) and that they act in concert to split adjacent protons into a triplet. (The spin-coupled protons may, of course, be further split by additional neighboring protons or heteronuclei.) The observation of nonequivalence in prochiral groups or the failure of prochiral protons to spin couple in the expected manner is frequently ascribed to slow rotation of that part of the molecule containing the prochiral moiety.

Enantiotopic nuclei or groups are capable of fulfilling all or, at least, most of the foregoing symmetry-related expectations. Their chemical shifts depend, in addition, on both the medium in which the NMR experiment is conducted and the spectral resolution of the spectrometer. The latter is influenced by, for example, the magnetic-field strength. Enantiotopic groups are isochronous in achiral or racemic media and constitute A₂, X₂, etc., systems. Moreover, they are potentially anisochronous in chiral media.

Many prochiral groups, however, cannot be interchanged by any type of symmetry operation, because of the presence of one or more chiral centers in the molecule. They are *diastereotopic* and anisochronous, and they constitute AB, AX, etc., systems. For this reason, when encountering prochiral groups, chemists should expect them to be diastereotopic and should be, perhaps, pleasantly surprised when they are not.

Before further investigating the matter of the chemical-shift nonequivalence of diastereotopic, prochiral groups in the presence of a chiral center, let us examine examples of

more familiar homotopic and enantiotopic groups to see how their NMR behavior differs critically from that of their diastereotopic counterparts. In particular, we will see why methyl protons are magnetically equivalent and why their chemical shifts are, indeed, averaged by fast rotation, while diastereotopic, prochiral protons are magnetically nonequivalent and their chemical shifts are not averaged by rapid rotation. In addition, there are many other classes of diastereotopic groups (Section 4-2), but these are not of interest in the present context.

A7-1 Homotopic Groups

Let us first consider the methyl protons of the molecule $H_aH_bH_cC-Cxyz$ illustrated in Figure A7-1. It is initially assumed that C–C rotation is rapid on the time scale of observation. It is well known that, even in the presence of an adjacent chiral center, methyl protons are chemically equivalent (and thus isochronous). The isochrony of methyl protons can be demonstrated in the following manner. For the sake of simplicity, only the three staggered conformations of one enantiomer (**A**, **B**, and **C** in the figure) are considered, and the populations of all other conformers are assumed to be negligible.

Furthermore, the chemical shift of any particular proton, say, H_a , is a function not only of its neighboring groups (including H_b and H_c in Figure A7-1), but also of the *geometrical* relationships that exist among these groups. For the purpose of their contributions to nearby chemical shifts (like those pictured in Figures A7-1 through A7-4), three types of neighboring groups can be identified from the Newman projections: (i) those which are immediately gauche to a proton in question (α), (ii) those which are, in turn, gauche to the first group (β), and (iii) that group which is anti to the subject proton (γ). The orientations of these substituents result in differential effects on the chemical shifts of their neighbors because of interactions *between* the groups (e.g., steric inhibition of resonance) that are specific to their particular geometric arrangements in the molecule.

The chemical shift of, for example, H_a in conformers **A**, **B**, and **C** can be expressed as a function of $\delta_{yH(b)z/xH(c)z}$, $\delta_{xH(b)y/zH(c)y}$, and $\delta_{zH(b)x/yH(c)x}$, respectively, where the substituents are given in the order α , β , γ for clockwise–counterclockwise viewing of the conformers in Figure A7-1. In addition, the mole fractions of conformers **A**, **B**, and **C** are n_A , n_B , and n_C , respectively. The average chemical shifts of H_a , H_b , and H_c are then given by the formulas

$$\delta_{H(a)} = n_A \delta_{yH(b)z/xH(c)z} + n_B \delta_{xH(b)y/zH(c)y} + n_C \delta_{zH(b)x/yH(c)x}, \quad (\text{A7-1})$$

$$\delta_{H(b)} = n_A \delta_{zH(c)x/yH(a)x} + n_B \delta_{yH(c)z/xH(a)z} + n_C \delta_{xH(c)y/zH(a)y}, \quad (\text{A7-2})$$

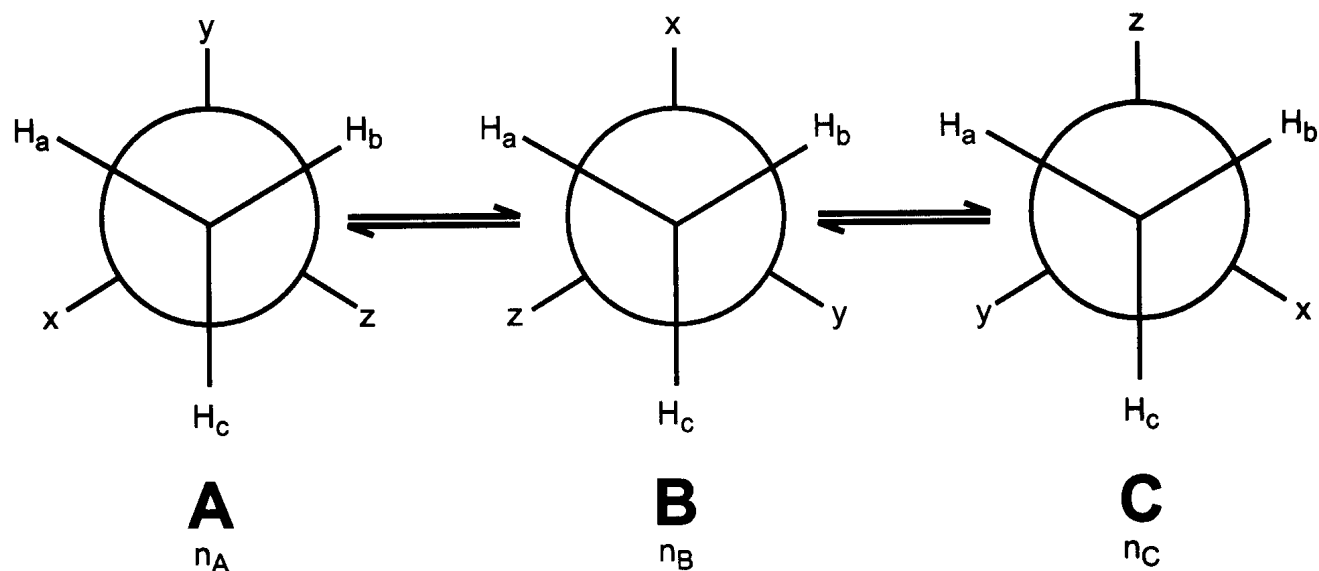


Figure A7-1 Homotopic ligands (H_a , H_b , H_c).

and

$$\delta_{H(c)} = n_A \delta_{xH(a)y/zH(b)y} + n_B \delta_{zH(a)x/yH(b)x} + n_C \delta_{yH(a)z/xH(b)z}. \quad (\text{A7-3})$$

For chemical-shift purposes, H_a , H_b , and H_c are, of course, indistinguishable, and $n_A = n_B = n_C = \frac{1}{3}$. The average chemical shifts of the methyl protons can be rewritten as

$$\delta_{H(a)} = \frac{1}{3} \delta_{yHz/xHz} + \frac{1}{3} \delta_{xHy/zHy} + \frac{1}{3} \delta_{zHx/yHx}, \quad (\text{A7-4})$$

$$\delta_{H(b)} = \frac{1}{3} \delta_{zHx/yHx} + \frac{1}{3} \delta_{yHz/xHz} + \frac{1}{3} \delta_{xHy/zHy}, \quad (\text{A7-5})$$

and

$$\delta_{H(c)} = \frac{1}{3} \delta_{xHy/zHy} + \frac{1}{3} \delta_{zHx/yHx} + \frac{1}{3} \delta_{yHz/xHz}, \quad (\text{A7-6})$$

and the average chemical shifts of H_a , H_b , and H_c can be expressed identically as

$$\delta_{H(a)} = \delta_{H(b)} = \delta_{H(c)} = \frac{1}{3} \delta_{yHz/xHz} + \frac{1}{3} \delta_{xHy/zHy} + \frac{1}{3} \delta_{zHx/yHx}. \quad (\text{A7-7})$$

We can see from eq. A7-7 that each methyl proton has the same three contributions to its overall chemical shift, and thus the three protons have *potentially* identical chemical shifts. If rotation about the $H_aH_bH_cC-Cxyz$ carbon-carbon bond were very slow, three equal-intensity, methyl proton signals would be observed. Since only one methyl proton NMR signal is actually detected, rotation about the subject carbon-carbon bond must be sufficiently rapid to average the three chemical-shift contributions (Section 4-2). On the time average, the methyl protons are, therefore, isochronous. It is important to recognize, however, that the signal of, for instance, H_a is able to be averaged with those of H_b and H_c only because the summed chemical-shift contributions of all three protons in the three equally populated conformers are identical. The three signals are, in fact, averaged because, in addition, the rotational speed about the carbon-carbon bond of $H_aH_bH_cC-Cxyz$ is very fast relative to the time scale of the NMR experiment.

Methyl protons also are known to be magnetically equivalent, which can be demonstrated, to an approximation, by first substituting H_1 and H_2 for substituents y and z in Figure A7-1 to produce Figure A7-2 and then determining whether couplings between

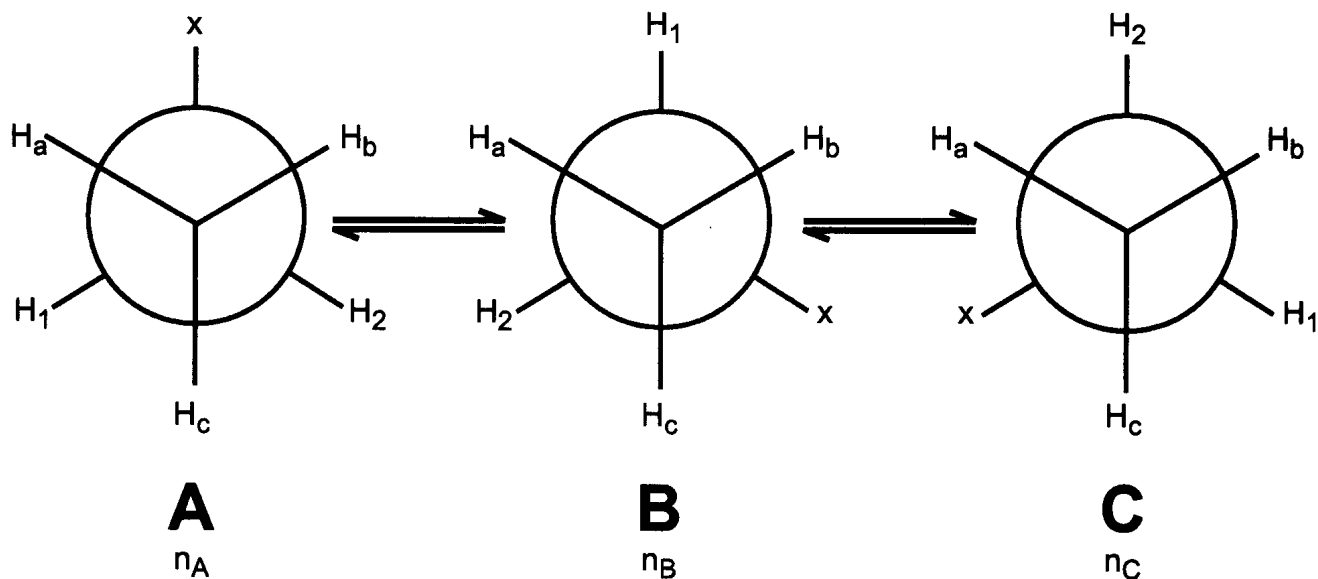


Figure A7-2 Coupling of homotopic ligands (H_a , H_b , H_c) with H_1 and H_2 .

H_a , H_b , and H_c , on the one hand, and H_1 and H_2 , on the other, are gauche or anti. The coupling constants between, for example, H_a and H_1 are gauche in conformers **A** and **B**, while that in **C** is anti. Examination of the three rotamers in Figure A7-2 shows that the average coupling constants between H_a , H_b , H_c and H_1 , H_2 are given by the following relationships:

$$J_{H(a)H(1)} = n_A J_{\text{gauche}} + n_B J_{\text{gauche}} + n_C J_{\text{anti}} = \frac{1}{3} J_{\text{anti}} + \frac{2}{3} J_{\text{gauche}} \quad (\text{A7-8})$$

$$J_{H(b)H(1)} = n_A J_{\text{anti}} + n_B J_{\text{gauche}} + n_C J_{\text{gauche}} = \frac{1}{3} J_{\text{anti}} + \frac{2}{3} J_{\text{gauche}} \quad (\text{A7-9})$$

$$J_{H(c)H(1)} = n_A J_{\text{gauche}} + n_B J_{\text{anti}} + n_C J_{\text{gauche}} = \frac{1}{3} J_{\text{anti}} + \frac{2}{3} J_{\text{gauche}} \quad (\text{A7-10})$$

$$J_{H(a)H(2)} = n_A J_{\text{anti}} + n_B J_{\text{gauche}} + n_C J_{\text{gauche}} = \frac{1}{3} J_{\text{anti}} + \frac{2}{3} J_{\text{gauche}} \quad (\text{A7-11})$$

$$J_{H(b)H(2)} = n_A J_{\text{gauche}} + n_B J_{\text{anti}} + n_C J_{\text{gauche}} = \frac{1}{3} J_{\text{anti}} + \frac{2}{3} J_{\text{gauche}} \quad (\text{A7-12})$$

$$J_{H(c)H(2)} = n_A J_{\text{gauche}} + n_B J_{\text{gauche}} + n_C J_{\text{anti}} = \frac{1}{3} J_{\text{anti}} + \frac{2}{3} J_{\text{gauche}} \quad (\text{A7-13})$$

If the various gauche couplings are essentially identical, and likewise for the different anti couplings, then we can easily determine, from these equations, that each of H_a , H_b , and H_c has the same *averaged* coupling constant to both H_1 and H_2 . By definition, the three protons are then magnetically equivalent. The same arguments that were invoked for the averaging of chemical-shift contributions into one detected signal are, similarly, employed here for the averaging of spin-coupling contributions into a single, observed coupling constant.

A7-2 Enantiotopic Groups

Let us next consider the methylene protons of the molecule $H_a H_b Y C - C R_1 R_2 X$, shown in Figure A7-3, and focus primarily on the prochiral group comprising H_a and H_b . If $R_1 = R_2$, these two protons are chemically equivalent and enantiotopic by virtue of a σ

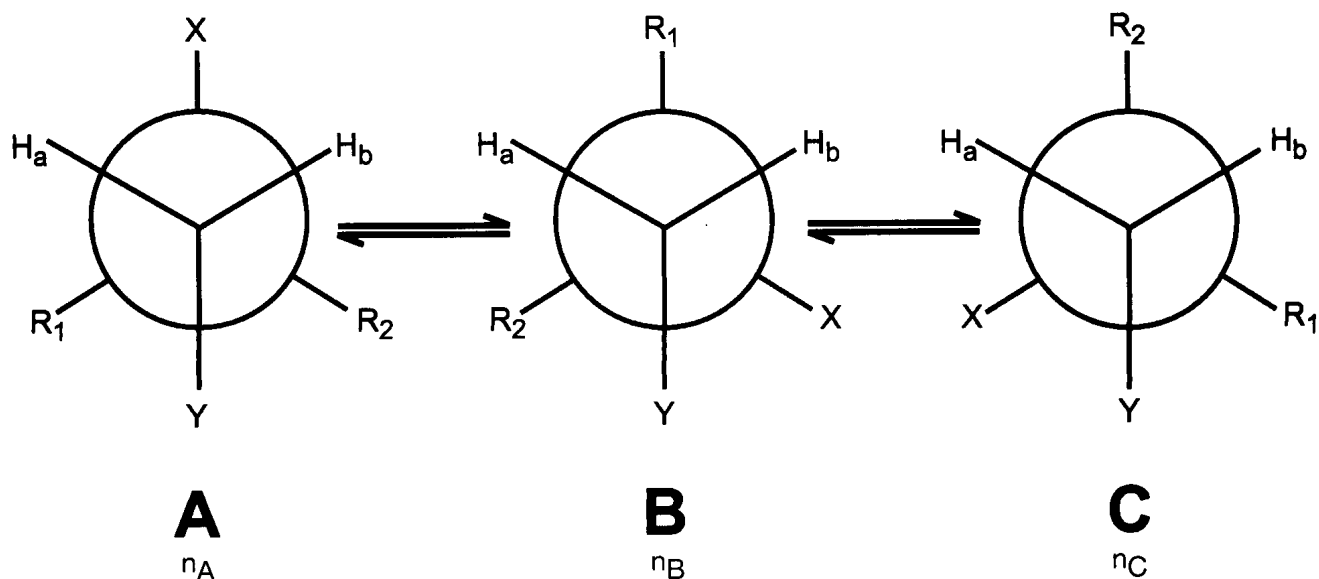


Figure A7-3 Enantiotopic ligands (H_a , H_b).

plane that bisects the X and Y groups in conformer **A**. They also are isochronous in achiral and racemic media. The more limited isochrony of H_a and H_b (when, of course, $R_1 = R_2$) can be established in the following way.

The same considerations and assumptions concerning three primary conformations, the insignificance of other conformers, and the geometric effects of neighboring groups on chemical shifts that were applied in Section A7-1 are now employed for the rotamers of Figure A7-3. With identical neighboring-group clockwise–counterclockwise substituent notation as before, the average chemical shifts of H_a and H_b are, respectively, given by

$$\delta_{H(a)} = n_A \delta_{XH(b)R(2)/R(1)YR(2)} + n_B \delta_{R(1)H(b)X/R(2)YX} + n_C \delta_{R(2)H(b)R(1)/XYR(1)} \quad (\text{A7-14})$$

and

$$\delta_{H(b)} = n_A \delta_{R(2)YR(1)/XH(a)R(1)} + n_B \delta_{XYR(2)/R(1)H(a)R(2)} + n_C \delta_{R(1)YX/R(2)H(a)X} \quad (\text{A7-15})$$

Again, for chemical-shift purposes, both R_1 and R_2 and H_a and H_b are indistinguishable when C–C rotation is fast. While $n_B = n_C$, n_A may not, however, be equal to these two mole fractions. The chemical shifts of H_a and H_b then can be rewritten, respectively, as

$$\delta_{H(a)} = n_A \delta_{XHR/RYR} + n_B \delta_{RHX/R YX} + n_C \delta_{RHR/XYR} \quad (\text{A7-16})$$

and

$$\delta_{H(b)} = n_A \delta_{RYR/XHR} + n_B \delta_{XYR/RHR} + n_C \delta_{RYX/RHX} \quad (\text{A7-17})$$

Since $\delta_{XHR/RYR} = \delta_{RYR/XHR}$, $\delta_{RHX/R YX} = \delta_{RYX/RHX}$, and $\delta_{RHR/XYR} = \delta_{XYR/RHR}$, the chemical shifts of H_a and H_b can be further expressed as

$$\delta_{H(a)} = \delta_{H(b)} = n_A \delta_{XHR/RYR} + n_B \delta_{RHX/R YX} + n_C \delta_{RHR/XYR} \quad (\text{A7-18})$$

We can see that each of H_a and H_b has the same three contributions to its overall chemical shift, and therefore, both protons have potentially identical chemical shifts. The same argument of very slow rotation, which was made for the *possible* observation of separate methyl proton signals, also applies to H_a and H_b (and R_1 and R_2). As we saw for the methyl protons, rapid rotation about the carbon–carbon bond of $H_a H_b YC-CR_1 R_2 X$ averages the three chemical-shift contributions, and the H_a/H_b (and R_1/R_2) pair is isochronous in achiral and racemic media. If groups X and Y, however, are very large, and bond rotation commensurately is slow, separate signals could, in principle, be detected.

If $R_1 = R_2 = H$, the appearance of H_a , H_b , H_1 , and H_2 depends upon (i) the relative populations of the three conformers (n_A , n_B , and n_C), (ii) the four coupling constants [$J_{H(a)H(1)}$, $J_{H(a)H(2)}$, $J_{H(b)H(1)}$, and $J_{H(b)H(2)}$], and (iii) the rate of rotation about the carbon–carbon bond of $H_a H_b YC-CH_1 H_2 X$. Since the bond rotational speed is almost always sufficiently rapid to average chemical-shift contributions (see earlier), the third criterion is not considered further with respect to the averaging of coupling-constant contributions.

The mole fractions of conformers **A**, **B**, and **C** and the aforesaid four coupling constants dictate whether H_a and H_b (and H_1 and H_2) are magnetically equivalent or nonequivalent. Overall couplings can be determined by a *gauche*–*anti* coupling-constant analysis similar to that carried out previously for the methyl protons. Examination of the three rotamers in Figure A7-3 (where $n_B = n_C$) shows that the average coupling constants between H_a , H_b , H_1 , and H_2 are given by

$$J_{H(a)H(1)} = n_A J_{gauche} + n_B J_{gauche} + n_C J_{anti}, \quad (\text{A7-19})$$

$$J_{H(b)H(1)} = n_A J_{anti} + n_B J_{gauche} + n_C J_{gauche}, \quad (\text{A7-20})$$

$$J_{H(a)H(2)} = n_A J_{anti} + n_B J_{gauche} + n_C J_{gauche}, \quad (\text{A7-21})$$

and

$$J_{H(b)H(2)} = n_A J_{\text{gauche}} + n_B J_{\text{anti}} + n_C J_{\text{gauche}}. \quad (\text{A7-22})$$

If $n_A = n_B = n_C$ and both the various gauche and the various anti couplings are essentially identical, then, from eqs. A7-19 through A7-22, H_a has the same coupling constants to H_1 and H_2 as has H_b . By definition, H_a is magnetically equivalent to H_b and H_1 is magnetically equivalent to H_2 , so they constitute an A_2B_2 or A_2X_2 spin system and appear as two triplets (excluding any coupling they might have to other nuclei). If anti and gauche couplings of approximately 13 and 4 Hz, respectively, are substituted into eqs. A7-19 through A7-22 (and for equally populated rotamers), an average of 7 Hz is obtained for each of the four coupling constants. This value is in good agreement with those typically observed for ethylene fragments. Such behavior is common for $H_aH_bYC-CH_1H_2X$ systems in which the X and Y groups are relatively small.

By contrast, if the X and Y groups are moderate in size, the population of conformer **A** can increase relative to the populations of **B** and **C**, where $n_A > n_B = n_C$. In this situation, $J_{H(a)H(2)} > J_{H(a)H(1)}$ and $J_{H(b)H(1)} > J_{H(b)H(2)}$. Due to the coupling-constant inequalities, both H_a and H_b and also H_1 and H_2 are magnetically nonequivalent, by definition, and constitute an $AA'BB'$ or $AA'XX'$ spin system. One such example is given in Figure 4-4. The spectral appearance of such systems depends not only on the relative conformer populations and coupling constants, but also on the chemical-shift separation between the AA' and BB' protons.

A7-3 Diastereotopic Groups

Finally, let us consider a compound of the type $CaabCxyz$, in which the "a" ligands are methylene protons. The molecule, which is shown in Figure A7-4, can be rewritten as $H_aH_bmC-Cxyz$. H_a and H_b constitute a prochiral group and cannot be interchanged by any type of symmetry operation, due to the presence of the $Cxyz$ chiral center. Gutowsky (1962) elegantly demonstrated that, in compounds of this type, the H_a and H_b ligands are inherently anisochronous. Moreover, as pointed out by Eliel and Wilen (1994), this intrinsic anisochrony is independent of the rate of rotation of the prochiral groups about the $H_aH_bmC-Cxyz$ carbon-carbon bond. The fundamental anisochrony of these diastereotopic groups can be developed in the following manner.

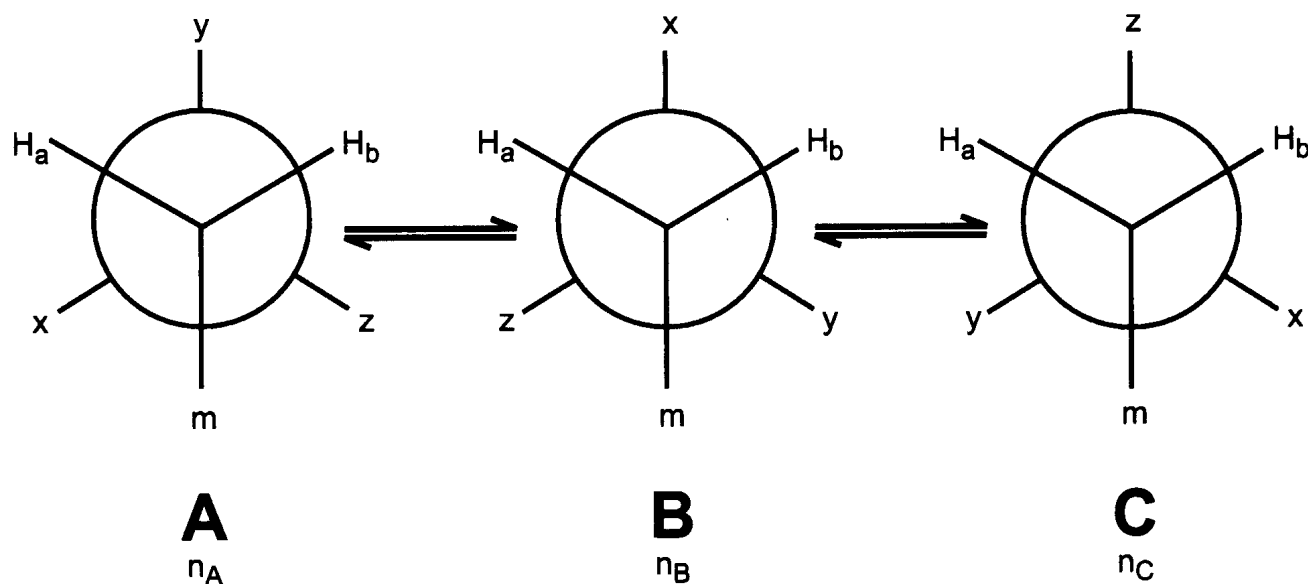


Figure A7-4 Diastereotopic ligands (H_a , H_b).

Once more, the same considerations and assumptions concerning three primary conformations, the insignificance of other conformers, and the geometric effects of neighboring groups on chemical shifts that were applied in Sections A7-1 and A7-2 are employed for the rotamers of Figure A7-4. The average chemical shifts of H_a and H_b are given by

$$\delta_{H(a)} = n_A \delta_{yH(b)z/xmz} + n_B \delta_{xH(b)y/zmy} + n_C \delta_{zH(b)x/ymx} \quad (\text{A7-23})$$

and

$$\delta_{H(b)} = n_A \delta_{zmx/yH(a)x} + n_B \delta_{ymz/xH(a)z} + n_C \delta_{xmy/zH(a)y} \quad (\text{A7-24})$$

Again, for chemical-shift purposes, H_a and H_b should have the same influence, and the chemical shifts of H_a and H_b then can be rewritten as

$$\delta_{H(a)} = n_A \delta_{yHz/xmz} + n_B \delta_{xHy/zmy} + n_C \delta_{zHx/ymx} \quad (\text{A7-25})$$

and

$$\delta_{H(b)} = n_A \delta_{zmx/yHx} + n_B \delta_{ymz/xHz} + n_C \delta_{xmy/zHy} \quad (\text{A7-26})$$

We can see from these expressions that the chemical-shift terms (expressed in the $n\delta_{abc/xyz}$ format) of H_a and H_b are similar, but not *identical*, in appearance. For example, the x , m , and z groups are located in the α , β , and γ positions (with respect to H_a) in conformer **A**, but their relative positions are reversed with respect to H_b in this rotamer. Moreover, the three substituents are clustered in this manner only in conformer **A**.

H_a and H_b in this system are, therefore, chemically distinct and diastereotopic and would be expected to be anisochronous in either achiral or racemic media. Since they constitute an AB or AX system and are magnetically nonequivalent by the chemical-shift criterion, any considerations of magnetic equivalence by the coupling-constant criterion are not applicable.

In sum, homomorphic ligands (i.e., those which are identical when detached from the molecule) can be classified as homotopic (equivalent) or heterotopic (nonequivalent). The latter can be further distinguished as diastereotopic or enantiotopic. These divisions are shown in Figure A7-5, and the descriptions presented for the different types of ligands are collected in Table A7-1.

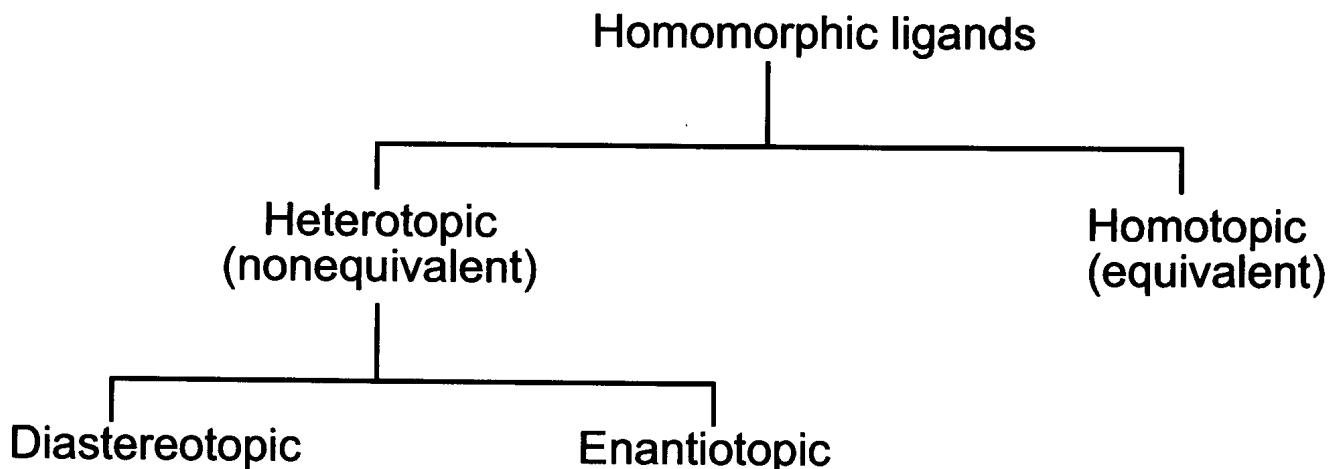


Figure A7-5 Classification of common ligands.

Table A7-1 Summary of Stereochemical Relationships

Topicity	Symmetry Type	Ligand Type	NMR Behavior
homotopic	rotation (C_n)	equivalent	isochronous
enantiotopic	plane/center	equivalent	isochronous in achiral or racemic media
diastereotopic	(none)	nonequivalent	potentially anisochronous in achiral or racemic media

Bibliography

A7.1. H. S. Gutowsky, *J. Chem. Phys.*, **37**, 2196 (1962).

A7.2. E. L. Eliel and S. H. Wilen, *Stereochemistry of Organic Compounds*. New York: Wiley-Interscience, 1994.

Index

- A_2 spectrum, 306–308, 310
 A_2B_2 spectrum, 339
 A_2X spectrum; *see* AX_2 spectrum
 A_2X_2 spectrum, 100, 116–117, 118, 339
 A_2X_3 spectrum, 16, 17, 103
AA'BB' spectrum, 101–102, 116–117, 136–137, 315–316, 339
AA'XX' spectrum, 100–102, 106, 115–117, 315–316, 339
AB spectrum, 98–99, 115, 144, 302–303, 308–314
 AB_2 spectrum, 115, 312–313
ABC spectrum, 111, 116, 314
Absolute-intensity representation, 59, 234
Absolute-value representation, 183, 244, 246, 250, 252
Absorption mode, 52–53, 183–185, 247, 300–301, 330; *see also* Real spectrum
ABX spectrum, 103, 105–106, 111, 116–117, 182, 313–314
Accordion excitation, 275; *see also* HMBC, 2J , 3J -HMBC modification
Acetaldehyde, ^{13}C chemical shift, 84, 88
 1H chemical shift, 71, 73
diethyl acetal, 103
HCC coupling, 108
Acetamide, 1H - ^{15}N coupling constant, 106
Acetic acid, ^{13}C chemical shift, 88
 1H chemical shift, 71, 75
Acetone, 12–13, 17, 26
 ^{13}C chemical shift, 84, 88
 1H chemical shift, 71
HCC coupling, 108
HCH coupling, 107
Acetonitrile, ^{13}C chemical shift, 86
 1H chemical shift, 71
 1H - ^{15}N coupling constant, 106
HCH coupling, 107
NH coupling, 167
solvent effect, 77–78
vicinal coupling, 111
Acetyl chloride, 1H chemical shift, 71
Acetylene; *see* Ethyne
Acid chlorides, ^{13}C chemical shifts, 88
Acquisition parameters, 1D, 39–48
2D, 241–243
Acquisition time, 1D, 42
2D, 242
Acrolein, dimethyl acetal, 194–195
Acrylonitrile, 1H spectrum 111
Active coupling, 182, 246, 254
Adiabatic relaxation, 320
Alcohols, ^{13}C chemical shifts, 84
 1H chemical shifts, 70, 75
Aldehydes, ^{13}C chemical shifts, 88
 1H chemical shifts, 73
shielding, 68
Aliasing, 40–41
folded signals, 41
noise, 46
see also Folding
Alkanes, ^{13}C chemical shifts, 82, 89
 1H chemical shifts, 69–71
 ^{13}C chemical shifts, 85–86, 90
 1H chemical shifts, 71–73
vicinal coupling, 111–112
Alkynes, ^{13}C chemical shifts, 86
 1H chemical shift, 71
Alkynic coupling, 113
Allene, long-range coupling, 113
Allenenes, ^{13}C chemical shifts, 81, 88
Allowed transitions, 304–307
Allylic coupling, 112–114, 282, 287–288
Alpha effect, on ^{13}C chemical shifts, 82–85
Amide bond rotation, 137
Amides, ^{13}C chemical shifts, 88
 1H chemical shifts, 70, 76
Amine inversion, 139–140
Amines, ^{13}C chemical shifts, 84
 1H chemical shifts, 70, 76
HCN coupling, 108
Ammonium ion, ^{14}N splitting, 136
 1H - ^{15}N coupling constant, 106
Ammonium salts, 1H chemical shifts, 70, 76
AMX spectrum, 103, 106, 111, 115, 182, 185–186
Angular frequency, 3
methyl group, 124
momentum, 1–2, 80–81, 296
Anhydrides, ^{13}C chemical shifts, 88
Aniline, ^{14}N line width, 167
Anilines, 1H chemical shifts, 76
Anisochronous, 334, 339–341
Anisole, 63, 74
Anisotropic rotation, 134–135
[16]Annulene, 65
[18]Annulene, 65
 γ -Anti effect, 83–84
Antiecho experiment, 331
Antiphase, 156, 158, 160, 163, 184, 187, 189
component, 325–331
Antisymmetric wave function, 310–312
Apodization, 50–51, 166, 244, 246, 248
APT; *see* Attached proton test
Aromatic solvent-induced shifts, 77–79
Aromatics, ^{13}C chemical shifts, 87, 90
 1H chemical shifts, 73–75
ortho coupling, 111
Artifacts, 2D, 196–197, 248, 250–252, 254, 259, 262, 268, 269
ASIS; *see* Aromatic solvent-induced shifts
Atomic inversion, 139–140
mass, 1–2
Attached proton test, 155, 161, 235–236
optimizing sensitivity, 235
Autogain feature, 45
Average energy of excitation, 80
AX spectrum, 13–14, 17, 98–99, 115, 148–149, 162, 174–175, 187, 303–304, 308, 310, 312
 AX_2 spectrum, 15, 17, 100, 115, 312–313
 AX_4 spectrum, 17
 AX_6 spectrum, 17
Axial peaks, 180; *see also* t_1 noise position, 66–67, 83–84, 110, 291–292
protons, relaxation, 134
Axial-equatorial interchange, 137
Aziridines, nitrogen inversion, 139
 B_0 (static magnetic field), 31, 36, 295
effects of inhomogeneity on spectra, 37–38
homogeneity; *see* Magnetic-field homogeneity
optimizing homogeneity, 37
 B_1 (radiofrequency magnetic field), calibration, 58–60
transmitter, 31–32
 B_2 (double resonance magnetic field), calibration, 60–61
decoupler, 32
Barbaralone, 141
Baseline correction, 54, 58
noise, 250
roll, 250
Benzaldehyde, ^{13}C chemical shift, 88
Benzene, ^{13}C chemical shift, 81, 86
 1H chemical shift, 64, 73
 1H spectrum, 4, 17
 1H - ^{13}C coupling constant, 105
long-range coupling, 113–114
shielding of, 64–65, 72
solvent effect, 77–78
Benzoquinones, 117
Benzylic coupling, 113–114
Beta effect on ^{13}C chemical shifts, 82–85
Biphenyl rotation, 138
BIRD, 189–192, 258–261, 265

- Bismethylene, 315–316
 Biuret, 136
 Bloch equations, 297–301, 322
 Bloch size, 45, 243; *see also* Interleaved acquisition
 Bloch-Siegert shift, 146
 Boltzmann population, 148, 151, 158
 Boltzmann's law, 3
 Bond anisotropy, 67, 71
 order, 81, 112
 shifts, 141–142
 Boron-11 couplings, 106
 Branching effect, 83–84
 Broadband decoupling, 35, 47, 146, 164, 204, 242
 Bromine relaxation, 320–321
 Bromochloromethane, 99–100
 Bromoethane, 99
 Brucine, ^1H spectrum, 204
 Buildup rate; *see* NOE
 Bullvalene, 141
 BURP, 166
 1,3-Butadiene, long-range coupling, 113–114
 1-Butene, ^{13}C chemical shift, 86
trans-2-Butene, ^1H chemical shift, 72
 ^{13}C chemical shift, 84, 86
 2-Butyne, long-range coupling, 113
 Butyroacetone, 101–102
- Calibrations, 58–61, 237
 decoupler pulses, 60–61
 pulse widths, 58–60
 Calicene, 138
 CAMELSPIN, 198
 Camphor, HMQC spectrum, 189–190
 Carbocations, shielding, 80
 Carbon disulfide, solvent effect, 77–78
 Carbon tetrachloride, ^{35}Cl line width, 136
 Carbon-13 couplings, 105–106, 108, 119, 121, 123, 162–163, 192–194, 199–200
 Carbonyl group, shielding, 67, 72, 80
 Carbonyl groups, ^{13}C chemical shifts, 88, 91
 Carboxylic acid, derivatives, ^{13}C chemical shifts, 88
 Carboxylic acids, ^1H chemical shifts, 68, 75
 Chair conformation, 110, 291
 Chemical equivalence, 99–103, 106, 117–118, 334–335, 337
 Chemical exchange, 136–143
 in 2D, 195–196, 198–199
 Chemical shielding anisotropy, 25
 relaxation, 132, 320
 Chemical shift, 5–8, 56, 62–88, 302–303
- Chemical-shift criterion, 102
 Chemical-shift difference, AB spectrum, 309
 1-Chloro-2-fluorobenzene, 69
 1-Chloro-4-nitrobenzene, ^1H spectrum, 13–14
 β -Chloroacrylic acid, 175–176
 COSY spectrum, 175
 4-Chlorobenzaldehyde, 74
 Chlorobenzene, relaxation time measurement, 133
 2-Chloroethanol, ^1H spectrum, 102, 316
 Chloroform, 14
 ^{13}C spectrum, 159–160
 ^1H chemical shift, 63
 INEPT spectrum, 159–160
 isotope effects, 79
 Cholestane, 215
 Cholesteryl acetate, ^{13}C spectrum, 155
 APT spectrum, 155
 Cleaning of NMR tubes, 33
 Closely coupled nuclei, 185–186; *see also* Second order effects
 Coalescence temperature, 142–143
 Coherence, 9, 326
 order, 204, 326–333
 selection, 165, 204
 Coherence-level diagram, 327–333
 COLOC, 192–193, 264–266
 Combination line, 115, 312
 Complete line shape analysis, 142–143
 Composite pulses, 148–165
 Conformation, 335–340
 anti, 335, 337–339
 gauche, 335, 337–339
 population effects, 335–336, 338–339
 Conjugated coupling, 113
 Conjugation; *see* Resonance effects
 Connectivity, 199, 203
 Contact shifts, 321
 Continuous-wave operation, 7, 31, 35
 Contour plot, 176, 250–251
 Cope rearrangement, 140–141
 COSY, 172–186, 196–198, 207, 208–212, 217, 219, 222–232, 252–253, 281–285, 328–332
 gradient version, 252; *see also* Long-range COSY, Phase-sensitive COSY
 COSY45, 181–182, 207, 211–212, 252–253
 Coupling, between equivalent nuclei, 98, 101, 107, 118–119
 Coupling constant, 13–19, 56, 98–130, 302–303, 305
 mechanism, 104–105
 relative signs, 105
- residual, 60–61
 sign, 104–105
 Coupling-constant criterion, 102, 122
 Cross peaks, 176, 330–333
 Cross polarization, 27, 185
 Cross sections, in spectral analysis, 250; *see also* Baseline noise, Contour plots
 Crotonaldehyde, ^1H chemical shift, 72
 Cubane, ^1H - ^{13}C coupling constant, 105
 CW; *see* Continuous wave
 Cyclobutane, ^{13}C chemical shift, 83
 ^1H chemical shift, 63, 69
 Cycloheptatriene, 124
 Cycloheptatrienylnit, 142–143
 1,3-Cyclohexadiene, HCCH coupling, 112
 ^1H chemical shifts, 72
 1,4-Cyclohexadiene, homoallylic coupling, 113
 Cyclohexane, 104
 ^{13}C chemical shift, 83
 dynamic ^1H spectrum, 24–25
 HCH coupling, 107
 isotope effects, 79
 ring reversal, 137
 Cyclohexane ring, shielding, 66
 Cyclohexanes, ^{13}C chemical shifts, 83–84, 89
 long-range coupling, 114
 vicinal couplings, 110
 Cyclohexanone, ^{13}C chemical shift, 88
 Cyclohexene, ^{13}C chemical shift, 86
 HCCH coupling, 112
 Cyclooctane, conformation, 139
 Cyclooctatetraene, bond shifts, 141–142
 ring reversal, 139
 Cyclooctatetreneiron tricarbonyl, 142
 1,3-Cyclopentadiene, ^1H chemical shifts, 72
 HCCH coupling, 112
 Cyclopentanol, ^{13}C chemical shift, 85–86
 Cyclopropane, ^{13}C chemical shift, 83
 ^1H chemical shift, 69
 ^1H - ^{13}C coupling constant, 105
 HCH coupling, 107
 shielding, 67
 Cyclopropanes, vicinal couplings, 110–111
 Cyclopropene, 100, 118–119
 HCCH coupling, 112
 CYCLOPS, 45, 165, 180
- DANTE, 166
 Data points, for 1D spectral description
 (np/2), 49–52
 number (np) for 1D spectral acquisition, 41, 49–51

- for first (ν_2) dimension spectral acquisition, 241, 247, 251
- for second (ν_1) dimension spectral acquisition, 247, 251
- Data-processing parameters, 243–250
- Data sets, imaginary, 247
 - real, 247
- DAVINS, 116, 314
- Decalins, 124
- Decane, carbon relaxation, 135
- 1-Decanol, 168
- Deceptive simplicity, 116–117, 315
- Decoupler, calibration, 60–61
 - field strength, 47, 60
 - modulation frequency, 58, 61
 - offset, 47
 - sample heating effects, 243, 258, 260
 - status, 47
- Decoupling, 18, 25, 46–47, 80, 105, 136, 144–146, 150, 152, 155, 158–160, 189; *see also* Homonuclear decoupling, Heteronuclear decoupling, and Double resonance
- Degassing, 34
- 1-Dehydrotestosterone, ^1H spectrum, 145
- Delay time, 132
- Dephasing, 203–204
- DEPT, 156–157, 161–162, 204, 207, 220, 221–222, 225–226, 229–231, 236–237, 280–282
- Depth gauge, 34
- Deuterated solvents, chemical shifts, 55
 - for locking, 33, 35
- Diamagnetic anisotropy, 64–69, 71–74, 81, 86
 - shielding, 62, 68, 80
 - susceptibility, 65–66
 - bulk, 77
- Diastereotopic groups, 103–104, 138, 140, 146, 179–180, 182, 189, 193, 261–262, 279, 334–335, 339–341
- 2,3-Dibromopropionic acid, COSY spectra, 181
- 1,2-Dichlorobenzene, ^1H spectrum, 101–102, 123
- cis*-1,2-Dichlorocyclopropane, 104
- Dichloroethene, HCC coupling, 108
- Dichlorophenols, ^1H spectra, 125–126
- Dielectric constant, 77–78
- Dienes, vicinal couplings, 112
- Diethyl ether, ^1H spectrum, 16
- Difference decoupling, 145
- Difference NOE, 151
- Difference spectra, 237; *see also* Subtraction experiments
- 1,1-Difluoroethene, 99–101, 109
- Difluoromethane, 99–100
- Digital resolution, in 1D spectra, 50–52, 180
 - in the first (ν_2) dimension in 2D spectra, 246–247
 - in the second (ν_1) dimension in 2D spectra, 246–247
 - optimizing, 247
- Digital signal filtration, 46
- Dihedral angle, 283, 285–286, 291, 293
- Dimensionless spin, 295, 298
- Dimethyl sulfoxide, nonexchanging solvent, 75
- 1,1-Dimethylallene, long-range coupling, 113
- N,N*-Dimethylformamide, 199
 - amide rotation, 137
 - solvent effects on, 70, 79
- 1,3-Dioxane, 123
- 1,4-Dioxane, isotope effects, 79
- Diphenylketimine, ^1H - ^{15}N coupling constant, 106
- Dipolar decoupling, 25, 27
- Dipole-dipole coupling, 25–26, 267
 - relaxation, 131–132, 150, 152, 195–196, 198, 205, 317–321, 331–332
- DIPSI-2, 256; *see* Isotropic mixing sequences
- Dirac notation, 303
- Direct coupling (*D*), 105
- Dispersion mode, 53, 183–184, 247, 300–301, 330; *see also* Imaginary spectrum
- Dispersive tails, in phase-sensitive COSY spectra, 252
 - with absolute-value data, 246; *see also* Line shape, phase-twisted
- Disulfides, hindered rotation, 138
- DNMR3, 142
- Double bond, shielding, 67–68
- Double irradiation, 26; *see also* Double resonance
- Double quantum coherence, 162–163, 165, 183, 189, 199, 204, 326–332
- Double quantum filtration, 183–185
- Double quantum transition, 304
- Double resonance, 18, 131, 136, 143–155, 160
- Doublet of doublets, 20
- DPFGSE, 205
- DPFGSE-NOE, 240, 268; *see also* Shaped pulses
- DQF-COSY, 183–184, 207, 214–216, 221, 246, 253–257, 332
- Dreiding model, 291
- Dummy scans; *see* Steady-state scans
- Dwell time, 40
- Dynamic effects, 23–25
 - NMR, 136–143
- EBURP, 166
- Echo experiment, 331
- Effective correlation time, 132, 135, 198, 317–319
 - nuclear charge, 106
 - spin-lattice relaxation time, 233
 - spin-spin relaxation time, 241, 248
- Electric-field effect, 77–79
 - shielding, 69
- Electromagnets, 31, 36–37
- Electron density, 80
 - spin relaxation, 321
- Electron spin resonance, 183
- Electronegativity, 6, 62–63, 81
 - and vicinal couplings, 111; *see also* Inductive effects
- Empirical correlations, for ^{13}C chemical shifts, 82–88, 92
 - for ^1H chemical shifts, 71–76, 91
- Enantiotopic groups, 99–100, 103, 279, 334–335, 337–341
- Energy-level diagram, 304–310
- Enol ethers, ^{13}C chemical shifts, 86
- Epoxides, vicinal coupling, 111
- Equatorial position, 66–67, 83–84, 110, 291–292
 - protons, relaxation, 134
- Ernst angle, 43
- Esters, ^{13}C chemical shifts, 88
 - ^1H chemical shifts, 70
- Ethane, ^{13}C chemical shift, 81–82
 - ^{13}C - ^{13}C coupling constant, 106
 - ^1H chemical shift, 63, 66, 69–70
 - HCC coupling, 108
- Ethanol, 68
- Ethene, ^{13}C chemical shift, 81
 - ^{13}C - ^{13}C coupling constant, 106
 - ^1H chemical shift, 63–64, 66, 71
 - ^1H - ^{13}C coupling constant, 105
 - HCC coupling, 108
 - HCH coupling, 107
- Ethers, ^{13}C chemical shifts, 84
 - ^1H chemical shifts, 70
- Ethyl *trans*-crotonate, 144
 - ^1H chemical shift, 63
 - ^1H spectrum, 19–20
- Ethylbenzene, 102–103
- Ethyne, ^{13}C chemical shift, 81
 - ^{13}C - ^{13}C coupling constant, 106
 - ^1H chemical shift, 63, 66, 71
 - ^1H - ^{13}C coupling constant, 105
 - HCC coupling, 108
- Evolution period, 173, 192
- EXAN II, 318

- Exchangeable protons, 75
Excitation sculpting, 205
Exponential weighting, 48–49
EXSY, 196, 198–199, 207, 232, 268–269, 331–332
 phase-sensitive, 199
Extreme narrowing condition, 318–321
 limit, 132, 149–151, 197
- False peaks, 180
Fast exchange, 23–24, 137, 143, 198
FDM; *see* Filter diagonalization method
Fermi contact mechanism, 104–105
F,F-COSY, 187
FID; *see* Free induction decay
Field sweep, 7
Filter bandwidth, 42, 57
Filter diagonalization method, 250
Filtering of sample solutions, 33–34
Filters, analog, 42, 46
 digital, 46
First-order spectra, 13, 56, 98–99, 101–102, 115, 123, 125, 145, 303–305
 pseudo, 56
Flip angle, 1D, 43–45
 2D, 242; *see also* Pulse width
Flip-flop mechanism, 134
FLOCK, 192–193, 264–266
 BIRD pulse functions, 265–266
Fluorine couplings, 109, 114–115, 119
3-Fluorocamphor, 211–212
Fluoromethane, 5
Fluxional molecules, 140–142
Folding, 180; *see also* Aliasing
Forbidden transitions, 304
Formaldehyde, HCH coupling, 107
Four-dimensional NMR, 203
Fourier analysis, 12
Fourier transformation, 13, 49, 172, 174, 183, 201, 330
 number, 50, 56
 spectrometer operation, 31–32
Free-induction decay, 11–13, 36, 172, 174, 187
Frequency domain, 13
FT; *see* Fourier transformation
Full width at half maximum, 52; *see also* Resolution
FWHM; *see* Full width at half maximum
- Gamma effect, on ^{13}C chemical shifts, 82–85
GARP, 258–259; *see also* Isotropic mixing sequences
Gated decoupling, 48, 151–152, 158
 γ -Gauche effect, 83
- Geminal coupling, 17, 105–109, 120, 123, 176, 182, 189, 207, 315
Gentamycin, DEPT spectra, 156–157
Glycine, 177–178, 180
Gradient coils, 39
 echo, 204–205
 pulse; *see* Pulsed field gradients, 203
Gyromagnetic ratio (γ), 2–4, 22, 106–107, 132, 146, 149–150, 153, 159, 193, 295, 319, 321
- Half-chair conformation, 291
Haloalkanes, ^{13}C chemical shifts, 80–81, 84–85
 ^1H chemical shifts, 62–63, 68, 71
 hindered rotation, 138
Halogenated alkanes, 138
Hamiltonian matrix, 304–305, 307–309
 operator, 302–304, 322–324
Hard pulses, 165
Hartmann-Hahn condition, 27, 185
Heavy atom effect, 81
Heisenberg uncertainty principle, 22
Heptamethylbenzenium ion, 198
HETCOR, 187–189, 193–195, 203, 207, 216–217, 220, 222–232, 261–262
Heterocycles, ring reversal, 139
Heteronuclear correlation, 187–195
 decoupling, 146–148, 151, 164–165
 multiple quantum coherence, 161
Heterotopic groups, 340
Hindered rotation, 137–139
HMBC, 193–194, 207, 262–264, 284
 2J , 3J -HMBC modification, 274–276
 gradient version, 263–264
 nongradient version, 263–264
HMQC, 189–190, 193, 201–202, 204, 207, 258–259
 gradient version, 258
HOHAHA, 185, 198
Homoallylic coupling, 113, 282, 287
Homogeneity; *see* Magnetic-field homogeneity
Homomorphic groups, 340
Homonuclear decoupling, 146, 151
Homotopic groups, 99–100, 335–337
3,4-Homotropilidine, 140
HSQC, 192–193, 258–261, 281–282
 gradient version, 259–261
 multiplicity-edited, 271–273
HSQC-TOCSY, 266–267
Hybridization, 63, 66–68
 and coupling, 105–106
Hydride shifts, 141
Hydrogen bonding, 78
Hydrogen-bonding effects, on ^1H chemical shift, 68, 75
- 3-Hydroxybutyric acid, 12–13
 ^{13}C spectrum, 18, 146
Hydroxyl protons, 75
 resonance, 23
11 β -Hydroxyprogesterone, NOE, 205–206
Hypercomplex Fourier transform, 241
Hyperconjugation, 107, 113
- Imaginary part, 49, 183, 299–300
 spectrum, 50; *see also* Dispersion mode
Imines, HCN coupling, 108
INADEQUATE, 106, 162–163, 165, 183, 189, 204
 2D, 199–200, 207, 213, 232, 332–333
Increments; *see* Time increments
Indene, allylic coupling, 113
Inductive effect, 63, 68–70, 72–74, 80, 84–85, 112, 182, 193; *see also* Electronegativity
INEPT, 156–162, 187, 192, 325
INEPT-INADEQUATE, 200, 207
Inhomogeneity effects, 37–38
Integration, 19, 21, 57–58
Interleaved acquisition, 237, 243; *see also* Block size
Inverse detection, 189–190
Inverse-gated decoupling, 48
Inversion recovery, 133, 135, 163–165, 168, 234, 327–328
Isobutane, ^{13}C chemical shifts, 83
Isobutylene, ^{13}C chemical shift, 86
 ^1H chemical shift, 71
Isochronous, 102, 334–336, 338
Isomontanolide, 213
Isonitrile, 167
Isopropyl group, 17, 103
Isotope effects, on chemical shifts, 79, 118
Isotropic groups, 63–64
Isotropic mixing sequences, DIPSI-2, 256
 GARP, 258–259
 MLEV-17, 256
 WALTZ-16, 256, 258, 262, 266
 WURST, 258–259
- J -filter, in HMBC experiment, 262
 J -resolved spectroscopy, 186–187, 207
Jeener experiment, 172, 176
- Karplus equation, 76, 109–112, 193, 285, 324
Ketones, ^{13}C chemical shifts, 88
- Laboratory time scale, 136
Lactones, ^{13}C chemical shifts, 88

- Lanthanide shift reagents, 116
 LAOCN3, 116, 314
 Larmor frequency, 3–4, 8–10, 12, 131, 143, 148, 162, 187, 190, 203, 296, 317–318, 321, 323–324, 328, 333
 Leucine, 177–180
 Line broadening, 48, 238, 240
 functions, 48–49
 parameter, 58–61
 Line shape, 36
 absorption mode, 52
 phase-twisted, 246, 252
 Line width, 10, 12, 302
 at half-height; *see* Full width at half maximum
 Linear prediction, 247–250
 backward, 250
 extensions, 248, 251, 258, 260
 Liquid crystal solvent, 105
 Local electron currents, 62–63
 Lock, external, 35
 internal, 35
 optimizing, 36
 phase, 35–36
 receiver, 35
 saturation, 35, 37, 237–238
 signal, 33, 35–36
 transmitter, 35
 Locking, automatic, 35
 field/frequency, 35–36
 Lone pair, shielding, 63–68
 Long-range COSY, 182–183, 207, 253
 coupling, 105, 112–115, 124, 177, 182–183, 192–193, 207
 Longitudinal relaxation; *see* Spin-lattice relaxation
 Lowering operator, 306
 Lutidines, ¹H spectra, 124–125
 Lysine, 184–185
 Magic angle, 65
 Magic-angle spinning, 26, 32
 Magnetic equivalence, 99–104, 106, 115, 117, 122, 334, 336–339
 moment, 1, 3, 5, 14, 131, 144, 295, 298, 302, 321
 resonance imaging, 203
 Magnetic-field homogeneity, 36, 52
 optimizing, 37
 Magnetization, 8–12, 131, 134, 158–159, 161, 163, 172–173, 175, 180, 184–185, 187, 189–190, 192, 195–197, 203–204, 297–301, 322–331
 transfer, 143, 146, 175–176, 181–183, 185, 187, 196–199; *see also* Saturation transfer
 Magnetogyric ratio, 2; *see also* Gyromagnetic ratio
 Magnets, permanent, 31
 superconducting, 31, 36–37
 Magnitude spectrum, 183
 Mannosan triacetate, ¹H spectrum, 145
 Matching; *see* Probes, adjustment
 McConnell equation, 65–67
 Medium, achiral, 334, 338, 340
 effects, 75–79, 214
 racemic, 334, 338, 340
 Menthol, 2D INADEQUATE spectrum, 199–200
 Methane, ¹³C chemical shift, 82
¹H chemical shift, 69
¹H-¹³C coupling constant, 105
 HCH coupling, 107
 solvent effects on, 78
 Methanol, ¹H chemical shift, 70
¹H spectrum, 23
 HCH coupling, 107
 hydroxyl exchange, 137
 Methano[10]annulene, 65
 Methaqualone, 218–219
 Methine shielding, 67, 70
 Methyl acetate, 5–7, 12–13, 18
 acetate, ¹H spectrum, 6
 shielding, 67, 70
 2-Methylacryloin, allylic coupling, 113
 Methylamine, ¹H chemical shift, 70
 3-Methylcyclopropene, 100
 Methylene shielding, 67, 70
 β-Methylglutaric acid, 117
 N-Methylpiperidine, 67
 Mixing period, 196–199, 204, 257, 267–270, 331
 MLEV-16, 148
 MLEV-17, 256; *see also* Isotropic mixing sequences
 Multiple quantum coherence, 161–162, 184, 189–190, 204
 filtration, 183–184
 Multiple resonance, 143–148
 Naphthalene, ¹³C chemical shift, 92
 HCCH coupling, 112
 Natural abundance, 21–22
 sensitivity, 21–22
 Negative absorption, 301
 dispersion, 301
 Neopentane, ¹³C chemical shift, 83
 Newman projections, 335
 Nitriles, ¹³C chemical shifts, 86
 Nitrobenzene, ¹³C chemical shift, 87
¹H chemical shift, 73–74
 Nitrogen inversion, 139–140
 Nitrogen-14 line widths, 136
 Nitrogen-15 couplings, 106, 108, 119, 121
 Nitromethane, ¹⁴N line width, 167
¹H chemical shift, 71
 NOE; *see* Nuclear Overhauser effect
 NOESY, 196–199, 201–203, 207, 215–216, 220, 268–269, 290–293, 331–332
 COSY and EXSY cross peak discrimination, 268
 mixing and repetition time considerations, 268
 phase-sensitive, 197, 268
 signal cancelation from COSY and EXSY artifacts, 268
 NOESY-HMQC, 202
 NOESY-TOCSY, 202
 Noise, 45
 aliased, 46
 decoupling, 47, 146
 digitization, 46; *see also* Digital signal filtration
 filtering, 42
 thermal, 45–46
 Nonlocal electron currents, 62–68
 Nonselective irradiation, 146
 Norbornanes, long-range coupling, 114
 Norbornene, ¹H chemical shifts, 67–68, 72
 Norbornyl cation, 141
 Normality, 303
 Nuclear Overhauser effect, 47–48, 57, 148–153, 192, 195–198, 209, 237–240, 321, 331
 buildup rate 196–197, 203
 difference, 205
 double pulsed field gradient spin echo-NOE experiment, 240
 NOE difference, 238–240
 PFG, 203–205
 steady-state, 237
 Number of data points; *see* Data points
 Nyquist condition, 40, 46
 Oblate ellipsoid, 64
 Observe pulse time; *see* Pulse width
 Off-diagonal peaks, 175–176
 Off-resonance decoupling, 146–147, 153
 in decoupler calibration, 60
 One-bond coupling, 104–106, 119, 123, 162–163, 190, 192–193
 One-dimensional NMR experiments, 35–36, 46–48, 52, 233–240
 Optically active solvent, 100

- Ortho coupling, 111–112
 Orthogonality, 303
 Overhauser enhancement factors, 149–150
 Oversampling, 46
 Oximes, ^{13}C chemical shifts, 88
- Parallel transition, 175–176, 181, 183
 Paramagnetic impurities, 321
 relaxation, 132, 153
 shielding, 80–82, 86, 118
 shift reagents, 118
 substances, 233
 Partial relaxation, 204
 Partially relaxed spectra, 135
 Pascal's triangle, 16–17, 98
 Passive coupling, 182, 254
 Pauli exclusion principle, 104
 Peak suppression, 135, 144, 146
 Penicillin, 152
 Pentane, ^{13}C chemical shifts, 83
 Perfluorocyclohexane, 69
 Permanent magnets; *see* Magnets
 PFG; *see* Pulsed field gradient
 Phase correction, 52–54
 first-order in 1D, 53–54, 57
 in 2D, 250
 zero-order in 1D, 53
 in 2D, 250
 Phase cycling, 45, 148, 162–165, 180, 184, 197, 204, 331–332
 number of scans to accommodate, 243
 Phase errors, correction, 52–54
 distorted signals, 41
 first-order, 53
 zero-order, 53
 Phase quadrants, 183–184
 Phase-sensitive COSY, 183–184, 252, 331
 dispersive tail problem, 252
 detectors, 41
 representation, 241, 244, 246–247, 250
 Phasing, 183, 185
 Phenanthro[3,4-b]thiophene, 212
 Phenols, ^1H chemical shifts, 75
 Phosphorus inversion, 140
 Phosphorus-31 couplings, 106, 109, 119
 Piperidine, INADEQUATE spectrum, 163
 Polarization transfer, 158, 187, 236, 261, 265
 Pople notation, 98, 100
 Population inversion, 11
 transfer; *see* Magnetization transfer
 Positive absorption, 301
 dispersion, 301
 Power-gated decoupling, 151
 P,P-COSY, 187
 Precession, 3, 11–12
- Probes, 32
 adjustment, 34–35
 Prochiral groups, 334, 337, 339
 Product-operator formalism, 322–323
 Progesterone, ^1H spectrum, 151
 Progressive transition, 175, 183
 Prolate ellipsoid, 64, 66
 Proline, 177–180
 Propyne, long-range coupling, 113
 Pseudoaxial position, 291
 Pseudoequatorial position, 291–292
 Pulse, read, 242
 ringdown, 250
 imperfections, 163–165
 width, 47
 calibration, 58–60
see also Flip angle
 Pulsed experiments, 11–13
 Pulsed field gradients, 189, 194, 200, 203–206, 232, 240, 332
 in 2D, 251–252
 Pulses, 90° , 43
 observation, 47, 52
 Pyramidal inversion, 139–140
 Pyridine, ^{13}C chemical shift, 87
 ^{13}C spectrum, 159
 ^1H chemical shift, 74
 ^1H - ^{15}N coupling constant, 106
 INEPT spectrum, 158–159
 Pyrimidine, 219
 Pyrrole, ^{13}C chemical shift, 87
 ^{14}N line width, 167
 ^1H chemical shift, 74
 ^1H spectrum, 136–137
- Quad images, 165, 180
 Quadrature detection, 165, 324–327
 phase detection, 41, 43, 45
 Quadricyclane, ^1H - ^{13}C coupling constant, 105
 Quadrupolar broadening, 178
 nuclei, 2, 4, 13, 22, 25–26, 76
 relaxation, 22, 76, 132, 135–136, 320–321
 Quadrupole moment, 22, 136
 Quaternary carbon, relaxation, 132, 152
 Quaternary carbons, in HETCOR, 188
 Quinoline, long-range coupling, 114
 NCC coupling, 109
 β -Quinolmethanol clathrate, 26
- R* value, 111
 Radial term, 80–81, 84, 86
 Raising operator, 306, 310–311
 Ramsay's equation, 80, 91
 Reaction rates, 136–143
 Read pulse, 242
- Real part, 49, 183, 299–300
 spectrum, 50; *see also* Absorption mode
 REBURP, 166
 Receiver, 35, 43, 45
 coils, 32, 34
 dead time, 57
 gain in 1D, 45–46
 gain in 2D, 243
 overload, 45
 phase, 41
 Receptivity, 21–22
 Reference, ^{13}C sensitivity standard, 60
 internal, 55–56
 primary, 55
 secondary, 55–56
 substances, 21–22
 Referencing; *see* Zero referencing
 Refocused INEPT, 159–160
 Regressive transition, 175, 183
 Relative signs, of coupling constant, 105, 314
 Relaxation, 10, 131–136
 delay time in 1D, 43–44, 47, 60
 delay time in 2D, 242–243, 251
 agents, 321
 time, 10, 12, 302
see also Spin-lattice relaxation and Spin-spin relaxation
 Relayed coherence transfer, 185, 194–195, 207
 Relayed COSY, 185–186
 Repetition time, 242–243, 268
 Resolution, 51–52
 digital, 50–52
 enhancement, 48–49
 spectral, 39, 44, 51
 Resonance effect, 63, 68, 72–74, 86–87, 112
 Ring currents, 64–66, 72–74
 Ring reversal, 24, 104, 110, 122–123, 167
 Rise time, 60
 ROESY, 197–199, 207, 269–270
 phase-sensitive, 198, 269
 spin-lock power and mixing time considerations, 269
 TOCSY and EXSY cross peak discrimination, 269
 Rotamers, 102–103, 338–340
see also Conformation
 Rotating coordinate system, 7, 11, 299, 324, 327
 frame, 7, 12, 197–198
 Rotational rates, effects on NMR spectra, 336, 338–339
- S/N ratio; *see* Signal-to-noise ratio
 Sample heating, in broadband decoupling, 242

- in HMQC, 258
- in HSQC, 260
- with high-dielectric solutions, 242
- Sample preparation, 33–34
 - size limitation, 32
 - solubility limitation, 32
- Sample spinning, 37
 - for resolution improvement, 36
 - not used in 2D, 251
 - shimming, 37, 39
 - sidebands, 37, 39
- Sample tubes, cleaning, 33
 - filling, 33
 - placement, 34
 - selection, 33
- Sampling rate, 39–40
- Satellite peaks, 18, 58, 118–119, 162–163, 189
- Saturation, 10, 35, 37
 - transfer, 143–144, 165; *see also* Magnetization transfer
- Scalar coupling; *see* Coupling constant relaxation, 132, 320
- Scan number, per time increment in 2D, 243
 - related to S/N improvement in 1D, 45
- Schrödinger equation, 302–303
- Second-order effects, 16, 98, 102, 116–118
 - spectra, 17, 56, 98–101, 115–116, 123, 186, 309–316
- Segmental motion, 135, 317
- Selection rule, 304, 306
- Selective decoupling, 175
- Selective excitation, 165
- Selective irradiation, 135, 146
- Sensitivity enhancement, by INEPT, 156–162
 - by NOE, 148–149, 152
 - Ernst-angle considerations, 43–44
 - oversampling, 46
- Shaped pulses, 166, 240, 270
- Shielding, 5, 25–26, 62
- Shim coils, 36
- Shimming, 36–39
 - automatic, 37
 - gradient, 39
- Shoolery's rule, 71, 91
- Sideband detection, 165
- Sigmatropic shifts, 142
- Signal averaging, 45
- Signal cancelation, in DEPT spectra, 237
 - in DQF-COSY spectra, 246
 - in multiplicity-edited HSQC spectra, 271–272
 - in NOESY spectra, 268
 - in ROESY spectra, 269
- phasing, 52–54, 58
- threshold level, 250, 279
- Signal-to-noise ratio, 57
 - improved by exponential weighting, 48
 - signal averaging, 45, 47
 - reduced by resolution enhancement, 49
- Single bonds, rotation about, 138–139
- Single quantum coherence, 161–163, 165, 183, 189–192, 194, 204, 326–327, 330–332
- Slow exchange, 23–24, 137, 142–143, 198
- Soft pulses, 166
- Solid-state NMR, 32, 35
- Solids, spectra of, 25–27
- Solvent anisotropy, 77–78
 - effects; *see* Medium effects
 - selection, 33
 - suppression, 135, 153, 204–205
- Solvent-solute interactions, 78
- Spectral analysis, 115–119, 153–156, 204
 - density, 317–319
 - editing experiments; *see* APT, DEPT subtraction, 46, 237
 - width, 1D, 41–42
 - 2D, 241–242
 - in calibration procedures, 58, 61
 - reduction in the first (ν_2) and second (ν_1) dimensions, 247
- Spectrometer components, 31–32
- Spin, 1, 21–22, 295
 - angular momentum, 295
 - decoupling; *see* Decoupling
 - diffusion, 134, 151–152, 197–198, 321
 - echo, 153, 159, 186, 204
- Spin locking, 27, 143, 185, 198, 243, 257, 266, 269, 319
 - in HSQC-TOCSY, 266
 - in TOCSY, 257
 - sample heating effects, 242
- Spin quantum number, 2
- Spin rotation relaxation, 132, 319
- Spin tickling, 144
- Spin wave function, 302–303
- Spin-diffusion limit, 321
- Spin-lattice relaxation, 10, 12, 27, 44, 131–136, 143, 152, 173, 192, 196, 233, 297, 317–321
 - time, measurement of, 133, 233–234, 321
- Spin-orbit coupling, 81, 84
- Spin-spin relaxation, 10, 12, 26, 51, 54, 134, 153, 174, 180, 192, 203, 297, 320
- Spin-spin splitting, 14; *see also* Coupling constant
- Spinner turbine, 34
- Spinning; *see* Sample spinning
 - sidebands, 37, 39
- Spiro[2.5]octane, 67
- Stacked plot, 175
- States method of signal detection, 241, 251; *see also* Quadrature phase detection
- Steady-state NOE, 237
- Steady-state scans, 1D, 46, 237–238, 240
 - 2D, 243, 251
 - in subtraction experiments, 237
- Stereochemical descriptors, α , 292–293
 - β , 292–293
- Stereochemistry, from NOE, 152
- Stereogenic center, 103
- Steric effects, 73–74, 76
- Stick diagrams, 20
- Styrene, ^1H chemical shifts, 72
- Subtraction artifacts, 205
- Subtraction experiments, DEPT, 236–237, 240
 - NOE difference, 238–240
 - optimizing results, 237–238
- Sucrose, ^1H spectrum, 205–206
- Sulfides, ^{13}C chemical shifts, 84
 - ^1H chemical shifts, 71
- Sulfonic acids, ^1H chemical shifts, 75
- Superconducting magnets; *see* Magnets
- Symmetric wave function, 306–308
- Symmetrization, 180, 250
- Symmetry, effect on spectra, 280
- T-ROESY, 198, 269
- t_1 noise, 180, 250, 254, 259–260, 263–264
- T_1 ; *see* Spin-lattice relaxation time
- T_2 ; *see* Spin-spin relaxation time
- T_2^* ; *see* Effective spin-spin relaxation time
- Temperature, performance of 2D experiments at constant, 251
 - performance of subtraction experiments at constant, 237–238
- Tesla, 2
- Tetramethylsilane, 6–7, 55
- Thiane 1-oxide, 123
- Three-dimensional NMR, 201–203
- Through space coupling, 114–115
- α -Thujene, 103
- Time domain, 13
- Time increments in the second (ν_1) dimension, with the States method, 241, 247, 251
 - with the TPPI method, 241
- Time scale, NMR, 136, 336

- Time-proportional phase incrementation, 241; *see also* Quadrature phase detection
- TMS; *see* Tetramethylsilane
- Tobey-Simon rule, 72–73
- TOCSY (1D), 270–272
(2D), 184–185, 198, 207, 256–257, 283
- TOCSY-HMQC, 202
- Toluene, ^{13}C chemical shift, 84, 87
 ^1H chemical shift, 71, 73
anisotropic rotation, 134–135
isotope effects, 79
- TPPI; *see* Time-proportional phase incrementation
- TQF-COSY, 185
- Transition energies, 304–305, 307–310
- Transition probability, 306–311
- Transmitter, 35, 58
coils, 32
frequency, 43
offset in 1D, 43
offset in 2D, 242
- Transverse relaxation; *see* Spin-spin relaxation
- 1,1,2-Trichloroethane, ^1H spectrum, 15
- Tricyclopentane, ^1H - ^{13}C coupling constant, 105
- Trifluoromethyl group, relaxation, 320
- Tripeptide, 177–180
- Triple quantum filtration, 185
resonance, 143
- Truncation, 50–51
artifacts, 50–51
of FID's, 50–51, 54, 244
suppression, 50–51
- Tubes; *see* Sample tubes
- Tumbling frequency, 317–318
- Tuning; *see* Probe adjustment
- Two-dimensional NMR experiments, 172–232, 240–251, 328–333
- Two-spin system, 13
- Uncertainty broadening, 135–136, 321
- α,β -Unsaturated ketones, ^{13}C chemical shifts, 86
- Valence tautomerization, 140–141
- van der Waals effect, 77–78
shielding, 68–69
- Vanillin, COLOC spectrum, 192
- Vicinal coupling, 17, 105, 109–112, 118, 120, 124, 176, 182, 189, 196, 207, 214, 315
- Vinyl acetate, ^{13}C spectrum, 146–147
- Vinyl group, 111
 ^1H chemical shift, 72
- Virtual coupling, 117–118
- Volume susceptibility, 77
- W coupling, 114, 253, 288; *see also* Zigzag coupling
- Wagner-Meerwein rearrangements, 141
- WALTZ, 47, 58, 256, 258, 262, 266;
see also Isotropic mixing sequences
- WALTZ-16, 148, 164–165
- Water suppression, 33
- WATERGATE, 204–206
- Weighting functions, 48–49, 244–246
exponential, 48, 50
Gaussian, 49
line broadening, 48–49
resolution enhancement, 48–49
sensitivity enhancement, 48, 51, 246
- WURST, 258–259; *see also* Isotropic mixing sequences
- X-ray crystallography, 1
- XCORFE experiment, 274
- Xylene, inversion recovery stack, 168
long-range coupling, 113
- Zeeman effect, 2, 296–297
- Zero filling, 49–50, 56, 58, 241, 243, 246–247, 249, 251
in the first (ν_2) and second (ν_1) dimensions, 241, 246–247, 251
use in conjunction with linear prediction, 249, 251
- Zero quantum coherence, 204, 326–327, 331–332
- Zero referencing, in 1D, 55–56
in 2D, 250
- Zigzag coupling, 114, 118, 145, 193; *see also* W coupling